AUSTRALIAN JOURNAL
OF PHYSICS

VOLUME 13

QC
1
A85
V.12
1959
Science
PER

Digitized by the Internet Archive
in 2024

https://archive.org/details/australian-journal-of-physics_1959_12

AUSTRALIAN JOURNAL OF PHYSICS

VOLUME 12

MELBOURNE
1959

AUSTRALIAN JOURNAL OF PHYSICS

Published by the Commonwealth Scientific and Industrial Research Organization. Volumes 1 to 5 of the Australian Journal of Physics and the Australian Journal of Chemistry issued as the Australian Journal of Scientific Research, Series A: Physical Sciences. Issued quarterly, £2 per annum.

BOARD OF STANDARDS

The Board of Standards for this Journal is appointed by the Commonwealth Scientific and Industrial Research Organization and the Australian Academy of Science and consists of Professor J. G. Wood (Chairman), Dr. N. S. Noble (Editor), Professor J. S. Anderson, Professor Sir Macfarlane Burnet, Professor Sir Leslie Martin, and Professor W. P. Rogers.

ADVISORY COMMITTEE

Acceptance of papers for this Journal is in the hands of an Advisory Committee appointed by the Board of Standards in consultation with the Institute of Physics (Australian Branch) and consisting of Dr. N. S. Noble (Chairman and Editor), Dr. G. H. Briggs, Professor L. G. H. Huxley, Professor Sir Leslie Martin, Dr. J. L. Pawsey, and Professor H. C. Webster.

◆

All enquiries and manuscripts should be forwarded to:

The Editor,
Australian Journal of Physics,
Commonwealth Scientific and Industrial Research Organization,
314 Albert Street, East Melbourne, C.2, Victoria

MELBOURNE

CONTENTS

Number 1, March 1959

PAGE

Zero-field Masers. By G. S. Bogle and H. F. Symmons 1

The Photoneutron Cross Section of ^{9}Be in the Intermediate Energy Range. By H. H. Thies, B. M. Spicer, and J. E. E. Baglin 21

Dirac Continuum Radial Wave Functions. By H. S. Perlman and B. A. Robson 30

The Effect of Sudden Ionospheric Disturbances (S.I.D.'s) on $2 \cdot 28$ Mc/s Pulse Reflections from the Lower Ionosphere. By F. F. Gardner.. 42

Theory of the Radio-echo Meteor Height Distribution in a Non-isothermal Atmosphere. By A. A. Weiss 54

Elevation, Height, and Electron Density of Echoing Points of Meteor Trails. By A. A. Weiss 65

The Detection of Time-correlated Photons by a Coincidence Counter. By R. Q. Twiss and A. G. Little 77

Short Communications

Irregular Coulomb Wave Functions. By A. Learner and B. A. Robson.. 94

Observations of Faculae bordering Small Sunspots near the Limb. By R. E. Loughhead and R. J. Bray 97

The Energy Spectrum of Protons from the $^7\text{Be}(d,p)^8\text{Be}$ Reaction. By R. H. Spear 99

The $^{58}\text{Ni}(n,p)^{58}\text{Co}$, $^{58}\text{Ni}(n,2n)^{57}\text{Ni}$, and $^{58}\text{Ni}(n,np)^{57}\text{Co}$ Cross Sections at $14 \cdot 1$ MeV. By K. H. Purser and E. W. Titterton 103

Electron Mobility in Liquid Argon. By F. D. Stacey 105

Number 2, June 1959

PAGE

The Microwave Spectra of Isotopic Molecules of Sulphur Dioxide. By W. E. Smith 109

The Temporal Variation of the Heights of Reflection Points of Meteor Trails. By A. A. Weiss 116

Neutral Hydrogen Gas in the Taurus-Orion Region observed with a Multichannel 21 cm Line Receiver. By R. X. McGee and J. D. Murray 127

Occultations of the Crab Nebula by the Solar Corona in June 1957 and 1958. By O. B. Slee 134

A Discussion of Ionospheric Demodulation near Gyro Frequency. By G. L. Goodwin 157

Radiative Transfer in Non-uniform Media. By R. G. Giovanelli .. 164

The Structure of a Stream of Electrons and Ions Drifting and Diffusing in a Gas when Ionization by Collision and Molecular Attachment are Present. By L. G. H. Huxley 171

The Shape of Spectral Lines: Tables of the Voigt Profile $(a/\pi)\int_{-\infty}^{\infty} e^{-y^2}dy/\{a^2+(v-y)^2\}$. By D. W. Posener 184

Short Communications

Photometric Observations of Subvisual Red Auroral Arcs at Middle Latitudes. By R. A. Duncan 197

Deviation from Matthiessen's Rule and Lattice Thermal Conductivity of Alloys. By P. G. Klemens 199

Number 3, September 1959

PAGE

The Use of Complete Temperature-Time Curves for Determination of Thermal Conductivity with particular Reference to Rocks. By J. C. Jaeger 203

The Optimum Line Width for the Transition used in a Reflection Cavity Maser Amplifier. By G. J. Troup 218

Seismic Recordings of Large Explosions in South-eastern Australia. By H. A. Doyle, I. B. Everingham, and T. K. Hogan 222

A Search for Levels of ^{7}Li between $9\cdot0$ and $9\cdot55$ MeV Excitation. By K. H. Purser 231

The Thermal Expansion of Solids. By G. C. Fletcher 237

Scattering of High Energy Polarized Nucleons by Complex Nuclei. By B. A. Robson 248

The Eta Carinae Nebula and Centaurus A near 1400 Mc/s. I. Observations. By J. V. Hindman and C. M. Wade 258

A 21 cm Survey of the Southern Milky Way. By F. J. Kerr, J. V. Hindman, and C. S. Gum 270

Short Communications

Spins and Parities of Levels of ^{9}Be below 15 MeV. By H. H. Thies and B. M. Spicer 293

Note on Band Transmission in Multilayer Dielectric Filters. By S. C. B. Gascoigne 296

Periodicities in Solar Radio Noise Emission. By N. C. Gerson 299

The Lorentz Transformations. By G. Builder 300

A New Method for Measuring the Attachment of Slow Electrons in Gases. By L. G. H. Huxley, R. W. Crompton, and C. H. Bagot 303

NUMBER 4, DECEMBER 1959

PAGE

Drift of a Charged Particle in a Magnetic Field of Constant Gradient. By P. W. Seymour 309

Radio-echo Observations of the Geminid Meteor Stream. By A. A. Weiss 315

High Resolution Observations of the Granular Structure of Sunspot Umbrae. By R. J. Bray and R. E. Loughhead 320

Solar Radio Bursts of Spectral Type II. By J. A. Roberts 327

Location of the Sources of 19 Mc/s Solar Bursts. By C. A. Shain and C. S. Higgins 357

An Investigation of the Speed of the Solar Disturbances responsible for Type III Radio Bursts. By J. P. Wild, K. V. Sheridan, and A. A. Neylan 369

An Association between Solar Radio Bursts at Metre and Centimetre Wavelengths. By A. A. Neylan 399

Solar Radio Emission of Spectral Type IV and its Association with Geomagnetic Storms. By D. J. McLean 404

The Eta Carinae Nebula and Centaurus A near 1400 Mc/s. II. Physical Discussion of the Eta Carinae Nebula. By C. M. Wade 418

Towards a Method for the Accurate Solution of the Schrödinger Wave Equation in Many Variables. I. Formulation of the Method for an Eigenvalue Problem without Symmetry Conditions. By I. M. Bassett 430

Towards a Method for the Accurate Solution of the Schrödinger Wave Equation in Many Variables. II. A Simple Numerical Illustration. By I. M. Bassett 441

Towards a Method for the Accurate Solution of the Schrödinger Wave Equation in Many Variables. III. Application of the General Method to the Wave Equation without Special Symmetry. By I. M. Bassett 449

The Lattice Thermal Conductivity of Some Gold Alloys. By J. A. Birch, W. R. G. Kemp, P. G. Klemens, and R. J. Tainsh 455

Short Communications

The Ionosphere of Jupiter. By H. Rishbeth 466

Analysis of Composite Spectral-sensitivity Functions. By J. S. Anderson, E. A. Faulkner, and D. F. Klemperer 469

The Extended Component of Centaurus A. By C. M. Wade 471

Index to Volume 12 477

ZERO–FIELD MASERS

By G. S. BOGLE* and H. F. SYMMONS*†

[*Manuscript received October* 6, 1958]

Summary

Solid state three-level masers operating with zero magnetic field are shown to be feasible and to have advantages over magnetic field masers in many applications. The requirements of the working substance are discussed and it is found that compounds of Cr^{2+}, Fe^{3+}, Ni^{2+}, and Gd^{3+} should be suitable. Diagrams and tables of maser properties of selected compounds are given ; on the basis of present knowledge a number of amplifying frequencies between 120 and 75,000 Mc/s should be available. The range of suitable compounds which has been studied is very small, and should be extended.

I. INTRODUCTION

A primary requirement of the three-level maser, which was stated by Bloembergen (1956) in his original proposal of the device, is that non-zero magnetic-dipole transition probabilities should exist between all three of the participating levels. This requirement is not fulfilled when the quantization of angular momentum is pure, since the selection rule $\Delta M = \pm 1$ applies. As a means of breaking down this selection rule, Bloembergen proposed that a paramagnetic salt possessing a Stark splitting due to its internal electric field should be subjected to a magnetic field inclined at an angle to the axis of the crystalline electric field. If the resulting Zeeman splittings are made comparable to the Stark splittings the quantization is very mixed and transitions may in general take place between all levels.

Use has been made of this principle, which one may call magnetic-field mixing, in a number of successful maser oscillators and amplifiers (for example, Scovil, Feher, and Seidel 1957 ; McWhorter and Meyer 1958).

In view of the great interest which has been aroused by the three-level maser it is surprising that no attention seems to have been paid to the possibility of realizing the device without using a magnetic field. It will be shown below that, among the paramagnetic substances already studied, there are several which provide the necessary transitions, between three levels, in zero magnetic field.

Such zero-field masers will not be tunable beyond the line width of the magnetic resonances involved, and so will hardly compete with magnetic-field masers where the profile of a naturally occurring radiation, such as the hydrogen line of radio astronomy, is to be studied. Nevertheless, zero-field masers possess some considerable advantages which may prove paramount in applications

---

* Division of Physics, C.S.I.R.O., University Grounds, Sydney.

† On leave from the Department of Physics, Otago University, New Zealand.

such as radar, communications, and high-sensitivity paramagnetic resonance experiments, where frequency, as such, is not important. The advantages are :

(1) The necessity for a magnet, which in magnetic-field masers has to fulfil exacting requirements of homogeneity, stability, and working space, is avoided.

(2) The orientation of the crystal loses its primary importance as an energy-determining factor. Thus large monocrystals of paramagnetic material will not be required ; indeed powders could be used, so that unit filling factor could be achieved without difficulty.

(3) As a corollary of (2) it is possible to utilize differently oriented but otherwise equivalent paramagnetic centres in the crystal, whereas in a magnetic-field maser only one type would, in general, be correctly oriented with respect to the field.

(4) Line broadening caused by inhomogeneity of the magnetic field, or of orientation of the crystal axes, is absent.

(5) A superconductor may be employed for the construction of the microwave circuits since no magnetic field is employed.

(6) Complicated or extended microwave structures, limited only by the requirement that they enter a Dewar vessel of reasonable size, may be used.

These advantages lead to great freedom in the design of masers. An attractive example is a travelling-wave maser consisting of a superconducting coaxial line filled with powdered paramagnetic and wound into a coil to permit convenient cooling of a considerable length.

In view of the advantages of zero-field masers we present a compilation of transition probabilities and frequencies calculated for a number of materials which, on the basis of present-day knowledge, are promising as working substances. The grounds for selection will also be given, and this will necessitate a consideration of maser and paramagnetic resonance theory.

II. The Three-level Maser

We refer at this point to Bloembergen's (1956) paper. Bloembergen considers a system with three energy levels $E_3>E_2>E_1$, to which is applied a strong microwave magnetic field at the frequency $\nu_{31}=(E_3-E_1)/h$ and a weak field at the frequency $\nu_{32}=(E_3-E_2)/h$. He gives an expression for the difference in population between levels for the case when all energy level differences are much less than kT. Preserving only terms of order $h\nu/kT$, we may ignore the distinction between w_{ij} and w_{ji}, thus obtaining

$$n_1-n_2=n_3-n_2=\tfrac{1}{3}\cdot\frac{hN}{kT}\cdot\frac{w_{21}\nu_{21}-w_{32}\nu_{32}}{w_{21}+w_{32}+W_{32}}. \qquad \ldots\ldots \quad (1)$$

The notation is Bloembergen's : N is the number of paramagnetic centres, the w's are the thermally induced (relaxation) transition probabilities, W_{32} is the transition probability between the levels E_3 and E_2 due to the microwave field $H(\nu_{32})$, and T is the absolute temperature. Without loss of generality one may suppose that $w_{21}\nu_{21}>w_{32}\nu_{32}$, for, if not, the labels 1 and 3 can simply be reversed. Then $n_3 > n_2$, and stimulated emission occurs at the frequency ν_{32}. The power emitted is

$$P_{\text{magn}} = \frac{Nh^2\nu_{32}(w_{21}\nu_{21} - w_{32}\nu_{32})W_{32}}{3kT(w_{21} + w_{32} + W_{32})}. \qquad \ldots\ldots\ldots\ldots \quad (2)$$

We now wish to express W_{32} in terms of the exciting field $H(\nu_{32})$, the matrix element $\langle 2 \mid H.S \mid 3\rangle$, and the width of the magnetic resonance line. At this point we depart from the nomenclature of Bloembergen and use the half-width at half-intensity $\Delta\nu$ instead of the relaxation time T_2. $(\Delta\nu = 1/(2\pi T_2).)$ Then the transition probability takes the form

$$W_{32} = \pi g^2\beta^2 \mid \langle 3 \mid H.S \mid 2\rangle \mid^2 / h^2\Delta\nu = \pi g^2\beta^2 H(\nu_{32})^2 \mid \langle 3 \mid S_H \mid 2\rangle \mid^2 / h^2\Delta\nu, \qquad \ldots\ldots\ldots\ldots\ldots\ldots \quad (3)$$

where g is the spectroscopic splitting factor, β the Bohr magneton, and S_H the projection of the spin operator in the direction of $H(\nu_{32})$.

Provided that the field $H(\nu_{32})$ is small, so that $W_{32} \ll w_{21} + w_{32}$, equation (2) shows that the power emitted is proportional to $H(\nu_{32})^2$. One may then define a magnetic quality factor Q_M by the equation

$$\frac{-1}{Q_M} = \frac{\text{power emitted per unit volume}}{2\pi\nu_{32} \times (\text{stored energy per unit volume})}.$$

This definition differs from that of Bloembergen in that unit volume of the paramagnetic is here considered, so that dependence on the volume of any conducting enclosure is avoided. We believe that this definition has the merit of embodying only properties characteristic of the paramagnetic material. Let the further stipulation be made that N shall be the number of paramagnetic centres per unit volume, so that equations (1) and (2) now refer to unit volume. Then

$$-\frac{1}{Q_M} = \frac{4\pi}{3kT} \cdot \frac{Ng^2\beta^2 \mid\langle 3 \mid S_H \mid 2\rangle\mid^2}{\Delta\nu} \cdot \frac{w_{21}\nu_{21} - w_{32}\nu_{32}}{w_{21} + w_{32}}. \qquad \ldots\ldots \quad (4)$$

The concept of magnetic Q is of central importance in any discussion of circuit properties of practical maser amplifiers. In the case of the cavity maser, for example, McWhorter and Meyer (1958) have shown that, under reasonable practical circumstances,

$$G^{\frac{1}{2}}B \doteqdot 2\nu_{32} / \mid Q_M \mid, \qquad \ldots\ldots\ldots\ldots\ldots\ldots\ldots \quad (5)$$

where G is the power gain, and B is the bandwidth.

As a very different example we shall take a travelling wave coaxial-line structure operating in the principal (TEM) mode. The gain per unit length attributable to the magnetic material is

$$G = (1/\mid Q_M \mid)(\nu_{23}/2v)(Z_0/Z) \text{ nepers}, \qquad \ldots\ldots\ldots\ldots \quad (6)$$

where Z_0 is the intrinsic impedance of the magnetic material, Z is the wave impedance of the filled coaxial line, and v is the group velocity of the wave in the filled coaxial line.

In both cases it is evident that the larger $1/\mid Q_M \mid$ the better the performance, and we shall therefore use it as a figure of merit of paramagnetic materials.

III. Extension of the Maser Equation to Four Levels and Extrapolation to More than Four Levels

The number of paramagnetics with precisely three levels is limited, and in fact the successful masers so far operated have used four or eight levels. In spite of this the equations of a multilevel maser do not appear to have been published. However, some estimate of the influence of extra levels is needed for the assessment of suitability of working substances.

For a four-level maser, we find that, with a natural extension of Bloembergen's notation, the equation analogous to equation (**1**) is

$$n_3-n_2=\frac{1}{4}\cdot\frac{hN}{kT}\cdot\frac{w_4(w_{21}\nu_{21}-w_{32}\nu_{32})+w_{24}(w_{14}\nu_{21}-w_{34}\nu_{32})}{w_4(w_{21}+w_{32})+w_{24}(w_{14}+w_{34})}, \quad .. \ (7)$$

where $w_4 \equiv w_{14}+w_{24}+w_{34}$.

If no relaxation transitions exist between the fourth level and the other three, i.e. $w_{14}=w_{24}=w_{34}=0$, the population difference n_3-n_2 turns out to be three-quarters of that given by equation (**1**), which accords with expectation since in this case only $\frac{3}{4}N$ centres are participating in the maser process. The same result is produced in quite a variety of circumstances: (i) if $w_{24}=0$; (ii) if $w_{14}=w_{34}=0$; (iii) if $w_{14}/w_{21}=w_{34}/w_{32}$; (iv) if all the w's are equal.

It may also be seen that the position of the fourth energy level is of no account. However, equation (**7**), like equation (**1**), rests on the assumption that all energy differences are small compared to kT.

Very little is at present known about the values of the relaxation frequencies w. We shall assume here that the effect of extra levels is simply to reduce the working population, so that for an x-level maser,

$$n_3-n_2 \div \frac{1}{x}\cdot\frac{hN}{kT}\cdot\frac{w_{21}\nu_{21}-w_{32}\nu_{32}}{w_{21}+w_{32}}. \quad .... \ (8)$$

The figure of merit then takes the form (cf. equation (**4**))

$$-\frac{1}{Q_M} \div \frac{4\pi}{xkT}\cdot\frac{Ng^2\beta^2\,|\langle 3\,|\,S_H\,|\,2\rangle|^2}{\Delta\nu}\cdot\frac{w_{21}\nu_{21}-w_{32}\nu_{32}}{w_{21}+w_{32}}. \quad .... \ (9)$$

IV. Requirements of the Spin and Hamiltonian for Zero-field Masers

In this section we shall discuss what values of spin are required to give three or more energy levels in zero field, and what components must be present in the spin Hamiltonian to provide transitions between the levels. It will be assumed that the nuclear spin is zero; its influence when it is not zero will be discussed in Section VII.

Paramagnetic resonance results are customarily presented in terms of the spin Hamiltonian formalism of Pryce (1950). The ground states of the paramagnetic centres are described in terms of a spin S, and the spin Hamiltonian is a function of spin operators with semi-empirical parameters. Once these are known all paramagnetic properties may be calculated, including those relevant to masers. A particularly useful compilation of spin Hamiltonian parameters has been given in the review article on paramagnetic resonance by Bowers and Owen (1955).

The number of independent states of an ion with spin S is $2S+1$; but, by virtue of Kramers' theorem (1930), the number of distinct energy levels cannot exceed $S+\frac{1}{2}$ for integer-plus-a-half spins. For integer spin the number of levels may be $2S+1$. In either case the full multiplicity allowed by Kramers' theorem may not be realized in crystal fields of high symmetry. Assuming low enough symmetry, the multiplicity is tabulated below as a function of spin:

Spin	1/2	1	3/2	2	5/2	3	7/2
Number of levels ..	1	3	2	5	3	7	4
Example	Cu^{2+}	Ni^{2+}	Cr^{3+}	Cr^{2+}	Fe^{3+}	—	Gd^{3+}

A spin higher than 7/2 is not expected to occur and no examples of spin 3 are known. It is seen that all values of spin except 1/2 and 3/2 are suitable for zero-field masers.

We come next to the required properties of the spin Hamiltonian. By far the commonest form of zero-field Hamiltonian, for $S>\frac{1}{2}$, is

$$\mathscr{H}=D\{S_z^2-\tfrac{1}{3}S(S+1)\}, \quad \ldots\ldots\ldots\ldots\ldots \quad (\mathbf{10})$$

where z is an axis of symmetry of the crystalline field. A zero-field maser is out of the question with this Hamiltonian. Since $\mathscr{H}$ commutes with S_z the eigenstates of the energy are simultaneous eigenstates of S_z. The eigenvalues of the Hamiltonian are

$$E_M=D\{M^2-\tfrac{1}{3}S(S+1)\}, \quad \ldots\ldots\ldots\ldots\ldots \quad (\mathbf{11})$$

where M is the eigenvalue of S_z. This gives a series of levels, in the order $M=0$, $M=\pm1$, $M=\pm2$, . . . for ions with integer spin and in the order $M=\pm1/2$, $M=\pm3/2$, $M=\pm5/2$, . . . for those with integer-plus-a-half spin. The pumping transition for a maser, which must always be a leap-frog transition, that is, one spanning two energy intervals, would here require $\Delta M=\pm2$. But this is forbidden since the states are pure eigenstates of S_z and the normal selection rule, $\Delta M=\pm1$, applies.

Fortunately for the zero-field maser, the term in S_z^2, equation (**10**), is quite frequently accompanied by other terms, though generally it remains predominant. The additional terms fall into two classes: those with axial symmetry, viz. S_z^4 and S_z^6; and those with lower symmetry. The axially symmetric terms make no improvement in the situation, for the Hamiltonian after their inclusion still commutes with S_z.

It is to the terms with lower symmetry—rhombic, trigonal, tetragonal, and hexagonal—that one must look in order to realize a zero-field maser. These terms are conventionally expressed as operator functions which transform under rotation in the same way as the spherical harmonics. Most of the terms met with in paramagnetic resonance are given in full in Bleaney and Stevens' (1953) review article (pp. 132, 137, and 150); it is invariably the case that a term with m-fold symmetry contains the operators S_+^m and S_-^m, where

$$S_+\equiv S_x+\mathrm{i}S_y, \qquad S_-\equiv S_x-\mathrm{i}S_y. \quad \ldots\ldots\ldots\ldots \quad (\mathbf{12})$$

These terms do not commute with S_z, and therefore the eigenstates of the Hamiltonian are not pure eigenstates of S_z, and normal selection rules no longer apply.

In general one may say that any paramagnetic with spin other than 1/2 or 3/2, which has a spin Hamiltonian of rhombic, trigonal, tetragonal, or hexagonal symmetry, is a candidate for a zero-field maser.

There is one exception to the rule. This is the case of perfect cubic symmetry, which has the Hamiltonian (Bleaney and Stevens 1953, p. 137)

$$\mathcal{H}_{\text{cubic}}=\tfrac{1}{6}a\{S_x^4+S_y^4+S_z^4-\tfrac{1}{5}S(S+1)(3S^2+3S-1)\}, \quad \ldots. \quad (\mathbf{13})$$

where a is a numerical coefficient. For all spins less than 3 this Hamiltonian gives fewer than three levels, and for $S=3$ and 7/2 the number of levels is three but the leap-frog transition probability turns out to be zero. It should be emphasized that this is true only of perfect cubic symmetry; $\mathcal{H}_{\text{cubic}}$ in conjunction with other operators has rhombic, trigonal, or tetragonal symmetry and the rule then applies.

V. Line Width and Ultimate Performance

The figure of merit, equation (**9**), depends on the line width $\Delta\nu$. In a zero-field maser three agencies can contribute to this: (1) the random magnetic fields of the nuclei of the diamagnetic neighbours of the paramagnetic centres; (2) a spread in the values of the spin Hamiltonian coefficients; (3) the fields of the paramagnetic centres themselves. In principle, (1) and (2) can be made small compared to (3) by choosing a host material in which the diamagnetic atoms have small nuclear moments and by obtaining a sufficiently perfect crystal structure. Then performance would depend only on the line width due to paramagnetic spin-spin interaction (3).

Kittel and Abrahams (1953) have calculated the line width for a dilute paramagnetic with a cubic lattice. With some adaptation of their result one obtains

$$\Delta\nu \doteqdot 6g^2\beta^2N\sqrt{\{S(S+1)\}}/h. \quad \ldots\ldots\ldots\ldots\ldots \quad (\mathbf{14})$$

We shall take this to be a fair indication of line width for any lattice, not merely cubic. Then the figure of merit becomes, using (**9**) and (**14**),

$$-\frac{1}{Q_M}\doteqdot\frac{2h(w_{21}\nu_{21}-w_{32}\nu_{32})\,|\langle 3\mid S_H\mid 2\rangle|^2}{xkT(w_{21}+w_{32})\sqrt{\{S(S+1)\}}}. \quad \ldots\ldots\ldots \quad (\mathbf{15})$$

The value of $|\langle 3\mid S_H\mid 2\rangle|^2$ will be typically of the order of $(\frac{1}{4})S^2$; the number of distinct energy levels, x, is $S+\frac{1}{2}$ and $2S+1$ for integer-plus-a-half and integer spins respectively; thus to a rough approximation (**15**) is independent of spin. Making now the simplifying assumption that $w_{21}\sim w_{32}$, and $\nu_{21}\gg\nu_{32}$, one obtains for the figure of merit

$$-\frac{1}{Q_M}\sim h\nu_{21}/4kT \quad \ldots\ldots\ldots\ldots\ldots\ldots\ldots \quad (\mathbf{16})$$

for integer-plus-a-half spin (Kramers degenerate ions). For integer spin the figure of merit is roughly halved.

It is interesting to compare (**16**), which should be valid for a magnetic-field maser as well as for a zero-field maser, with the results of McWhorter and Meyer (1958). In their experiment, $\nu_{21} \sim 6 \times 10^9$ c/s, $T = 1 \cdot 25$ °K, and $S = 3/2$. After adjustment for the doubling of multiplicity brought about by the presence of the magnetic field our theory predicts $-1/Q_M \sim h\nu_{21}/8kT$ or 1/35. In fact the experimentally measured figure, derived from the quoted gain-bandwidth product, by the use of equation (**5**), was 1/3300, or about 100 times worse than the ultimate predicted. The factor of 100 is made up in the following way. (*a*) The filling factor of the sample in the cavity was only 10 per cent., which contributes a factor 10. (*b*) The line width (derived from the quoted value of 5×10^{-9} sec for T_2) was 30 Mc/s, whereas that attributable to paramagnetic spin-spin interaction in the working population of 10^{19} per cm^3 was, according to equation (**14**), only 6 Mc/s. This contributes a factor 5. (*c*) The approximation made in deriving equation (**18**), namely, that $\nu_{21} \gg \nu_{32}$, is not justified; in fact $\nu_{32} \doteqdot \frac{1}{2}\nu_{21}$, which contributes a factor 2. The product of these factors is 100. The closeness of this agreement is only accidental, considering the approximations made in deriving equation (**16**).

The significant conclusion from the above comparison is that it is desirable to increase the paramagnetic concentration, or reduce other sources of line width, until the paramagnetic spin-spin width is dominant. The former course—increasing concentration—cannot necessarily be followed with impunity. For example, in their experiments with a 1400 Mc/s maser using dilute potassium chromicyanide, Autler and McAvoy (1958) found that, whereas ½ per cent. crystals ($N \sim 10^{19}$) functioned successfully, 1 per cent. crystals did not. This fact may be understood in terms of the theory of Giordmaine *et al.* (1958). According to this theory, the phonon frequencies near the spin resonances are considerably broadened by interaction with the spins. The phonon width $\Delta\nu_L$ is proportional to $N^{\frac{1}{2}}$, and, for a typical case, $\Delta\nu_L \sim 400$ Mc/s at $N = 10^{19}$. It follows that if the resonance at ν_{31} is saturated, as in pumping a maser, the temperature of all phonons in the range $\nu_{31} \pm \Delta\nu_L$ is raised and these will saturate in turn any other spin resonances which they overlap. It is clear that in this model maser action would not occur if $\Delta\nu_L > \nu_{32}$, for then the saturation of ν_{31} would spread to ν_{21} with the result that $n_1 = n_2 = n_3$. The same failure can occur even if $\Delta\nu_L < \nu_{32}$ because the lattice modes are not expected to show a sharp cut-off at $\nu \pm \Delta\nu_L$.

Since it may not be possible to increase paramagnetic concentration it is probable that the other course, of reducing the width due to diamagnetic neighbours, is the more promising. In most hydrated salts the protons in the water molecules cause a half-width of 20 Mc/s; by substituting heavy water this may be reduced to about 6 Mc/s (Bleaney and Stevens 1953, p. 119). By growing crystals which do not contain water of crystallization even greater improvements may be expected; for example, the diamagnetic neighbour width in dilute $K_3Cr(CN)_6$ crystals is only 3 Mc/s (Bowers 1952).

The other source of width—variation of spin Hamiltonian parameters—is more obscure. For example, it was found by Bleaney and Trenam (1954) that among the diluted ferric alums the ammonium, potassium, and thallium sulphates did not give narrow lines, whereas the rubidium and methylamine sulphates and potassium selenate did.

More experimental data are needed concerning causes of line width in paramagnetic compounds. However, it is reasonable to expect that ways will be found to utilize the full potential figure of merit given by equation (**16**).

To demonstrate the implications of this equation one may propose an example of a cavity maser with a Kramers degenerate working substance ($S=5/2$ or $7/2$) in which $\nu_{21}\sim20000$ and $\nu_{31}\sim3000$ Mc/s, $T\sim2$ °K, $G\sim30$ dB. From equations (**5**) and (**16**) the bandwidth would be 25 Mc/s. By contrast, the bandwidth so far achieved in a magnetic field maser at the same power gain is only 60 kc/s (McWhorter and Meyer 1958). The example shows that the present view of the maser as essentially a narrow-band device should be revised.

VI. Relaxation Times

The relaxation times for transitions between the three levels affect both the pumping power requirements and the figure of merit of the maser. We shall discuss first the pumping power.

The power absorbed at saturation, P_a, may be found by adapting the treatment of Eschenfelder and Weidner (1953), giving

$$P_a=\frac{N(h\nu)^2w}{3kT}=\frac{N(h\nu)^2}{6kT}\cdot\frac{1}{\tau}, \qquad\ldots\ldots\ldots\ldots \quad (\mathbf{17})$$

where w is the thermally induced (relaxation) transition probability between the two levels saturated, and τ is the associated spin-lattice relaxation time, which is equal to $1/(2w)$ (see, for example, Andrew 1955, p. 15). The power absorbed in pumping a maser is not correctly given, however, by direct substitution of ν_{31} for ν and w_{31} for w in equation (**17**) because the direct relaxations from level 3 to 1 are supplemented by those passing from 3 to 2 and thence to 1. From the Bloembergen equations we have derived the following general expression valid for three levels

$$P_a=\frac{N(h\nu_{31})^2}{6kT}\cdot\left(\frac{1}{\tau_{31}}+\frac{1}{\tau_{21}+\tau_{32}}\right), \qquad\ldots\ldots\ldots \quad (\mathbf{18})$$

where $\tau_{ij}=1/(2w_{ij})$.

We now consider the desirable limitations on the relaxation times. We shall use an effective time $\tau=\{1/\tau_{31}+1/(\tau_{21}+\tau_{32})\}^{-1}$; the experimental results available do not warrant a closer examination of the separate times.

The use of liquid helium temperatures is likely to be general since the figure of merit, equation (**16**), is inversely proportional to the absolute temperature. As a typical case, then, one may take $T\sim1$, $N\sim10^{19}$, $\nu_{31}\sim10^{10}$, and $x=4$, whence the power absorbed is about $1/10\tau$ mW/cm³. The volume of working substance will be some tens of cubic centimetres, so that $P_a\sim1/\tau$ mW. Postulating an upper limit of 1 W, which would evaporate about a litre of liquid helium per hour, one is led to the requirement that τ be a millisecond or longer.

Relaxation times of the order of milliseconds have indeed been measured at liquid helium temperatures (Gorter 1947; Benzie and Cook 1950; Eschenfelder and Weidner 1953; Giodmaine *et al.* 1958). It appears to be generally the case that, if a paramagnetic has a long enough relaxation time at room temperature to give observable resonance lines, then it has a relaxation time longer than 1 msec at liquid helium temperatures. We shall therefore assume that to be suitable for a maser a paramagnetic must give observable resonance lines at room temperature.

As Bloembergen (1956) has remarked, the w's may be expected to reflect the Debye (ν^2) phonon spectrum: if so, the figure of merit would contain $(\nu_{21}^3-\nu_{32}^3)/(\nu_{21}+\nu_{32})$. Accordingly we shall assume, for the purpose of this paper, that even if ν_{21} is only a few tens per cent. greater than ν_{32} the substance is a reasonable candidate for a zero-field maser.

VII. Influence of Hyperfine Structure

If the nucleus of a paramagnetic centre has odd mass number it will possess angular momentum and magnetic moment. A magnetic interaction will exist between the nucleus and the paramagnetic electrons, to account for which the term

$$\mathscr{H}_N=A_xS_xI_x+A_yS_yI_y+A_zS_zI_z \quad \ldots\ldots\ldots\ldots \quad \textbf{(19)}$$

must be added to the Hamiltonian, I_x, I_y, and I_z being the components of nuclear spin. An electric quadrupole interaction may also exist but is unimportant for the discussion in hand.

The effect of $\mathscr{H}_N$ is to increase considerably the number of levels. With electronic spin S and nuclear spin I the number of independent states is $(2S+1)(2I+1)$ and, although not all need correspond to distinct energy levels (see, for example, Fig. 8 of the paper by Bleaney and Ingram 1951), the number of levels, that is, x in equation (**9**), is often nearly an order of magnitude greater than the three required for maser action. The figure of merit is correspondingly reduced. Furthermore, hyperfine-structure masers, with their more closely spaced levels, are more likely to encounter the phonon-width trouble referred to in Section V.

For these reasons we do not regard hyperfine-structure masers as likely to be as important as fine-structure masers (masers with electronic splittings only). Nevertheless, hyperfine-structure masers merit some consideration because they hold the promise of extending the frequency coverage of zero-field masers. The energy splittings caused by $\mathscr{H}_N$ range from A to $(I+\frac{1}{2})A$; A is typically a few hundred Mc/s, and I may be as great as 7/2. Thus the band of frequencies covered is typically from 100 to 1000 Mc/s. We shall give one example of a hyperfine-structure maser in Section XI.

VIII. Eligible Ions

Since it is our aim to focus attention only on the most promising working substances for zero-field masers, we shall now apply rather liberally the disqualifications implied by the preceding sections.

Paramagnetism has been observed in compounds of the five transition groups, the iron, palladium, rare earth, platinum, and actinide groups, which are associated with unpaired electrons in the $3d$, $4d$, $4f$, $5d$, and $5f$ shells respectively.

We shall consider these groups in turn. Most of the available paramagnetic resonance data are collected together in the review article by Bowers and Owen (1955), to which we refer as B & O.

The most thoroughly investigated group is the *3d*. Most ions in the group give observable spectra at room temperature so that only a few need be disqualified by the relaxation-time criterion, leaving as eligible the ions VO^{2+}, V^{2+}, Cr^{2+}, Mn^{2+} (but not $[Mn(CN)_6]^{4+}$), Fe^{3+} (but not $[Fe(CN)_6]^{3+}$), Ni^{2+}, and Cu^{2+}. Next, the disqualification of ions which possess a large proportion of isotopes with hyperfine structure removes VO^{2+}, V^{2+}, Mn^{2+}, and Cu^{2+}. Those remaining which possess spin 1/2 or 3/2 must be disqualified for providing too few levels : Cr^{3+}, with $S=3/2$ is thus rejected, leaving Cr^{2+} ($S=2$), Fe^{3+} ($S=5/2$), and Ni^{2+} ($S=1$).

The next group, the *4d* group, provides rather few investigated compounds because chemical stability appears to go hand-in-hand with diamagnetic bonding. Of the compounds investigated, none have spin other than 1/2 or 3/2, so that the entire group is disqualified. The same applies to the *5d* group (B & O, p. 355).

In the *4f* or rare earth group relaxation times are generally very short and liquid hydrogen or helium temperatures have had to be employed in order to observe the spectra. The only ions giving observable spectra at room temperature are the iso-electronic Eu^{2+} and Gd^{3+}, which have $S=7/2$. Eu^{2+} is disqualified by its large proportion of isotopes with hyperfine structure (B & O, p. 363). Gd^{3+} has 30 per cent. isotopes with nuclear spin, but the associated hyperfine structure is so small that it eluded for years attempts to resolve it (Low 1956). The four electronic energy levels of Gd^{3+} are each thus effectively single and provide a good basis for a zero-field maser.

In the *5f* series the behaviour appears to resemble that in the *4f* series (Bleaney 1955 ; Hutchison *et al.* 1956), so that very short relaxation times are to be expected. Bleaney (1955) has pointed out that the ions Am^{2+}, Cm^{3+}, and Bk^{4+} are expected to behave analogously to Gd^{3+} and Eu^{2+}, with reasonably long relaxation times. However, the expense of these elements and the destruction of crystal structure which their radiations will cause, make it doubtful that they, or any other actinides, will be attractive candidates for zero-field masers and accordingly we shall not consider them further.

It is seen that the promising working substances for zero-field masers are the compounds of no more than four ions : Cr^{2+}, Fe^{3+}, Ni^{2+}, and Gd^{3+}. These will be discussed in detail in Section X.

IX. TRANSITION PROBABILITIES

The transition probability, equation (**3**), may be expressed in terms of an effective magneton number for the transition p analogous to that used in the description of magnetic susceptibilities. p is defined by

$$p^2H^2=g^2\,|\langle i\,|\,H\cdot S\,|\,j\rangle|^2. \qquad \ldots\ldots\ldots\ldots\ldots \quad (\mathbf{20})$$

The figure of merit then takes the form (cf. equation (**9**))

$$\frac{-1}{Q_M}=\frac{4\pi N\beta^2p^2}{\varkappa kT\Delta\nu}\cdot\frac{w_{21}\nu_{21}-w_{32}\nu_{32}}{w_{21}+w_{32}}. \qquad \ldots\ldots\ldots\ldots \quad (\mathbf{21})$$

If lmn are the direction cosines of H with respect to the axes xyz of the spin Hamiltonian,

$$p^2 = l^2 p_x^2 + m^2 p_y^2 + n^2 p_z^2, \quad \ldots\ldots\ldots\ldots\ldots\ldots \quad (22)$$

where $p_x^2 = g^2 \, |\langle i \mid S_x \mid j \rangle|^2$, and so on.

It is illuminating to notice that, for a free electron spin with oscillating field applied perpendicular to a steady field, $p^2 = g^2 \, |\langle -\frac{1}{2} \mid S_x \mid \frac{1}{2} \rangle|^2 = 1$ since $g = 2 \cdot 00$. Hence, in general, p^2 denotes the strength of a transition in terms of that for a free spin having the same line width: in other words, p^2 is the strength in free-spin units.

For powdered salts p^2 must be averaged over all directions of H, giving

$$p_{\mathrm{Av}}^2 = \tfrac{1}{3}(p_x^2 + p_y^2 + p_z^2). \quad \ldots\ldots\ldots\ldots\ldots\ldots \quad (23)$$

If the spectroscopic splitting factor g were anisotropic, equations (**20**) and (**21**) would require generalization; but for compounds suitable for masers it turns out that g is always nearly isotropic.

X. MASER PROPERTIES OF SELECTED COMPOUNDS

We shall now consider the suitability of those compounds of Cr^{2+}, Ni^{2+}, Fe^{3+}, and Gd^{3+} which have been studied by paramagnetic resonance. In many cases results have been observed at room temperatures, and the properties deduced from them must be taken only as an indication of what will apply at liquid helium temperatures.

Energies and eigenstates have been calculated from the spin Hamiltonian by standard methods. The eigenstates have been then used to calculate transition probabilities which in the diagrams that follow will be labelled by the value of $p^2 = l^2 p_x^2 + m^2 p_y^2 + n^2 p_z^2$ appropriate to the transition. The information in the diagrams will allow prediction of maser performance in case it should be desired to obtain optimum transition probabilities by mounting crystals of the working substance in a definite orientation in the oscillating fields.

It should be noted, however, that, when there are several differently oriented paramagnetic ions per unit cell of the crystal structure, it is not in general possible to mount crystals so as to use the most favourable component of p^2 for all ions: the spatial average p_{Av}^2 is then a useful guide to performance. Furthermore, one of the characteristic features of zero-field masers is the possibility they provide of using powdered material, which allows structural freedom and good filling factor. Therefore, in the tables of maser properties of specific compounds we shall quote the spatial average.

The ions Cr^{2+} and Ni^{2+} will be treated first. They both lack Kramers degeneracy and have larger splittings and probably shorter relaxation times than Fe^{3+} and Gd^{3+} which are Kramers degenerate.

Cr^{2+} : $S = 2$.

Only one compound, $CrSO_4.5H_2O$, has been studied (Ono *et al.* 1954). The results were obtained with undiluted crystals. There are two differently oriented ions per unit cell, each with the Hamiltonian

$$\mathscr{H} = D\{S_z^2 - \tfrac{1}{3}S(S+1)\} + E(S_x^2 - S_y^2). \quad \ldots\ldots\ldots\ldots \quad (24)$$

The g-value is nearly isotropic and equal to 2·0. The energy levels are (B & O, p. 336): $E_1=-2(D^2+3E^2)^{\frac{1}{2}}$, $E_2=-D-3E$, $E_3=-D+3E$, $E_4=2D$, and $E_5=2(D^2+3E^2)^{\frac{1}{2}}$. The transition probabilities are given in Figure 1.

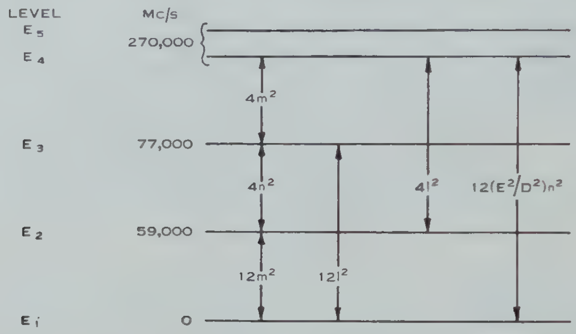

Fig. 1.—Transition probabilities for Cr^{2+} in free-spin units with oscillating field in the direction (lmn). The numerical values of the energy for $CrSO_4.5H_2O$ at room temperature are given; g^2 is taken as 4. For meaning of D and E, see equation (**24**).

The frequencies and spatially averaged transition probabilities are given in Table 1.

From Table 1 it is evident that a very promising possibility exists for a maser amplifying at about 18,000 Mc/s. The higher modes, b and c, may become practicable in the future.

Table 1

maser properties of Cr^{2+} and Ni^{2+} salts

Salt	Temperature of Measurement (°K)	Pumping Frequency (Mc/s)	Pumping Probability for Powdered Salt (free-spin units)	Amplifying Frequency (Mc/s)	Amplifying Probability for Powdered Salt (free-spin units)	Difference Frequency (Mc/s)
$CrSO_4.5H_2O$	290	(a) 77,000	4	18,000	1·3	59,000
		(b) 270,000	0·01	77,000	4	190,000
		(c) 270,000	0·01	59,000	4	210,000
$K_2Ni(SO_4)_2.6H_2O$ ..	290	115,000	1·7	30,000	1·7	85,000
$(NH_4)_2Ni(SO_4)_2.6H_2O$	90	75,000	1·7	29,000	1·7	46,000
$Tl_2Ni(SO_4)_2.6H_2O$ ..	290	80,000	1·7	6,000	1·7	74,000
$(NH_4)_2Ni(SeO_4)_2.6H_2O$	90	76,000	1·7	27,000	1·7	49,000
$NiSO_4.7H_2O$ ..	290	150,000	1·7	60,000	1·7	90,000

Ni^{2+}: $S=1$.

A number of nickel salts has been studied, and it has been found that where the crystalline environment has trigonal or higher symmetry the spin Hamiltonian provides only two distinct levels (Bleaney and Stevens 1953, p. 144) and so is useless for a zero-field maser. The majority of salts, however, are suitable, exhibiting rhombic symmetry with the same Hamiltonian as that of $CrSO_4.5H_2O$ given above. The g-value is nearly isotropic and equal to 2·25. The energies and transition probabilities are given in Figure 2.

Table 1 gives maser properties of suitable nickel salts (B & O, p. 350). The data refer to undiluted salts ; dilution may alter the frequencies by 20 per cent. In the Tutton salts there are two, and in $NiSO_4.6H_2O$ four differently oriented ions per unit cell.

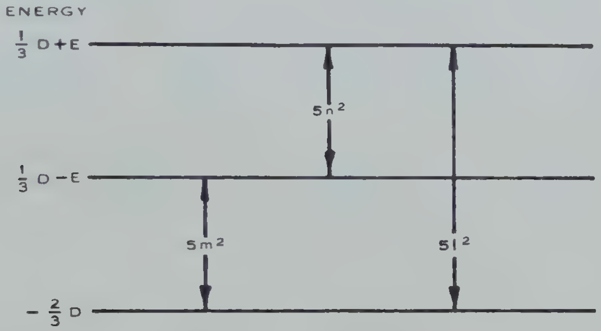

Fig. 2.—Energies and transition probabilities for Ni^{2+} assuming $g^2=5$. The transition probabilities are given in free-spin units and the oscillating field has the direction (lmn). For D and E, see equation (**24**).

It can be seen that a variety of amplifying frequencies is likely to be provided at liquid helium temperatures by nickel salts. The transition probabilities are substantial, being greater than the free-electron probability even for powdered salt.

That paramagnetic resonance has been observed in so few nickel salts is probably because the zero-field splittings for most salts are even greater than those in Table 1. These will constitute a reserve of maser materials for the future as the millimetre wave region develops.

Fe^{3+} : $S=5/2$.

The behaviour of ferric salts hitherto studied is described by the spin Hamiltonian of Bleaney and Trenam (1954) which in zero field takes the form

$$\mathscr{H}=D\left\{S_z^2-\frac{1}{3}S(S+1)\right\}+\frac{1}{6}a\left\{S_\xi^4+S_\eta^4+S_\zeta^4-\frac{707}{16}\right\}+\frac{7}{36}F\left(S_z^4-\frac{95}{14}S_z^2+\frac{81}{16}\right), \qquad \ldots\ldots\ldots\ldots\ldots\ldots \ (\mathbf{25})$$

where the coordinate system $\xi\eta\zeta$ refers to three mutually perpendicular axes with respect to which the z-axis is the (111) direction. Such a Hamiltonian is to be expected when the environment of the ion is predominantly cubic with cubic axes $\xi\eta\zeta$, with a superposed distortion along the (111) or z-direction such that the resulting symmetry is only trigonal with z as axis. The term in F is usually of small influence.

The term in a, or cubic term, has off-diagonal elements when expressed in the S_z-representation, as may be seen in the matrix given by Meijer (1951). These provide the leap-frog transitions which are necessary for zero-field maser action.

General formulae for the zero-field levels and eigenstates of the Hamiltonian (**25**) have been given by Bleaney and Trenam (1954). The energy levels are doublets at

$$\left.\begin{aligned} E_{1,2} &= \tfrac{1}{3}D-\tfrac{1}{2}(a-F)\pm\tfrac{1}{6}\{(18D+a-F)^2+80a^2\}^{\frac{1}{2}}, \\ E_3 &= -\tfrac{2}{3}D+a-F, \end{aligned}\right\} \quad \ldots . \quad (\mathbf{26})$$

and the eigenstates involve trigonometric functions of an angle α defined by

$$\tan\alpha = a\sqrt{20}/\{9D+\tfrac{1}{2}(a-F)\}. \quad \ldots\ldots\ldots\ldots\ldots\ldots \quad (\mathbf{27})$$

From these eigenstates transition probabilities may be calculated, which we present for the general case in Figure 3. The g-value is isotropic and equal to 2·00.

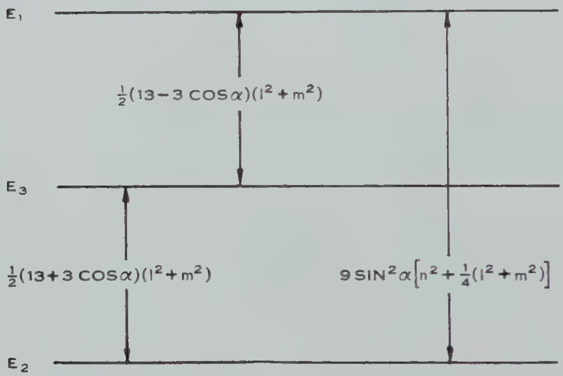
E_1
$\frac{1}{2}(13-3\cos\alpha)(l^2+m^2)$
E_3
$\frac{1}{2}(13+3\cos\alpha)(l^2+m^2)$
$9\sin^2\alpha\left[n^2+\frac{1}{4}(l^2+m^2)\right]$
E_2

Fig. 3.—Transition probabilities for Fe^{3+} in free-spin units with oscillating field in the direction (lmn), assuming $g^2=4$. The order of levels is appropriate to D positive and predominant. For $E_{1,2,3}$, α, and D, see equations (**25**), (**26**), and (**27**).

Although paramagnetic resonance has been observed in a wide variety of undiluted compounds (B & O, p. 342), the only compounds in which the spectrum of Fe^{3+} has been observed in diluted form (i.e. with high resolution) appear to be the alums (B & O, p. 342), the acetylacetonate (Jarrett 1957), MgO (Low 1957), and Al_2O_3 (sapphire) (Kornienko and Prokhorov 1957 ; Bogle and Symmons, paper in preparation).

Apart from MgO, where the Hamiltonian is purely cubic and need not be considered for a zero-field maser (Section IV), two classes of compounds may be distinguished.

The first class comprises the alums, except methylamine alum, and is characterized by comparable values of D and a, each being a few hundred Mc/s. This class is easy to pump and provides amplifying frequencies from 100 to 1000 Mc/s.

The second class comprises methylamine alum, the acetylacetonate, and sapphire; in these compounds D is some thousands of Mc/s while a remains a few hundred. The pumping transition probability reduces to $(20/9)(a^2/D^2)\{n^2+\frac{1}{4}(l^2+m^2)\}$ for $a \ll D$, which shows that this class is difficult to pump. It provides amplifying frequencies of the order of 10,000 Mc/s.

The maser properties of the above-mentioned compounds are given in Table 2. The methylamine alum is omitted because the pumping probability turns out to be only 0·003 free-spin unit. The acetylacetonate is included in spite of there being no data on the size of a, because the presence of off-diagonal terms is indicated by the failure of the Hamiltonian $D\{S_z^2-\frac{1}{3}S(S+1)\}$ to fit the measurements (Jarrett 1957).

The alums have four differently oriented ions per unit cell, the acetylacetonate two, and sapphire two.

TABLE 2

MASER PROPERTIES OF DILUTE Fe^{3+} AND Gd^{3+} COMPOUNDS

Ion	Diluent	Temperature of Measurement (°K)	Pumping Frequency (Mc/s)	Pumping Probability for Powdered Material (free-spin units)	Amplifying Frequency (Mc/s)	Amplifying Probability for Powdered Material (free-spin units)	Difference Frequency (Mc/s)
Fe^{3+}	$KAl(SeO_4)_2.12H_2O$	20	2,475	0·95	1,020	3·4	1,455
Fe^{3+}	Sapphire ..	4	31,300	0·02	12,030	5·3	19,270
Fe^{3+}	Cobalt acetylacetonate ..	290	17,000	—	6,000	5	11,000
Gd^{3+}	$Sm_2(SO_4)_3.8H_2O$	290	(*a*) 14,760	2·4	7,370	17	7,390
			(*b*) 25,040	0·04	10,280	5	14,760
			(*c*) 17,670	0·04	7,390	8	10,280

Gd^{3+} : $S=7/2$.

The general form of the spin Hamiltonian for gadolinium salts is given by B & O, p. 364. Recasting the Hamiltonian in terms of the b-coefficients, which are normally used to express experimental results, one obtains

$$\mathscr{H}=b_2^0\left\{S_z^2-\frac{1}{3}S(S+1)\right\}+\frac{1}{6}b_2^2(S_+^2+S_-^2)+\frac{1}{60}b_4^0P_4^0+\frac{1}{1260}b_6^0P_6^0+\frac{1}{2520}P_6^6(S_+^6+S_-^6). \qquad \ldots\ldots\ldots\ldots (28)$$

The operators P_4^0 and P_6^0 are rather complicated functions of S_z which are given explicitly by Elliott and Stevens (1953). The only case known not to be described by equation (28) is Gd^{3+} in CaF_2, which has been studied by Ryter (1957). Here the Hamiltonian has cubic symmetry and so does not provide a basis for a zero-field maser (see Section IV).

The dominant term in the Hamiltonian, except for cubic symmetry, is always the first, just as in the case of most iron group compounds. (D of equation (**10**) has the same meaning as b_2^0 of (**28**).) The energy levels are thus approximately those of $b_2^0(S_z^2-\frac{1}{3}S(S+1))$ acting alone, that is, $-5b_2^0$, $-3b_2^0$, b_2^0, and $7b_2^0$, so that the possible maser amplifier frequencies are about $2b_2^0$ and $4b_2^0$.

The Hamiltonian of equation (**28**) presents a generality not found in nature : in compounds so far studied it possesses either hexagonal symmetry, in which case $b_2^2=0$, or else rhombic symmetry, in which case $b_6^6=0$. Nevertheless, no misunderstanding need arise if the energy levels are written down as if all terms in (**28**) were simultaneously present. With the assumption that b_2^0 is the dominant term, the levels are given by the following equations, which are correct to the second degree in b_2^2 and b_6^6 :

$$\left.\begin{aligned}
E(\pm 7/2)&=7b_2^0+7b_4^0+b_6^0+(7/30)(b_2^2)^2/b_2^0+(2/21)(b_6^6)^2/b_2^0),\\
E(\pm 5/2)&=b_2^0-13b_4^0-5b_6^0+(5/6)(b_2^2)^2/b_2^0-(2/21)(b_6^6)^2/b_2^0,\\
E(\pm 3/2)&=-3b_2^0-3b_4^0+9b_6^0+(31/10)(b_2^2)^2/b_2^0,\\
E(\pm 1/2)&=-5b_2^0+9b_4^0-5b_6^0-(25/6)(b_2^2)^2/b_2^0.
\end{aligned}\right\} \quad .. \ (\mathbf{29})$$

The above expressions, except for the term in $(b_6^6)^2$, have in effect been given by B & O, pp. 365 and 368. Although the term in $(b_6^6)^2$ is unimportant for compounds studied hitherto we have included it for the sake of compounds which may be studied in the future.

When one comes to consider transition probabilities it proves desirable, for clarity, to present separate diagrams for the hexagonal and rhombic classes. This is done in Figures 4 and 5 respectively.

Class I. Gd^{3+} with hexagonal Hamiltonian

The only diluted compounds in this class which appear to have been studied in detail are the ethyl sulphate and double nitrate (B & O, p. 367) and the anhydrous chloride (Hutchison, Judd, and Pope 1957). In these salts the pumping transition probabilities are very small, namely, 3×10^{-6}, 6×10^{-5}, and 4×10^{-5} that of a free spin respectively. It is doubtful whether they will ever find application in a zero-field maser and we shall not consider them further.

Class II. Gd^{3+} with rhombic Hamiltonian

The only representative of this class for which data are available appears to be the sulphate octohydrate, which has been studied at room temperature with the corresponding samarium salt as diluent (B & O, p. 367). In this salt $r\equiv b_2^2/b_2^0=0\cdot60$, which is by no means small compared to unity. Consequently the energies and the transition probabilities are not given with sufficient accuracy by equation (**29**) and Figure 4. We have solved the problem numerically in order to obtain the results shown in Figure 6.

Table 2 shows that several possible pumping and amplifying frequencies exist, with substantial transition probabilities. To demonstrate this variety, which is a feature of Gd^{3+} in a rhombic environment, is the main purpose of the entry ; no great credence is to be attached to the actual magnitudes since (1) on cooling to liquid helium temperatures b_2^0 may be expected, by analogy with the ethylsulphate (Bleaney *et al.* 1951), to change by about 10 per cent., with the other b's not necessarily changing in proportion ; and (2) the diluent will have to be changed from paramagnetic samarium to diamagnetic yttrium. Lanthanum sulphate does not crystallize isomorphously with the gadolinium salt; yttrium sulphate does so, and the Gd^{3+} spectrum has been qualitatively observed in this diluent (Bogle, unpublished data).

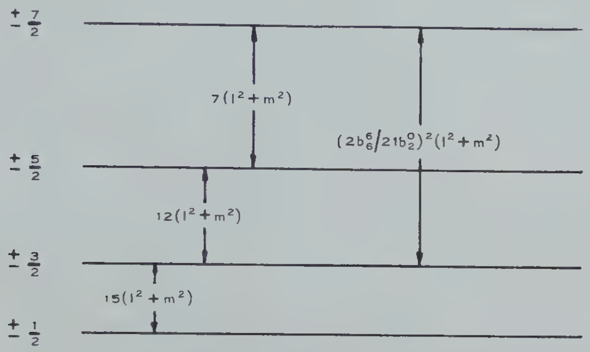

Fig. 4.—Transition probabilities in free-spin units for Gd^{3+} with a hexagonal Hamiltonian and with oscillating field in the direction (*lmn*). g^2 is taken as equal to 4. For b_6^6 and b_2^0, see equation (**28**). The order of levels is appropriate to b_2^0 positive and dominant.

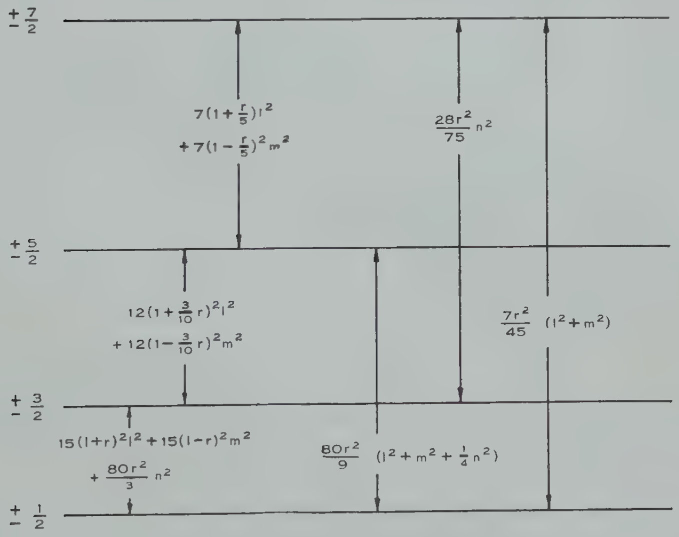

Fig. 5.—Transition probabilities in free-spin units for Gd^{3+} with a rhombic Hamiltonian and with oscillating field in the direction (*lmn*). g^2 is taken as equal to 4. $r = b_2^2/b_2^0$; for b_2^2 and b_2^0, see equation (**28**). The order of levels is appropriate to b_2^0 positive and dominant.

The conclusion to be drawn from the foregoing discussion is that gadolinium compounds with low symmetry are the most promising for zero-field masers. These have been neglected in the past, probably because both the presence of off-diagonal elements in the Hamiltonian and the frequent occurrence of several directionally inequivalent ions per unit cell have rendered analysis difficult. Some information is already available about the nitrate (Bleaney *et al.* 1951) and the chloride hexahydrate (Dieke and Leopold 1957) which suggests that they will be suitable working substances, with frequencies of similar order to those of the sulphate octohydrate. It can hardly be doubted that a wealth of gadolinium compounds of low symmetry awaits investigation.

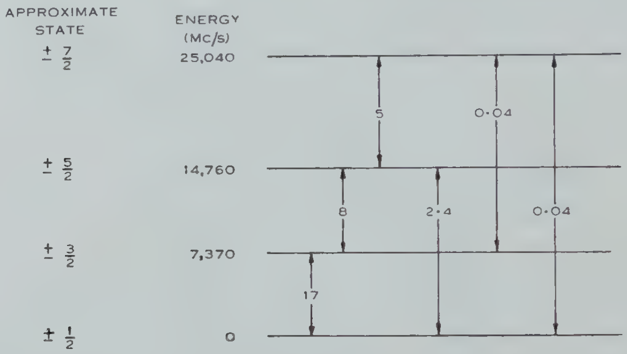

Fig. 6.—Energies and transition probabilities for Gd^{3+} in $Sm_2(SO_4)_3.8H_2O$ at 290 °K. The transition probabilities are averages for a powdered sample and are expressed in free-spin units.

XI. An Example of a Hyperfine-structure Maser

Ions satisfying the relaxation-time criterion (Section VI) and possessing a large proportion of isotopes with nuclear spin are (B & O, pp. 334, 363) V^{2+}, Mn^{2+}, Cu^{2+}, and Eu^{3+}. We choose for our example $(NH_4)_2Mn(SO_4)_2.6H_2O$ diluted with the corresponding zinc salt, which has been thoroughly investigated at 20 °K by Bleaney and Ingram (1951).

Manganese consists entirely of isotope 55 with nuclear spin equal to 5/2 ; the hyperfine-structure coupling is practically isotropic so that in zero field the Hamiltonian is (neglecting a small cubic term)

$$\mathscr{H}=D\{S_z^2-\tfrac{1}{3}S(S+1)\}+E(S_x^2-S_y^2)+AS.I. \quad \ldots\ldots\ldots \quad (30)$$

The electronic spin S is 5/2. The values of the parameters are : $D=830$, $E=150$, and $A=-280$ Mc/s. Because the parameters are all of comparable magnitude the quantization is very mixed and the calculation of the energy levels and eigenstates can only be effected by numerical methods. The energy levels are given numerically by Bleaney and Ingram (Fig. 8 of their paper) ; it may be seen that they extend in a series from 0 to 8500 Mc/s with gaps averaging 400 Mc/s and nowhere exceeding 900 Mc/s.

Expressing transition probabilities in free-spin units as before, one may say that a series of pumping frequencies exists between 4500 and 8500 Mc/s with probabilities of order $(E/D)^2$ or 0·03, and amplifying frequencies between 60 Mc/s and 2000 Mc/s with probabilities of order unity. If a non-resonant microwave structure were used, the salt would provide amplification at 2220, 2160, 2040, 1980, 1920, 1440, 1200, 720, 600, 480, 180, 120 Mc/s, the pumping frequency being required to vary only from 8500 to 7000 Mc/s.

XII. Conclusion

The important fact which has emerged from the search for zero-field maser materials is that even with the few compounds of the eligible ions Cr^{2+}, Fe^{3+}, Ni^{2+}, and Gd^{3+} which have been studied a wide range of frequencies should be available. That the number of known suitable compounds is not greater is simply a consequence of the fact that attention in the past has been concentrated on compounds with properties either inessential or detrimental to zero-field maser action : namely, compounds easily obtainable as large crystals ; likely to lead to the discovery of nuclear spins ; possessing few inequivalent ions ; or characterized by a simple spin Hamiltonian.

There is need for systematic research into that great majority of compounds of the ions named which is as yet untouched. Much of the work may be best pioneered by the classical cavity-resonator technique (fixed frequency and variable magnetic field). The loss of sensitivity occasioned by the necessity, where it exists, to use small crystals should be offset by application of the modern technique of high-frequency field modulation which has proved so simple and sensitive (see, for example, Buckmaster and Scovil 1956 ; Llewellyn 1957). At the same time direct measurements at zero-field will be needed, since the work of Bleaney, Scovil, and Trenam (1954), one of the few examples of zero-field measurements, has shown that the spin Hamiltonian which fits measurements at fixed frequency and variable field may not correctly predict the zero-field levels. In the case of dilute gadolinium ethyl sulphate the discrepancy amounted to 7 per cent. or 100 Mc/s. The theoretical basis of this anomaly is not yet understood and more experimental data on zero-field splittings are desirable for the solution of this problem as well as for maser design.

When data become available for a large proportion of the stable compounds of suitable ions, it is possible that zero-field masers will be able to supersede magnetic-field masers in the majority of applications.

XIII. References

Andrew, E. R. (1955).—" Nuclear Magnetic Resonance." (Cambridge Univ. Press.)

Autler, S. H., and McAvoy, N. (1958).—*Phys. Rev.* **110** : 280.

Benzie, R. J., and Cooke, A. H. (1950).—*Proc. Phys. Soc.* A **63** : 201.

Bleaney, B. (1955).—*Disc. Farad. Soc.* No. 19 : 112.

Bleaney, B., Elliot, R. J., Scovil, H. E. D., and Trenam, R. S. (1951).—*Phil. Mag.* **42** : 1062.

Bleaney, B., and Ingram, D. J. E. (1951).—*Proc. Roy. Soc.* A **205** : 336.

Bleaney, B., Scovil, H. E. D., and Trenam, R. S. (1954).—*Proc. Roy. Soc.* A **223** : 15.

Bleaney, B., and Stevens, K. W. H. (1953).—*Rep. Progr. Phys.* **16** : 108.

Bleaney, B., and Trenam, R. S. (1954).—*Proc. Roy. Soc.* A **223** : 1.

Bloembergen, N. (1956).—*Phys. Rev.* **104** : 324.

Bowers, K. D. (1952).—*Proc. Phys. Soc.* A **65** : 860.

Bowers, K. D., and Owen, J. (1955).—*Rep. Progr. Phys.* **18** : 304.

Buckmaster, H. A., and Scovil, H. E. D. (1956).—*Canad. J. Phys.* **34** : 711.

Dieke, G. H., and Leopold, L. (1957).—*J. Opt. Soc. Amer.* **47** : 944.

Elliott, R. J., and Stevens, K. W. H. (1953).—*Proc. Roy. Soc.* A **219** : 387.

Eschenfelder, A. H., and Weidner, R. J. (1953).—*Phys. Rev.* **92** : 869.

Giordmaine, J. A., Alsop, L. E., Nash, F. R., and Townes, C. H. (1958).—*Phys. Rev.* **109** : 302.

Gorter, C. J. (1947).—" Paramagnetic Relaxation." (Elsevier Publishing Co.: London.)

Hutchison, C. A., Judd, B. R., and Pope, D. F. D. (1957).—*Proc. Phys. Soc.* B **70** : 514.

Hutchison, C. A., Llewellyn, P. M., Wong, E., and Dorain, P. (1956).—*Phys. Rev.* **102** : 292.

Jarrett, H. S. (1957).—*J. Chem. Phys.* **27** : 1298.

Kittel, C., and Abrahams, E. (1953).—*Phys. Rev.* **90** : 238.

Kornienko, L. S., and Prokhorov, A. M. (1957).—*J. Expt. Theor. Phys.* **33** : 805 ; (translation : *Soviet Phys. JETP* **6** : 620 (1958)).

Kramers, H. A. (1930).—*Proc. Acad. Sci. Amst.* **33** : 959.

Llewellyn, P. M. (1957).—*J. Sci. Instrum.* **34** : 236.

Low, W. (1956).—*Phys. Rev.* **103** : 1309.

Low, W. (1957).—*Phys. Rev.* **105** : 792.

McWhorter, A. L., and Meyer, J. W. (1958).—*Phys. Rev.* **109** : 312.

Meijer, P. H. E. (1951).—*Physica* **17** : 899.

Ono, K., Koide, S., Sekiyama, H., and Abe, H. (1954).—*Phys. Rev.* **96** : 38.

Pryce, M. H. L. (1950).—*Proc. Phys. Soc.* A **63** : 25.

Ryter, C. (1957).—*Helv. Phys. Acta* **30** : 353.

Scovil, H. E. D., Feher, G., and Seidel, F. (1957).—*Phys. Rev.* **105** : 762.

THE PHOTONEUTRON CROSS SECTION OF ^{9}Be IN THE INTERMEDIATE ENERGY RANGE

By H. H. Thies,* B. M. Spicer,* and J. E. E. Baglin*

[*Manuscript received December* 4, 1958]

Summary

The photoneutron cross section of ^{9}Be has been measured in the region from 6·5 to 18 MeV, using filtered bremsstrahlung radiation from an 18 MeV synchrotron. The integrated cross section is in agreement with an earlier experiment, but increased resolution has shown a more complex shape, with sharp maxima at $11 \cdot 25 \pm 0 \cdot 2$ and $13 \cdot 25 \pm 0 \cdot 2$ MeV. The significant features of the cross section are discussed and compared with the level scheme as it is known at present.

I. Introduction

Several studies have been made of the level structure of ^{9}Be, covering mainly the region of excitation up to 7 MeV. A summary of these experiments is given by Ajzenberg and Lauritsen (1955). Experiments on the photodisintegration of ^{9}Be have, with one exception, used monochromatic radiation of energy below 8 MeV. A summary of these experiments is given by Edge (1957).

The level structure of ^{9}Be in the region of excitation 11–17 MeV is so far almost unexplored. This is due to the difficulty of forming ^{9}Be in this region of excitation, either as the compound nucleus or as the final nucleus in reactions induced by charged particles or neutrons. The study of inelastic proton scattering is not conclusive in this energy region, since here the deuterons from the reaction $^9\mathrm{Be}(p,d)^8\mathrm{Be}$ complicate the picture, at least in the study of Benveniste, Finke, and Martinelli (1956). This region of excitation is open for study by γ-induced reactions, and with sufficient resolution, some information on the level structure of ^{9}Be should be obtainable.

The only two competing modes of disintegration of ^{9}Be for excitations below the (γ,p) threshold (16·9 MeV) are

$$^9\mathrm{Be}+\gamma\rightarrow{}^8\mathrm{Be}+n\rightarrow\alpha+\alpha+n, \quad \ldots\ldots\ldots\ldots\ldots \quad (1)$$

$$^9\mathrm{Be}+\gamma\rightarrow{}^5\mathrm{He}+\alpha\rightarrow\alpha+n+\alpha. \quad \ldots\ldots\ldots\ldots\ldots \quad (2)$$

The probability of de-excitation by γ-emission is considered to be so small as to be negligible. Hence, if the total neutron yield from the photodisintegration of ^{9}Be is measured, the cross section obtained from it will be the sum of the cross sections of the reactions (**1**) and (**2**), and is to very good approximation the cross section for photon absorption by the ^{9}Be nucleus. Maxima in this cross section and their relative strengths will thus give information about the excited states of ^{9}Be.

---

* Physics Department, University of Melbourne.

Nathans and Halpern (1953) measured the γ-induced neutron yield from ^{9}Be from threshold (1·66 MeV) up to 24 MeV in 1 MeV steps, using bremsstrahlung from a 25 MeV betatron. The cross section computed from this yield curve had two broad maxima, one of 1·6 mbarn height at 10 MeV and one 3 mbarn high at 22 MeV.

II. The Experiment

The experiment performed by Nathans and Halpern (1953) has been repeated with the Melbourne 18 MeV synchrotron for the energy interval 4·5–18 MeV, with increase of resolution.

The experimental arrangement used was almost identical with the one described in an earlier paper (Spicer *et al.* 1958). As in the experiment of Nathans and Halpern, a graphite filter was used to " harden " the γ-ray beam before it struck the beryllium target. The thickness of the graphite absorber used was 28 cm. Because of the large decrease in the absorption coefficient of γ-rays in carbon between the energies of 1 and 5 MeV, and its relatively constant value from there up to 20 MeV, the graphite absorber was used to reduce the yield contribution from the cross section between the threshold of the reaction and 4 MeV. This reduction means that any detail in the yield curve at energies higher than 4 MeV is relatively enhanced. Nathans and Halpern (1953) tested this procedure by comparing the cross section for the ^{209}Bi(γ,n) reaction obtained by measuring the yield curve with the absorber in with that obtained from a yield curve measured with no absorber. They found no change in the shape of the cross section curve. Thus, the experimental accuracy in the region 10–18 MeV can be increased by this use of the carbon absorber.

The " filtered " γ-radiation was passed through a transmission ionization chamber, and struck the target which consisted of 100 g of beryllium powder of better than 99·5 per cent. purity contained in a thin-walled polystyrene cylinder. The target was located in the paraffin " house " and the neutron yield was measured with BF_3 counters.

The neutron yield (counts per roentgen) was measured in steps of 0·19 MeV from 5·5 to 18 MeV. Above 10 MeV, at least 40,000 counts per synchrotron energy setting were obtained during several different runs. These runs were taken over a period of some 3 months. Results of individual runs agreed within statistics. A background run was made with the container empty.

The measured doses were corrected for temperature and pressure variations. The counting loss of the detecting system was determined experimentally, and was kept small throughout this experiment. The counting efficiency of the detecting system was checked regularly with a standard Ra-Be source.

III. Analysis of Results

The cross section was derived from the yield curve using the Penfold-Leiss method (Penfold and Leiss 1958). The interposition of the carbon filter necessitated only a slight modification of the original method of analysis. This will now be described briefly.

In the discussion, the following symbols will be used. Reference to these symbols in the actual experimental layout is shown in Figure 1. The γ-ray beam emitted from the synchrotron has a spectral energy distribution $N(E,E_0)$ which is normalized so that $\int_0^{E_0} N(E,E_0)\mathrm{d}E=1$. The dose given at synchrotron energy E_0 is written I photons/cm^2, which gives $I.N(E,E_0)\mathrm{d}E$ photons/cm^2 in the energy interval E to $E+\mathrm{d}E$ at the plane y if no absorber or ionization chamber were interposed.

The γ-ray beam then passes through the carbon filter, the transmission ionization chamber, and the target, in that order. Their effective thicknesses and γ-ray absorption coefficients are X_1, $\mu_1(E)$, X_2, $\mu_2(E)$, X, $\mu_3(E)$ respectively. The target has atomic mass number A and density ρ g cm^{-3}. N is Avogadro's number. The efficiency of the neutron counting system is η, which is determined by measuring the count rate when the calibrated Ra-Be source is placed at the centre of the region covered by the beam in the plane y. $G(x)$ is a function of the target coordinates. It allows for the target not being totally immersed in the γ-ray beam, as well as the variation of the γ-ray intensity over the length of the target according to the inverse square law, and for the neutron counting efficiency being a function of x for a small source. $\sigma(E)$ is the cross section for the nuclear absorption of photons by the target. $Y(E_0)$ is the yield as measured (counts/Lucite roentgen). $k.m(E)$ is the registering efficiency of the γ-ray monitor. k is a numerical constant dependent on the intensity units used.

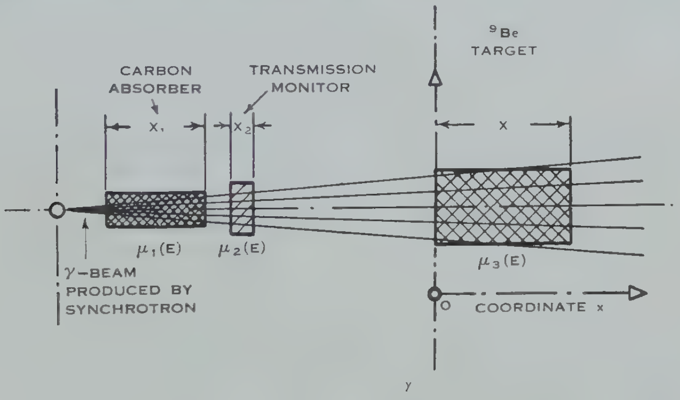

Fig. 1.—Relative positions of the carbon filter, transmission ionization chamber, and long beryllium target. The effective length and absorption coefficient symbols are shown with each object.

The following relation exists between $Y(E_0)$ and $\sigma(E)$

$$Y(E_0)=\frac{\int_0^{E_0} I.N(E,E_0)\exp\left[-\mu_1(E)X_1-\mu_2(E)X_2\right]\sigma(E)\mathrm{d}E\int_0^{X}(N\rho/A)\eta\exp\left[-\mu_3 x\right]G(x)\mathrm{d}x}{\int_0^{E_0} I.N(E,E_0)\exp\left[-\mu_1(E)X_1-\mu_2(E)X_2\right]k.m(E)\mathrm{d}E}. \quad \ldots\ldots\ldots\ldots\ldots\ldots (3)$$

The right-hand integral of the numerator is a function of E only. The integral in the denominator is a function of E_0 only. Thus one defines

$$J(E)=(N\rho/A)\int_0^X \eta \exp[-\mu_3(E)x]G(x)\mathrm{d}x, \quad \ldots\ldots\ldots\ldots\ldots\ldots\ldots\ldots \quad (4)$$

$$kF(E_0)=k\int_0^{E_0} N(E,E_0)\exp[-\mu_1X_1-\mu_2X_2]\,.\,m(E)\mathrm{d}E, \quad \ldots\ldots\ldots\ldots \quad (5)$$

and obtains finally for the " reduced yield " $y(E_0)$

$$y(E_0)=kF(E_0)\,.\,Y(E)=\int_0^{E_0} N(E,E_0)\exp[-\mu_1X_1-\mu_2X_2]\sigma(E)\,.\,J(E)\mathrm{d}E. \quad \ldots\ldots\ldots\ldots \quad (6)$$

Since the tables for the evaluation of the cross section are in terms of the intensity spectra $\varphi(E,E_0)$ rather than the number of photons spectra, $N(E,E_0)$, where $\varphi(E,E_0)=E.N(E,E_0)$, we define a " reduced cross section " $s(E)$ by the equation

$$s(E)=\{\sigma(E)J(E)\exp[-\mu_1X_1-\mu_2X_2]\}/E. \quad \ldots\ldots\ldots \quad (7)$$

Substituting this expression into (6) gives the integral equation in $s(E)$

$$y(E_0)=\int_0^{E_0} \varphi(E,E_0)s(E)\mathrm{d}E. \quad \ldots\ldots\ldots\ldots\ldots \quad (8)$$

Equation (8) is identical with the integral equation for which the Penfold-Leiss method gives solutions of $s(E)$ as functions of the $y(E_0)$. The function $\varphi(E,E_0)$ is known from bremsstrahlung theory, and is tabulated by Penfold and Leiss (1958). Thus one can obtain solutions for $s(E)$ and hence for $\sigma(E)$.

IV. Results

The experimental yield curve is shown in Figure 2. The absolute photoneutron cross section $\sigma(E)$, which was evaluated as outlined above, is shown in Figure 3. The photoneutron cross section covers only the region 6·5–18 MeV. The " area of statistical variation ", enclosing $\sigma(E)$, is computed from the statistical error of the measured yield curve points. Due to this factor and the finite resolution of this analysis, the cross section derived may deviate from its centre value within this region in any way provided it remains continuous and does not have a greater number of maxima, minima, and turning points than the centre value curve.

Since the cross section is that for nuclear absorption of photons by beryllium, the peaks in the cross section appear at the energies of excited states of ^{9}Be. Figure 4 shows the cross section curve plotted beside an energy level diagram (from Ajzenberg and Lauritsen 1955). Since Ajzenberg and Lauritsen's review paper, Almqvist, Allen, and Bigham (1955) have reported a previously unobserved level at 9·2 MeV. Except for this 9·2 MeV level, there is at least one independent confirmation of the existence of all known levels.

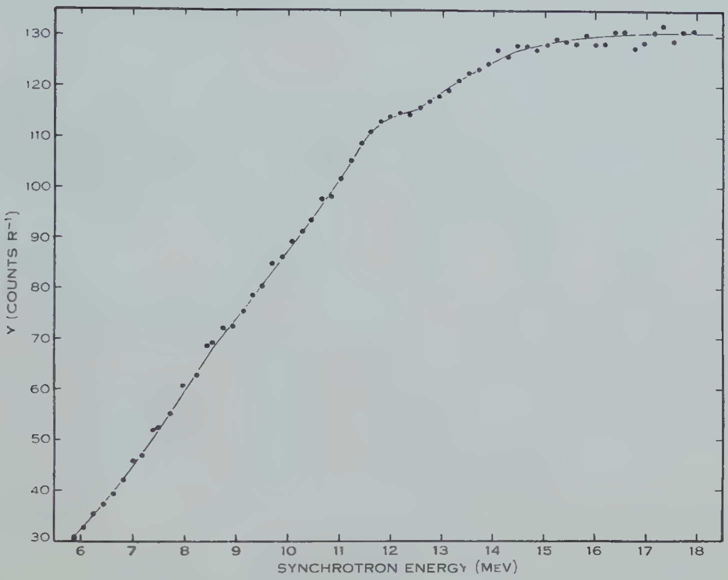

Fig. 2.—The experimental yield curve of photoneutrons from beryllium.

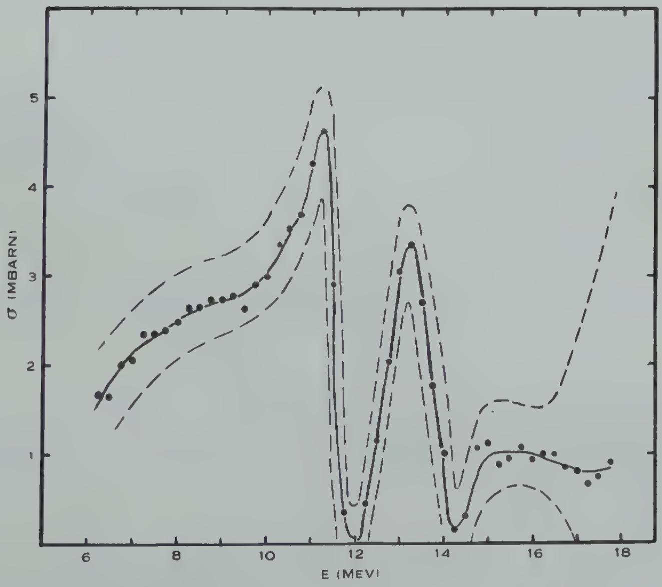

Fig. 3.—The cross section for production of photoneutrons from beryllium. The dashed lines represent the extremes of the area of statistical variation, which is to be interpreted as indicated in the text.

The maximum in the cross section curve at 11·25 ± 0·2 MeV unambiguously confirms the known level at 11·3 MeV. The known levels at 6·8 and 7·9 MeV are presumably responsible for the cross section in the energy region 6–8 MeV. The existence of considerable cross section between 8 and 11 MeV tends to confirm the existence of the 9·2 MeV level.

On the high energy side of the 11·25 MeV peak, the cross section has a maximum at 13·25 ± 0·2 MeV. This cannot be attributed to any known level. The peak has a width approximately the same as the 11·25 MeV level, and so the existence of one or more energy levels in this region is inferred. There is some support for the existence of an energy level at about 14 MeV in the work on the inelastic scattering of protons from beryllium described by Tyren and Maris (1958).

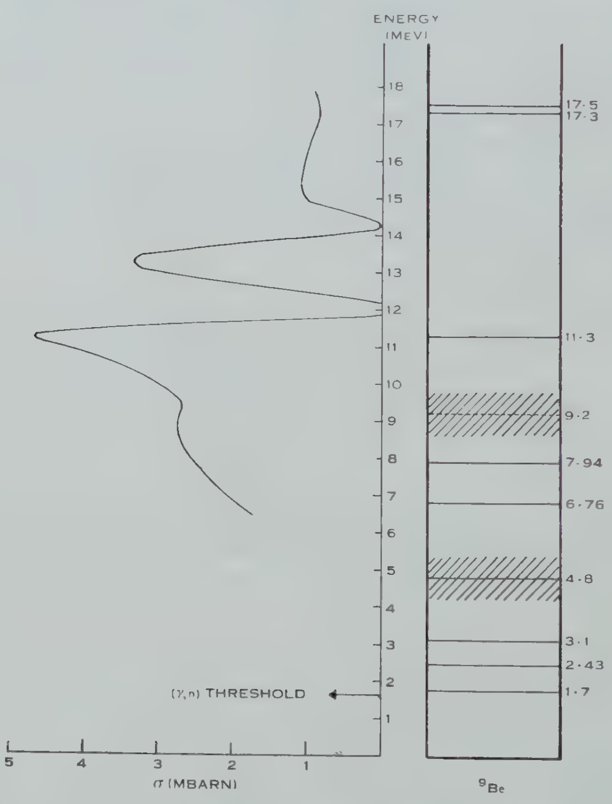

Fig. 4.—The cross section for nuclear absorption of photons in beryllium plotted beside a diagram of previously observed energy levels of ^{9}Be.

The integrated cross section for nuclear absorption of photons in ^{9}Be is 22 MeV-mbarn for the energy region from 6·5 to 18 MeV. This is in good agreement with a similar estimate based on the results of Nathans and Halpern (1953). These authors found a peak of height 3 mbarn at 22 MeV in the cross section derived from the yield of photoneutrons. If the 2·7 mbarn found by

Haslam *et al.* (1953) for the peak cross section of the 22 MeV resonance of the ^{9}Be(γ, p) reaction is added to the 3 mbarn noted above, we may give 5·7 mbarn as the height of the 22 MeV giant resonance of ^{9}Be. This giant resonance is considered to be due to electric dipole transitions.

V. Discussion of Results

It is of interest to seek information concerning the spin and parity of the 11·3 and the 13·3 MeV levels from the magnitude of the photon absorption cross section in these two cases. An estimate was made of the integrated cross section for absorption into these two levels, and is expected to be correct in absolute magnitude to within a factor of two. The estimate for the 13·3 MeV level is unambiguous, and involves only the assumption that the peak is due to one single level. In support of this assumption, it is noted that the levels of ^{9}Be at 4·8 and 9·2 MeV have widths exceeding 1 MeV. The shape of the 11·3 MeV level was deduced from the shape of the high energy side of it, since other levels interfere on the low energy side. The results are 4·0 and 3·9 MeV-mbarn respectively for the 11·3 and 13·3 MeV levels.

If the assumption is made that the levels are of Breit-Wigner shape, then

$$\int_{\text{level}} \sigma(E)\mathrm{d}E = \frac{7\cdot 7 S_0 \Gamma_\gamma}{E^2} G_n \text{ MeV-mbarn}, \quad \dots\dots\dots\dots \quad (9)$$

where E is the energy of the level in MeV,

S_0 is the statistical factor, which equals $(2J+1)/2(2I+1)$; here J is the spin of the excited state and I the spin of the ground state (for ^{9}Be, $S_0=(2J+1)/8$, since $I=3/2$),

Γ_γ is the radiative width of the level in electron-volts,

G_n is the branching ratio for neutron emission, which is unity here if we neglect decay of the excited state by radiation, compared to particle emission.

If a definite multipolarity is assumed for the γ-radiation absorbed by a particular level, then the possible values for the spin of that level are limited. Noting this, the minimum value for the Γ_γ of each of the levels may be calculated, and compared with the value of the rough single particle estimate of this radiative width (the Weisskopf unit (Weisskopf 1951)). This comparison is made in Table 1.

The values of the Weisskopf units were calculated from formulae given by Wilkinson (1956) in a summary of experimental data on radiative widths. In each case, the $E2$ Weisskopf unit is about 200 times smaller than the estimated radiative width. Wilkinson's survey indicates no radiative transition stronger than 14 times that indicated by the Weisskopf unit, and so it is inferred that the transitions to these two levels are not of the electric quadrupole type.

Further support to this idea is obtained from the sum rule for electric quadrupole transitions given by Levinger and Bethe (1950), namely,

$$\int_0^\infty \sigma(E2)\frac{\mathrm{d}E}{E} = \frac{4\pi^2}{137} \cdot \frac{2}{9} \cdot \frac{T.Z}{Mc^2}\langle r^2\rangle_{00},$$

where $\langle r^2\rangle_{00}$ is the expectation value of the squared displacement of the average nucleon from the centre of mass of the nucleus,

T is the average kinetic energy of the protons in the nucleus.

The insertion of the classical value of $0\cdot6R^2$ for $\langle r^2\rangle_{00}$ leads to too large a value of this quantity (Levinger and Bethe 1950; Levinger and Kent 1954) by a factor of approximately four. Bearing this in mind, we estimate $\int_0^\infty \sigma(E2)\mathrm{d}E/E$ for ^{9}Be to be approximately 0·2 mbarn. Computation of $\int(\sigma/E)\mathrm{d}E$ for the 11·3 MeV level and the 13·3 MeV level gives respectively 0·30 mbarn and 0·25 mbarn. It is scarcely possible that the sum rule would be exhausted by one single level, and so the possibility of electric quadrupole transitions is ruled out.

TABLE 1

COMPARISON OF THEORETICAL AND EXPERIMENTAL INFORMATION ON THE 11·3 AND 13·3 MeV LEVELS OF ^{9}Be

Property	11·3 MeV Level	13·3 MeV Level
$\int\sigma(E)\mathrm{d}E$	4·0 MeV-mbarn	3·9 MeV-mbarn
$\Gamma_\gamma(E1,M1),J_{\text{max.}}=5/2$	88 ev	119 ev
$\Gamma_\gamma(E2),J_{\text{max.}}=7/2$	66 ev	90 ev
$E1$ Weisskopf unit	686 ev	1120 ev
$M1$ Weisskopf unit	30 ev	49 ev
$E2$ Weisskopf unit	0·41 ev	0·74 ev
Γ_γ/E^3, dipole absorption assumed	0·061	0·051

The possibility of distinguishing between $E1$ and $M1$ transitions for these cases has now to be investigated. Wilkinson's survey of radiative widths (1956) indicated that $E1$ transitions have a most probable radiative width of about 0·032 Weisskopf unit, with a spread of about a factor of seven either way. The corresponding quantities for $M1$ transitions are a width of 0·15 Weisskopf units and a spread of a factor of 20 either way. Thus, on this basis, the observed transitions may be either $E1$ or $M1$.

Wilkinson suggests that a transition which shows a value of Γ_γ (eV)$/E^3$ (MeV) greater than 0·02 has about a 10 : 1 chance of being an $E1$ transition. Since, for the observed cases, Γ_γ/E^3 are 0·06 and 0·05, this suggests that they are electric dipole transitions.

A contrary argument comes from consideration of proton inelastic scattering data on ^{9}Be (Benveniste, Finke, and Martinelli 1956). In this work we consider the analysis of data on the 6·8 and 7·9 MeV levels. This can serve as a rough guide to expectations for the 11·3 and 13·3 MeV levels, since the integrated cross section for photon absorption by a single level is expected to increase approximately with E (Γ_γ varies as E^3, and there is a factor E^2 in the denominator of the expression for $\int\sigma\mathrm{d}E$). Benveniste, Finke, and Martinelli (1956) indicate that the 6·8 and 7·9 MeV levels have opposite parity. This conclusion is correct in spite of criticisms of their interpretation, which uses values for the nuclear radius of ^{9}Be that are too small (see Summers-Gill 1958). Since the cross section is approximately constant over the energy region 6–8 MeV in the photodisintegration, this indicates that there is not a large difference between the radiative widths for $E1$ and $M1$ transitions at these energies.

Thus we are unable to choose between $E1$ and $M1$ for the mode of absorption of photons into the 11·3 and 13·3 MeV levels. In any case, these two possibilities demand that the spin of the levels be 1/2, 3/2, or 5/2. Since the radiative transition in the region of 6–8 MeV is so strong, these possibilities also apply to the 6·8 and 7·9 MeV levels.

VI. CONCLUSIONS

The cross section for photon absorption by the ^{9}Be nucleus has been measured. Peaks in this cross section at 11·3 and 13·3 MeV are associated with levels in the beryllium nucleus at these energies. Consideration of the strength of the radiative transitions leads to the values of the spins of the levels of ^{9}Be at 6·8, 7·9, 11·3, 13·3 MeV coming from the possibilities 1/2, 3/2, 5/2, but no conclusion regarding the parity of these states was possible.

The study of this cross section in steps smaller than 0·25 MeV, as well as the study of the decay products of these levels, should throw further light on their properties.

VII. ACKNOWLEDGMENTS

The authors wish to acknowledge the encouragement given and the interest shown in this work by Professor Sir Leslie Martin. Two of us (H.H.T. and J.E.B.) wish to acknowledge research fellowships from Imperial Chemical Industries of Australia and New Zealand Ltd., which were held throughout this work.

VIII. REFERENCES

AJZENBERG, F., and LAURITSEN, T. (1955).—*Rev. Mod. Phys.* **27**: 77.

ALMQVIST, E., ALLEN, K. W., and BIGHAM, C. B. (1955).—*Phys. Rev.* **99**: 631A.

BENVENISTE, J., FINKE, R. G., and MARTINELLI, E. A. (1956).—*Phys. Rev.* **101**: 655.

EDGE, R. D. (1957).—*Nuclear Phys.* **2**: 485.

HASLAM, R. N. H., KATZ, L., CROSBY, E. H., SUMMERS-GILL, R. G., and CAMERON, A. G. W. (1953).—*Canad. J. Phys.* **31**: 210.

LEVINGER, J. S., and BETHE, H. A. (1950).—*Phys. Rev.* **78**: 115.

LEVINGER, J. S., and KENT, D. C. (1954).—*Phys. Rev.* **95**: 418.

NATHANS, R., and HALPERN, J. (1953).—*Phys. Rev.* **92**: 940.

PENFOLD, A. S., and LEISS, J. E. (1958).—Analysis of photo cross sections. Physics Research Laboratory, University of Illinois, Champaign, Illinois.

SPICER, B. M., THIES, H. H., BAGLIN, J. E. E., and ALLUM, F. R. (1958).—*Aust. J. Phys.* **11**: 298.

SUMMERS-GILL, R. G. (1958).—*Phys. Rev.* **109**: 1591.

TYREN, H., and MARIS, Th. A. J. (1958).—*Nuclear Phys.* **6**: 82.

WEISSKOPF, V. F. (1951).—*Phys. Rev.* **83**: 1073.

WILKINSON, D. H. (1956).—*Phil. Mag.* **1**: 127.

DIRAC CONTINUUM RADIAL WAVE FUNCTIONS

By H. S. Perlman* and B. A. Robson*

[*Manuscript received August* 12, 1958]

Summary

Tables of Dirac continuum radial wave functions for an electron in the Coulomb field of a mercury nucleus ($Z=80$) are presented for several energies and l's. Approximate methods of interpolation and extrapolation to regions not covered explicitly are indicated.

I. Introduction

The Dirac continuum wave functions for an electron in the Coulomb field of a heavy nucleus are required for the theoretical investigation of many atomic and nuclear problems. However, analytically, these functions are notoriously intractable. Firstly, they are non-separable in the many coordinate systems which induce separation in the Schrödinger wave functions and this imposes a severe restriction on the facility with which they can be used in certain problems. Allied difficulties such as non-integral parameters can also be cited. Furthermore, to the authors' knowledge, the only available tables of Dirac continuum radial wave functions are those of Glassgold and Mack (1954), which are valid only in the extreme relativistic energy region. For these reasons, the following tables, which were calculated during an investigation of specific ionization at relativistic energies, are presented separately.

II. Dirac Wave Functions for a Coulomb Field

The following units are used throughout: energy is measured in m_0c^2, length in $\hbar/m_0c$, and momentum in m_0c. Following Rose (1937), the four components, ψ_1, ψ_2, ψ_3, ψ_4, of the Dirac wave function for an electron, which has momentum p and energy $W=(p^2+1)^{\frac{1}{2}}$ in the continuum and which is in a Coulomb field due to Z times the electronic charge, may be expressed in spherical polar coordinates r, θ, φ for the two spin states $j=l\pm\frac{1}{2}$.

For $j=l+\frac{1}{2}$:

$$\left.\begin{aligned}
\psi_1&=\mathrm{i}\left(\frac{l-m+\frac{3}{2}}{2l+3}\right)^{\frac{1}{2}}Y_{l+1,\,m-\frac{1}{2}}f_\varkappa,\\
\psi_2&=\mathrm{i}\left(\frac{l+m+\frac{3}{2}}{2l+3}\right)^{\frac{1}{2}}Y_{l+1,\,m+\frac{1}{2}}f_\varkappa,\\
\psi_3&=\left(\frac{l+m+\frac{1}{2}}{2l+1}\right)^{\frac{1}{2}}Y_{l,\,m-\frac{1}{2}}g_\varkappa,\\
\psi_4&=-\left(\frac{l-m+\frac{1}{2}}{2l+1}\right)^{\frac{1}{2}}Y_{l,\,m+\frac{1}{2}}g_\varkappa,\\
&l\geqslant 0,\quad -(l+1)\leqslant m-\tfrac{1}{2}\leqslant l.
\end{aligned}\right\}\quad\ldots\ldots\ldots\ldots\quad(\mathbf{1a})$$

---

* Physics Department, University of Melbourne.

For $j=l-\frac{1}{2}$:

$$\left.\begin{aligned}\psi_1&=\mathrm{i}\left(\frac{l+m-\frac{1}{2}}{2l-1}\right)^{\frac{1}{2}}Y_{l-1,\,m-\frac{1}{2}}f_\varkappa,\\ \psi_2&=-\mathrm{i}\left(\frac{l-m-\frac{1}{2}}{2l-1}\right)^{\frac{1}{2}}Y_{l-1,\,m+\frac{1}{2}}f_\varkappa,\\ \psi_3&=\left(\frac{l-m+\frac{1}{2}}{2l+1}\right)^{\frac{1}{2}}Y_{l,\,m-\frac{1}{2}}g_\varkappa,\\ \psi_4&=\left(\frac{l+m+\frac{1}{2}}{2l+1}\right)^{\frac{1}{2}}Y_{l,\,m+\frac{1}{2}}g_\varkappa,\end{aligned}\right\}\quad\ldots\ldots\ldots\ldots\ \text{(1b)}$$

$$l\geqslant 1,\quad -l\leqslant m-\tfrac{1}{2}\leqslant l-1.$$

$Y_{l,m}(\theta,\varphi)$ are normalized spherical harmonics, and the $f_\varkappa(p,\rho)$, $g_\varkappa(p,\rho)$ are the radial wave functions, with $\rho=2pr$. j represents the total angular momentum quantum number, l the quantum number which in the non-relativistic limit is identified with the orbital momentum quantum number, and m the magnetic quantum number.

The parameter $\varkappa$ is defined so that

$$\left.\begin{aligned}\varkappa&=-(j+\tfrac{1}{2})=-(l+1),&&\text{when } j=l+\tfrac{1}{2},\\ \varkappa&=(j+\tfrac{1}{2})=l,&&\text{when } j=l-\tfrac{1}{2}.\end{aligned}\right\}\quad\ldots\ldots\ldots\ \text{(2)}$$

The regular continuum radial wave functions f, g, normalized in the energy scale, can be written

$$\left\{\begin{matrix}f_\varkappa(p,\rho)\\ g_\varkappa(p,\rho)\end{matrix}\right\}=N_\mp(\varkappa,\rho)[R_\varkappa(p,\rho)\mp R^*_\varkappa(p,\rho)],\quad\ldots\ldots\ldots\ldots\ \text{(3a)}$$

where

$$R_\varkappa(p,\rho)=\rho^{-3/2}K(\varkappa,p)M(\varkappa,p,\rho),\quad\ldots\ldots\ldots\ldots\ \text{(3b)}$$

$$N_\mp(\varkappa,p)=p^{\frac{1}{2}}(1\mp W)^{\frac{1}{2}}e^{\pi\eta/2}\,|\,\Gamma(\gamma+\mathrm{i}\eta)\,|\,[\pi^{\frac{1}{2}}\Gamma(2\gamma+1)]^{-1},\quad\ldots\ \text{(3c)}$$

$$M(\varkappa,p,\rho)=e^{-\mathrm{i}\rho/2}(\mathrm{i}\rho)^{\gamma+\frac{1}{2}}{}_1F_1(\gamma+1+\mathrm{i}\eta,\,2\gamma+1,\,\mathrm{i}\rho),\quad\ldots\ldots\ \text{(3d)}$$

$$K(\varkappa,p)=\mathrm{i}^{-\gamma-\frac{1}{2}}[(\gamma+\mathrm{i}\eta)(-\varkappa+\mathrm{i}\alpha Z/p)]^{\frac{1}{2}},\quad\ldots\ldots\ldots\ \text{(3e)}$$

$$\gamma=(\varkappa^2-\alpha^2Z^2)^{\frac{1}{2}},\quad\ldots\ldots\ldots\ldots\ \text{(3f)}$$

$$\eta=\alpha ZW/p,\quad\ldots\ldots\ldots\ldots\ \text{(3g)}$$

and α, the fine structure constant, is taken as 1/137.

The functions $M(\varkappa,p,\rho)$ are the Whittaker functions $M_{-\mathrm{i}\eta-\frac{1}{2},\,\gamma}(\mathrm{i}\rho)$ and are solutions of the differential equation (Erdelyi *et al.* 1953)

$$d^2M(\mathrm{i}\rho)/d\rho^2+\{\tfrac{1}{4}+\mathrm{i}(-\mathrm{i}\eta-\tfrac{1}{2})/\rho+(\tfrac{1}{4}-\gamma^2)/\rho^2\}M(\mathrm{i}\rho)=0.\quad\ldots\ \text{(4)}$$

Substituting

$$M=X+\mathrm{i}Y\quad\ldots\ldots\ldots\ \text{(5a)}$$

and

$$\tfrac{1}{4}+\mathrm{i}(-\mathrm{i}\eta-\tfrac{1}{2})/\rho+(\tfrac{1}{4}-\gamma^2)/\rho^2=F+\mathrm{i}G\quad\ldots\ldots\ldots\ \text{(5b)}$$

into (4) gives two coupled real equations :

$$X''+FX-GY=0, \quad \dots\dots\dots\dots\dots\dots \quad \textbf{(6a)}$$

$$Y''+FY+GX=0. \quad \dots\dots\dots\dots\dots\dots \quad \textbf{(6b)}$$

III. METHOD OF COMPUTATION OF THE RADIAL FUNCTIONS

The equations (**6a**), (**6b**) were solved by numerical integration from near the origin, using the recurrence formulae

$$(z_{n+1})_{\text{approx}}=2z_{n-1}-z_{n-3}+4h^2(z''_{n-1}+\tfrac{1}{3}\Delta^2 z''_{n-1}) \quad \dots\dots \quad \textbf{(7a)}$$

to integrate ahead, and

$$z_{n+1}=2z_n-z_{n-1}+h^2\left(z''_n+\frac{1}{12}\Delta^2 z''_n\right) \quad \dots\dots\dots\dots \quad \textbf{(7b)}$$

to provide the correction. It was assumed that the interval in ρ,h, was taken sufficiently small so that only one application of the above was required. For $0<\rho\leqslant 8$, h was taken to be $0\cdot 02$ while for $8<\rho\leqslant 16$, h was taken to be $0\cdot 2$. The initial values near the origin were computed using the series expansion for the Whittaker confluent hypergeometric functions.

These calculations were carried out on the CSIRAC (Physics Department, University of Melbourne) for $Z=80$ and for a range of $\varkappa$ and p.

The reason for solving for M rather than R is that M depends only upon $|\varkappa|$ and not $\varkappa$ and thus the values were obtained simultaneously for the two spin states. The complex gamma functions required for the coefficients N were obtained by interpolation from the National Bureau of Standards table (1954).

IV. DESCRIPTION OF TABLES

The radial wave functions were calculated for $\varkappa=\pm 1$, ± 2, ± 3, ± 4, and $p=0\cdot 2$, $0\cdot 4$, $0\cdot 6$, $0\cdot 8$. In terms of l, the above values of $\varkappa$ correspond, for the case $j=l+\frac{1}{2}$, to $l=0$, 1, 2, 3, and for the case $j=l-\frac{1}{2}$, to $l=1$, 2, 3, 4. The integrations were effected from near the origin to a distance $\rho=16$, which corresponds to a radial distance, for $p=0\cdot 8$, of five times the K shell radius of mercury.

The $M=X+\mathrm{i}Y$ are tabulated in Table 1 in terms of mantissa and power of ten. In the range $0<\rho\leqslant 8$, the values are accurate to better than $0\cdot 1$ per cent. In the range $8<\rho\leqslant 16$, the error in the values X and Y is considerably larger (generally $\sim$2 per cent.) on account of the larger interval employed in the numerical integration.

The $K=x+\mathrm{i}y$ are tabulated in Table 2 correct to $0\cdot 1$ per cent. The normalizing factors N are given in Table 3 to an accuracy of $0\cdot 5$ per cent.

The normalized radial wave functions can be written explicitly in terms of the tabulated functions

$$f_\varkappa(p,\rho)=2\mathrm{i}\rho^{-3/2}N_-(\varkappa,p)[y(\varkappa,p)X(\varkappa,p)+x(\varkappa,p)Y(\varkappa,p)], \quad \dots \quad \textbf{(8a)}$$

$$g_\varkappa(p,\rho)=2\rho^{-3/2}N_+(\varkappa,p)[x(\varkappa,p)X(\varkappa,p)-y(\varkappa,p)Y(\varkappa,p)]. \quad \dots \quad \textbf{(8b)}$$

Table 1

$M(\varkappa,p,\rho)=X(\varkappa,p,\rho)+\mathrm{i}Y(\varkappa,p,\rho)$

ρ	$\lvert\varkappa\rvert=1$															
	$p=0·2$				$p=0·4$				$p=0·6$				$p=0·8$			
	X		Y		X		Y		X		Y		X		Y	
0·2	−4·840	−2	8·250	−2	−5·405	−2	9·241	−2	−5·590	−2	9·566	−2	−5·677	−2	9·717	−2
0·4	−1·004	−1	1·539	−1	−1·263	−1	1·962	−1	−1·352	−1	2·109	−1	−1·394	−1	2·178	−1
0·6	−1·402	−1	1·900	−1	−2·006	−1	2·821	−1	−2·225	−1	3·159	−1	−2·332	−1	3·322	−1
0·8	−1·638	−1	1·909	−1	−2·706	−1	3·422	−1	−3·116	−1	4·013	−1	−3·319	−1	4·304	−1
1·0	−1·705	−1	1·624	−1	−3·324	−1	3·743	−1	−3·981	−1	4·627	−1	−4·312	−1	5·071	−1
1·2	−1·615	−1	1·122	−1	−3·832	−1	3·787	−1	−4·785	−1	4·982	−1	−5·275	−1	5·598	−1
1·4	−1·387	−1	4·840	−2	−4·209	−1	3·577	−1	−5·500	−1	5·079	−1	−6·179	−1	5·873	−1
1·6	−1·047	−1	−2·170	−2	−4·445	−1	3·141	−1	−6·105	−1	4·926	−1	−6·995	−1	5·895	−1
1·8	−6·232	−2	−9·152	−2	−4·531	−1	2·516	−1	−6·580	−1	4·541	−1	−7·702	−1	5·674	−1
2·0	−1·450	−2	−1·557	−1	−4·466	−1	1·742	−1	−6·911	−1	3·947	−1	−8·277	−1	5·223	−1
2·2	3·583	−2	−2·100	−1	−4·254	−1	8·576	−2	−7·088	−1	3·173	−1	−8·705	−1	4·563	−1
2·4	8·592	−2	−2·515	−1	−3·902	−1	−9·512	−3	−7·105	−1	2·248	−1	−8·973	−1	3·718	−1
2·6	1·333	−1	−2·781	−1	−3·422	−1	−1·077	−1	−6·961	−1	1·206	−1	−9·072	−1	2·714	−1
2·8	1·757	−1	−2·892	−1	−2·827	−1	−2·053	−1	−6·657	−1	8·093	−3	−8·995	−1	1·581	−1
3·0	2·114	−1	−2·848	−1	−2·133	−1	−2·987	−1	−6·198	−1	−1·094	−1	−8·743	−1	3·510	−2
3·2	2·390	−1	−2·655	−1	−1·358	−1	−3·851	−1	−5·590	−1	−2·285	−1	−8·317	−1	−9·446	−2
3·4	2·574	−1	−2·328	−1	−5·214	−2	−4·617	−1	−4·846	−1	−3·461	−1	−7·722	−1	−2·273	−1
3·6	2·661	−1	−1·886	−1	3·559	−2	−5·264	−1	−3·978	−1	−4·591	−1	−6·966	−1	−3·604	−1
3·8	2·649	−1	−1·351	−1	1·253	−1	−5·775	−1	−3·001	−1	−5·648	−1	−6·061	−1	−4·907	−1
4·0	2·538	−1	−7·493	−2	2·149	−1	−6·138	−1	−1·934	−1	−6·608	−1	−5·021	−1	−6·153	−1
4·2	2·334	−1	−1·058	−2	3·023	−1	−6·342	−1	−7·955	−2	−7·446	−1	−3·861	−1	−7·316	−1
4·4	2·044	−1	5·527	−2	3·855	−1	−6·386	−1	3·939	−2	−8·145	−1	−2·599	−1	−8·369	−1
4·6	1·678	−1	1·201	−1	4·627	−1	−6·270	−1	1·612	−1	−8·686	−1	−1·254	−1	−9·290	−1
4·8	1·248	−1	1·815	−1	5·321	−1	−5·994	−1	2·838	−1	−9·059	−1	1·524	−2	−1·006	
5·0	7·684	−2	2·372	−1	5·923	−1	−5·567	−1	4·049	−1	−9·255	−1	1·598	−1	−1·066	
5·2	2·540	−2	2·855	−1	6·420	−1	−4·998	−1	5·223	−1	−9·267	−1	3·059	−1	−1·109	
5·4	−2·795	−2	3·249	−1	6·800	−1	−4·299	−1	6·340	−1	−9·096	−1	4·512	−1	−1·133	
5·6	−8·164	−2	3·540	−1	7·054	−1	−3·486	−1	7·380	−1	−8·743	−1	5·935	−1	−1·137	
5·8	−1·341	−1	3·720	−1	7·178	−1	−2·577	−1	8·324	−1	−8·215	−1	7·305	−1	−1·101	
6·0	−1·840	−1	3·785	−1	7·167	−1	−1·588	−1	9·153	−1	−7·519	−1	8·598	−1	−1·086	
6·2	−2·298	−1	3·734	−1	7·024	−1	−5·386	−2	9·854	−1	−6·667	−1	9·795	−1	−1·031	
6·4	−2·703	−1	3·570	−1	6·747	−1	5·504	−2	1·041		−5·675	−1	1·087		−9·576	−1
6·6	−3·045	−1	3·297	−1	6·340	−1	1·658	−1	1·082		−4·561	−1	1·182		−8·666	−1
6·8	−3·314	−1	2·925	−1	5·809	−1	2·765	−1	1·106		−3·340	−1	1·262		−7·592	−1
7·0	−3·505	−1	2·465	−1	5·161	−1	3·850	−1	1·114		−2·035	−1	1·325		−6·370	−1
7·2	−3·610	−1	1·930	−1	4·406	−1	4·894	−1	1·105		−6·660	−2	1·370		−5·018	−1
7·4	−3·629	−1	1·335	−1	3·441	−1	5·638	−1	1·079		7·439	−2	1·397		−3·557	−1
7·6	−3·559	−1	6·958	−2	2·501	−1	6·457	−1	1·037		2·171	−1	1·405		−2·008	−1
7·8	−3·403	−1	3·003	−3	1·500	−1	7·165	−1	9·778	−1	3·592	−1	1·393		−3·927	−2
8·0	−3·164	−1	−6·453	−2	4·539	−2	7·751	−1	9·029	−1	4·983	−1	1·361		1·264	−1
8·2	−2·84	−1	−1·31	−1	−6·20	−2	8·20	−1	8·12	−1	6·32	−1	1·31		2·74	−1
8·4	−2·45	−1	−1·96	−1	−1·70	−1	8·51	−1	7·08	−1	7·58	−1	1·24		4·60	−1
8·6	−1·99	−1	−2·56	−1	−2·78	−1	8·66	−1	5·92	−1	8·74	−1	1·15		6·22	−1
8·8	−1·49	−1	−3·10	−1	−3·82	−1	8·66	−1	4·64	−1	9·78	−1	1·04		7·79	−1
9·0	−9·36	−2	−3·58	−1	−4·82	−1	8·51	−1	3·27	−1	1·07		9·15	−1	9·27	−1

TABLE 1 (*Continued*)

ρ	$\lvert\varkappa\rvert=1$															
	$p=0{\cdot}2$				$p=0{\cdot}4$				$p=0{\cdot}6$				$p=0{\cdot}8$			
	X		*Y*		*X*		*Y*		*X*		*Y*		*X*		*Y*	
9·2	−3·57	−2	−3·98	−1	−5·76	−1	8·20	−1	1·83	−1	1·15		7·76	−1	1·06	
9·4	2·40	−2	−4·28	−1	−6·63	−1	7·75	−1	3·39	−2	1·20		6·24	−1	1·19	
9·6	8·40	−2	−4·50	−1	−7·39	−1	7·15	−1	−1·18	−1	1·25		4·61	−1	1·30	
9·8	1·32	−1	−4·60	−1	−8·06	−1	6·42	−1	−2·71	−1	1·27		2·89	−1	1·39	
10·0	2·00	−1	−4·61	−1	−8·60	−1	5·57	−1	−4·23	−1	1·27		1·10	−1	1·46	
10·2	2·53	−1	−4·51	−1	−9·02	−1	4·61	−1	−5·71	−1	1·26		−7·31	−2	1·52	
10·4	3·02	−1	−4·31	−1	−9·30	−1	3·56	−1	−7·14	−1	1·23		−2·58	−1	1·55	
10·6	3·46	−1	−4·01	−1	−9·45	−1	2·44	−1	−8·49	−1	1·17		−4·43	−1	1·56	
10·8	3·82	−1	−3·62	−1	−9·44	−1	1·26	−1	−9·74	−1	1·10		−6·25	−1	1·55	
11·0	4·12	−1	−3·15	−1	−9·29	−1	4·22	−3	−1·09		1·01		−8·01	−1	1·52	
11·2	4·33	−1	−2·61	−1	−9·00	−1	−1·19	−1	−1·19		9·10	−1	−9·70	−1	1·47	
11·4	4·47	−1	−2·00	−1	−8·57	−1	−2·43	−1	−1·27		7·91	−1	−1·13		1·40	
11·6	4·51	−1	−1·35	−1	−8·00	−1	−3·63	−1	−1·34		6·59	−1	−1·27		1·30	
11·8	4·47	−1	−6·61	−2	−7·30	−1	−4·80	−1	−1·39		5·16	−1	−1·41		1·19	
12·0	4·33	−1	4·64	−3	−6·48	−1	−5·91	−1	−1·43		3·63	−1	−1·52		1·07	
12·2	4·12	−1	7·63	−2	−5·56	−1	−6·94	−1	−1·44		2·03	−1	−1·62		9·09	−1
12·4	3·82	−1	1·47	−1	−4·54	−1	−7·87	−1	−1·44		3·76	−2	−1·70		7·47	−1
12·6	3·44	−1	2·16	−1	−3·44	−1	−8·69	−1	−1·41		−1·31	−1	−1·75		5·72	−1
12·8	2·99	−1	2·80	−1	−2·27	−1	−9·39	−1	−1·37		−2·99	−1	−1·79		3·88	−1
13·0	2·48	−1	3·40	−1	−1·06	−1	−9·96	−1	−1·31		−4·66	−1	−1·80		1·96	−1
13·2	1·92	−1	3·94	−1	1·85	−2	−1·04		−1·23		−6·28	−1	−1·79		−2·03	−3
13·4	1·32	−1	4·41	−1	1·44	−1	−1·06		−1·13		−7·84	−1	−1·76		−2·02	−1
13·6	6·87	−2	4·71	−1	2·69	−1	−1·08		−1·01		−9·31	−1	−1·71		−4·03	−1
13·8	3·26	−3	5·09	−1	3·92	−1	−1·07		−8·86	−1	−1·07		−1·63		−6·00	−1
14·0	−6·32	−2	5·30	−1	5·11	−1	−1·05		−7·44	−1	−1·19		−1·53		−7·93	−1
14·2	−1·29	−1	5·40	−1	6·24	−1	−1·01		−5·91	−1	−1·30		−1·41		−9·77	−1
14·4	−1·93	−1	5·41	−1	7·29	−1	−9·60	−1	−4·28	−1	−1·39		−1·27		−1·15	
14·6	−2·54	−1	5·31	−1	8·26	−1	−8·93	−1	−2·57	−1	−1·47		−1·12		−1·31	
14·8	−3·12	−1	5·12	−1	9·12	−1	−8·12	−1	−8·16	−2	−1·53		−9·47	−1	−1·46	
15·0	−3·65	−1	4·82	−1	9·86	−1	−7·19	−1	9·73	−2	−1·56		−7·62	−1	−1·59	
15·2	−4·12	−1	4·44	−1	1·05		−6·14	−1	2·77	−1	−1·58		−5·65	−1	−1·70	
15·4	−4·52	−1	3·98	−1	1·09		−4·99	−1	4·55	−1	−1·57		−3·60	−1	−1·79	
15·6	−4·84	−1	3·43	−1	1·14		−3·75	−1	6·30	−1	−1·55		−1·47	−1	−1·86	
15·8	−5·09	−1	2·82	−1	1·14		−2·45	−1	7·98	−1	−1·50		6·92	−2	−1·91	
16·0	−5·25	−1	2·16	−1	1·15		−1·15	−1	9·58	−1	−1·44		2·87	−1	−1·93	
	$\lvert\varkappa\rvert=2$															
0·2	−1·423	−2	−1·127	−2	−1·510	−2	−1·195	−2	−1·538	−2	−1·217	−2	−1·551	−2	−1·227	−2
0·4	−6·536	−2	−5·415	−2	−7·379	−2	−6·102	−2	−7·659	2	−6·330	−2	−7·790	−2	−6·436	−2
0·6	−1·489	−1	−1·293	−1	−1·794	−1	−1·551	−1	−1·898	−1	−1·640	−1	−1·948	−1	−1·681	−1
0·8	−2·534	−1	−2·314	−1	−3·269	−1	−2·959	−1	−3·529	−1	−3·188	−1	−3·655	−1	−3·297	−1
1·0	−3·660	−1	−3·522	−1	−5·075	−1	−4·815	−1	−5·595	−1	−5·288	−1	−5·848	−1	−5·517	−1
1·2	−4·744	−1	−4·829	−1	−7·107	−1	−7·076	−1	−8·006	−1	−7·925	−1	−8·451	−1	−8·344	−1
1·4	−5·682	−1	−6·147	−1	−9·251	−1	−9·683	−1	−1·066		−1·107		−1·137		−1·176	
1·6	−6·394	−1	−7·396	−1	−1·140		−1·256		−1·344		−1·466		−1·449		−1·572	
1·8	−6·820	−1	−8·501	−1	−1·344		−1·563		−1·625		−1·864		−1·770		−2·018	
2·0	−6·925	−1	−9·397	−1	−1·528		−1·881		−1·897		−2·293		−2·090		−2·505	

TABLE 1 (*Continued*)

ρ	|κ|=2															
	$p=0\cdot2$				$p=0\cdot4$				$p=0\cdot6$				$p=0\cdot8$			
	X		*Y*		*X*		*Y*		*X*		*Y*		*X*		*Y*	
2·2	−6·695	−1	−1·003		−1·682		−2·200		−2·149		−2·744		−2·397		−3·028	
2·4	−6·138	−1	−1·038		−1·800		−2·513		−2·374		−3·208		−2·681		−3·575	
2·6	−5·279	−1	−1·041		−1·876		−2·811		−2·561		−3·675		−2·932		−4·139	
2·8	−4·156	−1	−1·012		−1·904		−3·086		−2·702		−4·137		−3·140		−4·707	
3·0	−2·817	−1	−9·509	−1	−1·882		−3·330		−2·792		−4·585		−3·297		−5·272	
3·2	−1·319	−1	−8·594	−1	−1·810		−3·535		−2·825		−5·010		−3·397		−5·825	
3·4	2·762	−2	−7·401	−1	−1·686		−3·695		−2·797		−5·400		−3·434		−6·352	
3·6	1·906	−1	−5·966	−1	−1·513		−3·805		−2·707		−5·748		−3·403		−6·845	
3·8	3·507	−1	−4·330	−1	−1·295		−3·861		−2·553		−6·045		−3·302		−7·292	
4·0	5·021	−1	−2·540	−1	−1·035		−3·859		−2·336		−6·282		−3·131		−7·684	
4·2	6·392	−1	−6·462	−2	−7·380	−1	−3·797		−2·060		−6·454		−2·890		−8·012	
4·4	7·574	−1	1·297	−1	−4·111	−1	−3·674		−1·728		−6·555		−2·580		−8·267	
4·6	8·524	−1	3·236	−1	−6·054	−2	−3·491		−1·343		−6·579		−2·205		−8·447	
4·8	9·211	−1	5·118	−1	3·061	−1	−3·250		−9·129	−1	−6·524		−1·768		−8·543	
5·0	9·614	−1	6·892	−1	6·810	−1	−2·953		−4·438	−1	−6·389		−1·276		−8·552	
5·2	9·719	−1	8·512	−1	1·056		−2·604		5·654	−2	−6·176		−7·353	−1	−8·470	
5·4	9·524	−1	9·934	−1	1·423		−2·208		5·798	−1	−5·882		−1·536	−1	−8·291	
5·6	9·033	−1	1·112		1·775		−1·771		1·117		−5·510		4·605	−1	−8·013	
5·8	8·261	−1	1·205		2·104		−1·299		1·658		−5·061		1·097		−7·639	
6·0	7·232	−1	1·269		2·403		−7·984	−1	2·194		−4·539		1·747		−7·168	
6·2	5·974	−1	1·302		2·665		−2·767	−1	2·715		−3·950		2·398		−6·605	
6·4	4·522	−1	1·305		2·884		2·581	−1	3·213		−3·301		3·042		−5·956	
6·6	2·917	−1	1·276		3·056		7·975	−1	3·678		−2·597		3·667		−5·225	
6·8	1·200	−1	1·217		3·177		1·333		4·100		−1·849		4·262		−4·422	
7·0	−5·810	−2	1·129		3·242		1·857		4·474		−1·064		4·819		−3·552	
7·2	−2·381	−1	1·013		3·251		2·361		4·790		−2·524	−1	5·327		−2·627	
7·4	−4·153	−1	8·734	−1	3·201		2·836		5·043		5·757	−1	5·777		−1·654	
7·6	−5·854	−1	7·119	−1	3·094		3·275		5·228		1·410		6·160		−6·467	−1
7·8	−7·441	−1	5·325	−1	2·929		3·671		5·339		2·238		6·469		3·850	−1
8·0	−8·874	−1	3·390	−1	2·709		4·017		5·374		3·051		6·698		1·428	
8·2	−1·01		1·35	−1	2·44		4·31		5·33		3·84		6·84		2·47	
8·4	−1·11		−7·36	−2	2·11		4·53		5·21		4·58		6·89		3·50	
8·6	−1·19		−2·84	−1	1·75		4·70		5·00		5·28		6·85		4·50	
8·8	−1·24		−4·90	−1	1·35		4·79		4·72		5·93		6·72		5·46	
9·0	−1·26		−6·89	−1	9·12	−1	4·81		4·37		6·50		6·49		6·38	
9·2	−1·25		−8·75	−1	4·53	−1	4·77		3·94		7·00		6·16		7·23	
9·4	−1·22		−1·05		−2·30	−2	4·65		3·44		7·42		5·75		8·00	
9·6	−1·15		−1·20		−5·09	−1	4·46		2·89		7·74		5·25		8·69	
9·8	−1·06		−1·33		−9·96	−1	4·20		2·28		7·97		4·66		9·29	
10·0	−9·50	−1	−1·43		−1·48		3·88		1·63		8·11		4·00		9·78	
10·2	−8·13	−1	−1·51		−1·94		3·49		8·50	−1	8·06		3·28		1·02	1
10·4	−6·56	−1	−1·55		−2·39		3·05		1·23	−1	7·97		2·49		1·04	1
10·6	−4·84	−1	−1·57		−2·80		2·56		−6·21	−1	7·78		1·66		1·06	1
10·8	−2·98	−1	−1·56		−3·18		2·03		−1·37		7·49		7·79	−1	1·06	1
11·0	−1·04	−1	−1·51		−3·52		1·47		−2·12		7·09		−1·26	−1	1·05	1
11·2	9·46	−2	−1·44		−3·81		8·70	−1	−2·85		6·61		−1·05		1·03	1
11·4	2·94	−1	−1·34		−4·04		4·60	−1	−3·55		6·03		−1·98		9·91	
11·6	4·91	−1	−1·21		−4·22		−3·70	−1	−4·23		5·36		−2·90		9·43	
11·8	6·79	−1	−1·06		−4·33		−9·98	−1	−4·85		4·62		−3·80		8·83	
12·0	8·57	−1	−8·84	−1	−4·38		−1·62		−5·42		3·82		−4·68		8·13	

TABLE 1 (*Continued*)

ρ	$\lvert\varkappa\rvert=2$															
	$p=0\cdot2$				$p=0\cdot4$				$p=0\cdot6$				$p=0\cdot8$			
	X		Y		X		Y		X		Y		X		Y	
12·2	1·02		−6·92	−1	−4·37		−2·22		−5·93		2·95		−5·63		7·00	
12·4	1·17		−4·86	−1	−4·29		−2·80		−6·37		2·04		−6·39		6·07	
12·6	1·29		−2·69	−1	−4·14		−3·35		−6·73		1·09		−7·09		5·06	
12·8	1·39		−4·44	−2	−3·94		−3·86		−7·00		1·41	−1	−7·71		3·98	
13·0	1·46		1·83	−1	−3·66		−4·32		−7·19		−8·72	−1	−8·25		2·83	
13·2	1·51		4·09	−1	−3·34		−4·72		−7·28		−1·86		−8·69		1·64	
13·4	1·53		6·30	−1	−2·95		−5·06		−7·28		−2·83		−9·02		4·17	−1
13·6	1·52		8·42	−1	−2·52		−5·34		−7·19		−3·78		−9·25		−8·26	−1
13·8	1·49		1·04		−2·05		−5·55		−6·99		−4·69		−9·37		−2·07	
14·0	1·42		1·22		−1·54		−5·68		−6·71		−5·55		−9·37		−3·31	
14·2	1·33		1·39		−1·00		−5·73		−6·33		−6·36		−9·25		−4·52	
14·4	1·21		1·53		−4·41	−1	−5·71		−5·86		−7·09		−9·02		−5·68	
14·6	1·07		1·64		1·34	−1	−5·62		−5·31		−7·74		−8·67		−6·80	
14·8	9·05	−1	1·73		7·15	−1	−5·44		−4·68		−8·30		−8·21		−7·84	
15·0	7·24	−1	1·79		1·29		−5·19		−3·99		−8·77		−7·65		−8·80	
15·2	5·29	−1	1·82		1·86		−4·87		−3·23		−9·13		−6·97		−9·67	
15·4	3·22	−1	1·82		2·41		−4·48		−2·42		−9·39		−6·21		−1·04	1
15·6	1·07	−1	1·78		2·93		−4·03		−1·57		−9·53		−5·36		−1·11	1
15·8	−1·12	−1	1·72		3·42		−3·52		−6·86	−1	−9·55		−4·43		−1·16	1
16·0	−3·31	−1	1·63		3·87		−2·95		2·18	−1	−9·46		−3·43		−1·20	1
	$\lvert\varkappa\rvert=3$															
0·2	2·343	−3	−1·091	−2	2·441	−3	−2·841	−3	2·473	−3	−2·878	−3	2·487	−3	−2·894	−3
0·4	2·369	−2	−2·674	−2	2·573	−2	−2·907	−2	2·640	−2	−2·982	−2	2·671	−2	−3·018	−2
0·6	8·874	−2	−9·712	−2	1·006	−1	−1·102	−1	1·045	−1	−1·146	−1	1·064	−1	−1·167	−1
0·8	2·210	−1	−2·344	−1	2·615	−1	−2·780	−1	2·753	−1	−2·929	−1	2·818	−1	−3·000	−1
1·0	4·397	−1	−4·513	−1	5·434	−1	−5·602	−1	5·796	−1	−5·985	−1	5·970	−1	−6·168	−1
1·2	7·579	−1	−7·524	−1	9·793	−1	−9·786	−1	1·059		−1·060		1·097		−1·099	
1·4	1·182		−1·134		1·599		−1·547		1·751		−1·706		1·826		−1·775	
1·6	1·712		−1·585		2·426		−2·273		2·693		−2·535		2·825		−2·663	
1·8	2·341		−2·088		3·479		−3·155		3·917		−3·571		4·134		−3·776	
2·0	3·057		−2·623		4·771		−4·184		5·321		−4·788		5·785		−5·119	
2·2	3·843		−3·166		6·307		−5·343		7·303		−6·235		7·806		−6·686	
2·4	4·677		−3·692		8·084		−6·611		9·498		−7·838		1·022	1	−8·466	
2·6	5·534		−4·177		1·009	1	−7·957		1·203	1	−9·593		1·303	1	−1·044	1
2·8	6·391		−4·597		1·232	1	−9·347		1·491	1	−1·147	1	1·625	1	−1·257	1
3·0	7·220		−4·930		1·473	1	−1·075	1	1·811	1	−1·343	1	1·988	1	−1·484	1
3·2	7·994		−5·157		1·731	1	−1·213	1	2·162	1	−1·543	1	2·390	1	−1·720	1
3·4	8·689		−5·264		2·002	1	−1·344	1	2·541	1	−1·744	1	2·828	1	−1·960	1
3·6	9·279		−5·240		2·280	1	−1·465	1	2·943	1	−1·941	1	3·300	1	−2·200	1
3·8	9·744		−5·077		2·563	1	−1·572	1	3·366	1	−2·129	1	3·802	1	−2·435	1
4·0	1·006	1	−4·774		2·846	1	−1·661	1	3·804	1	−2·303	1	4·329	1	−2·660	1
4·2	1·022	1	−4·335		3·125	1	−1·729	1	4·251	1	−2·459	1	4·875	1	−2·868	1
4·4	1·021	1	−3·766		3·394	1	−1·773	1	4·701	1	−2·591	1	5·434	1	−3·056	1
4·6	1·001	1	−3·079		3·649	1	−1·791	1	5·149	1	−2·696	1	6·000	1	−3·216	1
4·8	9·630		−2·289		3·883	1	−1·780	1	5·590	1	−2·769	1	6·566	1	−3·346	1
5·0	9·068		−1·414		4·094	1	−1·739	1	6·017	1	−2·806	1	7·128	1	−3·440	1

TABLE 1 (*Continued*)

ρ	$\|\varkappa\|=3$															
	$p=0\cdot2$				$p=0\cdot4$				$p=0\cdot6$				$p=0\cdot8$			
	X		*Y*		*X*		*Y*		*X*		*Y*		*X*		*Y*	
5·2	8·331		−4·749	−1	4·276	1	−1·667	1	6·422	1	−2·801	1	7·676	1	−3·494	1
5·4	7·428		5·059	−1	4·424	1	−1·563	1	6·802	1	−2·763	1	8·205	1	−3·504	1
5·6	6·372		1·504		4·534	1	−1·428	1	7·144	1	−2·677	1	8·704	1	−3·468	1
5·8	5·182		2·494		4·603	1	−1·261	1	7·447	1	−2·548	1	9·166	1	−3·383	1
6·0	3·879		3·451		4·628	1	−1·066	1	7·703	1	−2·374	1	9·583	1	−3·247	1
6·2	2·486		4·352		4·607	1	−8·448		7·906	1	−2·157	1	9·948	1	−3·059	1
6·4	1·029		5·173		4·537	1	−5·991		8·051	1	−1·897	1	1·025	2	−2·816	1
6·6	−4·652	−1	5·894		4·417	1	−3·327		8·133	1	−1·597	1	1·049	2	−2·521	1
6·8	−1·968		6·495		4·249	1	−4·916	−1	8·147	1	−1·257	1	1·066	2	−2·176	1
7·0	−3·451		6·960		4·033	1	2·474		8·091	1	−8·830		1·074	2	−1·783	1
7·2	−4·886		7·279		3·768	1	5·525		7·962	1	−4·777		1·074	2	−1·345	1
7·4	−6·247		7·439		3·456	1	8·611		7·760	1	−4·582	−1	1·066	2	−8·663	
7·6	−7·507		7·435		3·101	1	1·169	1	7·484	1	4·074		1·048	2	−3·515	
7·8	−8·642		7·267		2·704	1	1·470	1	7·136	1	8·761		1·022	2	1·938	
8·0	−9·631		6·934		2·271	1	1·760	1	6·714	1	1·354	1	9·857	1	7·635	
8·2	−1·04	1	6·44		1·81	1	2·03	1	6·22	1	1·83	1	9·40	1	1·35	1
8·4	−1·11	1	5·80		1·31	1	2·29	1	5·66	1	2·31	1	8·86	1	1·95	1
8·6	−1·15	1	5·01		7·98		2·52	1	5·03	1	2·78	1	8·23	1	2·55	1
8·8	−1·17	1	4·11		2·67		2·72	1	4·35	1	3·23	1	7·51	1	3·14	1
9·0	−1·17	1	3·10		−2·82		2·87	1	3·61	1	3·63	1	6·67	1	3·72	1
9·2	−1·15	1	2·00		−8·27		3·00	1	2·83	1	4·04	1	5·79	1	4·28	1
9·4	−1·11	1	8·40	−1	−1·36	1	3·08	1	2·00	1	4·40	1	4·84	1	4·80	1
9·6	−1·04	1	−3·59	−1	−1·90	1	3·12	1	1·15	1	4·72	1	3·83	1	5·29	1
9·8	−9·58		−1·57		−2·41	1	3·12	1	2·71		4·98	1	2·77	1	5·73	1
10·0	−8·57		−2·78		−2·90	1	3·07	1	−7·01		5·19	1	1·67	1	6·12	1
10·2	−7·39		−3·94		−3·35	1	2·98	1	−1·60	1	5·30	1	5·43		6·45	1
10·4	−6·07		−5·06		−3·77	1	2·84	1	−2·49	1	5·39	1	−6·04		6·71	1
10·6	−4·63		−6·09		−4·15	1	2·66	1	−3·37	1	5·40	1	−1·76	1	6·90	1
10·8	−3·09		−7·01		−4·47	1	2·43	1	−4·22	1	5·35	1	−2·91	1	7·02	1
11·0	−2·97		−7·82		−4·74	1	2·17	1	−5·03	1	5·23	1	−4·04	1	7·05	1
11·2	1·65	−1	−8·49		−4·96	1	1·87	1	−5·79	1	5·05	1	−5·14	1	7·00	1
11·4	1·82		−9·01		−5·12	1	1·54	1	−6·49	1	4·79	1	−6·20	1	6·87	1
11·6	3·47		−9·36		−5·21	1	1·18	1	−7·13	1	4·47	1	−7·20	1	6·66	1
11·8	5·07		−9·54		−5·23	1	7·89		−7·70	1	4·09	1	−8·14	1	6·36	1
12·0	6·59		−9·54		−5·19	1	3·83		−8·18	1	3·64	1	−9·00	1	5·98	1
12·2	8·01		−9·37		−5·09	1	−3·57	−1	−8·58	1	3·14	1	−9·78	1	5·52	1
12·4	9·32		−9·02		−4·92	1	−4·63		−8·89	1	2·60	1	−1·05	2	4·99	1
12·6	1·05	1	−8·49		−4·68	1	−8·91		−9·09	1	2·00	1	−1·10	2	4·38	1
12·8	1·15	1	−7·81		−4·39	1	−1·32	1	−9·20	1	1·37	1	−1·15	2	3·71	1
13·0	1·23	1	−6·97		−4·03	1	−1·73	1	−9·20	1	7·12		−1·18	2	2·98	1
13·2	1·29	1	−5·99		−3·62	1	−2·13	1	−9·10	1	2·89	−1	−1·21	2	2·20	1
13·4	1·32	1	−4·89		−3·16	1	−2·51	1	−8·89	1	−6·68		−1·21	2	1·38	1
13·6	1·34	1	−3·69		−2·66	1	−2·86	1	−8·58	1	−1·37	1	−1·21	2	5·20	
13·8	1·34	1	−2·41		−2·12	1	−3·17	1	−8·17	1	−2·07	1	−1·19	2	−3·58	
14·0	1·31	1	−1·06		−1·54	1	−3·45	1	−7·67	1	−2·76	1	−1·16	2	−1·25	1
14·2	1·26	1	3·18	−1	−9·44		−3·69	1	−7·07	1	−3·42	1	−1·12	2	−2·15	1
14·4	1·19	1	1·71		−3·29		−3·88	1	−6·38	1	−4·06	1	−1·06	2	−3·03	1
14·6	1·10	1	3·09		2·96		−4·02	1	−5·62	1	−4·66	1	−9·96	1	−3·90	1
14·8	9·92		4·44		9·22		−4·12	1	−4·78	1	−5·21	1	−9·17	1	−4·74	1
15·0	8·67		5·72		1·54	1	−4·15	1	−3·88	1	−5·71	1	−8·27	1	−5·54	1

TABLE 1 (*Continued*)

ρ	$\lvert\varkappa\rvert=3$															
	$p=0\cdot2$				$p=0\cdot4$				$p=0\cdot6$				$p=0\cdot8$			
	X		Y		X		Y		X		Y		X		Y	
15·2	7·26		6·92		2·15	1	−4·14	1	−2·93	1	−6·15	1	−7·27	1	−6·29	1
15·4	5·73		8·02		2·73	1	−4·07	1	−1·94	1	−6·52	1	−6·19	1	−6·98	1
15·6	4·09		9·00		3·29	1	−3·94	1	−9·15		−6·82	1	−5·02	1	−7·60	1
15·8	2·37		9·83		3·81	1	−3·76	1	1·28		−7·04	1	−3·80	1	−8·15	1
16·0	6·07	−1	1·05	1	4·28	1	−3·52	1	1·18	1	−7·19	1	−2·52	1	−8·61	1
	$\lvert\varkappa\rvert=4$															
0·2	5·343	−4	4·756	−4	5·515	−4	4·928	−4	5·570	−4	4·976	−4	5·595	−4	4·998	−4
0·4	1·084	−2	9·912	−3	1·156	−2	1·056	−2	1·179	−2	1·077	−2	1·189	−2	1·087	−2
0·6	6·090	−2	5·700	−2	6·707	−2	6·273	−2	6·910	−2	6·461	−2	7·005	−2	6·549	−2
0·8	2·020	−1	1·936	−1	2·299	−1	2·201	−1	2·393	−1	2·289	−1	2·437	−1	2·331	−1
1·0	5·014	−1	4·922	−1	5·903	−1	5·782	−1	6·206	−1	6·076	−1	6·350	−1	6·215	−1
1·2	1·035		1·041		1·261		1·265		1·340		1·343		1·377		1·380	
1·4	1·881		1·940		2·373		2·437		2·547		2·613		2·631		2·697	
1·6	3·111		3·291		4·065		4·276		4·410		4·633		4·577		4·804	
1·8	4·783		5·193		6·480		6·985		7·107		7·647		7·412		7·966	
2·0	6·940		7·738		9·757		1·078	1	1·082	1	1·192	1	1·134	1	1·248	1
2·2	9·603		1·100	1	1·402	1	1·589	1	1·572	1	1·776	1	1·656	1	1·868	1
2·4	1·277	1	1·505	1	1·938	1	2·253	1	2·198	1	2·544	1	2·327	1	2·689	1
2·6	1·641	1	1·990	1	2·592	1	3·091	1	2·974	1	3·529	1	3·164	1	3·748	1
2·8	2·047	1	2·558	1	3·369	1	4·126	1	3·911	1	4·761	1	4·182	1	5·082	1
3·0	2·487	1	3·206	1	4·270	1	5·373	1	5·017	1	6·269	1	5·394	1	6·725	1
3·2	2·952	1	3·930	1	5·295	1	6·849	1	6·298	1	8·081	1	6·807	1	8·711	1
3·4	3·431	1	4·723	1	6·437	1	8·565	1	7·754	1	1·022	2	8·426	1	1·107	2
3·6	3·910	1	5·573	1	7·687	1	1·053	2	9·379	1	1·271	2	1·025	2	1·384	2
3·8	4·377	1	6·468	1	9·030	1	1·275	2	1·117	2	1·557	2	1·227	2	1·704	2
4·0	4·817	1	7·393	1	1·045	2	1·521	2	1·310	2	1·880	2	1·448	2	2·068	2
4·2	5·215	1	8·331	1	1·192	2	1·792	2	1·516	2	2·241	2	1·686	2	2·479	2
4·4	5·557	1	9·265	1	1·343	2	2·085	2	1·732	2	2·640	2	1·939	2	2·937	2
4·6	5·830	1	1·018	2	1·494	2	2·400	2	1·956	2	3·077	2	2·204	2	3·442	2
4·8	6·020	1	1·105	2	1·643	2	2·734	2	2·184	2	3·550	2	2·477	2	3·994	2
5·0	6·117	1	1·186	2	1·787	2	3·084	2	2·413	2	4·057	2	2·756	2	4·590	2
5·2	6·112	1	1·259	2	1·923	2	3·446	2	2·639	2	4·595	2	3·035	2	5·230	2
5·4	5·993	1	1·323	2	2·047	2	3·818	2	2·860	2	5·161	2	3·312	2	5·909	2
5·6	5·759	1	1·374	2	2·157	2	4·194	2	3·070	2	5·750	2	3·582	2	6·624	2
5·8	5·411	1	1·412	2	2·249	2	4·570	2	3·265	2	6·357	2	3·840	2	7·369	2
6·0	4·949	1	1·435	2	2·320	2	4·944	2	3·442	2	6·976	2	4·081	2	8·139	2
6·2	4·378	1	1·442	2	2·368	2	5·311	2	3·594	2	7·602	2	4·299	2	8·928	2
6·4	3·704	1	1·432	2	2·389	2	5·665	2	3·719	2	8·228	2	4·489	2	9·729	2
6·6	2·937	1	1·404	2	2·381	2	6·001	2	3·811	2	8·850	2	4·647	2	1·054	3
6·8	2·086	1	1·358	2	2·343	2	6·314	2	3·867	2	9·462	2	4·767	2	1·134	3
7·0	1·168	1	1·294	2	2·274	2	6·599	2	3·883	2	1·006	3	4·844	2	1·214	3
7·2	1·951		1·211	2	2·171	2	6·850	2	3·856	2	1·062	3	4·874	2	1·292	3
7·4	−8·136		1·112	2	2·035	2	7·062	2	3·783	2	1·116	3	4·853	2	1·368	3
7·6	−1·840	1	9·957	1	1·866	2	7·231	2	3·664	2	1·166	3	4·777	2	1·440	3
7·8	−2·866	1	8·645	1	1·664	2	7·351	2	3·495	2	1·210	3	4·645	2	1·508	3
8·0	−3·872	1	7·197	1	1·430	2	7·419	2	3·276	2	1·249	3	4·453	2	1·571	3

TABLE 1 (*Continued*)

ρ	$\lvert\varkappa\rvert=4$															
	$p=0{\cdot}2$				$p=0{\cdot}4$				$p=0{\cdot}6$				$p=0{\cdot}8$			
	X		Y		X		Y		X		Y		X		Y	
8·2	−4·84	1	5·63	1	1·17	2	7·43	2	3·01	2	1·28	3	4·20	2	1·63	3
8·4	−5·74	1	3·96	1	8·73	1	7·38	2	2·69	2	1·31	3	3·89	2	1·68	3
8·6	−6·56	1	2·22	1	5·56	1	7·26	2	2·32	2	1·33	3	3·51	2	1·72	3
8·8	−7·29	1	4·25		2·17	1	7·08	2	1·91	2	1·34	3	3·08	2	1·75	3
9·0	−7·91	1	−1·39	1	−1·40	1	6·84	2	1·45	2	1·34	3	2·59	2	1·77	3
9·2	−8·39	1	−3·20	1	−5·11	1	6·54	2	9·52	1	1·33	3	2·04	2	1·78	3
9·4	−8·75	1	−4·98	1	−8·92	1	6·17	2	4·19	1	1·31	3	1·44	2	1·78	3
9·6	−8·95	1	−6·70	1	−1·28	2	5·73	2	−1·45	1	1·28	3	7·97	1	1·77	3
9·8	−9·00	1	−8·33	1	−1·66	2	5·24	2	−7·35	1	1·25	3	1·08	1	1·74	3
10·0	−8·89	1	−9·85	1	−2·04	2	4·70	2	−1·34	2	1·20	3	−6·17	1	1·71	3
10·2	−8·62	1	−1·12	2	−2·41	2	4·10	2	−1·99	2	1·11	3	−1·37	2	1·66	3
10·4	−8·19	1	−1·25	2	−2·76	2	3·45	2	−2·62	2	1·04	3	−2·15	2	1·60	3
10·6	−7·61	1	−1·35	2	−3·09	2	2·77	2	−3·25	2	9·61	2	−2·94	2	1·52	3
10·8	−6·89	1	−1·43	2	−3·39	2	2·05	2	−3·86	2	8·72	2	−3·73	2	1·43	3
11·0	−6·03	1	−1·50	2	−3·66	2	1·30	2	−4·46	2	7·74	2	−4·52	2	1·34	3
11·2	−5·05	1	−1·54	2	−3·89	2	5·32	1	−5·03	2	6·68	2	−5·31	2	1·23	3
11·4	−3·96	1	−1·56	2	−4·08	2	−2·49	1	−5·56	2	5·55	2	−6·07	2	1·10	3
11·6	−2·79	1	−1·55	2	−4·23	2	−1·04	2	−6·06	2	4·36	2	−6·80	2	9·73	2
11·8	−1·54	1	−1·52	2	−4·33	2	−1·82	2	−6·50	2	3·12	2	−7·50	2	8·32	2
12·0	−2·41		−1·47	2	−4·38	2	−2·59	2	−6·89	2	1·83	2	−8·15	2	6·84	2
12·2	1·08	1	−1·39	2	−4·38	2	−3·33	2	−7·22	2	5·23	1	−8·70	2	4·54	2
12·4	2·42	1	−1·29	2	−4·33	2	−4·05	2	−7·48	2	−8·04	1	−9·19	2	2·89	2
12·6	3·73	1	−1·17	2	−4·22	2	−4·73	2	−7·66	2	−2·14	2	−9·60	2	1·20	2
12·8	5·00	1	−1·04	2	−4·05	2	−5·37	2	−7·77	2	−3·46	2	−9·93	2	−5·20	1
13·0	6·22	1	−8·82	1	−3·83	2	−5·95	2	−7·80	2	−4·76	2	−1·02	3	−2·25	2
13·2	7·35	1	−7·13	1	−3·57	2	−6·47	2	−7·74	2	−6·03	2	−1·03	3	−3·97	2
13·4	8·37	1	−5·32	1	−3·25	2	−6·93	2	−7·60	2	−7·25	2	−1·03	3	−5·67	2
13·6	9·28	1	−3·41	1	−2·88	2	−7·31	2	−7·37	2	−8·40	2	−1·03	3	−7·34	2
13·8	1·01	2	−1·44	1	−2·47	2	−7·61	2	−7·05	2	−9·49	2	−1·01	3	−8·95	2
14·0	1·07	2	5·70		−2·02	2	−7·83	2	−6·65	2	−1·05	3	−9·81	2	−1·05	3
14·2	1·11	2	2·58	1	−1·54	2	−7·96	2	−6·17	2	−1·14	3	−9·42	2	−1·19	3
14·4	1·14	2	4·58	1	−1·03	2	−8·01	2	−5·61	2	−1·22	3	−8·92	2	−1·33	3
14·6	1·15	2	6·51	1	−4·96	1	−7·97	2	−4·98	2	−1·29	3	−8·32	2	−1·45	3
14·8	1·14	2	8·37	1	5·43		−7·83	2	−4·28	2	−1·34	3	−7·61	2	−1·57	3
15·0	1·11	2	1·01	2	6·15	1	−7·61	2	−3·51	2	−1·39	3	−6·82	2	−1·66	3
15·2	1·07	2	1·17	2	1·18	2	−7·30	2	−2·69	2	−1·41	3	−5·93	2	−1·74	3
15·4	1·01	2	1·32	2	1·74	2	−6·90	2	−1·83	2	−1·43	3	−4·96	2	−1·81	3
15·6	9·25	1	1·44	2	2·29	2	−6·43	2	−9·24	1	−1·43	3	−3·97	2	−1·86	3
15·8	8·29	1	1·55	2	2·82	2	−5·87	2	6·85	−1	−1·41	3	−2·82	2	−1·89	3
16·0	7·19	1	1·63	2	3·32	2	−5·25	2	9·55	1	−1·38	3	−1·67	2	−1·90	3

TABLE 2

$K(\varkappa,p)=x(\varkappa,p)+iy(\varkappa,p)$

$\varkappa$	$p=0{\cdot}2$		$p=0{\cdot}4$		$p=0{\cdot}6$		$p=0{\cdot}8$	
	x	y	x	y	x	y	x	y
1	2·775	−1·346	1·611	−0·7315	1·285	−0·5444	1·155	−0·4538
2	−1·700	−3·105	−1·438	−2·016	−1·269	−1·826	−1·195	−1·762
3	−3·240	2·651	−2·600	2·087	−2·477	1·953	−2·439	1·896
4	3·231	3·753	2·755	3·245	2·645	3·154	2·596	3·130
−1	2·176	−2·188	0·913	−1·516	0·5065	−1·301	0·3113	−1·201
−2	−3·336	−1·184	−2·476	−0·0267	−2·198	0·342	−2·064	0·520
−3	−0·367	4·176	0·736	3·257	1·092	2·963	1·264	2·823
−4	4·936	−0·398	3·993	−1·475	3·691	−1·824	3·545	−1·992

TABLE 3

$N_{\pm}(\varkappa,p)$

$\vert\varkappa\vert$	$p=0{\cdot}2$		$p=0{\cdot}4$	
	N_+	N_-	N_+	N_-
1	$8{\cdot}727\times10^{-1}$	$i8{\cdot}641\times10^{-2}$	$1{\cdot}017$	$i1{\cdot}958\times10^{-1}$
2	$2{\cdot}369\times10^{-1}$	$i2{\cdot}346\times10^{-2}$	$1{\cdot}522\times10^{-1}$	$i2{\cdot}932\times10^{-2}$
3	$2{\cdot}810\times10^{-2}$	$i2{\cdot}782\times10^{-3}$	$1{\cdot}251\times10^{-2}$	$i2{\cdot}410\times10^{-3}$
4	$2{\cdot}064\times10^{-3}$	$i2{\cdot}044\times10^{-4}$	$7{\cdot}302\times10^{-4}$	$i1{\cdot}406\times10^{-4}$

$\vert\varkappa\vert$	$p=0{\cdot}6$		$p=0{\cdot}8$	
	N_+	N_-	N_+	N_-
1	$1{\cdot}145$	$i3{\cdot}171\times10^{-1}$	$1{\cdot}271$	$i4{\cdot}460\times10^{-1}$
2	$1{\cdot}331\times10^{-1}$	$i3{\cdot}687\times10^{-2}$	$1{\cdot}303\times10^{-1}$	$i4{\cdot}572\times10^{-2}$
3	$9{\cdot}816\times10^{-3}$	$i2{\cdot}719\times10^{-3}$	$9{\cdot}185\times10^{-3}$	$i3{\cdot}223\times10^{-3}$
4	$5{\cdot}412\times10^{-4}$	$i1{\cdot}499\times10^{-4}$	$4{\cdot}963\times10^{-4}$	$i1{\cdot}642\times10^{-4}$

V. EXTENSION OF THE TABLES

For values of $Z\neq80$, it is evident that the use of these tables for $75\leqslant Z\leqslant85$ would involve errors of 5 per cent. or less.

In the region $|\varkappa|>4$, the Sommerfeld-Maue type of approximation (Bethe and Maximon 1954) is generally satisfactory.

For values of p not tabulated, the following possibilities arise

(i) extrapolation to $p<0{\cdot}2$;

(ii) interpolation for p in the region $0{\cdot}2<p<0{\cdot}8$;

(iii) extrapolation to $p>0{\cdot}8$.

For case (i), it usually suffices to approximate to the Dirac wave functions by means of the Darwin wave functions (Darwin 1928).

For case (ii), graphical interpolation of f,g will generally be accurate to a few per cent.

For case (iii), the following procedure is suggested. Plot the Whittaker functions for a given $\varkappa,\rho$, against $\eta = Z(1+p^2)^{\frac{1}{2}}/p$, using the tables. Then, determine the appropriate η corresponding to the required p ($>0\cdot8$) and read off the unknown Whittaker function from the extrapolated curve. This procedure is justified because the Whittaker functions are fairly smooth functions of η in the region from $\eta=1\cdot6$ ($p=0\cdot4$) through $\eta=1\cdot1$ ($p=0\cdot6$) and $\eta=0\cdot9$ ($p=0\cdot8$) to $\eta=0\cdot58$ ($p=\infty$). The method was used for a number of cases and found to yield radial wave functions near extrema to within a few per cent. Increased accuracy may possibly be secured if, in addition, the values of the Whittaker functions at $\eta=0$ are used. These are readily obtainable since, at $\eta=0$, the Whittaker functions can be expressed, with the help of contiguity relations, in terms of real Bessel functions.

VI. ACKNOWLEDGMENTS

The authors wish to thank Dr. F. Hirst and his computer staff for their willing assistance in the operation of CSIRAC, and Associate Professor C. B. O. Mohr for his encouragement and interest in this work.

VII. REFERENCES

BETHE, H. A., and MAXIMON, L. C. (1954).—*Phys. Rev.* **93** : 768.

DARWIN, C. G. (1928).—*Proc. Roy. Soc.* A **118** : 654.

ERDELYI, A., ET AL. (1953).—" Higher Transcendental Functions." Vol. I. Bateman Manuscript Project. (McGraw-Hill : New York.)

NATIONAL BUREAU OF STANDARDS (1954).—Tables of the gamma functions for complex arguments. Applied Mathematics Series No. 34.

ROSE, M. E. (1937).—*Phys. Rev.* **51** : 484.

THE EFFECT OF SUDDEN IONOSPHERIC DISTURBANCES (S.I.D.'S) ON 2·28 Mc/s PULSE REFLECTIONS FROM THE LOWER IONOSPHERE

By F. F. Gardner*

[*Manuscript received November 7, 1958*]

Summary

The effects of sudden ionospheric disturbances (S.I.D.'s) on the complicated structure of ionospheric echoes obtained with moderately high sensitivity at 2·28 Mc/s are described. The observations indicate that flares of classes 2 and 3 can produce high values of electron density near the base of the ionosphere. Mean electron density can exceed $1000/\text{cm}^3$ over the height range 60–75 km, where the greatest relative increase in ionization occurs. Nevertheless, the greater part of the S.I.D. absorption of waves reflected from the E region or above still occurs above 85 km.

The times of maximum disturbance at the different ionospheric levels agree within the experimental limit of about 1 min. The times of subsequent recovery at levels up to 85 km also seem to be simultaneous. However, the recovery of the E echo lags behind that of the 85–90 km echo group, by about 4 min on the average for large S.I.D.'s. It is quite likely that the delay is not wholly due to different recombination rates at different ionospheric levels, but is partly caused by a change in the quality of the incoming solar radiation during the life of the flare.

I. Introduction

The characteristic anomalies in the lower ionosphere associated with solar flares, known as sudden ionospheric disturbances (S.I.D.'s), have been studied in a number of ways (see review of the different effects by Ellison 1950). These include the absorption of short and medium radio waves, the change in the reflection characteristics of long radio waves, and geomagnetic " crochets ". While it is accepted that all three are manifestations of some change in the ionosphere below the E-layer maximum, which is little affected itself, it is still far from clear just what the change is. A few years back a preliminary investigation of the D region using the weak scattered reflections from irregularities below the main level of reflection for 2 Mc/s pulses was made (Gardner and Pawsey 1953), but during the periods of observation no S.I.D.'s occurred. However, a more extensive series of observations of vertical-incidence pulse reflections at 2·28 Mc/s has been made during which time some 70 S.I.D.'s were noted. The results, described in this paper, provide some definite information on the heights and magnitude of S.I.D. effects in the lower ionosphere.

II. Observation Procedure

The observations were made at the C.S.I.R.O. Radio Research Laboratory site at Camden.† Horizontal half-wave dipoles 60–70 ft above ground and about 400 ft apart were used for transmission and reception. The 2·28 Mc/s transmitter

---

* Division of Radiophysics, C.S.I.R.O., University Grounds, Chippendale, N.S.W.

† The site and facilities were kindly provided by Dr. G. H. Munro.

pulse length was ordinarily in the 30–40 μsec range. The power was about 10 kW, ten times higher than that used in the 1951–1952 observations, but the background noise, largely man-made, with an intensity approaching 10^6 °K equivalent temperature was more than 100 times the previous day-time noise level. The receiving bandwidth was around 50 kc/s. The receiver gain was switched cyclically to three positions with voltage gain ratios 1, 10, and 100 every 2 sec. When the intensity-modulated display was photographed on a slowly moving film the scans at the three gain settings merged and an approximately logarithmic intensity record was obtained. This record was supplemented by photographs of the class A display taken at 1-min intervals, each exposure lasting long enough to show a scan at each gain setting. Plate 1, Figures (*a*) and (*b*), shows the two records for a short S.I.D. on May 18, 1956. The 7·5 and 75 km range markers are provided by 50 and 500 μsec pips from a 100 kc/s crystal oscillator. In the amplitude photograph at 1129 the scan at low gain shows the *E* echo at 107 km just saturating, while echoes at shorter ranges 85 km and 95 km are small. At medium gain the three echoes saturate and at high gain saturating echoes fill the complete range interval from 85 to 130 km.

III. OBSERVATIONS

The observations were practically continuous (useful records for about three-quarters of the time) from February to December 1956. During this time 66 S.I.D.'s producing more than about 10 dB attenuation of the 1*E* echo were observed. This was a size that could be recognized easily and not confused with other absorption changes.

(*a*) *Association with Other S.I.D. Effects*

The radio records were compared with solar flare and S.I.D. data available from CRPL-F Part B publications, Kiepenheuer's daily maps of the Sun, and Ionospheric Prediction Service Series D publications, supplemented by local data. Of the 66 anomalies noted on the radio records :

49 were accompanied by short-wave fade-outs (S.W.F.'s) : of these 28 were " sudden start ", 3 " gradual ", and 18 " slow start " ;
22 were accompanied by sudden cosmic noise anomalies (S.C.N.A.'s) ;
20 were accompanied by effects on ionospheric *P′*-*f* records ;
4 were accompanied by sudden enhancements of atmospherics (S.E.A.'s) ;
31 were accompanied by flares of class 1 or above, of which 18 were class 1, 10 were class 2, and 3 were class 3.

The short-wave fade-outs (S.W.F.'s) are given both a widespread index ranging from 1 to 5, and an importance 1, 2, and 3 in CRPL-F. The median values of the indices for the 49 coincidences were 3 and 2 respectively. The corresponding flare size for the 31 coincidences was in the 1–2 range.

(*b*) *Effect of S.I.D.'s on the General Echo Pattern at 2·28 Mc/s*

The general pattern of the day-time echoes was similar to that shown in the previous paper and reproduced here as Figure 1. The echoes were in three main groups previously called the " 70 km ", " 90 km ", and *E*, and this grouping was found to be retained during S.I.D.'s. However, the " 70 km " echoes were often absent, and this can be accounted for by the noise background being higher than in the previous series. Figure 2 shows diagrammatically the variation in intensity of echoes at different heights during a moderately large S.I.D., associated with a class 2 flare. The E-echo amplitude drops by a factor of more than 10^3, to below the background noise. The echo reappears later as the ionosphere returns to normal. The 85 km echo fades out and recovers in a similar way, although the recovery is a few minutes in advance of the E. The echo at 70–75 km behaves differently. Following an initial enhancement its amplitude is reduced to below noise, while the reverse occurs during the subsequent recovery. The lowest echoes around 65 km are enhanced with a maximum enhancement near the time of S.I.D. maximum.

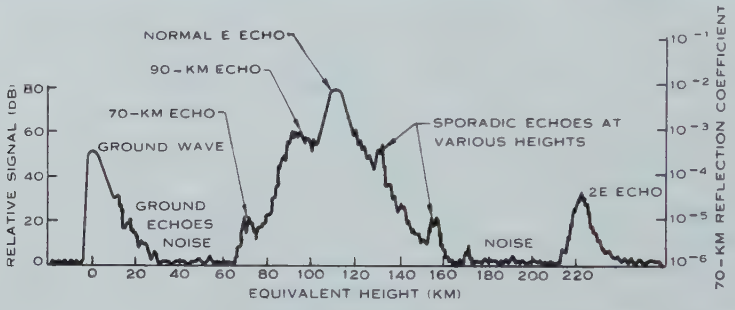

Fig. 1.—Sketch of typical midday echo pattern, reproduced from *J. Atmos. Terr. Phys.* **3**: 325 (1953).

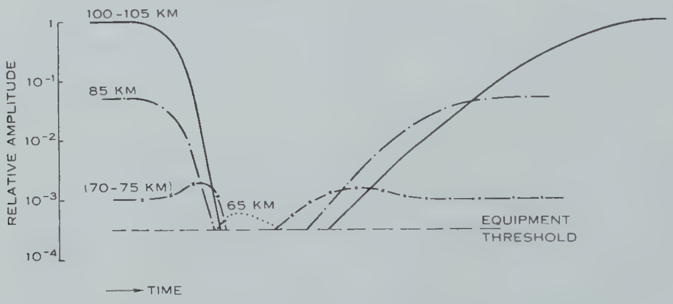

Fig. 2.—Diagram illustrating the variation in amplitude of echoes at different heights during a moderately large S.I.D.

Following the E echo in Figure 1 sporadic echoes are shown whose average intensity falls off rapidly with increasing range. These are thought to result from sideways scattering by irregularities below the E-region vertical-incidence reflection level. During an S.I.D. the intensity of these echoes decreases markedly, and variation in their maximum extent in range on the record provides a sensitive indication of the start and finish of the S.I.D. The variation in intensity of multiple E reflections is similar to, although greater than, that of the 1E, as would be expected. Echoes between about 90 km and the E tended to disappear even in small S.I.D.'s.

SUDDEN IONOSPHERIC DISTURBANCES

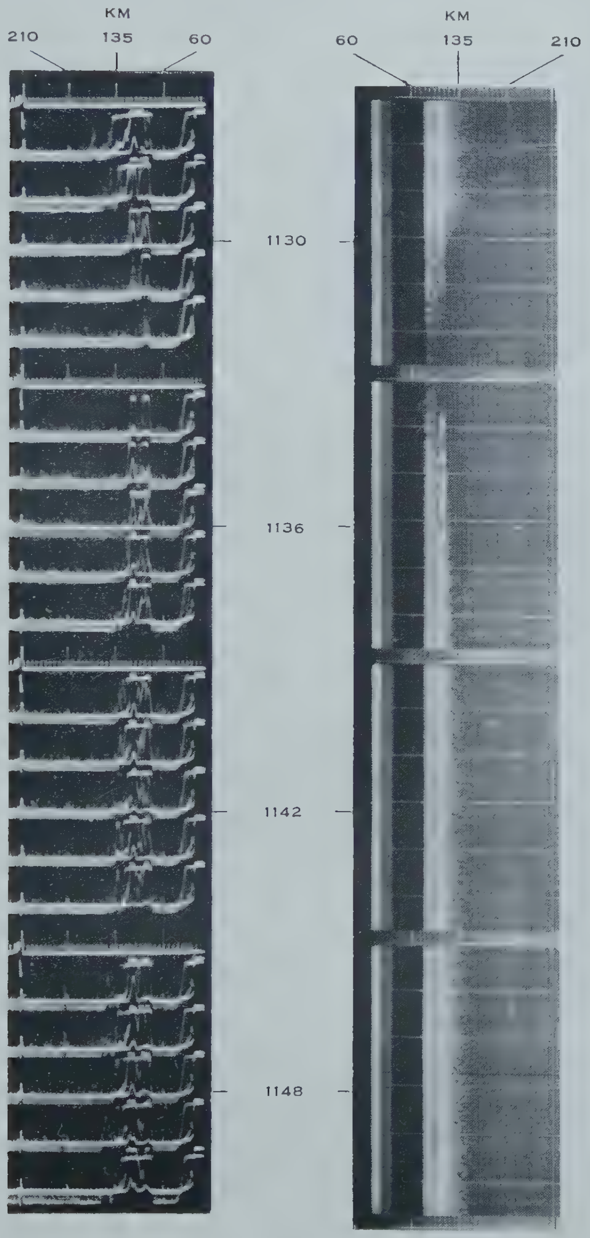

(a) (b)

Records for May 18, 1956 showing a short-lived S.I.D. (*a*) Amplitude record—A-scan photographs, with three different gains differing by ratios 1 : 10 : 100, taken at 1-min intervals. (*b*) Intensity record—scale is roughly logarithmic.

SUDDEN IONOSPHERIC DISTURBANCES

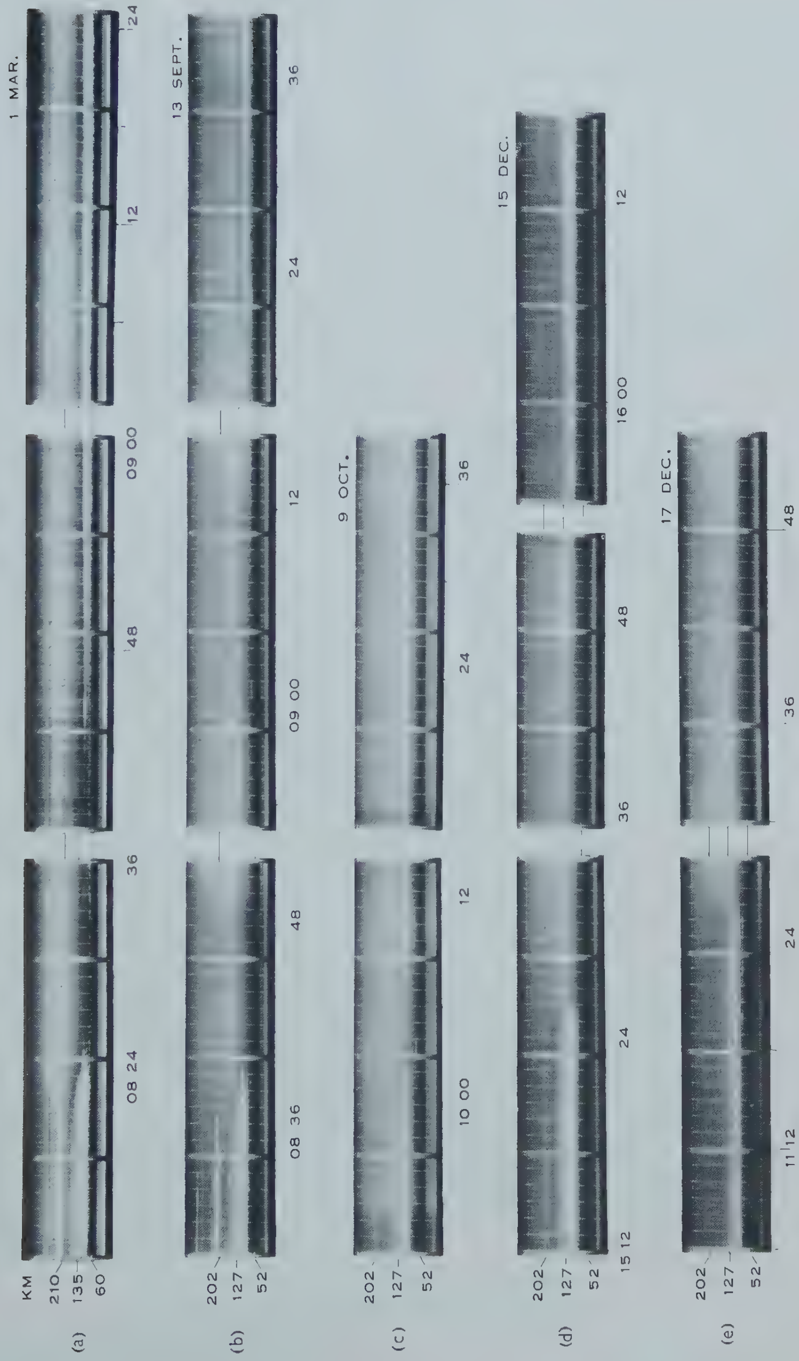

Intensity records for some typical S.I.D.'s during 1956. (*a*) March 1, (*b*) September 13, (*c*) October 9, (*d*) December 15, (*e*) December 17.

In about 10 per cent. of S.I.D.'s the normal E echo became spread, quite likely as the result of an increase in scattering by the " 90 km " region rather than an E-region change. In about the same percentage of cases the intensity of echoes in the 70–75 km range commenced some 2–5 min ahead of the first change in intensity of echoes from greater heights, as indicated by changes in the strength of $2E$ echoes or of echoes at the tail of the $1E$.

With S.I.D.'s smaller than the one illustrated in Figure 2 there is less progressive change in the strength of the different echoes before the S.I.D. starts to recover. Thus the dip in the intensity of the " 70 km " echo near S.I.D. maximum in Figure 2 may be absent. In addition, the features of individual S.I.D.'s differ in other respects, some of which are not due to changes of the incoming ionizing radiation. One difference is the result of the deep, irregular fading of the low-height echoes which tends to obscure changes in mean amplitude; another is the result of changes in the signal-to-noise ratio.

S.I.D.'s possessing some of the features discussed are shown in the intensity records of Plate 2. In (*a*) an echo at 67 km appears near the S.I.D. maximum, while the higher echo at 75 km varies in accordance with Figure 2 ; the echo at 90 km disappears and subsequently reappears ahead of the E. In (*b*) an echo at 68 km appears briefly during the S.I.D. (no echo at such a low height was received at any other time on the morning concerned) ; higher echoes disappear nearly simultaneously, but the 75 and 85 km ones reappear together ahead of the E. In (*a*) and (*b*) the S.I.D. absorption change is superimposed on the smooth diurnal increase in absorption which is quite rapid around 0900 hr ; it is the latter change which is mainly responsible for the change in strength of the multiple reflections and also of the echoes at the tail of the $1E$ between the beginning and end of the records shown. In the small S.I.D. (Plate 2 (*c*)) the echo at 79 km shows the typical behaviour of the " 75 km " echo in Figure 2. In Plate 2 (*d*) there is an initial intensification of an echo at 76 km at least 2 min ahead of the S.I.D. absorption increase of the E echo. The recovery is unusual in that the E reappears ahead of the 90 km echo. In Plate 2 (*e*) there is again an initial intensification of an echo at 73 km, at least 4 min earlier than the S.I.D. absorption commencement ; the 87 km echo reappears slightly ahead of the E.

The amplitude changes during a small S.I.D. can be seen in Plate 1 (*a*). At 1129, before the S.I.D. start, echoes are present to a little below 85 km. The E echo is large, with a mean amplitude of about 0·7 of saturation on the low gain, and between five and ten times the amplitude of the echo at 85 km. By 1130, however, the two echoes are practically equal, although both have been reduced. The E echo then disappears completely, implying a reduction approaching 1000/1, while the corresponding reduction for the 85 km echo which remains visible is about 30/1. The duration of this particular S.I.D. was very short, below a third of the average for its size.

(*c*) *Particular S.I.D. Effects*

(i) *Echo Heights during S.I.D.'s.*—In Figure 3 the distribution of heights of echoes up to 95 km, (*a*) whose intensities were increased during S.I.D.'s and (*b*) which were not, are compared. For echoes below 90 km, heights (*b*) were practically the same as those immediately before the S.I.D. The first thing to note in Figure 3 is that only the " 70 km " echoes are intensified. These are in two groups centred near 66–67 km and 73–74 km. This is the same grouping as ordinarily observed with a higher sensitivity equipment (see Fig. 7 (*d*) of Gardner and Pawsey (1953)). In Figure 3 there is a small difference of 1·5 km between the mean heights of the 70–75 km group of intensified and non-intensified echoes (the medians are 73·5 and 75 km respectively), although the most frequently occurring height, 75 km, is the same for both.

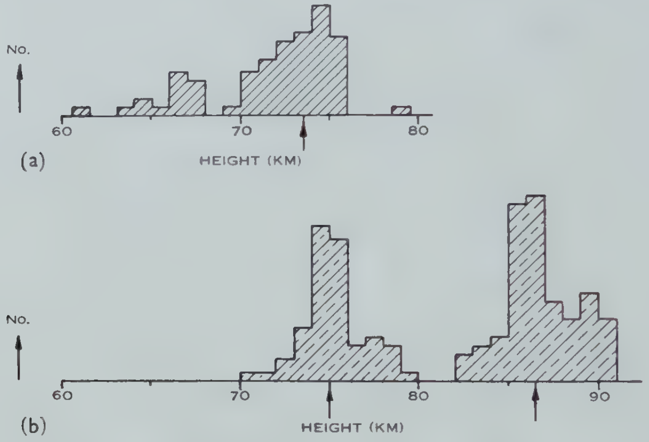

Fig. 3.—Histograms showing heights of echoes (*a*) whose intensity was increased during S.I.D.'s, (*b*) whose intensity was not increased—practically the same histogram as that of echoes immediately prior to the S.I.D. commencement.

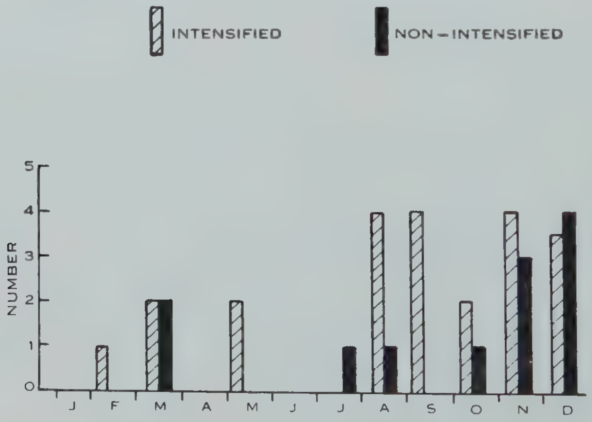

Fig. 4.—The frequency of occurrence of intensification and non-intensification of 70–75 km echoes during 1956.

Figure 3 shows a median height of 86·5 km for the " 90 km " echoes during S.I.D.'s, approximately the height of the lowest layer of the " 90 km " region under normal conditions.

(ii) *Changes in Echo Intensities during S.I.D.'s.*—It was found that the lowest group of echoes, those below 70 km, were intensified in seven cases. These echoes normally were not detectable, but in all cases when they were observable their intensity increased during an S.I.D. From our previous experience it is estimated that an increase in amplitude of at least 10/1 would normally be required for them to appear.

The 70–75 km echoes were intensified in 26 cases ; in 16 cases there was no change ; in the remaining 24 cases these echoes were below the sensitivity limit. The mean increase in amplitude was about 2/1. The subsequent reduction in amplitude at the S.I.D. maximum was as much as 8/1 below the pre-S.I.D. value. The relative frequency of occurrence of intensification and non-intensification appears to have a seasonal dependence as shown in Figure 4. It is more likely for the echo intensity to increase in winter than in summer.

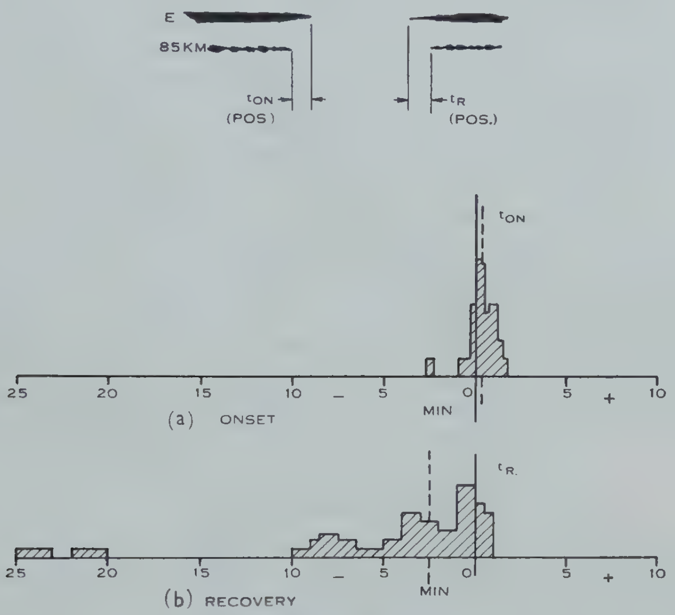

Fig. 5.—Distributions of the difference (*a*) of onset times t_{ON} and (*b*) of recovery times t_R of the " 90 km " and *E* echoes measured in accordance with the diagram at the top of the figure. The medians of the two histograms are shown by dashed lines.

Echoes above 80 km decreased in intensity during S.I.D.'s. In rare cases there might be a short-lived increase in the strength of an echo in this range. For the smaller S.I.D.'s where the 85–88 km and *E* echoes did not disappear it was observed that the proportional reduction of the *E* echo was considerably greater than that of the 85–88 km echo. In fact, when amplitude changes are expressed logarithmically, in nepers for example, the *E*-echo reductions were at least three times greater than those of the 85–88 km. With larger S.I.D.'s this was still the case during the portion of the S.I.D. when both echoes could be observed.

(iii) *Timing of Ionospheric Changes during S.I.D.'s.*—To the accuracy that variations in strength of fluctuating echoes could be timed, changes at different ionospheric heights were simultaneous in regard to times of start, maximum, and finish, apart from the recovery lag of the E echo behind the " 90 " of about 4 min and the intensification in some 10 per cent. of S.I.D.'s of the " 70 km " echo prior to the fade-out commencement.

The E-echo time lag can be demonstrated by noting time differences between corresponding points for the two echoes at the onset and at the recovery of the S.I.D. The most convenient are the times of disappearance and reappearance of the two echoes. This of course restricts attention to the larger S.I.D.'s, generally also those of longest duration. At the top of Figure 5 the two time differences measured are shown. The onset time t_{ON} is the time elapsing from the disappearance of the " 90 km " to the disappearance of the E ; t_R, the recovery time, is the time from the reappearance of the E to the reappearance of the " 90 km ". For a symmetrical disturbance and no real time lag t_{ON} and t_R should have the same sign and be equal. For a disturbance which decays, say, four times more slowly than it builds up, as does a typical S.I.D., t_R should equal $4t_{ON}$. Actually, Figure 5, which gives the distributions of t_{ON} and t_R, shows that the two times have different signs. t_{ON} is positive but t_R is negative (the " 90 km " both disappears and reappears ahead of the E). The median value of t_{ON} is $+0\cdot35$ min and that of t_R $-2\cdot5$ min. For a typical disturbance with a 1 : 4 onset : recovery ratio, the expected value of t_R for no lag is $4\times0\cdot35=1\cdot4$ min. The effective lag between the " 90 " and E echoes is therefore $1\cdot4+2\cdot5\approx4$ min.

IV. Discussion

(*a*) *Electron Density Changes*

It is obvious that changes in the pattern of ionospheric echoes during S.I.D.'s correspond to changes in the electron density-height distribution. There is, however, no direct method for deriving electron densities from echo intensities, and all that can be done is to see to what extent the observations fit the behaviour of simple models. The simplest explanation is to assume that changes in intensity are due solely to increases in absorption below the reflection levels, the correct explanation of the behaviour of echoes from above the region affected by the S.I.D., and therefore a good approximation for the E echo. Applied to the other echoes it gives a lower limit to the S.I.D. absorption increases. For the " 90 km " and E echoes the absorption values apply to the ordinary component alone, but with the " 70 km " echoes both components are involved. To produce the observed reduction of 8/1 in the amplitude of an echo near 75 km (Section III (*c*) (ii)), an increase in electron density of 1000/cm^3 over a height range of 15 km, say 60–75 km, is required,* an increase of some 10 times the pre-S.I.D. electron density.

---

* From the discussion of polarization behaviour by Gardner and Pawsey (1953), the reduction of 8/1 in amplitude implies almost complete absorption of the extraordinary component and at least $\frac{1}{2}$ neper increase for the ordinary. The electron densities follow from Figures 15 and 16 of their paper.

The absorption model does not explain the behaviour of echoes whose intensities increase during S.I.D.'s. An increase in reflectivity as well as an increase in underlying absorption must now take place. In the earlier investigation, when electron densities were measured it was found that average echo amplitudes were roughly proportional to electron densities when absorption effects were small. If such a proportionality continued to hold during an S.I.D., then the observed reflection coefficient R would be given by

$$R=\text{constant}\times N\exp(-\rho),$$

where N, the electron density, and ρ, the integrated absorption in nepers, are each a function of height. If R_0, N_0, and ρ_0 are the corresponding values prior to the S.I.D. commencement, then

$$R/R_0=(N/N_0)\exp\{-(\rho-\rho_0)\}. \quad \ldots\ldots\ldots\ldots\ldots \quad (1)$$

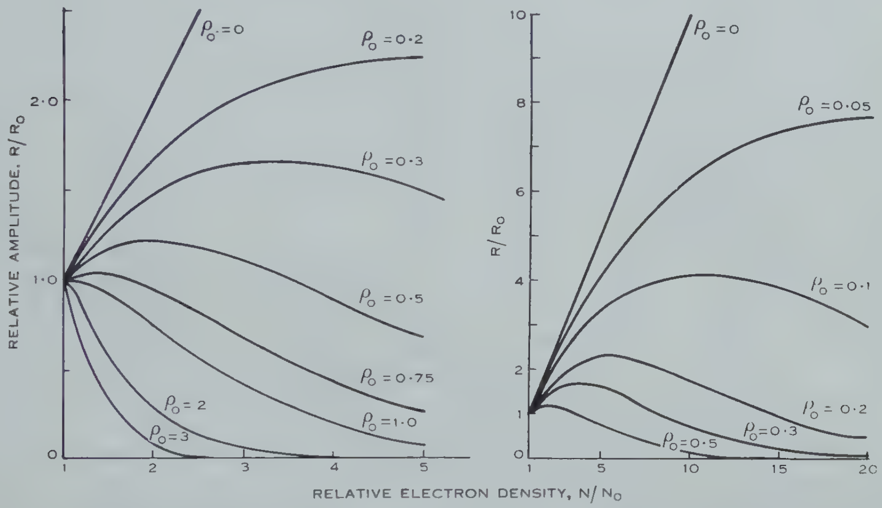

Fig. 6.—Variation of relative echo amplitude with increasing electron density, for different values of initial absorption ρ_0 in nepers. Two sets of curves with different scales are employed to cover the range of interest.

If the whole of the ionosphere below the reflection level for the echo concerned were affected in the same proportion, ρ would equal $(N/N_0)\rho_0$, and this is the basis for the next model. Substituting $\rho=(N/N_0)\rho_0$, equation (1) becomes

$$R/R_0=(N/N_0)\exp[-(N/N_0-1)\rho_0]. \quad \ldots\ldots\ldots\ldots \quad (2)$$

In Figure 6, R/R_0 is plotted as a function of N/N_0 for different values of ρ_0. For $\rho_0<1$, R/R_0 reaches a maximum $(R/R_0)_{\text{max.}}=(1/\rho_0)\exp(\rho_0-1)$ at $N/N_0=1/\rho_0$, and returns to unity at $N=N_1$. For $\rho_0>1$, R/R_0 decreases continuously with increase in N/N_0. Figure 7 gives $(R/R_0)_{\text{max.}}$ and N_1/N_0 as functions of ρ_0.

It can be seen from Figure 6 that this model will explain echoes, the intensity of which during S.I.D.'s

(i) decreases, $\rho_0>1$;

(ii) increases then decreases, $\rho_0<1$, $N/N_0>N_1/N_0$;

(iii) increases, $\rho_0<1$, $N/N_0<N_1/N_0$.

For a 10/1 increase in the amplitude of echoes from 65 km, ρ_0 (65 km) would have to be below 0·05 and the electron density must increase by more than 10/1 (with $\rho_0=0 \cdot 05$ in Fig. 6, $(R/R_0)_{\text{max.}}=10$, $N/N_0=20$). The same proportional increase in electron density would explain the intensification and subsequent diminution of the echo at 72–75 km if the appropriate value of ρ_0 was in the range 0·3 to 0·4 for $\rho_0=0 \cdot 36$, $(R/R_0)_{\text{max.}}=1 \cdot 5$, $N_1/N_0=6$. An increase in electron density of some 6/1 would be required before the echo intensity fell below the pre-flare value. The observed maximum increase in amplitude of this 72–75 km echo was somewhat higher than the $(R/R_0)_{\text{max.}}$ value of 1·5.* Qualitatively, the behaviour of echoes at heights greater than 75 km is in accord with the model behaviour for $\rho_0>1$, but, as the general behaviour is similar for different values of ρ_0, it is not possible to make quantitative estimates of ρ_0.

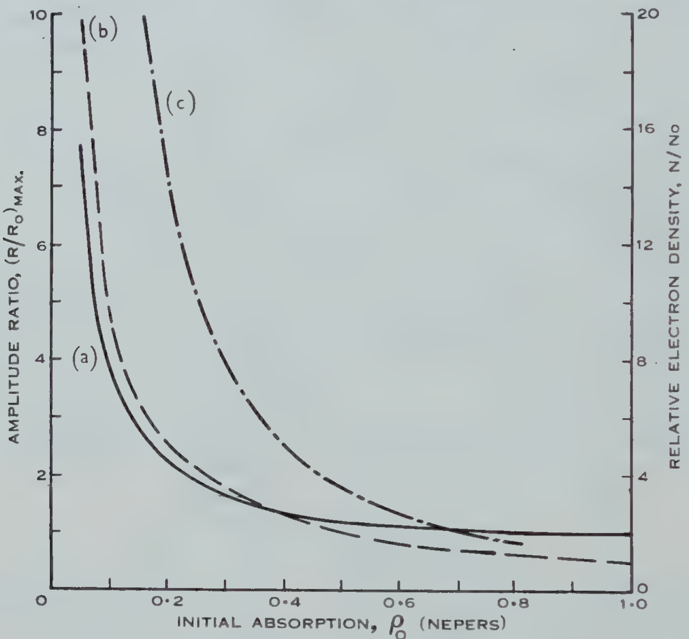

Fig. 7.—Variation of (*a*) $(R/R_0)_{\text{max.}}$, the maximum increase in echo amplitude expressed as a ratio of the pre-S.I.D. value; (*b*) $(N/N_0)_{\text{max.}}$, the value of N/N_0 at which this maximum occurs; and (*c*) the value, N_1/N_0, of N/N_0, at which R/R_0 returns to unity, each as a function of ρ_0, the initial absorption in nepers.

When polarization effects are included, the values of ρ_0 required to explain echo intensity variations are approximately the mean of the values for the two components at the lowest heights around 65 km, gradually changing with increasing height to the value appropriate to the ordinary magneto-ionic component, which alone is important above 80 km. Corresponding to the previous values of ρ_0, $0\cdot05$ and $0\cdot3$–$0\cdot4$, ρ_0 for the ordinary component will be less than $0\cdot05$ neper at 65 km, and around $0\cdot2$ neper at 72–75 km. These are in reasonable agreement with those derived in the previous observations ($0\cdot1$ neper for 72 km echoes on May 6, 1952) when electron densities were around 20 and $200/\text{cm}^3$ at the two heights. During S.I.D.'s these may increase by more than 10/1.

---

* If the reflectivity during an S.I.D. increased more rapidly than did the electron density, higher values of R/R_0 for a given value of ρ_0 would be obtained. This may have been the case with some of the S.I.D.'s.

It was found that " 70 km " echo intensities increased more frequently in winter than in summer (Section III (*c*) (ii) and Fig. 4). This fits the model behaviour, since ρ_0 will be smaller in winter than in summer.

In the model it has been assumed that N/N_0 is independent of height. This obviously cannot hold over the full range of echo heights. Some idea of the variation in electron density at heights above 75 km can be obtained from the *E*-echo variation. At the *E*-region maximum it is generally considered that the electron density is little affected. In the moderately large S.I.D.'s which we have been considering the overall absorption in nepers for waves completely traversing the *D* region might increase by a factor of 3.* As the centre of the absorbing region would be around 90 km, we obtain an N/N_0 variation of about 20/1 at 65 km, decreasing through 3/1 at 90 km to unity at 110 km. Notwithstanding the fact that the proportional increase is greatest around 70 km, it is concluded from the observations of the relative changes of the " 90 " and *E* echoes (Section III (*c*) (ii)) that, during an S.I.D., most absorption of the *E* echo still takes place between 85 km and the *E*-reflection level. In this region of the ionosphere the pre-S.I.D. electron densities are high and only small proportional increases are required to produce large increases in overall absorption.

The magnitude of the increases in electron density found for the 60–75 km range of heights, well over 1000 electrons/cm^3 in some cases, appears to be adequate to explain the variations in phase height of 16 kc/s waves at near-vertical incidence (Bracewell and Straker 1949). The reflection level, determined approximately by $N=100$, might fall some 10 km from 70 to 60 km and so produce a 360 degree phase change at 16 kc/s. Any fall in the reflection level could explain the worsening of long-distance propagation at frequencies below 8 kc/s causing a reduction in the strength of atmospherics at these frequencies (Gardner 1950), according to Budden's (1951) theory. The S.I.D. change in the electron density distribution with height might also explain the enhancement of atmospherics at frequencies between about 15 kc/s and 60 kc/s (Bureau 1937).

In a previous observation it was found that the ionospheric temperature, determined from the measurement of 2 Mc/s thermal radiation, increased by amounts of up to 40 °K during S.I.D.'s (Gardner 1954), but it was not obvious whether there was a real increase in electron temperature involved or whether the effect was due solely to a downward movement of the region of origin of the radiation to where the temperature was higher. From a consideration of the increases in electron density near the bottom of the ionosphere, together with the atmospheric temperature-height distribution, it appears that the latter effect alone is sufficient.

---

* This would increase *E*-echo absorption from about 3 to 12 nepers (25 to 100 dB). With the non-deviative absorption formula the corresponding cosmic noise absorption at 20 Mc/s would be about 1 dB.

(*b*) *Timing of S.I.D. Effects*

It was demonstrated that there was a mean time lag between the recoveries of 85 and 105 km echoes of at least 3 min. No lag (unlikely to be more than 1 min) was detectable between events at 85 km and at lower heights. The latter suggests that variations at the bottom of the ionosphere follow closely the variations in ionizing radiation, as was suggested by Bracewell and Straker (1949), who estimated from a study of sudden phase anomalies (S.P.A.'s) at 16 kc/s that the equivalent time constant of the ionosphere effects at heights around 65–75 km did not exceed $2\frac{1}{2}$ min. Ellison (1953), however, found that changes in Hα line width during flares are some minutes ahead of the corresponding lower ionospheric effects, there being a mean lag of 7 min between the two maxima. If the ionospheric effects are in step, to within 1–2 min with the ionization radiation, the latter's intensity cannot be dependent on the Hα line width alone.

The lag of the *E* recovery behind the 85 km recovery is not necessarily the result of different recombination rates at different ionospheric levels, as would be the case if the quality of the enhanced ionizing radiation remained constant through a solar flare and only the intensity varied. Rocket observations of solar spectra (Chubb *et al.* 1957) suggest that two types of radiation are enhanced in S.I.D.'s, namely Lyman-α line radiation and short X-rays. If this is so it is quite possible that the relative amounts of the two will vary during the progress of the flare. Our observations would require that the radiation producing its effect at the greater average height should tend to last longer than that effective at the lower height. Otherwise the time lag must be of ionospheric origin. In any case it would be expected that large flares S.P.A.'s (sudden phase anomalies), controlled by changes near the base of the ionosphere, would recover some 3–5 min earlier on the average than S.C.N.A.'s (sudden cosmic noise anomalies), controlled by the changes of total absorption through the ionosphere. Such a comparison does not appear to have been made.

The enhancement of the 70–75 km echo a few minutes before the commencement of the absorption increase at greater heights observed in 10–15 per cent. of the S.I.D.'s (Section III (*c*) (iii)) is puzzling, although it could be explained by the two-component ionization theory.

V. CONCLUSIONS

The main conclusion from the interpretation of these observations is that very large increases in electron density take place in the lower ionosphere. The relative increases in electron density are greatest near the bottom of the ionosphere: in a typical large S.I.D. associated with a class 2 or 3 flare the enhancement of ionization might vary from 20/1 at 65–70 km, through 3/1 at 90 km to unity at 110 km, while the actual electron density increase could average more than 1000/cm^3 over the height range 60–75 km.

It was found that, for moderately large S.I.D.'s, the *E*-echo recovery lagged about 4 min on the average behind the recovery of lower echoes around 85 km. Events at 85 km and lower heights appeared to be simultaneous.

While these observations have yielded new information on the effect of solar flares on the ionosphere, they have suffered from a lack of sensitivity and means for determining electron densities directly. If these deficiencies could be made good, more precise information on individual S.I.D.'s could be obtained. An increase in sensitivity of at least 10/1 in power would be necessary to show the detailed changes of strength of the " 70 km " echoes, which are the ones of interest. Electron densities could be obtained using polarized aerials in the way described in the previous paper. Because of the large increases in electron density involved, it would be best to work at frequencies in the 3–4 Mc/s range where the differential absorption of the ordinary and extraordinary waves is not too great.

Note :

A letter describing the effects of S.I.D.'s on *D*-region echo intensity records made on a frequency of 1·75 Mc/s at Christchurch has recently been published by Gregory (1958). The results quoted appear to agree reasonably with ours, although differences in detail on account of differences in frequency and location are to be expected.

VI. References

Bracewell, R. N., and Straker, T. W. (1949).—*Mon. Not. R. Astr. Soc.* **109** : 28.

Budden, K. G. (1951).—*Phil. Mag.* **42** : 1.

Bureau, R. (1937).—*Nature* **139** : 110.

Chubb, T. A., Friedman, H., Kreplin, R. W., and Kupperian, J. E., Jr. (1957).—*Nature* **179** : 861.

Ellison, M. A. (1950).—*Publ. R. Obs. Edinb.* **1** : 53.

Ellison, M. A. (1953).—*J. Atmos. Terr. Phys.* **4** : 226.

Gardner, F. F. (1950).—*Phil. Mag.* **41** : 1259.

Gardner, F. F. (1954).—*J. Atmos. Terr. Phys.* **5** : 298.

Gardner, F. F., and Pawsey, J. L. (1953).—*J. Atmos. Terr. Phys.* **3** : 321.

Gregory, J. B. (1958).—*J. Geophys. Res.* **63** : 273.

THEORY OF THE RADIO-ECHO METEOR HEIGHT DISTRIBUTION IN A NON-ISOTHERMAL ATMOSPHERE

By A. A. Weiss*

[*Manuscript received September* 29, 1958]

Summary

The theory of the distribution in height of the echoing points of shower meteors and of sporadic meteors belonging to a homogeneous velocity group, is extended to the case of a model atmosphere in which the scale height is a linear function of height. The mean and the r.m.s. deviation from the mean of the height distribution in this atmosphere are obtained in terms of tabulated functions, and the dependence of these parameters upon the scale height gradient is evaluated. Neither parameter varies strongly with the scale height gradient unless the incident meteors include a large proportion of massive particles. Experimental cut-off and the approximations made in the formulation of the theory limit the accuracy with which atmospheric scale height and density can be determined from observed heights of sporadic meteors.

I. Introduction

In two papers, Kaiser (1954*a*, 1954*b*) has presented a theory of the height distribution of the echoing points of meteors in an isothermal atmosphere, for both shower and sporadic meteors. He has shown that, apart from a small correction depending on the particular aerial system in use, the r.m.s. deviation of the height distribution for meteors of a particular shower, or for sporadic meteors in a narrow velocity range, depends only on the meteor mass distribution and on the scale height of the isothermal atmosphere. The atmospheric pressure and density at the mean height measured for meteors of a homogeneous velocity group are related to the physical properties of meteors (latent heat, density, velocity), the zenith angle of the meteor radiant, and the ionizing probability of an evaporated meteor atom.

The theory has been applied by Evans (1954, 1955) to the determination of atmospheric properties from simultaneous measurement of the height and velocity of sporadic meteors. He deduces an atmospheric scale height which increases by some 15 per cent. over the height range 90–100 km and atmospheric pressures and densities of the same order as those found by other techniques, e.g. rocket measurements. These results, in common with measurements by other methods, suggest that an isothermal atmosphere may not be the most appropriate model for the interpretation of the radio height measurements, and that an improvement in internal consistency and a more efficient use of observational data can be expected from a theory of the radio-echo height distribution based on a non-isothermal model atmosphere. The formulation of such a theory, starting with

---

* Division of Radiophysics, C.S.I.R.O., at Department of Physics, University of Adelaide.

an atmosphere whose scale height is a linear function of height, is the programme of this paper. This model atmosphere includes the isothermal atmosphere as a special case. It offers the distinct advantage that the moments of the theoretical height distribution, which form the link between theory and observation, are obtained in terms of tabulated functions. This feature greatly facilitates examination of the properties of the distributions.

II. Electron Density Profiles in a Linear Atmosphere

We assume a model atmosphere in which the scale height is a linear function of height. In such an atmosphere the scale height at any height h may be defined by

$$H=H_0+\{\delta/(1-\delta)\}(h-h_0), \quad \ldots\ldots\ldots\ldots\ldots \quad (1)$$

where H_0 is the scale height at some datum level h_0. The constant δ specifies uniquely the variation of the scale height with height. The density is

$$\rho=\rho_0(H/H_0)^{-1/\delta}, \quad \ldots\ldots\ldots\ldots\ldots\ldots\ldots \quad (2)$$

from which it is seen that $H\rho^\delta$ is an invariant for a particular atmosphere. This property is useful in changing the datum level.

The distribution of electron line density α along a meteor trail formed in this atmosphere is found by integrating the basic equations describing the evaporation of the meteor particle during its flight (Herlofsen 1947). By inserting the expression for the density gradient in this atmosphere, namely,

$$\frac{\mathrm{d}\rho}{\mathrm{d}h}=-\frac{\rho^{1+\delta}}{(1-\delta)H_0\rho_0^\delta},$$

at the appropriate points and accepting the usual approximations (see below), we obtain

$$\frac{\alpha}{\alpha_{\text{max.}}}=\frac{9}{4}\left(\frac{1-2\delta/3}{1-\delta}\right)^2\frac{\rho}{\rho_{\text{max.}}}\left[1-\frac{1}{3-2\delta}\left(\frac{\rho}{\rho_{\text{max.}}}\right)^{1-\delta}\right]^2, \quad \ldots\ldots \quad (3)$$

$$\alpha_{\text{max.}}=\frac{4}{9}(1-\delta)^2(1-2\delta/3)^{-3}\{\beta/(\mu H_{\text{max.}})\}m_\infty\cos\chi,$$

$$\rho_{\text{max.}}=\frac{8}{3}(1-2\delta/3)^{-1}\rho_m l r_\infty\cos\chi/(H_{\text{max.}}v_\infty^2),$$

$$r_{\text{max.}}=\frac{2}{3}(1-\delta)(1-2\delta/3)^{-1}r_\infty.$$

In these approximate expressions, the subscripts max., ∞ refer respectively to the point of maximum electron density in the trail and to the initial state of the meteor. $\beta=\beta_0 v_\infty^\eta$ is the ionizing probability, i.e. the probability that an evaporated meteor atom will produce a free electron ; the power-law form is assumed. The other quantities are : r, m, v, ρ_m=radius, mass, velocity, and density of the meteor ; χ=zenith angle of meteor radiant ; μ=mass of individual meteor atom ; l=latent heat of evaporation of a meteor atom, corrected for the efficiency of heat transfer.

The equations of which (**3**) is an approximate solution apply strictly to the evaporation of a spherical body with drag coefficient of unity. The following assumptions have also been made: (*a*) meteor deceleration is very small at all times; (*b*) $v^2 \gg 12l$; (*c*) $v^2 \gg 3l(2+\eta)$. The validity of these assumptions is open to question for slow meteors unless $l \ll 10^{11}$ erg/g (if v is measured in cm/sec) and $\eta \sim 0$ (Weiss 1958). Although these approximations have been retained in the interests of simplification, the departures of the approximate from the true electron density profiles are so large that consideration of their effects on the height distribution will be necessary at a later stage.

With $\delta=0$, the expressions (**3**) reduce to those for the isothermal atmosphere. Normalized electron densities are plotted in Figure 1 for three values of δ.

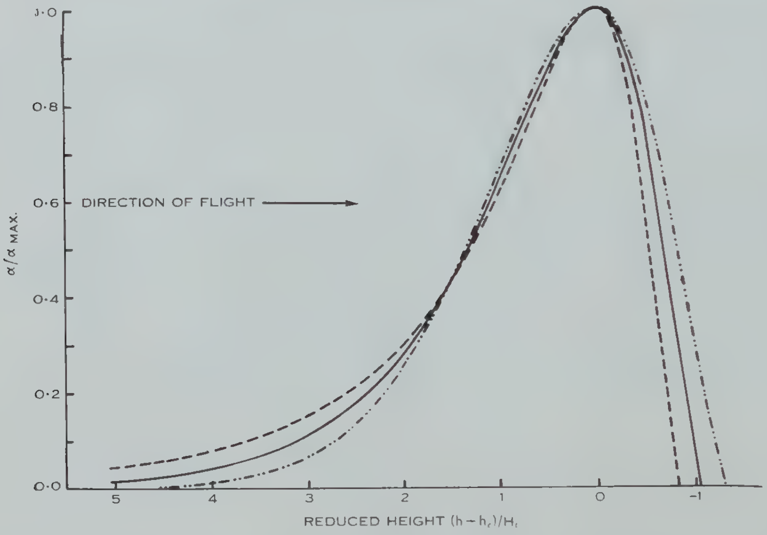

Fig. 1.—Electron density profiles in meteor trails formed in an atmosphere with a linear gradient of scale height H. h_c is the characteristic height for a given velocity, and δ defines the scale height gradient (see text). $\delta=-0{\cdot}2$, —··—··—·· ; $\delta=0$ (isothermal), ——————— ; $\delta=+0{\cdot}2$, — — — —.

From (**3**), we find that α electrons per unit length are produced, at a height where the density is ρ, by a meteor of mass

$$m=\left[\left(\frac{\alpha}{A_1\rho}\right)^{\frac{1}{2}}+\frac{\rho^{1-\delta}}{A_2\cos\chi}\right]^3, \quad \ldots\ldots\ldots\ldots\ldots\ldots \quad (4)$$

where

$$A_1=\{\pi\beta v^2/(2\mu l)\}\left(\frac{4}{3}\pi\rho_m\right)^{-2/3},$$

$$A_2=\{8\rho_m l/(v^2 H_0\rho_0^{\delta})\}\left(\frac{4}{3}\pi\rho_m\right)^{-1/3}.$$

Since the deceleration is assumed to be small, the velocity v in A_1 and A_2 refers to the initial state of the meteor and the subscript ∞ has been dropped.

III. The Elementary Height Distribution

Following the geometry of Figure I of Kaiser (1954*a*) and his development of the theory, we will restrict the treatment in this section to the echoing points of a homogeneous velocity group of meteors with a well-defined radiant, which are detected in a narrow sector $\theta-(\theta+d\theta)$ of the echo plane. We will further assume that the minimum detectable line density $\alpha_{\text{min.}}$ is a constant within this sector, independent of the range R of the echoing point. For given aerial gain and $\alpha_{\text{min.}}<10^{12}$ electrons/cm, $\alpha_{\text{min.}}$ is proportional to $R^{3/2}$. The heights of most echoing points, at least of sporadic meteors, extend from 70 to 120 km, so that in the given sector $\alpha_{\text{min.}}$ varies by a factor $(1\cdot 7)^{1\cdot 5}$, i.e. about 2. Neglect of this range factor will result in slight distortion in the elementary height distributions derived below, in the sense that the upper tail of the theoretical height distribution will be exaggerated relative to the lower tail.

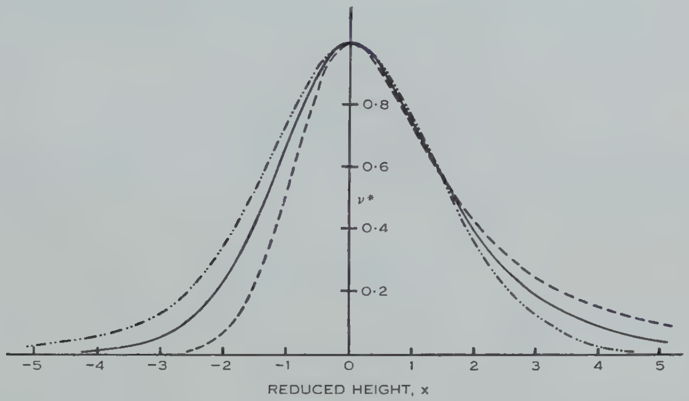

Fig. 2.—The dependence of the elementary height distribution ν^* upon the scale height gradient. Mass distribution parameter $s=1\cdot 5$. $x=(h-h_c)/H_c$. $\delta=-0\cdot 2$, —··—··—··; $\delta=0$, ————; $\delta=+0\cdot 2$, — — — —.

A characteristic density ρ_c is now introduced, such that

$$\rho_c=\{A_3^2\cos^2\chi\cdot\alpha_{\text{min.}}/4A_1\}^{1/(3-2\delta)}, \quad \ldots\ldots\ldots\ldots \quad (5)$$

where

$$A_3=A_2/(1-\delta).$$

ρ_c determines the height of detection of the smallest meteor of velocity v which it is possible to detect with the given equipment in the given sector. At any other height the smallest detectable meteor has a mass

$$m=\left(\frac{\alpha_{\text{min.}}}{A_1}\right)^{3(1-\delta)/(3-2\delta)}\left(\frac{2}{A_3\cos\chi}\right)^{3/(3-2\delta)}\left[z^{-\frac{1}{2}}+\frac{z^{1-\delta}}{2(1-\delta)}\right]^3, \quad \ldots \quad (6)$$

where $z=\rho/\rho_c$. With the usual frequency law for the distribution of meteor masses, namely,

$$N_m dm=m^{-s}dm, \quad \ldots\ldots\ldots\ldots\ldots\ldots \quad (7)$$

the normalized elementary height distribution becomes

$$\nu^*=\left[\frac{3-2\delta}{2(1-\delta)z^{-\frac{1}{2}}+z^{1-\delta}}\right]^{3(s-1)}, \qquad \ldots\ldots\ldots\ldots \quad (8)$$

in which z may be written

$$z=\rho/\rho_c=\{1+x\delta/(1-\delta)\}^{-1/\delta}. \qquad \ldots\ldots\ldots\ldots \quad (9)$$

x is the reduced height, measured in units of scale height H_c from the level of the characteristic density ρ_c.

With $\delta=0$, (8) and (9) reduce to Kaiser's elementary height distribution for the isothermal atmosphere. Figure 2 illustrates the dependence of the height distribution upon the gradient of the scale height for $s=1{\cdot}5$.

IV. PROPERTIES OF THE ELEMENTARY HEIGHT DISTRIBUTION

The mean and the r.m.s. deviation from the mean of the distribution (8) are determined through the integrals

$$I_p=\int_{-\infty}^{\infty}\nu^* x^p \mathrm{d}x, \qquad \ldots\ldots\ldots\ldots\ldots\ldots \quad (10)$$

with $p=0$, 1, 2. Evaluation of these integrals is straightforward. Use of (9) together with the substitution

$$z^{3/2-\delta}=2(1-\delta)(1-w)/w$$

leads to

$$I_p=K(s,\delta)\left(\frac{1-\delta}{\delta}\right)^{p+1}\sum_{r=0}^{p}\binom{p}{r}(-1)^{p-r}\{2(1-\delta)\}^{-2r\delta/(3-2\delta)}\mathrm{B}(a,b). \qquad \ldots\ldots\ldots\ldots\ldots\ldots \quad (11)$$

in which

$$K(s,\delta)=2\delta(3-2\delta)^{3s-4}\{2(1-\delta)\}^{-\varepsilon},$$

$\mathrm{B}(a,b)$ is the complete beta function $\int_0^1 w^{a-1}(1-w)^{b-1}\mathrm{d}w$ with

$$a=\{6s(1-\delta)-6+2\delta(r+4)\}/(3-2\delta),$$
$$b=\{3(s-1)-2\delta(r+1)\}/(3-2\delta),$$
$$\varepsilon=a-2r\delta/(3-2\delta).$$

The mean reduced height is

$$\bar{x}=I_1/I_0, \qquad \ldots\ldots\ldots\ldots\ldots\ldots\ldots\ldots \quad (12)$$

and the mean square deviation from the mean is

$$(\Delta x)^2=I_2/I_0-\bar{x}^2. \qquad \ldots\ldots\ldots\ldots\ldots\ldots \quad (13)$$

For the isothermal atmosphere

$$I_0=\int_{-\infty}^{\infty}\nu^*\mathrm{d}x=\{3^{3s-4}/2^{2s-3}\}\mathrm{B}(2s-2,\ s-1),$$

but for higher orders (12) and (13) reduce to indeterminate forms and the mean and r.m.s. deviation must be found as limits as $\delta\to0$. Figure 3 is a plot of the parameters of the height distribution for three values of s.

One feature arising in the evaluation of the moments through the integrals (**10**) is worthy of comment. The beta function $B(a,b)$ becomes infinite if either argument is zero. With $r=2$, $b=3(s-2\delta-1)/(3-2\delta)$. Values of s found for shower meteors using isothermal theory range from $s=1\cdot4$ to $s=2\cdot7$. In the actual atmosphere δ is essentially positive, at least in all but the lowest levels of the meteor region. With $s=1\cdot5$ and $r=2$, $b=3(0\cdot5-2\delta)/(3-2\delta)$, and quite moderate values of δ will produce a height distribution whose r.m.s. deviation Δx is large (compare Fig. 3). This behaviour is associated with the long upper tail of the height distribution, which in turn is the result of the slow rise of the meteor trail to maximum electron density. Even with $s=2\cdot0$, the value for sporadic meteors, Δx is quite sensitive to δ if $\delta>0$.

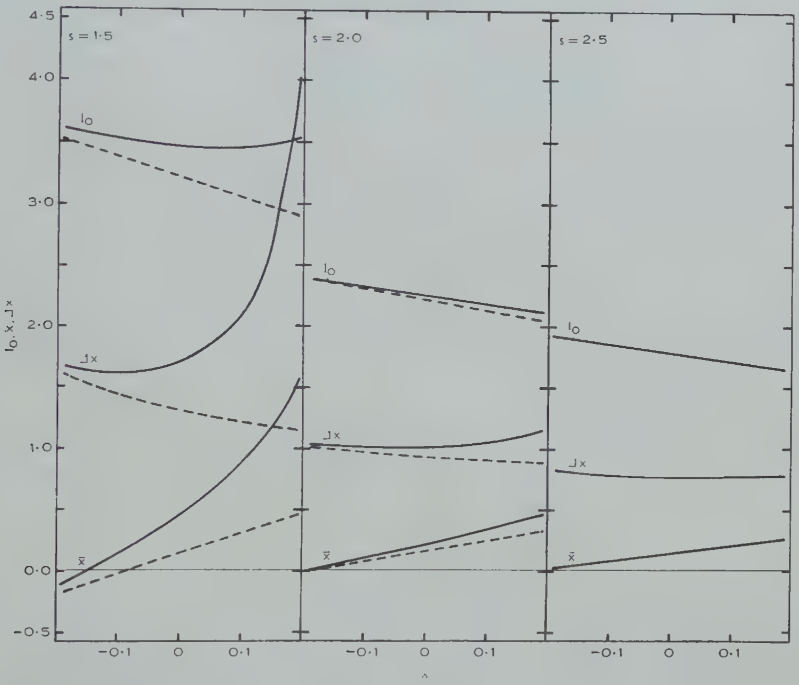

Fig. 3.—Properties of the elementary height distribution as functions of the scale height gradient and the mass distribution parameter s. I_0=zero moment, $\bar{x}$=mean, Δx=r.m.s. deviation from the mean, all in units of reduced height, $x=(h-h_c)/H_c$. ———— Full distribution; — — — — distribution truncated at $x=3$.

The contribution of the upper tail of the height distribution to $\bar{x}$ and Δx will now be examined in more detail, with the aid of numerical examples. If the height distribution is truncated at the height x_0, the contribution of the truncated tail to the integral I_p is

$$I'_p=\int_{x_0}^{\infty} \nu^* x^p \mathrm{d}x. \quad \ldots\ldots\ldots\ldots\ldots\ldots \quad (\mathbf{14})$$

For $x>3$ and $\delta<0\cdot2$, the term $z^{1-\delta}$ in ν^* is less than 2 per cent. of the other term $2(1-\delta)z^{-\frac{1}{2}}$ and may be neglected. Hence

$$I'_p=\left[\frac{3-2\delta}{2(1-\delta)}\right]^{3(s-1)}\int_{x_0}^{\infty} z^{3(s-1)/2}x^p\mathrm{d}x, \quad \ldots\ldots\ldots\ldots \quad (\mathbf{15})$$

For positive δ, with the substitution

$$w=\{1+x\delta/(1-\delta)\}^{-1}$$

and use of (**9**), (**15**) takes the form

$${}_+I'_p=\left[\frac{3-2\delta}{2(1-\delta)}\right]^{3(s-1)}\left(\frac{1-\delta}{\delta}\right)^{p+1}\mathrm{B}_{w_0}(c_+,d), \quad \ldots\ldots\ldots \quad (\mathbf{16})$$

where $\mathrm{B}_{w_0}(c,d)$ is the incomplete beta function $\int_0^{w_0} w^{c-1}(1-w)^{d-1}\mathrm{d}w$

with

$$c_+=\{3(s-1)/2\delta\}-p-1,$$
$$d=p+1.$$

For negative values of δ, the appropriate substitution is

$$w=1+x\delta/(1-\delta),$$

from which

$${}_-I'_p=\left[\frac{3-2\delta}{2(1-\delta)}\right]^{3(s-1)}\left(\frac{\delta-1}{\delta}\right)^{p+1}\mathrm{B}_{w_0}(c,d), \quad \ldots\ldots\ldots \quad (\mathbf{17})$$

where

$$c_-=1-3(s-1)/2\delta.$$

The parameters of the height distribution truncated at $x_0=3$ are also illustrated in Figure 3. The r.m.s. deviations of the full and the truncated distributions differ significantly for large positive values of δ even if s is as large as $2\cdot0$. For smaller values of s, the differences rapidly become very large.

V. The Complete Height Distribution

The complete height distribution for shower meteors is obtained by integrating the elementary height distribution (**8**), for the sector $\theta-(\theta+\mathrm{d}\theta)$ of the echo plane, with respect to θ over the whole echo plane, with due allowance for the collection sensitivity of the equipment which is also a function of θ. In the case of sporadic meteors belonging to a homogeneous velocity group a further integration is necessary, over all sporadic meteor radiants on the geocentric celestial sphere. The alterations to the mean and r.m.s. deviation necessitated by this passage from elementary to complete height distribution have been exhaustively discussed by Kaiser for the isothermal atmosphere. In general the corrections are small and only become serious as the mass distribution parameter s decreases well below $2\cdot0$; they are also insensitive to the form of the aerial polar diagram.

The parameters of the complete height distribution for the linear atmospheric model could be evaluated in the same way. However, in view of the smallness of the corrections for the isothermal model, there seems little to be gained by carrying through the calculations, which become very tedious. The corrections for the isothermal model, taken over unchanged, should be sufficiently accurate for all practical purposes unless $\delta \gg 0$ and $s \ll 2 \cdot 0$.

In the case of sporadic meteors, the extension from elementary to complete height distribution is made by first evaluating the rate of echoes and the height distribution (φ-distribution) observed in an element of solid angle $d\omega$ having coordinates (φ=elevation, θ=azimuth). For an assumed uniform geocentric distribution of radiants, and with $s=2 \cdot 0$, the mean $\bar{X}$ and the r.m.s. deviation ΔX of the φ-distribution are (Kaiser 1954*b*) :

$$\bar{X}-\bar{x}=-\frac{2}{3}\int_0^{\pi/2} \cos\xi \ln(\cos\xi)d\xi, \quad \ldots\ldots\ldots\ldots \quad (\mathbf{18})$$

$$(\Delta X)^2-(\Delta x)^2=-(\bar{X}-\bar{x})^2+\frac{4}{9}\int_0^{\pi/2} \cos\xi \ln^2(\cos\xi)\, d\xi, \quad \ldots \quad (\mathbf{19})$$

in which ξ is defined by $\cos\chi=\cos\varphi\cos\xi$. It is assumed that the equipment sensitivity is such that the minimum detectable line density is much less than 10^{12} electrons/cm over most of the aerial aperture. The parameters $\bar{X}$, ΔX are illustrated in Figure 4 as functions of δ.

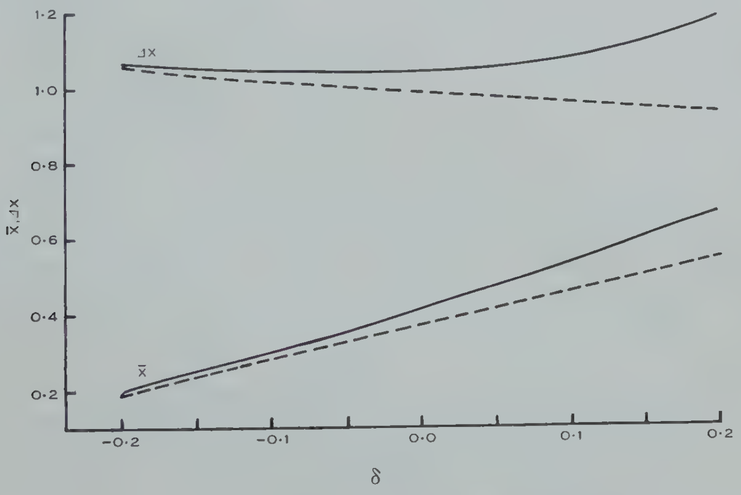

Fig. 4.—Properties of the complete sporadic height distribution observed within a narrow elevation interval. Aerial polar diagram is independent of azimuth. ———— Full distribution ; — — — — distribution truncated at x=3.

For the Adelaide equipment (Robertson, Liddy, and Elford 1953) which operates continuously for extended periods and whose aerial polar diagram is almost symmetrical about the zenithal direction and so is independent of azimuth θ, the assumption of a uniform radiant distribution is justified, and the elementary height distribution will be independent of azimuth. Weighted integration of the φ-distributions is still necessary to build up the complete distribution as observed. Proper weighting would be difficult for the Adelaide equipment, whose echo rate is determined by the line-of-sight velocity of drift of the meteor trails as well as by the aerial polar diagram. By selecting a narrow elevation interval over which the equipment sensitivity may be regarded as substantially constant, the final integration is eliminated (Kaiser 1954*b*) and Figure 4 may be taken as a sufficient approximation to the parameters of the complete sporadic meteor height distribution for a homogeneous velocity group. What constitutes a sufficiently narrow elevation interval can best be ascertained by a preliminary analysis of the records.

VI. Experimental and Theoretical Limitations

Two major limitations to the accuracy with which the derived theoretical height distributions can be expected to represent the measured distributions will now be examined.

Experimentally, the diffusion of the meteor trails will be of some consequence in modifying the upper portion of the height distributions. This acts in two ways. In the first place, diffusion of high meteor trails is so rapid that some are inevitably missed in a photographic radio record. Secondly, Hawkins (1956) has drawn attention to the existence of a diffusion ceiling, a critical height above which Fresnel zones will tend to disappear, thus preventing measurement of velocity even if the height is recorded. The importance of this diffusion cut-off will depend on the operating frequency and the method of recording, and may be ascertained in any particular case from a detailed examination of the records. The numerical examples already given (Figs. 3 and 4) for an elementary distribution truncated at $x=3$ indicate the order of magnitude of the errors which will be introduced by failure to recognize and correct for a severe diffusion cut-off.

The other limitation, a theoretical one, is associated with the assumptions leading to the approximate electron density profiles (**3**). The author (Weiss 1958) has already examined the discrepancy between the true and the approximate profiles for the special case of a spherical meteor evaporating in an isothermal atmosphere. The discrepancy in a linear atmosphere should not be greatly different for reasonable values of δ. An exact evaluation of the errors in the height distributions themselves is precluded by the alterations of the shape of the profiles introduced by the approximations. The approximations tend to understate the length of trail beyond the point of maximum electron density for meteors of all velocities ; in addition the trails of slow meteors do not rise to the sharp maximum predicted by the approximations. It seems reasonable to infer that the approximations will not seriously distort the theoretical height distributions for fast meteors but will tend to give too-peaked theoretical distributions for slow meteors.

Some useful conclusions regarding the error in the characteristic height for a given velocity group are also possible. This is so because the mean height for a given velocity will be determined largely by the smaller meteors accessible to the equipment. These small meteors, seen in the largest numbers, will be detected closer to the point of maximum electron density than is the case for the more massive meteors which contribute to the tails of the distribution.

Using the improved approximations suggested by the author (equations (5) of Weiss (1958)) for conditions near the maximum, we obtain the following relation, for $\alpha_{\text{max.}}=\text{constant}$:

$$\rho_{\text{max.}}=v_{\text{max.}}{}^{-(2+\eta/3)}F(\eta)^{-2/3}, \quad \ldots\ldots\ldots\ldots\ldots \quad (20)$$

where

$$v_{\text{max.}}=\left[v_\infty^2-12l\,.\,\ln\left\{\frac{1+2F(\eta)}{2F(\eta)}\right\}\right]^{\frac{1}{2}},$$

$$F(\eta)=1+3l(2+\eta)/v_\infty^2.$$

From the usual approximation (3)

$$\rho_{\text{max.}}=v_\infty{}^{-(2+\eta/3)}, \quad \ldots\ldots\ldots\ldots\ldots\ldots\ldots\ldots \quad (21)$$

which is independent of l. These two relations are compared in Figure 5, with 60 km/sec as datum velocity. Evidently the approximate expressions (3) used in formulating the theory will have little effect on the true relation between meteor velocity and height for fast meteors, and for slow meteors only if $l \gg 10^{11}$ erg/g, which is unlikely.

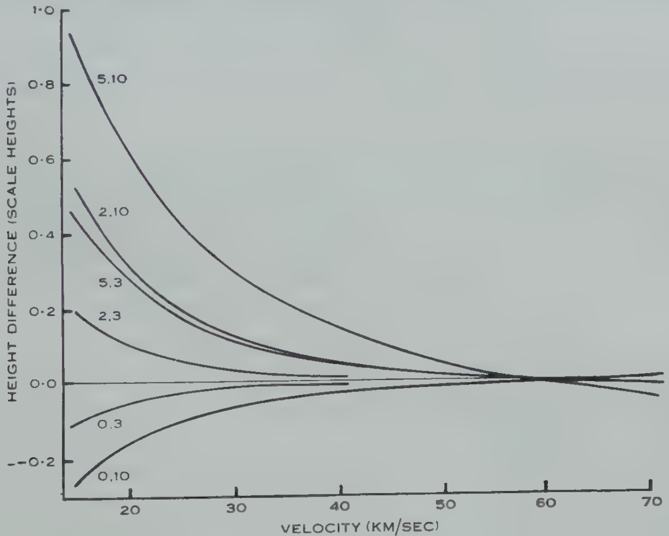

Fig. 5.—Approximate differences between characteristic heights with the usual and the improved approximations for trail shape. The code is (η, l'), where η=exponent in ionizing probability law, $l'=l\times10^{-11}$, l=effective latent heat of evaporation of a meteor atom (erg/g).

VII. Discussion

Atmospheric densities and scale heights and the gradient of the scale height, evaluated from the radio-echo meteor height distribution through the isothermal model atmosphere, already agree well with the results of measurements by other techniques. Nevertheless, the isothermal model can only make statements about the mean value of the scale height over the whole of the height range over which meteors of a given velocity are detected. Since the gradient of the scale height over the meteor region is not large, it cannot be expected that the linear model atmosphere will lead to any marked improvement in the numerical values of the atmospheric properties, although it will extend the domain over which they may be studied to the whole of the meteor region. The value of the new approach is rather to be sought in the more efficient use of data which it allows, in that the atmospheric properties can be derived from the height measurements treated as a whole, without a preliminary segregation into velocity groups.

The accuracy of numerical deductions from the theory is limited by diffusion and other experimental cut-off and by the approximations accepted in the formulation of the theory. Some allowance can be made for the experimental cut-off, but it seems that little can be done at present about the theoretical limitations, mainly because of ignorance of the absolute values of the meteor constants, particularly the latent heat, and of the velocity-dependence of the ionizing probability of an evaporated meteor atom. Ultimately, the failure of a linear scale height gradient to represent the actual atmosphere will become important, but a preliminary assessment, which indicates $\delta \sim 0 \cdot 15$, suggests that this model is acceptable over that part of the meteor region lying above 90 km.

Finally, it must be stressed that all the preceding considerations are based on the model of a spherical meteor particle and a simple evaporation process. If the phenomenon of fragmentation, advanced by Jacchia (1955) in explanation of anomalies in atmospheric densities derived from photographic meteors, is severe and widespread, this simple model will fail completely as a description of the actual meteor trail. The trails will form higher in the atmosphere and will be shorter in length. There is no real evidence either for or against fragmentation amongst faint radio meteors ; photographic meteors are very bright by radio standards and can constitute only a very small fraction of the meteors detected by a normal radio equipment. If the theory of the height distribution of the echoing points of meteor trails formed by evaporation can be made sufficiently precise, it can be used to advantage in assessing the extent to which the evaporation model corresponds with reality.

VIII. Acknowledgments

The author wishes to acknowledge the assistance of Dr. C. A. Hurst in the evaluation of the moments of the height distributions through beta-functions.

IX. References

Evans, S. (1954).—*Mon. Not. R. Astr. Soc.* **114** : 63.
Evans, S. (1955).—" Meteors." (Ed. T. R. Kaiser.) p. 86. (Pergamon Press : London.)
Hawkins, G. S. (1956).—*Proc. Inst. Radio Engrs., N.Y.* **44** : 1192.
Herlofsen, N. (1947).—*Rep. Prog. Phys.* **11** : 444.
Jacchia, L. G. (1955).—*Astrophys. J.* **121** : 521.
Kaiser, T. R. (1954*a*).—*Mon. Not. R. Astr. Soc.* **114** : 39.
Kaiser, T. R. (1954*b*).—*Mon. Not. R. Astr. Soc.* **114** : 52.
Robertson, D. S., Liddy, D. T., and Elford, W. G. (1953).—*J. Atmos. Terr. Phys.* **4** : 255.
Weiss, A. A. (1958).—*Aust. J. Phys.* **11** : 591.

ELEVATION, HEIGHT, AND ELECTRON DENSITY OF ECHOING POINTS OF METEOR TRAILS

By A. A. Weiss*

[*Manuscript received September* 29, 1958]

Summary

Continuous and systematic operation of a C.W. equipment which measures simultaneously several characteristics of meteor echoes, including the location in space of the reflection point, provides the basic material for an examination of the geometry of detection of meteor trails by radio equipments and of the processes underlying selection of echoes for measurements of different kinds.

At least 60 per cent. of all echoes are distorted in some degree, presumably by atmospheric turbulence or by non-specular reflection. This and selection in height due to diffusion of the trail are the two most important selection processes.

The distribution of the echoing points of sporadic meteors, in zenith angle and in height, is compared with theoretical expectation. Height distributions found for Arietid and ζ-Perseid meteors agree with other measurements. The height distribution for the Geminid shower is unexpectedly narrow, a fact for which no satisfactory explanation can be advanced. Distributions of electron line densities at reflection points agree qualitatively with known mass distributions and trail shapes.

I. Introduction

Since 1952 a 27 Mc/s C.W. equipment for observation of meteors has been in operation at Adelaide. Full details of the original installation and aerial system will be found in Robertson, Liddy, and Elford (1953). With this equipment the following characteristics of selected meteor echoes may be measured simultaneously: (*a*) direction and slant range of reflection point on the meteor trail relative to the observing station, (*b*) line-of-sight velocity of drift of the meteor trail, (*c*) echo amplitude, (*d*) rate of decay of echo. The first two quantities are required for measurement of wind in the meteor region (Elford and Robertson 1953). The first alone suffices for measurement of the heights of the reflection points. From the rate of decay of the echo and the height of the reflection point the height-dependence of the diffusion coefficient and its absolute value can be established (Weiss 1955*b*). Electron densities follow from the echo amplitude and the position of the echoing point. In addition, the azimuth of the reflection point and the time of occurrence of each echo, whether suitable for detailed measurement or not, lead to results of direct importance to meteor astronomy (Weiss 1957).

In all these studies the fully automatic equipment is operated systematically in routine and continuous surveys. This is followed by reading of all echoes

---

* Division of Radiophysics, C.S.I.R.O., at Department of Physics, University of Adelaide.

suitable for wind measurement and culminates in the establishment of diurnal and seasonal variations in the parameters measured. One unforeseen consequence of this routine operation is the automatic availability of a precise location of each reflection point whenever any meteor parameter (not winds) is under study. This, coupled with the relatively simple aerial system and its cylindrical symmetry, permits a ready assessment of the dependence of meteor parameters upon the elevation and range of the reflection point. This is a distinct advantage, as these geometrical factors are of some consequence in the interpretation of radio data. With the very great majority of radio equipments such a detailed examination of the geometry of detection is impossible.

The present treatment is largely confined to aspects of the distribution in height of reflection points for both shower and sporadic meteors. Some measurements of electron line densities are also analysed. The prerequisite for such measurements is of course the aerial gain in the direction of the reflection point, but, in addition, a careful selection of echoes is of prime importance. The reasons for rejection of echoes as unsuitable for measurement of the position of the reflection point and the line density are so illuminating that a full discussion is considered appropriate.

II. Selection of Echoes for Measurement

The selection of echoes for wind measurement is a rather severe process, which results in rejection of over 80 per cent. of echoes recorded. The effects of this selection will be noticed repeatedly in succeeding sections. Records for September 1953 have been analysed in detail.

Of 4730 meteors recorded, only 872, or 18·4 per cent., were suitable for wind measurement. Reasons for rejection were ascertained from 4 days' records embracing 500 meteors, of which 98, or 19·6 per cent., were read ; the details are summarized in Table 1. In amplification of the various categories of this table, the requirements for reading for winds may be stated : (*a*) the frequency of the Doppler beat pattern between sky and ground wave must not be too high or too low ; if too high, the positions of maxima (or minima) on some or all of the five direction-finding aerials cannot be determined with sufficient accuracy, and if too low the echo decays or is terminated by the automatic camera sequencing unit before a sufficient number of Doppler cycles are traversed ; (*b*) the duration of the echo must be sufficiently long to provide the requisite number of Doppler cycles ; (*c*) echo amplitude must not be too large or too small, if too large the maxima of the beat pattern are cut off by receiver saturation ; (*d*) the echo must not be severely distorted by turbulence, multiple centres, or other non-specular reflection ; (*e*) the slant radar range must be recorded. Since for no echo satisfying criteria (*a*) to (*d*) did the slant range fail to record, (*e*) is not a limitation in practice. In effect, echoes are rejected for wind measurement only because the direction of the reflection point cannot be ascertained.

A restriction on echo amplitude is essentially one imposed on the electron density in the trail at the reflection point, in relation to the aerial gain in this direction. Elimination of echoes on the grounds of distortion may be height-sensitive. A low Doppler beat frequency implies a small component of drift velocity in the line of sight. If this arises in a small actual drift velocity, echo selection will be azimuth-sensitive, perhaps mitigated by the diurnal changes in wind speed and direction. For reflection points close to the zenith, however, the line-of-sight wind component is always small, as the wind drift is essentially horizontal. Echo duration is related to the diffusion coefficient, which increases rapidly with height (Weiss 1955*b*); at 27 Mc/s height selection above 100 km may be severe. Since the height distribution of atmospheric and meteor parameters, found either from height correlations (e.g. winds, diffusion coefficients) or directly from the height distributions themselves, is one of the major contributions of meteor physics to the study of the atmosphere in the meteor region, selection of echoes by height is of considerable importance. It is one, moreover, to which every radio equipment is subject to an extent depending on the form of presentation of the echo and the operating frequency. Compared with this, selection in azimuth and in zenith angle is trivial.

TABLE 1

ANALYSIS OF ECHOES REJECTED AS UNSUITABLE FOR WIND MEASUREMENT

Type of Echo	Number of Echoes
Low Doppler beat frequency	60
High Doppler beat frequency	1
Echo decay too rapid	216
Low echo amplitude	45
High echo amplitude	14
Distorted echo waveform	66
Suitable for measurement	98
Total number of echoes	500

Of the 872 echoes for which reflection points could be located, echo amplitudes and hence electron densities were measured for 482. In the majority of cases rejection was associated with departures of the echo waveform from the smooth growth (persistent echoes only) and decay (all echoes) expected of a meteor trail dissipating by ambipolar diffusion in a quiescent atmosphere. Reference to Table 1 reveals 66 out of 164 otherwise readable echoes already rejected for distortion so severe that reflection points could not be located. We have here an additional 390 echoes (out of 872) which are less severely distorted. If these figures are representative, then at least 60 per cent. of all echoes are distorted in some degree by atmospheric turbulence, multiple reflection centres, or other non-specular reflection. This high rate may not apply without qualification to other equipments; indeed, less non-specular reflection and hence less distortion would be expected at higher frequencies. The importance of the result is that it emphasizes the danger of indiscriminate interpretation of echo amplitude and duration measurements on the basis of a theory of specular reflection by trails diffusing without distortion.

III. ZENITH ANGLES OF REFLECTION POINTS

(a) *Sporadic Meteors*

The distribution in zenith angle of the reflection points of sporadic meteors for September 1953 is illustrated in Figure 1. That this distribution is largely independent of the source distribution over the celestial sphere is shown by the absence of a marked diurnal variation (Weiss 1957) and the identical distribution found for March 1953.

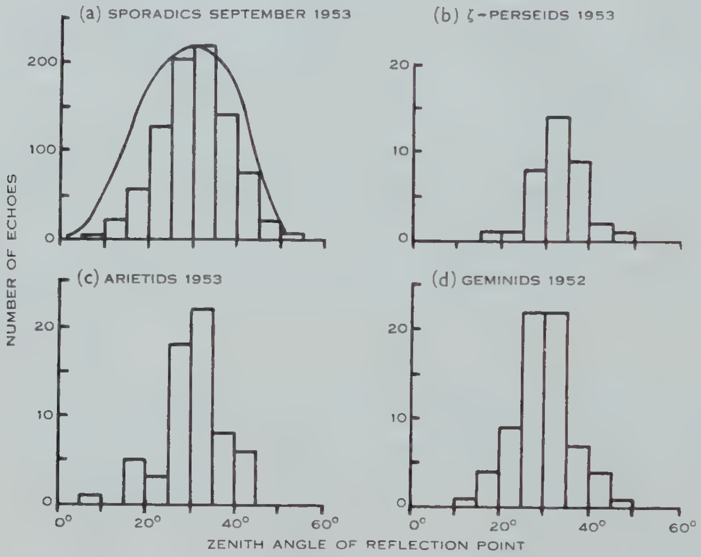

Fig. 1.—Zenith angles of reflection points of sporadic and shower meteors. The full line is the distribution predicted for a uniform sporadic radiant distribution.

This distribution may be compared with the prediction (Kaiser 1954*b*) for a uniform distribution of radiants on the geocentric celestial sphere. The number of echoes observed per unit zenith angle interval is

$$N_z = \text{const. } \sin^s z \cos^{(3s-7)/2} z\, S^{2(s-1)}(z), \quad \ldots\ldots\ldots\ldots \quad (1)$$

where z is the zenith angle of the reflection point, s the mass distribution parameter, and $S(z)$ the aerial polar diagram function (amplitude). In terms of power gains, $S^2(z) = (G_T G_R)^{\frac{1}{2}}$. For sporadic meteors $s = 2\cdot 0$.

Aerial power polar diagrams for the major lobes of the transmitting and receiving aerials and the composite polar diagram appear in Figure 2. Small departures from rotational symmetry are introduced by the separation of transmitting and receiving stations, and by asymmetry in the north-south and east-west traverses of the individual polar diagrams, but the composite polar diagram should apply to the majority of echoes.

Function (**1**) is included in Figure 1 (*a*). The positions of predicted and measured maxima agree excellently, but the measured distribution is sharper than predicted. At small zenith angles this could be due to discrimination against small zenith angles through low Doppler beat frequencies (Section II). At large zenith angles, where the composite power gain is less than 10 per cent. of the maximum gain, the aerial polar diagram of Figure 2 is least accurate, and the discrepancy could be eliminated by an increase in aerial gain by a factor of 2 or so.

(*b*) *Shower Meteors*

Distributions for three showers are also given in Figure 1. These are all sharper than the distribution for sporadic meteors. All three showers transit low in the north at Adelaide, and the sharpness of the distributions must be sought in different source distributions for showers and sporadics. Echoes cannot be detected at zenith angles numerically smaller than the elevation of the radiant, if specular reflection is assumed. For radiants near the horizon the collecting area for showers with compact radiants is much more limited than for sporadic meteors, whose radiants may lie in any azimuth. Accordingly, shower meteors should give fewer reflection points at small zenith angles than sporadic meteors, as observed. At the other extreme, the limited elevation reached by shower radiants should result in a deficiency of reflection points at large zenith angles. This will not be very marked, as the equipment sensitivity falls off rapidly as the radiant elevation increases beyond 30°.

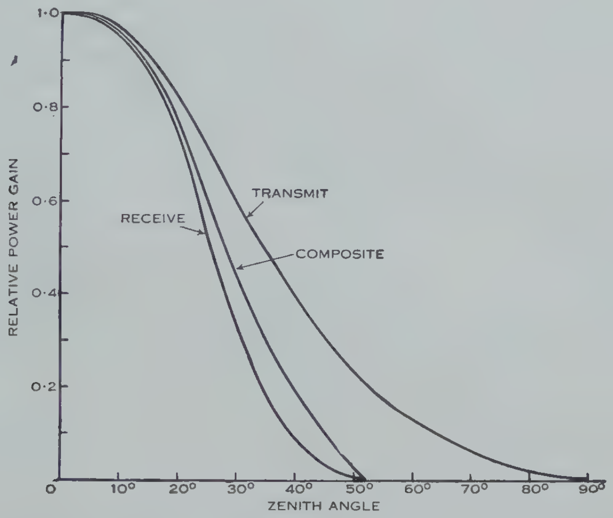

Fig. 2.—Power polar diagrams of the major lobes of the aerial system.

IV. Electron Line Densities

Figure 3 depicts distributions of echo amplitudes, relative to ground wave = 1 (measured at the receiver output), for three groups of sporadic meteors and three showers. The differences between the groups of echoes are barely significant

When echo amplitudes were measured, the form of each echo was noted. Two types of echo may be distinguished. The short, decay-type echo is characterized by an almost instantaneous rise to maximum amplitude, followed by an exponential decay; for such echoes the electron line density $\alpha < 2 \times 10^{12}$ electrons/cm. The other type, persistent echoes with $\alpha > 2 \times 10^{12}$, shows a slower rise to a flat maximum, followed by the exponential decay.

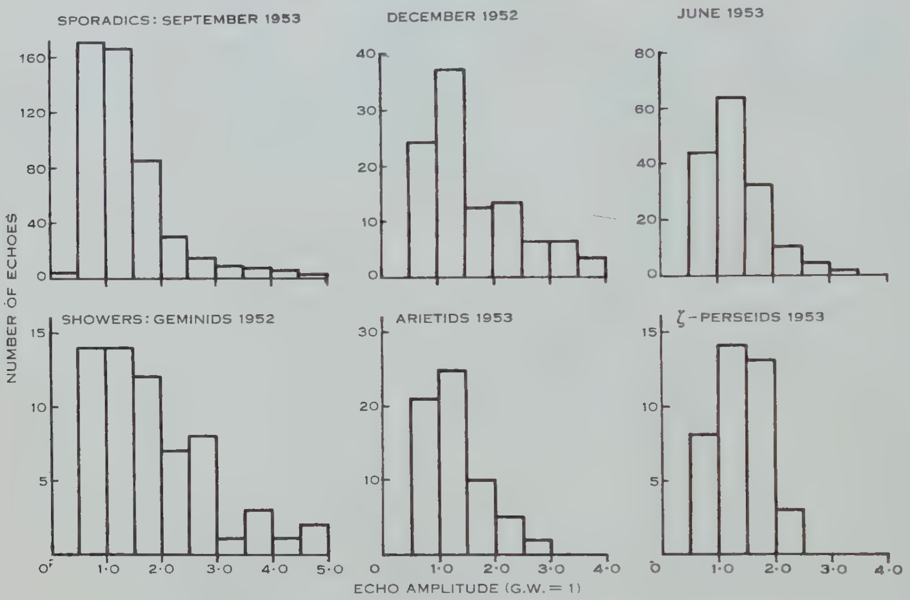

Fig. 3.—Distributions of echo amplitudes, relative to ground wave amplitude.

For short echoes, the line density is given by the Lovell-Clegg scattering formula

$$\alpha_S = (32\pi^2 R^3 \varepsilon / P G_T G_R \lambda^3)^{\frac{1}{2}} (mc^2/e^2), \quad \ldots\ldots\ldots\ldots \quad (2)$$

whilst for persistent echoes

$$\alpha_P = (54\pi^3 R^3 \varepsilon / P G_T G_R \lambda^3)^2 (mc^2/e^2). \quad \ldots\ldots\ldots\ldots \quad (3)$$

In these expressions, and for the equipment in question,

P = transmitter power = 250 W,
ε = echo power = 3×10^{-14} W minimum,
R = slant range to reflection point (m),
λ = wavelength = 11·2 m,
G_T = transmitting aerial power gain = 9·5 maximum,
G_R = receiving aerial power gain = 6·5 maximum.

With these equipment parameters, and echo amplitude A expressed in units of ground wave amplitude measured at the receiver output,

$$\alpha_S = 3A \times 10^9 (R^3/G_T G_R)^{\frac{1}{2}}, \quad \ldots\ldots\ldots\ldots\ldots \quad (4)$$

$$\alpha_P = 50A^4 (R^3/G_T G_R)^2. \quad \ldots\ldots\ldots\ldots\ldots\ldots \quad (5)$$

R is now in kilometres and the product $G_T G_R$ is normalized to 100 max.

All decay-type echoes have been reduced using the Lovell-Clegg formula (4). This procedure gave very few decay-type echoes with apparent line densities $>2\times10^{12}$ electrons/cm. Since neither formula (4) nor (5) is expected to be accurate for intermediate type echoes with $\alpha\sim2\times10^{12}$, echoes classed as persistent, which included quite a few of intermediate type, were reduced using whichever expression (4) or (5) gave the greater line density. Line densities computed on this basis may not be particularly accurate, but this procedure was justified in that it would accentuate any differences in the distributions of line densities which may exist between showers and sporadics and between showers *inter se*. A further source of inaccuracy in the computation of line densities for persistent echoes is the high powers to which the echo amplitude and the aerial gain are raised in (5).

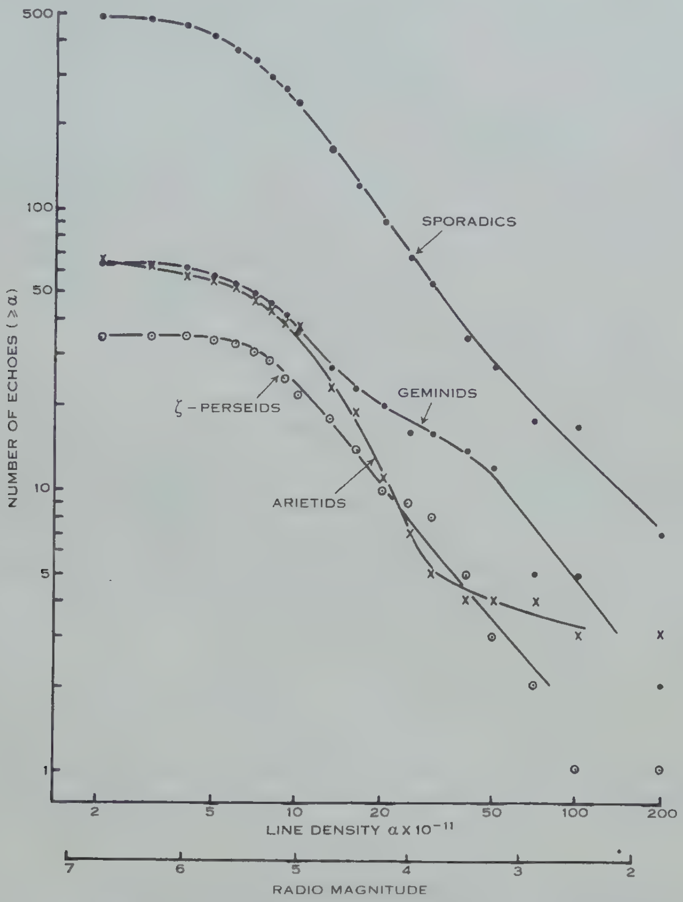

Fig. 4.—Distributions of measured electron densities (electrons/cm) for sporadic and shower meteors.

Figure 4 is a double logarithmic plot showing the number of echoes for which line densities exceed or are equal to α. Radio magnitudes M_r, on the definition of Kaiser (1955), are also shown. For the reasons given above, the distributions in Figure 4 can only be regarded as qualitative. They do, however, show up directly the excess of bright meteors in the Geminid stream, and their marked deficiency in the Arietid stream, which is to be expected from the mass distributions found by Browne *et al.* (1956). Although it is not very well brought out in Figure 4, all three showers exhibit a decrease, relative to sporadic meteors, in numbers of meteors fainter than $M_r \sim 5$. This may be a geometrical effect, or it may indicate a real deficiency of faint meteors in these streams. Further observations, with larger samples extending to fainter meteors, will be needed to settle this point.

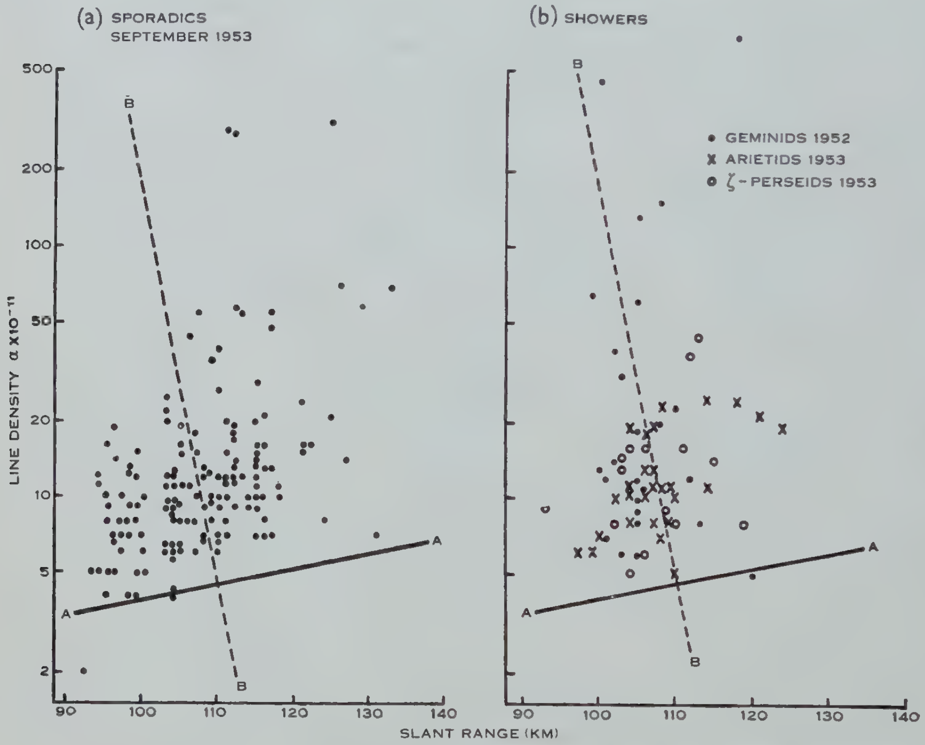

Fig. 5.—Range-electron density (electrons/cm) scatter diagrams for sporadic and shower meteors with $30 \leqslant z \leqslant 35$. *AA* is the locus of minimum detectable electron density, *BB* the locus of the points of maximum electron density in the trails, if atmospheric scale height = 7 km.

For sporadic meteors brighter than $M_r = 5 \cdot 5$, the empirical relation for the number of meteors with line densities $\geqslant \alpha$ detected by this equipment is

$$N(\geqslant \alpha) = \text{const. } \alpha^{-1 \cdot 33}.$$

In terms of radio brightness

$$N(\leqslant M_r) = \text{const. } 3 \cdot 40^{M_r}.$$

Finally, range-line density scatter diagrams for narrow intervals of zenith angle have been prepared. The one for $30 \leqslant z \leqslant 35°$ is reproduced in Figure 5. The curve *AA* is the limiting line density, corresponding to $A = \frac{1}{2}$, below which according to Figure 4 very few points should be situated. The measured line densities conform to this predicted relation between minimum detectable line density and slant range, and the agreement is equally good for other zenith angles. The line *BB*, whose position is arbitrary, is the locus of the points of maximum electron density of trails of meteors of constant velocity and radiant zenith angle. Its position, but not its slope, depends on these two quantities. For shower meteors, with narrow ranges of velocity and radiant zenith angle, there is a tendency for the points to concentrate to a locus of this form ; this is particularly so in the case of the brighter Geminids. It is the natural consequence of the distribution of electron density along the meteor trail, coupled with the rapid increase in numbers as the meteor mass decreases. For the fainter Geminids, indeed, the concentration to the locus of maxima is perhaps too marked ; a wide range distribution would be expected amongst the echoing points with lowest line densities, which should be situated near the extremities of the trails of more massive meteors as well as near the maximum points for the smallest meteors accessible to the equipment.

The position with respect to sporadics is not so obvious, because there is a spread in both velocity and radiant zenith angle which would have the effect of smearing out the locus of maxima into a band of considerable width.

V. THE SPORADIC METEOR HEIGHT DISTRIBUTION

Figure 6 is a smoothed contour diagram of equipment sensitivity, which has been prepared from distributions of the slant ranges of reflection points falling within narrow intervals of zenith angle, for September 1953 sporadic meteors. The most probable height is a function of zenith angle, but the form of the height distribution is almost independent of this angle.

The collection zone, within which the equipment will detect meteors, is formed by rotating this cross section about the zenithal axis. Its volume is $1 \cdot 2 \times 10^6$ km^3.

The full line *AA* in Figure 6 is the mean height of the smoothed distribution. From the theory of the sporadic meteor height distribution (Kaiser 1954*b*), it may be deduced that for constant meteor velocity the relation between the mean height and the zenith angle of detection is

$$h_z = h_0 + H \ln [\cos^{\frac{1}{2}} z \sin^{-\frac{2}{3}} z (G_T G_R)^{\frac{1}{3}}]. \quad \ldots\ldots\ldots\ldots \quad (6)$$

h_0 is here regarded as an arbitrary constant, although its absolute value can be determined from the atmospheric, meteor, and equipment constants. Relation (**6**) will also apply if the velocity distribution of sporadic meteors is independent of the zenith angle of detection, which will be approximately true if observations are continuous. Expression (**6**) is plotted in Figure 6 as the line *BB* ; a value of $H = 7$ km has been assumed. Agreement between theory and measurement is poor, especially at small zenith angles, a fact which may have some bearing on the derivation of atmospheric scale heights from the widths of measured sporadic height distributions.

Trails detected at very small zenith angles must proceed from radiants close to the horizon. For these trails, which are very long, the zenith angle is no longer constant, because the Earth's surface can no longer be regarded as flat. Qualitatively, the effect of this changing zenith angle is to elongate, and so lower the ends of, the trails. Whether this is sufficient to lower the measured mean height to the extent shown in Figure 6 can only be settled by calculation. In any case it is unlikely to afford an explanation of the discrepancy for $z > 10^\circ$.

Although it is not evident in Figure 6, the upper portions of the sensitivity contours must be influenced by cut-off due to high rates of diffusion. The cut-off is independent of zenith angle, which is not unexpected. Although it is not attempted here, a careful analysis of the form of the height distributions and of the scatter diagram of diffusion coefficient versus height would undoubtedly enable the nature of the diffusion cut-off to be established.

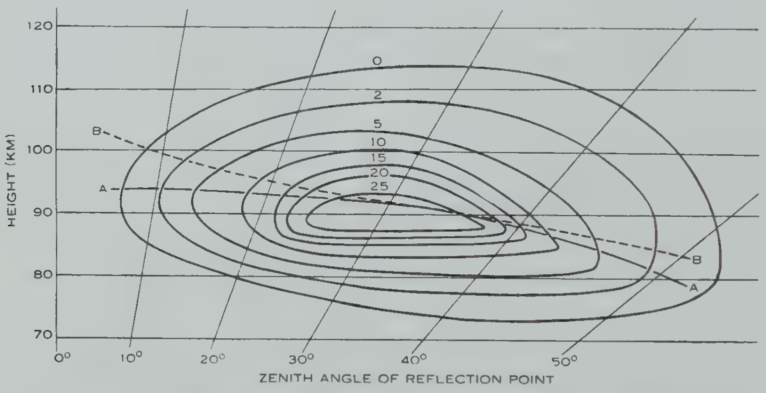

Fig. 6.—Zenith angle-height contours of equal equipment sensitivity. The numbers against the contours are relative sensitivities. The line *AA* gives the observed mean height, *BB* the mean height predicted for a uniform distribution of sporadic radiants.

VI. Shower Meteor Height Distributions

Height distributions for three showers are reproduced in Figure 7. Distributions for the Arietids and the ζ-Perseids are based on echoes selected by the geometrical method described by Weiss (1955*a*). That for the Geminids was determined by subtraction of the distribution for sporadic meteors on neighbouring days from the distribution for mixed sporadic and Geminid meteors found over the times of shower activity. Rather smaller samples of echoes for 1952 and 1953, known by the geometrical selection method to be Geminids, gave identical distributions.

The r.m.s. deviations for Arietids and ζ-Perseids are respectively $5\cdot10$ and $7\cdot16$ km. The theory of the shower meteor height distribution (Kaiser 1954*a*) relates these r.m.s deviations to the mass distribution parameter s and atmospheric scale height H. With $H=7$ km we find $s=2\cdot6$ for the Arietids and $s=1\cdot9$ for the ζ-Perseids, in the range of brightness $3 \leqslant M_r \leqslant 6$. These values of s are consistent with the line density distributions of Figure 4, if we accept $s=2\cdot0$ for sporadic meteors, and also with the values given by Browne *et al.* (1956).

For the Geminids, the r.m.s. deviation is 5·17 km, leading to $s=2\cdot5$. This value is consistent with the indication in Figure 5 that Geminid meteors are detected only near the points of maximum electron density in the trails; it is, however, very much larger than the values, 1·45 and 1·62, given by Browne *et al.* for fainter Geminids. This discrepancy is obvious from the very much broader height distribution measured at Jodrell Bank, and would be larger still were it not for the long tail of our distribution. No ready explanation suggests itself, but it must be due to failure to detect, or to measure, echoing points lying near the ends of the trails. Very low and very high heights of detection presumably arise in long trails of bright meteors seen at either extremity. It may be true that the Geminid trails, because of a larger proportion of bright meteors, are on the average much longer than for the other showers with steeper mass distributions. Near the beginning of a trail, $d\alpha/dh$ is proportional to $\exp(-h/H)$, hence a small decrease in equipment sensitivity, say due to cut-off by diffusion, will shorten the detectable length of trail very much more for a bright meteor than for a faint meteor. Now the height gradient of the diffusion coefficient for the Geminid meteors is about twice as large as that for the other showers and for sporadic meteors (Weiss 1955*b*; this result is also confirmed by measurements on the 1953 Geminids), so that Geminids should be abnormally sensitive to cut-off by diffusion. This could well explain the lack of high Geminids, but none of the selection processes considered in Section II should operate differentially on the lower portion of the height distribution. Perhaps the cause of the discrepancy is associated with the low elevation (<25°) of the Geminid radiant at Adelaide.

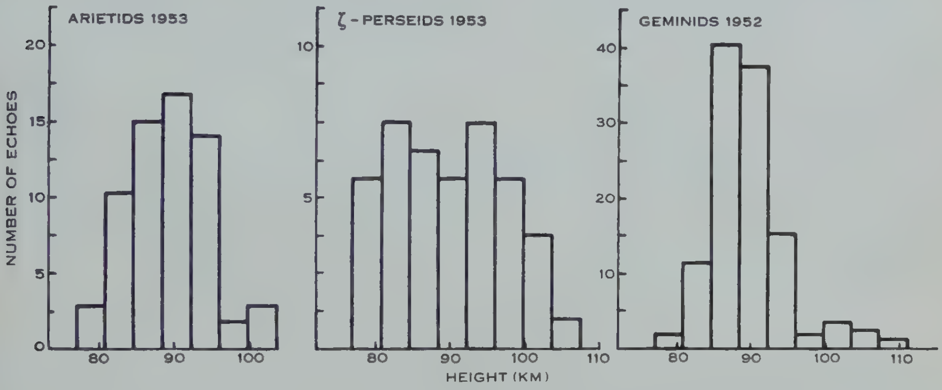

Fig. 7.—Height distributions of echoing points of shower meteors.

VII. Conclusions

Continuous recording, with the one equipment, of those characteristics of meteor echoes necessary for the location of the reflection point in space, and for measurement of echo amplitude, form, and rate of decay, permits a detailed examination of the principles underlying the selection of echoes for measurement, of the geometrical aspects of meteor detection, and of the influence of the selection process on the geometry of detection. With few exceptions, the manner in which the equipment responds to meteor trails agrees with theoretical expectation. The agreement between observed and expected distributions of electron densities, both in number and in height, engenders considerable confidence in the outcome of systematic studies of this kind, provided that a careful selection of echoes is first made on the basis of echo characteristics. Of the selection processes, selection of echoes in height is likely to prove the most troublesome. It not only affects the number-height distributions, which contain information on the atmospheric properties and the manner of ablation of a meteor particle in its flight through the atmosphere. Its influence can extend to the determination of height gradients of such quantities as the diffusion coefficient, in the form of incomplete scatter diagrams.

The conclusions regarding the high incidence of turbulent or other distortion in meteor echoes and the distribution of measured electron densities cannot be regarded as final. In their present state they do little beyond demonstrating the potentialities of the type of C.W. meteor equipment still under development at Adelaide. With the addition of a single simple outstation to the present equipment, comparison of echo amplitude and form can be made at two precisely known points on the trail of a shower meteor whose radiant position is already known. Further addition of accessory equipment for velocity measurement and (for some applications) of a second outstation, will render accessible the much more numerous sporadic meteors.

VIII. Acknowledgments

This work forms part of the meteor research programme of the University of Adelaide, which is under the general direction of Professor L. G. H. Huxley. The project is financed jointly by the University of Adelaide, the Division of Radiophysics, C.S.I.R.O., and the Radio Research Board. Many persons, of whom Dr. W. G. Elford should be especially mentioned, have contributed to the operation of the equipment and to preliminary reduction of data.

IX. References

Browne, I. C., Bullough, K., Evans, S., and Kaiser, T. R. (1956).—*Proc. Phys. Soc.* B **69** : 83.

Elford, W. G., and Robertson, D. S. (1953).—*J. Atmos. Terr. Phys.* **4** : 271.

Kaiser, T. R. (1954*a*).—*Mon. Not. R. Astr. Soc.* **114** : 39.

Kaiser, T. R. (1954*b*).—*Mon. Not. R. Astr. Soc.* **114** : 52.

Kaiser, T. R. (1955).—" Meteors." (Ed. T. R. Kaiser.) p. 55. (Pergamon Press : London.)

Robertson, D. S., Liddy, D. T., and Elford, W. G. (1953).—*J. Atmos. Terr. Phys.* **4** : 255.

Weiss, A. A. (1955*a*).—*Aust. J. Phys.* **8** : 148.

Weiss, A. A. (1955*b*).—*Aust. J. Phys.* **8** : 279.

Weiss, A. A. (1957).—*Aust. J. Phys.* **10** : 77.

THE DETECTION OF TIME-CORRELATED PHOTONS BY A COINCIDENCE COUNTER

By R. Q. Twiss* and A. G. Little*

[*Manuscript received November* 7, 1958]

Summary

The existence of a correlation between the arrival times of photons has been confirmed by measurements with a coincidence counter having a resolving time of $3\cdot5\times10^{-9}$ sec in three different experiments. In the first experiment it was found that the number of coincidence counts recorded from two photomultipliers, the apertures of which were optically superimposed, was significantly greater than when the light beams were incoherent. Furthermore, the number of these correlated counts was in satisfactory agreement with that predicted by theory. In the second experiment the change in the number of excess coincidences was measured as the degree of coherence of the light was altered by increasing the apparent separation of the photocathodes, and in this case also there was reasonable agreement between theory and experiment. In the final experiment it was shown that there was a significant difference between the number of coincidences observed when the light beams were in identical as opposed to orthogonal polarizations, and this last result especially makes it extremely improbable that the correlation could be caused by some spurious effect, such as plasma oscillations in the source, since the light source itself was found to be completely unpolarized.

I. Introduction

Hanbury Brown and Twiss (1956*a*, 1958*a*) have proposed a new type of stellar interferometer which is based upon the existence of a correlation between the times of arrival of photons at two points illuminated by coherent beams of light.

The reality of this correlation has been checked by a preliminary trial on Sirius (Hanbury Brown and Twiss 1956*b*, 1958*b*) and by two series of tests in the laboratory (1956*a*, 1957), in which the fluctuations in the anode currents of two phototubes were cross correlated in a linear multiplier.

On the other hand a negative result was obtained by Adam, Janossy, and Varga (1955) and also by Brannen and Ferguson (1956), who looked for a correlation by the direct method in which a coincidence counter recorded every event when two photoelectrons were simultaneously emitted from the cathodes of the two phototubes.

It was pointed out by Purcell (1956) and also by Hanbury Brown and Twiss (1956*c*) that these different results were not mutually inconsistent since the sensitivity of these counter experiments was too low by several orders of magnitude to yield a positive result. However, to remove any possible doubt as to the reality of the effect and to show that the correlation can be detected

---

* Division of Radiophysics, C.S.I.R.O., University Grounds, Chippendale, N.S.W.

directly with a coincidence counter, it was decided to repeat the experiment of Brannen and Ferguson with more sensitive equipment.

A preliminary account of such an experiment has been published elsewhere (Twiss, Little, and Hanbury Brown 1957) and in the present paper we shall give a more detailed discussion of this work together with an account of later experiments which were designed to test the existence of a correlation between photons in alternative ways. A similar test by Rebka and Pound (1957) has been reported, which also led to positive results in reasonable agreement with theory.

II. Basic Theory and Design of the Experiments

Consider the simple case in which a plane wave of randomly polarized light with a very narrow spectral bandwidth B is incident upon two identical photocathodes of quantum efficiency α. Let us assume that we are looking for coincidences between the emission times of electrons from these two photocathodes by means of an idealized coincidence counter which registers a count when, and only when, the difference between these emission times is less than τ_c, the resolution time.

If there were indeed zero correlation between the arrival times of photons we should expect, on the average, to observe $N_r(T_0)$ random coincidences in a time interval T_0 where

$$N_r(T_0)=2\alpha^2N_0^2\tau_cT_0, \quad \ldots\ldots\ldots\ldots\ldots\ldots \quad (1)$$

and where αN_0 is the average number of electrons emitted in unit time from either photocathode. However, if the arrival times of photons are partially correlated according to the theory given by Hanbury Brown and Twiss (1957) in a paper hereafter referred to as PI, and by Purcell (1956), we should expect to find an additional number $N_c(T_0)$ of coincidence counts where

$$N_c(T_0)=\tfrac{1}{2}\alpha^2N_0^2\tau_0T_0, \quad \ldots\ldots\ldots\ldots\ldots\ldots \quad (2)$$

and where τ_0, the *coherence time* of the light source defined in Appendix II, is approximately equal to $1/B$, the reciprocal light bandwidth. This expression is only valid as long as $\tau_c/\tau_0 \gg 1$ and this condition applies to all the experiments discussed in this paper.

In a physically realizable case the incident light beam will consist of a pencil of plane waves and N_c will be reduced by the *partial coherence factor* $\Delta(D,\nu_0)$, defined in PI, which is a function of the parameter

$$\pi aD\nu_0/cR_0,$$

where

a, D are the linear dimensions of the light source and of the photocathode respectively,
R_0 is the distance of the light source,
ν_0 is the midband frequency of the light.

If the photocathodes are not optically superimposed, the number of correlated coincidence counts is yet further reduced by the normalized *correlation factor* $\Gamma^2(d,\nu_0)$ which is a function of the parameters

$$\pi aD\nu_0/cR_0, \quad \pi ad\nu_0/cR_0,$$

where d/R_0 is the apparent angular separation of the photocathodes as seen from the light source.

Accordingly, the expected number of correlated coincidences in a practical case may be written

$$N_c(T_0)=\tfrac{1}{2}\alpha^2 N_0^2\tau_0 T_0\Delta(D,\nu_0)\Gamma^2(d,\nu_0)\gamma_1\gamma_2, \quad \ldots\ldots\ldots\ldots \tag{3}$$

where γ_1, γ_2 are factors introduced to allow for any loss of correlation in the optical and electronic system and for the effects of dark current and background light.

The ratio ρ_c of the numbers of correlated to random coincidences is therefore given by

$$\rho_c=\frac{N_c(T_0)}{N_r(T_0)}=\frac{1}{4}\frac{\tau_0}{\tau_c}\Delta(D,\nu_0)\Gamma^2(d,\nu_0)\gamma_1\gamma_2, \quad \ldots\ldots\ldots\ldots \tag{4}$$

The r.m.s. fluctuation in the number of random coincidences is given by

$$n_r(T_0)=\left[\overline{\{N_r(T_0)-\overline{N_r(T_0)}\}^2}\right]^{\frac{1}{2}}=\alpha N_0\sqrt{(2\tau_c T_0)}, \quad \ldots\ldots \tag{5}$$

assuming that these coincidences obey a Poisson distribution, and to achieve a significant result is it necessary that the signal-to-noise ratio S/N defined by

$$\frac{S}{N}=\frac{N_c(T_0)}{n_r(T_0)}=\tfrac{1}{2}\alpha N_0\tau_0\Delta(D,\nu_0)\Gamma^2(d,\nu_0)\gamma_1\gamma_2\left(\frac{T_0}{2\tau_c}\right)^{\frac{1}{2}} \quad \ldots\ldots \tag{6}$$

for the case of an unpolarized light source should be appreciably greater than unity.

The quantity $N_0\tau_0\Delta(D,\nu_0)$ is proportional to the average number of photons emitted into unit angle in unit frequency interval from unit area of the source, so that the sensitivity of the experiment is affected only by the brilliance, not by the bandwidth of the light source. This last fact is essential to the success of the experiment since there are two important reasons why the primary photocurrent must be held to a low value. In the first place, the coincidence counter would start to saturate once the average time interval between successive photoemissions was no longer appreciably greater than the resolution time of the counter ; in the second place, the photomultipliers would lose stability at the high gains ($\approx 10^8$) needed to operate the coincidence circuit from a single primary electron, if the anode current were appreciably to exceed 1 mA. These requirements made it impractical for us to employ the high-pressure mercury arc source used in the correlation experiment with a linear multiplier described in PI, and led us instead to the use of an electrodeless low-pressure ^{198}Hg isotope lamp.

If all the parameters in equations (4) and (6) are known it is possible to obtain a direct experimental check of the theory from the ratio of the number of coincidence counts obtained with coherent, as opposed to incoherent, light beams of the same intensity ; this procedure was adopted in the first experiment described in the present paper. However, it is difficult to make an accurate measurement of the effective resolution time τ_c, especially if τ_c is decreased as far as possible in order to improve the sensitivity ; furthermore, there is always the possibility of a loss of correlation in the electronic system, caused, for example, by a difference in the electron transit times through the photomultipliers. The effect of these uncertainties can be eliminated by taking the ratio of the " correlated " coincidences observed with two different values of $\Gamma^2(d,\nu_0)\Delta(D,\nu_0)$ which depends upon the geometry of the system but not upon τ_c, γ, or τ_0; this procedure was followed in the second experiment described in the present paper.

Finally, an experiment was carried out to find the ratio of the number of coincidences observed when the light beams reaching the photocathodes were linearly polarized first parallel and then orthogonal to each other.

III. Description of the Apparatus

(a) *The Optical Equipment*

A simplified outline of the optical equipment is shown in Figure 1. The light source consisted of an electrodeless ^{198}Hg isotope lamp, of the type developed by Meggers and Westfall (1950), which was excited by an EC 55 triode oscillator producing 1·5 W at 800 Mc/s; the visible area of the source was limited by a circular pinhole in a brass tube which fitted tightly over the discharge tube. In the first experiment the lamp bulb was cooled by an air blast; the tube was later fitted with a water jacket so that a circulating water system could be used. This latter arrangement was temperature-controlled by a thermostat to $\pm\frac{1}{2}$ °C. With a water temperature of 40 °C the light flux was measured to be 0·0013 W/cm^{-2} steradian^{-1}, which is about 30 per cent. of that emitted by the special lamp developed by Forrester, Gudmundsen, and Johnson (1955). To minimize the effects of variations in output light flux, the lamp was provided with a stabilizing circuit as shown in Figure 1.

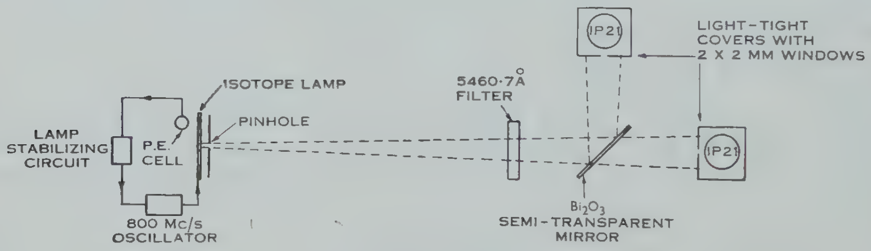

Fig. 1.—Arrangement of the optical system.

The 5461 Å line of the mercury spectrum was isolated by a Zeiss monochromatic filter having a peak transmission of 75 per cent., and the beam of light was split by a semitransparent dielectric mirror to illuminate the cathodes of the photomultiplier tubes. In the third experiment a sheet of " Polaroid " with a transmission of 64 per cent. in the accepted polarization was placed over each phototube. One of the " Polaroids " could be rotated between two alternative positions 90° apart.

In all cases the photocathode areas were limited by square apertures 2 by 2 mm and the distance from the pinhole to each cathode, which was of the order of 1–2 m, could be adjusted to an accuracy of ±1 mm.

In the early experiments one of the photomultipliers was mounted on a slide which enabled it to be moved transversely to the line of sight between two positions 5 mm apart. In one position the apertures of the photocathodes as viewed from the source were optically superimposed, in the other position their apparent angular separation was so large that the incident light beams were effectively uncorrelated.

In the second experiment, which was devised to measure the ratio of the correlation with different degrees of optical superimposition, the position of the fixed phototube could be adjusted in a series of steps so that the amount of optical overlap in the " coincidence " position could be varied from 100 to 0 per cent.

In the final experiment, with polarized light, the phototubes were kept fixed throughout the observations.

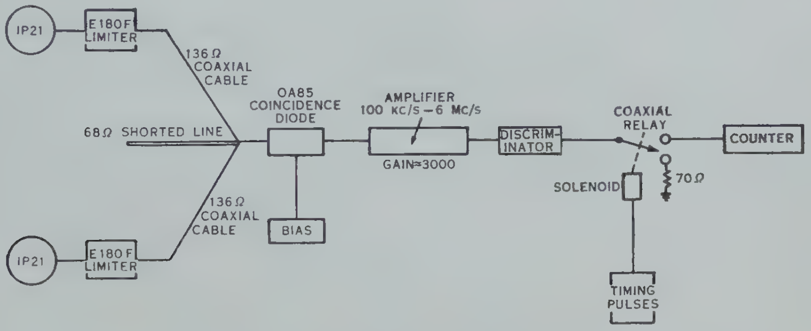

Fig. 2.—Schematic diagram of the coincidence counter.

(*b*) *The Electronic Equipment*

The phototubes were 1P21's working into a high speed coincidence counter essentially the same as that described by Bell, Graham, and Petch (1952), which is shown schematically in Figure 2. One advantage of this circuit is the pulse-limiting action of the pentodes which drive the coincidence diode ; however, to achieve this limiting it is necessary to operate the photomultipliers far in excess of their specified rating. We first tried to maintain an anode voltage of 2300 V, but under these conditions the dark current was excessively high and the stability of the small number of tubes that were tested was very poor. Accordingly, on the advice of Professor Bell (personal communication) we replaced the 6AK5 limiters with the higher gain, sharper cut-off E180F pentodes, which enabled us to obtain adequate limiting when the photomultipliers were operated at 1900 V, and we stabilized the voltages on the last few dynodes of the photomultipliers with voltage regulator tubes as described by Stump and Tallay (1954). With selected 1P21's the dark currents settled down to about 0·1 μA, after the H.T. voltages had been applied for a period of 1 hr, when the photomultipliers were run at room temperature ; the stability of the anode currents was greatly improved also, though occasional small jumps in these output currents were still observed. The stability could no doubt have been improved further by cooling the phototubes, but this complication proved unnecessary.

The output from the coincidence diode was passed through an amplifier having a passband from 0·1 to 6·0 Mc/s and a gain of about 3000 to an amplitude discriminator of the type described by Lewis and Wells (1954), which produced a standard pulse 0·3 μsec in duration and 1·0 V in height to drive a Hewlett-Packard counter-type frequency meter.

The bias on the germanium coincidence diode type 0A85 was maintained at 0·25 V during all the observations. The bias on the amplitude discriminator was set so that it never responded to break-through pulses from the coincidence diode. The screen voltages on the pulse-limiting pentodes were then adjusted so that the amplitude discriminator was never triggered as long as the H.T. voltage was only applied to one of the photomultipliers. Under these conditions a count could only be registered when coincident pulses were received from the pentode limiters, the combined height of which exceeded 0·25 V.

IV. Correlation between Photons Reaching Optically Superimposed Photocathodes

In this first experiment we aimed at getting an experimental check of theory by comparing the number of coincidences observed when the photocathodes were optically superimposed with the number observed when the photocathodes were so widely separated that the light beams incident from the pinhole source were effectively uncorrelated. The effect was expected to be small, of the order of 2 per cent., so to minimize the effects of drift the following experimental procedure was adopted.

(a) *Experimental Procedure*

When the photomultiplier currents had settled down to their steady value the photocathodes were optically superimposed for 2 min, the time interval being accurately determined by pulses from a crystal-controlled clock. At the end of this period the counter was isolated for a 30 sec dead period by a fast-acting relay, and the total number n_{1r} of the coincidences observed in the 2-min period were recorded; at the same time one of the photomultipliers was moved to the uncorrelated position. At the end of this dead period the counter was reconnected by the pulsed relay for a further 2 min and then disconnected for a second dead period, during which the total number n_{2r} of the coincidences observed in the " uncorrelated " position was recorded while the photomultiplier cathodes were optically superimposed again. The whole procedure was repeated ten times in a single run, which therefore took a total of 50 min to complete, allowing for the dead periods. The series N_1 and N_2, defined by

$$N_1 = \sum_{r=1}^{10} n_{1r}, \quad N_2 = \sum_{r=1}^{10} n_{2r} \quad \ldots\ldots\ldots\ldots\ldots \quad (7)$$

were recorded.

If the average light intensity reaching the movable photocathode had been equal in the coincident and displaced positions, the ratio $(N_1-N_2)/N_2$ would have given a measure of the ratio of the correlated to the random coincidences. In this initial experiment however, there were differences of the order of 0·5 per cent. between these two intensities, and to eliminate the effect of these a comparison run was made after each observation run with an extra length of 136 Ω cable in one channel of the coincidence counter circuit. This cable introduced an extra delay of 15 mμsec, which was about four times the resolution time of the coincidence counter, so that there was no chance of a count being registered by the simultaneous arrival of photons at the two photocathodes.*

The procedure in the comparison run was identical with that in the observation run and from this second set of results we computed the quantity

$$\rho_I=\sum_{r=1}^{10} n'_{2r}/\sum_{r=1}^{10} n'_{1r}=N'_2/N'_1, \quad \ldots\ldots\ldots\ldots\ldots\ldots \quad (8)$$

which was taken to represent the ratio of the light fluxes incident upon the movable photocathode in the "uncorrelated" and "correlated" positions respectively.

The ratio

$$\rho_c=(N_1\rho_I-N_2)/N_2 \quad \ldots\ldots\ldots\ldots\ldots\ldots\ldots\ldots\ldots \quad (9)$$

then represents the experimental value, for the ratio of the correlated to random coincidences in a given run

$$N_c=\rho_c N_2 \quad \ldots\ldots\ldots\ldots\ldots\ldots\ldots\ldots\ldots\ldots\ldots\ldots \quad (10)$$

may be taken as a corrected estimate of the number of correlated coincidences in the same run.

(b) *Experimental Results*

A total of six complete runs was made using the above procedure. Allowing for dead periods and comparison runs the total observation time was 10 hr, which was spread over two successive nights; it was not possible to observe during the day-time because of interference from other equipment in the building. The results are given in Table 1 and can be combined to give an experimental value

$$\rho_{\text{exp}}=0\cdot0193\pm0\cdot0016 \text{ (p.e.)} \quad \ldots\ldots\ldots\ldots\ldots \quad (11)$$

for the ratio of correlated to random coincidences. The quantity $N_c/2N_2^{\frac{1}{2}}$ in the final column represents the ratio of the number of correlated coincidences to the r.m.s. uncertainty in the number of random coincidences; the factor 2 arises because N_c was calculated from the four quantities N_2, N_1, N'_2, N'_1 which, it was assumed, were statistically independent.

As a final test a dummy run was made with a tungsten filament light source in place of the isotope lamp; no significant correlation was observed in this case and none was expected when using a source of such low surface brightness per unit bandwidth.

(c) *Calibration of the Equipment*

In order to compare the experimental results with theory an estimate is necessary of the parameters in equation (4), some of which could be measured directly, while others had to be calculated theoretically. Of the two in the latter class, $\Gamma^2(d,\nu_0)$ could be taken as unity by definition in the case in which the photocathodes were optically superimposed. The values of $\Gamma^2(d,\nu_0)$ at the displaced position and of $\Delta(D,\nu_0)$ were then calculated on the assumption that the photocathode sensitivity was uniform over the 2 by 2 mm aperture* from the theory and numerical results given in PI. For the case of the present experiment in which the light source was a pinhole 0·360 mm in diameter at a distance of 1·25 m,

---

* This was confirmed by tests with a millimicrosecond pulse generator in which pulses were simultaneously applied to the grids of the pentode limiter tubes.

TABLE 1

RATIO OF CORRELATED TO RANDOM COINCIDENCES WITH SUPERIMPOSED PHOTOCATHODES

Run No.	$\rho_c \times 100$ Percentage Ratio of Correlated to Random Coincidences	N_2 Number of Random Coincidences	N_c Number of Correlated Coincidences	$N_c/2N_2^{\frac{1}{2}}$ Signal-to noise Ratio*
1	2·20	135,446	2986	4·03
2	1·70	128,975	2190	3·05
3	1·73	136,250	2369	3·21
4	2·19	99,640	2185	3·46
5	1·94	96,326	1864	3·00
6	1·88	93,848	1761	2·87
Dummy run with white light source	0·22	81,576	185	0·32

* Ratio of correlated coincidences to r.m.s. uncertainty in random coincidences.

$$\Delta(D,\nu_0)=0\cdot475, \quad \ldots\ldots\ldots\ldots \quad (12)$$

and

$$\Gamma^2(d,\nu_0)<0\cdot01 \quad \text{for } d=5\text{ mm}, \quad \ldots\ldots\ldots \quad (13)$$

so that the decorrelation at the comparison position is effectively complete.

Since the action of the pentode limiters was not perfect, there were variations in the amplitudes of the current pulses driving the coincidence circuit, and it was found experimentally that the resolution time of the counter was a function of the sum of the amplitudes of these current pulses. To find the effective value of the resolution time of the counter the resolution time associated with a given pulse amplitude must be averaged over the amplitude probability distribution. The procedure for finding these quantities is given in Appendix I; under the conditions of this experiment it was found that

$$\tau_c=3\cdot5\times10^{-9}\text{ sec.} \quad \ldots\ldots\ldots\ldots \quad (14)$$

---

* In the case of the 1P21, in which a system of grid wires lies between the window and the photocathode, the assumption of uniform cathode sensitivity is not rigorously valid, but from the approximate treatment of an idealized case it seemed that the error introduced would not be significant, at least within the accuracy of the present experiment.

As discussed in Appendix II, the " coherence time " τ_0 of the light was measured with the aid of a Kösters interferometer (Bruce 1956) and it was found that

$$\tau_0 = 0 \cdot 73 \times 10^{-9} \text{ sec}, \quad \ldots\ldots\ldots\ldots\ldots\ldots \quad (15)$$

so that $\tau_0 \ll \tau_c$.

The factor γ_1 in equations (**4**) and (**5**), which represents the loss of correlation in the optical and electronic part of the equipment, receives a significant contribution from polarization effects in the semitransparent mirror. As discussed in Appendix III, this loss of correlation can be determined by measurements with an optical polarizer and, for the Bi_2O_3 mirror used in this experiment, contributed a factor of $0 \cdot 935$ to γ_1. Loss of correlation can also arise because of a difference in the electron transit times through the photomultipliers, and, if this were comparable with the mean resolution time of the counter, the effect would be serious, since one would tend to lose coincidences between small current pulses. However, in view of the fact that the total electron transit time through a 1P21 with an anode voltage of 2000 V is probably less than 10^{-8} sec, it seems reasonable that the differential delay should be appreciably less than $3 \cdot 5 \times 10^{-9}$ sec, the mean resolution time of the counter.

The factor $\gamma_1\gamma_2$ in equations (**4**) and (**5**) represents the fraction of random counts due to coincidences between pulses in one phototube and dark current or stray light pulses in the other. A typical value of γ_2, under the conditions of the present experiment, was $0 \cdot 92$, so that we took

$$\gamma_1\gamma_2 = 0 \cdot 86 \quad \ldots\ldots\ldots\ldots\ldots\ldots\ldots \quad (16)$$

as the factor representing the loss of correlation in the complete equipment.

(*d*) *Comparison with Theory*

Substituting into equation (**4**) the values of the various parameters given in equations (**12**)–(**16**), gives a theoretical value for ρ,

$$\rho_{\text{theor}} = 0 \cdot 0207. \quad \ldots\ldots\ldots\ldots\ldots\ldots \quad (17)$$

Perhaps the most uncertain quantity in this calculation is τ_c, the mean resolution time of the counter, though there could have been some additional loss of correlation in the coincidence counter for which no allowance has been made ; furthermore, the coherence time τ_0 was a function not only of ambient temperature at the light source but also of the output power of the driving oscillator. It is difficult to estimate accurately the combined magnitude of these potential errors, but we estimate that it is unlikely to be appreciably greater than $\pm 0 \cdot 002$, even when we allow for the variations in sensitivity over the photocathode apertures.

A comparison between equations (**11**) and (**17**) shows that they are in satisfactory agreement, the difference between the experimental and theoretical values being just less than the probable error.

V. THE VARIATION IN PHOTON CORRELATION AS A FUNCTION OF PHOTOCATHODE DISPLACEMENT

In order to obtain a check on the theory which depended on as few of the parameters of the equipment as possible, an experiment was performed in which the ratio of the number of correlated to random coincidences was compared for several values of the quantity $\Gamma^2(d,\nu_0)\Delta(D,\nu_0)$.

It would have been preferable, in a number of ways, to have kept the photocathodes superimposed, so that $\Gamma^2(d,\nu_0)$ stayed equal to unity, and varied $\Delta(D,\nu_0)$ by varying the apparent angular size of the pinhole source. For one thing, this procedure would have eliminated any possibility that the photocathodes were not illuminated by identical parts of the source. However, in order to vary $\Delta(D,\nu_0)$ appreciably, say by a factor of 4 to 1, it would be necessary to vary the apparent angular size of the source, and, therefore, of the light flux received by the photocathodes by factors of at least 3 to 1 and 9 to 1 respectively. Such a flux change would either have overloaded the photomultipliers at one end of the scale or would have led to an excessively low value of the signal-to-noise ratio at the other.

Accordingly, it was decided to keep $\Delta(D,\nu_0)$ constant and change $\Gamma^2(d,\nu_0)$ by moving the fixed phototube in steps away from the position of 100 per cent. optical overlap.

To improve the signal-to-noise ratio, the temperature of the light, which was controlled by the temperature of the circulating water, was adjusted to maximize $N_0\tau_0$, that is, to maximize the product of the light flux and the " coherence time ".* At the same time the resolution time of the counter was decreased by cutting down the length of short-circuited line by a factor of 0·6. As it turned out this move was probably mistaken, since the gain in signal-to-noise ratio was more than offset by a decrease in the stability of the anode photocurrents caused by the high currents, which led to an appreciable increase in the drift in the number of random coincidences. Under these circumstances the probable error in the measurements was almost certainly larger than that set by the fundamental random fluctuations.

The experimental procedure was similar to that adopted in the first experiment, with two major exceptions. Firstly, the degree of optical superimposition in the " correlated " position could be varied by changing the position of that photocathode which remained fixed throughout a given run, and measurements were taken with the cathodes displaced with respect to each other by 0, 1, 2, and 4 mm, that is, by 0, $\frac{1}{2}$, 1, and 2 times the cathode aperture. Secondly, considerable care was taken to equalize the light intensity reaching the movable photocathode in its two alternative positions. By comparing the number of single photon counts recorded by the frequency meter with only a small bias on the coincidence diode and with zero H.T. voltage on the movable photomultiplier, it was concluded that the intensity ratio was equal to unity within $\frac{1}{4}$ of 1 per cent. This result was confirmed by a dummy run with the extra cable inserted in one arm of the coincidence circuit, in which no significant difference was detected between the counts received in the two positions of the photocathode. Accordingly, it was decided to omit the comparison run which followed every observation run in the first experiment. In each run the photocathode was now alternated a total of 24 times between the " correlated " and " uncorrelated " positions, so that, allowing for the 30-sec dead periods, the total duration of the observations at any given position of the fixed photocathode was 1 hr.

---

* The " coherence time " was found approximately in this experiment by measuring the mirror separation in the Kösters interferometer at which the fringes first became invisible.

The experimental results are given in Table 2, the symbols in the first three columns having the same meaning as those in Table 1. In the fourth column we have given the theoretical values for $\Gamma^2(d)$, which were calculated from the results given in PI, for the case appropriate to the present experiment for which :

$$\pi a D/\lambda R=3\cdot 00, \quad D=2 \text{ mm}.$$

To find the experimental values of $\Gamma^2(d)$ as a function of d, the unknown parameter

$$(\tau_0/4\tau_c)\alpha N_0\gamma_1\gamma_2\Delta(D,\nu_0)$$

TABLE 2

CORRELATION BETWEEN PHOTONS AS A FUNCTION OF CATHODE SEPARATION

d Cathode Separation (mm)	N_R Number of Random Coincidences	N_c Number of Correlated Coincidences	$\Gamma^2_{\text{theor}}(d)$	$\Gamma^2_{\text{exp}}(d)$	p.e.	$\dfrac{\Gamma^2_{\text{theor}}(d)-\Gamma^2_{\text{exp}}(d)}{\text{p.e.}}$
0	350,871	7279	$1\cdot 0$	$1\cdot 078$	$\pm 0\cdot 085$	$0\cdot 918$
1	292,707	3524	$0\cdot 714$	$0\cdot 621$	$\pm 0\cdot 092$	$1\cdot 01$
2	307,412	885	$0\cdot 251$	$0\cdot 152$	$\pm 0\cdot 091$	$1\cdot 09$
4	259,526	—516	$0\cdot 013$	$-0\cdot 102$	$\pm 0\cdot 097$	$1\cdot 18$

was given the value of $0\cdot 0193$ which gave the best mean squares fit between the theoretical and experimental values of $\rho_c.\Gamma^2{}_{\text{exp}}(d)$, which is plotted in column 5 of Table 2 and shown graphically in Figure 3, was then calculated from the experimental values for ρ_c using equation (4). The probable errors given in column 6 were found on the assumption that the random counts obeyed a Poisson distribution. As may be seen, the residuals are all of the magnitude of the probable error so the agreement with theory is satisfactory, especially in view of the decreased stability in the anode currents of the photomultipliers, which were nearly four times larger than in the first experiment. It may be noted, incidentally, that the lack of a significant difference between the counts registered in the " correlated " and " uncorrelated " position at the maximum cathode spacing is further evidence that the light intensities at the two positions of the movable photocathode were equal.

VI. Experiments with Polarized Light Beams

As long as the light source emits unpolarized light, as was confirmed to be the case for the ^{198}Hg lamp, it is known, from classical radiation theory, that no interference phenomena can arise from the interaction of light beams with mutually orthogonal polarization. In particular, there should be no correlation between the arrival times of photons in orthogonally polarized beams. Hence, if the light source is sufficiently brilliant, there should be a significant difference between the number of coincidences recorded when the light beams reaching the two photocathodes are in identical as opposed to orthogonal states of polarization. To confirm that this is so, a final experiment was carried out with polarized light beams.

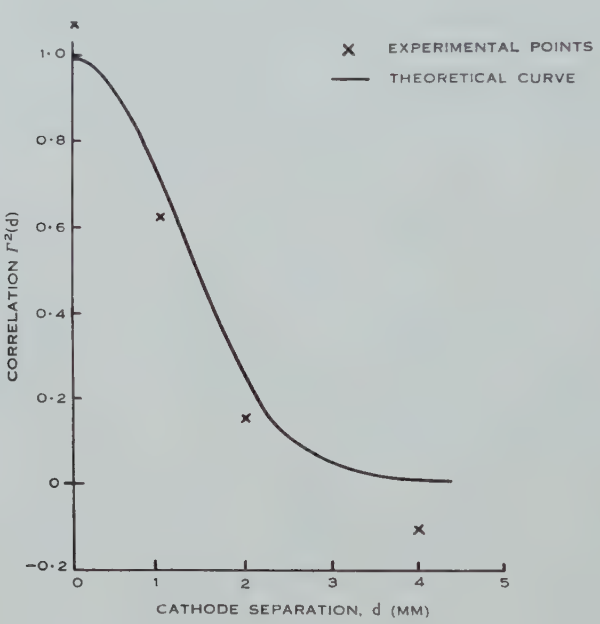

Fig. 3.—The change in correlation with separation of the photocathodes.

A complication now arises because the ratio of the light intensities in the reflected and transmitted beams is very different when the light is vertically from when it is horizontally polarized. However, this ratio should be equal in the case when the orthogonal states of linear polarization are inclined at ±45° to the vertical. Accordingly, the optical part of the equipment was set up as follows.

(a) *Setting up the Optical Equipment*

The apertures over the two photocathodes as seen from the source were optically superimposed and a piece of plane " Polaroid " was placed over each photocathode in a rotatable mount. The " Polaroid " in the reflected beam had two adjustable stops between which it could be rotated. The " Polaroid " in the direct beam, which could be fixed at an arbitrary angle to the vertical, was first rotated to maximize the direct photocurrent ; in this position, as can easily be shown, the incident light was polarized in the plane of the mirror. The " Polaroid " was then rotated through 45° and fixed in position. At this stage an auxiliary " Polaroid " was placed over the light source and rotated until the photocurrent in the direct light beam was zero ; the " Polaroid " in the reflected beam was then rotated until this photocurrent was also zero, and one of the adjustable stops was set up at this position in which the light beams incident upon the photocathodes were parallel-polarized. The " Polaroid " was then rotated through approximately 90° : the exact position of the second stop, which determined the " uncorrelated " position of the movable " Polaroid ", was adjusted to ensure the equality of the light intensities reaching the photocathode in the " correlated " and " uncorrelated " positions when the auxiliary " Polaroid " over the light source had been removed.

(*b*) *Operational Procedure and Results*

The operational procedure was very similar to that used in the earlier experiments, the only difference being that the phototubes were kept fixed in position throughout the run while the " Polaroid " in the reflected beam was rotated in successive dead periods between the " correlated " and " uncorrelated " positions. Two runs were made, each of 50 min total duration, and the results are shown in Table 3. As in the other experiments the fractional difference was of the order of 2 per cent., though a direct comparison with theory was not possible in this case since all the relevant parameters of the optical and electronic equipment were not known.

TABLE 3

DIFFERENCE BETWEEN COINCIDENCE COUNTS WITH PARALLEL AND ORTHOGONALLY POLARIZED LIGHT BEAMS

Run No.	N_R Number of Random Coincidences	N_c Number of Correlated Coincidences	$\rho\times 100$ Percentage Ratio of Correlated to Random Coincidences	$N_c/\sqrt{2}N_R^{\frac{1}{2}}$ Signal-to-noise Ratio
1	122,848	2512	2·0	5·0
2	104,282	1999	1·9	4·5

It may be noted that the number of random coincidences was very much less than in the second experiment, due to the fact that the temperature of the lamp was stabilized at an appreciably lower temperature. Under these conditions the stability of the anode currents of the phototubes was much improved and the drifts were also greatly reduced. Indeed, on the second run the r.m.s. variance in the individual readings, defined by

$$\left\{\frac{\sum_{r=1}^{10}[(n_{1r}-n_{2r})-N_c/10]^2}{10}\right\}^{\frac{1}{2}}$$

was less than the standard deviation, so that in this case, at least, no drifts were detectable.

VII. Discussion and Conclusions

In all the experiments described in the present paper there was positive evidence of a time correlation between photons in coherent beams of light. In the first experiment it was shown that the absolute magnitude of the effect agreed with that predicted by theory within the limits of accuracy of the measurements and in the second experiment it was shown that the correlation decreased in the expected manner as the separation of the photocathodes was increased. These results confirm the more accurate measurements described in PI, which were carried out by a quite different technique.

The objection has been raised (Brannen and Ferguson 1956) that the correlation reported in our original paper (Hanbury Brown and Twiss 1956*a*) might have been caused by spurious intensity fluctuations in the source produced, for example, by plasma oscillations. However, as was pointed out by Hanbury Brown and Twiss (1957) in their discussion of the results obtained with the linear multiplier technique, the quantitative agreement with theory over a whole range of cathode spacings makes this explanation very unlikely, and this conclusion is greatly strengthened by the results reported in the present paper, which were carried out with a radically different technique and with a quite different type of light source. In particular, it is virtually impossible to interpret the results with polarized light, reported above, in terms of spurious effects in the source, in view of the fact that the light beam from the source was found to be completely unpolarized.

VIII. Acknowledgments

The authors would like to express their gratitude to Professor R. E. Bell for very helpful advice in the operation of the coincidence counter; to Dr. D. Hollway for the loan of the isotope lamp and auxiliary equipment; and to J. P. Melos for the loan of a millimicrosecond pulse generator.

IX. References

Adam, A., Janossy, L., and Varga, P. (1955).—*Acta Phys. Hungarica* **4**: 301.
Bell, R. E., Graham, R. L., and Petch, H. E. (1952).—*Canad. J. Phys.* **30**: 35.
Brannen, E., and Ferguson, H. I. S. (1956).—*Nature* **178**: 481.
Bruce, C. F. (1956).—*J. Sci. Instrum.* **33**: 478.
Forrester, A. T., Gudmundsen, R. A., and Johnson, P. O. (1955).—*Phys. Rev.* **99**: 1691.
Hanbury Brown, R., and Twiss, R. Q. (1954).—*Phil. Mag.* **45**: 663.
Hanbury Brown, R., and Twiss, R. Q. (1956*a*).—*Nature* **177**: 27.
Hanbury Brown, R., and Twiss, R. Q. (1956*b*).—*Nature* **178**: 1046.
Hanbury Brown, R., and Twiss, R. Q. (1956*c*).—*Nature* **178**: 1447.
Hanbury Brown, R., and Twiss, R. Q. (1957).—*Proc. Roy. Soc.* **A 243**: 291.

Hanbury Brown, R., and Twiss, R. Q. (1958*a*).—*Proc. Roy. Soc.* A **248** : 199.
Hanbury Brown, R., and Twiss, R. Q. (1958*b*).—*Proc. Roy. Soc.* A **248** : 222.
Lewis, I. A. D., and Wells, F. H. (1954).—" Millimicrosecond Pulse Techniques." (Pergamon Press : London.)
Meggers, F., and Westfall, F. O. (1950).—*J. Res. Nat. Bur. Stand.* **44** : 447.
Purcell, E. M. (1956).—*Nature* **178** : 1449.
Rebka, G. A., and Pound, R. V. (1957).—*Nature* **180** : 1035.
Stump, R., and Tallay, H. E. (1954).—*Rev. Sci. Instrum.* **25** : 1132.
Twiss, R. Q., Little, A. G., and Hanbury Brown, R. (1957).—*Nature* **180** : 324.

Appendix I

Measurement of the Resolution Time of the Counter

The voltage pulses at the anodes of the photomultipliers have a large spread in amplitude owing to fluctuations in the gain of the electron multipliers. Since the action of the pentode limiters was not perfect there was also a spread in the amplitude of the current pulses at the coincidence diode. It was found experimentally that the resolution time of the counter depended upon the sum of the amplitudes of the current pulses in the pentode limiters. Accordingly, to find the value for τ_c which must be inserted in equations (**4**) and (**6**) in the text, one has to measure, firstly, the resolution time as a function of equal pulse amplitudes in the two channels of the coincidence counter and, secondly, the amplitude probability distribution of these current pulses.

To determine the first quantity we used a millimicrosecond pulse generator, which delivered negative-going pulses through a tapped coaxial line to the grids of the pentode limiters. With the bias on the coincidence diode set at the operating level of $0 \cdot 25$ V the amplitude of the pulse generator was adjusted to the level at which the resolution time of the counter was reduced to zero, that is, to the level at which no counts were found for any position of the tap on the coaxial line. One of the pentodes was then cut off and the bias on the coincidence diode was reduced to the level of $0 \cdot 09$ V, at which counts were observed from the current pulses in a single pentode.

The resolution time of the counter was then determined from the distance through which the tap could be moved before the amplitude discriminator ceased to trigger for a range of pulse heights from the generator. The amplitude of these pulses was defined by the bias V on the coincidence diode which just prevented any counts registering from the pulses in a single pentode limiter, where $0 \cdot 09 \leqslant V \leqslant 0 \cdot 25$. Finally, the relative number of pulses produced by a single phototube at its operating H.T. voltage, which triggered the counter when the coincidence diode bias was V, was recorded and from this data τ_c was evaluated assuming no significant difference between the resolution time of pulses from the photomultiplier and from the pulse generator respectively. No direct check was made of the truth of this, but, from the fact that the transit time spread in a 1P21 with 5000 V in the anode is only $0 \cdot 25 \times 10^{-9}$ sec (Lewis and Wells 1954), it may be concluded that the spread with 2000 V is still only $0 \cdot 4 \times 10^{-9}$ sec, which is only a little more than one-tenth the resolution time of the counter. The rise time of the pulse from the generator was also considerably faster than $3\cdot5\times10^{-9}$ sec, so the error introduced by any difference in the rate of rise of the two sets of pulses is not likely to be large, especially in view of the fact that the pulse length at the coincidence counter is determined largely by the length of the short-circuited line.

Appendix II

The Measurement of the Coherence Length of the Light

The quantity τ_0, the so-called coherence time of the light, can be defined (Purcell 1956) by the equation

$$\tau_0=\int_{-\infty}^{\infty} |g^2(\tau)|\,d\tau,$$

where $g(\tau)$, the autocorrelation function of the intensity of the incident light, is also the Fourier transform of $f(\nu-\nu_0)$, the normalized spectral response of the light centred on frequency ν_0, so that

$$g(\tau)=\int_{-\infty}^{\infty} f(\nu-\nu_0)\exp 2\pi i\nu\tau\,d\nu.$$

Instead of calculating $g(\tau)$ by first measuring the spectral response of the light source, a direct measurement was made on a Kösters interferometer (Bruce 1956), with which one can determine $g(2d/c)$ from the visibility of the fringes observed with a mirror spacing d. The fringe pattern was recorded photographically as a function of d at intervals of 0·25 in., the visibility curve was obtained from the photographs by means of a microphotometer, and the area under the curve was calculated numerically. As stated in the text, the value found in this way for τ_0 under the conditions of the first experiment was $0\cdot73\times10^{-9}$ sec.

Appendix III

The Loss of Correlation due to Polarization Effects in the Semitransparent Mirror

Consider an unpolarized light beam incident on a semitransparent mirror which splits the light into a direct and a reflected beam. The light from the source can be decomposed into two independent orthogonal linearly polarized components of equal intensity such that the electric vector in one polarization state lies in the plane of the mirror. Let us assume that the intensities of the light in the direct beam in these two states of polarization are $\alpha_1^2 I_0$ and $\alpha_2^2 I_0$ respectively so that the associated intensities in the reflected beam are $(1-\alpha_1^2)I_0$ and $(1-\alpha_2^2)I_0$ if we ignore the effects of absorption in the mirror.

The expected number of correlated coincidence counts is then proportional to

$$\alpha_1^2(1-\alpha_1^2)I_0^2+\alpha_2^2(1-\alpha_2^2)I_0^2.$$

However, if there had been no polarization effects in the mirror this number would have been proportional to

$$(\alpha_1^2+\alpha_2^2)(2-\alpha_1^2-\alpha_2^2)I_0^2/2,$$

so that γ_1, the factor representing the loss of correlation in the optical part of the equipment, is given by

$$\gamma_1=\frac{2[\alpha_1^2(1-\alpha_1^2)+\alpha_2^2(1-\alpha_2^2)]}{(\alpha_1^2+\alpha_2^2)(2-\alpha_1^2-\alpha_2^2)},$$

which may be written

$$\gamma_1=\frac{2(1+\sigma_1\sigma_2)}{(1+\sigma_1)(1+\sigma_2)},$$

where $\sigma_1=\alpha_1^2/\alpha_2^2$, $\sigma_2=(1-\alpha_1^2)/(1-\alpha_2^2)$.

The quantities σ_1, σ_2 were determined by placing a sheet of " Polaroid " in front of the light source and measuring the ratios of the maximum to minimum photocurrents both in the direct and in the reflected beams as the polarizer was rotated. For the Bi_2O_3 semitransparent mirror used in the experiments described in the text it was found that $\gamma_1=0\cdot935$.

SHORT COMMUNICATIONS

IRREGULAR COULOMB WAVE FUNCTIONS*

By A. Learner† and B. A. Robson‡

In a recent paper (Learner and Robson 1958), henceforth referred to as I, a skeleton table of values of the regular Coulomb wave functions was given in the integral representation. Here, the values of g_L and g_L' (defined in I) are presented in Table 1 for the same range of parameters, $\eta\leqslant 10$, $L=5$, 6, 10, and 11, $\Delta\rho=1$, and $\Delta\eta=1$.

In the notation of I, § the required values of G_L and G_L' are obtained by using the tabulated g_L and g_L' and noting that

$$G_L=A_L\rho^{L+1}g_L, \qquad \text{(1a)}$$

$$G_L'=A_L\rho^{L+1}\{g_L'+(L+1)g_L/\rho\}. \qquad \text{(1b)}$$

As for the regular functions, intermediate and other L values may be obtained by the recurrence formulae:

$$\rho^2 L g_{L+1}=2(2L+1)\{\eta\rho+L(L+1)\}g_L-4(L+1)(L^2+\eta^2)g_{L-1}, \qquad \text{(2a)}$$

$$\rho L g_L'=2(L^2+\eta^2)g_{L-1}-\{\eta\rho+L(2L+1)\}g_L, \qquad \text{(2b)}$$

and

$$2(L+1)g_L'=2\eta g_L-\rho g_{L+1}. \qquad \text{(2c)}$$

The table was checked in three ways using (i) the above recurrence formulae, (ii) the Wronskian relation $F_L'G_L-G_L'F_L=1$, and (iii) the tables of Coulomb wave functions for $L=0$ (Tubis 1958). The accuracy was found to be at least 0·1 per cent.

---

* Manuscript received September 4, 1958.

† Mathematics Department, University of Melbourne; present address: Trinity College, Cambridge.

‡ Physics Department, University of Melbourne.

§ Equations (3e) and (3f) of I should read: $A_L=2^{-1}(L^2+\eta^2)^{-\frac{1}{2}}A_{L-1}$ and $A_0=\{C_0(\eta)\}^{-1}.e^{-\pi\eta}$ respectively.

TABLE 1

VALUES OF g AND g'

ρ	$L=5$				$L=6$				$L=10$				$L=11$			
	g_5		g'_5		g_6		g'_6		g_{10}		g'_{10}		g_{11}		g'_{11}	
								$\eta=10$								
10	0·4074	5	−0·6882	5	0·1641	6	−0·3020	6	0·1531	9	−0·3826	9	0·1148	10	−0·3069	10
11	0·8174	4	−0·1248	5	0·2847	5	−0·4743	5	0·1418	8	−0·3212	8	0·9006	8	−0·2184	9
12	0·1910	4	−0·2642	4	0·5825	4	−0·8804	4	0·1630	7	−0·3366	7	0·8888	7	−0·1966	8
13	0·5115	3	−0·6409	3	0·1379	4	−0·1892	4	0·2259	6	−0·4270	6	0·1070	7	−0·2168	7
14	0·1554	3	−0·1758	3	0·3727	3	−0·4641	3	0·3699	5	−0·6410	5	0·1536	6	−0·2858	6
15	0·5314	2	−0·5396	2	0·1140	3	−0·1283	3	0·7028	4	−0·1118	5	0·2577	5	−0·4411	5
16	0·2038	2	−0·1837	2	0·3926	2	−0·3958	2	0·1530	4	−0·2233	4	0·4984	4	−0·7853	4
17	0·8760	1	−0·6905	1	0·1518	2	−0·1355	2	0·3786	3	−0·5057	3	0·1100	4	−0·1593	4
18	0·4206	1	−0·2863	1	0·6582	1	−0·5131	1	0·1057	3	−0·1286	3	0·2745	3	−0·3645	3
19	0·2233	1	−0·1318	1	0·3183	1	−0·2154	1	0·3320	2	−0·3650	2	0·7721	2	−0·9344	2
								$\eta=9$								
10	0·5486	4	−0·8736	4	0·2036	5	−0·3561	5	0·1468	8	−0·3560	8	0·1048	9	−0·2728	9
11	0·1214	4	−0·1733	4	0·3876	4	−0·6093	4	0·1464	7	−0·3208	7	0·8809	7	−0·2074	8
12	0·3138	3	−0·4016	3	0·8722	3	−0·1233	4	0·1813	6	−0·3607	6	0·9334	6	−0·1998	7
13	0·9350	2	−0·1068	3	0·2281	3	−0·2897	3	0·2715	5	−0·4919	5	0·1208	6	−0·2360	6
14	0·3186	2	−0·3222	2	0·6858	2	−0·7780	2	0·4809	4	−0·7946	4	0·1867	5	−0·3334	5
15	0·1236	2	−0·1091	2	0·2356	2	−0·2363	2	0·9926	3	−0·1495	4	0·3383	4	−0·5526	4
16	0·5442	1	−0·4133	1	0·9222	1	−0·8061	1	0·2360	3	−0·3229	3	0·7096	3	−0·1059	4
17	0·2692	1	−0·1756	1	0·4090	1	−0·3086	1	0·6422	2	−0·7935	2	0·1707	3	−0·2319	3
18	······		······		······		······		······		······		······		······	
19	0·7553	0	−0·4629	0	0·1081	1	−0·6525	0	0·7036	1	−0·6884	1	0·1464	2	−0·1609	2
20	0·4684	0	−0·2856	0	0·5931	0	−0·3615	0	0·2806	1	−0·2423	1	0·5191	1	−0·5063	1
								$\eta=8$								
10	0·7879	3	−0·1168	4	0·2663	4	−0·4387	4	0·1442	7	−0·3384	7	0·9751	7	−0·2467	8
11	0·1949	3	−0·2559	3	0·5626	3	−0·8246	3	0·1542	6	−0·3285	6	0·8834	6	−0·2014	7
12	0·5674	2	−0·6559	2	0·1412	3	−0·1837	3	0·2089	5	−0·3986	5	0·1010	6	−0·2084	6
13	0·1926	2	−0·1938	2	0·4159	2	−0·4766	2	0·3402	4	−0·5873	4	0·1412	5	−0·2646	5
14	0·7575	1	−0·6531	1	0·1426	2	−0·1421	2	0·6582	3	−0·1028	4	0·2367	4	−0·4030	4
15	0·3417	1	−0·2507	1	0·5651	1	−0·4837	1	0·1493	3	−0·2101	3	0·4674	3	−0·7219	3
16	······		······		······		······		······		······		······		······	
17	0·9363	0	−0·5598	0	0·1276	1	−0·8420	0	0·1203	2	−0·1340	2	0·2866	2	−0·3584	2
18	0·5091	0	−0·3242	0	0·6687	0	−0·4317	0	0·4236	1	−0·4140	1	0·8825	1	−0·9781	1
19	0·2503	0	−0·2048	0	0·3401	0	−0·2472	0	0·1691	1	−0·1460	1	0·3115	1	−0·3043	1
20	0·8467	−1	−0·1310	0	0·1464	0	−0·1492	0	0·7423	0	−0·5878	0	0·1240	1	−0·1080	1
								$\eta=7$								
10	0·1231	3	−0·1668	3	0·3724	3	−0·5699	3	0·1456	6	−0·3295	6	0·9289	6	−0·2278	7
11	0·3480	2	−0·4080	2	0·8881	2	−0·1189	3	0·1711	5	−0·3465	5	0·9107	5	−0·2003	6
12	0·1176	2	−0·1176	2	0·2547	2	−0·2956	2	0·2510	4	−0·4561	4	0·1129	5	−0·2236	5
13	0·4686	1	−0·3951	1	0·8694	1	−0·8624	1	0·4488	3	−0·7312	3	0·1721	4	−0·3073	4
14	······		······		······		······		······		······		······		······	
15	0·1090	1	−0·7121	0	0·1587	1	−0·1168	1	0·2443	2	−0·3145	2	0·6891	2	−0·9920	2
16	0·5670	0	−0·3804	0	0·7814	0	−0·5425	0	0·7309	1	−0·8237	1	0·1772	2	−0·2263	2
17	0·2723	0	−0·2257	0	0·3836	0	−0·2870	0	0·2550	1	−0·2508	1	0·5345	1	−0·5997	1
18	0·9394	−1	−0·1376	0	0·1648	0	−0·1634	0	0·1010	1	−0·8856	0	0·1868	1	−0·1841	1
19	−0·1185	−1	−0·7713	−1	0·3999	−1	−0·9168	−1	0·4328	0	−0·3591	0	0·7348	0	−0·6531	0
20	−0·6533	−1	−0·3199	−1	−0·2654	−1	−0·4435	−1	0·1866	0	−0·1624	0	0·3093	0	−0·2641	0

TABLE 1 (*Continued*)

p	L=5				L=6				L=10				L=11			
	g_5		g'_5		g_6		g'_6		g_{10}		g'_{10}		g_{11}		g'_{11}	
$\eta=6$																
10	0·2162	2	−0·2582	2	0·5693	2	−0·7905	2	0·1518	5	−0·3297	5	0·9076	5	−0·2149	6
11	0·7240	1	−0·7223	1	0·1578	2	−0·1863	2	0·1958	4	−0·3777	4	0·9692	4	−0·2047	5
12	…………		…………		…………		…………		…………		…………		…………		…………	
13	0·1338	1	−0·9780	0	0·2138	1	−0·1806	1	0·6334	2	−0·9582	2	0·2207	3	−0·3718	3
14	0·6542	0	−0·4692	0	0·9629	0	−0·7356	0	0·1534	2	−0·2031	2	0·4507	2	−0·6729	2
15	0·3047	0	−0·2566	0	0·4491	0	−0·3508	0	0·4462	1	−0·5122	1	0·1108	2	−0·1455	2
16	0·1077	0	−0·1473	0	0·1913	0	−0·1851	0	0·1530	1	−0·1530	1	0·3251	1	−0·3717	1
17	−0·3085	−2	−0·7871	−1	0·5340	−1	−0·9857	−1	0·5929	0	−0·5377	0	0·1114	1	−0·1120	1
18	−0·5657	−1	−0·3107	−1	−0·1699	−1	−0·4616	−1	0·2427	0	−0·2173	0	0·4275	0	−0·3945	0
19	−0·7027	−1	0·1203	−2	−0·4512	−1	−0·1275	−1	0·9481	−1	−0·9608	−1	0·1712	0	−0·1582	0
20	−0·5879	−1	0·1955	−1	−0·4700	−1	0·7004	−2	0·2861	−1	−0·4299	−1	0·6448	−1	−0·6848	−1
$\eta=5$																
11	0·1788	1	−0·1514	1	0·3277	1	−0·3300	1	0·2358	3	−0·4288	3	0·1072	4	−0·2160	4
12	0·7979	0	−0·6266	0	0·1292	1	−0·1123	1	0·4298	2	−0·6828	2	0·1611	3	−0·2868	3
13	0·3550	0	−0·3067	0	0·5562	0	−0·4644	0	0·9787	1	−0·1344	2	0·3028	2	−0·4735	2
14	0·1283	0	−0·1627	0	0·2312	0	−0·2210	0	0·2738	1	−0·3229	1	0·7029	1	−0·9553	1
15	0·9057	−2	−0·8236	−1	0·7195	−1	−0·1100	0	0·9113	0	−0·9391	0	0·1985	1	−0·2333	1
16	−0·4596	−1	−0·3128	−1	−0·5239	−2	−0·4977	−1	0·3398	0	−0·3254	0	0·6598	0	−0·6846	0
17	−0·5981	−1	0·8261	−3	−0·3575	−1	−0·1439	−1	0·1295	0	−0·1289	0	0·2430	0	−0·2370	0
18	−0·4941	−1	0·1770	−1	−0·3926	−1	0·5241	−2	0·4330	−1	−0·5426	−1	0·9038	−1	−0·9272	−1
19	−0·2857	−1	0·2221	−1	−0·2907	−1	0·1353	−1	0·7413	−2	−0·2170	−1	0·2906	−1	−0·3801	−1
20	−0·7839	−2	0·1811	−1	−0·1478	−1	0·1396	−1	−0·5753	−2	−0·6529	−2	0·4349	−2	−0·1456	−1
$\eta=4$																
10	0·1068	1	−0·9573	0	0·2003	1	−0·2089	1	0·1870	3	−0·3654	3	0·9535	3	−0·2074	4
11	0·4401	0	−0·3987	0	0·7550	0	−0·7022	0	0·3037	2	−0·5119	2	0·1245	3	−0·2368	3
12	0·1604	0	−0·1897	0	0·2967	0	−0·2875	0	0·6377	1	−0·9178	1	0·2108	2	−0·3484	2
13	0·2578	−1	−0·8975	−1	0·9873	−1	−0·1302	0	0·1689	1	−0·2070	1	0·4543	1	−0·6455	1
14	−0·3325	−1	−0·3330	−1	0·9557	−2	−0·5640	−1	0·5375	0	−0·5792	0	0·1217	1	−0·1486	1
15	−0·4866	−1	−0·7718	−3	−0·2535	−1	−0·1739	−1	0·1892	0	−0·1950	0	0·3869	0	−0·4199	0
16	−0·4038	−1	0·1499	−1	−0·3145	−1	0·2763	−2	0·6500	−1	−0·7415	−1	0·1345	0	−0·1410	0
17	−0·2276	−1	0·1855	−1	−0·2382	−1	0·1087	−1	0·1692	−1	−0·2876	−1	0·4519	−1	−0·5278	−1
18	−0·5835	−2	0·1444	−1	−0·1225	−1	0·1136	−1	−0·980	−3	−0·9601	−2	0·1130	−1	−0·1990	−1
$\eta=3$																
10	0·2147	0	−0·2432	0	0·4207	0	−0·4352	0	0·2268	2	−0·4111	2	0·1041	3	−0·2142	3
11	0·5002	−1	−0·1047	0	0·1415	0	−0·1698	0	0·4279	1	−0·6539	1	0·1541	2	−0·2724	2
12	−0·1781	−1	−0·3819	−1	0·2930	−1	−0·6865	−1	0·1051	1	−0·1357	1	0·3013	1	−0·4527	1
13	−0·3691	−1	−0·3887	−2	−0·1346	−1	−0·2241	−1	0·3141	0	−0·3590	0	0·7525	0	−0·9653	0
14	−0·3186	−1	0·1148	−1	−0·2350	−1	−0·5611	−3	0·1023	0	−0·1153	0	0·2250	0	−0·2584	0
15	−0·1796	−1	0·1472	−1	−0·1896	−1	0·7955	−2	0·3055	−1	−0·4107	−1	0·7246	−1	−0·8273	−1
16	−0·4683	−2	0·1113	−1	−0·1011	−1	0·8879	−2	0·5066	−2	−0·1415	−1	0·2138	−1	−0·2907	−1
$\eta=2$																
10	0·1584	−2	−0·4825	−1	0·5856	−1	−0·9351	−1	0·2996	1	−0·4939	1	0·1207	2	−0·2314	2
11	−0·2445	−1	−0·8989	−2	0·925	−3	−0·3102	−1	0·6643	0	−0·9163	0	0·2075	1	−0·3342	1
12	−0·2396	−1	0·7240	−2	−0·1523	−1	−0·5033	−2	0·1826	0	−0·2240	0	0·4717	0	−0·6438	0
13	−0·1413	−1	0·1093	−1	−0·1444	−1	0·4771	−2	0·5399	−1	−0·6727	−1	0·1305	0	−0·1601	0
14	−0·4190	−2	0·8323	−2	−0·8336	−2	0·6537	−2	0·1356	−1	−0·2197	−1	0·3841	−1	−0·4807	−1
$\eta=1$																
10	−0·1634	−1	0·2151	−2	−0·5876	−2	−0·1155	−1	0·4326	0	−0·6474	0	0·1511	1	−0·2653	1
11	−0·1085	−1	0·7241	−2	−0·9899	−2	0·1163	−2	0·1070	0	−0·1420	0	0·3036	0	−0·4465	0
12	−0·3928	−2	0·5997	−2	−0·6660	−2	0·4291	−2	0·2827	−1	−0·3895	−1	0·7630	−1	−0·1006	0

The authors wish to thank Dr. F. Hirst and his computer staff for their continued assistance in the operation of CSIRAC, and Associate Professor C. B. O. Mohr for his encouragement and interest in the project.

References

Learner, A., and Robson, B. A. (1958).—*Aust. J. Phys.* **11** : 138.

Tubis, A. (1958).—Tables of nonrelativistic Coulomb wave functions. Los Alamos Scientific Laboratory, Report LA2150.

OBSERVATIONS OF FACULAE BORDERING SMALL SUNSPOTS NEAR THE LIMB*

By R. E. Loughhead† and R. J. Bray†

It has long been known that there is a close association between sunspots and white-light faculae. No spots near the limb are observed without attendant faculae and, conversely, except for the polar faculae, which occur in zones where spots do not normally appear, there are few faculae which are not associated with spot groups at some stage of their lives. Photospheric faculae are visible only near the limb, where they may be described as consisting of a system of bright granules (ten Bruggencate 1940; Waldmeier 1955, cf. p. 205) seen against a background of material brighter than the surrounding photosphere; they are often arranged in the form of veins parallel to the limb.

During the course of the examination of a number of films‡ of spot groups near the limb we have noticed that there is a strong tendency for the facular streaks to lie in juxtaposition to any small spots in the vicinity. In such cases they appear as bright borders closely following the outlines of the spots and occurring almost invariably on the limb side.

Plate 1 gives two illustrations of this phenomenon: 1 (*a*) shows portion of an isolated group of small spots and 1 (*b*) some of the debris between the main components of a well-developed bipolar group. All the spots shown are devoid of penumbrae and appear somewhat elongated in the vertical direction owing to foreshortening (the heliocentric angles being 58 and 64° respectively). The bright borders are very conspicuous on some of the spots; their apparent widths lie between 1 and 2 sec of arc. Although there are several spots lacking a bright border and several facular veins unaccompanied by spots, there is no doubt that the phenomenon is real.

---

* Manuscript received September 26, 1958.

† Division of Physics, C.S.I.R.O., University Grounds, Chippendale, N.S.W.

‡ The films were taken with the 5-in. photoheliograph (Loughhead and Burgess 1958) of the C.S.I.R.O. Division of Physics Solar Observatory.

Photographs taken with the Sydney Hα-telescope, using solar image diameters of 15 and 75 mm, show normal hydrogen plages above the regions illustrated in Plate 1 but fail to reveal any detailed connexion between the hydrogen plages and the facular veins.

The same phenomenon has been observed in other spot groups near both limbs. Nevertheless, it is by no means universal: a number of spots similar to those illustrated, at comparable heliocentric angles, failed to show any bright borders. When present, however, they are almost invariably on the limb side. The effect has been observed only with spots devoid of penumbrae and sometimes occurs even with pores 1–2 sec of arc in diameter. It then takes the form of a bright point of light on the limb side of the pore, closely resembling a very bright photospheric granule.

One interpretation of the observations is that over the small umbral areas lie facular " clouds " of similar dimensions which, at the heliocentric angles concerned, appear displaced towards the limb by parallax; the observed displacements imply a height of about 1200 km (cf. Plate 1). In addition, the faculae are supposed to be semi-transparent—so that the spots remain visible underneath—but are sufficiently emissive to appear bright when their radiation is added to that of the normal photosphere. Apart from the earlier visual observations of faculae at the limb as " projecting hillocks " (Young 1895), there are three lines of evidence which suggest that faculae do indeed lie above the lower layers of the photosphere: the resemblance of faculae to the overlying calcium plages, the difference between the periods of solar rotation derived from measurements of faculae and spots, and finally, the interpretation of limb-darkening measurements of the faculae. The first two provide no estimates of height, and the present interpretation of the limb-darkening measurements is somewhat obscure. However, according to Waldmeier (1955, cf. p. 208), the contrast of the faculae reaches a maximum at a heliocentric angle of 71° and decreases nearer the limb. This would seem to imply that the faculae are located in the photosphere (see also Unsöld 1955); but the vertical extension of the photosphere does not exceed a few hundred kilometres, whereas the parallax explanation requires the faculae to lie at a height of about 1200 km.

Another possible explanation may lie in the lower absorption coefficient of the umbral gas compared with that of the photosphere. This causes the umbral boundary on the limb side to appear displaced away from the limb, so that any overlying facular cloud appears to project beyond the boundary.*

Whatever the explanation of the observed asymmetry in the location of the bright borders, the observations strongly suggest the existence of facular clouds directly overlying small umbral areas. A spot is a cool region surrounded by hotter gases, whereas a facula is a hot region surrounded by cooler gases. It

---

* The effect of a lower absorption coefficient would be to cause the umbra to become foreshortened, as the spot approached the limb, at a greater rate than that implied by geometrical foreshortening. A similar explanation has been used to account for the Wilson effect (Loughhead and Bray 1958). However, measurements made to detect any such anomalous foreshortening, based on the same data, have proved inconclusive owing to changes in the size of the spot during its passage across the disk and to irregularities in its umbral outline.

OBSERVATIONS OF FACULAE BORDERING SMALL SUNSPOTS NEAR THE LIMB

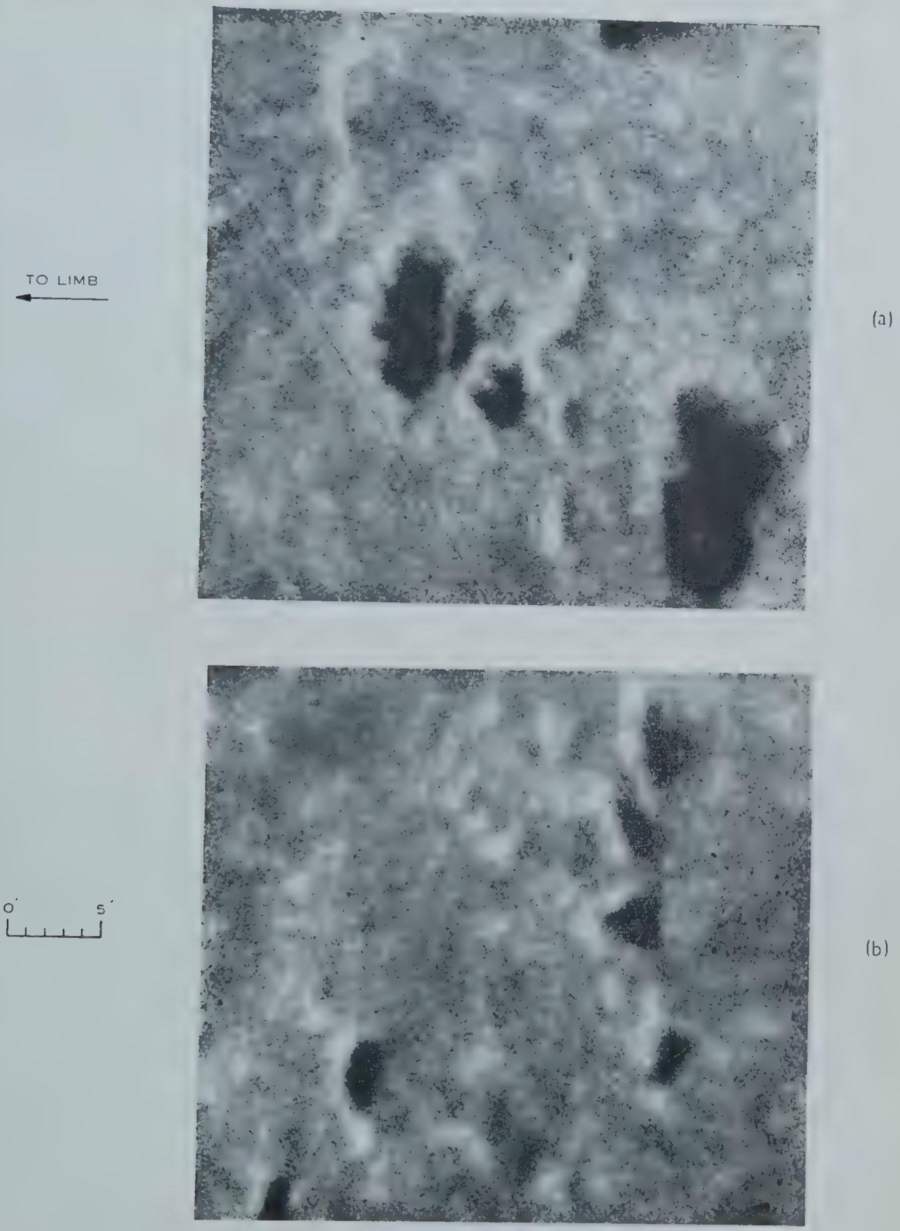

(*a*) Portion of an isolated group of small spots, photographed on January 10, 1958. Heliographic coordinates: 347° W., 23° N.; heliocentric angle, 58°.

(*b*) Small spots associated with a bipolar group, photographed on January 13, 1958. Heliographic coordinates: 298° W., 16° N.; heliocentric angle, 64°.

The spots are devoid of penumbrae and appear somewhat elongated in the vertical direction owing to foreshortening.

may well be a fruitful concept to consider spot and facula as two parts of a single physical system—the equivalent of a refrigerating engine (cf. Kiepenheuer 1953).

The authors are indebted to Miss M. McCabe and Mr. V. R. Burgess for supplying chromospheric photographs and to Mr. H. Gillett for processing the films and making the enlargements.

References

Kiepenheuer, K. O. (1953).—" The Sun." (Ed. G. Kuiper.) p. 375. (Univ. Chicago Press.)

Loughhead, R. E., and Bray, R. J. (1958).—*Aust. J. Phys.* **11** : 177.

Loughhead, R. E., and Burgess, V. R. (1958).—*Aust. J. Phys.* **11** : 35.

ten Bruggencate, P. (1940).—*Z. Astrophys.* **19** : 59.

Unsöld, A. (1955).—" Physik der Sternatmosphären." 2nd Ed. pp. 579–80. (Springer : Berlin.)

Waldmeier, M. (1955).—" Ergebnisse und Probleme der Sonnenforschung." 2nd Ed. (Geest u. Portig : Leipzig.)

Young, C. A. (1895).—" The Sun." p. 131. (Kegan Paul : London.)

THE ENERGY SPECTRUM OF PROTONS FROM THE ^{7}Be(d,p)^{8}Be REACTION*

By R. H. Spear†

The experimental evidence relating to the low-lying excited states of ^{8}Be has been discussed in a previous paper (Spear 1958). This note presents the results of a preliminary study of the energy spectrum of protons from the previously unreported ^{7}Be(d,p)^{8}Be reaction, undertaken with a view to obtaining further information on the problem.

The main difficulty of the experiment was to obtain a suitable ^{7}Be target ; ^{7}Be is unstable, and decays by K-capture with a half life of 53 days (Strominger, Hollander, and Seaborg 1958). The target was prepared by evaporating down a solution of ^{7}Be in hydrochloric acid onto a backing of gold foil of thickness $22 \cdot 7$ mg cm^{-2}. Unfortunately, the solution contained a good deal of impurity, and the solid material deposited on evaporation formed a thick and rather uneven target. The target covered an area of approximately $0 \cdot 3$ cm^{2}, and had an estimated activity of 20 μc.

The reaction was studied using the camera described by Martin *et al.* (1949), and each plate was given an integrated exposure of the order of 70,000 μC of $0 \cdot 85$ MeV deuterons from an electrostatic generator. The plates were processed

---

* Manuscript received October 14, 1958.

† Physics Department, University of Melbourne.

and proton ranges measured, by conventional methods. The proton energies E_p were determined from the range-energy relation given by Gibson, Prowse, and Rotblat (1954) for Ilford C2 emulsions.

Spectra have been obtained at three angles : 0, 90, and 270°, corresponding to mean values of φ, the true angle to the incident beam, of 13, 87, and 268° respectively. At each angle measurements were made over an area of approximately 1–2 cm² at a radial distance of approximately 4·7 cm from the point in the plate above the target spot. The absorbing foils were sufficiently thick to absorb the products of most contaminant reactions. So as to avoid tracks from the $^{14}N(d,p)^{15}N$ reaction ($Q=8\cdot609$ MeV), tracks were accepted only if their range was greater than two fields of view (approximately 390 μ).

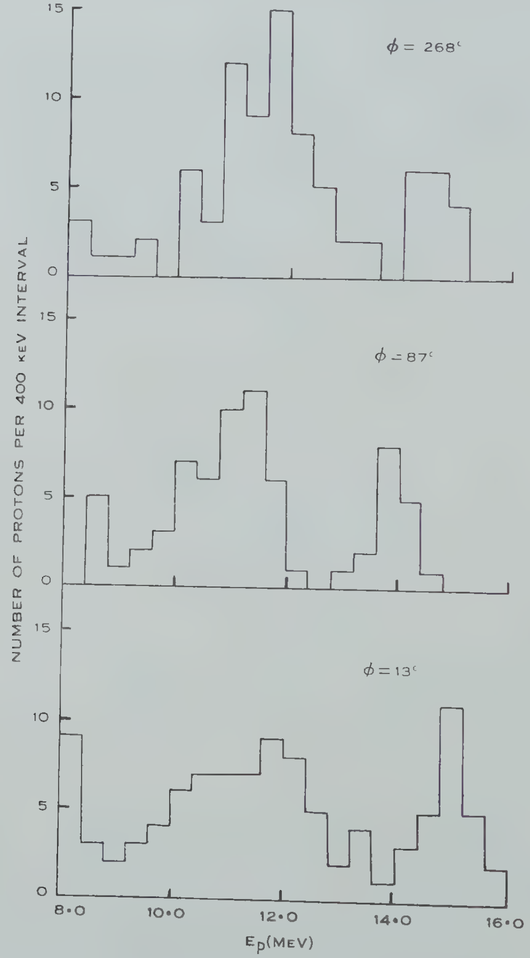

Fig. 1.—Energy spectrum of protons from $^{7}Be(d,p)^{8}Be$.

The results obtained from four plates (three 400 μ and one 200 μ) are shown in Figure 1. The tracks at 8·1 MeV on the 13° spectrum are probably due to the high energy tail of the ground state group from the $^{14}N(d,p)^{15}N$ reaction. In order to combine the results in terms of excitation energy E_{ex} in ^{8}Be, the following procedure was adopted. It was assumed that the high energy group at each angle was the ground state group from ^{7}Be$(d,p)^8$Be. From the energy of this group and the Q-value of 16·661 MeV for the reaction (as determined from the mass values), the total absorber thickness (i.e. target plus foils) at each angle was calculated. This thickness, obtained in centimetres air equivalent using the range-energy relation for protons in air given by Bethe and Ashkin (1953), was then used to find the relation between E_p and E_{ex} at each angle. The results for the three angles are plotted in terms of E_{ex} in Figure 2. The upper limit taken for E_{ex}, 5·8 MeV, corresponds to E_p=9·0, 8·1, and 9·1 MeV at 13, 87, and 268° respectively. There is no feasible contamination reaction which could give protons in the range of energies covered by Figure 2. The nearest would be the ^{10}B$(d,p)^{11}$B reaction (Q=9·227 MeV); if the target thickness were zero this would give protons of energies 8·2, 7·5, and 8·3 MeV at 13, 87, and 268° respectively.

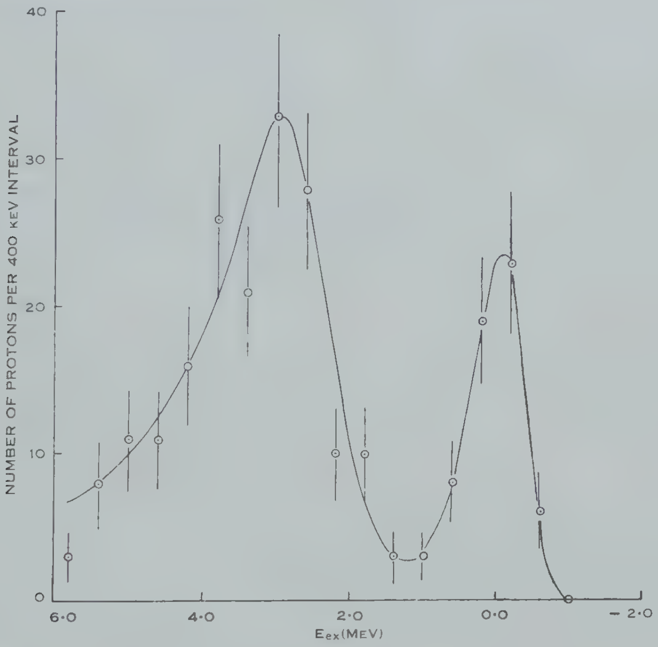

Fig. 2.—Energy spectrum of protons from ^{7}Be$(d,p)^8$Be (combination of results for φ=13, 87, and 268°).

The general shape of the spectrum is very similar to that obtained for the "mirror reaction" ^{7}Li$(d,n)^8$Be (Spear 1958), with a very broad group peaked at E_{ex}=2·95 MeV. The intensity of the ground state group relative to the 2·9 MeV state group is rather less than was obtained for the ^{7}Li$(d,n)^8$Be reaction. This may be explained by the fact that in the 200 μ plate many of the longer tracks passed right through the emulsion into the glass backing, and so were neglected; this would tend to suppress the high energy end of the spectrum.

The half-width of the ground state group is approximately 0·9 MeV. This relatively large width is due mainly to the use of a thick, uneven target and to the angular straggling caused by the necessity to scan a large area at each angle in order to obtain sufficient tracks. After allowing for experimental resolution, a value of 1·6±0·4 MeV is obtained for the width of the 2·9 MeV level, in good agreement with the value obtained from the ^{7}Li(d,n)^{8}Be reaction (Spear 1958).

Although the statistical accuracy of the measurements is not high, the results do not indicate the existence of any low intensity excited states of ^{8}Be in the region covered.

It is intended to extend the measurements using a purer sample of ^{7}Be in order to obtain a higher yield and better resolution.*

* *Note added in Proof.*—It has recently been brought to the author's attention that C. A. Barnes, R. W. Kavanagh, and J. B. Marion studied this reaction at the California Institute of Technology in 1956, using a scintillation spectrometer, but did not publish their results. Their 90° spectrum is similar to the present results.

The author is grateful to Professor Sir Leslie Martin for his continued interest in this work, and to Dr. D. N. F. Dunbar, who first suggested the experiment and has taken an active interest in it. Thanks are also due to Mr. P. Schwerdtfeger, who assisted with the preparation of the target and in making the exposures, and to the Radiochemistry Section of the Melbourne University Department of Chemistry for facilities provided. The ^{7}Be was supplied by the Isotopes Division, Atomic Energy Research Establishment, Harwell.

References

Bethe, H. A., and Ashkin, J. (1953).—" Experimental Nuclear Physics." Vol. 1. p. 166. (Ed. E. Segre.) (Wiley : New York.)
Gibson, W. M., Prowse, D. J., and Rotblat, J. (1954).—*Nature* **173** : 1180.
Martin, L. H., Bower, J. C., Dunbar, D. N. F., and Hirst, F. (1949).—*Aust. J. Sci. Res.* A **2** : 25.
Spear, R. H. (1958).—*Aust. J. Phys.* **11** : 502.
Strominger, D., Hollander, J. M., and Seaborg, G. T. (1958).—*Rev. Mod. Phys.* **30** : 585.

THE ^{58}Ni(n,p)^{58}Co, ^{58}Ni($n,2n$)^{57}Ni, AND ^{58}Ni(n,np)^{57}Co CROSS SECTIONS AT 14·1 MeV*

By K. H. Purser† and E. W. Titterton†

The energy spectrum of the protons which are emitted when nickel is bombarded with 14·1 MeV neutrons has been studied recently by several workers—Allan (1957), Colli, Facchini, *et al.* (1958), and Colli, Pignanelli, *et al.* (1958). The results of these experiments do not allow an accurate estimate of the relative importance of contributions from the (n,p) reaction and the (n,np) reaction. Such information is necessary when any reaction mechanism is postulated to account for the experimental results. In these experiments, therefore, activation techniques have been used to measure these two cross sections separately for the isotope ^{58}Ni at 14·1 MeV; in addition, the ^{58}Ni$(n,2n)^{57}$Ni cross section has been remeasured.

Reaction ^{58}*Ni*(n,p)^{58}*Co*

Nickel foils were irradiated with monoenergetic neutrons produced by the ^{3}H$(d,n)^{4}$He reaction, the neutron flux being measured by counting the associated α-particles emitted into a known solid angle. During irradiation, the nickel foils were placed 3·5 cm from the centre of the target. However, because the deuteron beam wanders slightly over the surface of the tritium target during an irradiation, an estimate of the flux through the sample based on the distance from the centre of the beam is unreliable; for this reason, copper disks were placed on either side of the irradiated nickel foil and the induced ^{65}Cu$(n,2n)^{64}$Cu activity compared with the same activity in disks which were placed 15 cm from the neutron source. This technique allowed the integrated flux at the specimen to be measured with an accuracy better than ±7 per cent.

^{58}Co formed by the (n,p) reaction during irradiation decays to an excited state of ^{58}Fe by positron emission and by the electron capture process. The k/β^+ branching ratio has been measured accurately by Good, Peaslee, and Deutsch (1946), and their value of 5·89 was used here. The number of ^{58}Co atoms produced during the irradiation was estimated by counting the positron annihilation quanta with a scintillation spectrometer, allowance being made for self-absorption in the nickel foils. The geometry of the counter was eliminated by calibrating the spectrometer with a standardized ^{22}Na source, and the counting errors were estimated to be less than 12 per cent. Three independent measurements of the cross section were made, and the weighted mean of these gave

$$^{58}\mathrm{Ni}(n,p)^{58}\mathrm{Co}\ \ (14\cdot1\ \mathrm{MeV}) = (560 \pm 110)\times10^{-27}\ \mathrm{cm}^2.$$

---

* Manuscript received October 28, 1958.

† Research School of Physical Sciences, Australian National University, Canberra.

Reaction ^{58}Ni(n,2n)^{57}Ni

The cross section of the reaction $^{58}\mathrm{Ni}(n,2n)^{57}\mathrm{Ni}$ has been measured previously by Paul and Clark (1953) using activation techniques, and they found a value of $(40\cdot6\pm10)\times10^{-27}$ cm^2. The method described above, applied to the positron emitted when ^{57}Ni decays to ^{57}Co with a half-life of 36 hr, was used to measure this cross section. The value found was $(38\pm8)\times10^{-27}$ cm^2—in good agreement with that of Paul and Clark.

Reaction ^{58}Ni(n,np)^{57}Co

The ratio of the cross sections for the two reactions $^{58}\mathrm{Ni}(n,2n)^{57}\mathrm{Ni}$ and $^{58}\mathrm{Ni}(n,np)^{57}\mathrm{Co}$ was measured by a method which depended upon the fact that the decay product from the 36-hr ^{57}Ni, produced by the $(n,2n)$ reaction, is 270-day ^{57}Co—the same nucleus as is produced directly by the (n,np) reaction. In other words, the number of ^{57}Co atoms produced at the end of the irradiation is proportional to the $^{58}\mathrm{Ni}(n,np)$ cross section, and the number present when the ^{57}Ni nuclei have decayed is proportional to the sum of the $^{58}\mathrm{Ni}(n,np)$ plus $^{58}\mathrm{Ni}(n,2n)$ cross sections.

A modified cobaltinitrite method (Mills and Vernon, personal communication) was used to separate the cobalt atoms from the nickel sample after irradiation, and the same separation technique was applied again to the nickel sample after one week had elapsed ; this removed all the ^{57}Co which had formed in the period due to the decay of ^{57}Ni. In both separations 5 mg cobalt carrier was used, and better than 99 per cent. recovery could be achieved in 45 min.

^{57}Co has a half-life of 270 days, decaying by electron capture to the 136 kV excited state of the stable isotope ^{57}Fe, while the ^{57}Fe decays to the ground state by emitting a 136 kV γ-ray. The ratio of the intensities of this γ-ray for the two separations is proportional to the ratio of the cross section $^{58}\mathrm{Ni}(n,np)^{57}\mathrm{Co} : {}^{58}\mathrm{Ni}(n,2n)^{57}\mathrm{Ni}$. The measured ratio was found to be $4\cdot2$, with a consistency of ±10 per cent. between the individual determinations. The cross section for the $^{58}\mathrm{Ni}(n,np)^{57}\mathrm{Co}$ reaction derived from this ratio is $(160\pm40)\times10^{-27}$ cm^2.

Discussion

There is evidence from experiments on the competitive modes of decay of ^{58}Ni bombarded by protons of 20 MeV energy for a preponderance of protons among the reaction products. Thus Cohen, Newman, and Handley (1955) find

$$\sigma(p,2p)/\sigma(p,pn)+\sigma(p,2n)=2\cdot8.$$

The results of the present experiment are somewhat similar in that they lead to the value

$$\sigma(n,np)/\sigma(n,2n)=4\cdot5\pm0\cdot9$$

for ^{58}Ni bombarded by $14\cdot1$ MeV neutrons. Thus, for proton and neutron bombardment of ^{58}Ni, proton emission from the excited nucleus appears to be favoured over neutron emission. Because of these facts a photonuclear experiment was carried out in this laboratory by Carver and Turchinetz (1959) to determine the (γp) and (γn) yields. They find the ratio of the integrated cross sections to be

$$\int_0^{32} \sigma(\gamma p)\mathrm{d}E \int_0^{32} \sigma(\gamma n)\mathrm{d}E = 2\cdot 35 \pm 0\cdot 2,$$

and again there is the predominance of proton emission. Such results are difficult to explain in terms of the usual statistical theory but may be influenced by the rounding off of the potential barrier as proposed by Scott (1954), by a difference in the level densities of the residual nuclei ^{57}Co and ^{57}Ni, or by a combination of the two.

References

Allan, D. L. (1957).—*Proc. Phys. Soc. Lond.* **70**: 195.

Carver, J. H., and Turchinetz, W. (1959).—*Proc. Phys. Soc.* (In press.)

Cohen, B. L., Newman, E., and Handley, T. H. (1955).—*Phys. Rev.* **99**: 723.

Colli, L., Facchini, U., Iori, I., Marcazzann, G., Sona, A., and Pignanelli, M. (1958).—*Nuovo Cim.* **7**: 400.

Colli, L., Pignanelli, M., Rytz, A., and Zurmühle, R. (1958).—*Nuovo Cim.* **9**: 280.

Good, W. M., Peaslee, D., and Deutsch, M. (1946).—*Phys. Rev.* **69**: 313.

Paul, E. B., and Clark, R. L. (1953).—*Canad. J. Phys.* **31**: 267.

Scott, J. M. C. (1954).—*Phil. Mag.* **45**: 441.

ELECTRON MOBILITY IN LIQUID ARGON*

By F. D. Stacey†

Experiments of Williams (1957) showed that the drift velocity of electrons in liquid argon to which an electric field F is applied is essentially independent of F. If the electrons remain free then their motion can be described by kinetic theory, from which it appears that electron mobility is proportional to $F^{-\frac{1}{2}}$ and drift velocity to $F^{\frac{1}{2}}$. This is the dependence reported by Malkin and Schultz (1951), but it is evident that the recent, more exhaustive work of Williams (1957) is correct on this point and therefore that kinetic theory is not applicable to the problem. This theory could in principle be extended to explain a field-independent velocity, by supposing a special dependence upon electron energy of the scattering cross section for the collision of electrons with argon atoms, but this is very artificial and unnecessary in view of the alternative explanation suggested here; in any case it leaves further serious objections, which will also be discussed briefly.

Williams (1957) calculated the scattering cross section needed to explain his electron mobility results by kinetic theory, observing that at high fields this gave electron kinetic energies up to 20 eV, several electron-volts in excess of the

---

* Manuscript received November 18, 1958.

† Department of Geophysics, Australian National University, Canberra.

first ionization energy of argon. This he concluded to be in agreement with observations of ionization currents in liquid argon (Williams and Stacey 1957), suggesting that some electron multiplication occurred at the highest fields. It has since been shown (Stacey 1958) that no electron multiplication is needed to explain the ionization current measurements and, further, that the maximum energy of electrons in columns of ionization formed by α-particles in liquid argon is of the order 7 eV, less than half the first ionization energy.

One of the reasons for experimenting with liquid argon as a conduction counter medium was that argon was considered to have no electron affinity, and the high electron mobility is in qualitative agreement with this supposition. However, the constant electron velocity is strongly suggestive of an attachment process, whereby heavy negative ions of very short lifetime are formed. This suggestion is now examined quantitatively.

If the cross section for the capture of electrons by neutral argon atoms is Q and the mean velocity of an electron between successive captures is v, then the probability that a free electron will be captured in a time $\mathrm{d}t$ is

$$NQv\mathrm{d}t,$$

N being the atomic density. The probability that a particular captive electron will escape in the same interval of time is

$$C\mathrm{e}^{-E/kT}\mathrm{d}t,$$

where E is the attachment energy, k is Boltzmann's constant, and T the absolute temperature. C is a frequency factor of the order kT/h, h being Planck's constant. The ratio of the times which an electron spends in the free and captive states is thus

$$(C/NQv)\mathrm{e}^{-E/kT},$$

and the observed electron velocity is

$$v'=v\cdot\frac{C\mathrm{e}^{-E/kT}}{NQv+C\mathrm{e}^{-E/kT}}, \quad \ldots\ldots\ldots\ldots\ldots\ldots \quad (1)$$

neglecting any contribution due to motion of the heavy negative ions during their lifetimes.

The mean free velocity v is a function of F, and if it is assumed that between successive captures an electron starts from rest and accelerates freely in the field, v is given by

$$v=\left(\frac{e}{m}\cdot\frac{F}{2QN}\right)^{\frac{1}{2}}, \quad \ldots\ldots\ldots\ldots\ldots\ldots \quad (2)$$

e/m being the electronic charge-to-mass ratio. If v' is independent of F (as is observed) it is evidently independent of v, a condition which is satisfied by equation (**1**) if

$$NQv \gg C\mathrm{e}^{-E/kT}, \quad \ldots\ldots\ldots\ldots\ldots\ldots \quad (3)$$

i.e. an electron is captive most of the time, so that equation (**1**) reduces to

$$v'=(C/NQ)\mathrm{e}^{-E/kT}. \quad \ldots\ldots\ldots\ldots\ldots\ldots \quad (4)$$

Numerical values of the interesting quantities, Q and E, cannot be obtained from equations (2) and (4), in which v is unknown. A proper experimental determination of Q and E would require the measurement of electron mobility over a range of temperatures, but as liquid argon at atmospheric pressure only exists over a very small temperature range, this would be a difficult undertaking. However, we can impose limits on the values of Q and E by simple physical arguments. The following three conditions must apply :

(i) The lifetime of the heavy negative ion is long by comparison with that of the free electron. This condition is expressed in equation (3).

(ii) The motion of the heavy ions does not contribute significantly to the measured electron velocities, since the negative ion mobility would only be of the same order as that for positive ions. Thus the ratio of the free electron to heavy ion lifetimes must be greater than the ratio of the positive ion mobility, μ_+, to the observed electron mobility, μ_e. This condition may be written

$$(C/NQv)\mathrm{e}^{-E/kT} \gg \mu_+/\mu_e. \qquad \dots\dots\dots\dots\dots\dots (5)$$

Since electron velocity is roughly constant over a wide range of fields, μ_e is not a quantity with much physical significance. However, the results of Williams (1957) indicate $\mu_e/\mu_+ \sim 4\times10^3$ at $F=10^5$ V/cm.

(iii) To be consistent with the theory of ionization of liquid argon by α-particles (Stacey 1958), the maximum electron energy should not exceed 7 eV, and therefore the mean kinetic energy of electrons in the free state should be less than 2 eV. This is expressed

$$\tfrac{1}{2}mv^2 = eF/4QN < 2\ \text{eV}. \qquad \dots\dots\dots\dots\dots\dots (6)$$

Conditions (i) and (ii) (equations (3) and (5)) may be written together as

$$(NQv/C)\mathrm{e}^{+E/kT} = f, \qquad \dots\dots\dots\dots\dots\dots (7)$$

where

$$1 \ll f \ll 4\times10^3,$$

so that the value of f may be taken as 60 within a factor of about 10. Thus from equations (4) and (7)

$$v = fv'. \qquad \dots\dots\dots\dots\dots\dots\dots\dots\dots\dots (8)$$

Combining equations (2) and (8) we obtain

$$Q = \frac{e}{m}\,\frac{F}{2N}\left(\frac{1}{v'f}\right)^2, \qquad \dots\dots\dots\dots\dots\dots\dots (9)$$

so that equation (4) then gives

$$E = kT\ln\,(C/NQv'). \qquad \dots\dots\dots\dots\dots\dots\dots (10)$$

The following numerical values may be used to estimate the magnitudes of Q and E from equations (9) and (10): $F=10^5$ V/cm$=333$ e.s.u., $e/m=5\cdot3\times10^{17}$ e.s.u./g, $m=9\cdot1\times10^{-28}$ g, $N=2\cdot1\times10^{22}$ per cm^3, $v'=10^6$ cm/sec

(Williams 1957), $k=8\cdot 6\times 10^{-5}$ eV °C^{-1}, $T=90$ °K, $h=6\cdot 6\times 10^{-27}$ erg sec. We then obtain

$$Q=1\cdot 7\times 10^{-18}\ \mathrm{cm}^2,$$
$$E=3\cdot 7kT=2\cdot 9\times 10^{-2}\ \mathrm{eV}.$$

Owing to its logarithmic dependence upon the uncertain values, E has been estimated more accurately than Q, for which it is suggested only that the above result is correct within a factor 10.

To test whether the above estimates are reasonable, condition (iii) can be applied. Using the same numerical values we find

$$\tfrac{1}{2}mv^2=1\ \mathrm{eV},$$

which shows that the above values are consistent with this condition.

Williams (1957) suggested that the electron mobility in liquid argon agreed with Eyring's (1936) theory of ionic mobility and related phenomena in liquids. It must be noted that Eyring's theory refers only to heavy ions, the potential wells responsible for trapping them being physical holes and not electrical potential wells. Eyring's theory has no application to electron mobility. Williams himself showed that this theory could not be successfully applied even to positive ions in argon, whose mobility gives much better agreement with Stokes's formula for spheres in a viscous fluid. It must be concluded that the trapping centres for the electrons are the neutral argon atoms; any trapping centres due to impurities would give heavy ion lifetimes far too long. The lifetime of the heavy negative ion in liquid argon (at 90 °K) can be estimated as $1/Ce^{E/kT}\sim 3\times 10^{-11}$ sec, which is sufficient explanation why such ions are not normally observed.

If the energy E of attachment of electrons to neutral atoms is comparable in liquid helium it can be seen immediately that at the lower temperature of helium the heavy negative ions will have very long lifetimes, and therefore that the observed negative ion mobility will be comparable with that of positive ions. This was found to be the case (Williams 1957), but in helium the detailed problem is rather more complex and an analysis will not be attempted here.

In conclusion it may be stated that the measured velocity of electrons in liquid argon is consistent with the formation of heavy negative ions having lifetimes of the order 3×10^{-11} sec, resulting from an electron affinity of neutral argon atoms, which gives an attachment energy of the order $0\cdot 03$ eV. The calculated capture cross section is of the order 10^{-18} cm^2. This picture is consistent with the theory of α-particle ionization of liquid argon (Stacey 1958) and indicates that no electron multiplication occurs.

References

Eyring, H. (1936).—*J. Chem. Phys.* **4**: 283.

Malkin, M. S., and Schultz, H. L. (1951).—*Phys. Rev.* **83**: 1051.

Stacey, F. D. (1958).—*Aust. J. Phys.* **11**: 158.

Williams, R. L. (1957).—*Canad. J. Phys.* **35**: 134.

Williams, R. L., and Stacey, F. D. (1957).—*Canad. J. Phys.* **35**: 928.

THE MICROWAVE SPECTRA OF ISOTOPIC MOLECULES OF SULPHUR DIOXIDE

By W. E. Smith*

[*Manuscript received November 5, 1958*]

Summary

Some new lines in the spectra of $^{34}SO_2$ and $^{33}SO_2$ have been measured and accounted for in terms of a semi-rigid rotor model with centrifugal distortion coefficients derived from Kivelson's (1954) published figures for $^{32}SO_2$, and rotational constants obtained from the measurements.

The hyperfine structure of the $^{33}SO_2$ $1_{11}\leftarrow 2_{02}$ transition has been analysed and found to agree with the quadrupole coupling constants of Bird and Townes (1954).

I. Introduction

The microwave spectrum of the asymmetric rotor sulphur dioxide has been the subject of investigation of a number of workers (Crable and Smith 1951; Sirvetz 1951; Kivelson 1954; Wertheimer and Clouard 1957) since the first rotational constants were reported by Dailey, Golden, and Wilson (1947). The early work neglected the effects of centrifugal distortion, which were shown by Sirvetz (1951) to be important in accounting for the observed spectrum. Kivelson (1954), by making use of a combination of microwave and infra-red data, has accurately fitted the microwave spectrum, obtaining at the same time a precise estimate of the molecular force constants. In the present work some new lines of the isotopic molecules $^{33}SO_2$ and $^{34}SO_2$, in addition to those found by Bird and Townes (1954), are reported and accounted for in terms of a semi-rigid model with centrifugal distortion coefficients calculated from Kivelson's force constants for $^{32}SO_2$.

II. Experimental

All measurements were made with a Stark-modulated spectroscope, the essential features of which have been described by Posener (1957). For the stronger lines 5 kc/s square-wave modulation was used, but the greater sensitivity of the 105 kc/s square-wave system was required for some of the weaker ones. Commercial grade sulphur dioxide was used and was consequently unenriched in ^{33}S, ^{34}S (natural abundance: ^{33}S, 0·74 per cent.; ^{34}S, 4·2 per cent.). The resulting low intensity of the $^{33}SO_2$ transitions necessitated the use of very narrow detector bandwidths (down to 0·01 c/s) with a.f.c. locking of the klystron frequency between harmonics of the laboratory frequency standard. In all frequency measurements small corrections for the time delay introduced by the finite detector bandwidths (Smith 1955) were made. The absorption cells could be cooled by dry ice either for enhancing the intensity or for identifying transitions.

---

* Division of Electrotechnology, C.S.I.R.O., University Grounds, Chippendale, N.S.W.

III. ^{34}SULPHUR DIOXIDE

The rotational constants of $^{34}SO_2$ may be estimated roughly from those of $^{32}SO_2$ by assuming the same molecular dimensions in evaluating the principal moments of inertia I_a, I_b about axes in the plane of the molecule, and the same inertia defect (Dailey, Golden, and Wilson 1947) to give I_c. These constants may then be used (neglecting distortion) to estimate line frequencies. Bird and Townes (1954) used this technique for finding two lines of $^{34}SO_2$ ($4_{04} \leftarrow 3_{13}$ 31,011·19 Mc/s ; $5_{24} \leftarrow 6_{15}$ 17,970·42 Mc/s). The same method has been used here to predict the $1_{11} \leftarrow 2_{02}$ transition at 10,550 Mc/s, which was subsequently measured and identified by its Stark effect at 10,547·91 ± 0·02 Mc/s.

The knowledge of these three transitions enables an accurate set of rotational constants to be calculated but for the effects of centrifugal distortion. The shifts in line frequencies due to distortion in $^{32}SO_2$ (Kivelson 1954) are quite small (<100 Mc/s) compared with the line frequencies and consequently need not be known to high precision. In view of the success in the prediction of line frequencies by assuming the molecular structure to be undisturbed by the isotopic substitution, it was concluded that the centrifugal distortion could be calculated with good accuracy using Kivelson's $^{32}SO_2$ force constants and structural parameters. Further examination shows that the four independent distortion constants τ_{aaaa}, τ_{bbbb}, τ_{aabb}, τ_{abab} (C_{2v} symmetry) for the various isotopic molecules may be simply related on this basis using expressions quoted by Kivelson (1954) for the τ's in terms of the force constants. The following interrelations are obtained :

$$\tau^{34}_{aaaa} = (a^{34}/a^{32})^2\, \tau^{32}_{aaaa}, \tag{1a}$$

$$\tau^{34}_{bbbb} = (b^{34}/b^{32})^2\, \tau^{32}_{bbbb}, \tag{1b}$$

$$\tau^{34}_{aabb} = (a^{34}b^{34}/a^{32}b^{32})\tau^{32}_{aabb}, \tag{1c}$$

$$\tau^{34}_{abab} = \left(\frac{a^{34}b^{34}}{a^{32}b^{32}}\right)\left(\frac{2M_0+M_s^{34}}{2M_0+M_s^{32}}\right)\left(\frac{M_s^{32}}{M_s^{34}}\right)\left(\frac{1+2(M_0/M_s^{32})\sin^2\theta}{1+2(M_0/M_s^{34})\sin^2\theta}\right)^2 \tau^{32}_{abab}, \tag{1d}$$

where a, b, c are rotational constants,

M_0 =mass of ^{16}O atom,
$M_s^{32,34}$=mass of ^{32}S, ^{34}S atoms,
2θ =S—O—S angle,
=119·536° (Kivelson 1954).

The remaining non-zero τ's may then be derived (Kivelson and Wilson 1953) :

$$\tau_{cccc} = (c/b)^4\, \tau_{bbbb} + (c/a)^4\, \tau_{aaaa} + 2(c^4/a^2b^2)\tau_{aabb}, \tag{2a}$$

$$\tau_{bbcc} = (c/b)^2\, \tau_{bbbb} + (c/a)^2\, \tau_{aabb}, \tag{2b}$$

$$\tau_{aacc} = (c/a)^2\, \tau_{aaaa} + (c/b)^2\, \tau_{aabb}. \tag{2c}$$

In this way the distortion coefficients listed in Table 1 were obtained. The same number of figures is retained for the τ's as was quoted by Kivelson but it must not be assumed in either case that they are all significant.

The usual D_J, D_{JK}, etc. (Nielsen 1951) were found from the τ's and used to set up the energy matrices. A set of rotational constants for $^{34}SO_2$ was then found which fitted the three known lines $1_{11} \leftarrow 2_{02}$; $4_{04} \leftarrow 3_{13}$; $5_{24} \leftarrow 6_{15}$. In these and other calculations the reduced energy was calculated by the continued fraction method (King, Hainer, and Cross 1943) modified (Posener 1953) where required to include the $H_{K,K\pm4}$ elements introduced by centrifugal distortion. The number of iterations required was reduced by the procedure of Posener (1956) for improving the convergence. The evaluation of any small changes of the rotational constants a, b, c is conveniently carried out using the variables $\alpha=(a+c)/2$, $\beta=(a-c)/2$, and $\varkappa$ the asymmetry parameter, together with the rigid rotor relations for the derivatives of the energy levels $W_{J\tau}$:

Table 1

DISTORTION COEFFICIENTS OF SULPHUR DIOXIDE MOLECULES

Molecule	τ_{aaaa} (Mc/s)	τ_{bbbb} (Mc/s)	τ_{aabb} (Mc/s)	τ_{abab} (Mc/s)
$^{32}SO_2$*	—9·8098	—0·039696	0·41170	—0·053203
$^{34}SO_2$	—9·2413	—0·039698	0·39960	—0·052739
$^{33}SO_2$	—9·5143	—0·039697	0·40546	—0·052966

* Kivelson (1954), " combined infra-red and microwave " results.

$$\partial W_{J\tau}/\partial\alpha=J(J+1), \qquad \text{(3a)}$$

$$\partial W_{J\tau}/\partial\beta=E_{J\tau}(\varkappa), \qquad \text{(3b)}$$

$$\partial W_{J\tau}/\partial\varkappa=\beta \mathrm{d}E_{J\tau}(\varkappa)/\mathrm{d}\varkappa, \qquad \text{(3c)}$$

where $E_{J\tau}$ is the reduced energy. $\mathrm{d}E_{J\tau}/\mathrm{d}\varkappa$ may in some cases be evaluated analytically, but otherwise may be estimated adequately for this purpose by differentiation of the fourth-order expansion of King, Hainer, and Cross (1943) for $E_{J\tau}$ in terms of the alternative asymmetry parameter $\delta(=(\varkappa+1)/2)$,

$$\mathrm{d}E_{J\tau}/\mathrm{d}\varkappa=\tfrac{1}{2}\mathrm{d}E_{J\tau}/\mathrm{d}\delta. \qquad \text{(4)}$$

The constants obtained in this manner are :

$$\left.\begin{aligned} a&=58{,}991\cdot27 \text{ Mc/s},\\ b&=10{,}318\cdot42 \text{ Mc/s},\\ c&=8{,}761\cdot42 \text{ Mc/s}, \end{aligned}\right\} \qquad \text{(5)}$$

together with the distortion coefficients of Table 1. These constants were then used to predict a number of $^{34}SO_2$ transitions which were later found and measured, and the results are listed in Table 2.

In the case of the $8_{17} \leftarrow 7_{26}$ line there was initially some ambiguity due to the presence of a weak line at 30,977·29±0·05 Mc/s. However, by cooling to dry ice temperatures this line was no longer detected, indicating that it arose from more excited levels, probably of $^{32}SO_2$.

The r.m.s. error on each of the measured frequencies of Table 2 is approximately 20 kc/s and the mean deviation from the frequencies computed by the rotational constants (**5**) together with the distortion coefficients of Table 1 is 120 kc/s, the largest individual deviation being 320 kc/s. The mean deviation for the prediction of new frequencies is 220 kc/s.

TABLE 2

$^{34}SO_2$ FREQUENCIES

Transition	Predicted Frequency from (**5**) (Mc/s)	Observed Frequency (Mc/s)	Final Calculated Frequency from (**6**) (Mc/s)	Shift Due to Distortion (Mc/s)
$1_{11} \leftarrow 2_{02}$	10,547·90	10,547·91	10,547·900	— 2·036
$4_{04} \leftarrow 3_{13}$	31,011·21	31,011·19*	31,011·144	— 0·469
$5_{24} \leftarrow 6_{15}$	17,970·40	17,970·42*	17,970·491	—20·363
$8_{26} \leftarrow 9_{19}$	20,699·43	20,699·30	20,699·247	—12·364
$10_{28} \leftarrow 11_{1,11}$	9,650·95	9,650·63	9,650·640	—13·269
$8_{17} \leftarrow 7_{26}$	30,975·61	30,975·39	30,975·421	+ 0·304

* Bird and Townes (1954).

To make maximum use of all of the experimental data a least-squares fit was then performed on the six lines to find the best values of *a*, *b*, *c*. Only linear changes in frequency for changes in *a*, *b*, *c* were taken in view of the smallness of the variations required, and the equations (**3**), (**4**) were used for computing the coefficients. For small changes in *a*, *b*, *c* the distortion shifts from the rigid-rotor frequencies were found to be unaffected, so the final calculations involved the evaluation of rigid-rotor energies only. The least-squares procedure was repeated until no further changes in *a*, *b*, *c* were indicated. The final results obtained are :

$$\left.\begin{aligned} a &= 58{,}991 \cdot 212 \text{ Mc/s}, \\ b &= 10{,}318 \cdot 404 \text{ Mc/s}, \\ c &= 8{,}761 \cdot 412 \text{ Mc/s}, \end{aligned}\right\} \quad \ldots\ldots\ldots\ldots\ldots\ldots \quad (\mathbf{6})$$

and the calculated frequencies appear in Table 2, where the mean deviation has now been reduced to only 37 kc/s, which is not far in excess of the r.m.s. error on each measurement. The final decimals in (**6**) are probably not fully significant considering the assumptions involved in the method, but rounding off to two decimals increases the mean deviation to 60 kc/s, indicating at least statistical significance. It will be noted that the differences from the initial set (**5**) are quite small, namely, —58, —16, and —8 kc/s, indicating good reliability for the process leading to the constants (**5**).

However, the small mean deviation cannot be taken as an estimate of the expected error on new predictions, since only a comparatively small number of lines has been taken and even these are either *P* or *R* type transitions of low or moderate J. Finally, of course, the predictions cannot very well be better than those of Kivelson for $^{32}SO_2$ since the distortion coefficients are derived from his. Kivelson obtained mean deviations of about 200 kc/s and it was decided to test the accuracy of prediction on the previously unobserved $1_{11} \leftarrow 2_{02}$ transition of $^{32}SO_2$ calculated to fall at 12,256·14 Mc/s. This line was found at 12,256·64 ± 0·02 Mc/s, showing a discrepancy of 500 kc/s.

IV. ^{33}SULPHUR DIOXIDE

The rotational constants of $^{33}SO_2$ were estimated roughly from those of $^{32}SO_2$ by the same method as used for $^{34}SO_2$ in the previous section. Bird and Townes (1954) have used this method to find the $5_{24} \leftarrow 6_{15}$ and $4_{04} \leftarrow 3_{13}$ transitions of $^{33}SO_2$ at 20,605·97 and 30,194·09 Mc/s respectively. The $1_{11} \leftarrow 2_{02}$ line was estimated here as falling near 11,378 Mc/s.

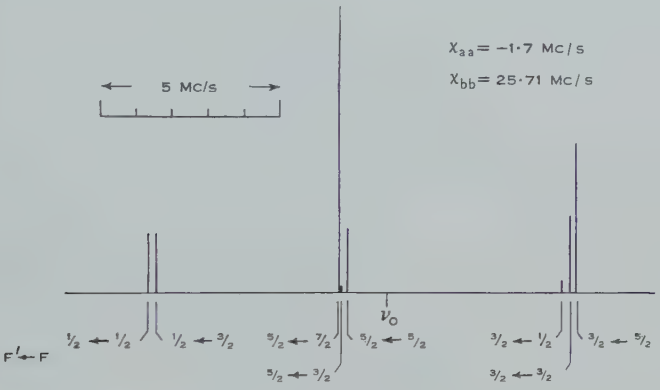

Fig. 1.—$^{33}SO_2$ $1_{11} \leftarrow 2_{02}$ hyperfine structure.

The spectrum of $^{33}SO_2$ is complicated by the hyperfine splitting due to the quadrupole moment of the ^{33}S nucleus ($I = \frac{3}{2}$) but Bird and Townes in their analysis of the $4_{04} \leftarrow 3_{13}$ transition deduced quadrupole coupling constants $\chi_{aa} = -1 \cdot 7 \pm 0 \cdot 2$ Mc/s, $\chi_{bb} = 25 \cdot 71 \pm 0 \cdot 03$ Mc/s. Fortunately, both the centrifugal distortion and the quadrupole splittings are small and each may be considered independently as a perturbation of a rigid rotor. Using these quadrupole coupling constants the splitting of the $1_{11} \leftarrow 2_{02}$ transition has been calculated by the usual first-order formula (Bragg and Golden 1949) and is shown in Figure 1. The initial approximation to $\varkappa$ gives sufficient accuracy for estimating this splitting and $dE(\varkappa)/d\varkappa$ may be found from the analytical forms of $E(\varkappa)$. The expected transitions give rise to what is essentially a triplet having intensities in the ratio 1 : 3 : 2.

A reasonable value of 20 Mc/s per mm for the line-breadth parameter gave an estimated absorption coefficient of approximately $3 \cdot 5 \times 10^{-9}$ cm^{-1} for the strongest (central) component with natural abundance of ^{33}S. Accordingly narrow detector bandwidths with klystron frequency stabilization, and in some runs dry ice cooling of the absorption cell was necessary to provide adequate sensitivity.

The triplet structure was subsequently confirmed, with measured peaks at 11,368·002±0·015, 11,373·286±0·015, and 11,379·825±0·015 Mc/s (r.m.s. errors). After allowing for the effects of the several transitions contributing to each component of the triplet, these results were found to be in good agreement with the coupling constants of Bird and Townes (1954) together with an unsplit frequency of 11,374·581±0·015 Mc/s. Unfortunately $^{33}SO_2$ is close to the symmetric rotor limit and χ_{aa}, χ_{bb} could not both be accurately determined from this transition. However, it was possible to estimate $\chi_{bb}-0{\cdot}514\chi_{aa}=26{\cdot}64\pm0{\cdot}05$ Mc/s, which compares well with 26·58±0·1 Mc/s derived from Bird and Townes's figures.

Centrifugal distortion constants obtained from those of $^{32}SO_2$ are listed in Table 1. A set of rotational constants was then obtained which accounted for the three known transition frequencies ($1_{11}\leftarrow2_{02}$; $4_{04}\leftarrow3_{13}$; $5_{24}\leftarrow6_{15}$) including effects of centrifugal distortion as was done to obtain the constants (5) for $^{34}SO_2$. The constants are:

$$\left.\begin{aligned} a&=59{,}856{\cdot}49\ \text{Mc/s},\\ b&=10{,}318{\cdot}20\ \text{Mc/s},\\ c&=\ \ 8{,}780{\cdot}23\ \text{Mc/s},\end{aligned}\right\}\qquad\ldots\ldots\ldots\ldots\ldots\quad(7)$$

and the results are summarized in Table 3.

TABLE 3

$^{33}SO_2$ FREQUENCIES

Transition	Observed Frequency (Mc/s)	Calculated Frequency from (7) (Mc/s)	Shift Due to Distortion (Mc/s)
$1_{11}\leftarrow2_{02}$	11,374·58	11,374·59	— 2·100
$4_{04}\leftarrow3_{13}$	30,194·09*	30,194·09	— 0·432
$5_{24}\leftarrow6_{15}$	20,605·97*	20,605·96	—21·227

* Bird and Townes (1954).

V. DISCUSSION OF RESULTS

It has been shown that a good account of the $^{34}SO_2$ spectrum is possible using centrifugal distortion coefficients derived from those of $^{32}SO_2$. Pierce (1956) also has found a similar technique useful in accounting for the spectrum of $^{16}O^{18}O^{16}O$ using the force constants of $^{16}O_3$. These results suggest that the procedure may also be applied to isotopic species of other molecules, but it must be remembered that the simplicity of the interrelations both in the present work and in the work of Pierce is a consequence of the C_{2v} symmetry of the molecules.

The method has also been applied to $^{33}SO_2$ using the same quantum transitions as were initially used for estimating the rotational constants (5) of $^{34}SO_2$. Although no further transitions of $^{33}SO_2$ have been observed, a similar accuracy of prediction would be expected from the constants (7) as was obtained from the constants (**5**) for $^{34}SO_2$. However, the necessity for caution is demonstrated by the comparatively poor fit of the $1_{11} \leftarrow 2_{02}$ transition of $^{32}SO_2$ to Kivelson's (1954) original figures.

The hyperfine structure of the $1_{11} \leftarrow 2_{02}$ transition of $^{33}SO_2$ has been analysed and found to be in complete accord with the published coupling constants of Bird and Townes (1954).

VI. ACKNOWLEDGMENT

The author would like to thank Dr. D. W. Posener for useful suggestions throughout the course of this work.

VII. REFERENCES

BIRD, G. R., and TOWNES, C. H. (1954).—*Phys. Rev.* **94** : 1203.

BRAGG, J. K., and GOLDEN, S. (1949).—*Phys. Rev.* **75** : 735.

CRABLE, G. F., and SMITH, W. V. (1951).—*J. Chem. Phys.* **19** : 502.

DAILEY, B. P., GOLDEN, S., and WILSON, E. B. (1947).—*Phys. Rev.* **72** : 871.

KING, G. W., HAINER, R. M., and CROSS, P. C. (1943).—*J. Chem. Phys.* **11** : 27.

KIVELSON, D. (1954).—*J. Chem. Phys.* **22** : 904.

KIVELSON, D., and WILSON, E. B. (1953).—*J. Chem. Phys.* **21** : 1229.

NIELSEN, H. H. (1951).—*Rev. Mod. Phys.* **23** : 90.

PIERCE, L. (1956).—*J. Chem. Phys.* **24** : 139.

POSENER, D. W. (1953).—M.I.T. Research Laboratory of Electronics Tech. Rep. No. 255.

POSENER, D. W. (1956).—*J. Chem. Phys.* **24** : 546.

POSENER, D. W. (1957).—*Aust. J. Phys.* **10** : 276.

SIRVETZ, M. H. (1951).—*J. Chem. Phys.* **19** : 938.

SMITH, W. E. (1955).—*J. Opt. Soc. Amer.* **45** : 227.

WERTHEIMER, R., and CLOUARD, M. (1957).—*C.R. Acad. Sci., Paris* **245** : 1793.

THE TEMPORAL VARIATION OF THE HEIGHTS OF REFLECTION POINTS OF METEOR TRAILS

By A. A. Weiss*

[*Manuscript received December* 11, 1958]

Summary

Heights of reflection points of over 6000 sporadic meteors measured with a 27 Mc/s combined C.W.-radar equipment are analysed. There is no significant seasonal variation in either the mean height or the width of the height distribution. The mean height alone shows a diurnal variation, with maximum height near midnight. A regrouping of the data reveals a dependence of both height parameters on the zenith angle of the apex of the Earth's way, with a large scatter. The observations are compared with height distributions computed for a uniform heliocentric distribution of sporadic meteors with uniform heliocentric velocities. Observed and predicted r.m.s. deviations are in agreement. The model reproduces correctly the form of the observed dependence of mean height on the zenith angle of the apex, for zenith angles less than 100°, but the extent of the predicted variation of mean height (12–20 km, depending on the assumptions) far exceeds the observed 3 km. This discrepancy may be reduced considerably by adding to the uniform model distribution a large component of sporadic meteors moving with low speeds in direct orbits whose inclination to the plane of the ecliptic is small.

I. Introduction

Three of the factors which determine the radio-echo height distribution of sporadic meteors are the properties of the atmosphere, the mass distribution of the incident meteors, and the characteristics of the equipment. These are either well established or can be measured. As a consequence, their virtual elimination from the height problem opens the way to a discussion of the two remaining factors, namely, the apparent distribution of sporadic meteor radiants over the celestial sphere and their velocity spread. The contributions of these two astronomical quantities to the observed height distributions are interrelated through the dependence of the apparent radiant upon velocity, which is imposed by the motion of the Earth. Inability to consider them separately is not, however, confined to the height data. It is common to every approach to the problem of the sporadic meteor distribution through temporal variations in quantities measured over an extended collecting area, and applies, for instance, to the interpretation of the measured velocity distributions themselves and to meteor rates.

The present paper deals with the heights of some 6400 sporadic meteors recorded from December 1952 to February 1955. The brightnesses of these meteors at their echoing points lie between the 3rd and 6th magnitudes. Meteors belonging to all showers resolvable with the equipment have been excluded.

---

* Division of Radiophysics, C.S.I.R.O., at Department of Physics, University of Adelaide.

II. Equipment

Heights of the reflection points have been measured with the 27 Mc/s equipment described by Robertson, Liddy, and Elford (1953). This is a combined C.W.-radar equipment. The direction cosines of each reflection point are determined by using spaced aerials associated with the C.W. portion of the equipment, and a superimposed radar pulse gives the slant range. Operation is semicontinuous, records being obtained on a 24-hr basis for periods of about a month at a time.

Measurements are accurate to within about 2 per cent., but there is reason to suspect that small changes of the same order have occurred in the absolute calibration of the system after 1953.

III. Analysis of Data

Table 1 indicates the periods selected for analysis, with some properties of the height distributions for these months.

Table 1

SUMMARY OF HEIGHT DATA ANALYSED

Month		Number of Meteors	Mean Height (km)	R.M.S. Deviation (km)
1952	December ..	683	91·2	6·98
1953	March	724	91·0	6·55
	June	596	89·9	7·06
	September ..	870	91·2	6·68
1954	May	1251	89·8	7·47
	July	740	88·9	7·16
	October	760	89·7	7·12
1955	February ..	743	90·3	6·62

A first appreciation of the diurnal and seasonal variations in the heights of echoing points is obtained from a more detailed examination of the data for the first four periods. Histograms showing the distribution of heights for each month separately are drawn in Figure 1. There is no evidence here of any stratification of the atmosphere into narrow " preferred " regions of high probability of detection of meteor trails, and no such tendency was found in the data for any of the other periods. Table 2 gives mean heights and r.m.s. deviations from the means, for 6-hr periods. There is no significant seasonal variation in either parameter. The diurnal variation in the r.m.s. deviation, if real, is scarcely significant. The only definite variation is the diurnal variation in the mean height, with minimum height near midday and maximum height near midnight.

The phase of the diurnal variation found from this crude division of the data is not obviously related to any property of the apparent sporadic radiant distribution. The most convenient and useful astronomical variable for relating height to apparent radiant distribution and velocity at any time is the zenith angle of the apex of the Earth's way. The azimuths of the reflection points, which reveal a marked concentration of sporadic radiants to the apex (Weiss 1957), suggest that this is a reasonable choice.

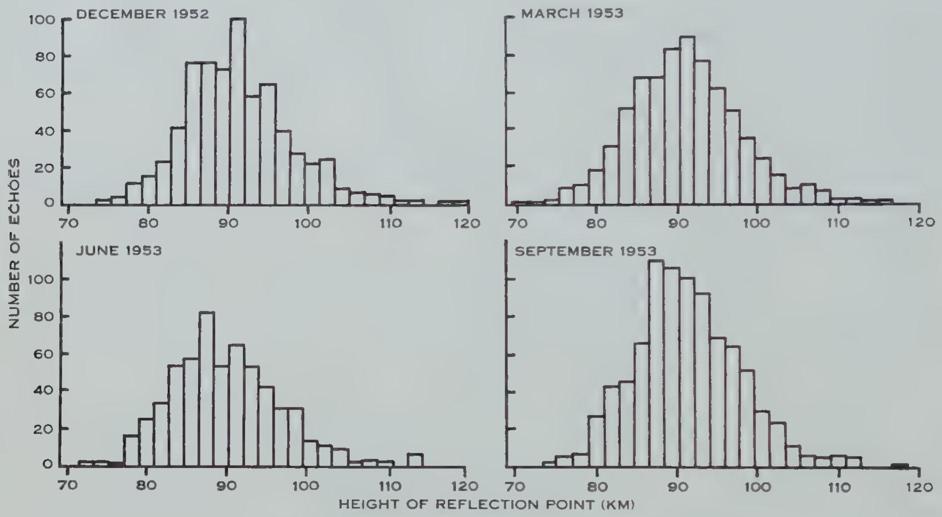

Fig. 1.—Height distributions for four observing periods.

Data for six periods have therefore been grouped by narrow (10°) intervals of the zenith angle Z of the apex. Uncorrected mean heights, and r.m.s. deviations from the means, are listed in Tables 3 and 4. Mean heights for the earlier periods differ consistently from those for the later periods, by up to 3 km. On the assumption that these differences are caused by calibration errors, the mean heights for all six periods have been reduced to a common basis by adjustment

Table 2

MEANS AND R.M.S. DEVIATIONS FOR 6-HR PERIODS

Month	Period (Local Time)			
	03–09	09–15	15–21	21–03
	(*a*) *Mean Height* (km)			
March	90·6	90·2	89·2	93·6
June	91·0	86·5	90·8	91·3
September	91·7	89·0	90·1	93·3
December	91·9	90·1	89·1	92·8
	(*b*) *R.M.S. Deviation* (km)			
March	6·8	6·7	6·2	7·3
June	7·9	5·5	6·4	6·8
September	6·9	6·5	5·3	6·7
December	6·6	5·8	6·7	7·6

TABLE 3

MEAN HEIGHTS (KM) AT 10° INTERVALS OF ZENITH ANGLE OF APEX

Zenith Angle of Apex (degrees)	Month					
	February 1955	March 1953	May 1954	July 1954	September 1953	October 1954
15		90·6				
25	89·3	90·1	89·2			
35	89·2	93·3	92·7			
45	90·6	91·4	90·2	89·2		
55	91·9	92·7	91·2	89·5		
65	90·6	91·6	89·0	90·1	92·1	90·2
75	91·6	92·9	88·9	89·4	93·0	90·2
85	89·2	92·8	90·2	87·4	92·7	91·3
95	89·5	92·3	88·1	89·1	90·1	89·1
105	89·5	92·1	88·8	87·9	90·6	89·1
115	89·9	89·6	89·3	87·9	91·1	90·1
125	92·8		90·5	89·6	91·1	88·4
135				87·4	93·9	89·6
145				89·8	90·2	88·7
155				88·4	90·8	86·1
165					90·5	89·6

TABLE 4

R.M.S. DEVIATIONS (KM) AT 10° INTERVALS OF ZENITH ANGLE OF APEX

Zenith Angle of Apex (degrees)	February 1955	March 1953	May 1954	July 1954	September 1953	October 1954
15		5·9				
25	6·5	7·1	6·9			
35	6·3	8·0	8·3			
45	6·7	6·8	8·5	6·6		
55	6·4	6·1	7·8	6·2		
65	6·2	6·8	7·7	9·1	6·6	7·2
75	7·2	5·5	7·9	6·9	8·3	8·3
85	6·7	7·9	8·4	7·3	7·9	7·4
95	8·0	6·8	6·4	8·2	5·7	6·2
105	6·8	7·8	7·7	7·6	6·1	8·1
115	6·9	6·3	7·0	5·5	6·1	7·7
125	6·3		6·9	7·1	6·5	7·1
135				6·8	6·9	6·7
145				8·4	5·5	5·8
155				6·3	5·1	6·6
165					5·3	6·4

for best fit over the interval of zenith angle 60–120°, where they all overlap. This correction does not affect the r.m.s. deviations.

Average mean heights $\bar{h}(Z)$, and average r.m.s. deviations $\delta h(Z)$, are plotted in Figure 2. There is a significant dependence of $\bar{h}$ on Z for $Z<100°$, i.e. only whilst the apex is close to or above the horizon. The width of the height distribution shows the reverse behaviour : δh is almost independent of Z whilst the apex lies above the horizon (there is perhaps a tendency for δh to decrease as Z becomes small) but decreases as the apex recedes towards the nadir. The plots of Figure 2 are obviously consistent with the failure to detect a seasonal variation, already noted.

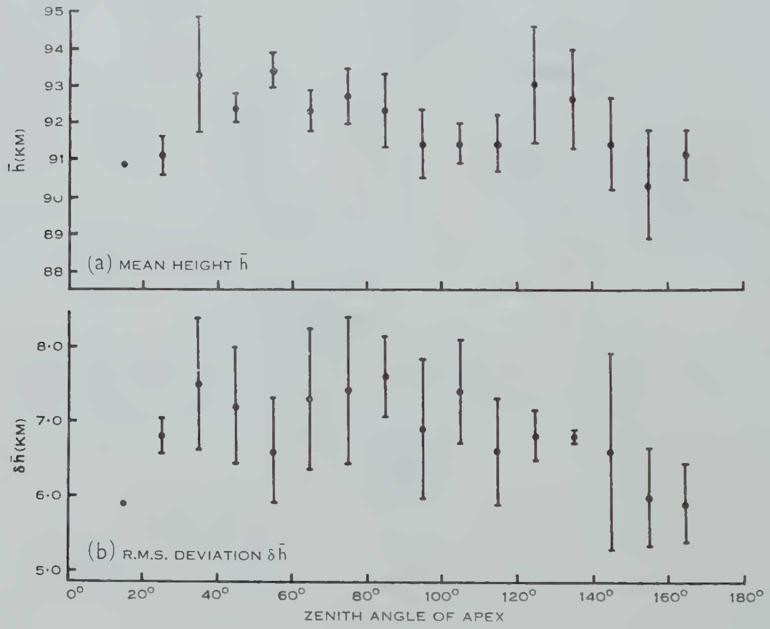

Fig. 2.—Mean heights and r.m.s. deviations from the means for the six periods summarized in Tables 3 and 4. Dots are values averaged over all periods ; barred lines show the r.m.s. deviations of the average values.

One noteworthy feature of the data summarized in Figure 2 and Tables 3 and 4 is their large scatter. It is perhaps not unexpected that for a given zenith angle of the apex considerable fluctuation should be encountered when data for periods widely separated in time are brought together in this way. This is especially so since a non-uniform apparent radiant distribution cannot be represented satisfactorily by only one independent variable. The phase of the diurnal variation for the 1953 data also raises the possibility of a small variation in local time, unrelated to the apex of the Earth's way. What is more surprising are the irregular and large differences between the mean heights and also the r.m.s. deviations, for successive narrow intervals of zenith angle for the same run. Each individual entry in Tables 3 and 4 is based on at least 40 echoes and usually considerably more. This leaves us with little alternative but to ascribe the scatter to short-lived irregular changes in the mass, radiant distribution, and velocity of the incident meteors.

The overall height distribution for the six periods of Table 3 appears in Figure 3, where it is compared with the heights of 367 sporadic meteors detected at Jodrell Bank, as tabulated by Evans (1954). The ranges of heights detected by the two equipments are similar, but the mean heights differ by about 4 km. This is probably connected with the different areas of the sky sampled by the two equipments. The resulting difference in the average radiant zenith angle will act in the correct sense to depress the Adelaide mean height. Another, but more unlikely, possibility is a larger deficiency of high reflection points at Adelaide, occasioned by failure to record or to measure echoes whose duration is limited by rapid diffusion of the trail after formation.

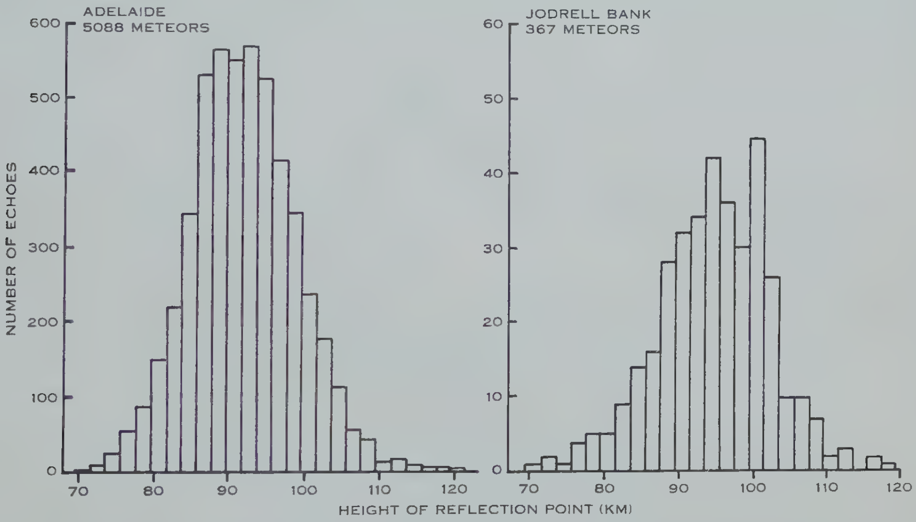

Fig. 3.—Total height distributions observed at Adelaide (six periods of Tables 3 and 4) and at Jodrell Bank (January-July 1952).

Mean hourly echo rates are plotted in Figure 4. Rates for September 1953 and October 1954 exhibit very similar behaviour, and data for these two months have been combined. The same applies to March 1953 and February 1955. In deriving these mean rates no attempt has been made to correct for short losses of operating time or interference to records. The close correspondence between the behaviour of the hourly rates for adjacent months in different years indicates that these omissions are not serious.

IV. Model Height Distributions

In an endeavour to account for the observational data, height distributions corresponding to some assumed distributions of sporadic meteor radiants and velocities have been determined. As the work proceeded it became evident that the experimental results could not be reproduced by any of the usual models, which are greatly oversimplified. The best representation has been obtained with a uniform heliocentric distribution of meteors moving with identical heliocentric velocities. These are the models U (Weiss 1957), which are not inconsistent with the total rate of all meteors detected by the equipment (not merely those whose heights are measured), and which are suggested by the azimuth data.

The sporadic radiant distribution may be regarded as built up from a large number of small radiant areas distributed over the whole of the celestial sphere. The first step in determining the theoretical height distribution is therefore to evaluate the relative sensitivity of the equipment as a function of the zenith angle χ of the radiant. This function has already been determined (Weiss 1957, Fig. 8 (*a*); only the major lobe is retained) but requires minor modification to take account of selection of echoes for height measurement, particularly of selection against radiants near the horizon which arises in an almost complete lack of measurable echoes near the zenith. The height distribution is not sensitive to small changes in the aerial polar diagram, and a quantitative estimate of the effects of echo selection on the response of the equipment is difficult. For these reasons correction of the theoretical response function of the equipment has not been attempted.

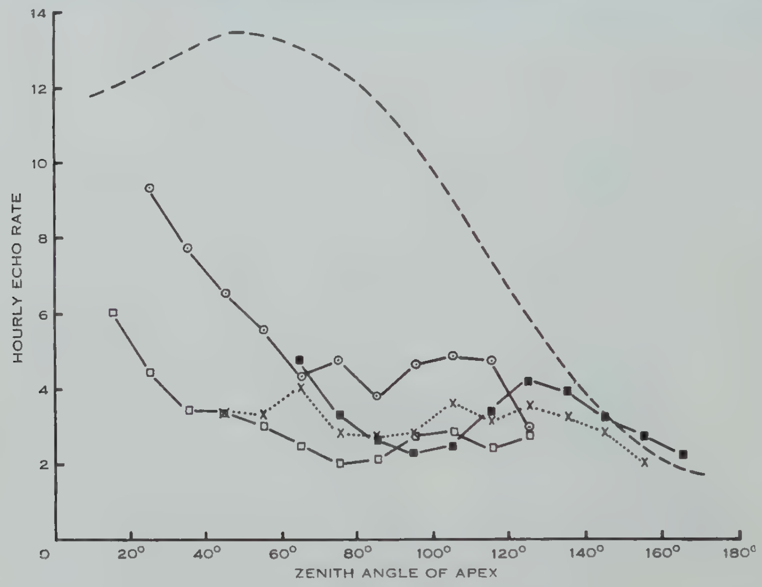

Fig. 4.—Observed and predicted echo rates. Observed rates: □———□ February-March; ⊙———⊙ May; ×······× July; ■———■ September-October. Rates predicted for model U_{42} (arbitrary scale) — — — — —.

In any model for which the heliocentric velocity of meteors is uniform, the geocentric velocity is a unique function of the apparent elongation of the radiant. Hence the observed velocity distribution is completely determined by the radiant distribution and the equipment response function (McKinley 1951). Typical echo rates as a function of *apparent* elongation ε for model U_{42} (heliocentric velocity 42 km/sec) are drawn in Figure 5. These illustrate the spread in apparent elongation of the radiants contributing to the height distribution at any time, and also the negligible contribution from radiants for which $\varepsilon > 120°$. The total echo rate as a function of Z is shown in Figure 4.

A relation between velocity and height is now all that is required to convert these echo rates into height distributions. Here the theory of the radio-echo height distribution in an isothermal atmosphere (Kaiser 1954) is applicable. The mean height of a homogeneous velocity group of meteors with a well-defined radiant is close to the characteristic height

$$x_c = \text{constant} + H \ln [\alpha_m{}^{-\frac{1}{3}} \cos^{-\frac{2}{3}} \chi \, v^2 \beta^{\frac{1}{3}}],$$

where H is the atmospheric scale height, v the meteor velocity, and α_m the minimum detectable line density at height x_c in the direction of maximum aerial gain in the echo plane. The new height variable x has been introduced to distinguish theory from observation. β, the probability that an evaporated meteor atom will produce a free electron, may be a function of velocity. The mean height x_m differs from the characteristic height by a small quantity, which depends on but is insensitive to the aerial polar diagram and the height, and it is sufficient to put $x_m = x_c + \text{constant}$. Since there is only a narrow spread in the elevation of echoing points (Weiss 1957), $\alpha_m{}^{-\frac{1}{3}}$ is substantially constant; the factor $\ln \cos^{-\frac{2}{3}} \chi$ also does not vary strongly except for radiants very close to the horizon, which are detected infrequently because of low maximum line density in the corresponding trails. Omitting these factors, the mean height $x_m(\varepsilon)$ becomes a function of apparent elongation only.

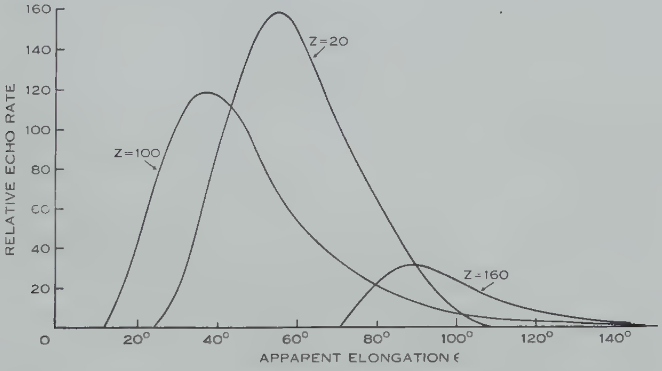

Fig. 5.—Relative echo rate as a function of apparent elongation of radiants from the apex of the Earth's way, for three values of Z=zenith angle of apex. Model U_{42}.

The form of the ionizing probability function β is not well established. Two forms, $\beta = \text{constant}$ and $\beta \propto v^3$ respectively, have been used in the numerical computations. Simultaneous velocity-height measurements by Evans (1954, 1955) suggest that β is insensitive to velocity, but there is other evidence in favour of a strong velocity dependence, in which case $\beta \propto v^3$ is more appropriate. Figure 6 shows the relation between x_m and ε for these two forms for β, with

$H=7$ km. The absolute values are arbitrary. Heights of beginning and end of trails of 480 sporadic meteors observed visually (Porter 1944) and analysed by elongation groups, also appear in this diagram.

The distribution of the mean heights for all elementary sporadic radiant areas accessible to the equipment at a given time (given Z) is found by combining the appropriate echo rate-ε relation (Fig. 5) with the x_m-ε relation (Fig. 6). Incorporation of the spread in heights associated with each elementary area finally leads to the complete height distribution, which is directly comparable with the distribution observed at the appropriate time. This additional spread is due to the spread in mass of the incident meteors and to the fact that a given trail may be detected at any point on its length, subject only to the limitations set by electron line density and specular reflection. It is approximately Gaussian in form (Kaiser 1954). Hence

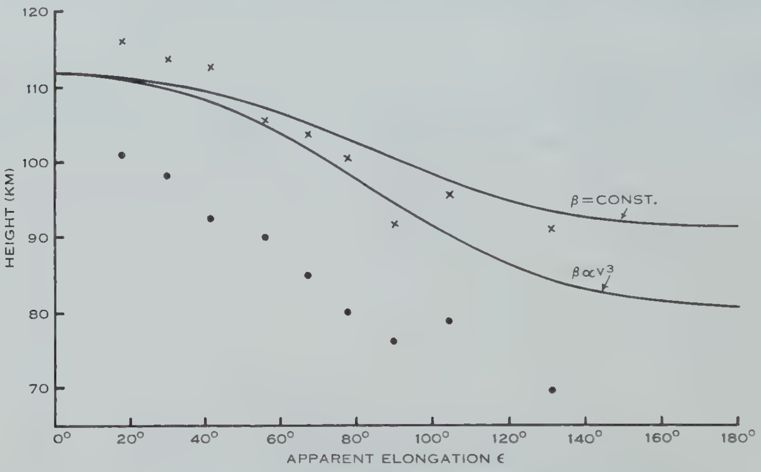

Fig. 6.—Mean height as a function of apparent elongation of radiant, model U_{42}. The position of the theoretical curves is arbitrary. β=ionizing probability of an evaporated meteor atom. Heights of visual trails (after Porter) : × beginning ; ● end.

$$\bar{x} \sim \bar{x}_m,$$
$$(\delta x)^2 \sim (\delta x_m)^2 + (\delta x_s)^2,$$

where $\bar{x}$, δx are respectively the mean and r.m.s. deviation from the mean of the complete theoretical height distribution, and δx_s is the r.m.s. deviation of heights for an elementary radiant area.

$\bar{x}$, δx_m, and δx for the model U_{42} are illustrated in Figure 7, in units of scale height. A uniform model with heliocentric velocity less than 42 km/sec will give substantially similar results, as the total geocentric velocity spread is insensitive to heliocentric velocity. The decrease of mean height $\bar{x}$ as Z decreases below 70° is caused by the movement of the region near the apex upwards away from the zenith angle (70°) of maximum equipment response, and eventually altogether outside the collecting area of the equipment. This behaviour will be typical of any equipment whose collecting area does not extend to the zenith.

The variation of δx_m with Z is a reflection of the orientation of the loci of constant apparent elongation relative to the loci of constant equipment response. According to Kaiser, $\delta x_s \sim 1$ scale height for the mass distribution appropriate to sporadic meteors. The resulting δx is shown in Figure 7. For heliocentric velocities lower than 42 km/sec, the range of δx will be slightly smaller. The width of the height distribution found in this way is always a minimum value, by virtue of the neglect of the factors α_m and χ in the derivation of the x_m.

A concentration of sporadic radiants to the plane of the ecliptic (model E of Weiss 1957), in combination with the x_m-ε relation of Figure 6, gives a mean height $\bar{x}$ which covers much the same range of heights as model U_{42}, but the r.m.s. deviation δx varies much more widely. Because of the greater population of apparent radiants near the antapex, δx is almost twice as large when the apex is near the horizon as it is when the apex is in either of its two extreme positions.

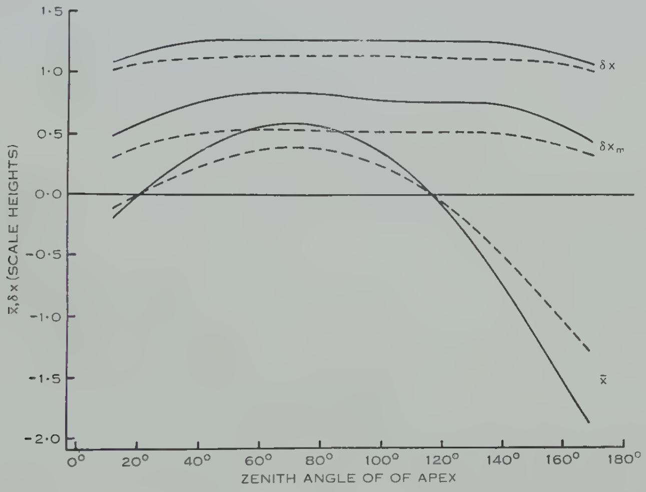

Fig. 7.—Mean height $\bar{x}$ and r.m.s. deviations δx_m, δx for model U_{42}. Position of $\bar{x}$ curves is arbitrary. ——— $\beta \propto v^3$; - - - - β=constant.

V. Interpretation of the Observations

Model U_{42} reproduces correctly the form of the dependence of mean height $\bar{h}$ on the zenith angle of the apex, for zenith angles less than 100°. In particular, it predicts the observed decrease in mean height at small zenith angles. The predicted height variation, however, far exceeds that observed and cannot be reconciled with it by any reasonable choice for the ionizing probability function β, or for the atmospheric scale height H. The small change observed in the r.m.s. deviation δh is also a feature of the model U_{42}; the observed values of this parameter, although a little low, do not lie outside the limits set by the uncertainties in β and in H. Observed and expected echo rates (Fig. 4) are quite incompatible.

It is well known that a uniform heliocentric distribution is far from representing the true distribution of sporadic meteors. The orbits of brighter meteors show a preference for the plane of the ecliptic, with a preponderance of direct orbits (e.g. Hawkins and Prentice 1957). The discrepancy between observed and predicted rates may be eliminated easily by postulating a greater concentration of apparent radiants to the antapex, which is what the facts demand ; but this solution only enhances the failure of the models in other directions. The excessive range of mean height is not reduced and the r.m.s. deviation becomes very large. This is true whether or not the additional radiants lie in the plane of the ecliptic. Evidently a further modification is required.

The pronounced helion and anthelion concentrations of sporadic radiants (Weiss 1957) in fact require that the meteors moving in direct orbits of low inclination have velocities not much in excess of the Earth's. These meteors have low geocentric velocities, and as they are non-uniformly distributed the x_m-ε relation drawn in Figure 6 will not apply to them. The incorporation of such a component into the model distributions already considered will exert a moderating influence on the variation of the mean height with zenith angle of the apex. However, a second (unpublished) survey of meteor activity at Adelaide in 1957–1958, using narrow-beam equipment, raises serious doubts as to whether the helion-anthelion component of meteors is sufficiently strong to reduce the variation of the mean height to the extent observed. It should also be pointed out that the visual observations summarized in Figure 6, although lacking in precision, are scarcely compatible with this hypothesis and that published distributions of velocities (McKinley 1951 ; Evans 1954) are not dominated by a large component of slow meteors.

The large number of variables involved and the necessity for considering the interaction between the meteor particle and the atmosphere make the prediction of temporal variations in the radio height distribution a problem of considerable complexity. It should, however, be profitable to re-examine the problem when firm data on the distribution of radiants, and more particularly of velocities, become available.

VI. Acknowledgments

This work forms part of the meteor research programme of the University of Adelaide, under the general direction of Professor L. G. H. Huxley. The project is financed jointly by the University of Adelaide, the Division of Radiophysics, C.S.I.R.O., and the Radio Research Board. The author is indebted to the many persons who have contributed to the operation of the equipment and to the tedious tasks of film reading and computation of heights.

VII. References

Evans, S. (1954).—*Mon. Not. R. Astr. Soc.* **114** : 63.

Evans, S. (1955).—" Meteors." (Ed. T. R. Kaiser.) p. 86. (Pergamon Press : London.)

Hawkins, G. S., and Prentice, J. P. M. (1957).—*Astr. J.* **62** : 234.

Kaiser, T. R. (1954).—*Mon. Not. R. Astr. Soc.* **114** : 39.

McKinley, D. W. R. (1951).—*Astrophys. J.* **113** : 225.

Porter, J. G. (1944).—*Mon. Not. R. Astr. Soc.* **104** : 257.

Robertson, D. S., Liddy, D. T., and Elford, W. G. (1953).—*J. Atmos. Terr. Phys.* **4** : 255.

Weiss, A. A. (1957).—*Aust. J. Phys.* **10** : 77.

NEUTRAL HYDROGEN GAS IN THE TAURUS–ORION REGION OBSERVED WITH A MULTICHANNEL 21 CM LINE RECEIVER

By R. X. McGee* and J. D. Murray*

[*Manuscript received December* 8, 1958]

Summary

A multichannel 21 cm hydrogen line receiver has been developed which is capable of producing a complete line profile in the very short time of 2 min.

To evaluate the large-scale survey potential of the instrument, the Taurus and Orion regions of approximately 3500 square degrees have been observed with a low-resolution (2·8° between half-power points) paraboloid.

The results suggest that a single large cloud or connected association of clouds of neutral hydrogen covers most of the region surveyed.

I. Introduction

One of the main limitations in the observation of neutral hydrogen by 21 cm line receivers has been the time required to obtain a single profile ; with the typical receivers in current use it is of the order of 2 hr. This has naturally restricted observations to those parts of the sky considered most likely to be rewarding. A new variation of H-line receiver has been developed at the Radiophysics Laboratory, Sydney, in which a complete line profile is observed and recorded in a very short time, at present every 2 min. The receiver is thus particularly suitable for large-scale surveys of the sky. As a preliminary investigation we have surveyed a region, some 3500 square degrees in area, containing the Taurus and Orion complexes. The results suggest that a single large cloud or connected association of clouds of neutral hydrogen covers the greater part of the region.

II. Equipment

The frequency bandwidth accepted by this instrument is divided into 48 separately recorded channels to give a continuous coverage of about 1½ Mc/s, capable of being centred on the natural line frequency (1420·405 Mc/s) or whatever Doppler-shifted frequency is appropriate to the observed region.

The receiver is of the double-conversion superheterodyne type having 31·8 and 6·74 Mc/s as the intermediate frequencies. By switching, at 385 c/s, the receiver output is arranged to be the difference between radiation from the sky accepted at 1420 Mc/s, the " signal frequency ", and 1424 Mc/s, the " reference frequency ". This latter frequency is believed to be well outside the widest H-line profile. The output of the second I.F. amplifier is passed into 48 double-tuned filters spaced at intervals of 32 kc/s ($\equiv 6\cdot 8$ km sec^{-1}). The shape of the filter pass bands is approximately Gaussian and their half-power width is 40 kc/s. A second detector is attached to each filter. The detected outputs, containing

---

* Division of Radiophysics, C.S.I.R.O., University Grounds, Chippendale, N.S.W.

contributions from the two switched frequencies, are passed through audio amplifiers and synchronous detectors for recovery of the wanted portion—the hydrogen line radiation. At this stage the fluctuations are smoothed by the introduction of a time constant of 2 min. A telephone-type uniselector samples each of the synchronous detector outputs once every 2 min. This information is displayed on a Speedomax recorder as a 48-point profile: frequency is the abscissa; H-line aerial temperature the ordinate. No absolute calibration has been made yet and the temperature scale was determined from many comparisons with galactic plane profiles obtained by Muller and Westerhout (1957) at Leiden. The adopted scale may have a small error due to a difference in aerial beamwidths.

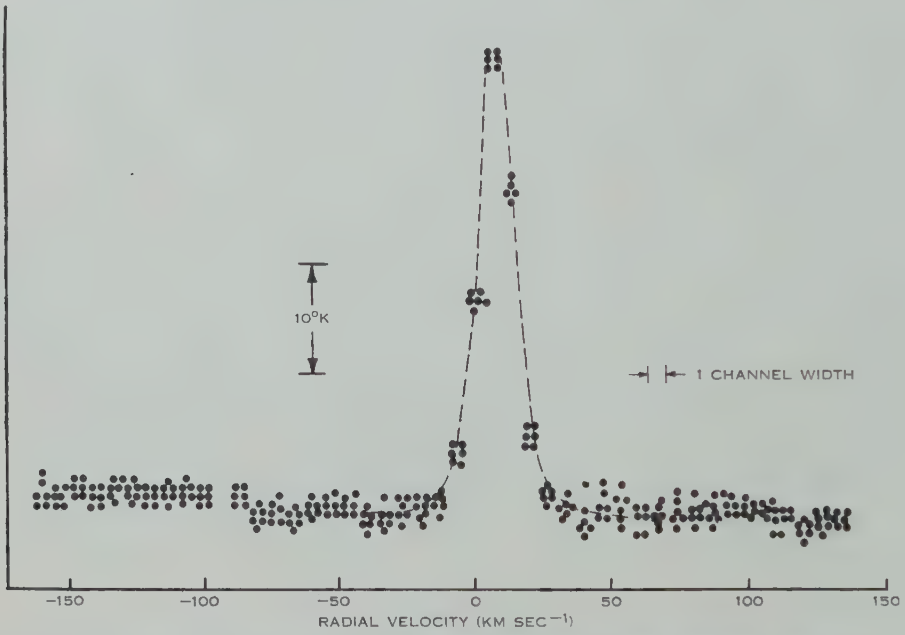

Fig. 1.—Composite H-line profile. The individual points of six successive profiles are plotted. $\delta=+14^{\circ}$, $\alpha=03^{\mathrm{h}}\ 49^{\mathrm{m}}$.

A composite profile for a mean position of $03^{\mathrm{h}}\ 49^{\mathrm{m}}$, $+14^{\circ}$ is given in Figure 1. The individual points of six successively recorded profiles from $03^{\mathrm{h}}\ 44^{\mathrm{m}}$ to $03^{\mathrm{h}}\ 54^{\mathrm{m}}$ have been plotted. The points along the base line illustrate the uncertainty caused by random noise fluctuations superimposed on a small inherent unevenness due to differences from channel to channel. However, it can be seen that a reliable zero level is easily established. The points on the profile show that the r.m.s. noise fluctuations are of the order of 1 °K.

In these initial operations the receiver is connected to a steerable parabolic aerial of beamwidth 2·8° between half-power points. Meridian transit observations are taken on fixed declinations over periods of 24 hr. This means that a low-resolution survey of the entire sky visible at latitude −34° could be made and checked in 3 months of operating time.

III. OBSERVATIONS

The original observations were made at 2° intervals in declination during the early testing period of the receiver. Most of these were repeated 3 months later and good agreement was found between both series. In some cases additional observations have been used to check the expected presence or absence of features.

Nearly all the profiles recorded in this survey were single peaked and appeared to have the same general shape and similar width (at least 3500 profiles were available for inspection). The average half-width of the profiles, calculated from a large randomly selected sample was 19 km $\sec^{-1}$ ($\equiv$90 kc/s) with standard deviation 2 km $\sec^{-1}$ ($\equiv 9 \cdot 5$ kc/s). For these reasons peak H-line aerial temperature ($T_{\mathrm{max.}}$) is regarded as a convenient indication of the areas under the profiles and hence of the amounts of hydrogen present.

In addition the combination of conditions enables a direct conversion to be made from $T_{\mathrm{max.}}$ to an approximate value of n_H, the number of hydrogen atoms in a line-of-sight column of 1 cm^2 section.

From the circumstances that 60 °K was the highest recorded aerial temperature and that no profile showed any tendency to flattening, it was inferred that the gas was optically thin at all points in these regions. Thus, the exact calculation of n_H following from Wild (1952) is obtained from the well-known relation,

$$n_H = 1 \cdot 835 \times 10^{13} \int_{-\infty}^{\infty} T(v) \mathrm{d}v,$$

where T is the H-line brightness temperature as a function of velocity. A mean profile with the above dimensions was integrated and the factor of proportionality $n_H/T_{\mathrm{max.}}$ was found to be $5 \cdot 0 \times 10^{19}$ per °K. Values of n_H calculated from $T_{\mathrm{max.}}$ and by the exact method were compared at a number of points; the mean error was ± 15 per cent. and no errors greater than ± 30 per cent. were found.

Contours of peak H-line aerial temperature ($T_{\mathrm{max.}}$), at intervals of $7 \cdot 5$ °K, are given in Figure 2. Both celestial (1958) and galactic coordinates (Ohlsson) are included. The same distribution in terms of n_H is presented in Figure 4.

To investigate the distribution of radial velocities, more than 350 uniformly distributed velocity values at the profile peaks have been worked out and corrected to the local standard of rest. The probable error involved here is ± 1 km $\sec^{-1}$. This represents approximately one velocity per aerial beamwidth over the region of interest. The velocities have been smoothed by taking means over suitable areas, generally 10° by 10°. In each area at least ten velocities were available; the maximum spread about a mean value is ± 3 km $\sec^{-1}$ in most cases. The mean velocities in km $\sec^{-1}$ are shown in large-print red numbers on about 30 adjacent areas in Figure 2.

IV. DISCUSSION

The outstanding conclusion from the observations is that most of the radiation over a great part of the survey area comes from a single large cloud or connected complex. This follows from two independent lines of evidence;

from the distribution of the quantity of hydrogen ($T_{\text{max.}}$ contours) and from the distribution of radial velocities.

Firstly, consider the $T_{\text{max.}}$ contours in Figure 2. They show a general decrease from left to right with increasing distance from the galactic plane. Superposed on this general slope are two lateral ridges: a large one in Taurus, longitude 140–160° approximately, extending in latitude from about $b=-10°$ to $b=-45°$, and a smaller one in Orion extending approximately along $l=183°$ from $b=-5°$ to $b=-35°$.

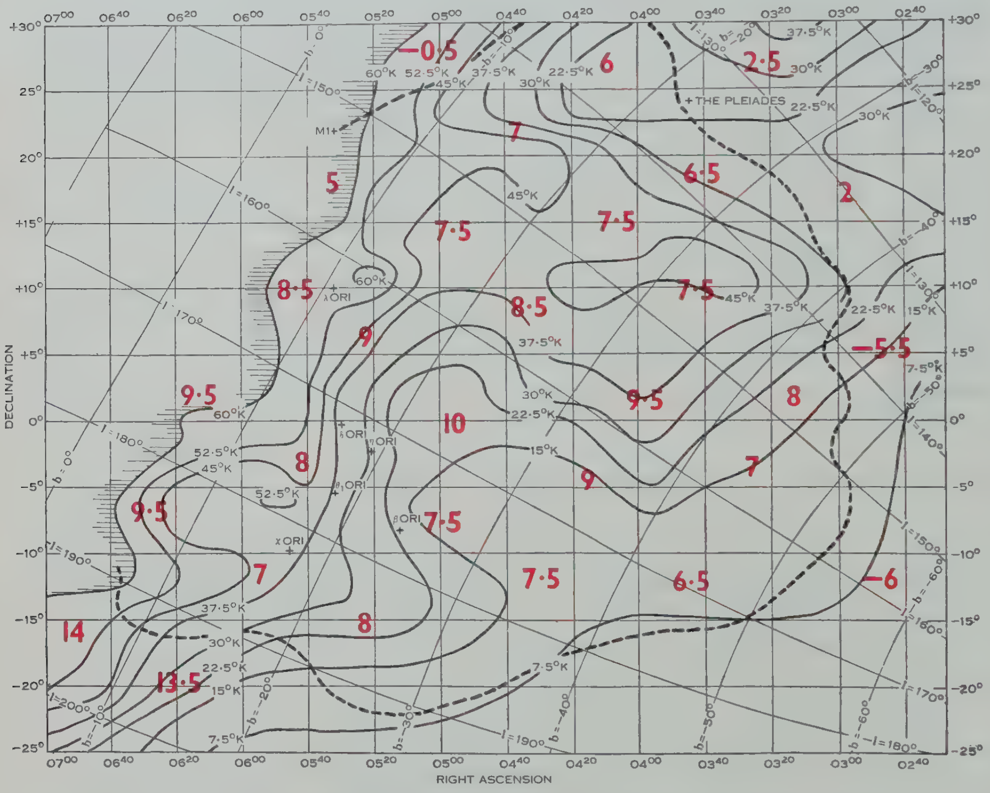

Fig. 2.—The Taurus-Orion neutral hydrogen complex. Contours at intervals of 7·5 °K represent peak H-line temperatures ($T_{\text{max.}}$). The large-print red numbers represent the mean radial velocities in km sec⁻¹ over areas usually 10° by 10°. Celestial coordinates: 1958; galactic coordinates: Ohlsson.

These large-scale features on the contour map must be due to physically associated complexes of hydrogen gas. If the radiation were due to a large number of randomly distributed small clouds the structure would be of the order of size of the aerial beamwidth: 3° instead of 20°.

Even stronger arguments follow from a consideration of velocities. It will be noticed immediately that the velocities over most of Figure 2 lie within a remarkably small range of values: in the region bounded by the dotted line, all but a few lie between $+6\cdot5$ and $+9$ km sec^{-1}, while outside this boundary the velocities change abruptly. The probable association between the two main features of the cloud is again demonstrated by the distribution of these velocities. On both ridges, extending to approximately $b=-40°$, the mean velocities are closely grouped about $7\cdot5$ km sec^{-1}. The central division occupying about 25° in b by 10° in l is one of increasing velocities up to 10 km sec^{-1}. In the outer regions of the cloud (i.e. close to the dotted line in Figure 2) the mean velocities are near $6\cdot5$ km sec^{-1} and suggest a halo of gas surrounding the double feature.

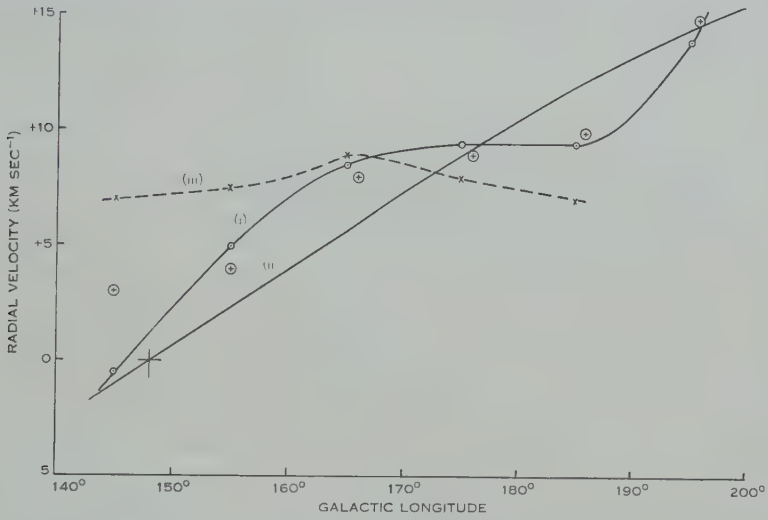

Fig. 3.—Radial velocity as a function of galactic longitude. Curve (i): the mean velocities over 10° longitude intervals between $b=-5°$ and $b=-10°$. Curve (ii): the differential galactic rotational curve through 0 at $l=148°$ and $+14$ km sec^{-1} at $l=193°$. Curve (iii): the mean velocities over 10° longitude intervals between $b=-10°$ and $b=-20°$. Points ⊕ are Leiden velocities at galactic latitude $-7\cdot5°$.

At the low galactic latitudes, the information on amount of hydrogen is cut off at the 60 °K contour. There is evidence in the recordings that parts of the cloud may extend inwards towards the galactic plane but in the vicinity of the 60 °K contour the profiles become complex, and in view of the low aerial resolution no attempt has been made to separate the relevant component.

In examining the effects of differential galactic rotation on the cloud, mean velocities taken over 10° longitude intervals between $b=-5°$ and $b=-10°$ have been plotted against galactic longitude in Figure 3. Incidentally, corresponding peak profile velocities obtained by Muller and Westerhout (1957) along $b=-7\cdot5°$ have been included and show good agreement. Figure 3 also gives the differential galactic rotational curve of best fit with values of 0 at $l=148°$ and $+14$ km sec^{-1} at $l=193°$. The mean observed velocity values $-0\cdot5$ and $+14$ km sec^{-1} may be seen from Figure 2 to represent regions outside the cloud boundary ; they are close enough to the rotational curve to indicate that they are determined almost entirely by galactic rotation. On the other hand, the low-latitude velocities inside the cloud boundary lie above the sine curve up to about the mid longitude (175°), then cross it to fall below to a maximum of approximately 3 km sec^{-1} in each case. These curves would suggest, firstly, that the two regions centred on $l=145°$, $b=-7\cdot5°$ and $l=195°$, $b=-7\cdot5°$ belong to background gas rotating as part of the general spiral structure. Its distance is estimated at 430 parsecs after extrapolation from the rotational velocities table of Kwee, Muller, and Westerhout (1954). Secondly, the recorded values of velocity within the cloud boundary could well be the result of a blend of peculiar velocities of the cloud and the velocities of background gas at the 430 parsecs distance. The amount by which the two sets of values would differ falls within a channel width (6·8 km sec^{-1}) of the receiver and the separation of such components would not be detected here.

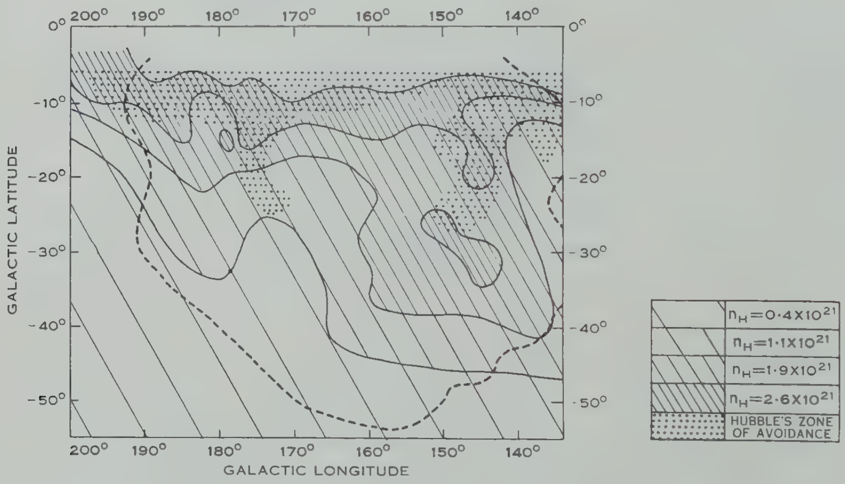
0° 200° 190° 180° 170° 160° 150° 140° 0°
-10°
-20°
-30°
-40°
-50°
200° 190° 180° 170° 160° 150° 140°
GALACTIC LONGITUDE
GALACTIC LATITUDE
$n_H=0\cdot4\times10^{21}$
$n_H=1\cdot1\times10^{21}$
$n_H=1\cdot9\times10^{21}$
$n_H=2\cdot6\times10^{21}$
HUBBLE'S ZONE OF AVOIDANCE

Fig. 4.—The distribution of neutral hydrogen in terms of n_H, the number of hydrogen atoms in a line-of-sight column of 1 cm^2 section, compared with Hubble's Zone of Avoidance in the Taurus-Orion region.

The third curve in Figure 3 in which the velocities of the adjacent regions within the cloud (centred on $b=-15°$) are plotted, illustrates that evidently very little differential galactic rotation occurs across the cloud : say, 1 km sec^{-1} at the most. Reference to Figure 2 will show that the same type of curve exists at all the higher latitudes inside the boundary.

The existence of these extensive regions where the peculiar velocities are predominant and no obvious gradient with longitude exists, would suggest that the cloud is quite close. For example, assuming that the differential galactic rotation across the cloud was 1 km sec^{-1} and that line-of-sight velocities depend on galactic rotational dynamics alone, we should place the cloud at about 20 parsecs from the Sun. The linear dimensions would then be 24 parsecs in l by 20 parsecs in b ; assuming a thickness of 25 parsecs an average density would be 23 hydrogen atoms per cm^3.

However, against these considerations is the possibility of the association of the cloud with dust complexes whose distances have long been established. Lilley (1955), using the results of a one-dimensional, 21 cm survey along $l=147°$ and $b=-15°$, has found good correlation between the optical depths of gas and dust. The degree of correspondence can be judged more readily from the two-dimensional evidence of Figure 4. The locations of the dust clouds have been indicated by reproducing Hubble's (1934) Zone of Avoidance for this part of the sky. The double-ridged feature exhibited by the n_H (or $T_{\text{max.}}$) contours coincides partially, particularly at the higher values, with the areas of dust. However, the hydrogen in each ridge covers a considerably larger area than the dust and in the Orion region the centre-line of the main ridge of hydrogen is displaced by almost 10° from the Orion flare of the Avoidance Zone.

If it now be assumed that the association of the dust clouds with the hydrogen cloud be genuine a very different estimate of dimensions and density results. Greenstein (1937) has given a distance of 145 parsecs for the absorbing clouds in Taurus and Orion. At this distance linear dimensions of 175 parsecs in l and 145 parsecs in b could be deduced and for a cloud thickness of 100 parsecs the average density would be 6 hydrogen atoms per cm^3. In making these deductions we have ignored considerations of galactic rotation effects on the cloud; the theoretical galactic rotational velocity gradient expected at 145 parsecs is 0 to $+5$ km sec^{-1}.

V. Conclusion

Our knowledge of the distribution of neutral hydrogen over the sky should include a general survey of the large-scale features as well as detailed studies of special features such as those reported by Menon (1956) and Wade (1957) in the Orion region. The results of this survey demonstrate that in the investigation of the general distribution a low-resolution aerial still has real value when coupled with a receiver capable of producing very many profiles. It would have been a long and difficult task to delineate such a large object as the Taurus-Orion cloud with the frequency-sweeping type of receivers in present use.

VI. Acknowledgments

The authors wish to acknowledge the assistance of their colleagues, Mr. C. J. Ohlston and Mr. M. W. Sinclair, whose skill and attention to detail made such a large contribution to the construction of the receiver. The authors are grateful to Mr. K. R. McAlister, who designed the aerial, and to Mr. J. P. Wild for his advice in the preparation of this paper and helpful criticisms.

VII. References

Greenstein, J. L. (1937).—*Ann. Harv. Coll. Obs.* **105**: 359–69.
Hubble, E. (1934).—*Astrophys. J.* **79**: 8–76.
Kwee, K. K., Muller, C. A., and Westerhout, G. (1954).—*Bull. Astr. Insts. Netherlds.* 458.
Lilley, A. E. (1955).—*Astrophys. J.* **121**: 559–68.
Menon, T. K. (1956).—Doctoral Thesis, Harvard University.
Muller, C. A., and Westerhout, G. (1957).—*Bull. Astr. Insts. Netherlds.* 475.
Wade, C. M. (1957).—Doctoral Thesis, Harvard University.
Wild, J. P. (1952).—*Astrophys. J.* **115**: 206–21.

OCCULTATIONS OF THE CRAB NEBULA BY THE SOLAR CORONA IN JUNE 1957 AND 1958

By O. B. Slee*

[*Manuscript received January 5, 1959*]

Summary

A description is given of some observations of the occultations of the Crab nebula by the solar corona in June 1957 and 1958, obtained with pencil-beam, fan-beam, and interferometer-type instruments. It is shown that the distribution of 85·5 Mc/s radiation on days when the angular separation is less than 10 solar radii is not consistent with a symmetrical scattering process. Better agreement is obtained by postulating the existence of scattering and regular refraction of comparable magnitude. Certain unexplained features of the pencil-beam distributions indicate that large-scale electron irregularities may be important in the scattering and refraction process. Additional evidence is presented for very short-term changes in the transmission properties of the corona.

I. Introduction

Since Machin and Smith (1951) and Vitkevitch (1951) suggested that the observation of discrete radio sources through the solar corona could provide hitherto unavailable information on the distribution of electron density in the solar atmosphere, a number of investigations have been made by English, Russian, French, and Australian observers. In June 1952, Machin and Smith (1952) used interferometers on wavelengths of 3·7 and 7·9 m to observe the Crab nebula (I.A.U. No. 05N2A) whose angular separation from the Sun at the time was between 5 and 20 solar radii. They found significant reductions in the amplitudes of the interference patterns over this range of angular separations, a result which could only be explained by postulating the existence of a large number of electron irregularities high in the corona ; these were regarded as an assembly of randomly distributed scattering centres, which, by scattering the incident radiation from the radio source, effectively increased its angular size and reduced the visibility of the interference fringes.

The observations were repeated on a more extensive scale in June 1953 by Hewish (1955), who confirmed the earlier work and showed that his observations were consistent with multiple scattering from electron density irregularities of rather large linear dimensions. The width of the scattered cone of radiation was found to be about 20 min of arc on the days of least angular separation at a wavelength of 3·7 m, and appeared to increase as the square of the wavelength.

Extensive observations were also carried out by Vitkevitch (1955*a*, 1955*b*) at the occultations of June 1952, 1953, and 1954, using interferometers on wavelengths of 6 and 3·5 m. He also concluded that the large reductions he noted

---

* Division of Radiophysics, C.S.I.R.O., University Grounds, Chippendale, N.S.W.

in the amplitudes of the interference patterns were due to a scattering mechanism, the angle of scattering increasing with wavelength. In addition, Vitkevitch found evidence for possible refraction effects and short-time changes in the scattering properties of the corona.

While it is theoretically possible to synthesize a source brightness distribution from records taken at a number of interferometer spacings, it is obvious that the method may be beset with uncertainties. In addition to the ever-present possibility of an unwanted solar contribution to the observed interferometer patterns, one is faced with the task of reconstructing a brightness distribution at a particular wavelength from a practically imposed limit of one or two interferometer spacings. Both the Russian and English results described above were obtained by using at most two interferometer spacings on a given wavelength. It is obvious that one or two Fourier components of the brightness distribution are not enough to reconstruct the distribution with any certainty, especially in the presence of possible asymmetry. With such observations one tends to adopt the simplest brightness distribution which will fit the restricted nature of the observations.

The first observations of a coronal occultation of the Crab nebula using a narrow-beam aerial were made by Slee (1956). Here the fan-shaped beam of the east-west arm of the 85·5 Mc/s cross-type aerial at Sydney was used. The apparent intensity of the radio source appeared to be significantly reduced on two days in June 1956 when the angular separation of the source and Sun was in the range 7–11 solar radii. These observations were explained by postulating that some of the radiation incident on the corona was being scattered to much larger angles ($\geqslant \pm 1^\circ$) than those deduced from the English and Russian interferometer observations. Hewish (1957), in describing the results of his observations at the same occultation, was unable to reconcile the fan-beam and interferometer measurements.

The purpose of the present paper is to present the results of measurements made at the occultations of the Crab nebula in June 1957 and 1958. In both years the observations were made by means of the pencil beam of the 3·5 m cross aerial, supplemented by recordings at the output of the fan beam of the east-west arm of the same aerial; in addition, during the 1957 occultation a 60λ spaced east-west interferometer was used on the same wavelength. These observations support the preliminary 1956 results to the extent that very significant modifications to the Crab nebula response patterns occurred on June 13, 14, 15, and 16 in each year. In addition, some new information regarding the distribution of the scattered radiation is presented and there is also more definite evidence for the short-term changes in the scattering properties of the corona first noted by the Russian observers.

II. The Observations

During the occultation of June 1957 recordings of the Crab nebula were obtained at the outputs of three distinct aerial systems all operating at a frequency of 85·5 Mc/s. These recordings will be called respectively fan-beam, pencil-beam, and interferometer observations. The observations in June 1958 were made with the fan and pencil beams only. Each system possessed its own advantages in rejecting interference from the Sun. It was hoped that a comparison of two or more records would result in obtaining information on the distribution of the Crab nebula emission with some certainty that solar interference had been taken into account.

Before describing the operation of the three systems, it is useful to have some information on the relative positions of the radio source and Sun on the days of least angular separation. This is given in Figure 1.

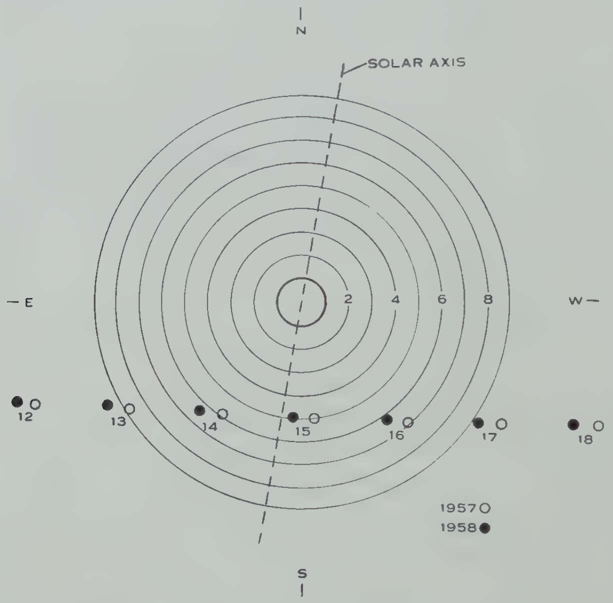

Fig. 1.—Relative positions of the Sun and the Crab nebula in the period June 12–18 in 1957 and 1958. The distance scale is marked in units of solar radii.

(a) The Fan-beam System

The east-west arm of the $85\cdot5$ Mc/s cross aerial has a beamwidth $0^\circ\cdot6$ east-west and 50° north-south to half-power points. During the observations the maximum of the beam was directed 15° north of the zenith, so that the Crab nebula was well within the fan beam for a few minutes about its transit time. The output of the array was connected to the receiver used in the Mills Cross operation, but some of the signal was withdrawn and amplified in a separate i.f. unit. After detection and D.C. amplification the signal was applied to a recording milliammeter. Because of the very narrow east-west beamwidth of this array, records of the Crab nebula could be obtained on every day of the occultation except on June 15 of each year when the Right Ascensions of the Sun and radio source were almost identical. The type of record obtained with the fan beam is illustrated in Figure 2, which shows tracings of drift patterns obtained on four days in June 1958. On June 14 and 16, the resolution of the fan beam was not good enough to see the complete response curve of the Crab nebula,

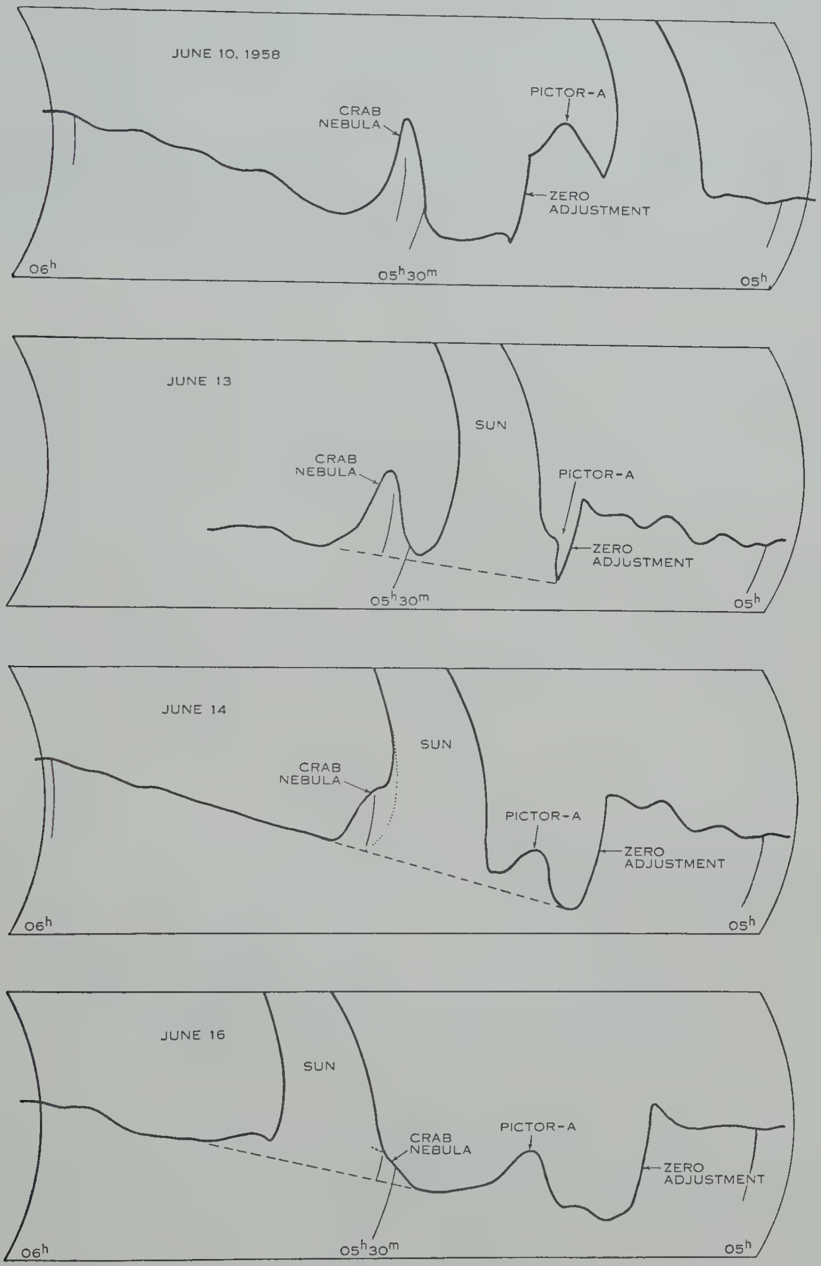

Fig. 2.—Fan-beam records taken during the occultation of June 1958. The vertical line inserted at sidereal time $05^h\ 31^m{\cdot}9$ in each record corresponds with the Right Ascension of the source.

but in these cases it was possible to trace the response at least as far as its normal transit time on the side remote from the Sun. The receiver was calibrated daily by means of a noise generator, and in addition the deflections due to less intense discrete sources served to check the overall sensitivity of the aerial and receiver.

It is obvious from Figure 2 that significant changes in the drift patterns of the Crab nebula occurred on June 13, 14, and 16; for example, on June 16 the recorder deflection at the normal transit time of the radio source, shown by the vertical line, was reduced to about 0·25 of the corresponding peak deflection on June 10. The response curves derived from this type of record will be discussed in more detail in a later section.

(*b*) *The Pencil-beam System*

The 85·5 Mc/s crossed aerial system has been described in some detail by Mills *et al.* (1958) and little further explanation is needed here. Briefly, by combining the outputs of two long aerial arrays arranged in the form of a cross, cyclically in and out of phase, it is possible to produce an effective pencil-beam type of response. The beam shape of this aerial when pointed 56° from the zenith to the declination of the Crab nebula is elliptical, being 50 min of arc east-west and 85 min of arc north-south to half-power points. With a beam of these dimensions it was realized that, on the days of closest approach of the Crab nebula to the Sun, the resolution in declination would not be adequate to reject the solar radiation completely; however, it was hoped that the recorder deflection due to the latter would be reduced to such a low level that the general east-west brightness distribution of the radio source could be deduced with some certainty.

Examples of pencil-beam records obtained during the occultation of June 1958 are shown in Figure 3. The upper record is a drift pattern obtained when the angular separation of the Sun and Crab nebula was 13 solar radii; the Crab nebula response on this record is typical of those obtained when the radio source was unaffected by the solar corona. The lower recording was taken on June 16 when the angular separation was 6·25 solar radii. Before an estimate can be made of the response pattern due to the Crab nebula from records such as this, the unwanted solar deflection must be subtracted from the observed response. A likely solar response on June 16, 1958 is shown by the broken curve in Figure 3. It can be seen that the response pattern of the radio source (obtained by subtracting one curve from the other) has been modified appreciably both in amplitude and shape. In particular, the response at the usual transit time of the source is much lower than its normal value. The means by which the solar contributions were estimated, and the resulting derived pencil-beam distributions will be discussed in the next section.

(*c*) *The Interferometer System*

During the occultation observations of June 1957, records were obtained with an east-west interferometer operating at 85·5 Mc/s, in addition to the fan- and pencil-beam records described above. The interferometer was formed by using the north-south arm of the cross in conjunction with two helical aerials, spaced 63λ from the former along a base line inclined at a slight angle to the east-west line. A schematic diagram of the interferometer system is shown in Figure 4 (*a*). The resulting interference fringes projected onto the celestial sphere are depicted by the set of sloping straight lines in Figure 4 (*b*), which also shows the paths of the Crab nebula and Sun relative to the fringe system. The already considerable north-south directivity of the array, combined with the north-south interference pattern of the two helices, resulted in a maximum response from the radio source and an effectively zero response from the Sun for about 20 min around the transit time of each source. The remainder of the equipment consisted of a conventional phase-switched receiver, phase detector, and D.C. amplifier driving a recording milliammeter.

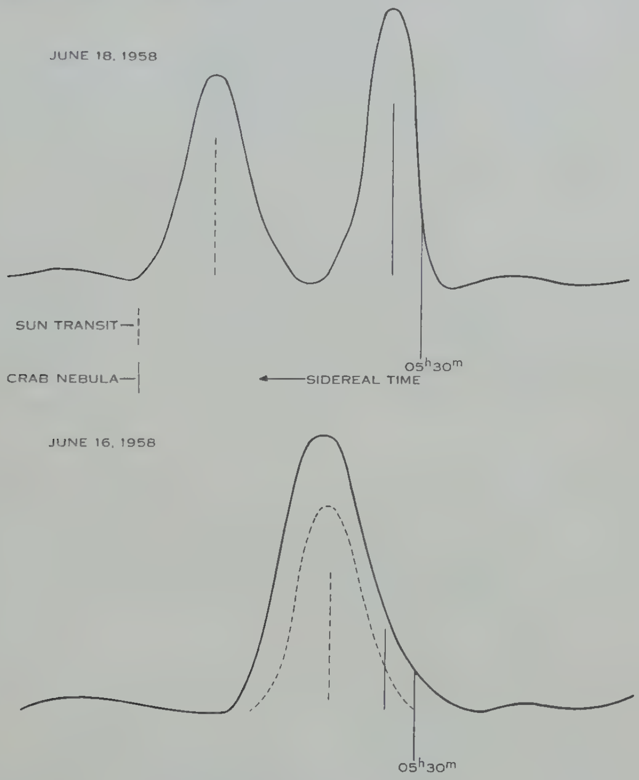

Fig. 3.—Pencil-beam recordings of the Crab nebula and the Sun for June 16 and 18, 1958. The broken line curve inserted on the record for June 16 represents the probable solar contribution to the observed response.

Some examples of the interferometer records obtained during the occultation of 1957 are given in Figure 5. The recording of July 5 is typical of the Crab nebula pattern obtained on days when the radio source was well separated from the Sun, while the other three patterns show the marked effects of the solar corona on the radiation from the Crab nebula. In interpreting the recordings shown in Figure 5, reference should be made to Figure 4 (*b*), which shows that, when the hour angles of the Sun and radio source are almost identical, a solar interference pattern will be produced on either side of the pattern due to the Crab nebula. For a time of the order of 10 min on either side of the transit time of the radio source, the steady solar radiation may be entirely neglected, and even solar bursts of the order of 1000 times the quiet level scarcely make any contribution to the observed output. The noticeable feature of the interferometer records is the great reduction in the amplitude of the interference pattern on days when the angular separation of the Crab nebula and Sun is small. An additional interesting characteristic is the sudden change in the amplitude of the Crab pattern at about $05^{\mathrm{h}}\ 36^{\mathrm{m}}$ on June 16 ; this is believed to be due to a genuine change in the transmission characteristics of the corona, since the possibility of solar interference

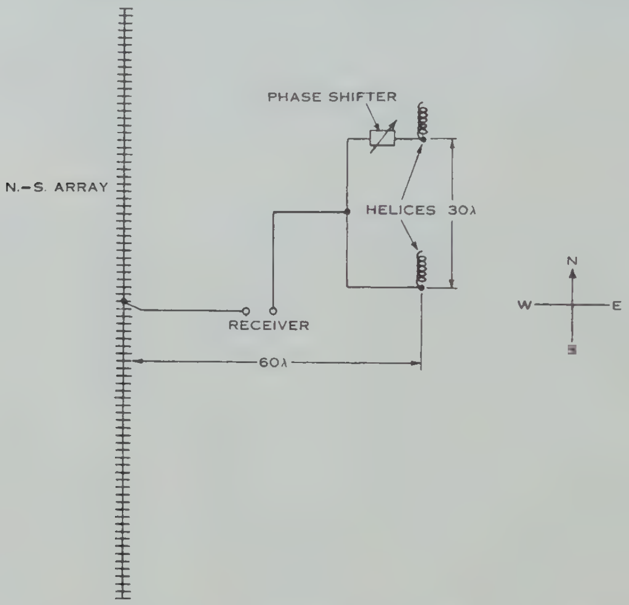

Fig. 4 (*a*).—Diagram illustrating the layout of the interferometer system used in June 1957.

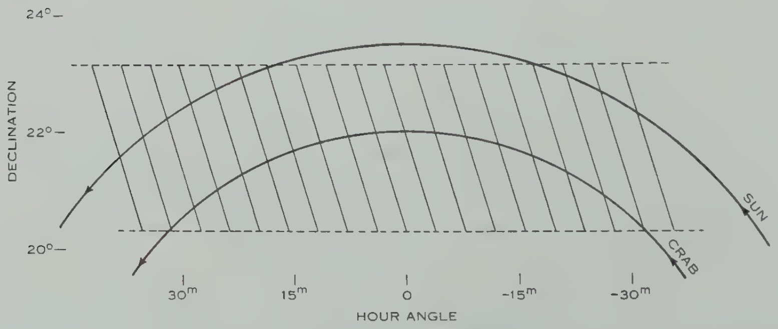

Fig. 4 (*b*).—Paths of the Sun and the Crab nebula relative to the interference fringes projected onto the celestial sphere.

at this time seems very remote. Although the intensity scale of the system was calibrated daily by means of a noise generator, it was not possible to perform an accurate calibration of the phase of the interferometer patterns ; this was mainly due to the use of a long length of coaxial cable from the receiver to the helical aerials, and it was common to find that the phase of the calibration pattern had changed by up to 30° from the beginning to the end of each day's observations, due, no doubt, to the changing ambient temperatures.

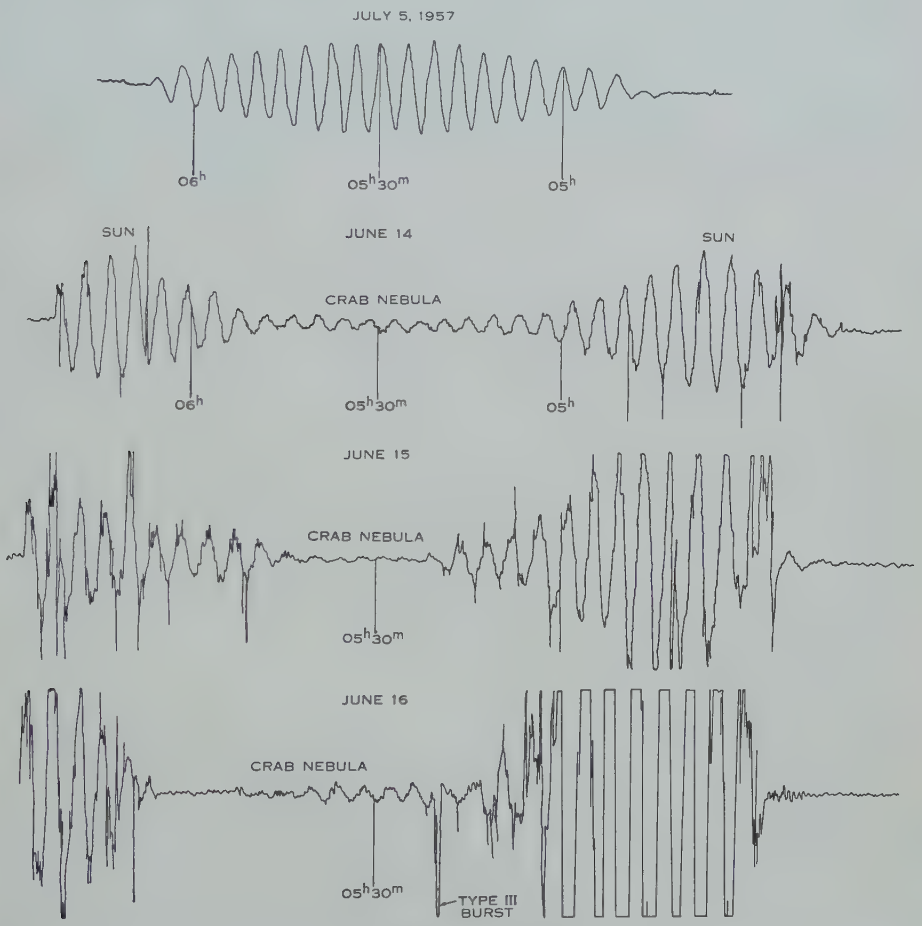

Fig. 5.—Examples of recordings obtained during the occultation of 1957 with an interferometer of east-west spacing 60λ. All times shown are sidereal.

III. Reduction of the Observations

The principal object of the analysis is to derive the main features of the east-west brightness distribution across the Crab nebula on days when the source is behind the solar corona. In this connexion the pencil-beam recordings assume the greatest importance, although the fan-beam and interferometer results can provide valuable confirmatory evidence, especially if there is doubt concerning the magnitude of the solar contribution to the former.

The information most easily obtained from the recordings is the response of the fan-beam and interferometer systems at the usual transit time of the Crab nebula. The daily observed values of this quantity for the occultations of 1957 and 1958 are plotted in Figure 6. Data for this figure are also given in Table 1. Also included in the table are the corresponding quantities from the pencil-beam recordings ; a description of their derivation will be given later in this section. All values plotted in Figure 6 and entered in Table 1 are relative to the average

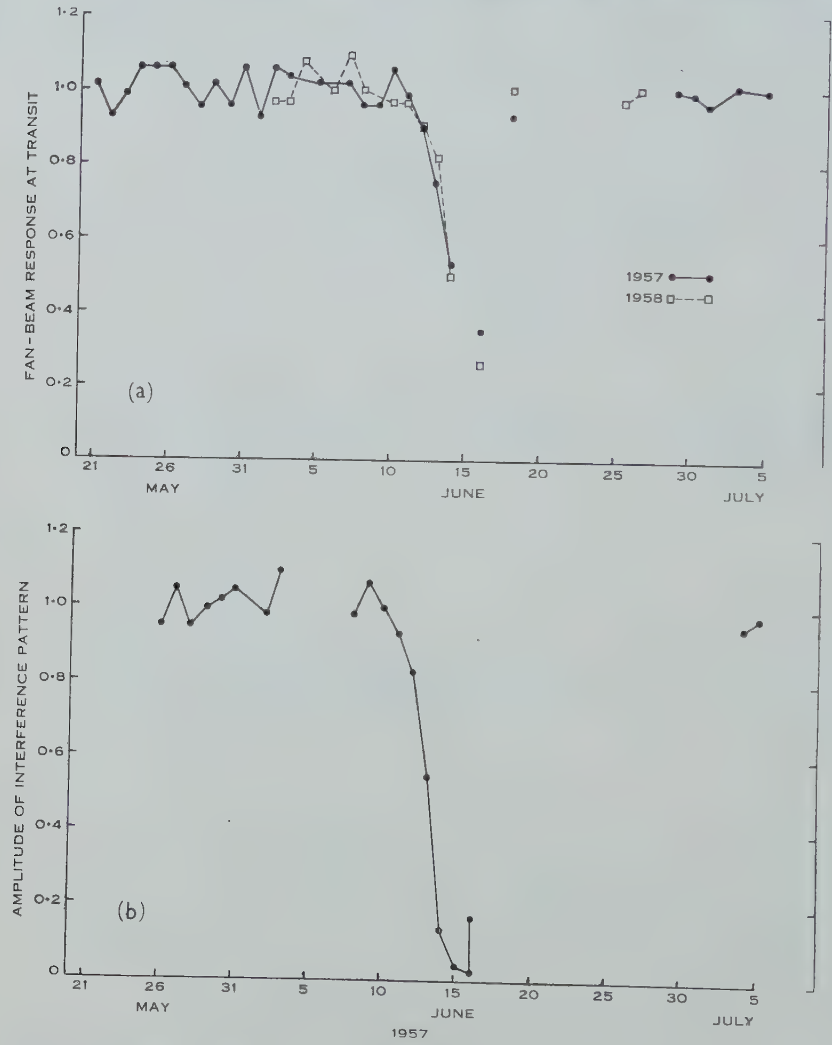

Fig. 6 (*a*).—Daily values of the fan-beam responses to the Crab nebula during June 1957 and 1958. All values are relative to the average response when the angular separation was greater than 20 solar radii.

Fig. 6 (*b*).—Amplitudes of the interferometer patterns during June 1957. Points plotted are relative to the average response when the angular separation was greater than 20 solar radii.

responses obtained when the angular separation of the Crab nebula and Sun was greater than 20 solar radii. It will be noted that no fan-beam record was obtained on June 15 of either year because the Crab nebula was lost in the much stronger solar response; in addition, recordings were not obtained on some other days because of interference or intense solar activity.

It is obvious from Figure 6 that the 3·5 m radiation from the Crab nebula was greatly modified by its passage through the solar corona between June 12 and 16 of each year, when the angular separation of the radio source and Sun was in the range 5–12 solar radii. Although the recordings obtained from both aerial systems showed pronounced effects over this period, the greatest reductions in the transit response occurred for the interferometer. This can only be interpreted as proving that the major part of the effect is not due to an absorption process in the corona. Since the interferometer is much more susceptible to changes in the east-west brightness distribution of a radio source than the fan beam, it must be concluded that the observations are consistent with a redistribution of the Crab nebula radio flux over a relatively large range of angles in the east-west direction. Such a process can occur either by scattering or refraction in the solar corona. Figure 6 and Table 1 also indicate that the effects were of similar magnitude in 1957 and 1958, and are not symmetrical about June 15, the day of closest approach.

TABLE 1

RESPONSES TO THE CRAB NEBULA AT ITS USUAL TRANSIT TIME

Date	1957			1958	
	Fan Beam	Interferometer	Pencil Beam	Fan Beam	Pencil Beam
June 10	1·06	1·00	0·98	0·97	1·04
11	0·99	0·93	1·11	0·97	1·04
12	0·90	0·83	0·82	0·90	0·98
13	0·75	0·55	0·84	0·82	0·80
14	0·53	0·14	0·79	0·50	0·80–0·86
15	—	0·05	0·43	—	0·32–0·61
16	0·35	0·17* 0·03	—	0·26	0·17–0·27
17	—	—	—	—	0·98
18	0·93	—	—	1·00	0·98

* Amplitude of interference pattern changed during observation.

Any attempt which is made to define the east-west brightness distribution across the Crab nebula on the days of closest approach to the Sun must in the main be restricted to an analysis of the fan-beam and pencil-beam recordings; it is obviously not possible to obtain an unambiguous distribution from the single 60λ Fourier component given by the interferometer record. The latter should, however, be useful in checking a likely distribution obtained, for example, from the pencil-beam response.

The drift patterns obtained with the fan beam on the interesting days of the occultations of June 1957 and 1958 are given in Figure 7. These patterns were derived from the type of recordings illustrated in Figure 2. No attempt was made to deduce the Crab nebula response while the Sun was in the fan beam, so that the patterns shown should be free of solar interference. In deciding the shape of the solar response, use was made of a supplementary low sensitivity fan-beam record. The response patterns for corresponding days in 1957 and 1958 show a pronounced similarity. It is not possible to deduce details of the Crab nebula east-west brightness distribution from the fan-beam drift patterns because only half the response pattern can be seen on the most interesting days. However, there is here ample evidence that the angular distribution of the radiation has been changed from its normal width of a few minutes of arc to values which appreciably exceed the east-west beamwidth of the array. Assuming for the present that all the radiation from the Crab nebula was being subjected to a symmetrical scattering process in the corona, the records of June 16, for example, indicate that the width of the scattered cone was some 2° to half-power points.

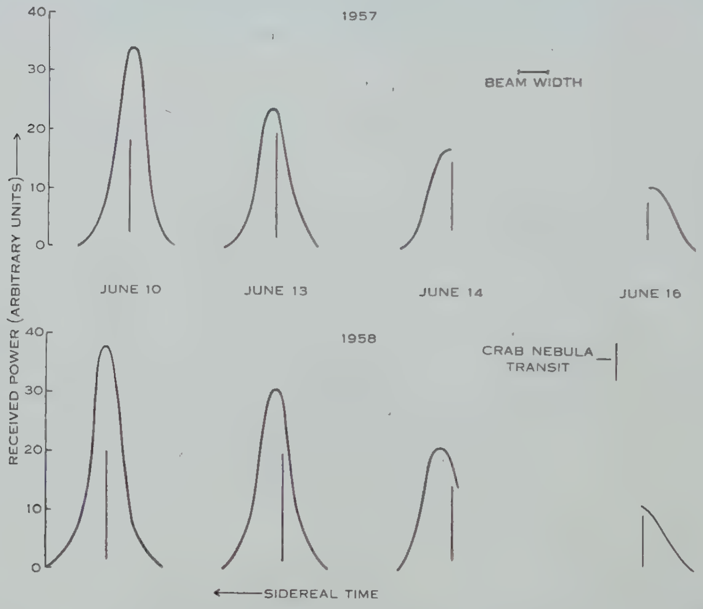

Fig. 7.—Fan-beam responses to the Crab nebula during the main phases of the occultations of 1957 and 1958.

Figure 8 shows some east-west drift patterns of the Crab nebula derived from pencil-beam recordings of the type shown in Figure 3. Before the Crab nebula response could be deduced from one of these records, it was necessary to extract an estimated solar contribution from the observed pattern. The solar deflection for any particular day was found as follows.

Pencil-beam records of the Sun were obtained as often as possible on the days preceding and following the main phase of the occultation. In addition, low sensitivity fan-beam records were taken each day. The solar responses on the two sets of records were compared, resulting in the establishment of a linear relationship between the two types of response; this relationship was subject to some random errors. On each of the three days when the Sun and Crab nebula could not be unambiguously separated by the pencil beam, the solar deflection on the low sensitivity fan-beam record was used to estimate a minimum and maximum solar pencil-beam response, corresponding to the standard deviation of the derived relationship.

The upper and lower series of curves in Figure 8 refer to observations in 1957 and 1958 respectively. An increase in solar activity prevented the taking of useful pencil-beam records after June 15, 1957, but it was found possible to obtain recordings on all the most interesting days in June 1958. The two curves outlined by the full and broken lines for each of the days, June 14, 15, and 16 correspond to the distributions obtained by subtracting the minimum and maximum solar contributions from the observed pencil-beam responses. The true distribution lies, in each case, somewhere between the two curves shown.

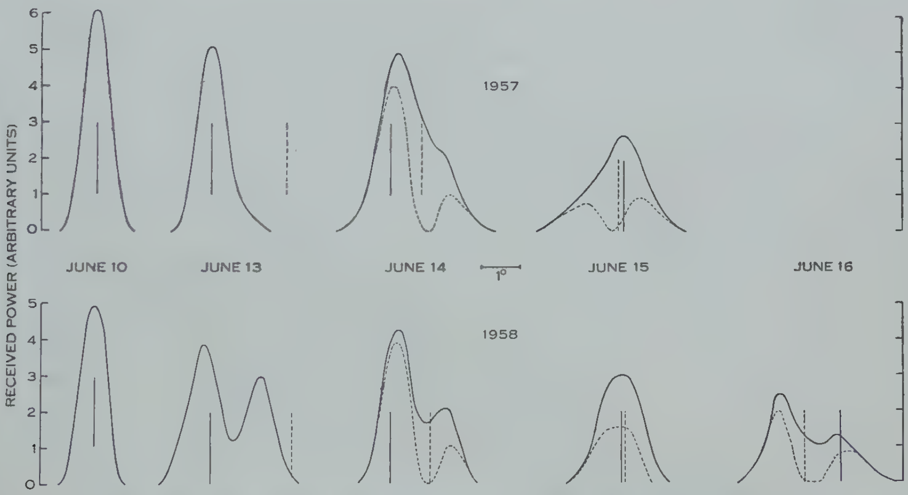

Fig. 8.—East-west pencil-beam distributions for the Crab nebula for June 1957 and 1958. The full and broken vertical lines represent the transit times of the Crab nebula and the Sun respectively. For June 14, 15, and 16 the true distribution lies somewhere between the two limiting curves shown.

On June 14 and 15, 1957, it was found possible to use the interferometer records of the same dates to ascertain which of the two curves shown in Figure 8 was nearer the true distribution. This was done by extracting the Fourier component of spatial frequency 60λ from a number of possible pencil-beam distributions obtained by allowing various solar deflections between the adopted limits. The amplitude and phase of each Fourier component was then compared with the observed interference pattern. It was found that distributions close to the shapes of the full-line curves for June 14 and 15, 1957, would give rise to the observed interference patterns; distributions similar to the broken-line curves would result in an interference pattern of far greater intensity than that recorded, and hence may be disregarded.

It is of interest to note that the integrated radio flux due to the true east-west distribution of June 14, 1957, is some 30 per cent. greater than that due to the Crab nebula when well separated from the Sun. Similarly, on June 14, 1958, although there is no means of defining the distribution as accurately as for the corresponding day in 1957, it can be said with some confidence that the integrated flux is equal to or higher than that of the unocculted source. On the other hand, for June 15 in both years and June 16, 1958, it appears that the integrated flux is less than or equal to the unocculted value. The solar contribution to the observed pencil-beam response of June 13, 1958 is negligible, and in this case it is possible to say that the integrated flux is 60 per cent. higher than the unocculted value.

In addition to the question of the total radio flux reaching the Earth, there are two other features of the pencil-beam distributions worthy of comment. Firstly, attention should be directed to the marked extensions of the curves in the direction toward the Sun on June 13, 14, and 16. In some cases there is definite evidence for a secondary peak in the distribution, especially for the records of June 13, 14, and 16, 1958 ; on these days appreciable radio flux is arriving at the receiver from points in the sky separated by as much as $1\frac{1}{2}°$ from the position of the Crab nebula in the east-west direction towards the Sun. In contrast to this behaviour, the records of June 15 of each year (the day of closest approach of the radio source to the Sun) show a much greater degree of symmetry about the position of the Crab nebula, although the response is greatly broadened and reduced in peak amplitude. The existence of the secondary maxima depends on the adopted shapes of the pencil-beam solar responses on the days concerned. All curves shown in Figure 8 were derived by assuming that the solar response curve was symmetrical about the time corresponding to the transit of the centre of the Sun's disk. An examination of the corresponding low sensitivity fan-beam records on which the peak Sun deflections exceed those of the Crab nebula by a factor of 10 supported the assumption of symmetry. Hence it was concluded that the secondary peaks were real features of the Crab nebula distributions on the days they occurred.

The second point of interest concerns the noticeable reductions in the pencil-beam responses at the normal transit time of the source indicated in Figure 8 by the continuous vertical lines. These quantities are set out in Table 1 alongside the fan-beam responses for the same days. For June 14, 15, and 16, 1958, two figures are given in the table for the pencil-beam response corresponding to the uncertainty in the solar contributions to the record. In principle it should be possible to relate the pencil-beam responses at transit with the corresponding quantities of the fan-beam records in order to deduce the size of the radio source in both east-west and north-south directions. The peak deflections of the pencil-beam records should suffer less diminution than those of the fan-beam responses because of the wider east-west beamwidth of the former aerial, provided that the size of the source in the north-south direction does not approach the north-south beamwidth of the pencil beam (85 min of arc). An inspection of Table 1 shows in fact that the pencil-beam response at transit was generally higher than that of the fan beam, with one notable exception, the record of June 16, 1958. The angular size of the Crab nebula, as deduced from these records, will be quantitatively discussed in the next section.

IV. Interpretation of Results

The east-west brightness distributions of the Crab nebula when occulted by the solar corona are obviously difficult to interpret unambiguously. In the first instance, we do not know the complete drift pattern for each day because of some uncertainty in the solar contribution to the records. In addition, granted that the distributions are correct, it is apparent that the resolving power of the aerial systems is not good enough to define with precision the relative positions of possible sources of radio energy. In attempting an interpretation of the results, the following characteristics of the records should be kept in mind: (*a*) the responses of the fan-beam and pencil-beam systems at the normal transit time of the Crab nebula are reduced; (*b*) the east-west distribution may be greatly extended in the direction toward the Sun, and in some cases a secondary peak is present; (*c*) the integrated radio flux of the Crab nebula may be greater than or less than the unocculted value. These experimental results are not consistent with the symmetrical scattering mechanism that has been proposed by the English and Russian authors to account for their interferometer observations of the Crab nebula when occulted by the corona. If scattering were the only process occurring, then the pencil-beam distributions of Figure 8 would remain symmetrical about the normal transit time of the radio source, although they would be widened and reduced in peak amplitude. As a possible alternative mechanism it is proposed to consider the effects of both coronal scattering and regular refraction on the Crab nebula radiation.

Imagine the solar corona to have a radial gradient of average electron density upon which is superposed random density variations of dimensions much greater than the operating wavelength. The average component will give rise to a regular refraction of the plane wave incident on the corona from a cosmic radio source. The irregular fluctuations in the density will cause a scattering of the same radiation. The problem of refraction in the solar corona has been given theoretical treatment by Link (1952) and Bracewell and Preston (1956). Both analyses were made on the assumption that the Sun was surrounded by a spherically symmetrical corona having a radial gradient of electron density of the form $N=a\rho^{-n}$ in which a is a constant, ρ is the distance from the solar centre, and n is a constant which may have values between 3 and 6. Recent optical determinations of the coronal electron density by Michard (1954) and Blackwell (1956) are consistent with a value of about 3 for the exponent over the range 2–10 solar radii. Calculations of the refraction using the approximate expression developed by Link shows that, at a frequency of 85·5 Mc/s, the Sun is surrounded by an occulting sphere of radius approximately 5 solar radii. A point cosmic radio source outside this sphere will be seen both by means of the direct ray, which will undergo slight refraction away from the Sun, and also by a " reflected " ray which is formed by the radiation which in traversing the corona inside the occulting sphere has been refracted through the angle between the direction of the radio source and the direction to the centre of the Sun. Hence to the observer on the Earth, an image of the source will appear within the occulting sphere. As the angular separation between the source and Sun decreases, the image will appear to approach the source until they are both located at the limb of the occulting sphere; at this point the source is occulted, the radio flux reaching the observer dropping rapidly to zero. The behaviour just described will be modified by the existence of scattering in the corona. To an observer at the Earth, scattering will increase the angular sizes of both radio source and its image. There is good reason for believing that the radiation which forms the image will be scattered through larger angles than that of the direct ray, since the former must traverse regions of higher electron density; hence it is likely that the image will appear extremely diffuse. It is believed that the absorption of the radiation forming the image will be negligible until the angular separation of the source and Sun is so great that the image falls within about 2 solar radii of the Sun's centre. Certainly absorption may be neglected when the angular separation is less than 10 solar radii.

Table 2

SCATTERING SUFFERED BY CRAB NEBULA—JUNE 1957, 1958

Date	Half-power Width of Scattered Cone (min of arc)	
	1957	1958
June 12	16	16
13	32	24
14	57	63
15	—	—
16	93	133

Some idealized calculations have been made of the refraction and scattering which may occur, based on the experimental results for June 1957 and 1958. The methods used are described in detail in Appendix I. For these calculations it was assumed that the corona exhibited spherical symmetry. It was also assumed that at any point in the corona the electron density was given by twice the value found by Michard and Blackwell, since their observations apply to sunspot minimum. The degree of scattering suffered by the direct ray was estimated from the reduction in the peak response of the fan beam at the normal transit time of the Crab nebula. The distribution of scattered radiation was taken to be Gaussian in all directions about the position of the source. The degree of scattering suffered by the radiation forming the image is not known, but a minimum value may be estimated from the fan-beam results. Values for the scattering angle to half-power points are set out in Table 2, and plotted as a function of the angular separation in Figure 9. It is apparent that the scattering angle increases rapidly when the angular separation of the Crab nebula and Sun is less than 10 solar radii, and continues the trend noted by Hewish (1958) from interferometer observations at larger angular separations during the same occultations. Some caution should, however, be used in interpreting the fan-beam reductions as being due solely to the increased size of the source; when the angular separation is small and the scattering angle very large it is likely that part of the reduction is caused by an eclipse of some of the scattered radio flux by the occulting sphere surrounding the Sun. Under these conditions, the scattering at the smallest angular separations will be over-estimated by this method, but it appears reasonable to assume that the radiation forming the image, which will lie mainly in the range 4–5 solar radii, will be scattered through angles of the order of 2–3° to half-power points.

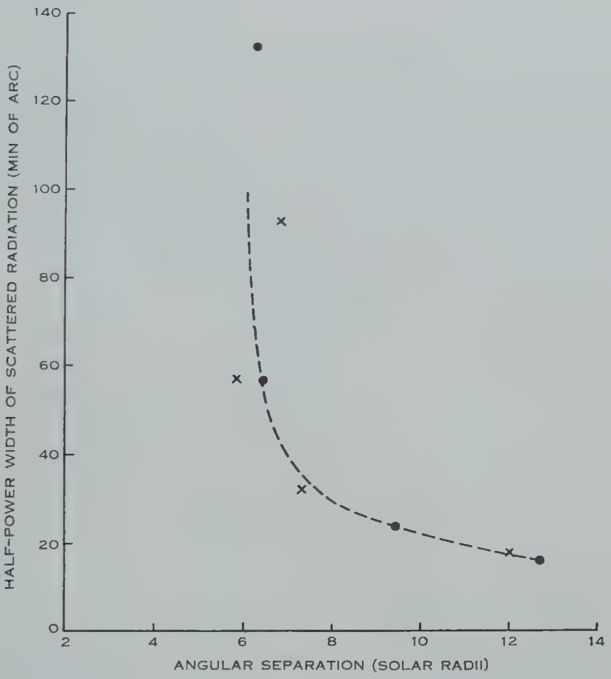

Fig. 9.—Half-power width of the scattered cone of radiation as a function of the angular separation between the Crab nebula and the Sun in June 1957, 1958. × 1957, ● 1958.

Figure 10 shows idealized sketches of the effects of scattering and refraction for June 13, 14, 15, and 16, 1958, calculated by making use of the above assumptions. The sketches for June 1957 would have a similar appearance. Since the scattering angle increases rapidly with decreasing angular distance from the Sun, the cross sections of the scattered radiation patterns will depart from the circular shapes expected at greater angular separations; part of the scattered radiation will, however, be blocked from the observer by the occulting disk on June 14, 15, and 16. The diffuse image of the Crab nebula will occupy an appreciable portion of the occulting disk, being elongated around and concentrated towards its periphery.

The model outlined above will account for some of the features of the pencil-beam distributions shown in Figure 8. For example, on June 13, the idealized distribution of Figure 10 predicts a distinct and well-resolved image of the Crab nebula separated from the radio source by about 1°·5 in the westerly direction toward the Sun; the experimental distribution of June 13, 1958 definitely agrees with the prediction but there is no clear evidence for an image on the corresponding day in 1957, although the tail of the distribution is extended somewhat in the Sun's direction. The experimental results for June 15 of both years agree qualitatively with the calculated distribution, which, it can be seen, is symmetrical about the position of the radio source and greatly broadened. On June 14 and 16, the model indicates that the distributions should be greatly extended in the direction toward and past the solar axis, the curve dropping smoothly to zero;

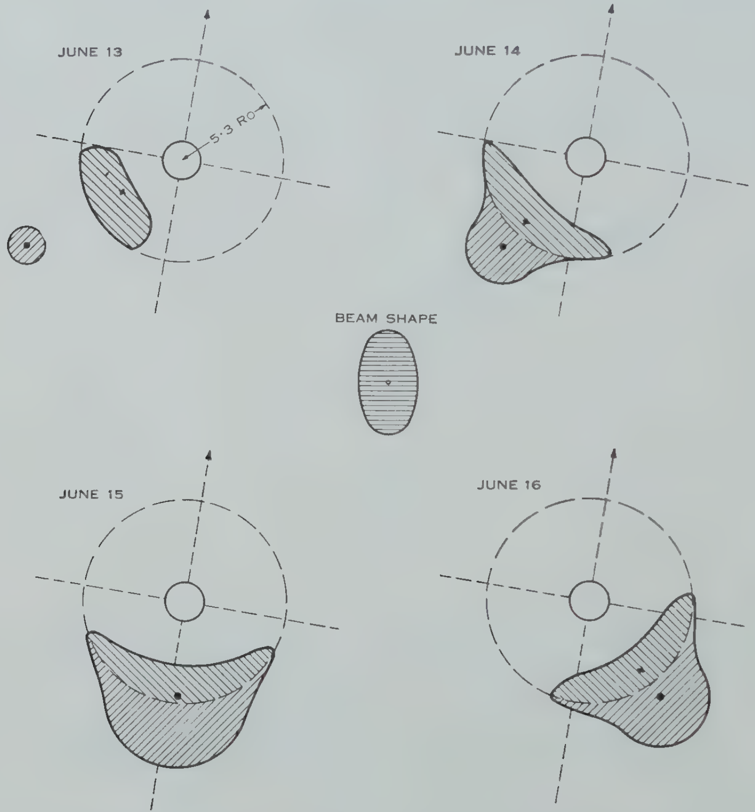

Fig. 10.—Idealized sketches showing the effects of scattering and refraction on the distribution of the Crab nebula radio flux in June 1958. The cross-hatched areas are contained within the half-power contours of the distributions. The positions of the point radio source and its image are shown by the filled-in circle and cross respectively.

the experimental curves for these days indicate that not only are the distributions extended in the predicted directions, but also show distinct secondary peaks.

It is clear that the spherical model does not adequately represent the observational results and that the distribution of Crab nebula radiation is markedly affected by refraction and scattering in large-scale coronal irregularities. The secondary peak, which represents the main departure of the observations from the simple spherical model, was recorded in both 1957 and 1958, and suggests the existence of semipermanent regions in the corona of higher than average electron density.

The question of the integrated radio flux in the presence of scattering and refraction is of interest. The existence of an image implies that the total radio flux reaching the observer can be appreciably increased. For any particular observation, this quantity will depend upon the amount of energy occulted and the distribution of scattered and refracted radio flux with respect to the aerial beam. The half-power contour of the aerial beam has been sketched in Figure 10. These diagrams show that on June 13 and 14 most of the scattered and refracted energy will be swept through the aerial beam, so that the integrated flux may be expected to be higher than normal. On June 15 and 16, however, a reasonable proportion of the radiation is either occulted or removed by the directivity of the aerial beam, so that a decrease in the integrated flux may be observed. These conclusions are supported by the measurements of integrated flux described in Section III. Evidence for large changes in integrated flux has also been obtained by other observers. Blum and Boischot (1957), while making observations of the Crab nebula during the 1957 occultation with a diffraction grating type of east-west interferometer at 169 Mc/s, found that the integrated radio flux was some 60 per cent. greater than normal on June 13, 1956; the increase was ascribed to the effects of refraction in the corona. Hewish (1958) describes observations made in 1956 with an interferometer of spacing 8λ at 38 Mc/s, and points out that, because the large fringe separation of approximately 7° probably exceeds the scattering angles likely to be produced, any reduction in the depth of modulation must be due to a decrease in the integrated radio flux reaching the observer. His results show that the amplitude of the interference pattern had fallen virtually to zero at an angular separation of about 7 solar radii. It can only be concluded that the radius of the solar occulting disk for 38 Mc/s radiation must extend to at least 7 solar radii near sunspot maximum. This is in keeping with the value of 5·3 solar radii deduced from the present pencil-beam results for 85·5 Mc/s radiation.

It is of some interest to re-examine the preliminary observations obtained by Slee (1956). As a result of the more complete observations in 1957 and 1958, it must be concluded that the reductions noted in the fan-beam responses of June 16 and 17 were wrongly interpreted. It is now apparent that the scattering experienced by the radio source is too complete to be described by a partial scattering process. Nearly all the energy is scattered from the radiation incident on the corona and redistributed in a different angular spectrum. This is in accord with the deductions of the English and Russian observers.

V. TEMPORAL CHANGES IN THE TRANSMISSION PROPERTIES OF THE CORONA

Hewish (1958) has given evidence that the scattering power of the corona increases markedly from sunspot minimum to maximum. This is especially true of the polar regions, where, during sunspot maximum, the electron density, and presumably the degree of inhomogeneity, approaches that of the equatorial regions.

There has also been some evidence for very short-term changes in the transmission properties of the corona, involving times of the order of minutes or seconds. Vitkevitch (1955*b*) describes relatively sudden disturbances to the amplitudes of interference patterns obtained during the occultations of 1953 and 1954 and attributes them to the occurrence of dynamic processes in the outer corona. Evidence for a similar effect was obtained by the author during the observations on June 16, 1957. This is evident from the interferometer record shown in Figure 5, which indicates that the amplitude of the interference pattern due to the Crab nebula was reduced to the noise level of the receiver in a time of the order of 6 min shortly after the transit time of the source. The possibility of a beat between an interference pattern due to the Sun and that of the radio source seems very unlikely, since the record shows no trace of a group of solar bursts which occurred between $05^h\ 30^m$ and $05^h\ 34^m$ sidereal time, proving that the solar contribution to the record was negligible at this time.

It is natural to interpret the observed modification to the interference pattern as a change in the transmission properties of the corona. For example, the propagation of streams of charged particles outward from an active area on the Sun's disk may progressively change either the dimensions or electron densities of the scattering irregularities. Alternatively, the ejection of a sufficiently large number of electrons into the corona may result in appreciable absorption or a marked increase in refraction of the Crab nebula radiation.

Assuming that the change in the interference pattern was due to the progressive growth of one of these effects, it is possible to obtain an approximate value for the velocity of the particles responsible. In order to account for the observed change in a time of 6 min, the disturbance would need to be propagated across a zone in the corona of about 1° angular diameter (allowing for the existing degree of scattered radiation) with a velocity of approximately 7×10^3 km/sec.

It is of some interest that an intense solar burst was recorded at $05^h\ 19^m$ sidereal time, the peak intensity of the burst being estimated at about 1000 times the quiet-Sun level. Due to the fact that the Sun had not completely passed out of the interference fringes at this time, the burst was seen on the record. Radio-spectrometer measurements of this burst (kindly supplied by Mr. J. P. Wild of this Laboratory) showed that it was of spectral type III. Assuming that a disturbance, coincident with the radio burst, was ejected into the corona in the right direction to intercept the ray paths from the Crab nebula to the Earth, it can be shown that it would need to have travelled with a velocity of about 5×10^3 km/sec in order to have been responsible for the observed effect 17 min later.

This value for the propagation velocity is consistent with the previous figure estimated from a different argument; it is, however, lower by an order of magnitude than the ejection velocities believed to be associated with type III bursts, and somewhat higher than the average velocity of particles causing terrestrial magnetic storms and aurorae. Unfortunately, the occurrence of strong, discrete solar radio bursts during occultation observations was not frequent enough to confirm their possible relationship with changes in coronal structure.

VI. CONCLUSIONS

The observations which have been described in this paper complement and in several important respects extend the results which have been obtained by the Russian and English observers over the past 7 years. They have been particularly valuable in extending the observations well into the corona at the peak of the present sunspot cycle; under these conditions the degree of scattering and occultation of radiation traversing the corona becomes so pronounced that interferometer observations, even on the closest spacings, can give little information on the distribution of the radio energy. The following is a summary of the results obtained by means of pencil-beam, fan-beam, and interferometer measurements in June 1957 and 1958.

(1) The angular distribution of the radio flux from a discrete radio source is greatly modified by its passage through the solar corona. When the angular separation between the Crab nebula and the Sun is less than 10 solar radii, the east-west distribution at 85·5 Mc/s becomes markedly asymmetrical about the position of the discrete source. It is then extended, and sometimes shows a secondary maximum, in the direction towards the Sun. The integrated radio flux on these occasions may be greater than or less than its unocculted value.

(2) The symmetrical scattering theory developed by the Russian and English workers to account for their interferometer observations is not consistent with the present results.

(3) A simple spherical coronal model, in which electron irregularities cause a scattering of up to 3° and the average electron content a regular refraction of the same order, is in better agreement with the pencil-beam observations. However, the lack of detailed agreement suggests that the effects of large semi-permanent regions of higher than average electron density may be important.

(4) There appears to be definite evidence for short-term changes in the transmission properties of the corona, possibly coupled with the ejection of disturbances from active areas on the Sun's disk.

The results of these observations demonstrate the feasibility and desirability of conducting occultation observations with fan-beam and pencil-beam type instruments. There is little doubt that, in the presence of the complex brightness distributions obtained at the smallest angular separations, the interpretation of interferometer results could be very misleading. Even during sunspot minimum there is a strong possibility that refraction effects would not be negligible. It would be of great interest to continue occultation observations by means of fan and pencil beams, if possible of higher resolution than those used here, in an attempt to obtain a detailed picture of the coronal electron density throughout the sunspot cycle.

VII. Acknowledgments

The author wishes to express his gratitude to all those who helped in various ways with the observations. In particular, great assistance was rendered by Mr. A. Watkinson in the construction of equipment and with the observations during the 1957 occultation. In addition, the author is indebted to Mr. E. R. Hill for valuable advice on some of the computational problems encountered, and to Dr. J. L. Pawsey for his continued stimulating interest throughout.

VIII. References

Blackwell, D. E. (1956).—*Mon. Not. R. Astr. Soc.* **116** : 56–68.
Blum, E. J., and Boischot, A. (1957).—*Observatory* **77** : 205–6.
Bracewell, R. N., and Preston, G. W. (1956).—*Astrophys. J.* **123** : 14–29.
Hewish, A. (1955).—*Proc. Roy. Soc.* A **228** : 238–51.
Hewish, A. (1957).—*Observatory* **77** : 151–3.
Hewish, A. (1958).—I.A.U.-U.R.S.I. Symposium on Radio Astronomy, Paris, July-Aug. 1958.
Link, F. (1952).—*Bull. Astr. Insts. Csl.* **3** : 6–12.
Machin, K. E., and Smith, F. G. (1951).—*Nature* **168** : 599–600.
Machin, K. E., and Smith, F. G. (1952).—*Nature* **170** : 319.
Michard, R. (1954).—*Ann. Astrophys.* **17** : 429–42.
Mills, B. Y., Little, A. G., Sheridan, K. V., and Slee, O. B. (1958).—*Proc. Inst. Radio Engrs., N.Y.* **46** : 67–84.
Slee, O. B. (1956).—*Observatory* **76** : 228–31.
Vitkevitch, V. V. (1951).—*C.R. Acad. Sci. U.R.S.S.* **77** : 585–8.
Vitkevitch, V. V. (1955*a*).—*Astr. J. Moscow* **32** : 150–64.
Vitkevitch, V. V. (1955*b*).—*C.R. Acad. Sci. U.R.S.S.* **101** : 429–32.

Appendix I

Refraction of Radiation from a Discrete Source in the Corona

Referring to Figure 11, (*a*) is a view in the line of sight of the observer; (*b*) is a diagram of the ray paths in a plane containing the Earth at E, the centre of the Sun at S, and the radio source. When the terrestrial observer looks towards the point A separated from the Sun by the angle θ and at position angle P, his line of sight intersects a point B on the celestial sphere which has the same position angle but is separated from the Sun by the angle φ. Obviously $\varphi=\theta+\omega$, where ω is the refraction suffered by the ray. A convenient method of finding the image, given the source position φ, consists of constructing a graph of $\theta+\omega$ as a function of θ, the values of refraction being calculated by an approximate expression due to Link (1952) or by ray tracing. Such a graph constructed for a frequency of 85·5 Mc/s and incorporating angles of refraction based on the electron density distribution described in the text is shown in Figure 12. To find the apparent positions of the source and its image, the graph is entered at the ordinate corresponding to the known source position and a horizontal line drawn to intersect the curve at points a and b. The abscissae of these points then define the image and apparent source positions respectively. The horizontal line $\varphi=\varphi_0$, which is tangent to the minimum point on the curve, corresponds to the radius of the circular zone on the celestial sphere occulted by the corona.

If the radio source is an extended object, the graph may again be used to find the apparent brightness distribution. Every value of φ over the extended source will give rise to two values of θ as before. The radial magnification of the image $d\theta/d\varphi$ will be negative and appreciably less than unity; the lateral magnification $\sin\theta/\sin\varphi$ will also be less than unity.

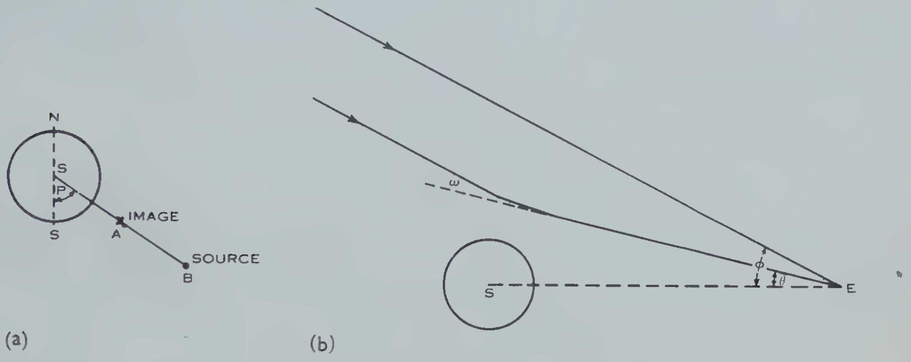

Fig. 11 (*a*).—View looking along the line of sight of the terrestrial observer towards a radio source and its image in the corona.

Fig. 11 (*b*).—View of the ray paths in the plane containing the radio source, the centre of the Sun, and the Earth.

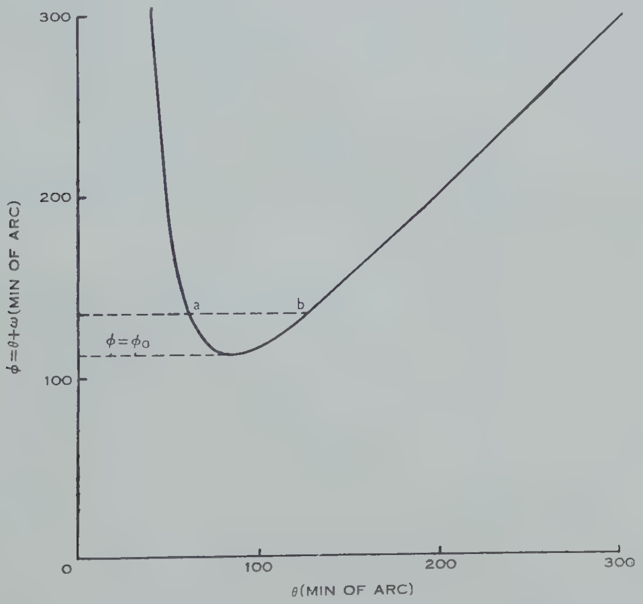

Fig. 12.—Relation between the true angular separation of the radio source and the Sun, φ, and the apparent separation θ, due to refraction in the corona.

For the case of a radio source which is both scattered and refracted in the corona, an approximate brightness distribution may be obtained provided the scattering angle is known as a function of the angular separation from the Sun.

In this case we may calculate the image brightness distribution on the assumption that it is due to an extended source of dimensions comparable with the scattering suffered by radiation traversing the inner parts of the corona. The approximate distributions of Figure 9 were derived on the assumption that the radiation forming the image had been scattered through an angle of 3° to half-power points. These diagrams are, however, highly idealized, since it is most likely that the scattering function will vary considerably over the region of the corona in which the image is formed, leading to departures from the distributions shown.

A DISCUSSION OF IONOSPHERIC DEMODULATION NEAR GYRO FREQUENCY

By G. L. Goodwin*

[*Manuscript received October* 20, 1958]

Summary

Observations made in Adelaide of the ionospheric demodulation of radio waves near gyro frequency at vertical incidence are discussed. The effect occurs in the region of about 90 km, and does not appear to decrease through dawn. An *F*-layer reflected wave is demodulated by unequal amounts during its two passages through the region. The large magnitude of the effect and its lack of dependence on modulation frequency seem to be inconsistent with the theory of wave interaction.

I. Introduction

The demodulation of radio waves was observed near gyro frequency by Cutolo (1952, 1953) and Mitra (1954), who received signals reflected from the ionosphere (probably the *E* region) at oblique incidence. Aitchison and Goodwin (1955) measured demodulation at a frequency of 1·55 Mc/s, near gyro frequency (approximately 1·60 Mc/s), by means of signals reflected at almost vertical incidence from the E_s layer and from the *F* layer, and subsequently confirmed their results by further observations. These results, which are discussed in the present communication, agree substantially with those of Cutolo and Mitra with regard to the magnitude of the observed demodulation, but cannot be explained by means of the theory of wave interaction.

II. Experimental Procedure

The experiments had already been designed to avoid possible sources of error mentioned later by Hibberd (1956).

Errors due to fading between a ground wave and waves reflected from the E_s and *F* layers were reduced to a small known amount by the following procedure: first, the ground wave was made very small by using a loop-aerial accurately adjusted during the day-time; secondly, measurements were not accepted unless the amplitude of one reflected wave was greater than three times the sum of the amplitudes of the other reflected waves and the ground wave. Comparatively few measurements (about 12 per cent. of those accepted) corresponded to an amplitude ratio greater than five. In practice, the accepted measurements represented signals for which one reflection was roughly four-fifths of the amplitude of the received signal.

It is conceivable that the modulation coefficient of the signal might possibly be reduced owing to sideband attenuation in the receiver, the effect being more pronounced at the higher modulation frequencies. In calibrating the receiving equipment, the signal was transmitted at each modulation frequency with a series of known modulation coefficients. The ground wave was received on a short simple aerial of variable length, and for each coefficient a calibration curve of audio-frequency amplitude against radio-frequency amplitude was drawn using arbitrary scales. The coefficient of an ionospherically reflected signal received with a loop-aerial could be found directly from the calibration curves, which were checked at intervals of about 2 min. Since any possible sideband attenuation in the receiver would affect equally the calibration and the measurements, it is extremely unlikely that errors due to this cause were present.

---

* Department of Physics, University of Adelaide; present address: Physics Department, University of Queensland, Brisbane.

III. INTERPRETATION OF RESULTS

The present experiments were carried out in Adelaide on 25 nights from May to December 1954 (Aitchison and Goodwin 1955) and confirmed by observations made on 15 nights from February to April 1955.

The mean virtual height of the E_s layer was estimated by means of regular pulse-modulated signals. At each modulation frequency, the coefficient of E_s-layer reflected signals was largely independent of the virtual height of the layer. The mean coefficient of F-layer reflected signals was approximately constant at each frequency when the virtual height of the E_s layer was between 98 and 122 km, but tended to be somewhat larger for heights outside this range; e.g. at 1000 c/s, the mean coefficients for F-layer reflections were $0 \cdot 128$, $0 \cdot 116$, and $0 \cdot 142$ respectively for the three ranges 86–98, 98–122, and 122–134 km. The data in Figure 1 are therefore restricted to observations made when the height of the E_s layer was between 98 and 122 km.

The received signal generally consisted of two waves reflected from the E_s and F layers, with a ground wave of much smaller amplitude, which may be neglected in this discussion. The coefficient of predominantly F-layer reflections depended markedly on the modulation frequency, whereas the coefficient of predominantly E_s-layer reflections was fairly constant, although a statistical analysis showed a small difference (at the 15 per cent. level of significance) between values observed at different frequencies. In particular, the coefficient of predominantly E_s-layer reflections oscillated with a " periodicity " similar to that of predominantly F-layer reflections, but with about one-quarter the amplitude, as illustrated in Figure 1. Taking into account the accuracy of the data, it is concluded that the oscillation was due solely to a small F-layer reflection received simultaneously with a larger E_s-layer reflection. The coefficient of a pure E_s-layer reflection would therefore be effectively constant without any marked dependence on frequency (at least between 120 and 4000 c/s), being about $0 \cdot 165$ for a transmitted coefficient of $0 \cdot 2$.

The oscillation in the coefficient of an F-layer reflected signal, which is exhibited by both sets of points in Figure 1, occurred about a mean coefficient of approximately $0 \cdot 12$. It remained essentially constant in amplitude for at least two " cycles ", being closely represented by a sine curve (full line in Fig. 1) with a " periodicity " of 900 c/s, and an amplitude equivalent to a coefficient of $0 \cdot 02$.

We shall consider the possibility that the theory of wave interaction (Bailey and Martyn 1934 ; Bailey 1937 ; Huxley 1952, 1956) may provide an explanation for the observations of demodulation close to gyro frequency. Since the " extraordinary " magneto-ionic component is very strongly absorbed in the E region, the " ordinary " is the only component received with appreciable amplitude after reflection from the E or F region. The " ordinary " and " extraordinary " components may be assumed to act as " wanted " and " disturbing " waves respectively. (Hibberd (1957) has also considered the possible disturbing effect of the " ordinary " component on itself.)

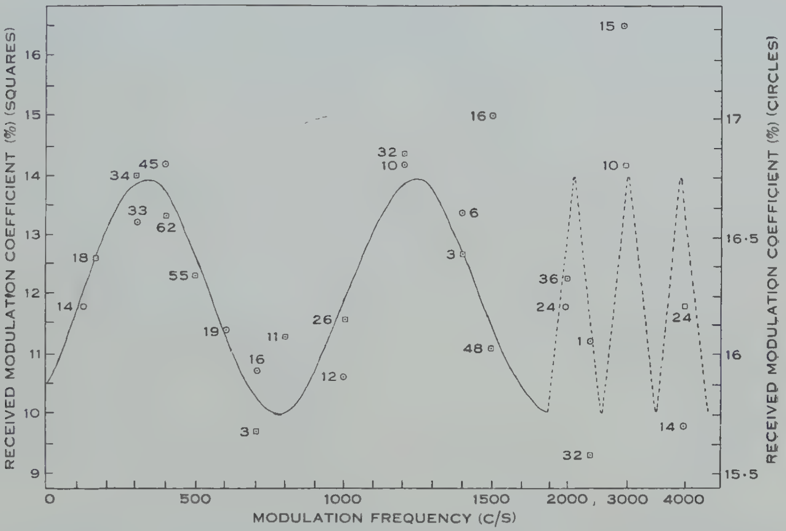

Fig. 1.—The dependence of the modulation coefficient of an F-layer reflection on the modulation frequency is shown for the height of the E_s-layer between 98 and 122 km. The squares represent an F-layer reflection received with a small E_s-layer reflection of about one-quarter the amplitude ; the circles denote an E_s-layer reflection with a small F-layer reflection of about one-quarter the amplitude. Each point is the mean of the number of measurements shown beside it. The squares carry four times the " weight " of the circles.

Let us consider a radio wave (originally modulated with a coefficient M) which has passed once through a demodulating region in the ionosphere. It may be shown (by extending the discussion of Aitchison (1957)) that (after detection) the amplitude of the audio component of the wave which is depicted in Figure 2 (a), may be written

$$M\cos\omega t - T_0\cos\varphi_\omega\cos(\omega t-\varphi_\omega) = (M-\tfrac{1}{2}T_0)\cos\omega t - \tfrac{1}{2}T_0\cos(\omega t-2\varphi_\omega)$$
$$= M_1\cos(\omega t+\chi_\omega),$$

where T_0 is the modulation coefficient transferred at an angular frequency $\omega\to 0$, φ_ω is given by the expression

$$\cos\varphi_\omega = 1/\{1+(\omega/Bn)^2\}^{\frac{1}{2}}, \quad \ldots\ldots\ldots\ldots\ldots\ldots\ldots\ldots \quad (1)$$

χ_ω is a phase angle, and the received modulation coefficient is

$$M_1 = \{(M-\tfrac{1}{2}T_0)^2 + (\tfrac{1}{2}T_0)^2 - T_0(M-\tfrac{1}{2}T_0)\cos 2\varphi_\omega\}^{\frac{1}{2}}. \quad \ldots\ldots \quad (2)$$

In experiments on cross-modulation (Ratcliffe and Shaw 1948; Huxley 1952) the value of Bn (or $G\nu$) was found to be about 2×10^3, n being the number of gas molecules in unit volume and B a constant. Assuming that this value might also apply for demodulation near gyro frequency, it would follow from equations (**1**) and (**2**) that M_1 is a known function of ω, if T_0 is known. In the case of an E_s-layer reflected wave, T_0 was approximately $0\cdot035$. The curves in Figure 3 corresponding to $Bn=2\times10^3$ and 8×10^3 lie above the experimental points (plotted with their standard deviations) and at the higher frequencies the curves are outside the limits of experimental error. It would appear that Bn is large, certainly greater than 8×10^3. This conclusion is substantiated by considering an F-layer reflected wave and neglecting initially the comparatively small sinusoidal oscillation observed in the modulation coefficient as the frequency is varied. This would also correspond to a wave which has passed once through the demodulating region. The received coefficient M_1 is taken to be essentially constant at $0\cdot12$ with a standard deviation of about $0\cdot025$, at least up to 4000 c/s. Since $T_0=0\cdot08$ and $M_1<0\cdot145$, it may be shown from equation (**2**) that $\varphi_\omega<30°$. In particular, when $\omega/2\pi=4000$, it follows from equation (**1**) that $Bn>4\cdot3\times10^4$. Thus, Bn is large, certainly greater than $4\cdot3\times10^4$.

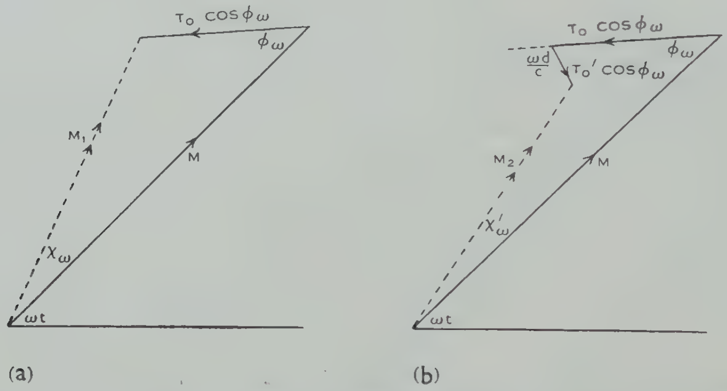

Fig. 2.—The expected modulation coefficient is shown for a wave which has passed (*a*) once, (*b*) twice, through the demodulating region in the ionosphere. (In the present experiments, φ_ω was found to be small.)

If we consider the case of an F-layer reflected wave which has passed twice through the demodulating region and assume that Bn has the generally accepted value of 2×10^3, it may be shown that the received modulation coefficient M_2 is expected to be a minimum when $\omega d/c$ is approximately 2π or multiples thereof, but that minima beyond the first should be of no consequence because of an increase expected in the value of φ_ω with increasing ω (Aitchison 1957). (Here, d is the group path length travelled by the wave between its two passages through the demodulating region and c is the velocity of the wave.) However, in the present experiments at least two maxima and two minima were present in the oscillation of M_2 (Fig. 1). It would appear therefore that the angle φ_ω was small and did not change appreciably with increasing ω, in agreement with the previous conclusion that φ_ω was certainly less than 30°.

If we take as an approximation $\varphi_\omega=0$, it may be shown that (after detection) the audio component of a wave which has passed twice through the demodulating region has the form

$$M_2 \cos(\omega t+\chi'_\omega)=(M-T_0)\cos\omega t-T'_0\cos(\omega t+\omega d/c),$$

where T_0 and T'_0 are the coefficients of transferred modulation, χ' is a phase angle, as shown in Figure 2 (*b*), and the received modulation coefficient is

$$M_2=\{(M-T_0)^2+T_0'^2-2T'_0(M-T_0)\cos\omega d/c)\}^{\frac{1}{2}}.$$

If $T'_0 \ll (M-T_0)$, the expression for M_2 may be simplified further, and becomes

$$M_2=(M-T_0)-T'_0\cos\omega d/c. \qquad \ldots\ldots\ldots\ldots\ldots\ldots\ldots (3)$$

Equation (3) indicates that to a close approximation M_2 has a constant component $(M-T_0)$ and a sinusoidal component of constant amplitude (T'_0). These implications of the theory agree very well with the experimental results.

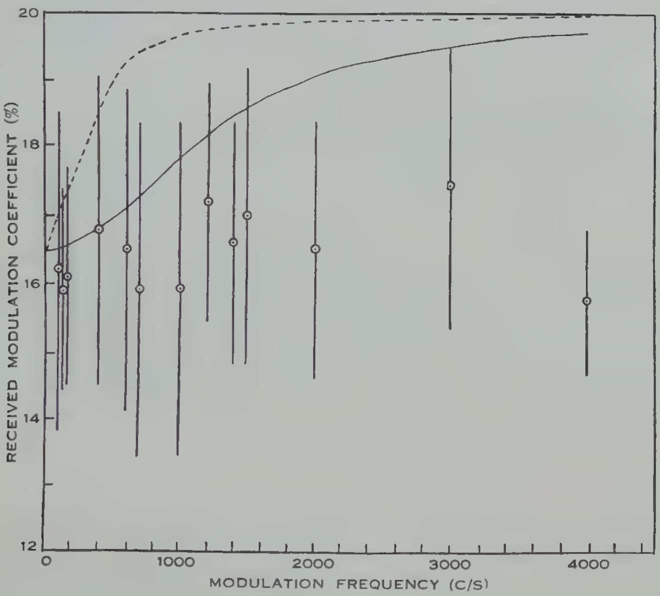

Fig. 3.—The modulation coefficients observed for E_s-layer reflections are shown with their standard deviations. The full line represents the theoretical variation of M_1 if $Bn=8\times10^3$ and the dotted line if $Bn=2\times10^3$.

Since reflections take place almost at vertical incidence, it would be expected from simple theory that T_0 and T'_0 would be practically equal. However, the present experimental observations suggest that $(M-T_0)$ was approximately 0·12 (at least up to 4000 c/s) and T'_0 was approximately 0·02 (at least up to 1500 c/s). It is concluded that in the present experiments an *F*-layer reflected wave, originally modulated with a coefficient of 0·2, was demodulated by about 0·08 and 0·02 during its two passages through the demodulating region ; that is, T_0 is approximately equal to $4T'_0$. The magnitudes of the two demodulations changed extremely slowly, if at all, with modulation frequency. It is difficult to find a simple explanation for the observed inequality of T_0 and T'_0.

In the above discussion, it appeared from the theory that Bn was very large, certainly greater than $4\cdot 3\times 10^4$. B has a value of $1\cdot 25\times 10^{-11}$ (personal communication from Professor L. G. H. Huxley), which suggests that $n>3\cdot 4\times 10^{15}$ cm^{-3}. It would follow from Table 1 of Huxley (1953) that demodulation near gyro frequency was a maximum at a height below 68 km. This theoretical estimate of the height may be compared with the following derivation from the experimental results. A periodicity of about 900 c/s was observed in the modulation coefficient of F-layer reflections, indicating that there was a time interval of 1/900 sec between the emergence of a radio wave from the demodulating region and its return to it after reflection from the F layer. Since the wave was almost vertically incident on the ionosphere, this suggests that the distance ($\frac{1}{2}d$) between the demodulating region and the reflection point in the F layer was of the order of 167 km. From pulse-modulated transmissions, the mean virtual height of the F layer for the data in Figure 1 was found to be 256 ± 17 km. It follows that demodulation was a maximum at a height of roughly 90 km.

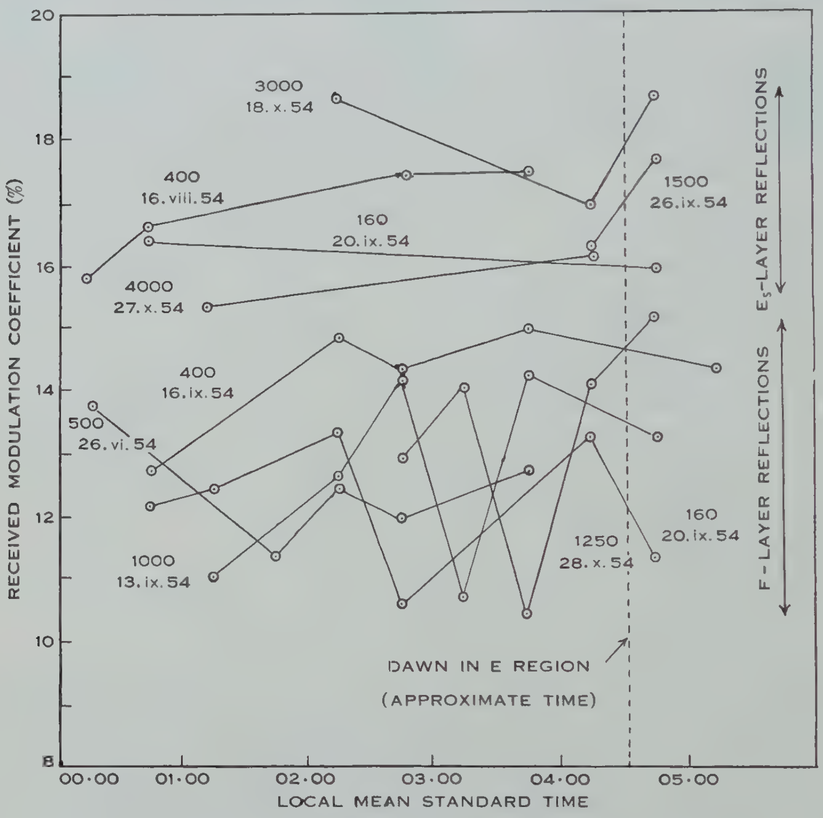

Fig. 4.—The received modulation coefficient is shown as a function of time for some typical results. The modulation frequency and date are given. Each point is the average of about seven measurements.

The deduction from theory that demodulation occurred largely below a height of 68 km disagrees with the direct estimate of 90 km. From a physical viewpoint, too, it is inconceivable that demodulation would occur below 68 km.

A statistical analysis of the results showed that a diurnal variation in the modulation coefficient was not present at the 5 per cent. level of significance for reflections either from the E_s layer or from the F layer, between 00·00 and 05·30 L.M.S.T. Some typical results are shown in Figure 4. In particular, there was apparently no decrease in demodulation through dawn in the present observations near gyro frequency, although such a " dawn " effect was observed by King (1957) at a frequency of 200 kc/s, which is remote from gyro frequency.

A discussion similar to that of Hibberd (1957) would show that the magnitude of demodulation, T_0, predicted by the theory, is about one hundred times smaller than the values observed in the present experiments.

The large magnitude of demodulation and its lack of dependence on modulation frequency at least up to 4000 c/s, appear to be inconsistent with the theory of wave interaction.

Carlevaro (1956) and Hibberd (1957) have also pointed out discrepancies between the theory and observations. It is concluded that the theory of wave interaction is inadequate to explain the present observations of demodulation near gyro frequency.

IV. Acknowledgments

The author wishes to thank Professor L. G. H. Huxley, who suggested the investigation, and Dr. G. J. Aitchison, in collaboration with whom the experimental work was carried out. Financial assistance was received from a Research Grant of the University of Adelaide and a scholarship from the Radio Research Board, C.S.I.R.O.

V. References

Aitchison, G. J. (1957).—*Aust. J. Phys.* **10** : 204.
Aitchison, G. J., and Goodwin, G. L. (1955).—*Nuovo Cim.* **1** : 722.
Bailey, V. A. (1937).—*Phil. Mag.* **23** : 774.
Bailey, V. A., and Martyn, D. F. (1934).—*Nature* **133** : 218.
Carlevaro, M. (1956).—*Nuovo Cim.* **4** (Suppl. No. 4) : 1422.
Cutolo, M. (1952).—*Nuovo Cim.* **9** : 687.
Cutolo, M. (1953).—*Nature* **172** : 774.
Hibberd, F. H. (1956).—*J. Atmos. Terr. Phys.* **8** : 120.
Hibberd, F. H. (1957).—*J. Atmos. Terr. Phys.* **11** : 102.
Huxley, L. G. H. (1952).—*Nuovo Cim.* **9** (Suppl. No. 9) : 59.
Huxley, L. G. H. (1953).—*Proc. Roy. Soc.* A **218** : 520.
Huxley, L. G. H. (1956).—*J. Atmos. Terr. Phys.* **8** : 118.
King, J. W. (1957).—*J. Atmos. Terr. Phys.* **10** : 166.
Mitra, S. N. (1954).—Conference on the Physics of the Ionosphere. Cavendish Laboratory, Cambridge. p. 7.
Ratcliffe, J. A., and Shaw, I. J. (1948).—*Proc. Roy. Soc.* A **193** : 311.

RADIATIVE TRANSFER IN NON-UNIFORM MEDIA

By R. G. Giovanelli*

[*Manuscript received December* 19, 1958]

Summary

The equation of radiative transfer incorporating Eddington's approximation is expressed in a form applicable to an inhomogeneous medium, as

$$\tfrac{1}{3}\nabla^2 J=\frac{1}{3\varkappa}\nabla J\,.\,\nabla\varkappa+\varkappa^2(\lambda J-4\pi S).$$

Here J is the total intensity, $\varkappa$ the attenuation coefficient, λ the ratio of absorption and attenuation coefficients, and S the source function.

A study is made of the emission from a simple model inhomogeneous semi-infinite medium, including the relative effects of variations in $\varkappa$, λ, and S across the surface. Particular attention is drawn to the significance of variations in attenuation coefficient in connexion with the appearance of chromospheric granulation.

I. INTRODUCTION

Solutions of the equation of radiative transfer used in astrophysics are customarily those for a plane parallel or spherically symmetrical medium. It is by no means clear, however, to what extent such solutions are applicable to atmospheres exhibiting granulation, and particularly whether they may be used in deducing from observation the spatial variation of physical conditions.

To study this question, the differential equation of radiative transfer, embodying Eddington's approximation, is generalized here for non-uniform media. A solution is obtained for a semi-infinite medium in which the attenuation coefficient, scattering parameter, and source function are independent of depth but may have small sinusoidal variations as functions of a coordinate parallel to the surface. This investigation yields some insight as to the effect of structure size on the appearance of granules, one of the important deductions being that, with structures that are not too coarse or too fine, variations in attenuation coefficient alone are sufficient to result in marked variations in brightness.

II. THE EQUATION OF RADIATIVE TRANSFER

Consider a coherently scattering medium in which $\varkappa$, λ, and S are functions of position, $\varkappa$ being the attenuation coefficient and λ the scattering parameter ($=1-\tilde{\omega}_0$, where $\tilde{\omega}_0$ is the albedo for single scattering), while S, the source function, is the ratio of the emission per unit volume and solid angle to the attenuation coefficient.

The intensity of radiation, I, is a function of direction and position. To establish an equation for the intensity we note that the change of intensity of a beam of radiation in traversing a distance ds is due to an attenuation loss $\varkappa I$ds

---

* Division of Physics, C.S.I.R.O., University Grounds, Chippendale, N.S.W.

and a gain due to scattering and emission. The gain due to isotropic coherent scattering is $(1/4\pi)\tilde{\omega}_0\varkappa J\mathrm{d}s$, where

$$J=\int_{4\pi} I\mathrm{d}\Omega$$

is the total intensity, and the contribution due to emission is $\varkappa S\mathrm{d}s$. So

$$\mathrm{d}I/\mathrm{d}s=-\varkappa I+(1/4\pi)\tilde{\omega}_0\varkappa J+\varkappa S.$$

In rectangular coordinates,

$$\sin\theta\cos\varphi\frac{\partial I}{\partial x}+\sin\theta\sin\varphi\frac{\partial I}{\partial y}+\cos\theta\frac{\partial I}{\partial z}=-\varkappa I+\frac{1}{4\pi}\tilde{\omega}_0\varkappa J+\varkappa S, \quad .. \ (1)$$

θ being the angle between the beam and the z-axis and φ the azimuth referred to the x-axis.

In its most general form, I may be expanded in a series of spherical harmonics

$$I=\sum_{n=0}^{\infty}\left[I_nP_n(\mu)+\sum_{m=1}^{n}(a_n^m\cos m\varphi+b_n^m\sin m\varphi)P_n^m(\mu)\right], \quad .. \ (2)$$

where $\mu=\cos\theta$, $P_n(\mu)$ and $P_n^m(\mu)$ being Legendre polynomials and associated Legendre functions respectively, and I_n, a_n^m, and b_n^m the corresponding amplitudes. Substituting (2) in (1) and integrating around φ, it follows that

$$\mu\frac{\partial}{\partial z}\sum_{n=0}^{\infty}I_nP_n(\mu)+\tfrac{1}{2}\sin\theta\sum_{n=1}^{\infty}\left(\frac{\partial a_n^1}{\partial x}+\frac{\partial b_n^1}{\partial y}\right)P_n^1(\mu)=-\varkappa\sum_{n=0}^{\infty}I_nP_n(\mu)+\frac{1}{4\pi}\tilde{\omega}_0\varkappa J+\varkappa S. \quad \ldots\ldots\ldots\ldots\ldots\ldots \ (3)$$

Multiplying by $P_m(\mu)\mathrm{d}\mu$ and integrating from -1 to $+1$, using the recurrence and integral relations for Legendre functions, and noting that $J=4\pi I_0$, it follows that

$$\left.\begin{aligned}\frac{1}{3}\frac{\partial I_1}{\partial z}+\frac{1}{3}\frac{\partial a_1^1}{\partial x}+\frac{1}{3}\frac{\partial b_1^1}{\partial y}&=-\varkappa\lambda I_0+\varkappa S \qquad (m=0).\\ \frac{\partial I_0}{\partial z}+\frac{2}{5}\frac{\partial I_2}{\partial z}+\frac{3}{5}\left(\frac{\partial a_2^1}{\partial x}+\frac{\partial b_2^1}{\partial y}\right)&=-\varkappa I_1 \qquad (m=1).\end{aligned}\right\} \quad \ldots . \ (4)$$

Subject to the approximation that I_2, a_2^1, and b_2^1 are zero, the latter equation becomes

$$\partial I_0/\partial z=-\varkappa I_1. \quad \ldots\ldots\ldots\ldots\ldots\ldots\ldots \ (5)$$

In the plane parallel case when a_1^1 and b_1^1 are zero and $\varkappa$ a function only of z, equations (4) and (5) lead to the well-known Eddington equation of radiative transfer.

When $\varkappa$ is a general function of position, we may note that, by symmetry, two other equations similar to (5) can be obtained immediately :

$$\partial I_0/\partial x=-\varkappa a_1^1, \qquad \partial I_0/\partial y=-\varkappa b_1^1.$$

From these and (5),

$$\nabla^2 I_0 = -\left(a_1^1 \frac{\partial\varkappa}{\partial x} + b_1^1 \frac{\partial\varkappa}{\partial y} + I_1 \frac{\partial\varkappa}{\partial z}\right) - \varkappa\left(\frac{\partial a_1^1}{\partial x} + \frac{\partial b_1^1}{\partial y} + \frac{\partial I_1}{\partial z}\right).$$

Using the same equations and (4), this leads to

$$\nabla^2 I_0 = \frac{1}{\varkappa}\left(\frac{\partial I_0}{\partial x}\frac{\partial\varkappa}{\partial x} + \frac{\partial I_0}{\partial y}\frac{\partial\varkappa}{\partial y} + \frac{\partial I_0}{\partial z}\frac{\partial\varkappa}{\partial z}\right) + 3\varkappa^2(\lambda I_0 - \varkappa S).$$

In terms of the total intensity, the generalized equation of radiative transfer may be written in the form

$$\frac{1}{3}\nabla^2 J = \frac{1}{3\varkappa}\nabla J \,.\, \nabla\varkappa + \varkappa^2(\lambda J - 4\pi S). \qquad \ldots\ldots\ldots\ldots\ldots\ldots\ldots \quad (6)$$

III. Radiative Transfer in a Model Sinusoidal Medium

In general, the solution of (6) is rather lengthy, though we can gain worthwhile insight as to the effect of structure in stellar atmospheres from a restricted study of a model semi-infinite medium in which the x and y axes lie in the surface, the z axis being directed outwards, and the quantities $\varkappa$, λ, and S are independent of y and z but have small sinusoidal variations, all of the same phase, in the x direction. Then

$$\left.\begin{aligned} \varkappa &= \varkappa_0 + \varkappa_1 \cos lx, \\ \lambda &= \lambda_0 + \lambda_1 \cos lx, \\ S &= S_0 + S_1 \cos lx. \end{aligned}\right\} \qquad \ldots\ldots\ldots\ldots\ldots\ldots \quad (7)$$

Here l is a measure of the structure size.

To solve (6), J may be expressed in the form

$$J = \sum_0^\infty \mathscr{J}_n(z) \cos nlx,$$

and, together with (7), substituted in the equation of radiative transfer. Now $\mathscr{J}_0(z)$ is the average value of J at depth z, while $\mathscr{J}_1(z)$ describes the variations of J with the same periodicity as the medium. Higher terms in $\mathscr{J}_n(z)$, $n \geqslant 2$, represent distortion of the intensity distribution and may be disregarded for small enough values of $\varkappa_1$, λ_1, and S_1. Then (6) becomes

$$\begin{aligned} \tfrac{1}{3}\mathrm{D}^2\mathscr{J}_0 + \tfrac{1}{3}(\mathrm{D}^2 - l^2)\mathscr{J}_1 \cos lx = {} & \tfrac{1}{3}(\varkappa_0 + \varkappa_1 \cos lx)^{-1}(l^2 \mathscr{J}_1 \varkappa_1 \sin^2 lx) \\ & + (\varkappa_0 + \varkappa_1 \cos lx)^2\{(\lambda_0 + \lambda_1 \cos lx)(\mathscr{J}_0 + \mathscr{J}_1 \cos lx) - 4\pi(S_0 + S_1 \cos lx)\}, \end{aligned}$$

where $\mathrm{D} \equiv \partial/\partial z$ and $\mathscr{J}_n \equiv \mathscr{J}_n(z)$.

Terms of the type $\cos^n lx$ are now replaced by a sum of terms in $\cos mlx$, in order to permit separation of equations for the various harmonic components. After some straightforward analysis in which terms involving second orders of small quantities are neglected, it is found that terms independent of x yield

$$\mathrm{D}^2\mathscr{J}_0 = 3\varkappa_0^2\lambda_0\mathscr{J}_0 + \left[\frac{3}{2}(2\varkappa_0\varkappa_1\lambda_0 + \varkappa_0^2\lambda_1) + \frac{1}{2}\, l^2 \frac{\varkappa_1}{\varkappa_0}\right]\mathscr{J}_1 - 12\pi\varkappa_0^2 S_0.$$

Terms involving $\cos lx$ yield

$$(\mathrm{D}^2-l^2)\mathcal{J}_1=3\varkappa_0^2\lambda_0\mathcal{J}_1+3(2\varkappa_0\varkappa_1\lambda_0+\varkappa_0^2\lambda_1)\mathcal{J}_0-12\pi(2\varkappa_0\varkappa_1S_0+\varkappa_0^2S_1).$$

The solutions of these simultaneous differential equations, subject to the boundary condition that the intensity remain finite deep within the medium, are

$$\left.\begin{aligned}\mathcal{J}_0&=Ae^{p_1z}+Be^{p_2z}+\frac{c(l^2+a)-(b+f)d}{a^2+al^2-2b(b+f)},\\ \mathcal{J}_1&=(p_1^2-a)(b+f)^{-1}Ae^{p_1z}+(p_2^2-a)(b+f)^{-1}Be^{p_2z}+\frac{ad-2bc}{a^2+al^2-2b(b+f)},\end{aligned}\right\} \qquad (8)$$

where $a=3\varkappa_0^2\lambda_0,$

$$b=\frac{3}{2}(2\varkappa_0\varkappa_1\lambda_0+\varkappa_0^2\lambda_1),$$

$$c=12\pi\varkappa_0^2S_0,$$

$$d=12\pi(2\varkappa_0\varkappa_1S_0+\varkappa_0^2S_1),$$

$$f=\frac{1}{2}\,l^2\,\frac{\varkappa_1}{\varkappa_0},$$

$$p_1=\left[\frac{1}{2}l^2+a+\frac{1}{2}(l^4+8b^2+8bf)^{\frac{1}{2}}\right]^{\frac{1}{2}},$$

$$p_2=\left[\frac{1}{2}l^2+a-\frac{1}{2}(l^4+8b^2+8bf)^{\frac{1}{2}}\right]^{\frac{1}{2}}.$$

The constants A and B are chosen to ensure zero inward flux at the boundary, $z=0$. In particular, this applies at points where $\partial J/\partial x=0$, or $\sin lx=0$; i.e. $\cos lx=\pm1$. As in the usual treatment of the plane parallel equation of transfer, this leads to the condition

$$\varkappa J=-\tfrac{2}{3}\mathrm{D}J,$$

when $z=0$, $\cos lx=\pm1$. Then, after some straightforward analysis, it is found that

$$A=(\gamma\varepsilon-\beta\eta)/(\varepsilon\alpha-\beta\delta),\qquad B=(\alpha\eta-\gamma\delta)/(\varepsilon\alpha-\beta\delta),$$

where $\alpha=\varkappa_0+\tfrac{1}{2}\varkappa_1(b+f)^{-1}[l^2+(l^4+8b^2+8bf)^{\frac{1}{2}}]+\tfrac{2}{3}p_1,$

$$\beta=\varkappa_0+\tfrac{1}{2}\varkappa_1(b+f)^{-1}[l^2-(l^4+8b^2+8bf)^{\frac{1}{2}}]+\tfrac{2}{3}p_2,$$

$$\gamma=-\{\varkappa_0[c(l^2+a)-(b+f)d]+\varkappa_1(ad-2bc)\}\{a^2+al^2-2b(b+f)\}^{-1},$$

$$\delta=\varkappa_1+(\tfrac{1}{2}\varkappa_0+\tfrac{1}{3}p_1)(b+f)^{-1}[l^2+(l^4+8b^2+8bf)^{\frac{1}{2}}],$$

$$\varepsilon=\varkappa_1+(\tfrac{1}{2}\varkappa_0+\tfrac{1}{3}p_2)(b+f)^{-1}[l^2-(l^4+8b^2+8bf)^{\frac{1}{2}}],$$

$$\eta=-\{\varkappa_1[c(l^2+a)-(b+f)d]+\varkappa_0(ad-2bc)\}\{a^2+al^2-2b(b+f)\}^{-1}.$$

To simplify these results, we note from physical considerations that, when l is small enough (very coarse structures), J at any point is the same as in a uniform medium having the same values of $\varkappa$, λ, and S. When l is large enough (very fine structures) the intensity variations are negligible, J being the same as in a uniform medium where the constants are $\varkappa_0$, λ_0, and S_0. The condition $l^4 \gg 8b(b+f)$ is satisfied almost throughout the entire transition between these extremes, in which case the average value of the total intensity at the surface is

$$\mathscr{J}_0 = \frac{2}{3}\,\frac{c}{\sqrt{a}\left(\varkappa_0+\frac{2}{3}\sqrt{a}\right)} = \frac{8\pi S_0}{\sqrt{(3\lambda_0)}(1+2\sqrt{(\lambda_0/3)})} \quad (z=0). \qquad \text{.. } \mathbf{(9)}$$

Thus the first important result emerges, that the mean value of J at the surface is unaffected by small sinusoidal variations in $\varkappa$, λ, or S in a direction parallel to the surface; it can also be shown that this conclusion applies to the mean value of J at all depths.

Under the same conditions, $l^4 \gg 8b(b+f)$, the fractional variation in J across the surface is

$$\begin{aligned} \frac{\mathscr{J}_1}{\mathscr{J}_0} = {} & \left\{c(a+l^2)\left[\varkappa_0+\frac{2}{3}\sqrt{(a+l^2)}\right]\right\}^{-1} \\ & \times\left\{-2\varkappa_0\frac{a}{l^2}bc[1-\sqrt{(1+l^2/a)}]-2\varkappa_0 bc+\varkappa_0 ad\sqrt{(1+l^2/a)}-\varkappa_1 ac(1+l^2/a)\right. \\ & \qquad \left.+\frac{2}{3}\sqrt{(a+l^2)}\,.\,(ad-2bc)\right\}. \qquad \ldots\ldots\ldots\ldots\ldots\ldots\ldots\ldots \quad \mathbf{(10)} \end{aligned}$$

This relation is easiest discussed in some special cases.

(i) As $l \to \infty$, $\mathscr{J}_1/\mathscr{J}_0 \to 0$.

(ii) When $l^2 \gg a$, i.e., for fine enough structures, greater changes are produced in the total intensity at the surface by a given fractional change in *attenuation* than by equal fractional changes in S or λ. This can be appreciated by noting that the dominant term in the numerator of (**10**) is then $-\varkappa_1 ac(1+l^2/a)$.

(iii) When $S_1=0$ and $\lambda_1=0$ (variations in $\varkappa$ alone),

$$\frac{\mathscr{J}_1}{\mathscr{J}_0} = \frac{\varkappa_1}{(1+l^2/a)\left[\varkappa_0+\frac{2}{3}\sqrt{(a+l^2)}\right]}\left\{-\frac{2a}{l^2}\left[1-\sqrt{\left(1+\frac{l^2}{a}\right)}\right]+2\sqrt{\left(1+\frac{l^2}{a}\right)}-3-\frac{l^2}{a}\right\} \quad (z=0).$$

Thus, when the variations in medium are of attenuation alone,

$$\begin{aligned} &\frac{\mathscr{J}_1}{\mathscr{J}_0} \to 0, && l^2 \ll a, \\ &\frac{\mathscr{J}_1}{\mathscr{J}_0} = -\frac{\varkappa_1(3-2\sqrt{2})}{\varkappa_0+\frac{2}{3}\sqrt{2}}, && l^2 = a, \\ &\frac{\mathscr{J}_1}{\mathscr{J}_0} \approx -\frac{\varkappa_1}{\varkappa_0+\frac{2}{3}l}, && l^2 \gg a, \\ &\frac{\mathscr{J}_1}{\mathscr{J}_0} \to 0, && l^2 \to \infty. \end{aligned}$$

This sequence shows that the variation in the total intensity across the surface, or the contrast, rises from zero to a maximum and decreases to zero again as the size of the structures diminishes. The maximum value of $\mathscr{J}_1/\mathscr{J}_0$ is of the order of but less than the fractional variation in $\varkappa$, and occurs for a value of l somewhere in the range $\sqrt{a}\lesssim l\lesssim 3\varkappa_0/2$. Maximum values of J across the surface correspond to minima of attenuation coefficient; this is because radiation can escape from greater depths at such positions.

(iv) When $\varkappa_1=0$ and $\lambda_1=0$ (variations in S alone),

$$\frac{\mathscr{J}_1}{\mathscr{J}_0}=\frac{S_1}{S_0\sqrt{(1+l^2/a)}}\cdot\frac{\varkappa_0+\frac{2}{3}\sqrt{a}}{\varkappa_0+\frac{2}{3}\sqrt{(a+l^2)}}\qquad(z=0).$$

Thus the contrast remains high from the coarsest structures down to those for which $l^2\approx a$, and diminishes for smaller structures. The maximum value of $\mathscr{J}_1/\mathscr{J}_0$ is S_1/S_0, maxima of J coinciding with maxima of S.

(v) When $\varkappa_1=0$ and $S_1=0$ (variations in λ alone),

$$\frac{\mathscr{J}_1}{\mathscr{J}_0}=-\frac{\lambda_1}{\lambda_0}\cdot\frac{\varkappa_0 a/l^2\{1-\sqrt{(1+l^2/a)}\}+\varkappa_0+2\sqrt{a}\sqrt{(1+l^2/a)}}{(1+l^2/a)\{\varkappa_0+\frac{2}{3}\sqrt{(a+l^2)}\}}\qquad(z=0).$$

Thus

$$\frac{\mathscr{J}_1}{\mathscr{J}_0}\rightarrow-\frac{\lambda_1}{2\lambda_0}\cdot\frac{4\lambda_0+\sqrt{(3\lambda_0)}}{2\lambda_0+\sqrt{(3\lambda_0)}},\qquad l\rightarrow 0,$$

which is of the order of $-\frac{1}{2}\lambda_1/\lambda_0$ for resonance radiation ($\lambda_0\ll 1$).

$$\frac{\mathscr{J}_1}{\mathscr{J}_0}=-\frac{\lambda_1}{2\lambda_0}\cdot\frac{2-\sqrt{2}+2\sqrt{(6\lambda_0)}}{1+\frac{2}{3}\sqrt{(6\lambda_0)}},\qquad l^2=a,$$

$$\frac{\mathscr{J}_1}{\mathscr{J}_0}=-\frac{\lambda_1}{\lambda_0}\cdot\frac{a(\varkappa_0+2l)}{l^2(\varkappa_0+\frac{2}{3}l)},\qquad l^2\gg a.$$

As the size of the structure diminishes, so does the contrast, being substantially reduced when $l^2=a$.

(vi) When the emission per unit volume and solid angle is proportional to the absorption coefficient, then S/λ is uniform throughout, and $ad=2bc$. Thus $\mathscr{J}_1$ vanishes deep in the medium, as is to be expected from very general considerations.

IV. Discussion

In showing that emission from a non-uniform medium is dependent on structure, the present work complements an earlier investigation by the author where, using a different method, the reflectance of a semi-infinite diffuse medium was also found to depend on structure (Giovanelli 1957*).

The most significant result obtained here is that, in a certain size range, variations in brightness of the medium are most sensitive to variations in attenuation coefficient, a quantity which in the case of a semi-infinite plane parallel medium does not appear explicitly in the expression for the brightness. For very coarse structures, variations in attenuation coefficient have no influence, but variations in scattering parameter and source function then have their greatest effects. As the structure size decreases, the effects of variations in λ and S become less significant and variations in $\varkappa$ become more important. After an optimum size, further decrease in the structure dimensions results in a reduction of brightness variations towards zero.

---

* Giovanelli, R. G.—*Aust. J. Phys.* **10**: 227.

The solutions obtained here are for a problem too simplified to have direct application to the Sun's atmosphere. However, it is instructive to calculate the orders of magnitude of the important structure sizes using data appropriate to the solar chromosphere. For example, if $\varkappa_0 \lesssim 2 \times 10^{-8}$ cm^{-1} in Hα and if $\lambda_0 \approx 10^{-2}$, then the structural dimensions corresponding to $l = 3\varkappa_0/2$ and $\sqrt{a}$ are $x = 2\pi/l \lesssim 2 \times 10^8$ cm and 2×10^9 cm respectively. This range includes such a large fraction of actual chromospheric structures that it is clearly essential to use appropriate solutions of the equation of radiative transfer, taking into account non-uniformities of the chromosphere, in deriving spatial variations of physical conditions there. Again, it would appear that even with perfect telescopic resolution there is a natural limit to the size of structure which can be detected with given contrast.

A further point requires stressing: the average intensity $\mathcal{J}_0$ is certainly influenced by structure when the variations in physical conditions are large.

V. ACKNOWLEDGMENT

This work was carried out at the Sacramento Peak Observatory, Geophysics Research Directorate, Sunspot, New Mexico, and the author's sincere thanks are due to its Director, Dr. J. Evans, for the opportunities and facilities provided.

THE STRUCTURE OF A STREAM OF ELECTRONS AND IONS DRIFTING AND DIFFUSING IN A GAS WHEN IONIZATION BY COLLISION AND MOLECULAR ATTACHMENT ARE PRESENT

By L. G. H. Huxley*

[*Manuscript received December* 8, 1958]

Summary

The theory is developed of the structure of a stream of electrons and ions drifting under the action of a uniform field and diffusing in a gas when either or both ionization by collision and electron attachment are present. The cases considered include a point source and a line source, and in the latter case the influence of a magnetic field is discussed.

The investigation provides a theoretical basis for methods of measuring electron attachment, about to be put into practice.

I. Introduction

In the well-known method devised by Townsend for studying the motions of slow electrons in gases (Townsend 1916) the ratio W/D of the drift velocity $\vec{W}$ to the coefficient of diffusion D is found by measuring the distribution of electrons in a stream moving through the gas in a steady state of motion in a uniform electric field. When separate measurements are made of the drift velocity $\vec{W}$ for a range of values of the ratio Z/p, of the electric field strength to the pressure p of the gas, of which ratio W and W/pD are functions, then the dependence of pD upon Z/p may be deduced.

From the quantities W/D, W, D, and p the microscopic details of the motion, such as mean energy of agitation Q of the electrons, the collisional cross sections of the molecules, and the mean rate at which electrons lose energy in collisions with molecules, are found as functions of Z/p (e.g. Healey and Reed 1941; Townsend 1947; Loeb 1955; Huxley 1957).

The experimental procedure is essentially as follows: a stream of electrons, having already acquired a steady state of motion in a uniform field Z, enters the diffusion chamber through an aperture (circular or rectangular) and moves through the gas under the same uniform field Z to a receiving electrode which is divided into separately insulated sections. In one method of division there is a central disk surrounded by one or more concentric annuli; in another, there is a central strip flanked by other strips or the remaining portions of the electrode.

The ratio R of the currents to any two portions of the electrode can be calculated in terms of W/D for a given apparatus, consequently, when the ratio of the currents is measured, W/D may be immediately derived from it.

---

* Department of Physics, University of Adelaide.

If the centre of the aperture of entry of the stream is taken as the origin of coordinates and the direction of drift $\vec{W}$ as the axis Oz, then the differential equation for the distribution of the concentration n of the electrons in unit volume in the steady stream is

$$\nabla^2 n = (W/D)\partial n/\partial z, \quad \ldots\ldots\ldots\ldots\ldots\ldots \quad (1)$$

a solution of which, satisfying the boundary conditions, is found and from it the ratio R (dimensions of apparatus, W/D) is calculated. In Townsend's work, since the dimensions of the aperture of entry to the diffusion chamber could not usually be considered as mathematically small in comparison with the dimensions of the chamber, the appropriate solutions of (**1**) were in the form of infinite series which were not convenient for calculating the ratio R. However, if the aperture is made small it may be regarded as a point source and simple solutions are found in the form of pole or dipole sources which with suitable image sources satisfy the boundary condition $n=0$ over the receiving electrode. The calculation of R is then a simple matter (Huxley and Zaazou 1949 ; Crompton, Huxley, and Sutton 1953).

In practice the pole solution (Crompton and Huxley 1955)

$$\left.\begin{aligned} n &= (S/4\pi Dr) \exp\,[\lambda(z-r)], \\ 2\lambda &= W/D, \end{aligned}\right\} \quad \ldots\ldots\ldots\ldots\ldots \quad (2)$$

together with a suitable image source accurately describes the actual distribution of n in the diffusion chamber.

The quantity S is the rate at which the pole source emits electrons.

Equation (**1**) and its solutions refer to situations in which electrons are neither lost to the stream by attachment to molecules to form negative ions nor gained by ionization of the molecules by collision. When either or both these processes are present to an important degree equation (**1**) and its solutions no longer accurately describe the distribution of n in the stream and that of the current over the receiving electrode. When the process of electron attachment occurs the stream becomes enriched with negative ions whose distribution is not precisely known. Many years ago V. A. Bailey (Healey and Reed 1941 ; Loeb 1955) devised methods for measuring the coefficient of attachment of electrons in such streams in which the unknown functions representing the distribution of negative ions, both entering the chamber and formed in the chamber by attachment, were eliminated by special but somewhat complicated experimental procedures.

Another special situation of interest is that in which ionization by collision is present and it is required to measure the mean energy of agitation of the electrons.

In view of the practical importance of measurements of coefficients of attachment and of ionization, in what follows the theory of the diffusing stream of electrons in a gas is extended to include the effects of electron attachment and ionization by collision.

New experimental procedures for measuring attachment coefficients and agitational energies Q in the presence of ionization are also discussed.

II. Extension of the Theory to include the Effects of Electron Attachment and Ionization by Collision

Consider the distribution of the concentration n of the electrons in a steady stream in which W is drift speed and D the coefficient of diffusion of the electrons. Adopt a system of coordinates in which the axis Oz is parallel to the direction of $\vec{W}$.

Let ν be the collisional frequency of an electron moving with a velocity of agitation c and suppose that the probability of attachment in single collisions of such electrons is f. It follows that the number of attachments that occur in time $\mathrm{d}t$ in an element of volume $\mathrm{d}\tau$ containing $n\mathrm{d}\tau$ electrons is $(\overline{f\nu})n\mathrm{d}\tau\mathrm{d}t$, where $(\overline{f\nu})$ is the mean value of $f\nu$ averaged over all speeds c. Similarly, if g is the probability of ionization by collision in single collisions, the number of new electrons and positive ions produced in $\mathrm{d}\tau$ in time $\mathrm{d}t$ is $(\overline{g\nu})n\mathrm{d}\tau\mathrm{d}t$. The equation of continuity for n is therefore

$$\mathrm{d}n/\mathrm{d}t = D\nabla^2 n - \vec{W}\cdot\text{grad}\, n - (\overline{f\nu}-\overline{g\nu})n. \qquad \ldots\ldots\ldots \qquad (3)$$

In a steady stream $\mathrm{d}n/\mathrm{d}t=0$, and when $W=W_z$ equation (3) reduces to

$$\nabla^2 n = 2\lambda\,\partial n/\partial z + 2\lambda\alpha n, \qquad \ldots\ldots\ldots\ldots\ldots\ldots \qquad (4)$$

where $2\lambda = W/D$ and $2\lambda\alpha = (\overline{f\nu}-\overline{g\nu})/D$. It follows from (4) that

$$\alpha = (\overline{f\nu}-\overline{g\nu})/W = \alpha_a - \alpha_i. \qquad \ldots\ldots\ldots\ldots\ldots \qquad (5)$$

The concentration N in unit volume of the negative ions in the stream satisfies the differential equation

$$D_1\nabla^2 N = W_1\,\partial N/\partial z - \alpha_a W n, \qquad \ldots\ldots\ldots\ldots \qquad (6)$$

where D_1 and W_1 are respectively the coefficient of diffusion and speed of drift of negative ions.

In what follows it is assumed that electrons enter the diffusion chamber through a small aperture which may be regarded as a point source.

Place the origin of coordinates at the aperture and let the axis Oz be parallel to the direction of $\vec{W}$ (that is, antiparallel to the field Z). The receiving electrode coincides with the plane $z=h$. Radial distances from the origin are denoted by $r=(x^2+y^2+z^2)^{\frac{1}{2}}$.

(a) *Distribution of* n

Write $n=\mathrm{e}^{\lambda z}V$ in equation (4); then after reduction this equation becomes

$$\nabla^2 V = (\lambda^2 + 2\lambda\alpha)V = \mu^2 V. \qquad \ldots\ldots\ldots\ldots \qquad (7)$$

The solution of this equation representing a simple pole source is

$$V = \text{constant} \times \mathrm{e}^{-\mu r}/r,$$

and the corresponding solution of equation (4) is

$$n = (s/4\pi D)\mathrm{e}^{\lambda z - \mu r}/r, \qquad \ldots\ldots\ldots\ldots\ldots \qquad (8)$$

in which the constant s is the number of electrons emitted by the source in unit time.

In order to make $n=0$ over the plane of the receiving electrode, $z=h$, when the electrode is absent, place an image source of suitable strength and negative sign at the point $(0,0,2h)$ to give the following distribution of n:

$$n=(s/4\pi D)e^{\lambda z}(e^{-\mu r}/r-e^{-\mu r'}/r'), \quad \ldots\ldots\ldots\ldots \quad (9)$$

where

$$r^2=\rho^2+z^2,\ r'^2=\rho^2+(2h-z)^2,\ \rho^2=x^2+y^2.$$

Equation (**9**) gives the distribution of n within the diffusion chamber to a good approximation in practice, since n is small over the plane $z=0$ except near the origin (e.g. Crompton and Huxley 1955).

In order to calculate the current to an annular division $a\leqslant\rho\leqslant b$ of the receiving electrode ($z=h$; $n=0$) it is necessary first to find $(\partial n/\partial z)_\rho$ at the plane $z=h$.

When ρ is constant, $r\mathrm{d}r=z\mathrm{d}z$; $r'\mathrm{d}r'=-(2h-z)\mathrm{d}z$.

From equation (**9**)

$$\left(\frac{\partial n}{\partial z}\right)_\rho=\lambda n+\frac{s}{4\pi D}\left[\frac{z}{r}\cdot\frac{\mathrm{d}}{\mathrm{d}r}\left(\frac{e^{-\mu r}}{r}\right)+\left(\frac{2h-z}{r'}\right)\frac{\mathrm{d}}{\mathrm{d}r'}\left(\frac{e^{-\mu r'}}{r'}\right)\right]e^{\lambda z}.$$

On the plane $z=h$; $r=r'$; $n=0$; $\rho\mathrm{d}\rho=r\mathrm{d}r$,

$$\left(\frac{\partial n}{\partial z}\right)_{z=h}=\frac{s}{4\pi D}\cdot\frac{e^{\lambda h}2h}{r}\cdot\frac{\mathrm{d}}{\mathrm{d}r}\left(\frac{e^{-\mu r}}{r}\right).$$

The current carried by diffusion to the annulus $a\leqslant\rho\leqslant b$ is

$$\begin{aligned}(i)_{ab}&=-2\pi\varepsilon D\int_a^b\left(\frac{\partial n}{\partial z}\right)_{z-h}\rho\mathrm{d}\rho\\&=s\varepsilon he^{\lambda h}\int_{d_a}^{d_b}\mathrm{d}\left(\frac{e^{-\mu r}}{r}\right)\\&=s\varepsilon he^{\lambda h}[e^{-\mu d_a}/d_a-e^{-\mu d_b}/d_b], \quad \ldots\ldots\ldots\ldots \quad (10)\end{aligned}$$

where ε is the electronic charge; $d_a^2=a^2+h^2$; $d_b^2=b^2+h^2$.

The total electronic current to the whole electrode ($a=0$; $b=\infty$) is

$$i=i_{0\infty}=\varepsilon se^{-(\mu-\lambda)h}=i_0e^{(\lambda-\mu)h} \quad (i_0=\varepsilon s). \quad \ldots\ldots \quad (11)$$

But from equation (**7**), $\mu^2-\lambda^2=2\lambda\alpha$; $(\mu-\lambda)=2\lambda\alpha/(\mu+\lambda)$, so that when $2\lambda\alpha\ll\lambda^2$, $\mu\simeq\lambda$, $\mu-\lambda\simeq\alpha$.

In this event,

$$i=i_{0\infty}=i_0e^{-\alpha h}. \quad \ldots\ldots\ldots\ldots\ldots\ldots \quad (12)$$

(*b*) *Ionization by Collision*

When $\alpha_a=0$, then $\alpha=-\alpha_i$ and equations (**11**) and (**12**) become

$$i=i_0e^{(\lambda-\mu)h};\ i\simeq i_0e^{\alpha_i h}, \quad \ldots\ldots\ldots\ldots\ldots \quad (13)$$

which is Townsend's well-known formula for the growth of current with increasing electrode separation h in a uniform field when ionization by collision is present.

It is seen that the quantity found from the exponential growth of currents between plane parallel electrodes is $\lambda-\mu$ and not α_i. In practice the difference between $\lambda-\mu$ and α_i would usually be unimportant.

(*c*) *Measurement of* μ *when* $\alpha_a=0$

The current to an annulus of the receiving electrode $a \leqslant \rho \leqslant b$ is (equation **10**)

$$i_{ab}=\varepsilon she^{\lambda h}[e^{-\mu d_a}/d_a - e^{-\mu d_b}/d_b], \quad \ldots\ldots\ldots\ldots \quad (\mathbf{14})$$

and that to another annulus $c \leqslant \rho \leqslant k$ $(c \geqslant b)$

$$i_{ck}=\varepsilon she^{\lambda h}[e^{-\mu d_c}/d_c - e^{-\mu d_k}/d_k]. \quad \ldots\ldots\ldots\ldots \quad (\mathbf{15})$$

The ratio R of these currents is independent of λ and εs and is a function of the dimensions h, a, b, c, k and of μ. Thus μ may be found by measuring R in an apparatus in which h, a, b, c, and k are known. Particular arrangements are: $a=0$, $b=c$, $k=\infty$; or $a\neq 0$, $b=c$, $k=\infty$. In such cases the formula for R is relatively simple.

Thus by separate measurements (at the same values of Z/p) of $\lambda-\mu$ and of μ, both λ and μ and therefore $\alpha_i=(\lambda^2-\mu^2)/2\lambda$ can be found accurately. The mean agitational energy Q of the electrons in the stream is derived from $\lambda=W/2D$. When both α_a and α_i are zero $\alpha=0$ and $\lambda=\mu$, which is the case that is most frequently investigated.

III. The Distribution of Negative Ions

This distribution is to be obtained as a solution of equation (**6**) in which n is distributed within the diffusion chamber according to equation (**9**). A formal solution of equation (**6**) is readily obtained either by the standard methods of potential theory using Green's formulae or from physical considerations as follows.

Let $d\tau$ be an element of volume at the point $P(x,y,z)$ containing $n d\tau$ electrons. This element acts as a point source of negative ions whose strength (rate of emission) is $\alpha_a W n d\tau$. This source therefore contributes to the total concentration N_0 of negative ions at a point $Q(x_0,y_0,z_0)$ an amount

$$dN=(\alpha_a W n d\tau/4\pi D_1)\exp[-\lambda_1\{r_1-(z_0-z)\}]/r_1,$$

where $r_1=[(x_0-x)^2+(y_0-y)^2+(z_0-z)^2]^{\frac{1}{2}}=$distance PQ.

The total concentration N_0 is obtained by integrating over all elementary sources $\alpha_a W n d\tau$ throughout the whole of space, devoid of electrodes, into which the original source of electrons s and its image at $(0,0,h)$ are emitting. Whence,

$$N_0=\frac{\alpha_a W}{4\pi D_1}\int_{\infty}\frac{n\exp[-\lambda_1\{r_1-(z_0-z)\}]d\tau}{r_1}, \quad \ldots\ldots \quad (\mathbf{16})$$

in which n is given by equation (**9**).

Equation (**16**) is the particular solution of equation (**6**) and it gives the distribution of the concentration N_0 of negative ions formed by electron attachment.

To this solution may be added a complementary function of equation (**6**) to allow for a stream of negative ions that may enter the diffusion chamber through the aperture of entry of the electrons. This complementary function is

$$N_c = \frac{C}{4\pi D_1} \frac{\exp\{-\lambda_1(r_0 - z_0)\}}{r_0}, \qquad \ldots\ldots\ldots\ldots \quad (\mathbf{17})$$

where C is the strength of the source and $r_0^2 = x_0^2 + y_0^2 + z_0^2$.

If the point $Q(x_0, y_0, z_0)$ lies on the receiving electrode, the flux of ions to an element of surface $\mathrm{d}S$ containing Q will be taken to be

$$\mathrm{d}I = (N_0 + N_c)W_1\mathrm{d}S = NW_1\mathrm{d}S.$$

When the point Q is sufficiently removed from the axis Oz (i.e. from the centre of the electrode) N_c becomes inappreciable and $N = N_0$.

In practice the receiving electrode would be divided into a central disk $\rho = a$ and two surrounding annular regions $a \leqslant \rho \leqslant b$, $b \leqslant \rho \leqslant \infty$, the radius a of the disk being chosen large enough to ensure that all but an unimportant proportion of the ions in the stream N_c reach the central disk. In order to appreciate the rough order of magnitude of the radius a consider a practical case in which the stream N_c is of the form described in equation (**17**).

According to equation (**14**) the proportion of the current carried by the ions N_c that impinge on the disk $0 \leqslant \rho \leqslant a$ is $(\lambda = \mu = \lambda_1)$

$$R_c = 1 - h\exp\{-\lambda_1(d_a - h)\}/d_a.$$

But for ions, $2\lambda_1 = W_1/D_1 = Z\varepsilon/kT$ (k is Boltzmann's constant, T is the absolute temperature, and ε is the ionic charge).

When $T = 288$ °K, and Z is expressed in volt/cm this relationship reduces to

$$\lambda_1 = 20 \cdot 15Z. \qquad \ldots\ldots\ldots\ldots\ldots\ldots \quad (\mathbf{18})$$

Since $d_a = h(1 + a^2/h^2)^{\frac{1}{2}}$, it follows that

$$\frac{\exp[-20 \cdot 15Zh\{(1 + a^2/h^2)^{\frac{1}{2}} - 1\}]}{(1 + a^2/h^2)^{\frac{1}{2}}} = 1 - R.$$

Suppose, as would be so in practice, that $(a/h)^2 \ll 1$, then the condition becomes

$$a \simeq \{(h/10Z)\ln[1/(1 - R)]\}^{\frac{1}{2}}. \qquad \ldots\ldots\ldots\ldots \quad (\mathbf{19})$$

Suppose $R = 90$ per cent., then $a = 0 \cdot 48(h/Z)^{\frac{1}{2}}$; if $R = 95$ per cent., then $a = 0 \cdot 3(h/Z)^{\frac{1}{2}}$; if $R = 99$ per cent., $a = 0 \cdot 68(h/Z)^{\frac{1}{2}}$.

Take, for instance, $h = 5$ cm, $Z = 10$ V/cm, then for $R = 90$ per cent., $a = 0 \cdot 33$ cm; for $R = 95$ per cent., $a = 0 \cdot 39$ cm.

The stream of electrons spreads, in general much more widely, since for electrons $\lambda = 20 \cdot 15Z(Q_0/Q)$, where Q/Q_0 is the ratio of the agitational energy of an electron to that of the molecules. The formula for a in terms of R now becomes

$$a \simeq \{(hQ/10ZQ_0)\ln[1/(1 - R)]\}^{\frac{1}{2}}. \qquad \ldots\ldots\ldots\ldots \quad (\mathbf{20})$$

Consequently

$$R=90 \text{ per cent., } a=0{\cdot}48(hQ/ZQ_0)^{\frac{1}{2}};$$
$$R=95 \text{ per cent., } a=0{\cdot}3(hQ/ZQ_0)^{\frac{1}{2}}.$$

Let $R=90$ per cent., $h=5$ cm, $Z=10$ V/cm, $Q/Q_0=10$, then $a=1{\cdot}05$ cm, whereas for ions $a=0{\cdot}33$ cm.

It is therefore possible to examine the distribution of electrons n and the ions N in the outer regions of the mixed stream which are virtually uncontaminated by the ions N_c that have entered through the aperture.

Although equation (**16**) provides a formal solution of equation (**6**) it does not lead to a simple formula for the distribution of the ions N formed by the attachment of electrons to molecules from which computations can be made for the measurement of α_a. It is therefore expedient to seek an approximate solution. To this end, advantage is taken of the fact of the disparity between λ for electrons and λ_1 for ions unless $Q/Q_0 \to 1$, as explained above. In many practical situations of interest, the actual spread of the elementary stream of ions arising from a source $\alpha_a W n \mathrm{d}\tau$ is small and these ions impinge on a small area of the electrode about a point whose x,y coordinates are the same as that of the elementary volume $\mathrm{d}\tau$.

Consider a hypothetical case in which the elementary sources are distributed in a plane layer $z=z_1$ with thickness $\mathrm{d}z$ parallel to and at a distance l from the receiving electrode $z=h$ and suppose that n is constant throughout the layer.

Let N be the concentration of ions at a point x,y,h on the electrode and consider what portion of the plane of the sources contributes a specified proportion, say X of the concentration N of ions. The point $O(x,y,z)$ is the point of intersection of the normal to the electrode at (x,y,h) and the layer $z=z_1$.

The contribution of an annular source with centre O, radius ρ, and width $\mathrm{d}\rho$ to N is

$$\frac{2\pi\alpha_a W n \mathrm{d}z}{4\pi D_1} \cdot \frac{\exp\{-\lambda_1(r-l)\}}{r} \cdot \rho \mathrm{d}\rho,$$

where $r^2=\rho^2+l^2$.

Thus the contribution of the circular disk with centre O and radius a is ($\rho\mathrm{d}\rho=r\mathrm{d}r$, $2\lambda_1=W_1/D_1$)

$$\mathrm{d}N=XN=\frac{\alpha_a W n \mathrm{d}z}{2D_1}\exp(\lambda_1 l)\int_l^{(l^2+a^2)^{\frac{1}{2}}}\exp(-\lambda_1 r)\mathrm{d}r$$
$$=\frac{\alpha_a W n \mathrm{d}z}{W_1}\Big\{1-\exp[-\lambda_1\{(l^2+a^2)^{\frac{1}{2}}-l\}]\Big\}.$$

The proportion of the total ionic current $I=\varepsilon W_1 N \mathrm{d}S$ received by an element of area $\mathrm{d}S$ of the electrode that is contributed by the disk with radius a is

$$XI=\varepsilon\alpha_a W n \mathrm{d}z\Big\{1-\exp[-\lambda_1\{(l^2+a^2)^{\frac{1}{2}}-l\}]\Big\}.$$

as $a\to\infty$, $X\to 1$, consequently $I=\varepsilon\alpha W n \mathrm{d}z$. Whence

$$X=1-\exp[-20{\cdot}15Z\{(l^2+a^2)^{\frac{1}{2}}-l\}]. \quad \ldots\ldots\ldots \quad (\mathbf{21})$$

When $a^2/l^2 \ll 1$, the following expression for a is derivable from equation (**21**)

$$a \simeq \{(l/10Z) \ln [1/(1-X)]\}^{\frac{1}{2}}. \qquad \ldots\ldots\ldots\ldots \quad (\mathbf{22})$$

Since equations (**19**) and (**22**) are identical it follows that :

$$X=90 \text{ per cent.}, \quad a=0\cdot48(l/Z)^{\frac{1}{2}}\,;$$
$$X=95 \text{ per cent.}, \quad a=0\cdot3(l/Z)^{\frac{1}{2}}\,;$$
$$X=99 \text{ per cent.}, \quad a=0\cdot68(l/Z)^{\frac{1}{2}}.$$

For instance, if $l=2$ cm, $Z=10$ V/cm, and $X=99$ per cent., then $a=0\cdot30$ cm. The total ionic current to a surface element dS of the electrode is carried in effect by ions that are formed in a small cylinder of the source layer centred on the normal to dS. When n is not uniform, but varies with radial distance, a good approximation to the current to dS is obtained in many cases by supposing that n is distributed uniformly throughout the layer with a value equal to that it possesses on the normal to dS.

It follows that an approximation to the total ionic current to dS when n is distributed throughout the whole of space above the receiving electrode is to be found by integration of n along the normal to dS. The current is JdS, where

$$J=\varepsilon\alpha_a W\int_{-\infty}^{h} n\mathrm{d}z. \qquad \ldots\ldots\ldots\ldots\ldots\ldots \quad (\mathbf{23})$$

This is the solution that is derived from equation (**6**) when the term $\nabla^2 N$ is omitted, that is to say, when ionic diffusion is neglected. In what follows it will be supposed that measurements are made under conditions in which the approximation implied by equation (**23**) is justified.

IV. CALCULATION OF THE TOTAL CURRENT TO AN ANNULUS OF THE ELECTRODE

The total current to an annulus $a \leqslant \rho \leqslant b$ of the electrode is the sum of the electronic current i_{ab} given by equation (**14**) and the ionic current $I_{ab}=\int J\mathrm{d}S$ (equation (**23**)) taken over the surface of the annulus. To this may be added the contribution, if necessary, of the ions N_c.

(*a*) *Ionic Current*

$$I_{ab}=\int J\mathrm{d}S=2\pi\varepsilon\alpha_a W\int_{-\infty}^{h}\int_{a}^{b} n\rho\mathrm{d}\rho\mathrm{d}z. \qquad \ldots\ldots\ldots \quad (\mathbf{24})$$

When the expression for n given in equation (**9**) is used and the integration is carried out with respect to ρ the following expression is obtained :

$$I_{ab}=\frac{\varepsilon\alpha_a s\lambda}{\mu}\int_{-\infty}^{h} \exp(\lambda z)\big[\exp\{-\mu(a^2+z^2)^{\frac{1}{2}}\}-\exp\{-\mu(b^2+z^2)^{\frac{1}{2}}\}$$
$$-\exp\{-\mu[a^2+(2h-z)^2]^{\frac{1}{2}}\}+\exp\{-\mu[b^2+(2h-z)^2]^{\frac{1}{2}}\}\big]\mathrm{d}z, \qquad \ldots \quad (\mathbf{25})$$

whereas, from equation (**14**) the electronic current is

$$i_{ab}=s\varepsilon h e^{\lambda h}[e^{-\mu d_a}/d_a - e^{-\mu d_b}/d_b]. \qquad \ldots\ldots\ldots\ldots \quad (\mathbf{26})$$

The total current εs to the whole electrode should, as a check, be given as the sum, $i_{\text{total}}=i_{0\infty}+I_{0\infty}$ by equations (**25**) and (**26**).

It is easily shown that, when $a=0$, $b=\infty$,

$$i_{\text{total}}=i_{0\infty}+I_{0\infty}=\varepsilon s\left[\mathrm{e}^{-(\mu-\lambda)h}+1-\frac{(\mu+\lambda)}{2\mu}\mathrm{e}^{-(\mu-\lambda)h}-\frac{(\mu-\lambda)}{2\mu}\mathrm{e}^{-(\mu+\lambda)h}\right].$$

Since $\alpha_a \ll \mu$ and λ; $\mu-\lambda=2\lambda\alpha_a/(\mu+\lambda)\simeq\alpha_a$; $\mu\simeq\lambda$; $(\mu+\lambda)h\gg 1$, the quantity in the bracket differs inappreciably from unity and $i_{\text{total}}=\varepsilon s$.

V. Procedures for Measuring α_a

(*a*) *Measurement of* α_a—*First Procedure*

The ratio of the currents to the annulus $a\leqslant\rho\leqslant b$ and to the portions of the electrode $a\leqslant\rho\leqslant\infty$ is (a large enough to eliminate current due to N_c)

$$\begin{aligned}R_1&=(i_{ab}+I_{ab})/(i_{a\infty}+I_{a\infty})\\&=1-(i_{b\infty}+I_{b\infty})/(i_{a\infty}+I_{a\infty})\\&=1-\frac{(h/d_b)\exp\{-\mu h(d_b/h)+\lambda h\}+\lambda h(\alpha_a/\mu)\int_{-\infty}^{1}\exp(\lambda hs)\,.\,B\mathrm{d}s}{(h/d_a)\exp\{-\mu h(d_a/h)+\lambda h\}+\lambda h(\alpha_a/\mu)\int_{-\infty}^{1}\exp(\lambda hs)\,.\,A\mathrm{d}s}\\&=F_1(b/h,\ a/h,\ \lambda h,\ \alpha_a h,\ \lambda/\mu)\ ;\ \ \mu\simeq\lambda+\alpha_a\ ;\ \ d_b^2=b^2+h^2,\ d_a^2=a^2+h^2\ ;\ \ \lambda/\mu\simeq 1,\end{aligned}\quad\ldots\ldots\ldots\ldots\ (\mathbf{27})$$

where $B=\exp\left[-\mu h(b^2/h^2+s^2)^{\frac{1}{2}}\right]-\exp\left[-\mu h\{b^2/h^2+(2-s)^2\}^{\frac{1}{2}}\right]$,
$A=\exp\left[-\mu h(a^2/h^2+s^2)^{\frac{1}{2}}\right]-\exp\left[-\mu h\{a^2/h^2-(2-s)^2\}^{\frac{1}{2}}\right]$.

Thus, if a set of curves is prepared for an apparatus in which a/h and b/h are given, showing R_1 as a function of λh for a range of values of the parameter α_a, then it is possible to measure α_a by measuring R_1 and λ.

An extensive set of such curves has been prepared by Dr. Barbara I. H. Hall and measurements are of α_a to be undertaken in this department.

(*b*) *Measurement of* α_a—*Second Procedure*

A second procedure by which the unknown contribution I_c to the current of the ions N_c may be eliminated, is the following.

The current to the central disk $\rho\leqslant a$ is

$(i_{0a})_{\text{total}}=i_{0a}+I_{0a}+I_c$, which, from equations (**25**) and (**26**), is

$$\begin{aligned}(i_{0a})_{\text{total}}=\varepsilon s\Big[&\exp(\lambda h)\{1-(h/d_a)\exp(-\mu d_a)\}\\&+(\lambda/\mu)\alpha_a h\Big\{\int_0^1\exp[-(\mu-\lambda)hs]\mathrm{d}s+\int_0^\infty\exp[-(\mu+s)hs]\mathrm{d}s\\&-\exp(-2\mu h)\int_{-\infty}^{1}\exp[(\mu+\lambda)hs]\mathrm{d}s-\int_{-\infty}^{1}\exp\left[\lambda hs-\mu h(a^2/h^2+s^2)^{\frac{1}{2}}\right]\\&+\int_{-\infty}^{1}\exp\left[\lambda hs-\mu h\{a^2/h^2+(2-s)^2\}^{\frac{1}{2}}\right]\mathrm{d}s\Big\}\Big]+I_c.\end{aligned}\quad\ldots\ldots\ldots\ (\mathbf{28})$$

Consider three distances h_1, h_2, and h_3 and let i_1, i_2, i_3 be the corresponding values of $(i_{0a})_{\text{total}}$ in an apparatus with a movable electrode.

The values of $(i_1 - I_c)$, $(i_2 - I_c)$, and $(i_3 - I_c)$ can then be calculated for given values of α_a, λ, and a.

Each typical current $(i_k - I_c)$ can be expressed as a function $f_k(a/h_k, \lambda h_k, \alpha_a h, \lambda - \mu)$ which can be represented by a family of curves in which f_k is shown as a function of λh_k for a range of values of the parameter α_a.

The ratio

$$R_2 = (i_1 - i_2)/(i_2 - i_3) = (f_1 - f_2)/(f_2 - f_3)$$

is independent of I_c and can be measured.

The ratio R_2, in an apparatus in which h_1, h_2, h_3 and a are given, is a function $F_2(\lambda, \alpha_a)$. Thus, from the curves for f_1, f_2, f_3, those showing R as a function of λ for a range of values of α_a can be constructed, and λ and α_a can be measured.

VI. THE EFFECT OF A TRANSVERSE MAGNETIC FIELD

Studies of the behaviour of a stream of electrons moving under the combined action of an electric field Z and a magnetic field B provide additional information about the motions of electrons in gases.

It is therefore of interest to attempt an extension of the theory to include the effects of ionization by collision and of electron attachment.

Let the source of electrons be a small aperture (or a short slot) at the origin of coordinates. Let the axis Oz be antiparallel to Z and suppose that the magnetic field B is transverse to Z and parallel to Oy. Let the components of the drift speed of electrons be W_z and W_x, that of the ions being $W_{1z} = W_1$ as before.

The coefficients of diffusion of electrons are D parallel to Oy and D_B in directions perpendicular to Oy.

The equation (3) of continuity for the electronic concentration in a steady stream now becomes

$$\frac{dn}{dt} = D_B \frac{\partial^2 n}{\partial x^2} + \frac{\partial^2 n}{\partial z^2} + D \frac{\partial^2 n}{\partial y^2} - \vec{W} \cdot \operatorname{grad} n - (\overline{f\nu} - \overline{g\nu})n = 0. \quad .. \ (29)$$

The variable y is eliminated by introducing in place of n the quantity $q = \int_{-\infty}^{\infty} n dy$. Integrate equation (29) with respect to y between the limits $+\infty$ and $-\infty$ and suppose that n and its derivatives have vanished at the lateral boundaries of the diffusion chamber. It follows that

$$D_B \frac{\partial^2 q}{\partial x^2} + \frac{d^2 q}{\partial z^2} - W_x \frac{\partial q}{\partial x} - W_z \frac{\partial q}{\partial z} - \alpha W_z q = 0,$$

that is,

$$\frac{\partial^2 q}{\partial x^2} + \frac{\partial^2 q}{\partial z^2} = 2\beta \frac{\partial q}{\partial x} + 2\gamma \frac{\partial q}{\partial z} + 2\gamma \alpha q, \quad \ldots\ldots\ldots\ldots \ (30)$$

where

$$2\beta = W_x/D_B,\ 2\gamma = W_z/D_B,\ \text{and}\ \alpha W_z = (\overline{f\nu} - \overline{g\nu}) = (\alpha_a - \alpha_i)W_z.$$

In equation (**30**) write $q = e^{\beta x + \gamma z}V$ to obtain

$$\frac{\partial^2 V}{\partial x^2} + \frac{\partial^2 V}{\partial z^2} = (\beta^2 + \gamma^2 + 2\gamma\alpha)V = \chi^2 V. \quad \ldots\ldots\ldots\ldots \quad (\mathbf{31})$$

Solutions of equation (**30**) are sought in which q is the two-dimensional concentration of electrons per unit length from an equivalent simple line source along the axis Oy. The appropriate solution of equation (**31**) is $V = A\mathrm{K}_0(\chi r)$ where A is a constant and K_0 is the modified Bessel function of the second kind and of zero order.

If s is the rate of emission of electrons per unit length of the equivalent line source it may be shown from the property $\mathrm{K}_0(v) \to -\log v,\ v \to 0$, that the solution of equation (**31**) that is sought is

$$q = (s/2\pi D_B)e^{\beta x + \gamma z}\mathrm{K}_0(\chi r), \quad \ldots\ldots\ldots\ldots\ldots \quad (\mathbf{32})$$

where $r^2 = x^2 + y^2$.

The solution that gives $q = 0$ over the receiving electrode $z = h$ is obtained by adding an image source at $(0,0,2h)$, that is,

$$q = (s/2\pi D_B)e^{\beta x + \gamma z}[\mathrm{K}_0(r) - \mathrm{K}_0(r')], \quad \ldots\ldots\ldots \quad (\mathbf{33})$$

where $r'^2 = x^2 + (2h - z)^2$.

It follows from equation (**33**) that

$$\frac{\partial q}{\partial z} = \frac{s}{2\pi D_B}\left[\gamma q + e^{\beta x + \gamma z}\left\{\frac{z}{r} \cdot \frac{\mathrm{d}}{\mathrm{d}r}\mathrm{K}_0(\chi r) + \frac{(2h - z)}{r'} \cdot \frac{\mathrm{d}}{\mathrm{d}r'}\mathrm{K}_0(\chi r')\right\}\right],$$

whence

$$(\partial q/\partial z)_{z=h} = -(s/2\pi D_B)e^{\beta x + \gamma h}2\chi h\mathrm{K}_1\{\chi(h^2 + x^2)^{\frac{1}{2}}\}/(h^2 + x^2)^{\frac{1}{2}}.$$

The current received by a strip of the electrode with width $a \leqslant x \leqslant b$ whose edges are parallel to Oy is

$$\begin{aligned} i_{ab} &= -\varepsilon D_B \int_a^b \left(\frac{\partial q}{\partial z}\right)_{z=h} \mathrm{d}x \\ &= \frac{\varepsilon s \chi h e^{\gamma h}}{\pi} \int_a^b \frac{e^{\beta x}\mathrm{K}_1\{\chi(h^2 + x^2)^{\frac{1}{2}}\}\mathrm{d}x}{(h^2 + x^2)^{\frac{1}{2}}} \\ &= \frac{\varepsilon s \chi h e^{\gamma h}}{\pi} \int_{a/h}^{b/h} \frac{e^{\beta h s}\mathrm{K}_1\{\chi h(1 + s^2)^{\frac{1}{2}}\}\mathrm{d}s}{(1 + s^2)^{\frac{1}{2}}}. \quad \ldots\ldots\ldots \quad (\mathbf{34}) \end{aligned}$$

The total current carried by electrons to the electrode is obtained by extending the limits of integration in equation (**34**) to $\pm\infty$. Thus,

$$\begin{aligned} i_{\text{total}} = i_{-\infty,\,\infty} &= \frac{2\varepsilon s \chi h \exp(\gamma h)}{\pi} \int_0^\infty \frac{\cosh \beta x \,.\, \mathrm{K}_1\{\chi(h^2 + x^2)^{\frac{1}{2}}\}\mathrm{d}x}{(h^2 + x^2)^{\frac{1}{2}}} \\ &= \frac{\varepsilon s \chi h}{\pi} \cdot \frac{\pi}{\chi h} \exp(\gamma h) \,.\, \exp\{-h(\chi^2 + \beta^2)^{\frac{1}{2}}\} \\ &= \varepsilon s \exp\{\gamma - (\gamma^2 + 2\gamma\alpha)^{\frac{1}{2}}h\}. \end{aligned}$$

But $\alpha \ll \gamma$, consequently $\gamma^2+2\gamma\alpha=(\gamma+\alpha)^2-\alpha^2 \simeq (\gamma+\alpha)^2$ and

$$i_{\text{total}}=\varepsilon s \exp(-\alpha h)=i_0 \exp(-\alpha h)=i_0 \exp\{-(\alpha_a-\alpha_i)h\}, \quad .. \ \textbf{(35)}$$

in agreement with equation (**12**) except that here $\alpha=(\overline{f\nu}-\overline{g\nu})/W_z$ whereas in equation (**12**) $\alpha=(\overline{f\nu}-\overline{g\nu})/W$. However, W_z does not usually differ significantly from W in practice.

(*a*) *Distribution of Negative Ions*

Equation (**6**) now becomes

$$\frac{\partial^2 N}{\partial x^2}+\frac{\partial^2 N}{\partial y^2}+\frac{\partial^2 N}{\partial z^2}=2\lambda_1\frac{\partial N}{\partial z}-(\alpha_a W_z/D_1)n.$$

Put $Q=\int_{-\infty}^{\infty} N\mathrm{d}y$ and integrate N in the equation with respect to y to obtain, as before,

$$\frac{\partial^2 Q}{\partial x^2}+\frac{\partial^2 Q}{\partial z^2}=2\lambda_1\frac{\partial Q}{\partial z}-(\alpha_a W_z/D_1)q,$$

with the formal particular solution, for the value Q_0 of Q at (x_0,y_0,z_0),

$$Q_0=(\alpha_a W_z/2\pi D_1)\int_{\infty} q\mathrm{e}^{\lambda_1(z_0-z)}\mathrm{K}_0(\lambda_1 r_1)\mathrm{d}\tau, \quad \ldots\ldots \ \textbf{(36)}$$

in which q is given in equation (**33**) and $r_1^2=(x_0-x)^2+(y_0-y)^2+(z_0-z)^2$.

As before, the general solution is intractable and the approximate solution

$$(N)_{z=h}=(\alpha_a W_z/2\lambda_1 D_1)\int_{-\infty}^{h} q\mathrm{d}z=(\alpha_a W_z/W_1)\int_{-\infty}^{h} q\mathrm{d}z$$

is adopted.

The ionic current to the strip $a \leqslant x \leqslant b$ is therefore

$$\begin{aligned} I_{ab} &= \varepsilon\alpha_a W_z\int_{-\infty}^{h}\int_a^b q\mathrm{d}z\mathrm{d}x \\ &= \frac{\varepsilon s\alpha_a W_z}{2\pi D_B}\int_{-\infty}^{h}\int_a^b \mathrm{e}^{\beta x+\gamma z}[\mathrm{K}_0(\chi r)-\mathrm{K}_0(\chi r')]\mathrm{d}z\mathrm{d}x, \end{aligned}$$

where $r^2=x^2+z^2$, $r'^2=x^2+(2h-z)^2$.

Thus, the total current to the strip is

$$\begin{aligned} (i_{ab})_{\text{total}}=\varepsilon s\Bigg[&\frac{h\chi\mathrm{e}^{\gamma h}}{\pi}\int_a^b \frac{\mathrm{e}^{\beta x}\mathrm{K}_1\{\chi(h^2+x^2)^{\frac{1}{2}}\}\mathrm{d}x}{(h^2+x^2)^{\frac{1}{2}}} \\ &+I_c+\frac{\alpha_a W_z}{2\pi D_B}\int_{-\infty}^{h}\int_a^b \mathrm{e}^{\beta x+\gamma z}\{\mathrm{K}_0(\chi r)-\mathrm{K}_0(\chi r')\}\mathrm{d}z\mathrm{d}x\Bigg], \end{aligned}$$

$$\ldots\ldots\ldots\ldots\ldots\ldots \ \textbf{(37)}$$

where, as before, I_c is the current from ions entering through the aperture, and $\chi^2=\beta^2+\gamma^2+2\gamma\alpha$, $\gamma=W_z/2D_B$.

The procedures for measuring α_a described in Section IV become inaccurate or inapplicable in conditions where the spread of the stream of electrons does not differ greatly from that of the ions N_c, that is to say when $\lambda \rightarrow \lambda_1$. However, by the application of a transverse magnetic field the stream of electrons is deflected from that of the ions N_c, consequently, methods for measuring α_a based upon the analyses of this section should prove useful under conditions where $\lambda \rightarrow \lambda_1$.

VII. APPROXIMATIONS

When the receiving annulus or strip is narrow then approximate values of integrals such as those appearing in equations (27) and (34) may be found as the product of the range of integration and the value of the integrand at the centre of the range. Also the lower limit $-\infty$ of integrals such as those in equation (28) may be replaced by the physically more correct value of zero, with little error. These changes greatly simplify the computations.

VIII. ACKNOWLEDGMENTS

The author is indebted to Drs. R. W. Crompton, C. A. Hurst, B. I. H. Hall, and R. H. Healey for discussions on the subject matter of this paper.

IX. REFERENCES

Crompton, R. W., and Huxley, L. G. H. (1955).—*Proc. Phys. Soc.* B **68** : 381.

Crompton, R. W., Huxley, L. G. H., and Sutton, D. J. (1953).—*Proc. Roy. Soc.* A **218** : 507.

Healey, R. H., and Reed, J. W. (1941).—" The Behaviour of Slow Electrons in Gases." (Amalgamated Wireless (Australasia) Ltd. : Sydney.)

Huxley, L. G. H. (1957).—*Aust. J. Phys.* **10** : 118.

Huxley, L. G. H., and Zaazou, A. A. (1949).—*Proc. Roy. Soc.* A **196** : 402.

Loeb, L. B. (1955).—" Basic Processes of Gaseous Electronics." (University of California Press.)

Townsend, J. S. (1947).—" Electrons in Gases." (Hutchinson : London.)

THE SHAPE OF SPECTRAL LINES: TABLES OF THE VOIGT PROFILE

$$\frac{a}{\pi}\int_{-\infty}^{\infty}\frac{\mathrm{e}^{-y^2}\mathrm{d}y}{a^2+(v-y)^2}$$

By D. W. Posener*

[*Manuscript received February* 3, 1959]

Summary

A brief discussion is given of some methods of computing the line shape, commonly known as the *Voigt profile*, resulting when a spectral line is broadened simultaneously by Gaussian and Lorentz effects, and tables and curves are presented for representative values of the variables.

I. Introduction

When the broadening of a spectral line is due to contributions from a Gaussian shape (e.g. Doppler effect) and from an independent Lorentz shape (e.g. natural line width), the resulting intensity distribution may be expressed by (Mitchell and Zemansky 1934, pp. 97, 160)

$$H(a,v)=\frac{a}{\pi}\int_{-\infty}^{\infty}\frac{\mathrm{e}^{-y^2}\mathrm{d}y}{a^2+(v-y)^2}. \quad \ldots\ldots\ldots\ldots \quad (\mathbf{1a})$$

Here $v=(\nu-\nu_0)/\frac{1}{2}\Delta\nu'_G$ and is the distance from the line centre ν_0 in units of $\frac{1}{2}\Delta\nu'_G$; $\Delta\nu'_G=(\ln 2)^{-\frac{1}{2}}\Delta\nu_G$, where $\Delta\nu_G$ is the Gauss half-width (in frequency units) that the line would have if no Lorentz effect were present; and $a=\Delta\nu_L/\Delta\nu'_G$, where $\Delta\nu_L$ is the Lorentz half-width.

Alternatively, $H(a,v)$ can be related to the error function of a complex variable through (Born 1933, p. 483; Harris 1948)

$$H(a,v)=2\pi^{-\frac{1}{2}}\mathrm{Re}\left\{\mathrm{e}^{z^2}\int_{z}^{\infty}\mathrm{e}^{-t^2}\mathrm{d}t\right\}, \quad \ldots\ldots\ldots\ldots \quad (\mathbf{1b})$$

where $z=a+\mathrm{i}v$.

In the common case of a line broadened by Doppler and collision effects the two processes are not independent (Mitchell and Zemansky 1934, p. 160), but it appears that even in this event the use of equation (**1**) is a sufficiently good approximation for most purposes.

In some cases, $H(a,v)$ may also be used to approximate to the measured intensity distribution when the influence of the observing apparatus has to be taken into account (Dennison 1928; van de Hulst 1946; van de Hulst and Reesinck 1947).

The intensity distribution (**1**) is commonly called by astrophysicists a *Voigt profile* because of the original discussion of this effect by Voigt (1912). Its application to the solution of a number of practical problems has been well discussed in an important paper by van de Hulst and Reesinck (1947).

---

* Division of Electrotechnology, C.S.I.R.O., University Grounds, Chippendale, N.S.W.

II. Numerical Evaluation of the Integral

The numerical evaluation of $H(a,v)$ over the whole range of the variables presents some difficulties.

Zemansky (1930) has described a series expansion, due to T. H. Gronwall, which works well for small v and a, and he has tabulated $H(a,v)$ for $a=0\cdot5$, 1, and $1\cdot5$, for different ranges of v; these tables have been extended by Mitchell and Zemansky (1934, p. 328), and the values therein have now been checked and found to be substantially correct. Examination of the formula used shows that the largest term to contribute to the sum occurs when the summation index n equals v^2, so it is apparent that the calculation becomes rather unwieldy for large v. To illustrate, for small a and for $v=24$ the only terms which contributed to 1 part in 10^7 were found to be those for $n=483$ to 651, and the answer was then correct to only 1 part in 10^6 because of truncation errors. Further, for values of a greater than about 4, the recurrence formula for $I_n(a)$ given by Zemansky (1930) breaks down in practice after a very few terms because a small error in the initial term is rapidly propagated and magnified. Even if the recurrence relation is replaced by the equivalent series it is found that this is asymptotic (see, for example, Bromwich 1949, p. 332) and in fact becomes divergent for large enough n. Thus Zemansky's series is usable only for values of a less than about four.

An alternative expansion of equation (**1a**), due to Dr. D. G. Lampard (personal communication), runs as follows:

$$\begin{aligned} H(a,v) &= \frac{1}{\pi a}\int_{-\infty}^{\infty}\frac{\mathrm{e}^{-y^2}\mathrm{d}y}{1+\{(y-v)/a\}^2} \\ &= \frac{1}{\pi a}\sum_{n=0}^{s-1}\frac{1}{a^{2n}}\int_{-\infty}^{\infty}(-\mathrm{i}v+\mathrm{i}y)^{2n}\,\mathrm{e}^{-y^2}\mathrm{d}y+R_s \\ &= \frac{1}{\pi^{\frac{1}{2}}a}\sum_{n=0}^{s-1}\frac{H_{2n}(-\mathrm{i}v)}{(2a)^{2n}}+R_s, \qquad \ldots\ldots\ldots\ldots\ldots\ldots\ldots \quad (\mathbf{2}) \end{aligned}$$

where the series is obtained on long division by the denominator, and the integral representation of the Hermite polynomials (Morse and Feshbach 1953, p. 786) has been used. The remainder R_s is given by

$$R_s=\frac{1}{\pi a}\int_{-\infty}^{\infty}\frac{[\mathrm{i}(y-v)/a]^{2s}\mathrm{e}^{-y^2}\mathrm{d}y}{1+\{(y-v)/a\}^2},$$

so that

$$|R_s|<\left|\frac{1}{\pi^{\frac{1}{2}}a}\cdot\frac{H_{2s}(-\mathrm{i}v)}{(2a)^{2s}}\right|.$$

However,

$$\frac{H_{2n}(-\mathrm{i}v)}{(2a)^{2n}}=\mathrm{i}^{2n}\left\{\left(\frac{v}{a}\right)^{2n}+\ldots+\frac{1\cdot3\ \ldots\ (2n-1)}{2^n}\cdot\frac{1}{a^{2n}}\right\},$$

so when the series (**2**) is not divergent it is asymptotic, and its usefulness depends on the values of v/a and a. It is found that sufficient accuracy is obtainable if $a\geqslant4$, provided $v/a\leqslant\frac{1}{2}$.

Born (1933, p. 482) has given series expansions of equation (**1b**) for large and small values of v/a, and has essentially tabulated $H(a,v)$ for $a=0\cdot5$, 1, 2, and

10, with $v/a=0(0\cdot2)4$. In the present work the range of applicability of his series has not been investigated, but the numerical values of his tables have been checked by other methods and found to be substantially correct, except for $a=0\cdot5$, where for $v/a\geqslant2\cdot0$ the tabulated values are systematically too large.

For astrophysical purposes only small values of a seem to have been of interest, and Hjerting (1938) has discussed calculations in this region and has given tables of $H(a,v)$ for $v=0(0\cdot25)5$ and $a=0(0\cdot01)0\cdot2(0\cdot1)0\cdot5$; his values for $a=0\cdot1$, $0\cdot2$, and $0\cdot5$ have now been checked by other methods and found correct.

Harris (1948) has given the coefficients in a Taylor series expansion of equation (**1b**) also for small a, but usable for larger values of v than available with Hjerting's formula.

The present study has been undertaken in connexion with another problem, for which it was found that published methods of computation were unsuitable and that existing tables of $H(a,v)$ were inadequate.

For the numerical integration of equation (**1a**), a standard method* of numerical analysis is the use of Gauss-Hermite quadrature (Kopal 1955):

$$\int_{-\infty}^{\infty} \mathrm{e}^{-y^2}f(y)\mathrm{d}y=\sum_{j=1}^{n} H_j f(a_j)+R_n, \qquad \ldots\ldots\ldots\ldots \quad (\mathbf{3})$$

with the quantities H_j and a_j given by Kopal (1955) for n up to 20. Essentially, the method involves approximating $f(y)$ by a suitable polynomial; difficulty in its use lies in the estimation of the remainder R_n in those cases, such as the present, where it is not known to vanish.

A contribution of the present work is to report that for $n=20$ the integral $H(a,v)$, as given by equation (**1a**), may be conveniently and accurately evaluated by Gauss-Hermite quadrature except for simultaneously small values of v and a. The error involved in using equation (**3**) has been determined by comparison of the results obtained by it with those computed by the Zemansky and Lampard series expansions in their ranges of usefulness, and with Born's tabulated values for $a=10$ and v up to 40. The general agreement is such as to justify extrapolation to those regions in which the above series expansions cannot be used.

Figure 1 shows the *maximum* percentage error in $H(a,v)$ computed by means of equation (**3**) when $n=20$; for very small a (e.g. $0\cdot01$) the error is particularly large for values of v at or very near to the Hermite polynomial roots a_j. For practical reasons the last two pairs of H_j and $|\,a_j\,|$ were not used; their omission does not affect the results of this work to the accuracies quoted, but causes the curves in Figure 1 to level off in the vicinity of $0\cdot0001$ per cent. Neglect of the next last two pairs introduces tails on these curves levelling off around $0\cdot001$ per cent.

Figure 2, derived from the curves of Figure 1, indicates the regions of usefulness of equation (**3**) for given error limits.

The quantity w, which is the effective half-width in units of $\Delta\nu_G'$ and is defined by $H(a,w)=\frac{1}{2}H(a,0)$, is shown in Figure 3; it can be roughly approximated by $w \sim (1+a^2)^{\frac{1}{2}}$ over most of its range.* Rather better approximations have been given by Burger and van Cittert (1927) and graphically summarized by Minkowski and Bruck (1935), in fair agreement with the present results which were obtained by a method of successive approximations.

---

* The author is indebted to Dr. J. M. Bennett, of the Adolph Basser Computing Laboratory, for telling him of this method.

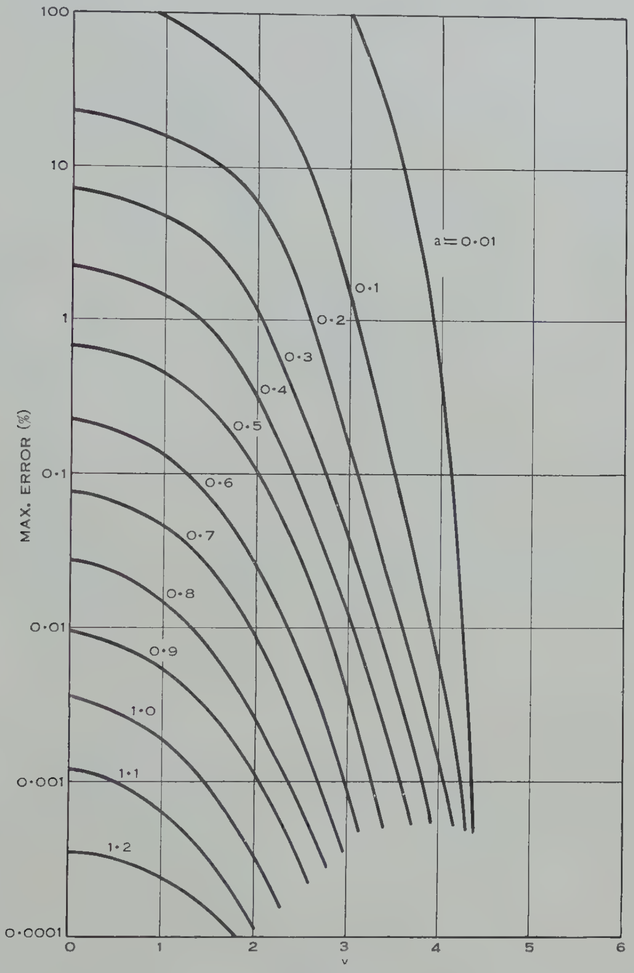

Fig. 1.—Maximum percentage error in $H(a,v)$ computed by Gauss-Hermite quadrature (equation (**3**)).

III. Tabulation

Apart from the cases $a=0$ and $a=\infty$, Table 1 was constructed using Zemansky's series for $v<5-2a$ if $a<1\cdot2$, and Gauss-Hermite quadrature elsewhere; for $a<1\cdot2$, $H(a,0)$ was calculated by a polynomial approximation (Hastings 1955, pp. 42, 169), although it can be obtained from tables of the error function. The values tabulated in Table 1 have errors of less than one unit

---

* Danos and Geschwind (1953) give $\Delta\nu_{\text{eff.}} \sim (\Delta\nu_G^2+\Delta\nu_L^2)^{\frac{1}{2}}$, or, in the present notation, $w \sim (\ln 2+a^2)^{\frac{1}{2}}$, an approximation which is adequate for many purposes.

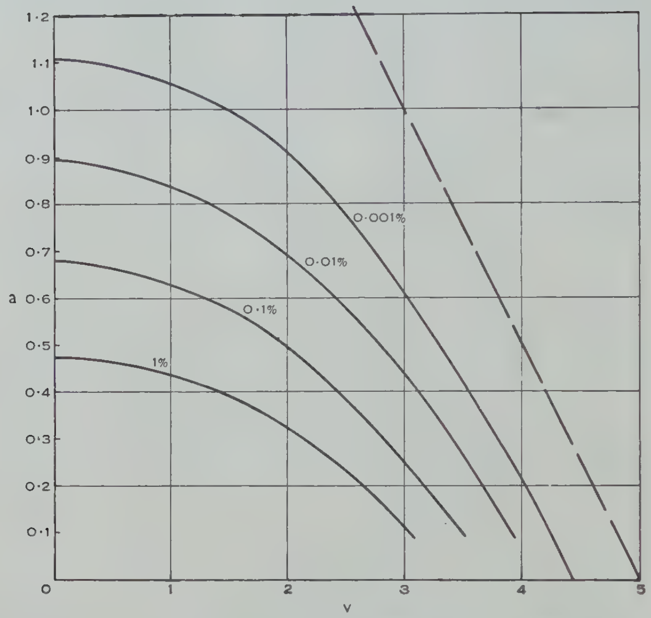

Fig. 2.—Regions of usefulness of Gauss-Hermite quadrature for given error limits. The dashed lines $v=5-2a$, $a=1\cdot2$, separate the regions in which different methods were used for the computation of Table 1.

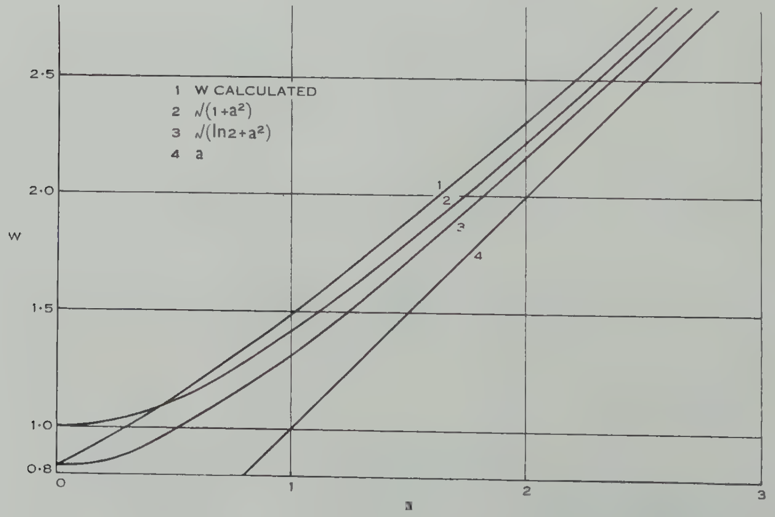

Fig. 3.—The quantity w as a function of a, compared with various approximations and with the line $w=a$.

in the last place (due mainly to round-off), and have been given to five decimal places—more than adequate for most line shape problems—because of the possibility that to this accuracy the integral may be of use in other fields.

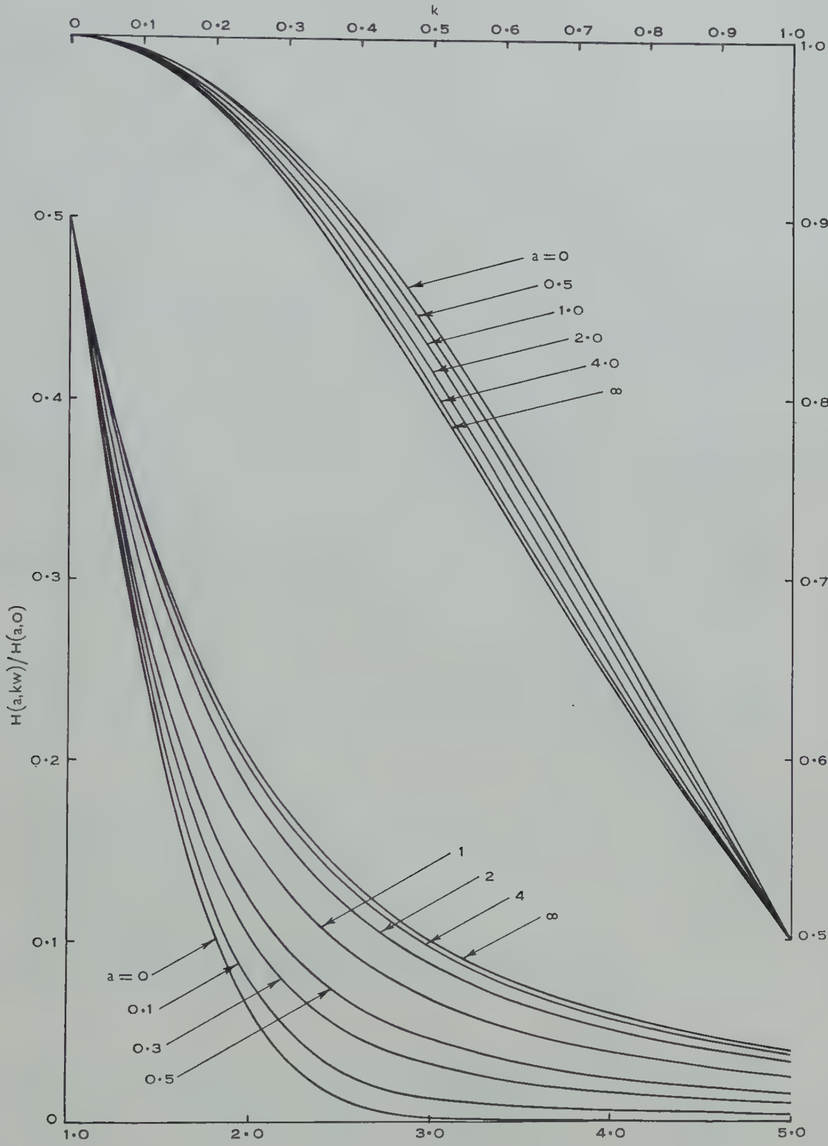

Fig. 4.—Values of the function $H(a,kw)/H(a,0)$ for representative values of a.

In preference to listing $H(a,v)$ directly, the table shows, for each value of a, the quantities $H(a,0)$ and w, and tabulates the normalized profiles at multiples k of the effective half-width w, i.e. lists $H(a,kw)/H(a,0)$ for selected values of k in the range 0–20. The values of a were chosen in an attempt to cover the region fairly evenly, but with a bias to small a (<1) where the calculations are rather

TABLE 1

VALUES OF $H(a,kw)/H(a,0)$

a	0·00	0·01	0·02	0·03	0·04	0·05	0·06	0·07	0·08	0·09
$H(a,0)$	1·00000	0·98882	0·97783	0·96703	0·95642	0·94599	0·93574	0·92567	0·91576	0·90603
w	0·83255	0·83789	0·84326	0·84865	0·85407	0·85952	0·86500	0·87050	0·87603	0·88158
k										
0·0	1·00000	1·00000	1·00000	1·00000	1·00000	1·00000	1·00000	1·00000	1·00000	1·00000
0·1	0·99309	0·99308	0·99307	0·99306	0·99305	0·99304	0·99303	0·99302	0·99301	0·99300
0·2	0·97265	0·97262	0·97258	0·97254	0·97250	0·97246	0·97242	0·97238	0·97234	0·97230
0·3	0·93952	0·93944	0·93936	0·93928	0·93920	0·93911	0·93903	0·93895	0·93887	0·93878
0·4	0·89503	0·89490	0·89477	0·89464	0·89451	0·89438	0·89425	0·89412	0·89399	0·89386
0·5	0·84090	0·84073	0·84055	0·84038	0·84021	0·84004	0·83987	0·83970	0·83952	0·83935
0·6	0·77916	0·77897	0·77877	0·77857	0·77837	0·77817	0·77798	0·77778	0·77758	0·77738
0·7	0·71203	0·71183	0·71163	0·71143	0·71123	0·71103	0·71083	0·71063	0·71043	0·71023
0·8	0·64171	0·64154	0·64137	0·64120	0·64104	0·64087	0·64070	0·64053	0·64036	0·64019
0·9	0·57038	0·57028	0·57018	0·57007	0·56997	0·56987	0·56976	0·56966	0·56956	0·56946
1·0	0·50000	0·50000	0·50000	0·50000	0·50000	0·50000	0·50000	0·50000	0·50000	0·50000
1·1	0·43227	0·43241	0·43254	0·43268	0·43281	0·43295	0·43309	0·43322	0·43336	0·43349
1·2	0·36857	0·36887	0·36917	0·36947	0·36977	0·37007	0·37036	0·37066	0·37095	0·37125
1·3	0·30993	0·31041	0·31090	0·31138	0·31186	0·31234	0·31281	0·31329	0·31376	0·31423
1·4	0·25703	0·25771	0·25839	0·25906	0·25973	0·26040	0·26106	0·26172	0·26238	0·26303
1·5	0·21022	0·21110	0·21197	0·21283	0·21369	0·21454	0·21539	0·21624	0·21707	0·21791
1·6	0·16958	0·17063	0·17168	0·17272	0·17376	0·17479	0·17581	0·17683	0·17784	0·17884
1·7	0·13490	0·13612	0·13734	0·13854	0·13973	0·14092	0·14210	0·14326	0·14442	0·14557
1·8	0·10584	0·10720	0·10855	0·10989	0·11122	0·11254	0·11384	0·11514	0·11642	0·11769
1·9	0·08190	0·08337	0·08483	0·08627	0·08770	0·08912	0·09053	0·09192	0·09330	0·09466
2·0	0·06250	0·06405	0·06559	0·06710	0·06861	0·07010	0·07157	0·07303	0·07448	0·07591
2·2	0·03492	0·03653	0·03813	0·03971	0·04127	0·04282	0·04434	0·04585	0·04734	0·04882
2·4	0·01845	0·02003	0·02159	0·02313	0·02465	0·02615	0·02763	0·02910	0·03054	0·03197
2·6	0·00923	0·01069	0·01214	0·01357	0·01499	0·01638	0·01776	0·01911	0·02045	0·02177
2·8	0·00436	0·00569	0·00699	0·00828	0·00955	0·01080	0·01204	0·01326	0·01446	0·01565
3·0	0·00195	0·00312	0·00427	0·00540	0·00652	0·00763	0·00872	0·00980	0·01086	0·01191
3·2	0·00083	0·00184	0·00285	0·00384	0·00481	0·00578	0·00674	0·00768	0·00861	0·00953
3·4	0·00033	0·00121	0·00209	0·00295	0·00380	0·00465	0·00548	0·00631	0·00712	0·00793
3·6	0·00013	0·00090	0·00166	0·00241	0·00316	0·00390	0·00463	0·00535	0·00607	0·00678
3·8	0·00004	0·00072	0·00139	0·00205	0·00271	0·00336	0·00401	0·00465	0·00528	0·00590
4·0	0·00002	0·00061	0·00121	0·00179	0·00238	0·00295	0·00353	0·00409	0·00466	0·00521
4·2	0·00000	0·00054	0·00107	0·00159	0·00211	0·00263	0·00314	0·00365	0·00415	0·00465
4·4	0·00000	0·00048	0·00095	0·00143	0·00189	0·00236	0·00282	0·00327	0·00373	0·00418
4·6	0·00000	0·00043	0·00086	0·00129	0·00171	0·00213	0·00255	0·00296	0·00337	0·00378
4·8	0·00000	0·00039	0·00078	0·00117	0·00155	0·00194	0·00231	0·00269	0·00307	0·00344
5·0	0·00000	0·00036	0·00071	0·00107	0·00142	0·00177	0·00211	0·00246	0·00280	0·00314
5·5	0·00000	0·00029	0·00058	0·00087	0·00115	0·00144	0·00172	0·00200	0·00228	0·00255
6·0	0·00000	0·00024	0·00048	0·00072	0·00096	0·00119	0·00143	0·00166	0·00189	0·00212
6·5	0·00000	0·00020	0·00041	0·00061	0·00081	0·00101	0·00120	0·00140	0·00160	0·00179
7·0	0·00000	0·00017	0·00035	0·00052	0·00069	0·00086	0·00103	0·00120	0·00137	0·00153
8·0	0·00000	0·00013	0·00026	0·00039	0·00052	0·00065	0·00078	0·00091	0·00104	0·00116
9·0	0·00000	0·00010	0·00021	0·00031	0·00041	0·00051	0·00061	0·00071	0·00081	0·00091
10·0	0·00000	0·00008	0·00017	0·00025	0·00033	0·00041	0·00049	0·00057	0·00066	0·00074
12·0	0·00000	0·00006	0·00011	0·00017	0·00023	0·00028	0·00034	0·00040	0·00045	0·00051
15·0	0·00000	0·00004	0·00007	0·00011	0·00015	0·00018	0·00022	0·00025	0·00029	0·00032
20·0	0·00000	0·00002	0·00004	0·00006	0·00008	0·00010	0·00012	0·00014	0·00016	0·00018

TABLE 1 (*Continued*)

a	0·10	0·12	0·14	0·16	0·18	0·20	0·22	0·24	0·26	0·28
$H(a,0)$	0·89646	0·87779	0·85974	0·84228	0·82538	0·80902	0·79318	0·77784	0·76297	0·74857
w	0·88716	0·89841	0·90976	0·92121	0·93278	0·94444	0·95621	0·96809	0·98007	0·99215
k										
0·0	1·00000	1·00000	1·00000	1·00000	1·00000	1·00000	1·00000	1·00000	1·00000	1·00000
0·1	0·99299	0·99297	0·99295	0·99292	0·99290	0·99288	0·99286	0·99284	0·99282	0·99280
0·2	0·97226	0·97218	0·97210	0·97202	0·97194	0·97185	0·97177	0·97169	0·97161	0·97153
0·3	0·93870	0·93853	0·93837	0·93820	0·93803	0·93786	0·93770	0·93753	0·93736	0·93719
0·4	0·89373	0·89347	0·89320	0·89294	0·89268	0·89242	0·89215	0·89189	0·89162	0·89136
0·5	0·83918	0·83883	0·83849	0·83814	0·83779	0·83745	0·83710	0·83675	0·83640	0·83606
0·6	0·77718	0·77678	0·77639	0·77599	0·77559	0·77519	0·77479	0·77440	0·77400	0·77360
0·7	0·71003	0·70963	0·70923	0·70883	0·70843	0·70803	0·70764	0·70724	0·70685	0·70645
0·8	0·64002	0·63968	0·63935	0·63901	0·63868	0·63834	0·63801	0·63768	0·63735	0·63702
0·9	0·56936	0·56915	0·56895	0·56875	0·56855	0·56834	0·56814	0·56795	0·56775	0·56755
1·0	0·50000	0·50000	0·50000	0·50000	0·50000	0·50000	0·50000	0·50000	0·50000	0·50000
1·1	0·43362	0·43389	0·43415	0·43442	0·43468	0·43494	0·43520	0·43545	0·43571	0·43596
1·2	0·37154	0·37212	0·37270	0·37328	0·37384	0·37441	0·37497	0·37552	0·37607	0·37661
1·3	0·31470	0·31563	0·31655	0·31746	0·31837	0·31926	0·32014	0·32102	0·32188	0·32273
1·4	0·26368	0·26497	0·26625	0·26751	0·26875	0·26998	0·27120	0·27239	0·27358	0·27474
1·5	0·21874	0·22038	0·22200	0·22359	0·22517	0·22672	0·22826	0·22977	0·23125	0·23272
1·6	0·17983	0·18180	0·18374	0·18564	0·18752	0·18937	0·19119	0·19298	0·19474	0·19647
1·7	0·14671	0·14896	0·15118	0·15336	0·15550	0·15760	0·15967	0·16170	0·16369	0·16564
1·8	0·11895	0·12144	0·12388	0·12628	0·12863	0·13094	0·13320	0·13542	0·13759	0·13972
1·9	0·09602	0·09868	0·10129	0·10385	0·10636	0·10882	0·11123	0·11358	0·11589	0·11814
2·0	0·07732	0·08011	0·08283	0·08550	0·08811	0·09067	0·09316	0·09560	0·09799	0·10032
2·2	0·05028	0·05314	0·05593	0·05866	0·06133	0·06393	0·06646	0·06893	0·07135	0·07370
2·4	0·03338	0·03615	0·03884	0·04147	0·04403	0·04652	0·04895	0·05132	0·05363	0·05587
2·6	0·02308	0·02564	0·02813	0·03055	0·03292	0·03522	0·03745	0·03963	0·04176	0·04382
2·8	0·01682	0·01912	0·02136	0·02354	0·02566	0·02773	0·02974	0·03170	0·03361	0·03547
3·0	0·01295	0·01498	0·01696	0·01889	0·02077	0·02261	0·02439	0·02613	0·02783	0·02948
3·2	0·01044	0·01223	0·01397	0·01567	0·01732	0·01894	0·02052	0·02206	0·02356	0·02502
3·4	0·00873	0·01029	0·01182	0·01332	0·01478	0·01620	0·01760	0·01896	0·02029	0·02159
3·6	0·00748	0·00886	0·01021	0·01153	0·01282	0·01408	0·01532	0·01653	0·01771	0·01887
3·8	0·00652	0·00774	0·00894	0·01012	0·01126	0·01239	0·01349	0·01457	0·01563	0·01667
4·0	0·00576	0·00685	0·00792	0·00897	0·01000	0·01101	0·01199	0·01296	0·01391	0·01484
4·2	0·00514	0·00612	0·00708	0·00802	0·00895	0·00985	0·01075	0·01162	0·01248	0·01332
4·4	0·00462	0·00550	0·00637	0·00722	0·00806	0·00888	0·00969	0·01048	0·01126	0·01203
4·6	0·00418	0·00498	0·00577	0·00654	0·00730	0·00805	0·00879	0·00951	0·01022	0·01092
4·8	0·00381	0·00453	0·00525	0·00596	0·00665	0·00734	0·00801	0·00867	0·00932	0·00996
5·0	0·00348	0·00415	0·00480	0·00545	0·00609	0·00672	0·00734	0·00794	0·00854	0·00913
5·5	0·00283	0·00337	0·00391	0·00444	0·00496	0·00548	0·00598	0·00648	0·00697	0·00746
6·0	0·00235	0·00280	0·00325	0·00369	0·00413	0·00456	0·00498	0·00540	0·00581	0·00621
6·5	0·00198	0·00237	0·00275	0·00312	0·00349	0·00385	0·00421	0·00457	0·00492	0·00526
7·0	0·00170	0·00203	0·00235	0·00267	0·00299	0·00330	0·00361	0·00392	0·00422	0·00451
8·0	0·00129	0·00154	0·00179	0·00203	0·00227	0·00251	0·00274	0·00298	0·00320	0·00343
9·0	0·00101	0·00121	0·00140	0·00159	0·00178	0·00197	0·00216	0·00234	0·00252	0·00270
10·0	0·00082	0·00097	0·00113	0·00129	0·00144	0·00159	0·00174	0·00189	0·00203	0·00218
12·0	0·00056	0·00067	0·00078	0·00089	0·00099	0·00110	0·00120	0·00130	0·00140	0·00150
15·0	0·00036	0·00043	0·00050	0·00057	0·00063	0·00070	0·00077	0·00083	0·00090	0·00096
20·0	0·00020	0·00024	0·00028	0·00032	0·00036	0·00039	0·00043	0·00047	0·00050	0·00054

TABLE 1 (*Continued*)

a	0·30	0·35	0·40	0·45	0·50	0·55	0·60	0·65	0·70	0·75
$H(a,0)$	0·73460	0·70150	0·67079	0·64225	0·61569	0·59093	0·56780	0·54618	0·52593	0·50694
w	1·00433	1·03523	1·06675	1·09887	1·13160	1·16491	1·19878	1·23321	1·26818	1·30367
k										
0·0	1·00000	1·00000	1·00000	1·00000	1·00000	1·00000	1·00000	1·00000	1·00000	1·00000
0·1	0·99277	0·99272	0·99267	0·99261	0·99256	0·99251	0·99245	0·99240	0·99235	0·99229
0·2	0·97145	0·97124	0·97104	0·97083	0·97063	0·97042	0·97022	0·97002	0·96982	0·96963
0·3	0 93702	0·93660	0·93618	0·93576	0·93534	0·93492	0·93451	0·93410	0·93370	0·93330
0·4	0·89110	0·89044	0·88978	0·88912	0·88847	0·88783	0·88719	0·88655	0·88593	0·88531
0·5	0·83571	0·83485	0·83399	0·83313	0·83229	0·83145	0·83062	0·82980	0·82899	0·82819
0·6	0·77321	0·77223	0·77125	0·77028	0·76932	0·76838	0·76744	0·76652	0·76562	0·76473
0·7	0·70606	0·70508	0·70412	0·70316	0·70222	0·70129	0·70038	0·69948	0·69860	0·69775
0·8	0·63669	0·63588	0·63508	0·63429	0·63351	0·63275	0·63200	0·63127	0·63056	0·62986
0·9	0·56736	0·56687	0·56639	0·56593	0·56547	0·56502	0·56459	0·56416	0·56375	0·56334
1·0	0·50000	0·50000	0·50000	0·50000	0·50000	0·50000	0·50000	0·50000	0·50000	0·50000
1·1	0·43621	0·43682	0·43742	0·43800	0·43856	0·43911	0·43964	0·44016	0·44065	0·44113
1·2	0·37714	0·37846	0·37974	0·38098	0·38217	0·38333	0·38445	0·38553	0·38656	0·38756
1·3	0·32358	0·32564	0·32763	0·32956	0·33141	0·33320	0·33491	0·33656	0·33813	0·33964
1·4	0·27589	0·27870	0·28140	0·28400	0·28649	0·28888	0·29116	0·29335	0·29543	0·29741
1·5	0·23416	0·23766	0·24102	0·24424	0·24731	0·25024	0·25304	0·25570	0·25822	0·26063
1·6	0·19817	0·20230	0·20623	0·20998	0·21355	0·21695	0·22017	0·22323	0·22612	0·22887
1·7	0·16756	0·17219	0·17660	0·18079	0·18476	0·18852	0·19208	0·19544	0·19862	0·20162
1·8	0·14181	0·14684	0·15160	0·15612	0·16038	0·16441	0·16820	0·17178	0·17515	0·17832
1·9	0·12035	0·12565	0·13066	0·13539	0·13984	0·14404	0·14798	0·15169	0·15518	0·15845
2·0	0·10260	0·10806	0·11321	0·11805	0·12260	0·12687	0·13088	0·13464	0·13817	0·14148
2·2	0·07599	0·08147	0·08661	0·09143	0·09594	0·10016	0·10411	0·10781	0·11127	0·11450
2·4	0·05806	0·06327	0·06815	0·07271	0·07697	0·08096	0·08468	0·08816	0·09142	0·09446
2·6	0·04583	0·05062	0·05510	0·05929	0·06320	0·06686	0·07028	0·07348	0·07647	0·07927
2·8	0·03728	0·04160	0·04563	0·04941	0·05295	0·05626	0·05935	0·06225	0·06496	0·06751
3·0	0·03109	0·03494	0·03855	0·04193	0·04510	0·04807	0·05086	0·05347	0·05592	0·05822
3·2	0·02645	0·02987	0·03309	0·03611	0·03895	0·04161	0·04412	0·04647	0·04868	0·05075
3·4	0·02286	0·02590	0·02877	0·03147	0·03402	0·03641	0·03867	0·04079	0·04278	0·04466
3·6	0·02000	0·02272	0·02529	0·02771	0·03000	0·03216	0·03419	0·03611	0·03791	0·03961
3·8	0·01768	0·02012	0·02243	0·02461	0·02667	0·02862	0·03047	0·03220	0·03384	0·03538
4·0	0·01576	0·01796	0·02004	0·02202	0·02389	0·02566	0·02733	0·02891	0·03040	0·03181
4·2	0·01414	0·01614	0·01803	0·01982	0·02152	0·02313	0·02466	0·02610	0·02746	0·02875
4·4	0·01278	0·01459	0·01631	0·01795	0·01950	0·02097	0·02237	0·02369	0·02494	0·02612
4·6	0·01160	0·01326	0·01483	0·01633	0·01776	0·01911	0·02039	0·02160	0·02275	0·02384
4·8	0·01059	0·01210	0·01355	0·01493	0·01624	0·01748	0·01866	0·01978	0·02084	0·02184
5·0	0·00970	0·01110	0·01243	0·01370	0·01491	0·01606	0·01715	0·01818	0·01916	0·02009
5·5	0·00793	0·00908	0·01018	0·01123	0·01223	0·01318	0·01409	0·01495	0·01577	0·01654
6·0	0·00661	0·00757	0·00850	0·00938	0·01022	0·01102	0·01179	0·01251	0·01320	0·01386
6·5	0·00560	0·00642	0·00720	0·00795	0·00867	0·00936	0·01001	0·01063	0·01122	0·01178
7·0	0·00480	0·00551	0·00618	0·00683	0·00745	0·00804	0·00861	0·00914	0·00965	0·01014
8·0	0·00365	0·00419	0·00471	0·00520	0·00568	0·00613	0·00656	0·00698	0·00737	0·00774
9·0	0·00287	0·00330	0·00370	0·00410	0·00447	0·00483	0·00517	0·00550	0·00581	0·00610
10·0	0·00232	0·00266	0·00299	0·00331	0·00361	0·00390	0·00418	0·00445	0·00470	0·00494
12·0	0·00160	0·00184	0·00207	0·00229	0·00250	0·00270	0·00290	0·00308	0·00326	0·00342
15·0	0·00102	0·00117	0·00132	0·00146	0·00160	0·00173	0·00185	0·00197	0·00208	0·00219
20·0	0·00057	0·00066	0·00074	0·00082	0·00090	0·00097	0·00104	0·00111	0·00117	0·00123

TABLE 1 (*Continued*)

a	0·80	0·85	0·90	0·95	1·00	1·10	1·20	1·30	1·40	1·50
$H(a,0)$	0·48910	0·47233	0·45653	0·44164	0·42758	0·40173	0·37854	0·35764	0·33874	0·32159
w	1·33968	1·37618	1·41315	1·45059	1·48848	1·56553	1·64419	1·72434	1·80586	1·88866
k										
0·0	1·00000	1·00000	1·00000	1·00000	1·00000	1·00000	1·00000	1·00000	1·00000	1·00000
0·1	0·99224	0·99219	0·99214	0·99209	0·99204	0·99195	0·99186	0·99177	0·99169	0·99161
0·2	0·96943	0·96924	0·96905	0·96887	0·96868	0·96833	0·96798	0·96766	0·96734	0·96704
0·3	0·93290	0·93251	0·93213	0·93175	0·93138	0·93066	0·92997	0·92931	0·92868	0·92808
0·4	0·88470	0·88410	0·88351	0·88294	0·88237	0·88127	0·88022	0·87923	0·87828	0·87738
0·5	0·82741	0·82664	0·82589	0·82515	0·82443	0·82304	0·82171	0·82046	0·81927	0·81816
0·6	0·76386	0·76301	0·76218	0·76136	0·76057	0·75904	0·75760	0·75624	0·75496	0·75376
0·7	0·69691	0·69609	0·69529	0·69451	0·69375	0·69230	0·69094	0·68966	0·68847	0·68736
0·8	0·62918	0·62852	0·62788	0·62726	0·62665	0·62550	0·62443	0·62343	0·62250	0·62164
0·9	0·56295	0·56257	0·56220	0·56185	0·56151	0·56086	0·56026	0·55970	0·55918	0·55871
1·0	0·50000	0·50000	0·50000	0·50000	0·50000	0·50000	0·50000	0·50000	0·50000	0·50000
1·1	0·44160	0·44204	0·44246	0·44287	0·44327	0·44400	0·44467	0·44529	0·44585	0·44636
1·2	0·38851	0·38942	0·39030	0·39114	0·39193	0·39342	0·39478	0·39601	0·39712	0·39813
1·3	0·34108	0·34246	0·34377	0·34502	0·34621	0·34841	0·35041	0·35220	0·35382	0·35528
1·4	0·29930	0·30110	0·30281	0·30443	0·30597	0·30881	0·31136	0·31365	0·31570	0·31754
1·5	0·26290	0·26506	0·26711	0·26904	0·27087	0·27424	0·27725	0·27994	0·28234	0·28448
1·6	0·23146	0·23391	0·23622	0·23840	0·24046	0·24424	0·24760	0·25058	0·25324	0·25560
1·7	0·20444	0·20711	0·20961	0·21198	0·21420	0·21827	0·22187	0·22506	0·22790	0·23041
1·8	0·18131	0·18412	0·18675	0·18923	0·19156	0·19581	0·19956	0·20288	0·20582	0·20842
1·9	0·16152	0·16440	0·16711	0·16965	0·17203	0·17637	0·18020	0·18357	0·18655	0·18920
2·0	0·14458	0·14749	0·15021	0·15277	0·15516	0·15951	0·16334	0·16672	0·16970	0·17235
2·2	0·11753	0·12036	0·12302	0·12550	0·12782	0·13204	0·13575	0·13902	0·14191	0·14446
2·4	0·09730	0·09997	0·10246	0·10479	0·10697	0·11094	0·11442	0·11750	0·12021	0·12261
2·6	0·08188	0·08433	0·08663	0·08878	0·09079	0·09445	0·09767	0·10051	0·10303	0·10525
2·8	0·06989	0·07212	0·07421	0·07617	0·07801	0·08135	0·08431	0·08691	0·08922	0·09127
3·0	0·06037	0·06240	0·06429	0·06608	0·06775	0·07079	0·07349	0·07587	0·07798	0·07985
3·2	0·05270	0·05453	0·05625	0·05787	0·05939	0·06216	0·06461	0·06679	0·06871	0·07043
3·4	0·04642	0·04808	0·04964	0·05111	0·05249	0·05501	0·05725	0·05923	0·06099	0·06256
3·6	0·04121	0·04272	0·04414	0·04547	0·04673	0·04903	0·05107	0·05288	0·05450	0·05593
3·8	0·03684	0·03821	0·03951	0·04072	0·04187	0·04397	0·04584	0·04750	0·04898	0·05030
4·0	0·03314	0·03439	0·03557	0·03669	0·03774	0·03966	0·04137	0·04290	0·04426	0·04547
4·2	0·02997	0·03112	0·03220	0·03322	0·03419	0·03595	0·03753	0·03893	0·04018	0·04130
4·4	0·02724	0·02829	0·02929	0·03023	0·03111	0·03274	0·03419	0·03549	0·03664	0·03767
4·6	0·02487	0·02584	0·02676	0·02762	0·02844	0·02994	0·03128	0·03248	0·03355	0·03450
4·8	0·02279	0·02369	0·02454	0·02534	0·02610	0·02749	0·02873	0·02984	0·03083	0·03172
5·0	0·02097	0·02180	0·02259	0·02333	0·02403	0·02533	0·02648	0·02751	0·02843	0·02925
5·5	0·01727	0·01797	0·01862	0·01925	0·01983	0·02092	0·02188	0·02275	0·02352	0·02421
6·0	0·01448	0·01506	0·01562	0·01615	0·01665	0·01756	0·01839	0·01912	0·01978	0·02037
6·5	0·01231	0·01281	0·01329	0·01374	0·01417	0·01496	0·01567	0·01630	0·01686	0·01737
7·0	0·01060	0·01103	0·01145	0·01184	0·01221	0·01289	0·01351	0·01406	0·01455	0·01499
8·0	0·00809	0·00843	0·00875	0·00905	0·00934	0·00987	0·01034	0·01077	0·01115	0·01149
9·0	0·00639	0·00665	0·00691	0·00715	0·00737	0·00779	0·00817	0·00851	0·00881	0·00908
10·0	0·00517	0·00538	0·00559	0·00578	0·00597	0·00631	0·00662	0·00689	0·00714	0·00736
12·0	0·00358	0·00373	0·00388	0·00401	0·00414	0·00438	0·00460	0·00479	0·00496	0·00512
15·0	0·00229	0·00239	0·00248	0·00257	0·00265	0·00280	0·00294	0·00306	0·00318	0·00328
20·0	0·00129	0·00134	0·00139	0·00144	0·00149	0·00159	0·00165	0·00172	0·00179	0·00184

TABLE 1 (*Continued*)

a	1·60	1·70	1·80	1·90	2·00	2·20	2·40	2·60	2·80	3·00
$H(a,0)$	0·30595	0·29166	0·27856	0·26651	0·25540	0·23559	0·21850	0·20361	0·19055	0·17900
w	1·97262	2·05767	2·14370	2·23065	2·31843	2·49624	2·67667	2·85932	3·04386	3·23002
k										
0·0	1·00000	1·00000	1·00000	1·00000	1·00000	1·00000	1·00000	1·00000	1·00000	1·00000
0·1	0·99153	0·99146	0·99139	0·99132	0·99126	0·99115	0·99105	0·99096	0·99089	0·99082
0·2	0·96676	0·96649	0·96624	0·96600	0·96577	0·96536	0·96499	0·96466	0·96438	0·96412
0·3	0·92751	0·92698	0·92648	0·92600	0·92555	0·92474	0·92402	0·92339	0·92283	0·92234
0·4	0·87654	0·87574	0·87499	0·87429	0·87363	0·87243	0·87138	0·87046	0·86965	0·86894
0·5	0·81711	0·81612	0·81520	0·81434	0·81353	0·81208	0·81081	0·80971	0·80874	0·80790
0·6	0·75264	0·75159	0·75062	0·74971	0·74886	0·74735	0·74604	0·74491	0·74392	0·74307
0·7	0·68632	0·68536	0·68447	0·68365	0·68288	0·68152	0·68035	0·67935	0·67849	0·67774
0·8	0·62085	0·62011	0·61944	0·61881	0·61824	0·61722	0·61635	0·61561	0·61498	0·61444
0·9	0·55828	0·55787	0·55751	0·55717	0·55686	0·55632	0·55586	0·55547	0·55514	0·55486
1·0	0·50000	0·50000	0·50000	0·50000	0·50000	0·50000	0·50000	0·50000	0·50000	0·50000
1·1	0·44682	0·44724	0·44762	0·44797	0·44828	0·44883	0·44929	0·44967	0·45000	0·45027
1·2	0·39904	0·39986	0·40060	0·40128	0·40189	0·40295	0·40382	0·40455	0·40517	0·40568
1·3	0·35659	0·35777	0·35884	0·35980	0·36067	0·36216	0·36340	0·36442	0·36528	0·36600
1·4	0·31919	0·32067	0·32200	0·32319	0·32427	0·32613	0·32765	0·32891	0·32996	0·33085
1·5	0·28639	0·28811	0·28964	0·29102	0·29226	0·29439	0·29613	0·29757	0·29876	0·29977
1·6	0·25771	0·25960	0·26128	0·26279	0·26415	0·26647	0·26837	0·26993	0·27123	0·27232
1·7	0·23265	0·23465	0·23643	0·23803	0·23946	0·24191	0·24391	0·24556	0·24692	0·24807
1·8	0·21074	0·21280	0·21464	0·21629	0·21776	0·22028	0·22234	0·22403	0·22544	0·22661
1·9	0·19154	0·19363	0·19549	0·19716	0·19865	0·20120	0·20327	0·20498	0·20640	0·20759
2·0	0·17469	0·17677	0·17863	0·18029	0·18178	0·18432	0·18639	0·18809	0·18951	0·19070
2·2	0·14673	0·14874	0·15053	0·15214	0·15358	0·15603	0·15804	0·15969	0·16106	0·16221
2·4	0·12475	0·12664	0·12834	0·12985	0·13121	0·13353	0·13542	0·13698	0·13828	0·13936
2·6	0·10723	0·10899	0·11057	0·11197	0·11324	0·11540	0·11716	0·11862	0·11983	0·12084
2·8	0·09309	0·09471	0·09616	0·09746	0·09863	0·10062	0·10226	0·10360	0·10472	0·10567
3·0	0·08152	0·08301	0·08434	0·08554	0·08661	0·08845	0·08995	0·09119	0·09223	0·09310
3·2	0·07196	0·07332	0·07454	0·07564	0·07662	0·07831	0·07970	0·08084	0·08179	0·08259
3·4	0·06396	0·06521	0·06633	0·06734	0·06824	0·06979	0·07107	0·07212	0·07300	0·07374
3·6	0·05722	0·05836	0·05939	0·06032	0·06115	0·06257	0·06374	0·06471	0·06552	0·06620
3·8	0·05148	0·05253	0·05348	0·05432	0·05509	0·05640	0·05748	0·05837	0·05912	0·05975
4·0	0·04655	0·04752	0·04839	0·04917	0·04988	0·05109	0·05209	0·05291	0·05360	0·05418
4·2	0·04230	0·04319	0·04399	0·04472	0·04537	0·04649	0·04741	0·04817	0·04881	0·04934
4·4	0·03860	0·03942	0·04017	0·04083	0·04144	0·04247	0·04332	0·04403	0·04462	0·04512
4·6	0·03536	0·03612	0·03681	0·03743	0·03799	0·03895	0·03974	0·04040	0·04095	0·04141
4·8	0·03251	0·03322	0·03386	0·03444	0·03496	0·03585	0·03658	0·03719	0·03771	0·03814
5·0	0·02999	0·03065	0·03125	0·03178	0·03227	0·03310	0·03378	0·03435	0·03483	0·03523
5·5	0·02484	0·02539	0·02589	0·02635	0·02675	0·02746	0·02804	0·02852	0·02892	0·02926
6·0	0·02090	0·02138	0·02180	0·02219	0·02254	0·02314	0·02363	0·02404	0·02439	0·02468
6·5	0·01783	0·01824	0·01861	0·01894	0·01924	0·01976	0·02019	0·02054	0·02084	0·02109
7·0	0·01539	0·01574	0·01606	0·01635	0·01662	0·01707	0·01744	0·01775	0·01801	0·01823
8·0	0·01180	0·01207	0·01232	0·01255	0·01275	0·01310	0·01339	0·01363	0·01383	0·01400
9·0	0·00933	0·00955	0·00975	0·00993	0·01009	0·01037	0·01060	0·01079	0·01095	0·01109
10·0	0·00756	0·00774	0·00790	0·00805	0·00818	0·00841	0·00860	0·00876	0·00889	0·00900
12·0	0·00526	0·00538	0·00549	0·00560	0·00569	0·00585	0·00598	0·00609	0·00618	0·00626
15·0	0·00337	0·00345	0·00352	0·00359	0·00365	0·00375	0·00383	0·00391	0·00396	0·00402
20·0	0·00189	0·00194	0·00198	0·00202	0·00205	0·00211	0·00216	0·00220	0·00223	0·00226

TABLE 1 (*Continued*)

a	3·50	4·00	4·50	5·00	6·00	7·00	8·00	9·00	10·00	Infinity
$H(a,0)$	0·15529	0·13700	0·12248	0·11070	0·09278	0·07980	0·06999	0·06231	0·05614	Lorentz
w	3·70112	4·17840	4·66013	5·14515	6·12213	7·10531	8·09252	9·08245	10·07435	
k										
0·0	1·00000	1·00000	1·00000	1·00000	1·00000	1·00000	1·00000	1·00000	1·00000	1·00000
0·1	0·99067	0·99057	0·99049	0·99042	0·99034	0·99028	0·99024	0·99021	0·99019	0·99010
0·2	0·96361	0·96322	0·96293	0·96270	0·96238	0·96218	0·96204	0·96194	0·96187	0·96154
0·3	0·92134	0·92060	0·92004	0·91961	0·91901	0·91862	0·91836	0·91817	0·91804	0·91743
0·4	0·86752	0·86647	0·86568	0·86508	0·86424	0·86371	0·86334	0·86309	0·86290	0·86207
0·5	0·80623	0·80501	0·80410	0·80341	0·80245	0·80184	0·80143	0·80114	0·80093	0·80000
0·6	0·74139	0·74017	0·73927	0·73859	0·73766	0·73706	0·73667	0·73639	0·73619	0·73529
0·7	0·67628	0·67524	0·67447	0·67389	0·67311	0·67261	0·67228	0·67205	0·67188	0·67114
0·8	0·61338	0·61263	0·61209	0·61168	0·61113	0·61078	0·61055	0·61038	0·61027	0·60976
0·9	0·55432	0·55393	0·55366	0·55345	0·55317	0·55300	0·55288	0·55280	0·55274	0·55249
1·0	0·50000	0·50000	0·50000	0·50000	0·50000	0·50000	0·50000	0·50000	0·50000	0·50000
1·1	0·45079	0·45115	0·45141	0·45160	0·45186	0·45202	0·45213	0·45220	0·45226	0·45249
1·2	0·40667	0·40734	0·40783	0·40819	0·40867	0·40897	0·40917	0·40931	0·40941	0·40984
1·3	0·36737	0·36831	0·36899	0·36948	0·37015	0·37056	0·37083	0·37102	0·37116	0·37175
1·4	0·33252	0·33367	0·33449	0·33509	0·33590	0·33640	0·33673	0·33696	0·33712	0·33784
1·5	0·30167	0·30297	0·30390	0·30459	0·30550	0·30607	0·30644	0·30670	0·30688	0·30769
1·6	0·27438	0·27579	0·27680	0·27754	0·27853	0·27914	0·27954	0·27982	0·28003	0·28090
1·7	0·25023	0·25172	0·25277	0·25355	0·25459	0·25523	0·25565	0·25594	0·25615	0·25707
1·8	0·22883	0·23036	0·23144	0·23224	0·23330	0·23396	0·23439	0·23469	0·23491	0·23585
1·9	0·20984	0·21137	0·21247	0·21327	0·21435	0·21501	0·21545	0·21575	0·21597	0·21692
2·0	0·19293	0·19446	0·19556	0·19636	0·19743	0·19809	0·19853	0·19883	0·19905	0·20000
2·2	0·16437	0·16586	0·16692	0·16770	0·16874	0·16938	0·16981	0·17010	0·17031	0·17123
2·4	0·14142	0·14283	0·14383	0·14457	0·14556	0·14617	0·14657	0·14685	0·14705	0·14793
2·6	0·12276	0·12408	0·12502	0·12571	0·12664	0·12721	0·12759	0·12786	0·12804	0·12887
2·8	0·10745	0·10867	0·10954	0·11019	0·11105	0·11158	0·11194	0·11218	0·11236	0·11312
3·0	0·09474	0·09588	0·09669	0·09728	0·09808	0·09857	0·09890	0·09913	0·09930	0·10000
3·2	0·08411	0·08516	0·08590	0·08645	0·08719	0·08765	0·08795	0·08816	0·08831	0·08897
3·4	0·07513	0·07610	0·07679	0·07729	0·07798	0·07840	0·07868	0·07903	0·07901	0·07962
3·6	0·06749	0·06838	0·06902	0·06949	0·07012	0·07051	0·07076	0·07094	0·07107	0·07163
3·8	0·06094	0·06176	0·06235	0·06278	0·06336	0·06372	0·06402	0·06413	0·06425	0·06477
4·0	0·05528	0·05604	0·05658	0·05698	0·05752	0·05786	0·05808	0·05823	0·05834	0·05882
4·2	0·05036	0·05107	0·05157	0·05194	0·05244	0·05275	0·05296	0·05310	0·05320	0·05365
4·4	0·04607	0·04672	0·04719	0·04753	0·04800	0·04855	0·04847	0·04861	0·04870	0·04912
4·6	0·04229	0·04290	0·04333	0·04365	0·04408	0·04435	0·04453	0·04465	0·04474	0·04513
4·8	0·03895	0·03952	0·03992	0·04022	0·04063	0·04088	0·04104	0·04115	0·04124	0·04160
5·0	0·03599	0·03652	0·03690	0·03718	0·03758	0·03779	0·03794	0·03805	0·03813	0·03846
5·5	0·02991	0·03035	0·03067	0·03091	0·03123	0·03143	0·03156	0·03165	0·03171	0·03200
6·0	0·02523	0·02562	0·02589	0·02614	0·02637	0·02654	0·02665	0·02673	0·02678	0·02703
6·5	0·02157	0·02190	0·02214	0·02231	0·02255	0·02270	0·02279	0·02286	0·02291	0·02312
7·0	0·01864	0·01893	0·01914	0·01929	0·01950	0·01963	0·01971	0·01977	0·01981	0·02000
8·0	0·01433	0·01455	0·01471	0·01483	0·01499	0·01509	0·01516	0·01521	0·01524	0·01538
9·0	0·01135	0·01153	0·01166	0·01175	0·01188	0·01196	0·01202	0·01205	0·01208	0·01220
10·0	0·00921	0·00936	0·00946	0·00954	0·00965	0·00971	0·00975	0·00978	0·00981	0·00990
12·0	0·00641	0·00651	0·00659	0·00664	0·00672	0·00676	0·00679	0·00681	0·00683	0·00690
15·0	0·00411	0·00418	0·00423	0·00426	0·00431	0·00434	0·00436	0·00437	0·00438	0·00442
20·0	0·00232	0·00235	0·00238	0·00240	0·00243	0·00245	0·00246	0·00246	0·00247	0·00249

lengthy. Behaviour of the tabulated values is illustrated by the representative curves shown in Figure 4.

It should be observed that the useful tables of van de Hulst and Reesinck (1947) are in effect a short inverse tabulation of the present work, and give k as a function of a for selected values of $H(a,v)/H(a,0)$; their notation is related to that used here by

$$\beta_1,\ \beta_2,\ c,\ h,\ b/h \rightarrow \tfrac{1}{2}\Delta\nu_L,\ \tfrac{1}{2}\Delta\nu'_G,\ H(a,0),\ w\Delta\nu'_G,\ k.$$

The " Working graph of the parameters " given in their Figure 2 has been checked and is correct to one scale division except for the curve of $b_{0\cdot1}/h$ which is in error by as much as 5 per cent. Since this curve is of some importance in data analysis the following values of $b_{0\cdot1}/h$ may be used to sketch in a correction :

β_1/h ..	0·200	0·225	0·250	0·275	0·300	0·325	0·350	0·375	0·400	0·425	0·450	0·475	0·500
$b_{0\cdot1}/h$ ..	2·11	2·17	2·23	2·30	2·37	2·45	2·52	2·60	2·68	2·76	2·84	2·92	3·00

The columns in their Table 1, headed 0·2 and 0·05, and corresponding to the fifth- and twentieth-widths respectively, have also been checked and found to be essentially correct.

Most of the numerical work reported here was carried out on SILLIAC, the electronic digital computer of the Adolph Basser Computing Laboratory, School of Physics, University of Sydney. Because of the large number of small values of a, the computing time was relatively long, and preparation of Table 1 required 35 minutes of machine time.

IV. Acknowledgment

The author wishes to thank Mr. W. E. Smith for useful criticism and suggestions during the preparation of this paper.

V. References

Born, M. (1933).—" Optik." (Springer : Berlin.)

Bromwich, T. J. I'A. (1949).—" An Introduction to the Theory of Infinite Series." 2nd Ed. (Macmillan : London.)

Burger, H. C., and van Cittert, P. H. (1927).—*Z. Phys.* **44** : 58–69.

Danos, M., and Geschwind, S. (1953).—*Phys. Rev.* **91** : 1159–62.

Dennison, D. M. (1928).—*Phys. Rev.* **31** : 503–19.

Harris, D. L. (1948).—*Astrophys. J.* **108** : 112–5.

Hastings, C. (1955).—" Approximations for Digital Computers." (Princeton Univ. Press.)

Hjerting, F. (1938).—*Astrophys. J.* **88** : 508–15.

van de Hulst, H. C. (1946).—*Bull. Astr. Insts. Netherlds.* **10** : 79–81.

van de Hulst, H. C., and Reesinck, J. J. M. (1947).—*Astrophys. J.* **106** : 121–7.

Kopal, Z. (1955).—" Numerical Analysis." (Chapman and Hall : London.)

Minkowski, R., and Bruck, H. (1935).—*Z. Phys.* **95** : 299–301.

Mitchell, A. C. G., and Zemansky, M. W. (1934).—" Resonance Radiation and Excited Atoms." (Cambridge Univ. Press.)

Morse, P. M., and Feshbach, H. (1953).—" Methods of Theoretical Physics." Part I. (McGraw Hill : New York.)

Voigt, W. (1912).—*S.B. bayer Akad. Wiss.* **1912** : 603–20.

Zemansky, M. W. (1930).—*Phys. Rev.* **36** : 219–38.

SHORT COMMUNICATIONS

PHOTOMETRIC OBSERVATIONS OF SUBVISUAL RED AURORAL ARCS AT MIDDLE LATITUDES*

By R. A. DUNCAN†

A photometer (Roach *et al.* 1958) sensitive to the red oxygen emission at 6300 Å has been in operation at Camden, near Sydney (geomagnetic latitude 42°), since July 1958. In this period three bright aurorae have been seen in southern Australia; on July 8–9, September 4–5, and September 25–26. Following the first two the photometer detected a subvisual stable red arc the next night. On the night after the third aurora, observation was prevented by cloud.

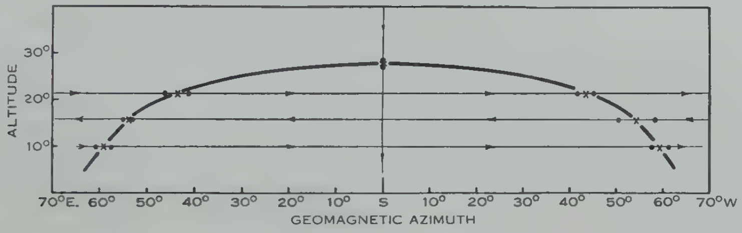

Fig. 1.—Shape of auroral arc observed between 1930^{h} and 2330^{h} September 5, 1958. The photometer scanned the sky along the paths indicated by the fine arrowed lines. A complete sky scan was completed once every 5 min. The crosses show the mean positions at which the arc was intercepted. The dots are the quartile points.

These arcs had the following characteristics:

(1) They occurred on the night following a bright visual aurora. By this time the magnetic disturbance index (K) at Watheroo had fallen to 5 or less.

(2) Periodic checks on the 5577 Å emission showed no departure from the quiet airglow pattern. Indeed, during the previous 15 months 5577 Å emission was intensively studied and auroral activity was never detected at this wavelength unless the disturbance index (K) equalled or exceeded 6.

(3) The arcs were centred (to within 1 or 2°) on geomagnetic south, and maintained these positions for some hours. The arc seen on September 5–6 is shown in Figure 1. It maintained this position from 1938 till 2330 E.S.T. After this it began to sink slowly, being 5° lower by 0245.

(4) The intensities of the arcs varied steadily with time (Fig. 2) in marked contrast to the rapid fluctuations which we usually observe during visual aurorae.

---

* Manuscript received December 15, 1958.

† Upper Atmosphere Section, C.S.I.R.O., Camden, N.S.W.

Using a photometer at Haute Provence (geomagnetic latitude 45·7°) Barbier (1957) found a red arc on January 21, 1957, but this was during a great magnetic storm ($Kp = 9$). Störmer (1955) states that only four visual red arcs were observed in southern Norway in the 40 years ending 1955.

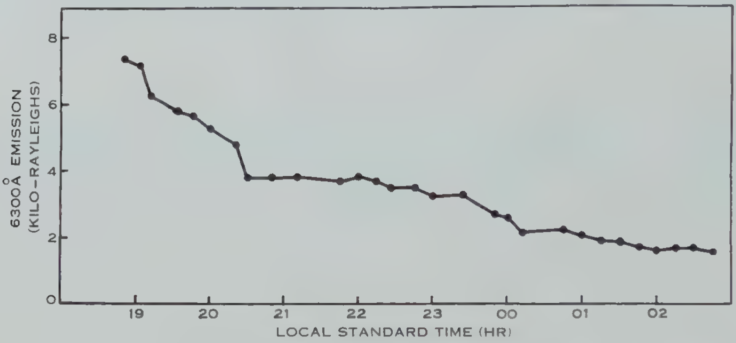

Fig. 2.—Time variation of the brightness of the red auroral arc observed on September 5–6, 1958. The brightness plotted here is that of a point on the eastern limb 15·7° above the horizon (see Fig. 1) but is representative of all parts of the arc.

The existence of auroral arcs at middle latitudes during times of only moderate geomagnetic disturbance does not appear to have been previously reported.

This work forms part of the research programme of the Upper Atmosphere Section of the Commonwealth Scientific and Industrial Research Organization. The photometer was lent by the United States National Bureau of Standards as an I.G.Y. contribution.

The author has to thank Mr. R. O. Errey for help in the observations.

References

Barbier, D. (1957).—*C.R. Acad. Sci., Paris* **244** : 1945.
Roach et al. (1958).—*J. Atmos. Terr. Phys.* **50** : 171.
Störmer, C. (1955).—“The Polar Aurora.” (Clarendon Press : Oxford.)

DEVIATION FROM MATTHIESSEN'S RULE AND LATTICE THERMAL CONDUCTIVITY OF ALLOYS*

By P. G. Klemens†

The purpose of this note is to point out that the difference in the ideal electronic thermal conductivity between an alloy and a pure metal can be estimated from the corresponding difference in the ideal electrical resistivity, using the Wiedemann-Franz law. This allows the separation of the thermal conductivity into an electronic and a lattice component to be made with greater confidence, particularly at liquid oxygen temperatures.

Matthiessen's rule states that the electrical resistivity of metals is composed of an ideal and a residual resistivity

$$\rho=\rho_i+\rho_0, \quad \ldots\ldots\ldots\ldots\ldots\ldots\ldots \quad (1)$$

where $\rho \to \rho_0$ as $T \to 0$, ρ_0 is independent of temperature T, and $\rho_i(T)$ is independent of ρ_0. The ideal resistivity ρ_i arises from the scattering of electrons by lattice waves, while ρ_0 is due to the scattering by imperfections and impurities.

On going from a metal to an alloy, the residual resistivity is substantially increased. However, this is not the only change, for the number of free electrons is generally affected, and hence the band structure. Consequent changes in ρ_0 cannot be separated from changes due to the increased number of scattering centres, but in general a change in band structure causes a change in ρ_i, which can be observed. Thus we may write for an alloy

$$\rho=\rho_0+\rho_i+\Delta\rho_i, \quad \ldots\ldots\ldots\ldots\ldots\ldots\ldots \quad (2)$$

where now ρ_i is the ideal resistivity of the parent metal and $\Delta\rho_i$ the change in ideal resistivity on alloying.

In analogy to (**1**), the electronic thermal conductivity $\varkappa_e$ is limited by the scattering of electrons by imperfections and impurities, leading to a residual thermal resistivity W_0, and by the lattice waves, leading to an ideal thermal resistivity W_i (see, for example, Klemens 1956). Thus

$$1/\varkappa_e=W_e=W_0+W_i. \quad \ldots\ldots\ldots\ldots\ldots\ldots \quad (3)$$

Furthermore, it can be shown that W_0 and ρ_0 are related by the Wiedemann-Franz-Lorenz relation

$$\rho_0=LW_0T, \quad \ldots\ldots\ldots\ldots\ldots\ldots\ldots \quad (4)$$

where $L=\pi^2/3(K/e)^2$ is the Sommerfeld value of the Lorenz number (K is the Boltzmann constant, e the electronic charge). For the ideal resistivities, however,

$$\rho_i<LW_iT, \quad \ldots\ldots\ldots\ldots\ldots\ldots\ldots \quad (5)$$

except at high temperatures, where the two are equal (e.g. Klemens 1956).

---

* Manuscript received February 16, 1959.

† Division of Physics, C.S.I.R.O., University Grounds, Chippendale, N.S.W.

The thermal conductivity of metals and alloys is additively composed of the electronic component $\varkappa_e$ and a lattice component $\varkappa_g$, the latter arising from the heat transport by lattice waves (Koenigsberger 1907 ; for proof of additivity see Klemens 1956). Thus

$$\varkappa=\varkappa_e+\varkappa_g, \quad \ldots\ldots\ldots\ldots\ldots\ldots \quad (6)$$

but in pure metals $\varkappa_g \ll \varkappa_e$. In alloys, where $\varkappa_e$ is small because W_0 is large, $\varkappa_e$ and $\varkappa_g$ are often of comparable magnitude, and if $\varkappa_e$ can be calculated, one can deduce $\varkappa_g$ from the measured values of $\varkappa$. To obtain $\varkappa_e$ it is necessary to measure ρ_0 and hence to deduce W_0.

In recent years a number of systematic investigations of the thermal and electrical conductivities of alloys have been undertaken so as to evaluate their lattice thermal conductivities (for reviews see Olsen and Rosenberg (1953) and Klemens (1956, 1958)). In order to deduce $\varkappa_g$ at very low temperatures (say, below 20 °K) it is usually sufficient to consider only W_0, derived from ρ_0, when calculating $\varkappa_e$ from (**3**), W_i being negligibly small. However, at higher temperatures W_i cannot be neglected, even in alloys. Kemp *et al.* (1954, 1956) have considered the term W_i in (**3**) to calculate $\varkappa_e$—and hence obtain $\varkappa_g$—at temperatures up to about 90 °K. This procedure has been followed in subsequent investigations (see Klemens 1958), and from the behaviour of $\varkappa_g$ at these higher temperatures it has been possible to obtain information concerning the scattering of lattice waves by various point defects and by anharmonicities.

Unfortunately there is no direct information about the value of W_i in alloys, for $\varkappa_e$ can be directly measured only in the pure parent metal. It has thus been assumed in all such work on the lattice thermal conductivity of alloys that in the alloy W_i is the same as in the parent metal. As long as $W_i \ll W_0$, an error in W_i will not be serious, but the higher the temperature and the more dilute the alloy, the greater will be the relative contribution of W_i to W_e and of $\varkappa_e$ to $\varkappa$, and the more important will be errors of W_i in calculating $\varkappa_g$.

Since Matthiessen's rule (**2**) is not obeyed when going from a pure metal to an alloy, but ρ_i changes by $\Delta\rho_i$ due to changes in the band structure, one would expect (**3**) to break down similarly, so that the electronic thermal resistivity becomes

$$W_e=W_0+W_i+\Delta W_i, \quad \ldots\ldots\ldots\ldots\ldots \quad (7)$$

where W_i is now the ideal thermal resistivity of the parent metal. Since ΔW_i cannot be observed directly, there is some uncertainty in the separation of $\varkappa_g$ and $\varkappa_e$ from observations of $\varkappa$ and ρ_0. Paradoxically, uncertainties due to ΔW_i are greatest for dilute alloys, even though ΔW_i is then probably small, because of the increased necessity, as pointed out above, of knowing $W_i+\Delta W_i$ accurately.

It is the purpose of this note to point out that ΔW_i can be calculated from $\Delta\rho_i$ by means of a relation analogous to (**4**)

$$\Delta\rho_i=LT\Delta W_i, \quad \ldots\ldots\ldots\ldots\ldots\ldots \quad (8)$$

and since $\Delta\rho_i$ can be deduced from measurements of the electrical conductivity of the alloy, it is possible to calculate $\varkappa_e$ with greater confidence.

The ideal electrical and thermal resistivities arise from interactions between electrons and phonons which take electrons from a region of momentum space where there are too many electrons into a region where there are too few, relative to the equilibrium concentration. As pointed out elsewhere (Klemens 1956), the deviations g of the distribution function from the equilibrium distribution f^0 are of the form

$$g(\mathbf{k}) \propto f(\mathbf{k}_1)\, \mathrm{d}f^0/\mathrm{d}\varepsilon, \qquad \ldots\ldots\ldots\ldots\ldots\ldots \quad (\mathbf{9a})$$

for electrical conduction, and

$$g(\mathbf{k}) \propto f(\mathbf{k}_1)\, \varepsilon\, \mathrm{d}f^0/\mathrm{d}\varepsilon, \qquad \ldots\ldots\ldots\ldots\ldots\ldots \quad (\mathbf{9b})$$

for thermal conduction, where $\mathbf{k}$ is the electron wave-vector, $\mathbf{k}_1$ is a unit vector specifying the direction of $\mathbf{k}$, $f(\mathbf{k}_1)$ is some function of $\mathbf{k}_1$ depending on the shape of the Fermi surface and the zone structure, and is the same function in both cases, and ε is the reduced electron energy ($\varepsilon=(E-\zeta)/KT$, ζ being the Fermi energy).

In the case of electrical conduction the sign of g depends upon $f(\mathbf{k}_1)$ and thus on the direction of $\mathbf{k}$. Hence ρ_i is due to the motion of electrons (through interaction with phonons) to distant regions on the Fermi surface, involving substantial changes in $\mathbf{k}_1$ (horizontal movement).

In the case of thermal conduction, the sign of $g(\mathbf{k})$ can be reversed not only by changing $\mathbf{k}_1$ but also by changing ε. Thus W_i is due to two types of motion in $\mathbf{k}$-space: horizontal movement through large angles on the Fermi surface, and vertical movement through values of ε comparable to unity. To a first approximation each movement contributes to W_i in an additive manner, so that

$$W_i = W_{Hi} + W_{Vi}. \qquad \ldots\ldots\ldots\ldots\ldots\ldots \quad (\mathbf{10})$$

Since $f(\mathbf{k}_1)$ is the same in the cases of electrical and of thermal conduction, horizontal movement is equally efficacious in both cases, so that W_{Hi} and ρ_i are related by the Wiedemann-Franz relation (**4**)

$$\rho_i = LTW_{Hi}. \qquad \ldots\ldots\ldots\ldots\ldots\ldots \quad (\mathbf{11})$$

It is the occurrence of the term W_{Vi} in (**10**) which is responsible for the inequality (**5**). This term is particularly important at low temperatures.

Now W_{Vi} is relatively insensitive to changes in the band structure, being mainly governed by a local property of the Fermi surface. On the other hand W_{Hi}, being due to motion of electrons over large distances on the Fermi surface (large changes in $\mathbf{k}_1$), is sensitive to the overall shape of the Fermi surface, particularly in regard to its position relative to the zone boundaries (Klemens 1954, 1956).

The change $\Delta\rho_i$ on alloying is due to the sensitivity of the horizontal movement to changes in the band structure; it is reflected by changes in W_{Hi} which must be much larger than any change in W_{Vi}. Thus from (**11**) we obtain (**8**) as a good approximation.

Using (**7**) and (**8**), one can deduce $\varkappa_e$ for alloys with more confidence than previously, since values of ρ_0 and $\Delta\rho_i$ can be obtained from measurements of ρ.

This eliminates one source of uncertainty in the evaluation of $\varkappa_g$. There still remains a second limitation: since $\varkappa$ is measured only with limited precision, $\varkappa_g$ cannot be determined from (**6**) if $\varkappa_e \gg \varkappa_g$, even if $\varkappa_e$ is accurately known. Thus studies of $\varkappa_g$ are still confined to alloys which are not too dilute. However, the correction (**7**) and (**8**) should make possible a more reliable estimate of $\varkappa_g$ at higher temperatures in the case of many dilute alloys which previously could be analysed only at low temperatures.

References

Kemp, W. R. G., Klemens, P. G., Sreedhar, A. K., and White, G. K. (1954).—*Proc. Phys. Soc. Lond.* A **67**: 728.

Kemp, W. R. G., Klemens, P. G., Sreedhar, A. K., and White, G. K. (1956).—*Proc. Roy. Soc.* A **233**: 480.

Klemens, P. G. (1954).—*Aust. J. Phys.* **7**: 70.

Klemens, P. G. (1956).—"Encyclopedia of Physics." Vol. 14, Pt. 4. (Springer: Berlin.)

Klemens, P. G. (1958).—*Solid State Physics* **7**: 1.

Koenigsberger, J. (1907).—*Phys. Z.* **8**: 237.

Olsen, J. L., and Rosenberg, H. M. (1953).—*Advanc. Phys.* **2**: 28.

AUSTRALASIAN MEDICAL PUBLISHING CO. LTD.
SEAMER AND ARUNDEL STS., GLEBE, SYDNEY

THE USE OF COMPLETE TEMPERATURE–TIME CURVES FOR DETERMINATION OF THERMAL CONDUCTIVITY WITH PARTICULAR REFERENCE TO ROCKS

By J. C. Jaeger*

[*Manuscript received May* 7, 1959]

Summary

Most of the transient methods at present in use for the determination of thermal conductivity involve the study of the asymptote of a temperature-time curve. This implies that they require relatively long times of experiment and make no use of the information contained in measurements of temperature at smaller times.

A simple method of reducing observations is described which uses measurements of temperature at equally spaced intervals of time, together with a curve calculated from the theory. Such curves are given for a number of experimental situations likely to be useful for the measurement of the thermal conductivities of rocks. Among these are the line source : (i) in the semi-infinite solid, (ii) along the axis of a cylinder, (iii) along the surface of a cylinder. These methods yield values for both the thermal conductivity and diffusivity, and the desirability of such measurements is stressed. The application of the method to the thermal conductivity probe and to the measurement of the diffusivity of solids in the form of slabs and cylinders is also discussed. An alternative method of the same type, using the times at which specified temperatures are attained, is also described.

I. Introduction

In the early literature of conduction of heat many transient methods were given for determining the thermal diffusivity of specimens of simple geometrical shapes. These usually involve cooling the body from a constant initial temperature and use only the late stages of the cooling curve in which the theoretical solution reduces to a single exponential term (for references see Carslaw and Jaeger (1959), Sections 6.5, 8.5, 9.5). More recently, " time-lag " methods which involve an experimental situation in which the temperature-time curve has a linear asymptote (cf. Barrer 1939), and " probe " methods in which there is an asymptote linear in the logarithm of the time (cf. Blackwell 1954 ; de Vries and Peck 1958) have enjoyed a considerable vogue.

These methods all have the disadvantage that they completely waste the information available in the early parts of the temperature-time curves. Also, since they involve the approach to an asymptote they require relatively long experimental times when applied to specimens of poor conductors and of moderate size.

The object of the present paper is to describe a simple numerical method of discussing complete temperature-time curves which is applicable to a wide variety of cases.

---

* Australian National University, Canberra.

In many simple experimental situations, the temperature $v(t)$ measured at some point at time t after the beginning of the experiment has the theoretical form

$$v(t)=A(K,\varkappa)f(\varkappa t/a^2), \quad \ldots\ldots\ldots\ldots\ldots\ldots \quad (1)$$

where A is a constant depending on the thermal conductivity K and the diffusivity $\varkappa$ of the material, and $f(\varkappa t/a^2)$ is a function of the dimensionless quantity $\varkappa t/a^2$, where a is a length which specifies the size of the specimen. The diffusivity $\varkappa=K/\rho c$, where ρ is the density and c the specific heat of the material.

It follows from (**1**) that

$$\frac{v(2t)}{v(t)}=\frac{f(2\varkappa t/a^2)}{f(\varkappa t/a^2)}, \quad \ldots\ldots\ldots\ldots\ldots\ldots\ldots \quad (2)$$

so that the value of $\varkappa t/a^2$ can be found from an experimental value of $v(2t)/v(t)$ with the aid of a theoretical curve of the function $f(2T)/f(T)$.

In practice, a convenient unit of time t_0 is chosen and the values $v(nt_0)$ of the temperature at times nt_0, $n=1, 2, \ldots$, are measured. Each ratio $v(2nt_0)/v(nt_0)$ gives a value of $\varkappa t_0/a^2$ and these should agree within experimental error. If they show any systematic drift it is a valuable indication that the theory does not adequately represent the experimental situation. When $\varkappa t_0/a^2$ has been found, the value of $A(K,\varkappa)$ follows from (**1**) by comparing the observed values of $v(t)$ with the theoretical value $A(K,\varkappa)f(\varkappa t/a^2)$. In this way both K and $\varkappa$ can be found. Even if both are not needed the fact that $K/\varkappa=\rho c$, the heat capacity of the material per unit volume, which is usually known approximately, provides a useful check of the method. There is, of course, no need except practical convenience for the choice of the particular number 2 in (**2**), any other number can be used in the same way if desired.

The above method of reduction is most useful when temperatures are recorded continuously. If readings are made manually with a galvanometer or potentiometer it is much more convenient to record the times at which the temperature attains a definite value. Suppose that t and t_N are, respectively, the times at which temperatures v and Nv are attained, then by (**1**)

$$f(\varkappa t_N/a^2)=N\,f(\varkappa t/a^2), \quad \ldots\ldots\ldots\ldots\ldots\ldots \quad (3)$$

and $\varkappa t/a^2$ can be determined from a theoretical curve of the root T of $f(Tt_N/t)=N\,f(T)$ as a function of t_N/t.

Either of these methods of reduction can be applied to a great many methods for the determination of thermal conductivity. The necessary theoretical results for a number of systems likely to arise in connexion with measurements of the conductivities of rocks are given below and illustrated by reducing results obtained with actual experiments on the systems. The reason for the choice of these systems is given in Section II. The case of a line source in an infinite medium is discussed in Section III. It has already been described by Jaeger (1959) for the corresponding hydrological problem. The case of a line source along the axis of a circular cylinder is discussed in Section IV, and that of a line source on the surface of a cylinder in Section V. The application of the method to the thermal conductivity probe is given in Section VI. Finally, in Section VII the determination of diffusivity from slabs, cylinders, and spheres with constant initial and surface temperatures, as in many of the classical methods, is discussed.

In all cases where numerical values are given, units will be c.g.s., calorie, and degC.

II. The Determination of the Thermal Conductivity of Rocks

The measurement of the thermal conductivity of rocks is a relatively slow and difficult matter. The standard steady-state method, the divided bar (Benfield 1939), involves the use of a set of disks with accurately ground surfaces, and even when these have been made takes considerable experimental time. The " probe " methods, used for measurement of conductivities *in situ* in drill holes, are also slow and cumbersome.

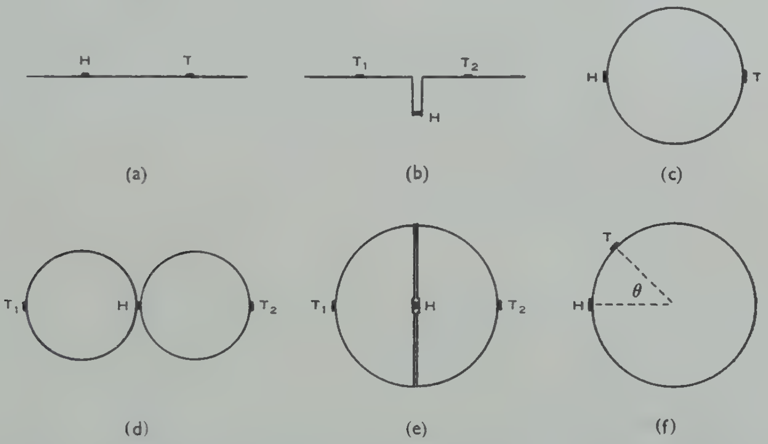

Fig. 1.—Cross sections of some possible systems for the determination of the thermal conductivity of rock specimens. *H*, heater wire ; T, T_1, T_2, thermocouples.

An ideal method requires (i) small experimental time, and (ii) small time of preparation of specimens. Condition (i) suggests, not merely that transient methods should be used, but also that the early part of the regime in which asymptotes have not been attained should be studied, this has the additional advantage that heat losses from insulated surfaces should be negligible. Condition (ii) implies that preparation of specimens should all be done with diamond tools and should involve no hand finishing.

The mechanical operations which can rapidly and accurately be performed on rocks with diamond tools are : (i) drilling cylindrical cores, (ii) facing off their ends to make finite cylinders, (iii) cutting flat surfaces. Surfaces cut by a saw will not be accurately flat so that, for example, a wire pressed between two of them will not be in contact over the whole of the length ; however, it is easy with an accurate wheel or saw to take off a shaving over a limited strip which will be plane to within $0 \cdot 001$ cm or better (cf. Fig. 1 (*e*)).

A number of experimental situations which may be obtained by the operations described above and are covered by the theory given below are shown in Figure 1. They are:

(i) A semi-infinite solid whose plane surface has a long straight heater wire H and a thermocouple T attached to it and covered with insulating material (Fig. 1 (*a*)). This simple situation, which must be viewed with some suspicion because of possible heat losses from the heater, may readily be replaced by that described in (ii) below.

(ii) A semi-infinite solid with a heater wire H in a narrow slot filled with cement to give good contact (Fig. 1 (*b*)). These methods can be used on nearly plane surfaces *in situ* or on large specimens of friable rock which cannot be machined readily.

(iii) If thin core only, say <2 cm in diameter is available, the heater H and thermocouple T may be placed along diametrically opposite generators (Fig. 1 (*c*)). A more satisfactory arrangement, Figure 1 (*d*), has narrow flats ground on two cylinders with the heater H pressed between. Two thermocouples T_1 and T_2 in parallel or series are used.

(iv) Core of moderate diameter, say 5 cm, may be slit along an axial plane and have an axial heater wire H between narrow, accurately ground, slots (Fig. 1 (*e*)).

(v) For core of greater diameter which it is not desired to cut, the heater H and thermocouple T may be on the surface along generators distant θ apart (Fig. 1 (*f*)).

(vi) Many other systems suggest themselves immediately, for example, slabs or finite cylinders with constant initial and surface temperatures.

III. THE CONTINUOUS LINE SOURCE* IN AN INFINITE MEDIUM

The temperature $v(t)$ at time t at distance a from a continuous line source which emits heat at the constant rate Q per unit length per unit time for $t>0$ is given by (cf. Carslaw and Jaeger 1959, Section 10.4)

$$v(t)=-\frac{Q}{4\pi K}\mathrm{Ei}\left(-\frac{a^2}{4\varkappa t}\right), \qquad \ldots\ldots\ldots\ldots \quad (4)$$

where K and $\varkappa$ are the thermal conductivity and diffusivity of the surrounding medium and

$$-\mathrm{Ei}(-x)=\int_x^\infty \frac{e^{-u}}{u}\mathrm{d}u \qquad \ldots\ldots\ldots\ldots\ldots\ldots\ldots \quad (5)$$

is the tabulated exponential integral. For the present purposes the Works Projects Administration Tables (1940) are the most convenient, but a useful shorter table is given by Jahnke and Emde (1933).

---

* The justification for using the simple line-source formula for the case of a thin heating wire at the distances $a>1$ cm contemplated here is essentially contained in the theoretical and experimental results on thin probes. Calculation shows that the effect of small finite diameter of the probe is negligible at the distances considered here, and experimental agreement of conductivities measured by thin probes with those determined by steady-state methods implies that for quite small times the heat flow outside the probe is determined by (4).

The result corresponding to (**2**) is

$$\frac{v(2t)}{v(t)}=\frac{\mathrm{Ei}(-a^2/8\varkappa t)}{\mathrm{Ei}(-a^2/4\varkappa t)}. \quad \ldots\ldots\ldots\ldots\ldots\ldots \text{(6)}$$

Values of $\mathrm{Ei}(-x)/\mathrm{Ei}(-2x)$ are shown in curve I of Figure 2, and values of $-\mathrm{Ei}(-x)$ in curve II.

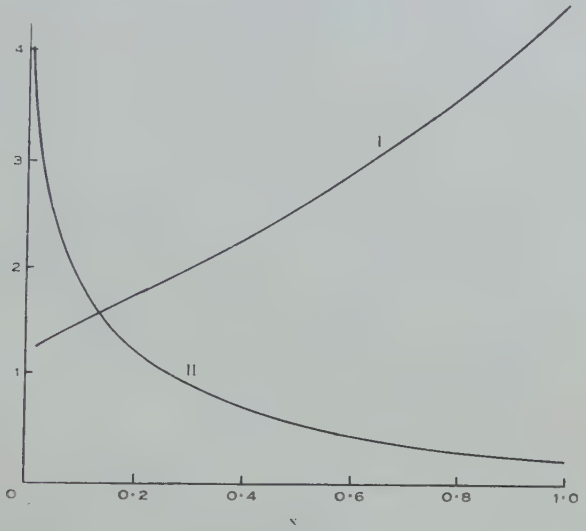

Fig. 2.—Curve I: values of $\mathrm{Ei}(-x)/\mathrm{Ei}(-2x)$. Curve II: $-\mathrm{Ei}(-x)$.

The method is, of course, ideally adapted for use with powders, but to illustrate its application to rocks the results of an experiment on a block of granite using the system of Figure 1 (*b*) are shown in Table 1. The surface of the solid was covered with lightweight insulating powder to minimize heat loss. The thickness of the block was greater than 10 cm, so that for the purposes of the present calculation it may be regarded as semi-infinite. A heating wire of

TABLE 1

REDUCTION OF OBSERVATIONS ON A LINE SOURCE IN AN INFINITE MEDIUM

n	$v(nt_0)$	$v(2nt_0)/v(nt_0)$	$a^2/8\varkappa nt_0$	$a^2/8\varkappa t_0$	$-0\cdot6\ \mathrm{Ei}(-4\cdot66/n)$
0	0·000				0·000
1	0·000				0·000
2	0·014				0·019
3	0·054	3·67	0·81	2·43	0·055
4	0·100	2·84	0·59	2·36	0·100
5	0·146	2·48	0·47	2·35	0·148
6	0·198	2·20	0·38	2·28	0·194
7	0·241	2·06	0·33	2·31	0·239
8	0·284	1·94	0·28	2·24	0·283
10	0·362				0·362
12	0·436				0·434
14	0·497				0·498
16	0·550				0·557

resistance $0 \cdot 278\ \Omega$/cm was placed at the base of a narrow slot $0 \cdot 5$ cm deep, which was filled with cement to ensure good contact. The heater current was $0 \cdot 57$ A. Temperatures in the surface were measured by thermocouples T_1, T_2, in parallel, each distant $1 \cdot 23$ cm from the heater.

Actual temperatures $v(nt_0)$ measured from the recorder at times nt_0, $n=1, 2, \ldots$, where $t_0=7 \cdot 5$ sec, are shown in the second column. The third column shows the values of $v(2nt_0)/v(nt_0)$ and the fourth the values of $a^2/8\varkappa nt_0$ which are the abscissae of curve I of Figure 2 corresponding to the ordinates $v(2nt_0)/v(nt_0)$. The values of $a^2/8\varkappa t_0$ in the fifth column are seen to be approximately constant, as they should be, with a mean value of $2 \cdot 33$. Using this mean value, the observed temperatures should be proportional to $\mathrm{Ei}(-4 \cdot 66/n)$.

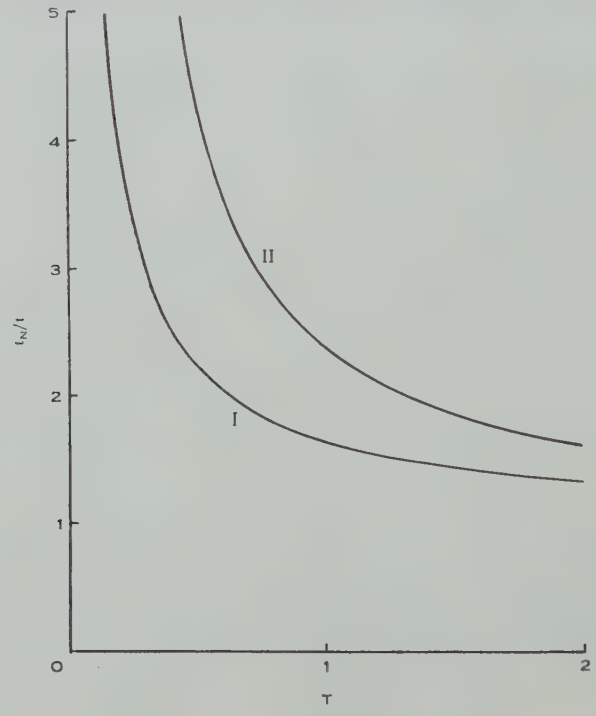

Fig. 3.—Values of t_N/t for which $\mathrm{Ei}(-tT/t_N)=N\mathrm{Ei}(-T)$. Curve I: $N=2$; curve II: $N=3$.

The mean value of the constant of proportionality calculated from the values $n=3, \ldots, 8$ is $0 \cdot 60$ and the last column shows values of $-0 \cdot 6\ \mathrm{Ei}(-4 \cdot 66/n)$, which are seen to agree to within experimental error with the observed temperatures. By (1), allowing for an image source, the value of the constant of proportionality is $Q/2\pi K$ and this leads to the result $K=0 \cdot 0057$. It should be noticed that this result does not require a knowledge of the distance a, which might be uncertain.

If the value of a is known, $\varkappa$ follows from $a^2/8\varkappa t_0=2 \cdot 33$, and using the measured value $a=1 \cdot 23$ cm gives $\varkappa=0 \cdot 0108$. This value of $\varkappa$ does not involve a knowledge either of the heat input or of the calibration of the thermocouples.

From these values of K and $\varkappa$, the heat capacity ρc per unit volume of the rock is found to be $0\cdot53$, which is consistent with the density of the rock and the specific heat of granite. This provides a valuable check on the overall reliability of the method.

If the second method of reduction described in the Introduction is applied to this problem, (3) becomes, using (4),

$$\mathrm{Ei}(-tT/t_N)=N\,\mathrm{Ei}(-T), \qquad (7)$$

where $T=a^2/4\varkappa t$. In Figure 3 values of t_N/t satisfying (7) are shown as a function of T for the values 2 and 3 of N.

TABLE 2

ALTERNATIVE REDUCTION OF THE EXPERIMENT OF TABLE 1

n	$v(x_n t_0)$	x_n	x_{2n}/x_n	$a^2/4\varkappa x_n t_0$	$a^2/4\varkappa t_0$
0	0				
1	0·062	3·18	1·43	1·45	4·61
2	0·124	4·54	1·57	1·07	4·86
3	0·186	5·80	1·76	0·82	4·76
4	0·248	7·14	1·94	0·65	4·64
6	0·372	10·22			
8	0·496	13·86			

The treatment by this method of the curve reduced in Table 1 is shown in Table 2. Choosing the same unit of time $t_0=7\cdot5$ sec, the times $x_n t_0$ at which the temperatures attain the values $n\times0\cdot062$ degC, $n=1, 2, \ldots$, are shown in the third column. The fourth column shows the ratios x_{2n}/x_n and the fifth the value of $a^2/4\varkappa x_n t_0$ read off from curve I of Figure 3. The last column shows $a^2/4\varkappa t_0$, which should be the same for all rows. The mean value of $a^2/4\varkappa t_0$ is $4\cdot72$, which may be compared with $4\cdot64$ found earlier. The determination of K and $\varkappa$ now proceeds as before.

IV. A CIRCULAR CYLINDER WITH AXIAL HEATING

The cylinder is supposed to be initially at zero temperature and to have a continuous line source of heat along its axis which emits Q heat units per unit time per unit length for $t>0$. The surface of the cylinder is assumed to be insulated, so that its length does not enter the problem.

With the previous notation, the temperature $v(t)$ at time t at a point of the surface of the cylinder is given by (Carslaw and Jaeger 1959, Section 14.18 (**11**), (**12**))

$$v(t)=\frac{Q}{\pi K}f_1(\varkappa t/a^2), \qquad (8)$$

where

$$f_1(T)=T-\tfrac{1}{8}-\sum_{s=1}^{\infty}\frac{1}{\alpha_s^2 J_0(\alpha_s)}\exp(-\alpha_s^2 T), \qquad (9)$$

and the α_s, $s=1, 2, \ldots$, are the positive roots of $J_1(\alpha)=0$.

For large values of t, v tends to a straight line of slope $Q/\pi a^2 \rho c$ and intercept $a^2/8\varkappa$ on the t-axis. By measuring both of these, both K and $\varkappa$ can be determined. This is an example of the "time-lag" methods referred to earlier.

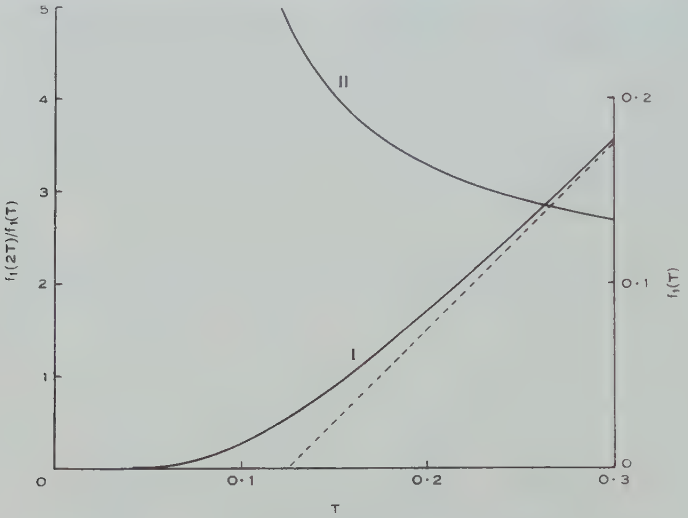

Fig. 4.—Curve I : $f_1(T)$, right-hand scale ; the asymptote is shown dotted. Curve II : $f_1(2T)/f_1(T)$, left-hand scale.

To enable the present method to be used for smaller values of time along the lines described in Section I, values of $f_1(T)$ and $f_1(2T)/f_1(T)$ calculated from (9) are shown in Figure 4.

Table 3

REDUCTION OF OBSERVATIONS FOR AXIAL HEATING OF A CIRCULAR CYLINDER

n	$v(nt_0)$	$v(2nt_0)/v(nt_0)$	$\varkappa nt_0/a^2$	$\varkappa t_0/a^2$	$1\cdot 34 f_1\,(0\cdot 036n)$
0	0				
1	0·000				
2	0·001				0·003
3	0·020				0·023
4	0·051	4·31	0·140	0·0350	0·052
5	0·090	3·49	0·182	0·0364	0·090
6	0·131	3·14	0·215	0·0358	0·131
7	0·177	2·86	0·257	0·0367	0·176
8	0·220				0·221
10	0·314				0·316
12	0·411				0·411
14	0·506				0·508

As an example of a practical case, Table 3 shows the surface temperature of a cylinder of quartz-porphyry of diameter 4·76 cm heated by an axial wire of resistance 0·278 Ω/cm carrying a current of 0·64 A for $t > 0$. The cylinder was immersed in lightweight insulating powder.

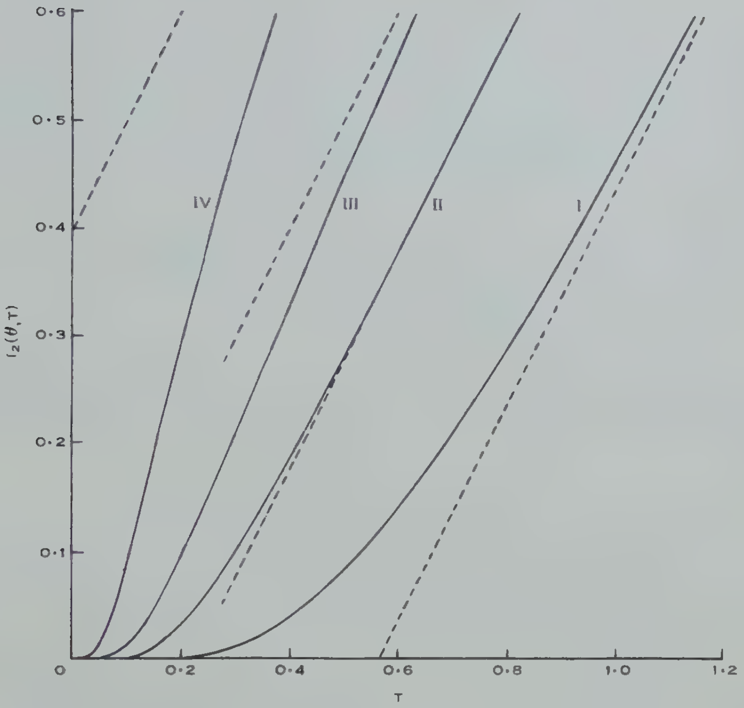

Fig. 5.—Values of $f_2(\theta,T)$. Curves I, II, III, IV are for $\theta=180$, 90, 69, 45° respectively. The asymptotes are shown by dotted lines.

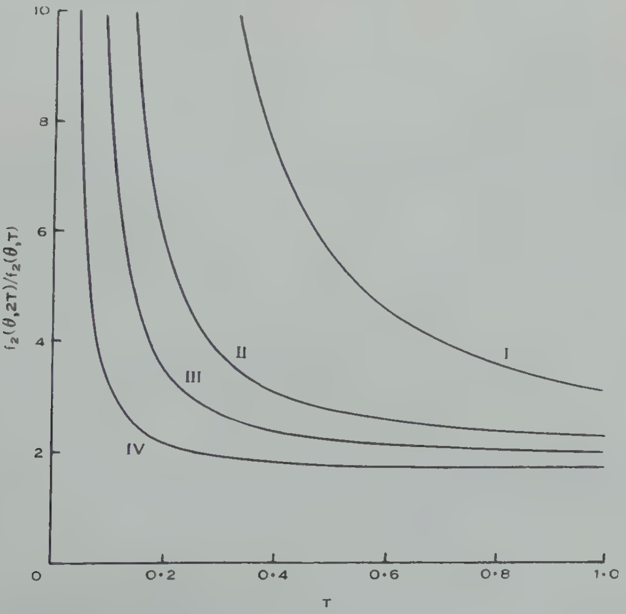

Fig. 6.—Values of $f_2(\theta,2T)/f_2(\theta,T)$. Curves I, II, III, IV are for $\theta=180$, 90, 69, 45° respectively.

The unit of time chosen is $t_0=15$ sec; the second column gives the temperature $v(nt_0)$ at time nt_0, and the third the ratio $v(2nt_0)/v(nt_0)$. The fourth column gives values of $\varkappa nt_0/a^2$ read off from curve II of Figure 4. The mean of the values of $\varkappa t_0/a^2$ in the fifth column is 0·036 and, choosing a constant of proportionality of 1·34, the calculated results in the last column agree well with the experimental values.

From $Q/\pi K=1\cdot34$, we get $K=0\cdot0064$, and $\varkappa t_0/a^2=0\cdot036$ gives $\varkappa=0\cdot0136$. These give $\rho c=0\cdot47$, leading, with $\rho=2\cdot7$, to the reasonable value $c=0\cdot17$.

V. A CIRCULAR CYLINDER HEATED ALONG A GENERATOR

The cylinder is supposed to be initially at zero temperature and to have a continuous line source along a generator which emits Q heat units per unit length per unit time for $t>0$. There is supposed to be no loss of heat from the surface of the cylinder, so its length does not matter.

TABLE 4

REDUCTION OF OBSERVATIONS ON A CIRCULAR CYLINDER HEATED ALONG A GENERATOR

n	$v(nt_0)$	$v(2nt_0)/v(nt_0)$	$\varkappa nt_0/a^2$	$\varkappa t_0/a^2$	$1\cdot53f_2(\pi,\ 0\cdot055n)$
0	0				0
4	0·002				0·004
5	0·010				0·012
6	0·027	10·3	0·323	0·054	0·027
7	0·050	8·04	0·38	0·054	0·050
8	0·082	6·5	0·443	0·056	0·081
10	0·171				0·168
12	0·278				0·275
14	0·402				0·401
16	0·533				0·540

The temperature $v(t)$ at time t at a point on the surface at an angular distance θ from the source is (Carslaw and Jaeger 1959, Section 14.18 (**11**), (**12**))

$$v(t)=\frac{Q}{\pi K}f_2(\theta,\varkappa t/a^2), \qquad \text{(10)}$$

where

$$f_2(\theta,T)=T+\tfrac{1}{8}-\ln\,(2\sin\tfrac{1}{2}\theta)-\sum_{n=0}^{\infty}\varepsilon_n\cos n\theta\sum_{m=1}^{\infty}\frac{\exp\,(-\alpha_{n,m}^2T)}{(\alpha_{n,m}^2-n^2)}, \qquad \text{(11)}$$

where $\varepsilon_1=1$, $\varepsilon_n=2$ if $n\geqslant2$, and the $\alpha_{n,m}$, $m=1, 2, \ldots$, are the roots of $J_n'(\alpha)=0$. These are tabulated by Smith, Rodgers, and Traub (1944).

For large values of the time, $v(t)$ is asymptotically a straight line of slope $Q/\pi a^2\rho c$ and intercept $a^2\{8\ln\,(2\sin\frac{1}{2}\theta)-1\}/8\varkappa$ on the t-axis. If $0<\theta<69°$, approximately, this intercept is negative and if $69°<\theta<180°$ it is positive. Values of $f_2(\theta,T)$ for the values 45, 69, 90, and 180° of θ are shown in Figure 5. These results lead to a "time-lag" method for determining both K and $\varkappa$;

it may be remarked that the asymptote is approached most rapidly when θ is about 90°.

For use with the present method the values of the ratios $f_2(\theta,2T)/f_2(\theta,T)$ for the values 45, 69, 90, 180° of θ are shown in Figure 6.

As an example, Table 4 shows some observations for the case $\theta=\pi$ made with a heating wire of resistance $0{\cdot}278\ \Omega/\text{cm}$ carrying a current of $0{\cdot}8$ A and running between two dolerite cylinders of diameter $2{\cdot}22$ cm in the arrangement of Figure 1 (*d*). The unit of time t_0 is $7{\cdot}5$ sec, and temperatures at times nt_0 are shown in the second column. The third column gives the ratios $v(2nt_0)/v(nt_0)$, and the fourth shows values of $\varkappa nt_0/a^2$ read off from curve I of Figure 6. The mean of the values of $\varkappa t_0/a^2$ in the fifth column is $0{\cdot}055$, leading to $\varkappa=0{\cdot}0090$. Choosing a constant of proportionality of $1{\cdot}53$, the theoretical values in the last column are obtained which agree reasonably well with the measured temperatures. The result $Q/\pi K=1{\cdot}53$ now gives $K=0{\cdot}0044$, $\rho c=0{\cdot}49$.

VI. The Thermal Conductivity Probe

This is the extension of the line source theory of Section III to cover the case in which the source has a finite diameter and thermal capacity. The simplest idealization of such a system is as follows: an infinitely long circular cylinder of radius a is surrounded by an infinite medium of thermal properties K, ρ, c, $\varkappa$ and contains perfect conductor of thermal capacity S per unit length to which heat is supplied at the constant rate Q per unit length per unit time for times $t>0$. There is a thermal contact resistance $1/H$ per unit area at the surface $r=a$. Then, if the whole system is at zero temperature at time $t=0$, the temperature v of the perfect conductor at time t is given by

$$Kv/Q=G(h,\alpha,\tau), \qquad \ldots\ldots\ldots\ldots \quad (\mathbf{12})$$

where

$$\tau=\varkappa t/a^2, \quad \alpha=2\pi a^2\rho c/S, \quad h=K/aH, \qquad \ldots\ldots \quad (\mathbf{13})$$

and $G(h,\alpha,\tau)$ is a complicated integral expression for which some numerical values are given by Jaeger (1956).

In principle, the use of a probe containing a heater and a temperature-measuring element in a hole drilled in rock provides a simple method of measuring rock conductivities *in situ*. In fact the experiments are difficult to interpret since all three parameters (**13**) occurring in (**12**) have to be determined, and, while (**12**) has a logarithmic asymptote from which K may be determined directly, to do so in a hole of diameter 4 cm requires an experiment of 2 hr or more in duration, which is most undesirable.

In order to be able to use the earlier parts of the temperature-time curve, Blackwell (1954) has proposed to use several terms of the asymptotic expansion of $G(h,\alpha,\tau)$, while Beck, Jaeger, and Newstead (1956) have suggested a method of curve fitting. The present method is very suitable for the reduction of these results, though more numerical results than those given by Jaeger (1956) are needed for its complete application.

Firstly, it should be said that in most cases a reasonably accurate estimate of the value of α can be made from a knowledge of the dimensions and material of the probe and the nature of the surrounding rock. Secondly, for the case of holes containing water it may be assumed that h is zero or small, whereas, if there is an air-space between the probe and the rock, h will be relatively large. Only the former case will be discussed here, and in Figure 7 values of $G(0,\alpha,\tau)$ and $G(0,\alpha,2\tau)/G(0,\alpha,\tau)$ for various values of α are shown. These have been taken from Jaeger (1956), where some information about the case $h>0$ is also given.

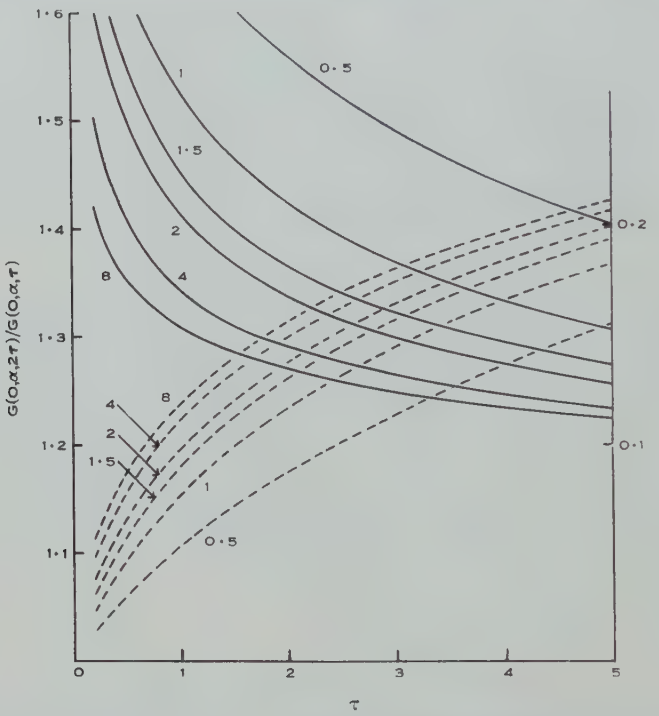

Fig. 7.—Values of $G(0,\alpha,\tau)$: dotted lines, right-hand scale. Values of $G(0,\alpha,2\tau)/G(0,\alpha,\tau)$: full lines, left-hand scale. The numbers on the curves are the values of α.

As an illustration, some observations made in a water-filled hole of diameter 3·5 cm in vesicular basalt are shown in Table 5. They are reduced on the assumption (derived from the dimensions of the probe) that $\alpha=2$. The unit of time t_0 is 300 sec.

As usual, the second column shows values of the observed temperature at time nt_0, the third gives the ratio $v(2nt_0)/v(nt_0)$, the fourth gives the values of $\varkappa nt_0/a^2$ read off from Figure 7 for the case $\alpha=2$. The mean of the values of $\varkappa t_0/a^2$ is 0·62, and the last column shows calculated temperatures for this value with a constant of proportionality $Q/K=52$.

The value of Q was $0{\cdot}22$ cal cm^{-1} sec^{-1}, so that from (**12**) it follows that $K=0{\cdot}0042$. Also since $\varkappa/a^2=0{\cdot}0021$ and $a=1{\cdot}75$ cm we find $\varkappa=0{\cdot}0063$. These results lead to the rather high value $\rho c=0{\cdot}67$, which may be attributed to water filling the vesicles in the rock.

The above reduction is incomplete since it merely assumed that $h=0$ and $\alpha=2$. An actual experimental curve can usually be fitted equally well for a range of values of both h and α. There are, however, two additional criteria which are usually available: (i) if the assumed values of h or α are flagrantly incorrect the values of $\varkappa t_0/a^2$ in the fifth column of the table will cease to be approximately constant, (ii) the value of ρc obtained must be consistent with that assumed in α. This last criterion is not available for the example given in Table 5 because of the peculiar nature of the material, so that the reduction cannot be carried further.

TABLE 5

REDUCTION OF OBSERVATIONS MADE WITH A THERMAL CONDUCTIVITY PROBE

n	$v(nt_0)$	$v(2nt_0)/v(nt_0)$	$\varkappa nt_0/a^2$	$\varkappa t_0/a^2$	$52G(0,2,0\cdot62n)$
0	0				0
2	5·69	1·381	1·32	0·66	5·72
3	6·92	1·344	1·86	0·62	6·92
4	7·86	1·318	2·42	0·60	7·90
5	8·68	1·297	3·00	0·60	8·68
6	9·30				9·36
8	10·36				10·40
10	11·26				11·23

VII. MEASUREMENT OF DIFFUSIVITY FROM SLABS OR CYLINDERS WITH CONSTANT INITIAL AND SURFACE TEMPERATURE

These represent some of the oldest and simplest of the classical methods for measuring diffusivity. The formulae are all well known.

(i) For the slab of thickness $2a$ with zero initial temperature and surface temperature V, the temperature $v(t)$ on the mid-plane of the slab at time t is given by (Carslaw and Jaeger 1959, Section 3.4)

$$v=V-\frac{4V}{\pi}\sum_{n=0}^{\infty}\frac{(-1)^n}{2n+1}\exp\{-\tfrac{1}{4}(2n+1)^2\pi^2T\}, \quad \ldots\ldots \quad (14)$$

where

$$T=\varkappa t/a^2. \quad \ldots\ldots \quad (15)$$

Numerical values of v at close intervals of T are given by Olson and Schultz (1942). Values of the ratio $v(2t)/v(t)$ for this case are shown in Figure 8, curve I.

(ii) For an infinite circular cylinder of radius a with zero initial temperature and surface temperature V, the temperature on the axis is given by (Carslaw and Jaeger 1959, Section 7.6)

$$v=V-2V\sum_{n=1}^{\infty}\frac{\exp(-\alpha_n^2T)}{\alpha_nJ_1(\alpha_n)}, \quad \ldots\ldots \quad (16)$$

where T is given by (**15**) and α_n, $n=1, 2, \ldots$, are the positive roots of $J_0(\alpha)=0$. Numerical values of (**16**) are given by Olson and Schultz (1942). Values of the ratio $v(2t)/v(t)$ are shown in Figure 8, curve II.

(iii) Numerical values of the temperatures in finite circular cylinders with zero initial and constant surface temperatures can readily be obtained (Carslaw and Jaeger 1959, Section 8.4; or Olson and Schultz 1942). In curve III of Figure 8 values of the ratio $v(2t)/v(t)$ for the centre temperature of a finite cylinder of length $2a$ and diameter $2a$ are shown.

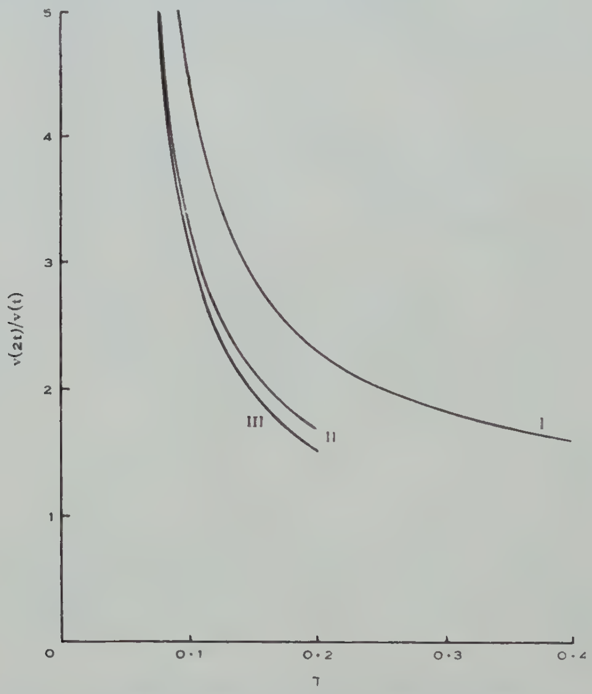

Fig. 8.—Values of $v(2t)/v(t)$ at the centre of a solid with zero initial temperature and constant surface temperature as a function of $T=\varkappa t/a^2$. Curve I: a slab; curve II: a cylinder; curve III: a finite cylinder whose length is equal to its diameter.

These methods have the well-known disadvantage that it is difficult to be certain that the prescribed temperature is in fact maintained at the surface. This disadvantage is less important for poor conductors, and it may be noted that such methods are particularly well suited to rocks whose diffusivities have to be measured when saturated with water.

As an example, Table 6 shows the recorded temperature changes (on an arbitrary scale) measured by a thermocouple at the centre of a finite circular cylinder whose length and diameter were both 5·08 cm and which was initially at a constant temperature and was immersed at $t=0$ in a well-stirred mixture of ice and water. The mean of the values of $\varkappa t_0/a^2$ in the fourth column is 0·0079 and the unit of time t_0 was 3·75 sec, leading to $\varkappa=0{\cdot}0136$. The material of the cylinder was the quartz porphyry previously studied in Section IV, where the same value of $\varkappa$ was found. While the complete agreement is, of course, accidental, it suggests that the boundary condition of zero surface temperature may in fact have been fairly well realized in the present experiment. It will be noticed that the absolute values of the temperature are not needed in the present method.

TABLE 6

REDUCTION OF OBSERVATIONS ON THE DIFFUSIVITY OF A FINITE CYLINDER

n	$v(nt_0)$	$v(2nt_0)/v(nt_0)$	$\varkappa nt_0/a^2$	$\varkappa t_0/a^2$
0	0			
8	0·085	6·73	0·064	0·0080
9	0·128	5·53	0·071	0·0079
10	0·182	4·61	0·079	0·0079
11	0·236	4·08	0·085	0·0077
16	0·572			
18	0·708			
20	0·839			
22	0·962			

VIII. REFERENCES

BARRER, R. M. (1939).—*Trans. Faraday Soc.* **35** : 628.

BECK, A., JAEGER, J. C., and NEWSTEAD, G. (1956).—*Aust. J. Phys.* **9** : 286.

BENFIELD, A. E. (1939).—*Proc. Roy. Soc.* A **173** : 428.

BLACKWELL, J. H. (1954).—*J. Appl. Phys.* **25** : 137.

CARSLAW, H. S., and JAEGER, J. C. (1959).—" Conduction of Heat in Solids." 2nd Ed. (Oxford Univ. Press.)

JAEGER, J. C. (1956).—*Aust. J. Phys.* **9** : 167.

JAEGER, J. C. (1959).—*J. Geophys. Res.* **64** : 561.

JAHNKE, E., and EMDE, F. (1933).—" Tables of Functions." (Teubner : Berlin.)

OLSON, F. C. W., and SCHULTZ, O. T. (1942).—*Industr. Engng. Chem.* **34** : 874.

SMITH, D. B., RODGERS, L. M., and TRAUB, E. H. (1944).—*J. Franklin Inst.* **237** : 301.

DE VRIES, D. A., and PECK, A. J. (1958).—*Aust. J. Phys.* **11** : 255.

WORKS PROJECTS ADMINISTRATION (1940).—" Tables of Sine, Cosine, and Exponential Integrals." (U.S. National Bureau of Standards.)

THE OPTIMUM LINE WIDTH FOR THE TRANSITION USED IN A REFLECTION CAVITY MASER AMPLIFIER

By G. J. Troup*

[*Manuscript received April 8, 1959*]

Summary

The line width of the amplifying transition in a reflection cavity maser is shown to have an optimum value, which will give maximum amplification bandwidth at a fixed gain. Difficulties associated with achieving the optimum line width in practice for the paramagnetic maser are briefly discussed.

I. Introduction

The bandwidth of a resonant cavity maser amplifier at a fixed gain depends upon the line width of the amplifying transition and is always considerably less than this line width (Gordon, Zeiger, and Townes 1955 ; Gordon and White 1958 ; Stich 1958). It will be shown below that, for a given reflection cavity maser system, there is an optimum transition line width which will give maximum amplification bandwidth at constant gain. The value of the optimum line width is a function of various amplifier parameters (frequency, filling factor for the active medium, etc.), of the dipole moment for the transition, and of the concentration of excess molecules in the emissive condition. (Molecule will be used throughout as a generic term.)

In order to take full advantage of the low noise input temperature of a maser amplifier, it must be operated at a gain of the order of 20 dB if followed by a conventional microwave receiver (see, for example, Wittke 1957). At such gains, reported cavity maser bandwidths are narrow ; for example, Morris, Kyhl, and Strandberg (1959) report a bandwidth of 4 Mc/s at $\sim$9000 Mc/s with a gain of 20 dB, actually a vast improvement on previously reported masers (for example, McWhorter and Meyer 1958 ; Autler and McAvoy 1958). Bandwidth increase is desirable, and the knowledge of the optimum transition line width is therefore useful.

Moreover, any limitation of the concentration of excess upper-state molecules in a maser also limits the obtainable bandwidth, and operation of the system at optimum line width may then be the only method of bandwidth increase. This is important in the case of the three-level paramagnetic maser (Bloembergen 1956), for the device cannot be placed in an emissive condition when the concentration of paramagnetic ions exceeds a certain value. One is led to the idea that the maximum bandwidth obtainable with a Bloembergen cavity maser will

---

* Weapons Research Establishment, Salisbury, S. Aust.

occur when the concentration of active centres is close to the limiting value and operation at optimum line width is used. A prediction of the ultimate bandwidth obtainable from a Bloembergen system then becomes possible, but this will not be undertaken here.

II. The Reflection Cavity Maser

Only the reflection cavity maser is considered, since it is superior in all respects (noise factor, bandwidth at a fixed gain, etc.) to the transmission cavity amplifier (Gordon and White 1958). Maser performance depends upon the "molecular Q" Q_m, which is defined by

$$-Q_m=\frac{2\pi f\times\text{Average energy stored in the cavity}}{\text{Average power emitted in the cavity}}. \quad \ldots\ldots (1)$$

Here, f is the resonant frequency of the cavity, taken as equal to the frequency of amplification and to the central frequency of the molecular response.

It can be shown (e.g. Strandberg 1957) that Q_m is of the form

$$|Q_m|=(K\delta/N^*), \quad \ldots\ldots\ldots\ldots\ldots\ldots (2)$$

where δ is the line width of the amplifying transition, N^* is the number density of the excess molecules in the emissive state, and K is a constant for the particular molecules and amplifier system. K includes the square of the dipole moment for the amplifying transition and the filling factor for the active medium in the cavity. (This last is the ratio of the field energy coupled to the molecules to the total field energy stored in the cavity.)

Subject to certain assumptions, the gain G of the reflection cavity maser can be written

$$G\simeq(|Q_m|+Q_L)^2(|Q_m|-Q_L)^{-2}, \quad \ldots\ldots\ldots\ldots (3)$$

where Q_L is the loaded Q of the cavity. The assumptions are:

(i) that the gain has a reasonably high value (>10, say);

(ii) that the cavity has a high unloaded Q, so that the loaded Q is determined mainly by the external coupling to the cavity (McWhorter and Meyer 1958).

The bandwidth B of the reflection cavity maser, after some manipulation of the results of Gordon and White (1958) and of Stich (1958) (which are identical), can be written

$$B\simeq\delta[(|Q_m|/Q_L)-1][1+(\delta|Q_m|/f)]^{-1}, \quad \ldots\ldots\ldots\ldots (4)$$

where f is the centre frequency of the molecular response and of the cavity resonance, as previously; a Lorentz line shape is assumed for the transition. The amplification bandwidth B is seen to be always less than the line width δ, both because of the factor $[(|Q_m|/Q_L)-1]$, which may be regarded as the gain-dependent term (see equation (3)), and because of the form of the remainder of the expression.

III. OPTIMUM LINE WIDTH FOR THE REFLECTION CAVITY MASER

From equation (2), any alteration in the line width δ will alter the molecular Q, and hence (equation (3)) the gain. However, the gain can be kept constant by suitably adjusting the loaded Q of the cavity. Then only the terms $\delta[1+(\delta\,|\,Q_m\,|/f)]^{-1}$ need be considered to determine whether the transition line width has an optimum value at constant gain. Using equation (2), the expression governing the bandwidth is rewritten as

$$\delta[1+(\delta\,|\,Q_m\,|/f)]^{-1}=b=\delta[1+(K\delta^2/N^*f)]^{-1}. \quad \ldots\ldots \quad (5)$$

N^*, the concentration of excess emissive molecules, is taken as constant for the amplifier system. Differentiation of this expression with respect to δ then shows that b has a maximum value

$$b_{\text{max.}}=\tfrac{1}{2}(K/N^*f)^{-\frac{1}{2}}, \quad \ldots\ldots\ldots\ldots\ldots\ldots\ldots \quad (6)$$

when

$$\delta=(K/N^*f)^{-\frac{1}{2}}=2b_{\text{max.}}.$$

Hence the amplification bandwidth of a given reflection cavity maser system can be given a maximum value by the adjustment of the line width of the amplifying transition to an optimum value.

Two conditions must be fulfilled before the optimum line width can be realized. Firstly, alteration of the line width must not alter N^*, the concentration of excess emissive molecules, i.e. the efficiency of excitation must remain constant. Secondly, any method used to alter the line width must not affect the magnitude of the dipole moment for the amplifying transition (contained in the factor K). This last requirement is not unrealistic. In the case of the three-level paramagnetic maser, the energy levels are mixtures of states, dependent on the strength and direction of a steady magnetic field : the use of magnetic field inhomogeneity to increase the line width might therefore affect the dipole moment of the amplifying transition.

For completeness, an important practical case is considered next. When paramagnetic ions are diluted in a host lattice, the transition line width can be directly proportional to the concentration of the ions, N (Bogle and Symmons 1959). Since N^*, the concentration of excess ions in the emissive state, will also be directly proportional to the total ionic concentration N, the molecular Q can be a constant, independent of the line width (equation (2)). If variation of the line width is then carried out solely by variation of the ionic concentration, equation (5) shows that the best width is the broadest obtainable ; for

$$\left.\begin{array}{r} b\rightarrow(f/|\,Q_m\,|) \text{ as } \delta\rightarrow\infty, \\ \text{i.e. as } N\rightarrow\infty, \end{array}\right\} \quad \ldots\ldots\ldots\ldots\ldots \quad (7)$$

since δ/N is a constant.

Equations (6) and (7) show that the cavity maser amplification bandwidth is influenced by the concentration of excess emissive molecules. Therefore, limiting this concentration also limits the bandwidth at constant gain. The fact that operation of the Bloembergen maser cannot be achieved when the concentration of paramagnetic ions reaches a certain critical value (Autler and McAvoy 1958 ; Giordmaine *et al.* 1958) indicates that adjustment of the transition line width may become an important method of bandwidth increase (see also Bogle and Symmons 1959).

IV. Practical Considerations for Paramagnetic Masers

The actual realization of the optimum line width for a given maser system may not be easy. Increasing the effective line width for paramagnetic transitions might be done relatively simply, by the use of magnetic-field inhomogeneity. Decreasing the line width is more difficult, since this will involve changing the maser crystal in some way—for example, by using special isotopes to reduce hyperfine broadening. It is desirable to work with a substance in which the line width is less than the optimum width for a given maser system, but which will still give a low molecular Q when the line width is increased. Much research into the causes of line widths of paramagnetic ions in crystals still needs to be done ; in many cases the line widths are considerably in excess of calculated spin-spin widths (Bogle and Symmonds 1959).

V. Conclusion

It has been shown that there is an optimum line width for the transition used in a cavity maser, such that the amplification bandwidth is a maximum at a fixed gain. The realization of this optimum line width may be difficult in practice, since the line width must be variable without changing any other amplifier parameters.

VI. Acknowledgments

The author is indebted to Dr. G. S. Bogle and Dr. H. F. Symmons for the communication of their paper (Bogle and Symmons 1959) prior to publication. The present paper is published with the permission of the Chief Scientist, Australian Department of Supply.

VII. References

Autler, S. H., and McAvoy, N. (1958).—*Phys. Rev.* **110** : 280.
Bloembergen, N. (1956).—*Phys. Rev.* **104** : 324.
Bogle, G. S., and Symmons, H. F. (1959).—*Aust. J. Phys.* **12** : 1.
Giordmaine, J. A., Alsop, L. E., Nash, F. R., and Townes, C. H. (1958).—*Phys. Rev.* **109** : 302.
Gordon, J. P., and White, L. D. (1958).—*Proc. Inst. Radio Engrs., N.Y.* **46** : 1588.
Gordon, J. P., Zieger, H. Z., and Townes, C. H. (1955).—*Phys. Rev.* **99** : 1264.
McWhorter, A. C., and Meyer, J. W. (1958).—*Phys. Rev.* **109** : 312.
Morris, R. J., Kyhl, R. L., and Strandberg, M. W. P. (1959).—*Proc. Inst. Radio Engrs., N.Y.* **47** : 80.
Stich, M. L. (1958).—*J. Appl. Phys.* **29** : 782.
Strandberg, M. W. P. (1957).—*Phys. Rev.* **106** : 617.
Wittke, J. P. (1957).—*Proc. Inst. Radio Engrs., N.Y.* **45** : 291.

SEISMIC RECORDINGS OF LARGE EXPLOSIONS IN SOUTH-EASTERN AUSTRALIA

By H. A. Doyle,[*] I. B. Everingham,[†] and T. K. Hogan[‡]

[*Manuscript received April* 29, 1959]

Summary

Three very large quarry explosions of between 50 and 100 tons of high explosive in the Snowy Mountains area were recorded by seismographs at distances up to 375 km. P and S wave velocities within the Earth's crust for this part of south-eastern Australia were formally determined to be $6 \cdot 04$ ($\pm 0 \cdot 04$) and $3 \cdot 62$ ($\pm 0 \cdot 03$) km/sec, respectively. The P_n velocity was found to be $8 \cdot 03$ km/sec, with an estimated error of $0 \cdot 2$ km/sec. Assuming a uniform layer above the Mohorovičić discontinuity with these velocities, the discontinuity was formally estimated to be at a depth of 37 km.

I. Introduction

During 1956 and 1957 three very large explosions of between 50 and 100 tons were detonated at Eaglehawk quarry in the Snowy Mountains area of New South Wales to provide rock-fill for the Adaminaby dam. The positions and times of these explosions (Table 1) were determined accurately and the ground waves produced were recorded at 13 different stations (Fig. 1) by the Scientific Services Division of the Snowy Mountains Hydro-Electric Authority (S.M.H.E.A.), the Geophysics Department of the Australian National University, and the Geophysical Section of the Bureau of Mineral Resources.

The aim of this programme was to obtain accurate seismic velocities for the study of the Earth's " crust " in this region, and to assist in the location of naturally occurring earth tremors. The S.M.H.E.A. has recently set up seismic stations at Wambrook, Jindabyne, Cabramurra, and Geehi (Jaeger and Browne 1958) for engineering purposes, while the National University has established stations at Canberra and Inveralochy (Fig. 1). The Bureau of Mineral Resources has a station at Melbourne, and until recently ran a temporary one at Warragamba in conjunction with the Sydney Water Board. A Century prospecting seismograph was used at Mt. Stromlo, as its distance (96 km) was near the best distance for critical reflection from the Mohorovičić discontinuity. In addition temporary recording sites were used at Cooma, Indi, Berrima, and Marulan (N.S.W.) by the S.M.H.E.A. and the University, and at Whitfield (Vic.) by the Bureau of Mineral Resources. Radio warnings of the expected times of the explosions were broadcast from the S.M.H.E.A. station VL2PA Wambrook, and from the Cooma commercial station 2XL. The times of the explosions were determined with an error of less than 10 msec by transmitting a pulse by radio from the detonation apparatus to the Cooma laboratories of the Scientific Services Division

---

[*] Department of Geophysics, Australian National University, Canberra.

[†] Bureau of Mineral Resources, Geology and Geophysics, Melbourne.

[‡] Scientific Services Division, Snowy Mountains Hydro-Electric Authority, Cooma, N.S.W.

where it was recorded by a Minirack recorder. Second impulses (with the 59th second omitted) were produced by a crystal clock at the Cooma laboratories and broadcast over the radios and also recorded on the Minirack. The crystal clock was rated from WWVH to an accuracy of ±5 msec. The detonations had delays of less than 10 msec. The geographic positions of the explosions were obtained from survey marks related to the S.M.H.E.A. grid with an error less than 0·01 km (Table 1).

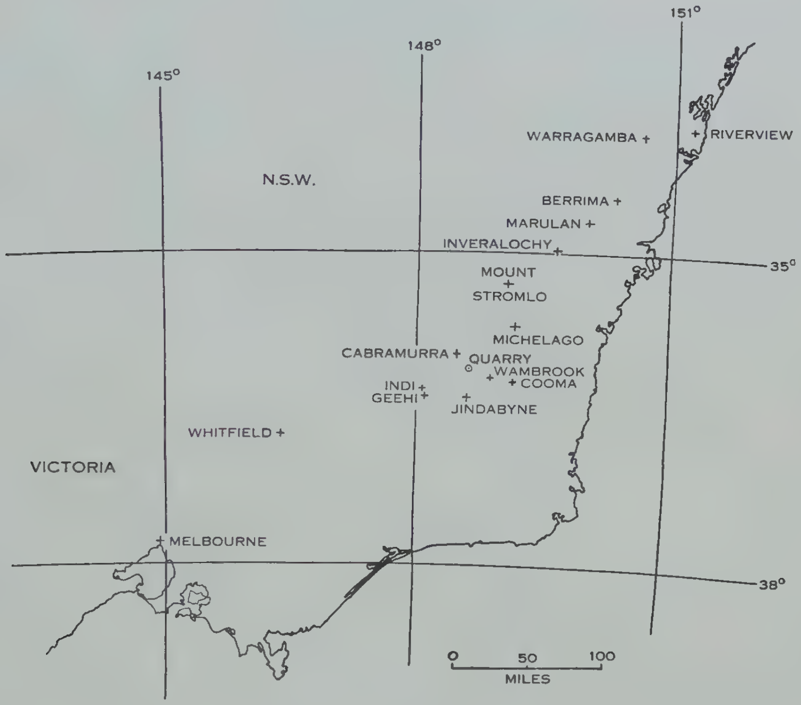

Fig. 1.—Recording sites.

The distances to each recording station were calculated with an error no greater than ½ km (Table 3). The maximum height difference between sites was about 1 km and so no height correction was made. The travel-times were usually measured to about ±0·2 sec, but some instruments gave much better accuracy (e.g. at Cooma).

Table 1

DETAILS OF EXPLOSIONS

Explosion	Date	Time (G.M.T.)	Geographic Coordinates φ	λ	Size (tons)
A	23. xii.56	02 19 49·6	36° 08′·2	148° 37′·7	60
B	10. ii.57	03 00 54·5	36° 07′·6	148° 36′·8	50
C	7.viii.57	00 23 41·1	36° 08′·2	148° 37′·7	100

The instruments used were generally of short period and high magnification (Table 2). They ranged from permanent observatory-type instruments (Benioff and Wood-Anderson), portable observatory-type (Willmore), to refraction survey seismographs (Century) and composite units put together temporarily for the work (e.g. Willmore geophone plus Minirack amplifier and recorder, as used at Cooma).

TABLE 2

STATION INSTRUMENTATION

Station	Explosion	Instruments	Components	Paper Speed (mm/sec)
Wambrook	A	Willmore	1Z, 1H	1
	C	Wood-Anderson	2H	1
Cabramurra	B	Willmore	1Z	1
	C	Willmore	1Z	1
Indi	B	S.M.A. recorder with Willmore geophone	1Z	50
Jindabyne	C	S.M.A. recorder with Willmore geophone	1Z	50
Cooma	B	Minirack recorder and Willmore geophone	2Z, 2H	95
	C	Minirack recorder and Willmore geophone		25
Geehi	C	Century	4Z	15
Mt. Stromlo	B	Century	12Z	95
Inveralochy	C	B.P.I. recorder*	2Z	4
Marulan	C	B.P.I. recorder	2Z	4
Whitfield	B	Willmore	1Z	1
Berrima	C	Willmore	1Z	1
Warragamba	B, C	Willmore	1Z	1
Melbourne	A, B, C	Benioff	1Z, 2H	1

* Kindly loaned by the Bernard Price Institute, Johannesburg.

It was considered most important to measure accurately the first P arrival (P_1) at the near stations, as this velocity is required for the locations of near earthquakes by the P difference method. For this reason there was not so much concern at this stage with the recording of later arrivals such as P_n.

II. PHYSIOGRAPHY AND GEOLOGY

The recording sites formed two long traverse lines, one to the north-east towards Sydney, and one to the south-west towards Melbourne, with a total span of approximately 600 km (Fig. 1).

The traverse lines crossed the south-east portion of the " Great Divide ", otherwise called the South-eastern Highlands. These Highlands consist of elevated tableland country, generally 2000–3000 ft above sea-level, with higher areas culminating in the Kosciusko horst, which reaches 7000 ft above sea-level.

Rock types are mainly Palaeozoic shales and slates, occurring in ill-defined meridional belts and separated by granitic intrusions, which are sometimes in the form of large batholiths (David 1950). At the northern end of the traverse line two stations (Warragamba and Riverview) were situated on the Sydney basin. This is a shale and sandstone basin of considerable thickness. Recent seismic reflection surveys have shown at least 14,000 ft of sediments (C. S. Robertson, Bureau of Mineral Resources, unpublished data 1957).

III. Discussion of Results

Only reasonably clear "phases" are listed in Table 3 and graphed in Figure 2. The Benioff and Willmore records in particular contained other possible arrivals. In the case of some stations (e.g. Mt. Stromlo and Inveralochy) the large amplitude of the first arrival and the lack of automatic volume control made the reading of arrivals other than the first very difficult, and so no P_n, reflected waves, or S waves were observed at these stations. This was unfortunate, particularly in the case of the expected reflected wave at Mt. Stromlo. Riverview Observatory reported only very small amplitudes from explosion C, while Brisbane reported no observable motion, so that these stations could not be included.

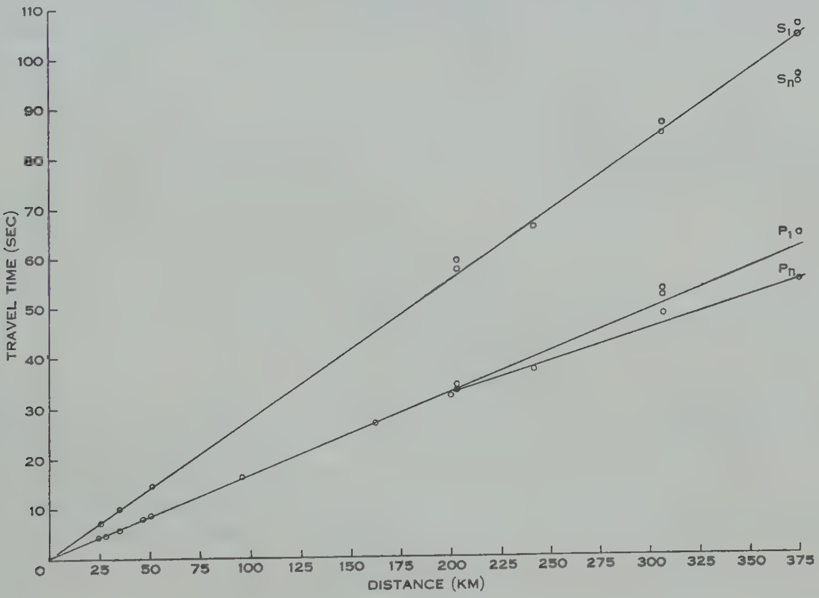

Fig. 2.—Travel-time curves.

It can be seen from Figure 2 that the arrivals are divisible into three groups. For the closer stations out as far as Inveralochy (160 km), the plot of travel-times of the first arrivals against distance gave a consistent velocity close to 6 km/sec. This phase, denoted P_1, was also recorded at some of the distant stations as a second arrival, but with less certainty. It was interpreted as the longitudinal wave in the Earth's "crust". The curve of first arrivals changes at about 180 km to a velocity near 8 km/sec. This was interpreted as the arrival of longitudinal waves (P_n) from below the Mohorovičić discontinuity. The third group of arrivals was taken as the transverse wave S_1. It was a wave of larger amplitude, usually of longer period, with a velocity of about $3\frac{1}{2}$ km/sec.

(a) *The* P_1 *Phase*

The travel-time equation for P_1 was calculated using the method of least squares. Only first arrivals were used in the final calculation because of the lack of ambiguity and the greater accuracy obtained by using first arrivals only. The omission of the distant stations from the calculation was also justified by their larger residuals. The Melbourne residuals were about +1·8 sec compared with the standard deviation of 0·12 sec for the closer stations.

P_1 recordings from two explosions were used at Wambrook, Cabramurra, and Cooma (Table 3). The Cooma times were used in the calculation separately as they were much more accurate, so giving Cooma double weight. However, for the other two stations the average travel-time was used. Thus in effect nine results were used to determine the formal P_1 travel-time equation

$$t=0\cdot335\ (\pm0\cdot073)+0\cdot1655\ (\pm0\cdot0010)\Delta\ \text{sec},$$

where Δ is the distance in kilometres.

This corresponds to a P_1 velocity of 6·04 (±0·04) km/sec. The standard errors of course measure the internal consistency of the observations but do not reveal systematic errors. The largest residuals amongst the close stations were only 0·18 sec for Cooma and Jindabyne. At Cooma there appears to be a slight delay compared to the other stations. This delay may be related to a wide belt of Ordovician sediments lying between Wambrook and Cooma.

It is noteworthy that if only P_1 phases are used that are second arrivals at distant stations, a lower apparent velocity of between 5·8 and 5·9 km/sec is obtained. This is probably due to the first part of the phase being missed, and, as is well known, probably explains the low velocities obtained in early near earthquake studies when the amplitudes were small.

(b) *The* P_n *Phase*

The P_n equation was not very well determined. In preliminary calculations it was found that the indefinite first arrival at Warragamba had a large residual (2–3 sec) from both the P_n and P_1 curves and so it was not used in the later calculations for either. This left only four stations that could be used for P_n, Marulan and Berrima to the north-east, and Whitfield and Melbourne to the south-west. All three explosions were recorded at Melbourne and these three values were averaged.

The two groups of stations, to the north-east and to the south-west, were treated separately to avoid the effect of the different time delays in the two directions. The velocity and time intercept obtained using the two Victorian stations, Whitfield and Melbourne, were 7·96 km/sec and 7·8 sec, while those for the northern stations Marulan and Berrima were both appreciably higher, 8·3 km/sec and 8·2 sec respectively. The values gave a weighted mean P_n velocity of 8·03 km/sec and a mean time intercept of 8·0 sec. Errors for these last two figures were estimated by assuming errors of ±0·2 sec in the travel-times to each station and calculating the mean velocity and time intercept in the extreme cases. These estimated errors were ±0·2 km/sec and ±1·0 sec respectively.

The formal P_n travel-time equation is then

$$t=8\cdot0(\pm1\cdot0)+0\cdot124(\pm0\cdot003)\Delta \text{ sec.}$$

More recordings of P_n from timed explosions are required in this area to check this equation.

(c) *The* S_1 *Phase*

The two Warragamba S_1 times were averaged. One of the three Melbourne recordings was treated separately and the other two averaged, so giving Melbourne extra weight. The eight results then gave the following travel-time equation :

$$t=0\cdot48(\pm0\cdot49)+0\cdot276(\pm0\cdot002)\Delta \text{ sec.}$$

This is equivalent to an S_1 velocity of 3·62(±0·03) km/sec.

Whitfield and Berrima had much higher residuals (1·1 and 1·2 sec) than the other stations. It was found that by omitting these two stations the large standard error in the time intercept was greatly reduced, showing the intercept to be significantly above zero. The standard deviation was reduced from 0·62 to 0·18 sec, but little difference was made to the velocity 3·613(±0·007). The equation is then

$$t=0\cdot44(\pm0\cdot13)+0\cdot2768(\pm0\cdot0005)\Delta \text{ sec.}$$

As is usual in explosion work, the S amplitudes were not much greater than the P amplitudes ; for example, at Melbourne the S amplitudes were 1·5 times those of P.

(d) *Other Phases*

The only S_n phases worth listing were recorded at Melbourne. On the Cooma records P_1 was followed a second later by a sharp arrival (P_s) of twice the amplitude. This is shown clearly in Figure 3. It could not be correlated by ordinary ray theory with phases at other stations. However, less definite waves following P_1 and S_1 were noticed at Melbourne. It is suggested that this arrival is either a P wave guided by slower material near the surface, particularly in the sediments west of Cooma, or a surface wave produced by conversion from the P wave at inhomogeneities as described by Tatel and Tuve (1955).

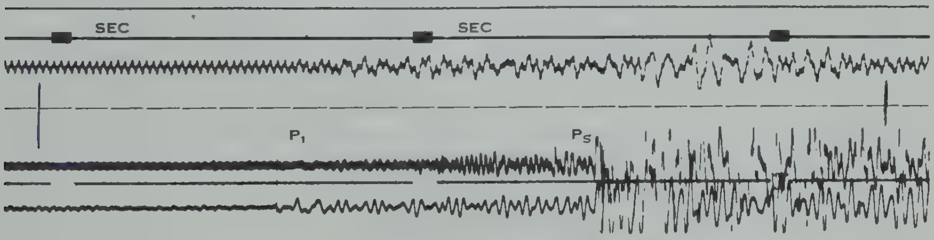

Fig. 3.—P_1 and P_s at Cooma.

Hodgson (1953) noted large phases closely following P_1 at epicentral distances between 66 and 120 km. Katz (1955) described small P_1 first arrivals each “ followed within one second by a much larger arrival that could not be correlated

TABLE 3

PHASES AND TRAVEL-TIMES

Station	Explosion	Distance (km)	Travel-time (sec)	Phase	Residual (sec)
Wambrook	A	23·7	4·3	P_1	+0·02 (mean)
	B	25·2	4·5	P_1	
			(7·2)	S_1	—0·25
Cabramurra	B	27·2	4·6	P_1	—0·14 (mean)
	C	29·05	5·1	P_1	
Jindabyne	C	34·62	5·89	P_1	—0·18
			9·97	S_1	—0·08
			12·62	L	
Cooma	B	47·0	8·29	P_1	+0·18
			9·17	P_s?	
	C	45·23	7·98	P_1	+0·16
Indi	B	46·8	8·06	P_1	—0·02
Geehi	C	50·57	8·73	P_1	+0·02
			14·73	S_1	+0·27
Mt. Stromlo	B	95·9	16·20	P_1	—0·01
Inveralochy	C	160·7	26·9	P_1	—0·03
Marulan	C	200·0	32·2	P_n	—0·7
Whitfield	B	202·8	33·3	P_n	—0·1
			34·4*	P_1	(+0·5)
			57·6	S_1	+1·06
			(59·4)		
Berrima	C	241·7	37·2	P_n	—0·9
			66·1	S_1	—1·20
Warragamba	B	307·2	48·3*	(eP)	(+2·1)
			52·0*	P_1	(+0·8)
			85·0	S_1	+0·10 (using mean of B & C)
			(87·1)		
	C	307·2	48·4	(eP)	(+2·2)
			52·4*	P_1	(+1·2)
			(53·3)		
			86·0	S_1	+0·10 (mean B & C)
			(87·0)		
Melbourne	A	375·5	55·1	P_n	+0·4
			64·2*	P_1	(+1·8)
			95·0	S_n	
			104·5	S_1	—0·04 (mean A & C)
	B	375·0	54·7	P_n	0·0
			64·4*	P_1	(+2·0)
			104·3	S_1	+0·15
	C	375·5	55·0	P_n	+0·3
			63·6*	P_1	(+1·2)
			96·5	S_n	
			(104·0)	S_1	—0·04 (mean A & C)
			(106·8)		

* Not used in final calculation.

with any arrivals on other seismograms ". Gane *et al.* (1956) reported similar phases, describing them as follows : " These data suggest that these second phases follow at a roughly constant time after the first arrivals." All these above cases are difficult to explain by simple refraction in a second crustal layer and may have been caused by local trapping of energy near the surface.

Another possible explanation is a reflection from a Conrad discontinuity at 10–15 km depth, but no consistent evidence was seen for further layering above the Mohorovičić discontinuity. However, later arrivals would be difficult to see on most records owing to the high " noise-level " caused by the early arrivals.

The very small amplitude of the Riverview recording was mainly because of the longer period instruments. Also the high noise level at short periods at that site makes the recording of quarry explosions and near earthquakes difficult.

If the first arrival at Warragamba is a P_n phase, its large positive residual (2·1–2·2 sec) from the P_n curve is possibly caused by the thickness of the sediments of the Sydney basin.

IV. CRUSTAL STRUCTURE

Assuming a uniform " crust " above the Mohorovičić discontinuity with a P_1 velocity of 6·04 km/sec, a P_n velocity of 8·03 km/sec, and time intercept 8·0 sec, the depth to the discontinuity was formally calculated as 37 km. Although this figure is approximate only, it is to be noted that it is close to the value normally obtained in continental regions such as the shield areas of Western Australia (Doyle 1957 ; Bolt, Doyle, and Sutton 1958), Canada (Hodgson 1953), and South Africa (Gane *et al.* 1956).

In earlier published explosion recordings in Western Australia (Doyle 1957 ; Bolt, Doyle, and Sutton 1958) a good determination was made of the P_n velocity (8·2 km/sec), and a less accurate one of P_1 velocity (6·0–6·1 km/sec), the reverse of the case in this work. At about the same time, the Bureau of Mineral Resources made seismic recordings at the eastern end of the Nullarbor Plain in South Australia. The velocities found were 6·3 km/sec for P_1 and 3·6 km/sec for S_1. The depth to the Mohorovičić discontinuity was found to be 35–42 km by reflection and refraction measurements (I. B. Everingham, unpublished data 1958).

From the evidence obtained so far, the Nullarbor and Eastern Highlands regions do not appear very different seismically, though the former is a flat shield area reaching only 1000 ft in height, while the latter extends to 7000 ft in height. In both areas the sediments are thin (about 0·3 and 1–2 km respectively) compared with crustal dimensions, and the underlying basements have similar velocities. It is uncertain whether there is any significant difference between the depths to the Mohorovičić discontinuity in the two areas because of the uncertainties in the depth determinations (3–5 km). Future reflection recordings in south-eastern Australia will be useful to elucidate this.

Marshall and Narain (1954) found gravity Bouguer values which decreased from positive values at the coast to about —50 mgal in the South-eastern Highlands region. On the basis of the seismic results it appears most likely that the negative gravity values are not caused by a depression of the Mohorovičić discontinuity below the normal continental depth (35 km), but by emplaced granite masses having a relatively low density. In Western Australia, Gunsen and Van der Linden (Bureau of Mineral Resources, unpublished data 1956) recorded a large negative anomaly which has been similarly interpreted, and Innes (1957) has recently discussed a Canadian example.

V. Acknowledgments

Special acknowledgment is due to Mr. T. A. Lang, formerly Associate Commissioner of the S.M.H.E.A., and to Professor J. C. Jaeger of the National University who made this work possible. The cooperation of the contractors Kaiser-Walsh-Perini-Raymond and of the Quarry Superintendent, Mr. Chrisman, is gratefully acknowledged. Also that of Mr. D. Norris, Mr. K. Vale, Mr. A. Kelso of Wambrook radio station, and the various members of survey parties. Mr. John Scott kindly broadcast time signals from Station 2XL.

A seismograph was loaned by the Bernard Price Institute, Johannesburg, and two chronometers by the Hydrographic Branch of the Royal Australian Navy, Sydney.

The authors would like to thank the Director of the Bureau of Mineral Resources and the Commissioner of the S.M.H.E.A. for permission to carry out and publish this work. The views expressed are those of the authors and not necessarily those of the Authorities.

VI. References

Bolt, B. A., Doyle, H. A., and Sutton, D. (1958).—*Geophys. J.* **1** : 135–45.

David, T. W. E. (1950).—" The Geology of the Commonwealth of Australia." Vol. I. (Arnold & Co.: London.)

Doyle, H. A. (1957).—*Nature* **180** : 132–4.

Gane, P. G., Atkins, A. R., Sellschop, J. P. F., and Seligman, P. (1956).—*Bull. Seismol. Soc. Amer.* **46** : 293–316.

Hodgson, J. H. (1953).—*Publ. Dom. Obs., Ottawa* **16** : 113–63.

Innes, M. J. J. (1957).—*Trans. Amer. Geophys. Un.* **38** : 156–65.

Jaeger, J. C., and Browne, W. R. (1958).—*Aust. J. Sci.* **20** : 225–8.

Katz, S. (1955).—*Bull. Seismol. Soc. Amer.* **45** : 303.

Marshall, C. E., and Narain, H. (1954).—*Mem. Dept. Geol. Univ. Sydney* No. 2, pp. 58–60.

Tatel, H. E., and Tuve, M. A. (1955).—*Spec. Pap. Geol. Soc. Amer.* No. 62, pp. 35–50.

A SEARCH FOR LEVELS OF ^{7}Li BETWEEN 9·0 AND 9·55 MeV EXCITATION

By K. H. Purser†

[*Manuscript received May 25, 1959*]

Summary

The cross section of the reaction ^{6}Li(n,^{3}H)^{4}He has been measured, with good energy resolution, over the neutron range 2·0–2·65 MeV. This corresponds to an excitation of ^{7}Li from 9·0 to 9·55 MeV, a region in which photodisintegration experiments indicate the presence of one or more levels. No resonance structure was observed in this experiment and possible reasons for this are discussed.

I. Introduction

Cross-section measurements for the neutron-induced reaction ^{6}Li(n,^{3}H)^{4}He have been made from thermal energies to a maximum neutron energy of 18·3 MeV (Frye 1954; Weddell and Roberts 1954; Hughes and Harvey 1955; Ribe 1956; Bonner 1958; Kern and Kreger 1958). These results show that, with the exception of the broad p-wave resonance at 255 keV, no resonance structure is apparent over the whole of the measured energy range. This is surprising as several fairly well-established levels are known to be present in the compound system, ^{7}Li*.

In the experiments reported here, the cross section of ^{6}Li(n,^{3}H)^{4}He was measured, with good energy resolution, over a neutron energy range 2·0–2·65 MeV; this corresponds to an excitation of the compound ^{7}Li system from 9·0 to 9·55 MeV where a fairly well-established level of ^{7}Li is known to be present (Ajzenberg and Lauritsen 1955). From a knowledge of the neutron and triton partial widths which have been established for this level by γ-ray absorption experiments it would appear that, to an order of magnitude, the resonance cross section to this level by neutron absorption in ^{6}Li should be several hundred millibarns. The experimental techniques used here were sufficiently sensitive so that a 10 per cent. change in the cross-section curve having a 40 keV half-width should be readily detected.

II. Evidence for Level of ^{7}Li at 9·3 MeV and Its Possible Character

The existence of a level of ^{7}Li in the neighbourhood of 9·3 MeV was first demonstrated by Titterton and Brinkley (1953), who used nuclear emulsion techniques to measure the differential cross section of the reaction ^{7}Li(γ,^{3}H)^{4}He. Their cross section went through a peak at 9·3 MeV with an experimental half-width of several hundred keV. By comparing these results with cross-section measurements which were carried out by Titterton (1953), who used 14·8 and 17·6 MeV γ-rays, from the ^{7}Li(p,γ)^{8}Be reaction, an approximate integrated cross section of $0 \cdot 2 \times 10^{-3}$ MeV barns can be associated with this level. Stoll and Wächter (1953), Erdos *et al.* (1954), Stoll (1954), and Miwa (1955) have also found resonance absorption of γ-rays between $9 \cdot 0$ and $9 \cdot 5$ MeV in similar experiments. Goldemberg and Katz (1954) have measured an integral spectrum for the reaction $^7\text{Li}(\gamma,n)^6\text{Li}$; their results show a prominent break in the yield curve which they ascribe to a level in ^{7}Li at $9 \cdot 6$ MeV, and their approximate integrated cross section is also $0 \cdot 2 \times 10^{-3}$ MeV barns. Further evidence for the existence of the level has been provided by inelastic scattering data of Allen (1954), who scattered 14 MeV neutrons from ^{7}Li. Silver (1957) has scattered $31 \cdot 8$ MeV protons from ^{7}Li and reported a level of ^{7}Li about $9 \cdot 6$ MeV. Recently, Titterton (personal communication) has remeasured the differential cross section using synchrotron bremsstrahlung of maximum energy 12 MeV. His preliminary results confirm the existence of resonant absorption of γ-rays around $9 \cdot 3$ MeV ; the results also eliminate the possibility that the level which is present is populated by γ-ray cascade processes from levels at higher excitation of ^{7}Li. In this work we have assumed that the $9 \cdot 3$ MeV level, excited by the $^7\text{Li}(\gamma,{}^3\text{H})^4\text{He}$ experiments, is the same level as that found at $9 \cdot 6$ MeV by Goldemberg and Katz (1954).

---

† Department of Nuclear Physics, Australian National University, Canberra.

III. Experimental

Neutrons from the $d(d,n)^3$He reactions were used to bombard an enriched ^{6}LiI(Eu) crystal which served both as the target and scintillation detector for ^{6}Li neutron-induced reactions within the crystal volume. Energy variation of the neutrons arriving at the crystal was achieved by rotating the ^{6}LiI crystal about a vertical axis through the heavy ice target, maintaining the deuteron beam energy constant at 350 keV. The neutron flux was monitored by a boron-loaded 2 in. scintillation-detector* placed in line with the ^{6}LiI crystal as shown in Figure 1.

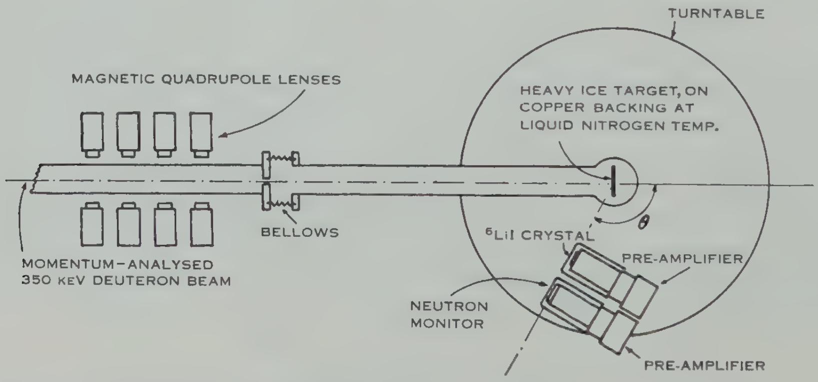
TURNTABLE
MAGNETIC QUADRUPOLE LENSES
HEAVY ICE TARGET, ON COPPER BACKING AT LIQUID NITROGEN TEMP.
BELLOWS
θ
^{6}LiI CRYSTAL
PRE-AMPLIFIER
MOMENTUM-ANALYSED 350 KEV DEUTERON BEAM
NEUTRON MONITOR
PRE-AMPLIFIER

Fig. 1.—Schematic diagram showing experimental arrangement.

The crystal detector consisted of a rectangular piece of ^{6}LiI(Eu) (96 per cent. ^{6}Li) of density $3 \cdot 93$ g/cm^3 and dimensions $0 \cdot 525$ by $0 \cdot 534$ by $0 \cdot 090$ in. The centre of the crystal was placed $14 \cdot 7 \pm 0 \cdot 2$ cm from the heavy ice target.

---

* Nuclear Enterprise Ltd., Ne400 scintillator.

Light pulses from the ^{6}LiI detector were viewed by a Dumont 6292 photomultiplier whose output was amplified and fed to a pulse height analyser and scaler of known bias level. Figure 2 shows a typical pulse height distribution from the ^{6}LiI detector recorded for a neutron energy of 2·6 MeV. The low energy peak, centred around 18 V, is due to the reaction ^{6}Li(n,^{3}H)^{4}He induced by the background of thermal and epithermal neutrons which are present in the experimental area from scattering and from the carbon contamination in the beam tube. The half-width of this thermal peak is about 8 per cent. for a freshly mounted crystal, and provides a useful calibration line of known width to check the electronics.

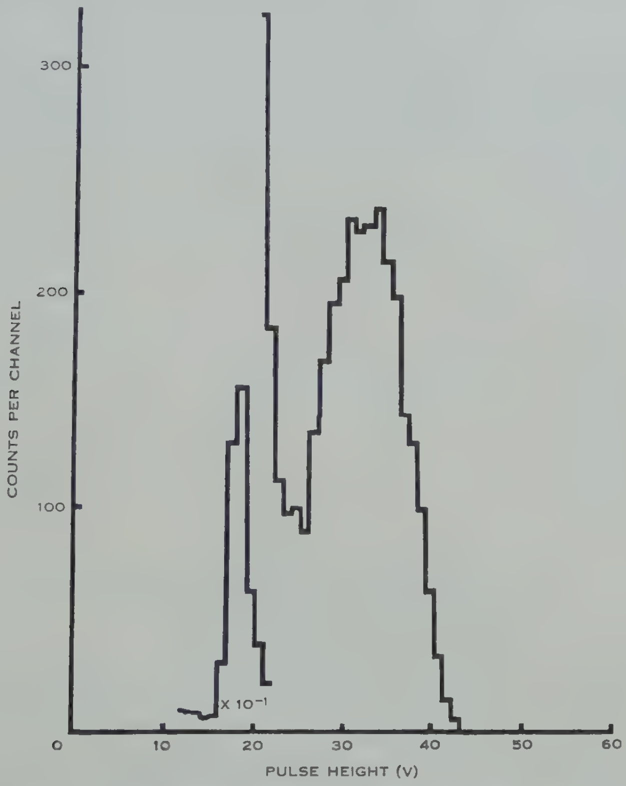

Fig. 2.—Pulse height distribution from ^{6}LiI(Eu) detector.

The high energy peak in Figure 2 arises from (n,t) reactions induced in the crystal by fast neutrons; it has a half-width considerably greater than the resolution of the equipment. Kern and Kreger (1958), Murray (1958), and Ophel (1958) have shown that this large width is due to the difference between the triton and α-particle scintillation response, which is effective because centre of mass motion causes the emitted tritons and α-particles to have a range of energies available to each of them in the laboratory system. The shape of the peak also depends on the angular distribution of the reaction. Spectra taken at various neutron energies showed that the shape of the high energy peak is the same over the whole energy range. To carry through a cross-section measurement a bias level was set at a known point in the high energy peak and all events producing a pulse greater than this were taken to be ^{6}Li(n,^{3}H)^{4}He events. The bias level was set sufficiently high so that no pulses from the thermal peak were counted by the scaler. Corrections were made to allow for the pulses, from the high energy peak, which were missed because of the high setting of the bias level.

The production of monoenergetic neutrons from the $d(d,n)^3$He reaction is made difficult because of the large background of neutrons which are produced in the accelerator beam tube owing to collisions of the beam with the defining stops and from the target backing. Because of this background flux it is necessary to use relatively thick targets, so that the yield is well above the background level. Unfortunately, thick targets reduce the range of the angle θ (or neutron energy) which is available for a given energy resolution. In these experiments a continually replenished target of heavy ice was used. The thickness of the target was monitored by a measurement of the total neutron yield and was maintained throughout at 100 keV. Figure 3 shows the energy resolution of the neutrons obtained from a 100 keV thick target for a deuteron beam energy of 350 keV as a function of the emitted neutron energy and the angle θ as calculated from the tables of Fowler and Brolley (1956).

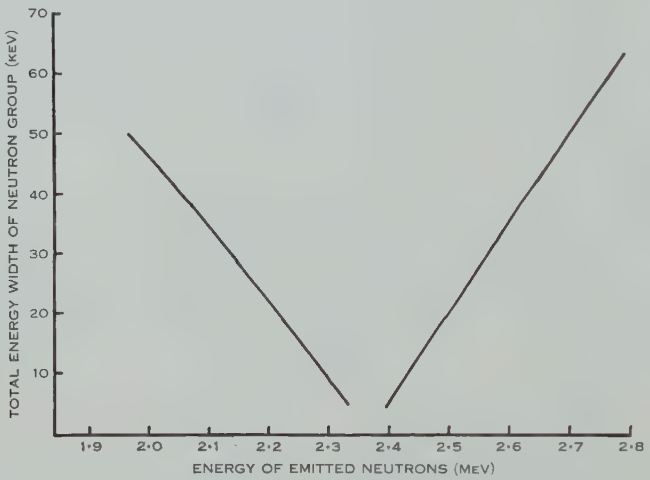

Fig. 3.—Energy resolution of neutrons obtained from a 100 keV thick heavy ice target using an incident deuteron beam of energy 350 keV.

The chief sources of background neutrons in the experimental area were at the analysing-magnet vacuum box, at the defining apertures, and at the backing of the heavy ice target. These background neutrons were reduced to less than 10 per cent. of the direct flux from the target by shielding and by locating the defining stops in the beam tube to be as far from the target as possible. Background counts in the detector and the monitor were measured by counting without a heavy ice target, for the same time-integrated beam current as was used in the experiments.

The time-integrated neutron flux density in the experiments was determined with the aid of a boron-loaded scintillator by the ^{10}B(n,^{4}He)^{7}Li reaction. Cadmium and boron shielding was placed around the monitor to reduce the counts due to the epithermal background in the experimental area. This monitor was calibrated absolutely at 2·55 MeV by means of a triple-coincidence proton-recoil counter similar, in principle, to that described by Bame *et al.* (1957).

IV. Results and Discussion

Figure 4 shows the results of these cross-section measurements. The horizontal bars indicate the energy spread inherent in this type of neutron source; the vertical bars are the estimated errors in the measurements.

The main sources of error at each point when determining the shape of the cross-section curve are: the background subtractions, 3 per cent.; uncertainties in the geometry, 5 per cent.; counting errors, 4 per cent. The absolute determination of the cross section is also dependent upon geometry of the recoil-counter telescope and its location with respect to the heavy ice target; this introduces a further uncertainty of 7 per cent.; the total error ±10 per cent.

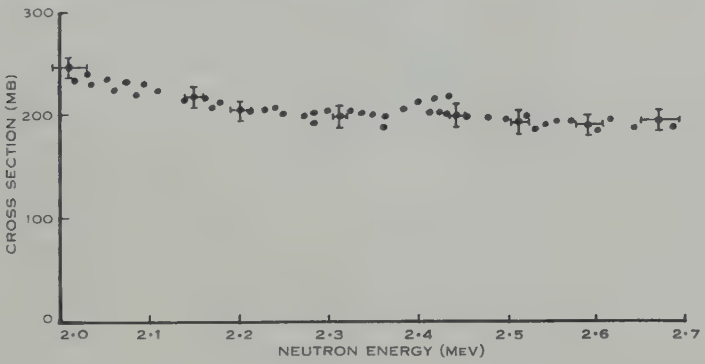

Fig. 4.—Experimental cross-section data.

Over the energy range of 2·0–2·7 MeV the cross-section data show no significant indication of resonance structure but fall smoothly with increasing neutron energy. This suggests either that no levels are present in this energy range or that if they are present the triton partial width is so small (10 keV or less) that the energy resolution of the experiment prevented them being seen.

If the level under discussion has a spin and parity of $5/2^{+}$ both the neutron and triton partial waves entering the reaction will be d-waves. The low transparency of the centrifugal barrier to these particles would give the narrow partial widths necessary to account for these experimental results and the apparent lack of compound nucleus formation.

An explanation which accounts for the bulk of the cross section of the ^{6}Li(n,^{3}H)^{4}He reaction and the measured angular distribution, above about 2 MeV, has been suggested by Dabrowski and Sawicki (1955) and Sawicki (1955). These authors have considered an "α plus d" model for ^{6}Li and have calculated the inverse-stripping cross section for ^{6}Li(n,^{3}H)^{4}He assuming a pick-up process which does not go through the intermediate system, ^{7}Li*. Sawicki's calculations, which include Coulomb corrections, are in reasonable agreement with the cross-section and angular distribution measurements of Darlington *et al.* (1953), Frye (1954), and Weddell and Roberts (1954). It seems likely that part of the reaction, at least, goes through direct processes for neutron energies greater than 2 MeV. However, while the direct process matrix elements appear to be very strong, it is still difficult to understand the apparent absence of resonance peaks corresponding to levels that are known to exist from γ-ray experiments on ^{7}Li.

V. ACKNOWLEDGMENTS

The author wishes to express his appreciation to Professor E. W. Titterton for many helpful discussions and suggestions throughout the course of this work, and is also indebted to Dr. F. Barker for assistance in interpreting the theoretical implication of the results.

VI. REFERENCES

AJZENBERG, F., and LAURITSEN, T. (1955).—*Rev. Mod. Phys.* **27** : 77.

ALLEN, D. L. (1954).—*Nature* **174** : 267.

BAME, S. J., HADDARD, E., PERRY, J. E., and SMITH, R. K. (1957).—*Rev. Sci. Instrum.* **28** : 997.

BONNER, T. (1958).—U.C.R.L. 5226.

DABROWSKI, J., and SAWICKI, J. (1955).—*Acta Phys. Polon.* **14** : 323.

DARLINGTON, L. E., HAUGSNES, J., MANN, H. M., and ROBERTS, J. H. (1953).—*Phys. Rev.* **90** : 1049.

ERDOS, P., STOLL, P., WÄCHTER, M., and WATAGHIN, V. (1954).—*Nuovo Cim.* **12** : 639.

FEENBERG, E. (1955).—" Shell Theory of the Nucleus." (Princeton Univ. Press.)

FOWLER, J. L., and BROLLEY, J. E. (1956).—*Rev. Mod. Phys.* **28** : 103.

FRYE, G. M. (1954).—*Phys. Rev.* **93** : 1086.

GOLDEMBERG, J., and KATZ, L. (1954).—*Phys. Rev.* **95** : 471.

HUGHES, D. J., and HARVEY, J. A. (1955).—B.N.L. 325.

KERN, B. D., and KREGER, W. E. (1958).—*Phys. Rev.* **112** : 926.

MIWA, M. (1955).—*J. Phys. Soc. Japan* **10** : 173.

MURRAY, R. B. (1958).—*Nuclear Instruments* **2** : 237.

OPHEL, T. R. (1958).—*Nuclear Instruments* **3** : 45.

RIBE, F. L. (1956).—*Phys. Rev.* **103** : 741.

SAWICKI, J. (1955).—*Nuovo Cim.* **1** : 957.

SILVER, R. (1957).—U.C.R.L. 3887.

STOLL, P. (1954).—*Helv. Phys. Acta* **27** : 395.

STOLL, P., and WÄCHTER, M. (1953).—*Nuovo Cim.* **10** : 347.

TITTERTON, E. W. (1953).—*Proc. Phys. Soc.* A **66** : 519.

TITTERTON, E. W., and BRINKLEY, T. A. (1953).—*Proc. Phys. Soc.* A **66** : 194.

WEDDELL, J. B., and ROBERTS, J. H. (1954).—*Phys. Rev.* **95** : 117.

THE THERMAL EXPANSION OF SOLIDS

By G. C. FLETCHER*

[*Manuscript received February* 18, 1959]

Summary

From the theory of normal vibrations of a lattice, a practical means of obtaining the equation of state of an ionic solid is developed from which the thermal expansion can be derived. Using previous work by Kellermann, application is made to the case of sodium chloride and the results compared with experiment. Possible reasons for the discrepancy between theory and experiment, which is very large at high temperatures, are discussed. The variation with temperature of the specific heat at constant volume and the isothermal compressibility are also investigated.

I. INTRODUCTION

In a previous paper by the author (Fletcher 1957) it was pointed out that a number of workers have attempted to draw qualitative and quantitative conclusions regarding the presence of defects in solids from their behaviour as regards thermal expansion, particularly at high temperatures. It was pointed out that this procedure was a dubious one since almost nothing was known of the thermal expansion of ideal solids, i.e. not containing defects. In that paper an equation of state, based on the theories of Debye and Grüneisen and from which the thermal expansion could be obtained, was developed and applied to an ionic solid, potassium chloride. In the present work an attempt has been made in Section II to develop a more accurate equation of state, based on the theory of normal modes of vibration of a lattice. In Section III this has again been applied to an ionic solid, sodium chloride, since one is most justified in ignoring the electrons explicitly for such a case. A wide discrepancy between theory and experiment, not explicable by the presence of defects, is found and possible reasons for this are discussed in Section V. In attempting to explain the discrepancy it was considered useful to calculate the specific heat C_V and compressibility $\varkappa_T$ also, as described in Section IV. Here agreement with experiment is considerably better.

II. EQUATION OF STATE

A brief resumé of part of a paper by Kellermann (1940) will be given first in order to define certain quantities $\begin{bmatrix} \varkappa & \varkappa' \\ x & y \end{bmatrix}$ used later. Consider a crystal, in which unit cell of volume v_a is determined by lattice vectors $\mathbf{a}_1$, $\mathbf{a}_2$, $\mathbf{a}_3$ and contains s particles, whose positions in the cell are given by the basis vectors

---

* Department of Mathematics, University of Sydney.

$\mathbf{r}_\varkappa$ $(\varkappa=1, 2, \ldots, s)$. Let the $\varkappa$th particle in cell $\mathbf{l}=(l_1, l_2, l_3)$ (l_i integral or zero), whose equilibrium position is

$$\mathring{\mathbf{r}}_\varkappa^{\mathbf{l}}=\mathbf{a}^{\mathbf{l}}+\mathring{\mathbf{r}}_\varkappa=l_1\mathbf{a}_1+l_2\mathbf{a}_2+l_3\mathbf{a}_3+\mathring{\mathbf{r}}_\varkappa, \qquad \ldots\ldots\ldots\ldots \quad (1)$$

suffer a displacement $\mathbf{u}_\varkappa^{\mathbf{l}}$ to the position $\mathbf{r}_\varkappa^{\mathbf{l}}$. Assuming central forces between pairs of particles and neglecting external forces on the particles, the total potential energy of the crystal may be written

$$\Phi=\tfrac{1}{2}\sum_{\varkappa,\varkappa'}\ \sideset{}{'}\sum_{\mathbf{l},\mathbf{l}'} \varphi_{\varkappa\varkappa'}^{\mathbf{l}\mathbf{l}'}(|\,\mathbf{r}_\varkappa^{\mathbf{l}}-\mathbf{r}_{\varkappa'}^{\mathbf{l}'}\,|), \qquad \ldots\ldots\ldots\ldots \quad (2)$$

where

$$\varphi_{\varkappa\varkappa'}^{\mathbf{l}\mathbf{l}'}=\varphi_{\varkappa\varkappa'}(|\,\mathbf{r}_\varkappa^{\mathbf{l}}-\mathbf{r}_{\varkappa'}^{\mathbf{l}'}\,|) \qquad \ldots\ldots\ldots\ldots\ldots\ldots\ldots\ldots \quad (3)$$

is the mutual potential energy of the $(\mathbf{l}, \varkappa)$ and $(\mathbf{l}', \varkappa')$ particles, assumed to be a function only of their distance apart, and terms with $\varkappa=\varkappa'$, $\mathbf{l}=\mathbf{l}'$ are omitted from the summation in (2). Expansion of this in powers of the Cartesian components $u_{\varkappa x}^{\mathbf{l}}$, $u_{\varkappa y}^{\mathbf{l}}$, $u_{\varkappa z}^{\mathbf{l}}$ of the displacements $\mathbf{u}_\varkappa^{\mathbf{l}}$ up to the second order gives $\Phi\simeq\Phi_0+\Phi_2$, where

$$\Phi_0=\tfrac{1}{2}\sum_{\varkappa,\varkappa'}\ \sideset{}{'}\sum_{\mathbf{l},\mathbf{l}'} \varphi_{\varkappa\varkappa'}^{\mathbf{l}\mathbf{l}'}(|\,\mathring{\mathbf{r}}_\varkappa^{\mathbf{l}}-\mathring{\mathbf{r}}_{\varkappa'}^{\mathbf{l}'}\,|), \qquad \ldots\ldots\ldots\ldots\ldots \quad (4)$$

$$\Phi_2=-\tfrac{1}{2}\sum_{\varkappa,\varkappa'}\ \sum_{\mathbf{l},\mathbf{l}'}\ \sum_{x,y} (\varphi_{\varkappa\varkappa'}^{\mathbf{l}\mathbf{l}'})_{xy}u_{\varkappa x}^{\mathbf{l}}u_{\varkappa' y}^{\mathbf{l}'}, \qquad \ldots\ldots\ldots\ldots \quad (5)$$

where

$$(\varphi_{\varkappa\varkappa'}^{\mathbf{l}\mathbf{l}'})_{xy}=\left[\frac{\partial^2\varphi_{\varkappa\varkappa'}(r)}{\partial x\partial y}\right]_{\mathbf{r}} \quad (\mathbf{r}=\mathring{\mathbf{r}}_\varkappa^{\mathbf{l}}-\mathring{\mathbf{r}}_{\varkappa'}^{\mathbf{l}'}),\ \ (\varphi_{\varkappa\varkappa}^{\mathbf{l}\mathbf{l}})_{xy}=-\sum_{\varkappa'}\ \sideset{}{'}\sum_{\mathbf{l}'}(\varphi_{\varkappa\varkappa'}^{\mathbf{l}\mathbf{l}'})_{xy},$$

and $\sum\limits_x$ refers to summation over the three Cartesian directions. The Lagrangian equations of motion for the system are then

$$m_\varkappa\ddot{u}_{\varkappa x}^{\mathbf{l}}-\sum_{\varkappa'}\sum_{\mathbf{l}'}\sum_{y}(\varphi_{\varkappa\varkappa'}^{\mathbf{l}\mathbf{l}'})_{xy}u_{\varkappa' y}^{\mathbf{l}'}=0. \qquad \ldots\ldots\ldots\ldots\ldots \quad (6)$$

where $m_\varkappa$ is the mass of the $(\mathbf{l}, \varkappa)$ particle. Assumption of a normal mode of vibration of the form

$$\mathbf{u}_\varkappa^{\mathbf{l}}=\mathbf{U}_\varkappa \exp\,[\mathrm{i}(2\pi\mathbf{k}\cdot\mathring{\mathbf{r}}_\varkappa^{\mathbf{l}}-\omega t)], \qquad \ldots\ldots\ldots\ldots \quad (7)$$

where t denotes the time variable, leads to a $3s$-dimensional secular equation

$$\left|\ \begin{bmatrix}\varkappa & \varkappa' \\ x & y\end{bmatrix}+m_\varkappa\omega^2\delta_{\varkappa\varkappa'}\delta_{xy}\ \right|=0, \qquad \ldots\ldots\ldots\ldots\ldots \quad (8)$$

where

$$\begin{bmatrix}\varkappa & \varkappa' \\ x & y\end{bmatrix}=\sum_{\mathbf{l}}(\varphi_{\varkappa\varkappa'}^{\mathbf{l}\mathbf{0}})_{xy} \exp 2\pi\mathrm{i}\mathbf{k}\cdot(\mathring{\mathbf{r}}_{\varkappa'}^{\mathbf{l}}-\mathring{\mathbf{r}}_\varkappa^{\mathbf{0}}), \qquad \ldots\ldots\ldots\ldots \quad (9)$$

for each vector $\mathbf{k}$. Here $\mathbf{0}$ denotes the triumvirate of numbers $\mathbf{l}'=(0, 0, 0)$. Application of the usual cyclic boundary condition restricts $\mathbf{k}$ to the values $\mathbf{k}=k_1\mathbf{b}_1+k_2\mathbf{b}_2+k_3\mathbf{b}_3$, where $\mathbf{a}_i\cdot\mathbf{b}_j=\delta_{ij}$, $k_i=h_i/n$ $(h_i=0, 1, \ldots, n-1)$, and $n^3=N$ is the number of cells in the lattice.

If it is assumed further that the interparticle potential energy may be expressed as the sum of two terms

$$\varphi=\varphi_C+\varphi_R=-c\rho^{-m}+b\rho^{-n}, \quad \ldots\ldots\ldots\ldots \quad (\mathbf{10})$$

ρ being the interparticle distance, then $\begin{bmatrix}\varkappa & \varkappa' \\ x & y\end{bmatrix}$ may correspondingly be rewritten

$$\begin{bmatrix}\varkappa & \varkappa' \\ x & y\end{bmatrix}={}^{C}\begin{bmatrix}\varkappa & \varkappa' \\ x & y\end{bmatrix}+{}^{R}\begin{bmatrix}\varkappa & \varkappa' \\ x & y\end{bmatrix}. \quad \ldots\ldots\ldots\ldots \quad (\mathbf{11})$$

A lattice parameter a may be chosen so that $\mathbf{a}_i \propto a$, $\mathbf{b}_i \propto a^{-1}$, and $v_a \propto a^3$. Then obviously $\mathbf{k}\cdot(\mathring{\mathbf{r}}^{1}_{\varkappa'}-\mathring{\mathbf{r}}^{1}_{\varkappa})$ is independent of a so that

$$\left.\begin{aligned}{}^{C}\begin{bmatrix}\varkappa & \varkappa' \\ x & y\end{bmatrix} &\propto a^{-m-2}\propto v_a^{-\frac{1}{3}(m+2)}, \\ {}^{R}\begin{bmatrix}\varkappa & \varkappa' \\ x & y\end{bmatrix} &\propto v_a^{-\frac{1}{3}(n+2)}.\end{aligned}\right\} \quad \ldots\ldots\ldots\ldots \quad (\mathbf{12})$$

Defining

$$\begin{pmatrix}\varkappa & \varkappa' \\ x & y\end{pmatrix}=v_a^{\frac{1}{3}(m+2)}e^{-2}(m_{\varkappa}m_{\varkappa'})^{-\frac{1}{2}}\begin{bmatrix}\varkappa & \varkappa' \\ x & y\end{bmatrix}, \quad \ldots\ldots\ldots\ldots \quad (\mathbf{13})$$

where, for future convenience, e is the magnitude of the charge on the electron, then ${}^{C}\begin{pmatrix}\varkappa & \varkappa' \\ x & y\end{pmatrix}$ is independent of v_a while ${}^{R}\begin{pmatrix}\varkappa & \varkappa' \\ x & y\end{pmatrix}\propto v_a^{\frac{1}{3}(m-n)}$ and (**8**) may be rewritten

$$\left|\,{}^{C}\begin{pmatrix}\varkappa & \varkappa' \\ x & y\end{pmatrix}+{}^{R}\begin{pmatrix}\varkappa & \varkappa' \\ x & y\end{pmatrix}+\Omega^2\delta_{\varkappa\varkappa'}\delta_{xy}\,\right|=0, \quad \ldots\ldots\ldots \quad (\mathbf{14})$$

where

$$\Omega^2=v_a^{\frac{1}{3}(m+2)}e^{-2}\omega^2. \quad \ldots\ldots\ldots\ldots\ldots\ldots \quad (\mathbf{15})$$

If now ${}^{C}\begin{pmatrix}\varkappa & \varkappa' \\ x & y\end{pmatrix}$ and ${}^{R}\begin{pmatrix}\varkappa & \varkappa' \\ x & y\end{pmatrix}$ are calculated for one value a_0 of a (the suffix zero will be used hereafter to refer to this value) and equation (**14**) solved for all $\mathbf{k}$, it is comparatively simple to repeat this process for any other value of a. Putting $g=v_a/v_0=a^3/a_0^3$,

$$\left.\begin{aligned}{}^{C}\begin{pmatrix}\varkappa & \varkappa' \\ x & y\end{pmatrix} &= {}^{C}\begin{pmatrix}\varkappa & \varkappa' \\ x & y\end{pmatrix}_0, \\ {}^{R}\begin{pmatrix}\varkappa & \varkappa' \\ x & y\end{pmatrix} &= {}^{R}\begin{pmatrix}\varkappa & \varkappa' \\ x & y\end{pmatrix}_0 g^{\frac{1}{3}(m-n)},\end{aligned}\right\} \quad \ldots\ldots\ldots\ldots \quad (\mathbf{16})$$

so that it is only necessary to multiply the ${}^{R}\begin{pmatrix}\varkappa & \varkappa' \\ x & y\end{pmatrix}_0$ by a factor independent of $\mathbf{k}$ to obtain the equations determining the normal frequencies of vibration of the crystal for any value of the lattice parameter.

Denoting these frequencies by $\omega(\mathbf{k},i)$, where $i=1, 2, \ldots, 3s$, the energy of a given state of the crystal is

$$E_m=\Phi_0+\sum_{\mathbf{k},i}[m(\mathbf{k},i)+\tfrac{1}{2}]\hbar\omega(\mathbf{k},i), \quad \ldots\ldots\ldots\ldots \quad (17)$$

where the $m(\mathbf{k},i)$ are positive integers or zero (not to be confused with the index m in (**10**)). The relevant partition function at temperature T is

$$Z=\sum_m \exp(-E_m/kT)=\exp(-\Phi_0/kT)/\prod_{\mathbf{k},i}[2\sinh(\hbar\omega/2kT)]. \quad \ldots \quad (18)$$

The free energy of the crystal is therefore

$$\left.\begin{aligned}F=-kT\ln Z&=\Phi_0+kT\sum_{\mathbf{k},i}[\ln 2+\ln\sinh(\hbar\omega/2kT)]\\ &=\Phi_0+\mathscr{T}.\end{aligned}\right\} \quad \ldots \quad (19)$$

The equation of state for the crystal may be obtained from the equilibrium condition

$$p=-\left(\frac{\partial F}{\partial V}\right)_T=-\left(\frac{\partial\Phi_0}{\partial V}\right)_T-\left(\frac{\partial\mathscr{T}}{\partial V}\right)_T, \quad \ldots\ldots\ldots\ldots \quad (20)$$

which is sufficient to give the variation of volume with temperature at constant pressure.

III. Application to Sodium Chloride

It was decided to apply this method to determine the theoretical thermal expansion of sodium chloride, for which Kellermann (1940) had determined the normal frequencies of vibration at room temperature. It was possible, therefore, to use this work as a starting point, apart from the relative simplicity of investigating an ionic crystal, for which the assumption that the interparticle potential energy depends only on the interparticle distance is most likely to be valid (see Fletcher (1957) for a discussion of this point). Kellermann did not consider the electrons explicitly but treated the Na^+ and Cl^- ions as basic particles so that $s=2$ and, taking a as the nearest-neighbour distance, $v_a=2a^3$. Then in (**10**), with $c=\pm e^2$ and $m=1$, the first term corresponds to the Coulomb force between two ions and the second to all other forces, e.g. van der Waals. In the case of the latter he ignored all but nearest-neighbour interactions (see Section V), thereby obtaining

$$-\alpha_M e^2/a+6v(a)=-\alpha_M e^2/a+6b/a^n, \quad \ldots\ldots\ldots\ldots \quad (21)$$

where α_M is the Madelung number for the lattice, as the contribution per cell to Φ_0. To determine values of b and n for use in calculating $\begin{pmatrix}\varkappa & \varkappa'\\ x & y\end{pmatrix}$ he used the relations

$$(\mathrm{d}\Phi_0/\mathrm{d}r)_{r=a}=0 \text{ and } 9V\varkappa_T^{-1}=(r^2\mathrm{d}^2\Phi_0/\mathrm{d}r^2)_{r=a}, \quad \ldots\ldots \quad (22)$$

where $\varkappa_T$ is the compressibility. Neither of these is correct; this point and correction for the error introduced are discussed in Section IV. Kellermann tabulated $(v_a/e^2)\,{}^{C}\begin{bmatrix}\varkappa & \varkappa' \\ x & y\end{bmatrix} = (m_\varkappa m_{\varkappa'})^{\frac{1}{2}}\,{}^{C}\begin{pmatrix}\varkappa & \varkappa' \\ x & y\end{pmatrix}$ and $(m_\varkappa m_{\varkappa'})^{\frac{1}{2}}\,{}^{R}\begin{pmatrix}\varkappa & \varkappa' \\ x & y\end{pmatrix}$ for about 50 wave vectors **k** covering the relevant region of **k**-space. Using these as ${}^{C}\begin{pmatrix}\varkappa & \varkappa' \\ x & y\end{pmatrix}_0$ and ${}^{R}\begin{pmatrix}\varkappa & \varkappa' \\ x & y\end{pmatrix}_0$, the six normal frequencies of vibration were calculated in the present work by means of a digital computer for these vectors **k** and for $g=1(0\cdot01)1\cdot14$, a range designed to cover the possible change of volume from room temperature to the melting point. For each **k** and i $\omega(\mathbf{k},i)$ was tabulated against g and $\partial\omega/\partial g$, $\partial^2\omega/\partial g^2$ evaluated by numerical methods.

Considering now one mole of the crystal, for which $V=2Na^3$,

$$\Phi_0=N(-\alpha_M e^2 a_0^{-1} g^{-\frac{1}{3}}+6ba_0^{-n} g^{-\frac{1}{3}n}), \quad \ldots\ldots\ldots\ldots\ldots\ldots \quad (23)$$

and

$$(\partial\Phi_0/\partial V)_T=(2Na_0^3)^{-1}(\mathrm{d}\Phi_0/\mathrm{d}g)=a_0^{-4}(\tfrac{1}{6}\alpha_M e^2 g^{-4/3}-nba_0^{-n+1} g^{-\frac{1}{3}(n+3)}), \quad \ldots\ldots\ldots\ldots\ldots\ldots \quad (24)$$

while

$$\left(\frac{\partial\mathscr{T}}{\partial V}\right)_T=\frac{\hbar}{4Na_0^3}\sum_{\mathbf{k},i}\coth\left(\frac{\hbar\omega(\mathbf{k},i)}{2kT}\right)\left(\frac{\partial\omega(\mathbf{k},i)}{\partial g}\right)_T. \quad \ldots\ldots\ldots\ldots \quad (25)$$

Since the normal frequencies had been calculated only for certain points in **k**-space, the relevant region of **k**-space was divided into cells, volume ΔK, each containing one of these points. If the total volume of **k**-space for each i, and therefore corresponding to N states of the crystal, is K, (**25**) may be rewritten

$$\left(\frac{\partial\mathscr{T}}{\partial V}\right)_T=\frac{\hbar}{4Ka_0^3}\sum_{\mathbf{k},i}\coth\left(\frac{\hbar\omega(\mathbf{k},i)}{2kT}\right)\left(\frac{\partial\omega(\mathbf{k},i)}{\partial g}\right)_T\Delta K, \quad \ldots \quad (26)$$

summation now being carried out only over the values of **k** for which $\omega(\mathbf{k},i)$ had been calculated.

The actual procedure used was for a given value of g, to evaluate (**24**) and also (**26**) for two or more suitable values of T. By interpolation it was then possible to find the temperature for which (**20**) was satisfied, i.e. corresponding to the value of g chosen (p was in fact neglected since at normal pressure its magnitude was less than $0\cdot01$ per cent of either of the other terms).

IV. Determination of Parameters

The form of interparticle potential energy assumed by Kellermann and the present author involves two parameters, b and n. Although these could be calculated in principle from atomic theory, Kellermann's determination of them from experimental data appears more realistic for the purpose of the present approximate theory. As will be seen, this amounts to fitting the theoretical (V,T) and $(\varkappa_T,T)$ curves to experiment at one point. It is convenient to introduce here two parameters defined by Kellermann

$$A=4a_0^3 e^{-2}(\mathrm{d}^2v/\mathrm{d}r^2)_{r=a_0}=4n(n+1)be^{-2}a_0^{-n+1}, \quad \ldots\ldots \quad (27)$$

and

$$B=4a_0^2 e^{-2}(\mathrm{d}v/\mathrm{d}r)_{r=a_0}=-4nbe^{-2}a_0^{-n+1}, \quad \ldots\ldots\ldots\ldots \quad (28)$$

whence

$$n=-A/B-1 \text{ and } b=-\tfrac{1}{4}e^2n^{-1}a_0^{n-1}B. \quad \ldots\ldots\ldots \quad \mathbf{(29)}$$

In terms of these the condition (**20**) becomes, using (**26**),

$$\left(\frac{\alpha_M}{6}+\frac{B}{4}\right)\frac{e^2}{a_0^4}g^{-4/3}+\frac{\hbar}{4Ka_0^3}\sum_{\mathbf{k},i}\coth\left(\frac{\hbar\omega}{2kT}\right)\left(\frac{\partial\omega}{\partial g}\right)_T\Delta K=-p. \quad \ldots\ldots \quad \mathbf{(30)}$$

Further, the isothermal compressibility is given by

$$\begin{aligned}\varkappa_T^{-1}&=-V(\partial p/\partial V)_T=V[(\partial^2\Phi_0/\partial V^2)_{T,T}+(\partial^2\mathscr{T}/\partial V^2)_{T,T}]\\&=(-8\alpha_M+3A-6B)e^2/36a_0^4g^{4/3}\\&\quad+\frac{\hbar g}{4Ka_0^3}\sum_{\mathbf{k},i}\left[\coth\left(\frac{\hbar\omega}{2kT}\right)\left(\frac{\partial^2\omega}{\partial g^2}\right)_{T,T}-\frac{\hbar}{2kT}\operatorname{cosech}^2\left(\frac{\hbar\omega}{2kT}\right)\left\{\left(\frac{\partial\omega}{\partial g}\right)_T\right\}^2\right]\Delta K.\end{aligned} \quad \ldots\ldots\ldots\ldots\ldots\ldots \quad \mathbf{(31)}$$

The aim of choosing A and B so that (**30**) and (**31**) are satisfied by experimental values of T, a_0, and $\varkappa_T$ cannot be attained before calculating the normal frequencies, however, since the frequencies are required for evaluating certain terms in these relations. Thus it is necessary to obtain approximate values at first by some such means as that used by Kellermann, namely, the use of (**22**), which is equivalent to ignoring the frequency-dependent terms. Having calculated the normal frequencies ω_1, using these incorrect values, A_1, B_1, n_1, b_1, of the parameters, the present author obtained approximate corrections to them as follows. These ω_1 and their derivatives were substituted into (**30**) and (**31**) to obtain new values of the parameters, A_2, B_2, n_2, and b_2. Now ${}^{C}\begin{bmatrix}\varkappa & \varkappa' \\ x & y\end{bmatrix}$ is independent of the parameters and it can be shown that

$$\left.\begin{aligned}&{}^{R}\begin{bmatrix}\varkappa & \varkappa \\ x & x\end{bmatrix}v_0/e^2=-(A+2B)\,;\quad {}^{R}\begin{bmatrix}\varkappa & \varkappa' \\ x & y\end{bmatrix}=0 \qquad\qquad (x\neq y),\\&{}^{R}\begin{bmatrix}\varkappa & \varkappa' \\ x & x\end{bmatrix}v_0/e^2=A\cos 2\pi k_xa_0+B(\cos 2\pi k_ya_0+\cos 2\pi k_za_0) \quad (\varkappa\neq\varkappa').\end{aligned}\right\} \ldots \mathbf{(32)}$$

The approximation was made of assuming all ${}^{R}\begin{bmatrix}\varkappa & \varkappa' \\ x & y\end{bmatrix}\propto(A+2B)$: then consideration of (**16**) shows that a recalculation with the new values, A_2, B_2, would produce the same values of Ω for different values, g_2, of g instead of those, g_1, used before, where

$$(A_2+2B_2)g_2^{\frac{1}{3}(1-n_2)}=(A_1+2B_1)g_1^{\frac{1}{3}(1-n_1)}. \quad \ldots\ldots\ldots \quad \mathbf{(33)}$$

From (**15**) the frequencies ω_2 corresponding to g_2 are

$$\omega_2=(g_1/g_2)^{\frac{1}{2}}\omega_1. \quad \ldots\ldots\ldots\ldots\ldots\ldots \quad \mathbf{(34)}$$

By this means a new tabulation of ω against g was prepared, interpolation made for $g_2=1$, and further values of the parameters found by substitution in (**30**) and (**31**). This procedure was repeated until self-consistency was obtained. The final results were

$$A=10\cdot 68\,;\ B=-1\cdot 048\,;\ n=9\cdot 188\,;\ b=9\cdot 902\times 10^{-83},$$

as compared with Kellermann's values

$$A=10\cdot 18\,;\ B=-1\cdot 165\,;\ n=7\cdot 738\,;\ b=1\cdot 148\times 10^{-71},$$

both being based on the values $\alpha_M=1\cdot 7476$; $e=4\cdot 8\times 10^{-10}$ e.s.u. ; $a_0=2\cdot 814\times 10^{-8}$ cm ; and $\varkappa_T=4\cdot 16\times 10^{-12}$ cm²/dyne, corresponding to $g=1$; $T=288$ °K.

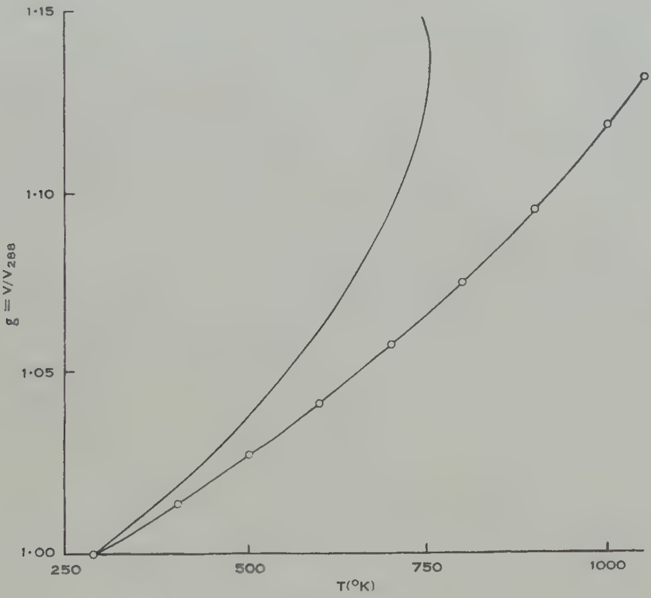

Fig. 1.—Expansion of sodium chloride.
—o—o— Experimental (Eucken and Dannöhl 1934).
———— Theoretical.

With these corrected values of the parameters, the procedure described in Section III was carried out to obtain V as a function of T at constant (zero) pressure. The results are shown in Figure 1 ; the experimental curve was obtained from the values of Eucken and Dannöhl (1934) for the thermal expansion of sodium chloride. Owing to the wide discrepancy between theory and experiment, it was decided to try to check the tables of normal frequencies by calculating the specific heat at constant volume and the isothermal compressibility. To do this it was necessary to obtain temperatures T corresponding to the values of g, under which the frequencies were tabulated, and for this Eucken and Dannöhl's figures were used. The expression (**31**) was used to evaluate $\varkappa_T$, while for the specific heat

$$E=\Phi_0+\frac{N\hbar}{2K}\sum_{\mathbf{k},i}\ \omega(\mathbf{k},i)\coth\left(\frac{\hbar\omega(\mathbf{k},i)}{2kT}\right)\Delta K, \qquad \ldots\ldots\ldots \quad (\mathbf{35})$$

and

$$C_V=\left(\frac{\partial E}{\partial T}\right)_V=\frac{N\hbar^2}{4KkT^2}\sum_{\mathbf{k},i}\omega^2\operatorname{cosech}^2\left(\frac{\hbar\omega}{2kT}\right)\Delta K. \quad \ldots\ldots (36)$$

The results are shown in Figures 2 and 3. The experimental values for C_V were taken from Hunter and Siegel (1942) while those for $\varkappa_T$ were obtained from their values of $\varkappa_s$ by use of the relation

$$\varkappa_T=\varkappa_s+\alpha^2VT/C_p, \quad \ldots\ldots\ldots\ldots\ldots\ldots (37)$$

together with the figures quoted by Hunter and Siegel for C_p and the results of Eucken and Dannöhl (1934) for V and for the coefficient of thermal expansion α.

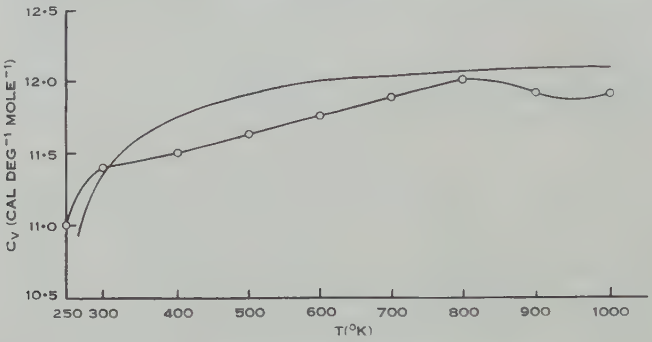

Fig. 2.—Specific heat of sodium chloride.
—o—o— Experimental (Hunter and Siegel 1942).
——— Theoretical.

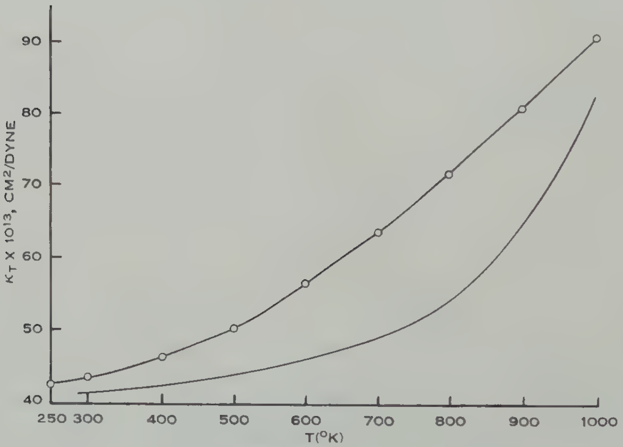

Fig. 3.—Compressibility of sodium chloride.
—o—o— Experimental (Hunter and Siegel 1942).
——— Theoretical.

V. Comparison with Experiment and Discussion

Figure 1 shows that the theory used here predicts a much more rapid increase of volume with temperature than is found experimentally. Analysis of this discrepancy is complicated by the fact that the form of potential energy assumed and the values used for the parameters A, B, n, and b affect both $(\partial\Phi_0/\partial V)_T$

and $(\partial\mathscr{T}/\partial V)_T$, although the total effect on the (V,T) curve of quite large changes in these parameters was found to be surprisingly small. Essentially the method used has involved the finding of a temperature T to which a given set of ω's, and hence a given value of V, corresponds. The good agreement with experiment in the case of C_V might seem to indicate that the ω's are tabulated against the correct values of V (and hence of T). However, cosech x is so insensitive a function of x when x is small, as $x=\hbar\omega/2kT$ is here, especially for high temperatures, that one could vary T considerably (and hence alter the tabulation of the ω's against V) without affecting this agreement appreciably. It does indicate that the ω's obtained are of the right order of magnitude. In the case of $\varkappa_T$, however, the frequency-dependent terms are both very sensitive to the choice of T, are relatively independent of one another, and their magnitudes are $\sim$25 and 40–50 per cent. of the other terms in (**31**). The reasonable agreement with experiment does, therefore, suggest that the ω's are correctly tabulated against V and that the fault lies elsewhere in the development of the theory of thermal expansion used here.

Assuming for the moment that the form assumed for the potential energy and the values used for the parameters are essentially correct, $(\partial\Phi_0/\partial V)_T$ is determined, but inclusion of anharmonic terms in the expansion of Φ would affect $(\partial\mathscr{T}/\partial V)_T$. With cubic symmetry quartic terms in the $\mathbf{u}_\varkappa^l$ are the first to be considered; their coefficients will be of the same sign as those of the quadratic terms and by perturbation theory they will contribute to E_m terms proportional to $(m^2+m+\frac{1}{2})/\omega^2$. Thus E_m would be increased, which can be interpreted in terms of a larger effective ω. Since the important factors in $(\partial\mathscr{T}/\partial V)_T$ are the coth $(\hbar\omega/2kT)$, this would mean a larger value of T would be necessary to keep $-(\partial\mathscr{T}/\partial V)_T=(\partial\Phi_0/\partial V)_T$. Thus inclusion of anharmonic terms would improve agreement with experiment. An attempt to assess this was made but it seemed obvious that a fairly exact calculation would be necessary before any worthwhile conclusions could be drawn.

As far as the form assumed for the potential energy Φ is concerned, Kellermann makes the point that only nearest-neighbour interactions are considered for the repulsive part. This does not seem so, however, since, provided one assumes a repulsive interparticle potential energy proportional to ρ^{-n}, the contribution to Φ_0 from all particles will be of the form C/a^n, where C is just the coefficient of a^{-n} determined here (from experiment), and similarly for Φ_2. Regarding the constancy of the form of Φ, e.g. of the parameters, assumed here, one expects an increase in temperature to spread out the electron clouds about the ions. Provided these clouds stay spherically symmetrical, the Coulomb terms $\pm e^2/\rho$ will be unchanged, but the others will be increased owing to greater repulsion between the electrons. This would increase the restoring force on a displaced ion, increase the ω's, and decrease $-(\partial\mathscr{T}/\partial V)_T$ ($\partial\mathscr{T}/\partial V$ is negative) if T is kept fixed. On the other hand, $-B$, which is essentially the repulsive force between two ions, would be increased; this increase would result in a decrease in $(\partial\Phi_0/\partial V)_T$ also. Thus, one cannot say without further investigation whether one would have to increase or decrease T, thereby improving or worsening agreement with experiment, to maintain $-(\partial\mathscr{T}/\partial V)_T=(\partial\Phi/\partial V)_T$.

One further point is that, if some or all of the electrons were considered as separate particles, they would be expected to perform high frequency oscillations, thereby increasing the average normal frequency and decreasing $-(\partial\mathscr{T}/\partial V)_T$. The effect on $(\partial\Phi/\partial V)_T$ is difficult to estimate, since it would involve Coulomb, correlation, and exchange effects between the electrons.

Reference to Figure 1 shows that the theoretical coefficient of thermal expansion eventually becomes infinite and then negative. Obviously this has no connexion with observations where α becomes zero and then negative. With regard to the theoretical work of Blackman (1958) on this point, practically all $\gamma_\nu=-(\partial \ln \nu/\partial \ln V)_T$ are positive, but for a few wave vectors $\mathbf{k}\gamma_\nu$ is negative and the number of these increases as V, i.e. T, decreases.

One further point is that the approximate summation procedure introduced over the wave vectors **k**, for which the normal frequencies had been calculated, may have affected the results obtained. Error is most likely to enter through the factors $\partial\omega/\partial g$ since these do vary quite rapidly with **k** in some regions of **k**-space. Since, however, the summation was carried out over 384 wave vectors, the overall effect on the calculations was not considered serious.

VI. Conclusions

An attempt, based on lattice theory, has been made to calculate the theoretical thermal expansion of sodium chloride. The agreement with experiment is very poor, the theoretical value of α increasing far too rapidly with temperature, eventually becoming infinite and then negative. Investigation of the variation with temperature of C_V and $\varkappa_T$ using the tables of normal frequencies of vibration of the crystal obtained in the work, indicates that these frequencies are essentially correct in absolute magnitude and as functions of the volume of the crystal. The discrepancy between theoretical and experimental values of α seems most likely to be due to the neglect of anharmonic terms in the expansion of the potential energy Φ but may partly be caused by the assumptions as to the form of Φ and the constancy of this form.

With regard to future work along the lines indicated here, it would be relatively simple to obtain correct values of the parameters A, B, n, and b exactly by an iterative process, since at each stage it would only be necessary to recalculate the ω's for three or four values of g covering the value at which (**30**) and (**31**) are to be satisfied, using a digital computer. It would be simplest and most satisfactory to do this at 0 °K, since then the frequency-dependent terms are greatly simplified; however, experimental values of a_0 and $\varkappa_T$ at 0 °K would be difficult to obtain accurately. If some other temperature is chosen, the method is easily extended to lower temperatures by considering values $g<1$; this was not done here owing to an oversight in carrying out the calculations.

VII. Acknowledgments

The author wishes to thank the Adolph Basser Computing Laboratory, University of Sydney, for the use of SILLIAC; their staff for advice and assistance in programming the problem; and Dr. P. G. Klemens of C.S.I.R.O. for useful discussions in connexion with the work.

VIII. REFERENCES

BLACKMAN, M. (1958).—*Phil. Mag.* **3** : 831.
EUCKEN, A., and DANNÖHL, W. (1934).—*Z. Electrochem.* **40** : 814.
FLETCHER, G. C. (1957).—*Phil. Mag.* **8** : 639.
HUNTER, L., and SIEGEL, S. (1942).—*Phys. Rev.* **61** : 84.
KELLERMANN, E. W. (1940).—*Phil. Trans.* **A 238** : 513.

SCATTERING OF HIGH ENERGY POLARIZED NUCLEONS BY COMPLEX NUCLEI

By B. A. Robson*

[*Manuscript received May* 20, 1959]

Summary

The elastic scattering of 220 MeV polarized nucleons by carbon and calcium is studied using a new expression for the polarization. Except at small angles of scattering, substantial agreement is obtained with the results of calculations using a simplified form of the WKB method. Optical model parameters are found which are compared with those obtained by other workers for this energy region.

I. Introduction

The elastic scattering of polarized protons by complex nuclei has been investigated (Hafner 1958) for incident energies of 220 MeV with sufficient accuracy to permit a severe test of the optical model. At this energy, the polarization shows large fluctuations with scattering angle. For most scattering angles, the polarization as usually defined (equation (**3**)) is large and positive. However, the polarization is negative for those angles for which the differential cross section shows a minimum. Both the latter two effects are diffraction phenomena associated with the scattering.

The theoretical interpretation of the experimental data has generally been carried out by the addition of a spin-orbit term to the complex central potential of the optical model. Fermi (1954) obtained qualitative agreement for the polarization of 340 MeV protons by carbon using the Born approximation. However, the Born approximation is not even qualitatively correct at large angles. Other workers have used the WKB approximation in a partial wave analysis. This method is discussed in Section III (*b*). It has been found to give excellent fits to the experimental data at all except small angles for a Woods-Saxon (1954) complex central potential with a spin-orbit term of the Thomas type. Unfortunately, the partial wave method tends to conceal the physics of the problem, which can be more easily understood in an approach such as the Born approximation. It is for this reason that an attempt has been made to obtain a closed formula for the polarization which does not have the defects of the Born approximation.

II. Approximations for Polarization

The nuclear potential is taken to be

$$V(r)=-(V+\mathrm{i}W)g(r)+\gamma r^{-1}(\mathrm{d}g/\mathrm{d}r)\mathbf{L}\,.\,\boldsymbol{\sigma}, \qquad \ldots\ldots\ldots \quad (\mathbf{1})$$

where $g(r)$ is the shape of the central potential, V and W are positive real functions so that the central force is attractive and absorptive, and γ is a positive real quantity corresponding to the sign of the spin-orbit force in the shell model. $\mathbf{L}$ and $\boldsymbol{\sigma}$ represent the orbital and spin angular momenta of the nucleon.

---

* Physics Department, University of Melbourne.

The differential cross section and the polarization for the elastic scattering of unpolarized nucleons by a spinless target are given by

$$\mathrm{d}\sigma(\theta)/\mathrm{d}\Omega=|A(\theta)+B(\theta)\boldsymbol{\sigma}\,.\,\mathbf{n}|^2=A^*A+B^*B, \quad \ldots\ldots\ldots \quad (2)$$

and

$$\mathbf{P}(\theta)=P(\theta)\mathbf{n}=(A^*B+B^*A)\mathbf{n}/(A^*A+B^*B), \quad \ldots\ldots \quad (3)$$

where $A(\theta)$ and $B(\theta)$ are the amplitudes for spin-independent and spin-dependent scattering respectively and $\mathbf{n}$ is a unit vector given by

$$\mathbf{n}=\mathbf{k}_i\times\mathbf{k}_f/k^2\sin\theta, \quad \ldots\ldots\ldots\ldots\ldots\ldots \quad (4)$$

where $\mathbf{k}_i$ and $\mathbf{k}_f$ are $\hbar^{-1}$ times the initial and final momenta of the nucleon.

In the Born approximation, it may be shown that for neutrons

$$A(\theta)=2m(V+\mathrm{i}W)\hbar^{-2}\int_0^\infty \mathrm{j}_0(Kr)r^2g(r)\mathrm{d}r, \quad \ldots\ldots\ldots \quad (5)$$

$$B(\theta)=\mathrm{i}2m\gamma k^2\hbar^{-2}\sin\theta\int_0^\infty \mathrm{j}_0(Kr)r^2g(r)\mathrm{d}r, \quad \ldots\ldots\ldots \quad (6)$$

where $K=2k\sin\frac{1}{2}\theta$, m is the reduced mass of the nucleon, and j_0 is the zero order spherical Bessel function. Hence

$$P(\theta)=\frac{2\gamma k^2W\sin\theta}{V^2+W^2+\gamma^2k^4\sin^2\theta}. \quad \ldots\ldots\ldots\ldots\ldots \quad (7)$$

This result for the polarization has the following defects :

(*a*) the polarization is proportional to the absorption potential, so that $P(\theta)=0$ for $W=0$;

(*b*) the polarization is independent of $g(r)$ and is therefore the same for all nuclei for a given incident energy (assuming γ and W constant) ;

(*c*) the polarization vanishes only when $\theta=0$ or π for finite W.

These defects are a consequence of $A(\theta)$ and $B(\theta)$ having the same angular dependence apart from the $\sin\theta$ factor, so that the integral over r is the same for both amplitudes.

The Montroll and Greenberg (MG) approximation has been shown (Mohr and Robson 1956) to give better results for the differential cross section than the Born approximation, although both approximations are rather unsatisfactory for complex potentials, when absolute magnitudes are concerned. If the approximate Montroll and Greenberg (1952) wave function is used instead of a plane wave, one obtains for neutrons :

$$A(\theta)=2m(V+\mathrm{i}W)\hbar^{-2}p\int_0^\infty \{\mathrm{j}_0(K_-r)+q\mathrm{j}_0(K_+r)\}r^2g(r)\mathrm{d}r, \quad \ldots\ldots \quad (8)$$

$$B(\theta)=\mathrm{i}2m\gamma kk_1\hbar^{-2}p\sin\theta\int_0^\infty \{\mathrm{j}_0(K_-r)+q\mathrm{j}_0(K_+r)\}r^2g(r)\mathrm{d}r, \quad \ldots\ldots \quad (9)$$

where $K_{\pm}=\{k^2+k_1^2\pm 2kk_1\cos\theta\}^{\frac{1}{2}}$ (N.B.—Im $\{k_1\}$ is neglected here),

$$p=2k_1\exp\{\mathrm{i}a(k_1-k)\}/(k_1+k)(1-q^2),$$
$$q=(k_1-k)\exp\{2\mathrm{i}ak_1\}/(k_1+k),$$
$$k_1^2=k^2-U,$$
$$U=-2m(V+\mathrm{i}W)\hbar^{-2},$$

and a is the radius of the equivalent sphere of the diffuse boundary spherical scatterer $g(r)$. The assumption involved is that the MG approximate wave function does not differ too greatly from the accurate wave function in the diffuse boundary region of $g(r)$. The polarization is given by

$$P(\theta)=\frac{2\gamma k^2W\sin\theta}{V^2+W^2+\gamma^2k^2k_1k_1^*\sin^2\theta}. \qquad \ldots\ldots\ldots\ldots (10)$$

Equation (**10**) differs only slightly from equation (**7**) and has the same defects. Both the Born and MG approximations for the polarizations fail for the same reason ; $A(\theta)$ and $B(\theta)$ have the same angular dependence under the integral over r. The fluctuations in the polarization arise from a change in wavelength and amplitude of the wave function over the diffuse nuclear boundary.

A simple approximate wave function which has changes in wavelength and amplitude is

$$\left.\begin{aligned}\psi(r)&=p\exp(\mathrm{i}k_1\mathbf{n}_0.\mathbf{r})+pq\exp(-\mathrm{i}k_1\mathbf{n}_0.\mathbf{r}), && r\leqslant a,\\ &=\exp(\mathrm{i}k\mathbf{n}_0.\mathbf{r}), && r>a.\end{aligned}\right\} \quad \ldots . (11)$$

where $\mathbf{n}_0$ is a unit vector along the incident direction, and a is some appropriate value of r. The above wave function is discontinuous at $r=a$ (although it is nearly continuous at high energies), its wavelength and amplitude changing abruptly at this radius. On the other hand, the wavelength and amplitude of the exact wave function will change gradually over the whole diffuse nuclear boundary. However, it will be seen that the use of a " two-step " wave function is sufficient to account for the observed fluctuations of the polarization, which are not predicted by either the Born or MG approximations, which use " single-step " wave functions.

In the following calculations $g(r)$ is taken, for convenience, to be of trapezoidal form

$$\left.\begin{aligned}g(r)&=1, && \text{for } 0<r\leqslant a,\\ &=(b-r)/(b-a), && a<r\leqslant b,\\ &=0, && b<r<\infty.\end{aligned}\right\} \quad \ldots\ldots\ldots\ldots (12)$$

For simplicity, the " two-step " wave function was taken to be

$$\left.\begin{aligned}\psi(r)&=p\exp(\mathrm{i}k_1\mathbf{n}_0.\mathbf{r})+pq\exp(-\mathrm{i}k_1\mathbf{n}_0.\mathbf{r}), && 0<r\leqslant a,\\ &=\exp(\mathrm{i}k\mathbf{n}_0.\mathbf{r}), && a<r\leqslant b.\end{aligned}\right\} \quad \ldots\ldots (13)$$

so that the change in the wavelength and amplitude takes place at $r=a$ rather than at $r=r_0=\frac{1}{2}(a+b)$, the radius of the equivalent sphere. It was found that substantially the same results were obtained if the discontinuity of the wave function was taken at either $r=a$ or $r=r_0$. One finds for neutrons

$$A(\theta)=2m(V+\mathrm{i}W)\hbar^{-2}\{Z(a)+I(a)\}, \quad \ldots\ldots\ldots\ldots\ldots \quad (\mathbf{14})$$

$$B(\theta)=\mathrm{i}2m\gamma k^2\hbar^{-2}\sin\theta\{Z'(a)+I(a)\}, \quad \ldots\ldots\ldots\ldots \quad (\mathbf{15})$$

where $I(a)=\int_a^b \mathrm{j}_0(Kr)r^2g(r)\mathrm{d}r,$

$$Z(a)=a^2p\{[\mathrm{j}_i(K_-a)/K_-]+[q\mathrm{j}_1(K_+a)/K_+]\},$$
$$Z'(a)=a^2\mathrm{j}_1(Ka)/K.$$

$Z(a)$ and $Z'(a)$ are equal only if $k_1=k$, so that $p=1$, $q=0$, and $K_-=K$. $Z(a)$ arises from the region $0<r<a$ of the $A(\theta)$ integration, while $Z'(a)$ arises from the region $a<r<b$ of the $B(\theta)$ integration and the difference between them is due entirely to the different wave functions in these regions. The polarization is

$$P(\theta)=\frac{2\gamma k^2L(a)\{W\lambda(a)+V\mu(a)\}\sin\theta}{(V^2+W^2)(\lambda^2+\mu^2)+\gamma^2k^4L^2\sin^2\theta}, \quad \ldots\ldots\ldots \quad (\mathbf{16})$$

where $L(a)=Z'+I$, $\lambda(a)=\mathrm{Re}\{Z\}+I$, $\mu(a)=\mathrm{Im}\{Z\}$.

The polarization, given by equation (**16**), does not exhibit the same defects as those given by the Born approximation (equation (**7**)) or the MG approximation (equation (**10**)). Firstly, $P(\theta)\neq 0$ if $W=0$, since the polarization depends also upon V. Secondly, the polarization vanishes whenever $L=0$ or $\{W\lambda+V\mu\}=0$. These two conditions are satisfied for slightly different scattering angles and give rise to the observed fluctuations of the polarization. Moreover, the differential cross section given by the denominator of equation (**16**) (apart from a factor $4m^2\hbar^{-4}$), does not become zero at the diffraction minima, as in the Born and MG approximations, since the two terms do not vanish simultaneously. (It should be noted that the denominators of equations (**7**) and (**10**) are not the differential cross sections for the Born and MG approximations.) Thirdly, the polarization depends upon $g(r)$ and is therefore different for different nuclei.

III. Comparison of Theory with Experiment

(*a*) *Carbon*

Figure 1 (*a*) shows the experimental results of Chesnut, Hafner, and Roberts (1956) and Hafner (1958) for 220 MeV protons elastically scattered by carbon, together with the theoretical curve of Hafner, who used the WKB phase shift method. The full curve is the prediction of equation (**16**) for neutrons of the same energy. The potential used was nearly that of Hafner, $V=10$ MeV, $W=25$ MeV, $\gamma=4\cdot 7$ MeV f^2 (f$\equiv$1 fermi$=10^{-13}$ cm), the mean nuclear radius $r_0=\frac{1}{2}(a+b)=2\cdot 4$ f and the diffuseness parameter $\Delta=\frac{1}{2}(b-a)=0\cdot 2$ f.

Since the calculation is for neutrons, a discrepancy can be expected at small angles. Also, Fernbach, Heckrotte, and Lepore (1955) have shown that the effect of the Coulomb interference is to decrease the first maximum and to increase the angular width of the diffraction dip of the polarization. Thus, the full curve may be considered as a satisfactory prediction for the polarization of 220 MeV neutrons by carbon.

In the present calculations, it was found that the zeros of the polarization are largely determined by the radius r_0. Changing r_0 from $2 \cdot 4$ f to $2 \cdot 8$ f moved the zeros to smaller angles by about 4°, so the choice of r_0 is rather critical. A value of $3 \cdot 0$ f, corresponding to $1 \cdot 3\ A^{\frac{1}{3}}$ for r_0, gives the dip of the polarization at too small an angle. The largest radius, which is consistent with the polarization data, is about $1 \cdot 2\ A^{\frac{1}{3}}$. This agrees very well with the information about nuclear radii obtained from electron scattering experiments. It was found, in disagreement with Hafner, that reasonable changes in Δ (e.g. from $0 \cdot 2$ f to $0 \cdot 4$ f) did not change the polarization appreciably.

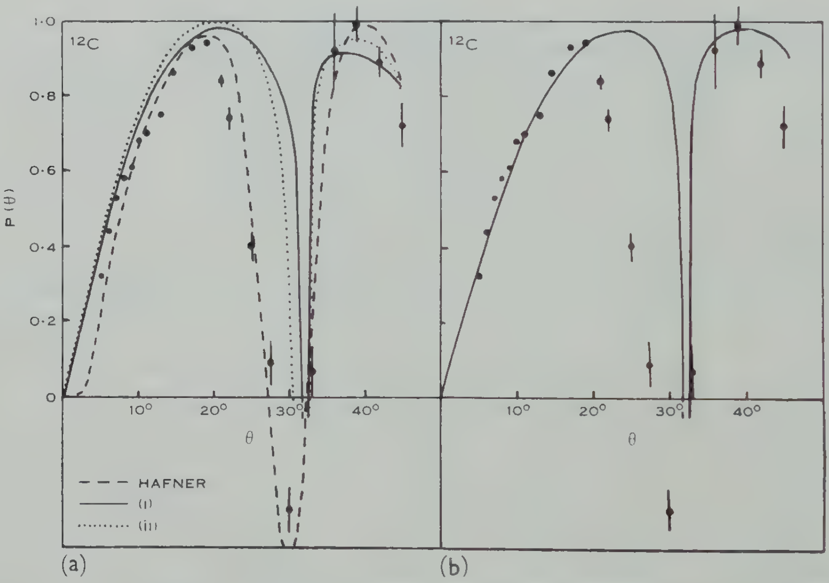

Fig. 1.—Polarization in elastic scattering of 220 MeV nucleons from ^{12}C. The points are the experimental results of Hafner for protons. (*a*) shows the theoretical predictions of Hafner (with $V=10$ MeV, $W=25$ MeV, $\gamma=5 \cdot 0$ MeV f^2, $r_0=2 \cdot 4$ f, and $\Delta=0 \cdot 1$ f) and of equation (**16**) (with (i) $V=10$ MeV, $W=25$ MeV, $\gamma=4 \cdot 7$ MeV f^2, $r_0=2 \cdot 4$ f, $\Delta=0 \cdot 2$ f and (ii) $V=10$ MeV, $W=40$ MeV, $\gamma=6$ MeV f^2, $r_0=2 \cdot 4$ f, $\Delta=0 \cdot 2$ f). (*b*) shows the theoretical prediction of equation (**20**) (with $V=10$ MeV, $W=20$ MeV, $\gamma=3 \cdot 0$ MeV f^2, $\varepsilon=-0 \cdot 5$, $r_0=2 \cdot 4$ f, $\Delta=0 \cdot 2$ f).

The effect of changes in V, W, and γ may be studied by considering the two angles $\theta=20$ and 40°, where $P(\theta)$ is a maximum. The theoretical curve cannot be a poor fit, if both the maxima and the zeros of the polarization data are satisfied. Figure 2 shows the predictions of $P(20°)$ and $P(40°)$ as a function of W and γ for $V=10$ and 20 MeV respectively. The polarization for these two angles is between $0 \cdot 9$ and $1 \cdot 0$. Table 1 shows the values of γ with the corresponding values of W for which fits at both angles may be obtained. Figure 1 (*a*) shows that a satisfactory fit is also obtained for $V=10$ MeV, $W=40$ MeV, and $\gamma=6$ MeV f^2.

(*b*) *Calcium*

Figure 3 shows the method applied to the heavier nucleus, calcium. It is seen that a satisfactory result is obtained for $V=10$ MeV, $W=25$ MeV, $\gamma=4\cdot7$ MeV f^2, $r_0=3\cdot9$ f, and $\Delta=0\cdot4$ f. For comparison, Hafner's parameters are $V=10$ MeV, $W=25$ MeV, $\gamma=4\cdot7$ MeV f^2, $r_0=3\cdot6$ f, and $\Delta=0\cdot1$ f. Such a value of the diffuseness parameter, which is considerably smaller than that ($\sim0\cdot4$ f) given by electron scattering experiments, causes the differential cross section to be too large at angles greater than the first diffraction minimum (Hafner 1958). This discrepancy would appear to arise from the failure of the WKB approximation at small angles.

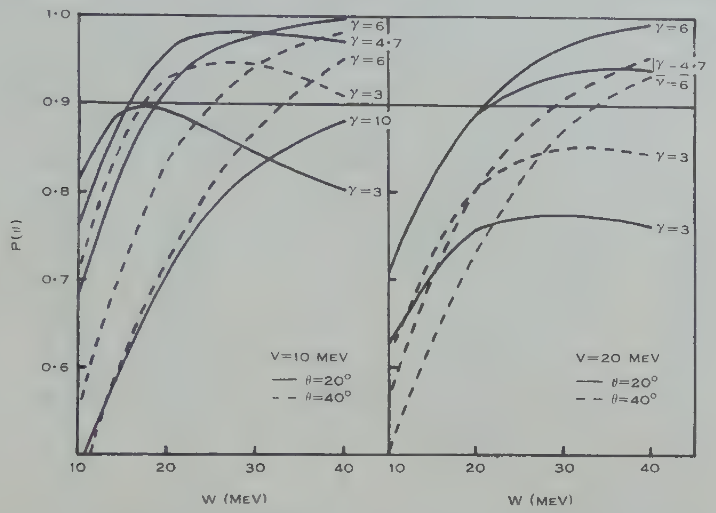

Fig. 2.—Polarization in elastic scattering of 220 MeV nucleons from ^{12}C at $\theta=20$ and 40°. The experimental polarization lies between $0\cdot9$ and $1\cdot0$ for both angles. The predictions of $P(20°)$ and $P(40°)$ given by equation (**16**) are shown for several values of γ and W for $V=10$ MeV and $V=20$ MeV.

Table 1

VALUES OF THE NUCLEAR POTENTIAL PARAMETERS

V (MeV)	γ (MeV f^2)	W (MeV)
10	~3	~18
	$4\cdot7$	$\gtrsim25$
	6	$\gtrsim34$
20	~4	~27
	$4\cdot7$	$\gtrsim29$
	6	$\gtrsim34$

The effect of increasing or decreasing γ is to move the maxima to smaller or larger angles respectively and make the peaks asymmetrical (Fig. 3 (*b*)).

The zeros of the polarization are unaffected by variations of γ and again they require the radius to be given by $1\cdot 1\, A^{\frac{1}{3}} \leqslant r \leqslant 1\cdot 2\, A^{\frac{1}{3}}$. As for carbon, one can expect that an equally satisfactory fit may be obtained for a larger value of γ with a greater value of W.

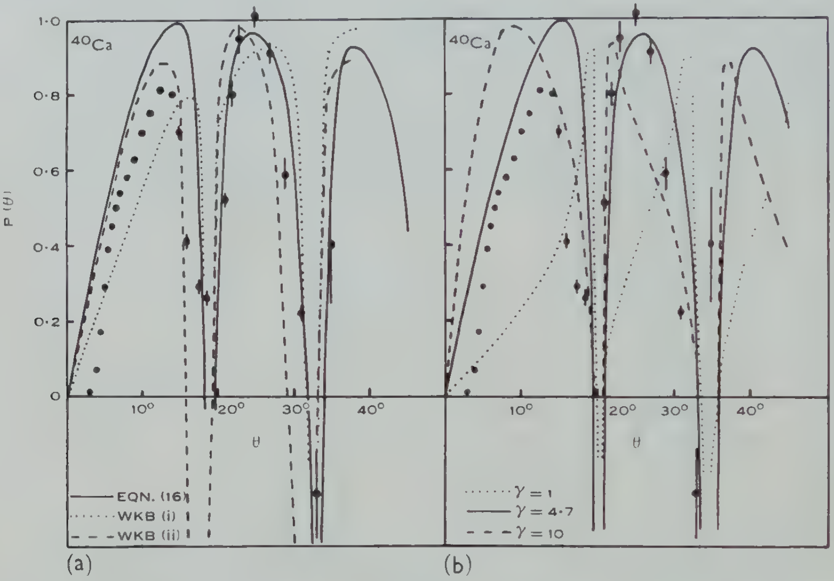

Fig. 3.—Polarization in elastic scattering of 220 MeV nucleons from ^{40}Ca. The points are the experimental results of Hafner for protons. (*a*) shows the theoretical predictions of equation (**16**) (with $V=10$ MeV, $W=25$ MeV, $\gamma=4\cdot 7$ MeV f^2, $r_0=3\cdot 9$ f, $\Delta=0\cdot 4$ f) and of simplified WKB calculations (with $V=10$ MeV, $W=25$ MeV, $r_0=3\cdot 8$ f, $\Delta=0\cdot 4$ f and (i) $\gamma=4\cdot 7$ MeV f^2, (ii) $\gamma=10$ MeV f^2. (*b*) shows the theoretical predictions of equation (**16**) (with $V=10$ MeV, $W=25$ MeV, $r_0=3\cdot 7$ f, $\Delta=0\cdot 4$ f, and (i) $\gamma=1$ MeV f^2, (ii) $\gamma=4\cdot 7$ MeV f^2, (iii) $\gamma=10$ MeV f^2.

Figure 3 (*a*) also shows a comparison with the calculations obtained with a simplified form of the WKB approximation. In this approximation, the phase shifts δ_l are given by

$$\delta_l=\tfrac{1}{2}\int^{\infty}\frac{v\mathrm{d}r}{[k^2-(l+\frac{1}{2})^2/r^2]^{\frac{1}{2}}}, \qquad \ldots\ldots\ldots\ldots\ldots \quad (\mathbf{17})$$

where $v=2m\hbar^{-2}V(r)$. Writing $\delta_l=x_l+iy_l$, then, for the trapezoidal potential of equations (**1**) and (**12**), one finds

$$x_l=\frac{\alpha V\nu^2}{(B-A)}\left[\frac{\rho}{\nu}\sinh\left(\operatorname{arcosh}\frac{\rho}{\nu}\right)-\operatorname{arcosh}\frac{\rho}{\nu}\right]_{\rho=A}^{\rho=B}$$

$$+2\alpha\gamma k^2\mathrm{d}g/\mathrm{d}\rho\mathbf{L}.\boldsymbol{\sigma}\left[\operatorname{arcosh}\frac{\rho}{\nu}\right]_{\rho=A}^{\rho=B}, \qquad \ldots\ldots \quad (\mathbf{18})$$

$$y_l=\frac{\alpha W\nu^2}{(B-A)}\left[\frac{\rho}{\nu}\sinh\left(\operatorname{arcosh}\frac{\rho}{\nu}\right)-\operatorname{arcosh}\frac{\rho}{\nu}\right]_{\rho=A}^{\rho=B}, \qquad \ldots\ldots \quad (\mathbf{19})$$

where $\alpha=\frac{1}{2}m\hbar^{-2}k^{-2}$, $\nu=l+\frac{1}{2}$, $\rho=kr$, $A=ka$, and $B=kb$.

It is seen that the two approximations agree qualitatively. Quantitatively, the main difference between the two methods exists at small angles, where the WKB approximation is least satisfactory on account of its phase shift cut-off. At larger angles, both approximations show a similar movement of the polarization maxima as γ is varied but in the WKB approximation the polarization zeros also move and the shape of the polarization curve shows less asymmetry.

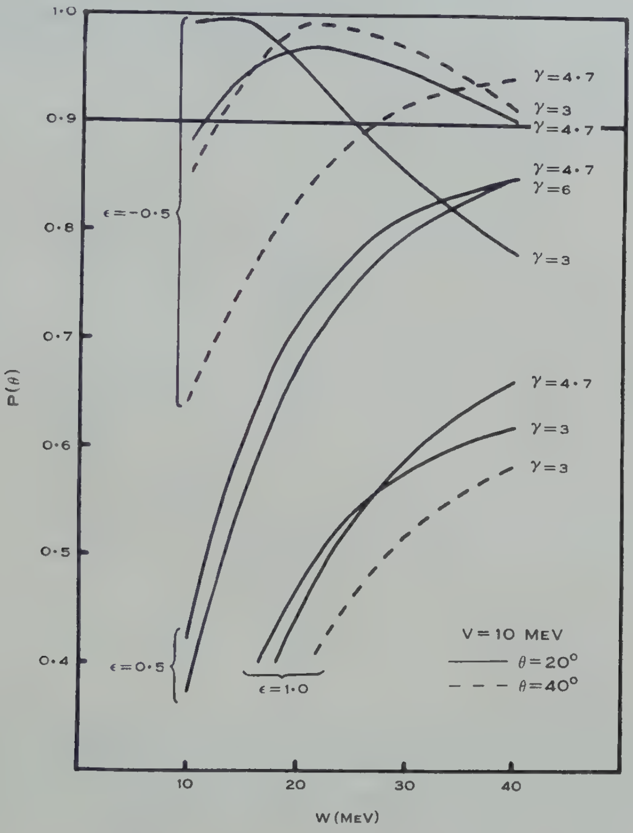

Fig. 4.—Polarization in elastic scattering of 220 MeV nucleons from ^{12}C at $\theta=20$ and 40°. The experimental polarization lies between $0\cdot9$ and $1\cdot0$ for both angles. The theoretical predictions of $P(20°)$ and $P(40°)$ given by equation (**20**) are shown for several values of γ and W for $\varepsilon=1\cdot0$, $0\cdot5$, and $-0\cdot5$ and $V=10$ MeV.

IV. Complex Spin-orbit Potential

So far the discussion has been restricted to real spin-orbit interactions. However, Heckrotte (1956) required the spin-orbit potential to have an imaginary term in order to fit the small-angle elastic scattering polarization of 300 MeV protons by carbon. He found that, if the ratio of imaginary to real spin-orbit potential ε was $\sim -0\cdot5$ to $-1\cdot0$, satisfactory agreement could be obtained with experiment. It is thus of interest to investigate the effect of making $\varepsilon \neq 0$. Replacing γ by $\gamma_c = \gamma(1+i\varepsilon)$, the polarization is

$$P(\theta)=\frac{2\gamma k^2 L(a)\{W\lambda+\mu V+\varepsilon(W\mu-V\lambda)\sin\theta\}}{(V^2+W^2)(\lambda^2+\mu^2)+\gamma^2k^4(1+\varepsilon^2)L^2\sin^2\theta}. \quad \ldots\ldots \ (20)$$

Figure 4 shows the predictions for $P(20°)$ and $P(40°)$ as a function of W, γ, and ε for $V=10$ MeV. Taking $\varepsilon=0{\cdot}5$ or $1{\cdot}0$ is seen to give too small values at both angles. Further changes in γ would not cause a significant increase. On the other hand, an appreciable amount of negative ε may be added and agreement with experiment can still be maintained. Figure 1 (*b*) gives the result of using $\varepsilon=-0{\cdot}5$, $V=10$ MeV, $W=20$ MeV, and $\gamma=3{\cdot}0$ MeV f². Table 2 shows for comparison the values of γ_c determined by other workers.

TABLE 2

VALUES OF THE SPIN-ORBIT COUPLING CONSTANT

Reference	Energy (MeV)	Re$\{\gamma_c\}$ (MeV f²)	Im$\{\gamma_c\}$ (MeV f²)
Present paper	220	3 to 6	0 to —3
Sternheimer (1958)	150	11·2	0 to —11·2
Riesenfeld and Watson (1956)	190	(A) 2·4	—2·7
		(B) 3·3	—2·8
Hafner (1958)	220	5·0	0
Ohnuma (1958)	220	(GT) 3·3	—0·6
		(SM) 7·2	—1·1
Jastrow and Harris (1959)	287	4	+1
Bjorklund, Blandford, and Fernbach (1957)	300	2·2	—2·6
Batty (1958)	310	6·4	0 to —1·6
Bethe (1958)	310	3·6	—1·1

The two sets of results (A and B) refer to the two sets of nucleon-nucleon phase-shifts of Feshbach and Lomon (1956) used by Riesenfeld and Watson to calculate the optical model potential. Similarly, Ohnuma used the phase-shift data of Gammel and Thaler (1957) (GT) and of Signell and Marshak (1958) (SM).

V. ACKNOWLEDGMENTS

The author wishes to thank Associate Professor C. B. O. Mohr for his close interest in this work, and Dr. P. Swan for helpful discussions.

VI. REFERENCES

BATTY, C. J. (1958).—*Proc. Phys. Soc.* **73** : 185.
BETHE, H. A. (1958).—*Ann. Phys. N.Y.* **3** : 190.
BJORKLUND, F., BLANDFORD, I., and FERNBACH, S. (1957).—*Phys. Rev.* **108** : 795.
CHESNUT, W. G., HAFNER, E. M., and ROBERTS, A. (1956).—*Phys. Rev.* **104** : 449.
FERMI, E. (1954).—*Nuovo Cim.* **11** : 407.
FERNBACH, S., HECKROTTE, W., and LEPORE, H. (1955).—*Phys. Rev.* **97** : 1059.
FESHBACH, H., and LOMON, E. (1956).—*Phys. Rev.* **102** : 891.

GAMMEL, J. L., and THALER, R. M. (1957).—*Phys. Rev.* **107** : 291.
HAFNER, E. M. (1958).—*Phys. Rev.* **111** : 297.
HECKROTTE, W. (1956).—*Phys. Rev.* **101** : 1406.
JASTROW, R., and HARRIS, I. (1959).—*Nuc. Phys.* **9** : 437.
MOHR, C. B. O., and ROBSON, B. A. (1956).—*Proc. Phys. Soc.* A **69** : 365.
MONTROLL, E. W., and GREENBERG, J. M. (1952).—*Phys. Rev.* **86** : 889.
OHNUMA, S. (1958).—*Phys. Rev.* **111** : 1173.
RIESENFELD, W. B., and WATSON, K. M. (1956).—*Phys. Rev.* **102** : 1157.
SIGNELL, P. S., and MARSHAK, R. E. (1958).—*Phys. Rev.* **109** : 1229.
STERNHEIMER, R. M. (1958).—*Phys. Rev.* **112** : 1785.
WOODS, R. D., and SAXON, D. S. (1954).—*Phys. Rev.* **95** : 577.

THE ETA CARINAE NEBULA AND CENTAURUS A NEAR 1400 Mc/s

I. OBSERVATIONS

By J. V. Hindman* and C. M. Wade*

[*Manuscript received May* 27, 1959]

Summary

Observations of two strong southern radio sources, the Eta Carinae Nebula (NGC 3372) and Centaurus A (13S4A), at a frequency near 1400 Mc/s, are described. The observations were made with a 36 ft transit-mounted paraboloidal aerial and a 21 cm hydrogen-line receiver modified for the reception of continuum radiation.

The flux density of the Eta Carinae Nebula near 1400 Mc/s is $5 \cdot 82 \times 10^{-24}$ W m^{-2} (c/s)$^{-1}$, with an estimated uncertainty of less than ±20 per cent. This source appears to be fairly symmetrical, with a strong central condensation.

The flux density of Centaurus A is $1 \cdot 3 \times 10^{-23}$ W m^{-2} (c/s)$^{-1}$, with an estimated uncertainty of ±20 per cent. The great angular extent of the object previously found at metre wavelengths is confirmed; at 1400 Mc/s the source covers 7° in declination and about 3° in Right Ascension. The central source associated with NGC 5128 is responsible for about 23 per cent. of the total flux, with the remainder arising in the extended part of the source. There is a well-marked secondary maximum in the extended component at $\alpha_{1950} \approx 13^{\mathrm{h}}\ 21^{\mathrm{m}}$, $\delta_{1950} \approx -44° \cdot 7$.

I. Introduction

(*a*) *The Eta Carinae Nebula*

One of the most prominent galactic emission nebulae is NGC 3372, commonly known as the " Eta Carinae Nebula ". Photographs taken in Hα light show that it consists of a bright core less than half a degree in diameter, crossed by several absorption lanes, with fainter outer extensions which increase its overall angular diameter to 2° (Gum 1955). According to Bok, Bester, and Wade (1955), there may be a very faint Hα emission field underlying the nebula and extending for several degrees; this feature is probably unrelated to NGC 3372. Recently Mills, Little, and Sheridan (1956) have shown that the object is a strong emitter of radio waves at 85·5 Mc/s.

Despite the prominence of NGC 3372, very little is known about its physical properties—temperature, density, mass, excitation, etc. Aside from an early study by Bok (1932), who found a density of 60 ions cm^{-3} for the inner regions of the nebula, the published data are almost entirely of a descriptive nature (Bailey 1908; Cederblad 1946; Gum 1955). The observations described in the present paper were undertaken to provide data for a determination of the general physical properties of the object; these will be discussed in the second paper of this series (Wade 1959). A secondary reason for the observational programme was that NGC 3372 is the only important galactic emission nebula too far south to be included in Westerhout's (1958) comprehensive survey at 1400 Mc/s.

* Division of Radiophysics, C.S.I.R.O., University Grounds, Chippendale, N.S.W.

(*b*) *Centaurus A*

The strong southern radio source Centaurus A (13S4A) was one of the first to be identified with an optically observable object. Bolton, Stanley, and Slee (1949) suggested that it is associated with the peculiar galaxy NGC 5128. This identification still appears to be correct. NGC 5128 is an anomalous object, appearing to be a spheroidal galaxy of Hubble type E_0 crossed by a dark band of obscuration. The radio-frequency counterpart of NGC 5128, Centaurus A, is no less peculiar. Early interferometric observations (Stanley and Slee 1950) indicated that it consists of two components: one, a strong source of small angular size coinciding in position with NGC 5128; the other, a broad, faint extended source surrounding NGC 5128. The extended source has been shown in good detail by recent pencil-beam observations at 19·7 Mc/s (Shain 1958) and at 85·5 Mc/s (Sheridan 1958). It is highly elongated in the north-south direction and covers an area of more than 20 square degrees. In the present paper we describe observations made to extend the picture to decimetre wavelengths. The results will be discussed in a later paper.

II. Instrumentation

The equipment used to make the observations described in the present paper consisted of units of the hydrogen-line receiver (at Potts Hill, near Sydney) used by Kerr, Hindman, and Gum (1959), modified to permit broadband detection of continuum radiation.

(*a*) *The Aerial*

The 36 ft transit-mounted paraboloidal reflector at Potts Hill was employed. The feed is a flanged horn attached to a four-legged support based on the rim of the reflector. Four separate calibrations were required to fix the aerial constants:

- (i) *Calibration of the declination indicator.*—This has been described in detail by Kerr, Hindman, and Gum (1959). The declination setting is accurate to within 0°·05.
- (ii) *Determination of the instrumental meridian.*—Observations of discrete sources with well-determined positions show that the instrumental meridian does not deviate perceptibly from the true meridian.
- (iii) *Measurement of the shape of the radiation pattern.*—This was done by observing the Sun and several discrete sources (Kerr, Hindman, and Gum 1959). The main lobe of the aerial pattern is circular, with a very nearly Gaussian cross section. The separation of the half-power points is 1°·4. The first side lobes are 23 dB below the peak of the main lobe. Figure 1 shows a section of the beam, with a Gaussian curve for comparison.
- (iv) *Measurement of the aperture efficiency.*—This was accomplished by comparing the gain of the aerial with the known gain of a sectoral horn, using the Sun as a transfer source. The peak gain of the paraboloid is $41\cdot8\pm0\cdot3$ dB, corresponding to an aperture efficiency of $0\cdot56\pm0\cdot04$.

When deriving the flux density of an extended object, one must know the gain of the aerial throughout a solid angle large enough to include the entire object for every beam position at which there is a measurable aerial temperature. In effect, this means that one must know how to convert observations of aerial temperature into a (smoothed) map of brightness temperature. The desired conversion factor, which we shall call the *net efficiency*, may be defined as that fraction of the total input power which would go into the main lobe if the aerial were used to transmit instead of to receive. In the case of the Potts Hill aerial, we have a net efficiency of 0·78 at 1400 Mc/s. It should be noted that the net efficiency must be multiplied by a factor depending on the angular extent of the source, if the source covers an appreciable fraction of 4π steradians.

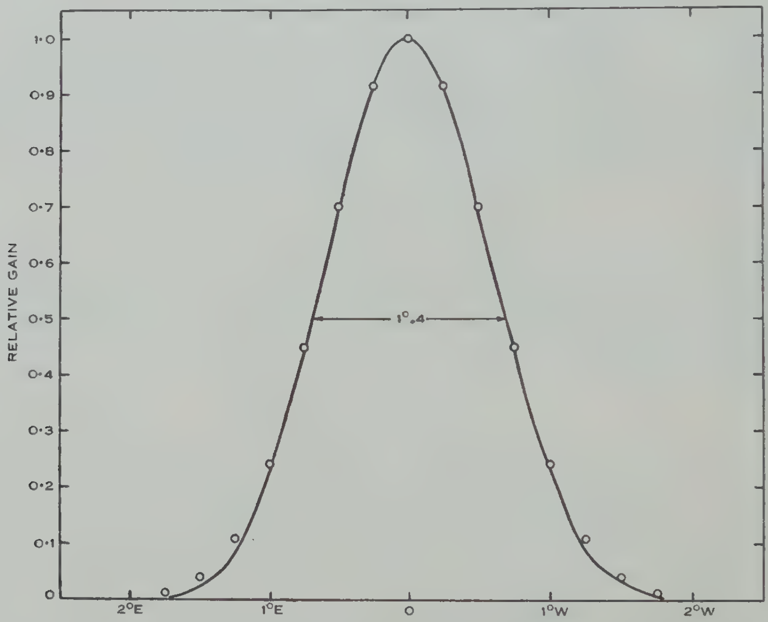

Fig. 1.—The measured shape of the main lobe of the radiation pattern of the 36 ft paraboloid at a frequency of 1400 Mc/s. The open circles indicate the form of a Gaussian curve with the same width between half-power points.

(*b*) *The Receiver*

Figure 2 is a block diagram of the receiving system. The i.f. bandwidth was approximately 2·7 Mc/s. No image rejection was used, so the system accepted noise from two bands each 30 Mc/s from the local oscillator frequency, 1393 Mc/s. Neither band included radiation from galactic neutral hydrogen. The receiver was a D.C. comparison radiometer which, in the present programme, measured the difference between the receiver output voltage and the voltage of a stable D.C. source. Long-term stability of the receiver was achieved by temperature control; the zero level remained constant to within about 2 °K for several hours at a time. No time constant other than that inherent in the pen recorder was used, because a short time constant facilitated the recognition of impulsive interference (mainly due to vehicles). The envelope of the noise fluctuations usually had a width of about 2 °K. The records could be read with an accuracy of about ±0·2 °K ; hence the short instrumental time constant had little influence on the attainable reading accuracy. The effective time constant introduced by averaging in the reduction process was about 30 sec.

The receiver calibration consisted of two steps. The first was a measurement of the receiver noise temperature with the aid of a discharge-tube noise generator. The measurement was made at the output of the second detector because of the limited range of the D.C. amplifier. The noise temperature of the receiver is given by

$$T_R=(1+\alpha)T_0\frac{T_s/T_0-P_1/P_0}{P_1/P_0-1}, \quad \ldots\ldots\ldots\ldots\ldots \quad (1)$$

where α=fraction of the image band accepted (=1 in our case),
T_0=ambient temperature,
T_s=effective temperature of the noise generator,
P_0=output power with the noise generator turned off, and
P_1=output power with the noise generator turned on.

T_0, T_s, and α are all known quantities. Hence the measurement required only a determination of P_1/P_0. During the period of observation, T_R was near 1800 °K.

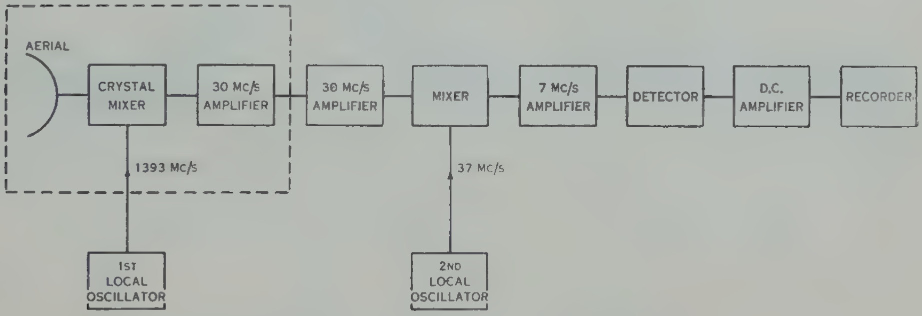

Fig. 2.—Block diagram of the receiving system.

The second step in the calibration was to relate a change in aerial temperature to the corresponding change in the deflection of the pen recorder. The fractional change in input power at the second detector corresponding to a small change ΔT_a in aerial temperature is

$$\frac{\Delta P}{P}=\frac{(1+\alpha)\Delta T_a}{T_R+(1+\alpha)T_a}. \quad \ldots\ldots\ldots\ldots\ldots\ldots \quad (2)$$

The detector of the Potts Hill radiometer is linear within the accuracy of our measurement. In the case of a linear detector, the fractional change in detector output voltage corresponding to $\Delta P/P$ is

$$\Delta V/V=\tfrac{1}{2}\Delta P/P. \quad \ldots\ldots\ldots\ldots\ldots\ldots\ldots \quad (3)$$

Combining equations (2) and (3), we get

$$\Delta T_a=\frac{2T_R}{1+\alpha}\cdot\frac{\Delta V}{V}, \quad \ldots\ldots\ldots\ldots\ldots\ldots \quad (4)$$

provided $T_R \geqslant (1+\alpha)T_a$, which was true in the present series of measurements. Calibration of the D.C. amplifier gave the relation between $\Delta V/V$ and recorder deflection, from which one immediately obtains the increment in aerial temperature required to shift the recorder pen by one chart unit. During the present programme, the sensitivity was near 0·5 °K per chart division.

III. THE OBSERVATIONS

The observations consist of drift curves made during meridian transit at intervals of $\frac{1}{2}°$ in declination. Three to five observations were made on each declination, and from these a set of mean sections was derived. During many of the observations the aerial was directed towards the South Celestial Pole for 2 min every 10 or 15 min in order to obtain a fairly continuous check on the zero-level stability of the receiver over the period of the observation. The zero level adopted for the reduction of each observation was that corresponding to the south pole. The actual zero level, however, depended on the declination setting of the aerial because the amount of radiation received from the ground through the side and back lobes of the aerial pattern varied with the altitude towards which the main lobe was directed. Therefore the variation of receiver output level as a function of declination had to be determined separately in order that all the mean sections could be referred to a common zero level. While the corrections were all small, some were large enough to be significant; the largest amounted to 2 °K. A further check on the calibration of the zero levels was obtained by scanning the regions in declination several times during transits. A selected record is shown in Figure 3.

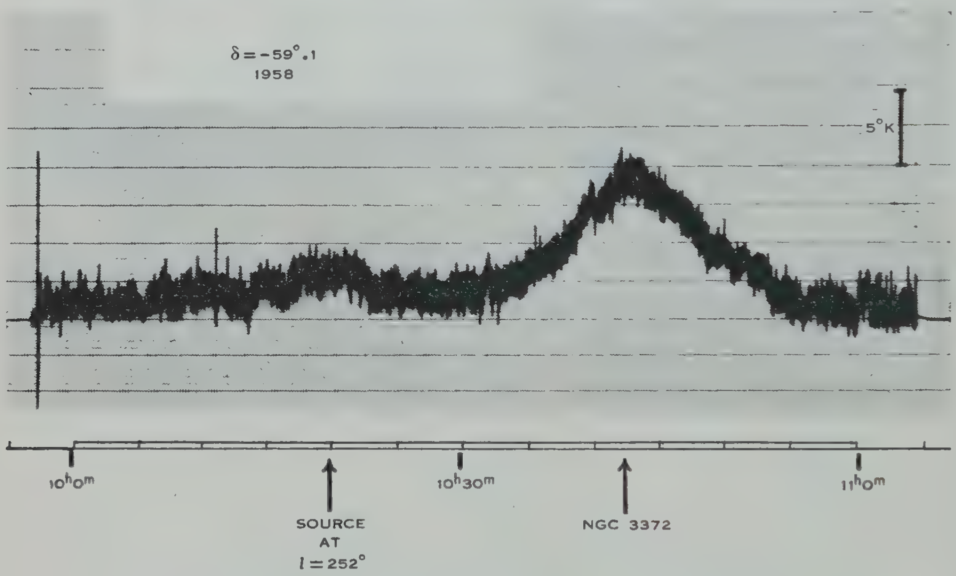

Fig. 3.—A constant-declination record taken at $\delta_{1958} = -59°\cdot1$. This strip passes 0°·5 north of NGC 3372 and 1°·5 south of the source at $l = 252°$. Right Ascensions for the epoch 1958·0 are indicated. The sensitivity is 0·55 °K per small chart division.

(*a*) *The Eta Carinae Region*

The contour diagram of the Eta Carinae region (Fig. 4) was drawn from the mean sections. The outer contour, marked 0 °K, delineates the boundary of detectable radiation. The quantity shown is aerial temperature as a function of position (in galactic coordinates, referred to Ohlsson's pole). The distribution of brightness temperature (as smoothed by the aerial beam) may be found by dividing the aerial temperatures by the net efficiency factor for the aerial. The source at $l=255°$ is NGC 3372 ; the other source, at $l=252°$, is not related to any object known optically, but it was recorded in the survey by Hill, Slee, and Mills (1958) at $3 \cdot 5$ m wavelength. It is evident that an appreciable amount of radiation from the galactic disk is present on the high longitude side of NGC 3372, with the maximum intensity of the ridge occurring at $b \approx -0° \cdot 8$.

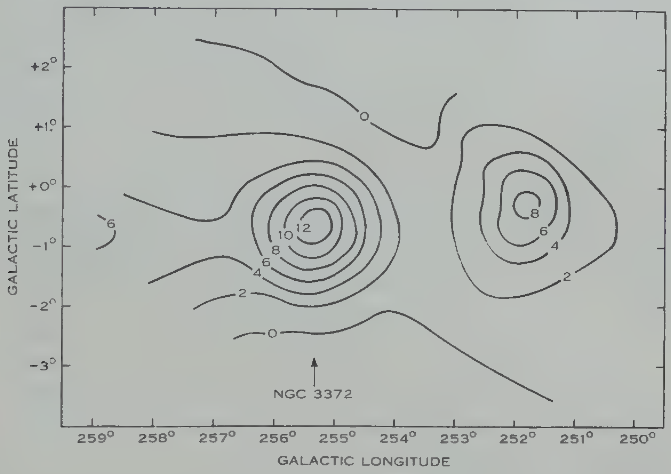

Fig. 4.—Map of aerial temperature as a function of position in the vicinity of NGC 3372. The contour interval is 2 °K. The contours marked 0 °K show the limits of detectable radiation. The coordinates are based on Ohlsson's galactic pole, $\alpha_{1900}=12^h\ 40^m$, $\delta_{1900}=+28°$.

Before deriving the flux density of NGC 3372, it was necessary to subtract the radiation due to the galactic disk. This was accomplished by a linear interpolation between constant longitude sections outside the nebula on either side, at $l=253° \cdot 5$ and at $l=257° \cdot 5$. The resulting form for the estimated distribution of the disk radiation is shown in Figure 5. Subtraction of this from the observed distribution yields the source brightness distribution shown in Figure 6. The maximum net aerial temperature, 10 °K, occurs at $l=255° \cdot 3$, $b=-0° \cdot 6$. Table 1 shows the agreement between this position and previous radio and optical determinations. The small discrepancy between the two optically determined positions is due to the difficulty in defining accurately the centre of an extended and somewhat irregular object.

Integration of the contours shown in Figure 6 leads to a value of $5 \cdot 82 \times 10^{-24}$ W m^{-2} (c/s)$^{-1}$ for the flux density of NGC 3372 near 1400 Mc/s.

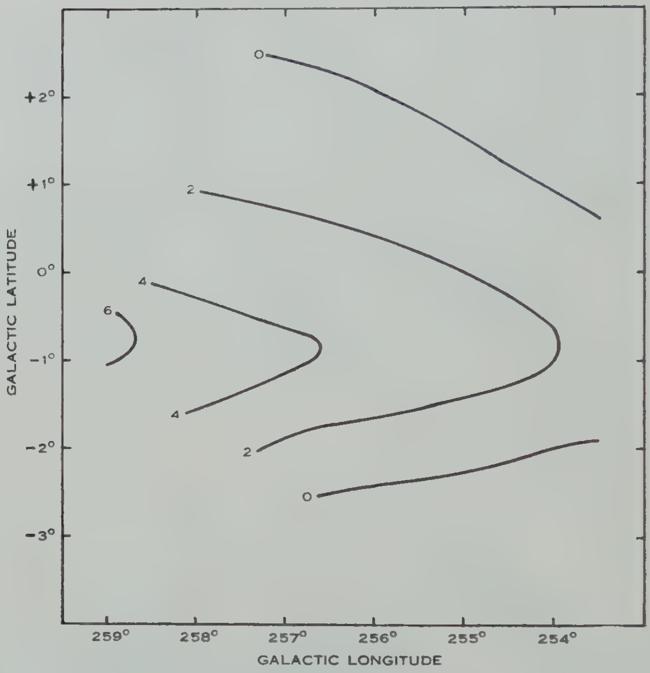

Fig. 5.—Estimated distribution of the galactic disk radiation in the vicinity of NGC 3372.

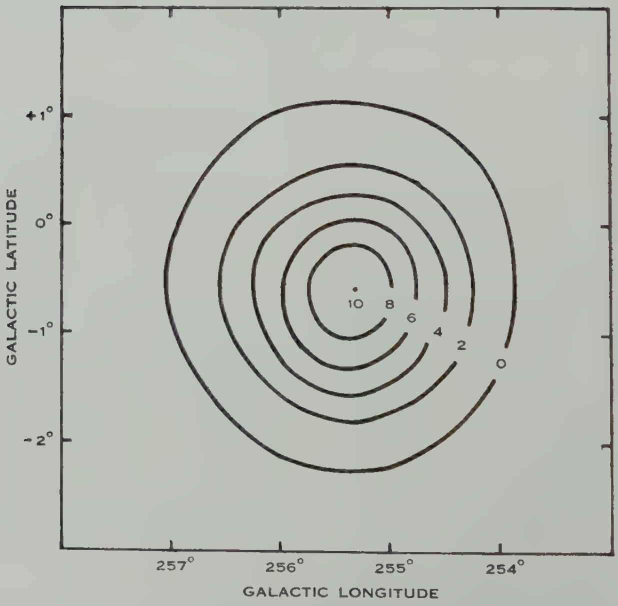

Fig. 6.—Contours of NGC 3372 after subtraction of the galactic disk radiation.

The accuracy of this figure is not easy to estimate, since several sources of uncertainty must be considered. These are :

(i) *Aerial calibration.*—The relevant quantity is the net efficiency, which depends on the aerial gain and the form of the radiation pattern. The latter is known quite accurately, but the gain is less well determined. We estimate that the maximum error in the net efficiency is about ±10 per cent.

(ii) *Receiver calibration.*—This measurement is straightforward and should be accurate to within ±10 per cent.

(iii) *Errors in the mean sections and in the subtraction of the galactic disk radiation.*—The mean sections are subject to some uncertainty because of the thermal noise fluctuations in the receiver output and residual errors in the adopted zero levels. While the procedure used to subtract the galactic disk radiation was impersonal, it certainly was not perfectly accurate. The estimated maximum error from these causes is ±10 per cent.

The uncertainty due to the above causes probably is under ±20 per cent. The greatest error, which would apply if all of the above uncertainties were additive, does not exceed ±30 per cent.

The flux density of the source at $l=252°$ is 5×10^{-24} W m^{-2} (c/s)$^{-1}$. This result is only approximate, since our observations do not cover an area large enough to permit a good estimate of the galactic background level under the source.

TABLE 1

COMPARISON OF RADIO AND OPTICAL POSITIONS FOR NGC 3372

Frequency	l	b	Estimated Maximum Error	Reference
1400 Mc/s	255°·3	—0°·6	±0°·1	Present paper
85·5 Mc/s	255°·4	—0°·7	±0°·1	Hill, Slee, and Mills (1958)
Optical	255°·3	—0°·5	—	Cederblad (1946)
Optical	255°·2	—0°·8	—	Gum (1955)

(*b*) *Centaurus A*

The observed distribution of 1400 Mc/s radiation from Centaurus A is shown in Figure 7. The limit of detectable radiation is indicated by the contour marked " 0 ". The object lies nearly 20° from the galactic plane, and there is no detectable galactic continuum emission in its vicinity. The region north of $\delta=-41°$ is too faint to be well observed with our equipment, so the contours in that region are shown as dashed lines. The source evidently comprises two distinct components :

(i) A primary maximum at $\alpha_{1950}=13^{\mathrm{h}}\,22^{\mathrm{m}}\cdot9$, $\delta_{1950}=-42°\,45'$, which seems almost certainly to be associated with the peculiar galaxy NGC 5128.

(ii) A very extensive source covering some 20 square degrees, which probably is associated physically with the primary source. There is a strong, broad maximum in the intensity of this component at $\alpha_{1950} \approx 13^{\mathrm{h}}\ 20^{\mathrm{m}}\cdot 5$, $\delta_{1950} \approx -44^{\circ}\cdot 7$. Two weak secondary maxima are suspected in the northern part of the object, at $\alpha_{1950} \approx 13^{\mathrm{h}}\ 20^{\mathrm{m}}$, $\delta_{1950} \approx -40^{\circ}\cdot 3$ and at $\alpha_{1950} \approx 13^{\mathrm{h}}\ 24^{\mathrm{m}}$, $\delta_{1950} \approx -39^{\circ}\cdot 1$.

On the whole, Figure 7 bears a remarkably close resemblance to the 85·5 Mc/s chart published by Sheridan (1958).

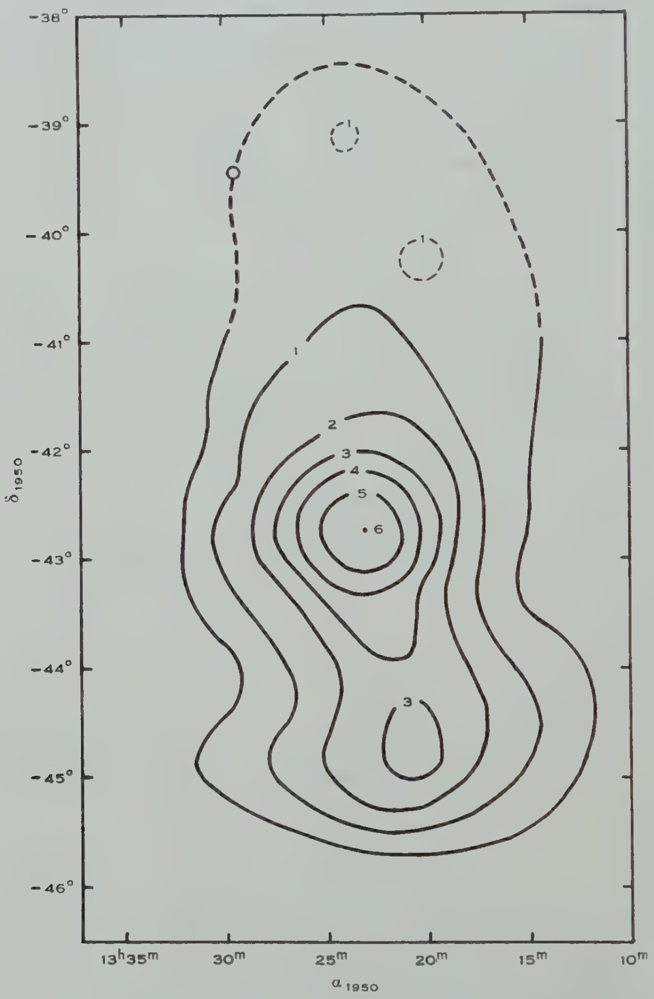

Fig. 7.—Map of aerial temperature for Centaurus A as a function of position in equatorial coordinates (epoch 1950).

The position found for the primary maximum is in satisfactory agreement with the results obtained previously at metre wavelengths, as shown in Table 2. The slightly higher value for the Right Ascension determined at 1400 Mc/s may be due partly to the skewness of the primary source, observed by Sheridan

TABLE 2

POSITION MEASUREMENTS FOR CENTAURUS A

Frequency	α_{1950}	δ_{1950}	Reference
1400 Mc/s	$13^h\ 22^m{\cdot}9\pm0^m{\cdot}5$	$-42°\ 45'\pm6'$	Present paper
100 Mc/s	$13^h\ 22^m{\cdot}5\pm0^m{\cdot}07$	$-42°\ 46'\pm2'$	Mills (1952)
85·5 Mc/s	$13^h\ 22^m{\cdot}4\pm0^m{\cdot}2$	$-42°\ 41'\pm4'$	Sheridan (1958)
Optical (NGC 5128)	$13^h\ 22^m{\cdot}4$	$-42°\ 45'$	de Vaucouleurs (1956)

with a beamwidth of 50′. The skewness is such that the primary source profile is less steep on the eastern side, hence the greater beamwidth of our aerial (nearly twice that used by Sheridan) probably results in a slight shift of the observed maximum intensity towards a higher Right Ascension at 1400 Mc/s.

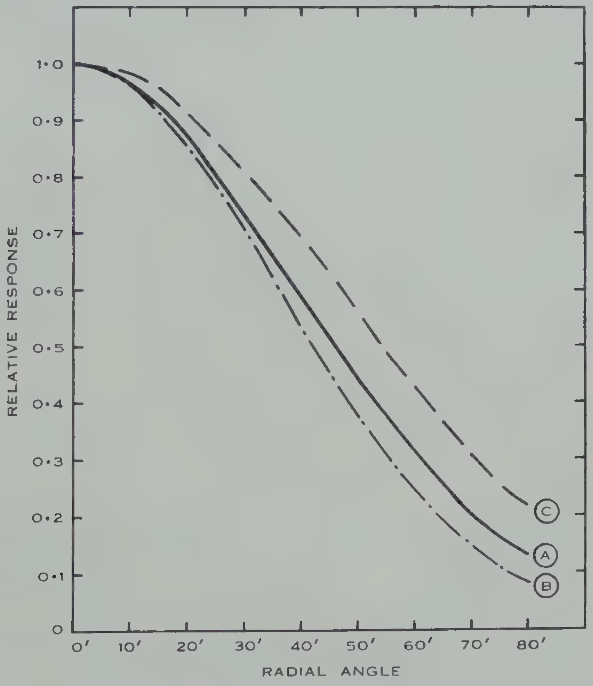

Fig. 8.—Apparent radial brightness distributions: *A*, observed mean for NGC 3372; *B*, point source smoothed by the aerial beam; *C*, uniform optically thin sphere 2°·0 in diameter smoothed by the aerial beam.

The integrated flux density of the entire object is $1{\cdot}3\times10^{-23}$ W m^{-2} (c/s)$^{-1}$ at 1400 Mc/s, with an estimated probable error of ±20 per cent. Of this about 3×10^{-24} W m^{-2} (c/s)$^{-1}$, or 23 per cent., arises in the primary source; the remainder is due to the extended component.

IV. Conclusions

(a) *The Eta Carinae Nebula*

Figure 6 suggests that NGC 3372 possesses a high degree of radial symmetry in its overall surface brightness distribution. This is implied by the circularity of the contours and by the central location of the maximum observed brightness. Small-scale irregularities, if present, cannot be seen because the aerial beam has a size of the same order as that of the object. Nevertheless, any strong large-scale asymmetry would result in a noticeable distortion of the contours.

The true surface brightness distribution across NGC 3372 cannot be derived from the observed distribution (Bracewell and Roberts 1954). It is possible, however, to judge whether the source shows an appreciable central condensation. Curve *A* in Figure 8 is the observed mean radial brightness distribution. Curve *B* is the expected response to a point source (see Fig. 1). Curve *C* is the computed response to a uniform optically thin sphere (semi-elliptical true radial surface brightness distribution) with the same angular diameter as NGC 3372 ($2^\circ\cdot 0$). Comparison of curves *A* and *B* indicates that the source must have an appreciable angular width, while comparison of curves *A* and *C* implies that it must be strongly concentrated towards its centre. This conclusion is in agreement with unpublished measurements in Hα light made by C. S. Gum, which show that the object has an intense central core about 24′ in diameter, and that the surface brightness in the outer regions is much lower.

The observational results may be summarized as follows:

(i) The flux density of NGC 3372 near 1400 Mc/s is $5\cdot 82\times 10^{-24}$ W m^{-2} (c/s)$^{-1}$, with an estimated probable error less than ± 20 per cent.

(ii) There is no marked large-scale asymmetry in its surface brightness distribution.

(iii) The source is strongly concentrated towards its centre.

The results will be discussed in a second paper (Wade 1959).

(b) *Centaurus A*

We have found that the appearance of Centaurus A (13S4A) at 1400 Mc/s is similar to that previously observed at $85\cdot 5$ Mc/s by Sheridan (1958). The source consists of two components: one is a point source evidently associated with the peculiar galaxy NGC 5128; the other is a very large extended source with no known optical counterpart. A striking feature is the strong maximum in the intensity of the extended source, about 2° south of the point source. The total flux density at 1400 Mc/s is $1\cdot 3\times 10^{-23}$ W m^{-2} (c/s)$^{-1}$, with an estimated probable error of ± 20 per cent. Of this, about 23 per cent. arises in the point source, and 77 per cent. comes from the extended source.

The results will be discussed in a subsequent paper.

V. Acknowledgment

One of us (C.M.W.) is indebted to the Commonwealth Scientific and Industrial Research Organization for a Junior Research Fellowship.

VI. References

Bailey, S. I. (1908).—*Ann. Harv. Coll. Obs.* **60** : 199.
Bok, B. J. (1932).—Harv. Repr. No. 77.
Bok, B. J., Bester, M. J., and Wade, C. M. (1955).—*Proc. Amer. Acad. Arts Sci.* **86** : 9.
Bolton, J. G., Stanley, G. J., and Slee, O. B. (1949).—*Nature* **164** : 101.
Bracewell, R. N., and Roberts, J. A. (1954).—*Aust. J. Phys.* **7** : 615.
Cederblad, S. (1946).—Medd. Lunds Astr. Obs. (II) No. 119.
Gum, C. S. (1955).—*Mem. R. Astr. Soc.* **67** : 155.
Hill, E. R., Slee, O. B., and Mills, B. Y. (1958).—*Aust. J. Phys.* **11** : 530.
Kerr, F. J., Hindman, J. V., and Gum, C. S. (1959).—*Aust. J. Phys.* **12** : 270.
Mills, B. Y. (1952).—*Aust. J. Sci. Res.* A **5** : 456.
Mills, B. Y., Little, A. G., and Sheridan, K. V. (1956).—*Aust. J. Phys.* **9** : 218.
Shain, C. A. (1958).—*Aust. J. Phys.* **11** : 517.
Sheridan, K. V. (1958).—*Aust. J. Phys.* **11** : 400.
Stanley, G. J., and Slee, O. B. (1950).—*Aust. J. Sci. Res.* A **3** : 234.
de Vaucouleurs, G. (1956).—Mem. Commonw. Obs. Aust. No. 13.
Wade, C. M. (1959).—*Aust. J. Phys.* **12** (4). (In press.)
Westerhout, G. (1958).—*Bull. Astr. Insts. Netherlds.* **14** : 215.

A 21 CM SURVEY OF THE SOUTHERN MILKY WAY

By F. J. Kerr,* J. V. Hindman,* and C. S. Gum*

[*Manuscript received May* 25, 1959]

Summary

A study has been made of 21 cm hydrogen-line radiation around the Southern Milky Way, using a beamwidth of 1°·4 and a bandwidth of 40 kc/s (8·5 km/sec).

The surveyed strip of sky was sampled by recording the intensity of the radiation along 41 discrete tracks across the galactic equator, in the longitude range 175°–5° (" old " system of coordinates). The tracks were generally spaced 5° apart in longitude, and were in most cases along lines of constant declination. The range of galactic latitude of the tracks varied from 9° to 1°·5, for reasons connected with the programming of the survey.

The observations were taken on a four-channel statically balanced receiver; one run along a track yielded the variation of intensity as a continuous function of sky position at four fixed frequencies. Records were taken at a sufficient number of discrete frequencies to cover the full frequency range of the line.

The results are presented in the form of contour diagrams showing the 21 cm intensity along each track as a function of latitude and radial velocity. In addition, line profiles are given for a series of points around the " new " galactic equator.

A combination of this survey and that carried out for the northern sky by the Leiden group gives a coverage of the whole galactic circle at approximately the same resolution. There is good agreement between the two sets of results in the common range of longitude.

I. INTRODUCTION

Observations of the 21 cm line from interstellar atomic hydrogen provide the best of the known methods for investigating the large-scale structure of the Galaxy. Not only is radiation detectable from substantially the whole Galaxy but contributions from different distances can generally be distinguished, through the Doppler dispersion produced by galactic rotation effects. By contrast, optical studies are restricted to the solar neighbourhood, while radio continuum observations can only provide an integrated intensity along each line of sight.

The first survey of 21 cm radiation over a substantial part of the sky was carried out in Sydney by Christiansen and Hindman (1952), soon after the initial detection of the line by Ewen and Purcell (1951). This early survey showed the high degree of concentration towards the galactic plane, and gave the first 21 cm indication of spiral arms. The strip of sky in the vicinity of the galactic equator has special interest for studies of large-scale galactic structure. An extensive investigation of the northern part of this strip has been carried out by the Leiden group (van de Hulst, Muller, and Oort 1954; Muller and Westerhout 1957) and this has led to a picture of the spiral structure of the Galaxy over the range of longitude accessible from Holland (Schmidt 1957; Westerhout 1957).

---

* Division of Radiophysics, C.S.I.R.O., University Grounds, Chippendale, N.S.W.

The outstanding uncertainty in deriving the three-dimensional distribution of galactic hydrogen from 21 cm observations is the choice of a rotational velocity model for relating Doppler shifts and distance. Observations from a southern hemisphere observatory, besides being important in themselves for completing a galactic survey, are essential for a test of the assumptions made in interpreting the observations, and particularly of the rotation model adopted.

The present paper gives the results of a survey covering the southern part of the Milky Way strip, using a beamwidth of 1°·4 and a bandwidth equivalent to 8·5 km/sec. In order to study the thin layer of hydrogen, observations were taken along 41 " tracks " crossing the galactic equator in the longitude range 175°–5° (" old " system of coordinates). In most cases these tracks were lines of constant declination, the observations being made with a stationary aerial; the frequency of the receiver always remained constant during an observation. Four separate channels were used, providing simultaneous records in four adjacent 40 kc/s bands, which could be set to any desired position in the frequency range of the line.

This method of observation was chosen because the aerial was limited to meridian operation. The combination of transit aerial and fixed-frequency receiver was very suitable for obtaining the variation of intensity across the sky, for example, in locating the galactic plane. On the other hand, line profiles had to be derived from a series of observations along each track at a number of discrete frequencies.

The results of the survey are presented in the form of contour diagrams, each showing the variation of brightness temperature as a function of galactic latitude and radial velocity for a particular track. Line profiles may be derived from diagrams of this type by taking horizontal sections. A set of profiles for points on the new galactic equator has also been included in the paper; such profiles are the most significant for galactic structure studies and they also provide a quick assessment of the variation with longitude.

This paper is appearing during the transition period when the " old " system of galactic coordinates (Ohlsson 1932) is being superseded by a " new " system (Blaauw *et al.* 1959). The results are presented primarily in terms of the old coordinates, as the survey was carried out in terms of that system, but the new coordinates are also given in the diagrams as far as possible. The symbols l^{I}, b^{I} are used throughout for the old coordinates and l^{II}, b^{II} for the new.

Taken together, the Leiden and Sydney surveys cover the full 360° range of galactic longitude, at approximately the same resolution in angle and velocity. There is sufficient overlap in longitude to permit a good check of the homogeneity of the combined data.

A progress report on the analysis of the southern survey has been given by Kerr, Hindman, and Carpenter (1957), and the results have also been used by Oort, Kerr, and Westerhout (1958) in a first discussion of the combined Leiden and Sydney data. In addition, IAU Subcommission 33b has taken into account the new information on the shape of the hydrogen layer in its revision of the system of galactic coordinates (Gum and Kerr 1958; Gum and Pawsey 1958; Blaauw *et al.* 1959). The present paper gives the observational results only; these results will be discussed in later papers.

II. AERIAL

The observations were taken with the Radiophysics Laboratory's 36 ft. paraboloid, which is mounted on an east-west axis as a transit instrument.* The aerial is located at Potts Hill, near Sydney, at latitude 33°·9 S. and longitude 151°·0 E.

The aerial is fed by a flanged horn, carried on a four-legged support attached to the rim of the dish, and both the waveguide crystal mixer and the intermediate-frequency pre-amplifier are located near the feed point. The polarization of the electric vector is horizontal, i.e. parallel to the east-west axis.

(*a*) *Beam Characteristics*

The directional diagram was derived with the Sun as a source by sweeping in declination during the period of a solar transit; allowance was made for the finite diameter of the solar disk. Check measurements were made on several discrete sources of cosmic noise, but these were less accurate owing to the lower intensity.

The main beam was found to be nearly Gaussian, with a half-power width of 1°·4 and an approximately circular cross section. The near side lobes were 23 dB below the peak intensity.

To derive the brightness temperature in the sky from measured values of aerial temperature, we must determine the *net efficiency*† of the aerial. This may be defined as that fraction of the total input power which would go into the main lobe if the aerial were used to transmit instead of receive. It takes account of losses in the system, and also discriminates between the radiation in the main beam and its adjoining side lobes and that in the " stray " field, the remainder of the sphere.

The gain of the aerial was measured by a comparison with a known horn, using the Sun as a reference source. The gain was found to be 41·8±0·3 dB, leading to a value for the *aperture efficiency* of the paraboloid (the ratio of the effective area to the geometrical area) of 0·56±0·05. The *net efficiency* was then derived by integrating over the full beam, with the absolute level fixed by the gain measurement. The value obtained was 0·78.

(*b*) *Position Measurement*

The primary position calibration was carried out on the strong radiation from the Sun over the range of declination covered by the ecliptic. By moving the aerial in small steps during a solar transit, calibration points in declination were obtained with an accuracy of ±0°·03. The calibration was extended over the rest of the declination range by visual sights across the face of the dish during the transit of stars. These visual checks depended on the assumption that the dish and feed structures moved as a single unit when the declination was changed. This assumption is known to be valid over the Sun's range of declination, but cannot be tested so precisely outside this range. An additional check was provided by a position measurement on the source Centaurus A (Hindman and Wade 1959).

---

* A photograph of the aerial has been published by Kerr, Hindman, and Robinson (1954).

† This quantity is related to, but differs from, the " diffractive efficiency " defined by Seeger, Westerhout, and van de Hulst (1956) (Wade, in preparation). It must be multiplied by a factor which depends on the angular extent of the source, if the source covers an appreciable fraction of the whole sky.

Scale errors of a few tenths of a degree were found to occur in some parts of the declination range, arising from distortion of the structure which supports the dish. These errors were closely reproducible and were satisfactorily allowed for through a calibration table. Periodical checks were made on the Sun to ensure that the scale zeros had not moved significantly, and the whole process of Sun and star checks was carried out on three separate occasions.

TABLE 1

COMPARISON BETWEEN SYDNEY AND LEIDEN AERIAL SCALES THROUGH MEASUREMENTS ON THE SOURCE SGR A

Aerial	Beamwidth	Right Ascension (1950)	Declination (1950)	Reference
Sydney, Potts Hill	1°·4	$17^{\mathrm{h}}\ 42^{\mathrm{m}}\cdot 7 \pm 0^{\mathrm{m}}\cdot 2$	$-29^\circ\ 01' \pm 5'$	
Leiden, Kootwijk	1°·8 by 2°·8			
1954 . .		$17^{\mathrm{h}}\ 42^{\mathrm{m}}\cdot 0 \pm 0^{\mathrm{m}}\cdot 8$	$-28^\circ\ 58' \pm 15'$	Westerhout (personal communication)
1955 . .		$17^{\mathrm{h}}\ 42^{\mathrm{m}}\cdot 1 \pm 0^{\mathrm{m}}\cdot 8$	$-29^\circ\ 02' \pm 15'$	
IAU Comm. 33b mean	—	$17^{\mathrm{h}}\ 42^{\mathrm{m}}\cdot 6 \pm 0^{\mathrm{m}}\cdot 06$	$-28^\circ\ 57' \pm 1'$	Gum and Pawsey (personal communication)

The Right Ascension calibration was based on the same radio and visual observations. The alignment of the radio axis with the meridian was checked in this way to an accuracy of ±0°·02. In addition, allowance had to be made for the time delay in the receiver, which produced an apparent shift of Right Ascension on a constant declination track. Other factors which affect the accuracy of the position measurements are: rounding-off errors in setting the scale (in the case of declination), errors in reading time from the records (in the case of Right Ascension), and, finally, the slight errors introduced in the conversion from equatorial to galactic coordinates. The overall uncertainty of the position measurements in the survey is estimated to be ±0°·07 in each galactic coordinate.

A combination of the Sydney and Leiden surveys is necessary to give an overall picture of the whole Galaxy; consequently, some direct comparisons have been made to guard against the possibility of systematic position errors in either set of data. The most precise of these comparisons was made through the discrete source Sagittarius A (IAU 17S2A), with the results shown in Table 1. The Leiden survey was carried out with the Kootwijk aerial. For comparison, the table includes a recent mean position derived by IAU Subcommission 33b from measurements made with the larger reflectors at Dwingeloo, Stockert, and Washington (Blaauw *et al.* 1959). The Sydney and Kootwijk values agree with one another and with the more accurate position to well within their probable errors.

III. Receiver

(*a*) *Description of Receiver*

The receiver used in the survey departed from the usual practice of switching between two frequencies, one of which is on the line and the other away from it. Instead, the difference in the receiver output at the two frequencies was measured continuously by connecting the two channels to opposite sides of a differential D.C. amplifier. The front portion of the receiver followed conventional practice, with intermediate frequencies at 30 and 7 Mc/s. A block diagram of the later sections is shown in Figure 1.

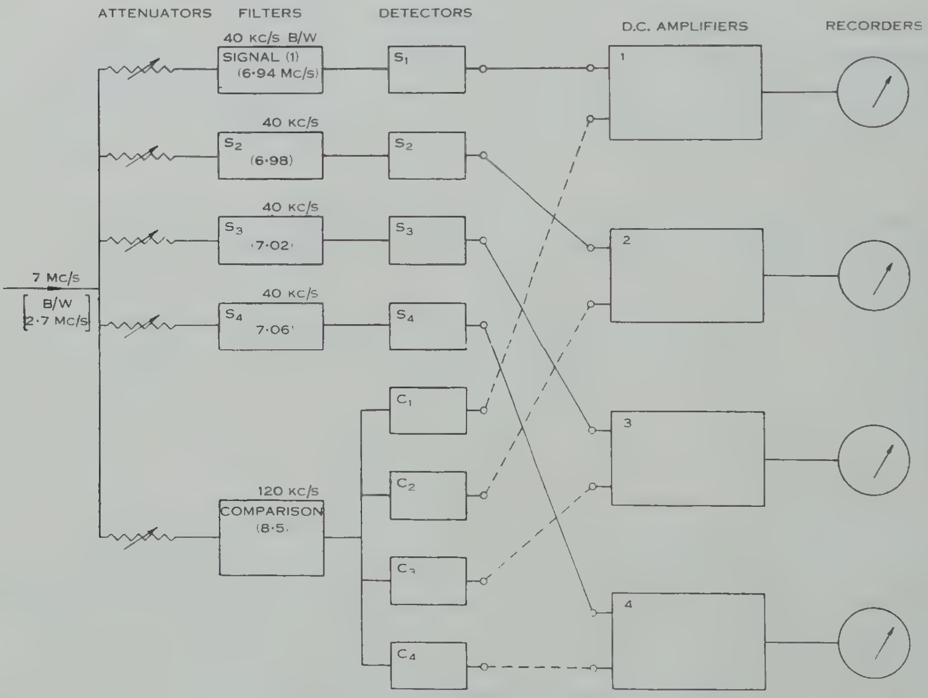

Fig. 1.—Block diagram of later sections of receiver.

The receiver noise factor, measured with a continuous-spectrum source, varied between 6 and 8 dB during the period of the survey. The effective noise factor for the detection of line radiation was about 3 dB higher, since the contributions of receiver noise at the signal and image frequencies were approximately equal.

The first local oscillator, at 1390 Mc/s, was variable in frequency, so that the block of signal channels could be moved across a line profile; a temperature-controlled oscillator, operating at about 5·7 Mc/s, was followed by five tripling stages. The second local oscillator was a self-excited oscillator at 37 Mc/s.

The main i.f. amplifiers, whose overall bandwidth was 2·7 Mc/s, were followed by a system of passive filters which selected specific portions of this pass band. Four of these filters were used as signal channels to receive the line; their half-power bandwidth was 40 kc/s and they were spaced about 40 kc/s apart. Single-tuned circuits were used in the filters; 90 per cent. of the noise response was within a band of 70 kc/s. A fifth filter, placed 1·6 Mc/s away from the signal filters, was used as the comparison channel. Its bandwidth was made somewhat larger (120 kc/s) to reduce the noise fluctuations in the receiver output. The levels in the various channels were controlled by attenuators at the output of the 7 Mc/s amplifier.

The outputs of the filters were fed to diode detectors which were linear to within 1 per cent. over the observed range of brightness temperatures. Four separate detectors were attached to the comparison filter to minimize interaction between the four channels.

Following the detectors, the difference voltage between each pair of signal and comparison channels was fed to an integrating circuit and a D.C. amplifier. The overall time delay of the whole receiver was measured on simulated galactic crossings which were produced by varying the output of an artificial signal source; a value of 25 sec was obtained.

The receiver was balanced with the aerial pointed towards a " cold " part of the sky. In any other direction, the output of the D.C. amplifier was then proportional to the amount of line radiation in the " signal " channel.

Most 21 cm line work to date has been done with receivers which are swept over the frequency range containing the line, and the levels on and off the line are compared by switching rapidly between the signal and comparison channels.

The statically balanced receiver avoids two of the major problems which must be overcome in stabilizing the switched and swept type of receiver. These are the maintenance of a flat base line while tuning over a wide frequency band and the precise equalizing of local oscillator output and front-end performance in the two switched positions. Instead of these, a new difficulty arises, owing to the fact that the signal and comparison channels use different parts of the i.f. pass band: the gain of the two channels can change differentially for quite small changes in the shape of the pass band.

In practice, the receiver proved difficult to stabilize, but close temperature control of the whole i.f. amplifier and the filter units and careful work on all critical parts of the system have brought the performance to a state where the base line follows a straight line to within ±1 °K over a period of half an hour or so. During the period occupied by this survey, the receiver performance gradually improved but the observational data were all satisfactorily tied together.

The normal method used to establish the zero level was to make a measurement at the South Celestial Pole before and after each galactic crossing. This type of check is difficult if motion of the aerial itself produces a significant change in the receiver output level as the orientation of the pre-amplifier and other units varies. Such an effect was present during part of the survey, but it was monitored throughout the whole programme by checking the output level over a wide range of declination in the cold parts of the sky.

(b) *Temperature Calibration*

The absolute temperature scale of the receiver was calibrated by a two-step process: the noise factor of the receiver was first obtained and then a calibration of the D.C. amplifier was used to relate a change in aerial temperature to the corresponding change in the receiver output voltage. The noise factor was measured with the aid of a gas-discharge noise generator of waveguide type, connected to a horn which was placed immediately in front of the feed horn.

The overall result of these measurements showed that one recorder scale unit corresponded to 3·2 °K of aerial temperature when the receiver was operating in the condition which was adopted as the standard. The probable error of this absolute calibration is estimated to be about ±15 per cent.; relative checks of the day-to-day variations in sensitivity could, however, be made with an accuracy of ±7 per cent., using the methods to be described in the next section.

The corresponding values of brightness temperature T_b are less certain: the conversion from aerial temperature to brightness temperature is complex because the amount of galactic radiation picked up by the stray field varies as the aerial points to different directions in the sky. The net efficiency of the aerial, as described in Section II (*a*) above, was found to be $0\cdot78\pm0\cdot06$. Therefore, on the average,

$$T_b \approx 1\cdot28 T_a,$$

with the proportionality factor varying by a few per cent. from point to point in the sky.

(c) *Frequency Calibration*

The receiver was tuned by varying the first local oscillator. Measuring the operating frequency for each signal channel involved a measurement of its three components, the frequencies of the two local oscillators (1390 and 37 Mc/s) and the associated narrow-band filter (about 7 Mc/s). With an overall pass band of 40 kc/s, an accuracy of several kilocycles per second was required in each case; thus only the first of the three measurements offered any difficulty.

The method adopted made use of a crystal-controlled oscillator (occasionally checked against WWVH) as a local reference standard for measuring the frequency of the 5·7 Mc/s oscillator. The beat note between the two oscillators, which was in the range from zero to 5000 c/s, was continuously monitored on a cathode-ray tube against a calibrated audio oscillator. The sign of the frequency difference was checked by producing a known frequency shift in the tunable oscillator. For convenience, the second local oscillator was adjusted so that zero beat was obtained when the receiver frequency corresponded to zero radial velocity (1420·405 Mc/s). Then, for other settings of the receiver, the beat note was a direct measure of the radial velocity at which observations were being made. By this procedure, the receiver frequency could be measured to an accuracy of about 0·5 kc/s (0·1 km/sec in velocity). In the later stages of the survey, the frequency was always stable to about one part in 10^6, i.e. 1·5 kc/s, over the period of a galactic crossing.

IV. Observing Programme

In this section we discuss the layout of the "tracks" which were used to sample the Southern Milky Way strip and the manner in which the observations were arranged in order to cover the full frequency range for each track.

(*a*) *Area Covered*

Observations have been taken over the whole stretch of the Milky Way which is accessible from Sydney, but the main attention has been concentrated on the southern part. The results presented in this paper cover the range of longitude from 175° to 5° (old system): this range provides a good overlap with the Leiden observations in the regions $l^{\mathrm{I}}=175°$–$220°$ and $320°$–$5°$. A number of records have also been obtained in the rest of the accessible range ($l^{\mathrm{I}}=115°$–$175°$ and $5°$–$65°$); these have been used in a study of the flatness of the hydrogen layer but have not otherwise been reduced.

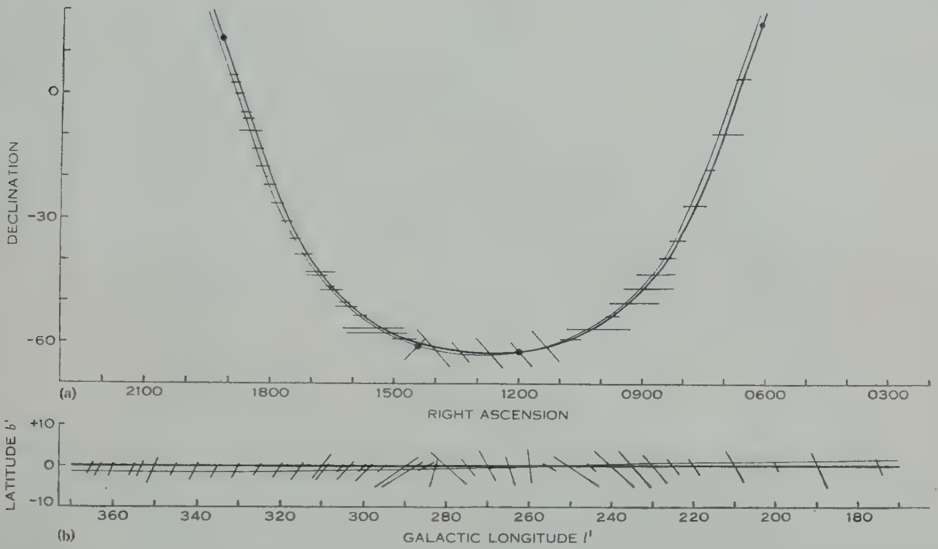

Fig. 2.—Layout of the 41 tracks along which observations were taken, showing also the old (——) and new (——) galactic equators. (*a*) Celestial coordinates (epoch 1955). The dots represent check points. (*b*) Old galactic coordinates.

(*b*) *Track System*

The surveyed area was sampled by taking observations along 41 tracks crossing the galactic equator. On each day of the programme, observations were made along a series of these tracks, with a check to the South Celestial Pole for a zero reference between successive tracks.

The layout of the track system on the sky is shown in Figure 2, in both celestial and (old) galactic coordinates. Most of the tracks were at constant declination, except in the southernmost region, where the latitude changes very slowly along a constant-declination line. In this section several special tracks were used, in which the declination was varied by the operator at a rate of 0°·2 per minute during the period of the observation. The declination values for the constant-declination tracks are given in the titles of the contour diagrams (Plates 1–41); the special tracks are defined in Table 2.

The galactic coordinates, in the old system, of any point on the tracks can be obtained from Figure 3. For many purposes, however, the tracks can be regarded as effectively normal to the galactic equator, because the intensity varies much more slowly with longitude than with latitude. For the remainder of the paper, the tracks are identified by the (old) longitude at which they cross the old galactic equator.

TABLE 2

SPECIFICATION OF THE VARIABLE-DECLINATION TRACKS IN THE SOUTHERNMOST REGION

$l^{\rm I}$ at Old Equator	Declination (1955)	$l^{\rm II}$ at New Equator
260°·0	$-64^\circ\cdot 8+0^\circ\cdot 2\,(\alpha-11^{\rm h}\,00^{\rm m})_{\rm min.}$	292°·3
264°·8	$-64^\circ\cdot 2+0^\circ\cdot 2\,(\alpha-11^{\rm h}\,48^{\rm m})$	297°·1
269°·9	$-66^\circ\cdot 4+0^\circ\cdot 2\,(\alpha-12^{\rm h}\,22^{\rm m})$	302°·0
274°·8	$-64^\circ\cdot 8+0^\circ\cdot 2\,(\alpha-13^{\rm h}\,10^{\rm m})$	306°·8
279°·8	$-66^\circ\cdot 2+0^\circ\cdot 2\,(\alpha-13^{\rm h}\,38^{\rm m})$	311°·5
282°·7	$-58^\circ\cdot 2-0^\circ\cdot 2\,(\alpha-14^{\rm h}\,17^{\rm m})$	315°·1

In the longitude range 220°–5°, there is a track crossing the galactic equator at least every 5°,* with some additional tracks in the range corresponding to the inner region of the Galaxy. These extra tracks were chosen to pass through points which were exactly symmetrical about the galactic centre with points on the main programme, in order to study the symmetry of the velocity pattern.

The latitude ranges of the individual tracks varied from 9° to 1°·5. The track lengths were chosen in such a way that a number of tracks could always be followed in each observing session. A few of the tracks were uncomfortably short, but most of the gas in the thin hydrogen layer is contained in the surveyed strip. In southern longitudes, the bulk of the gas that we are studying is at large distances and is therefore confined to a small latitude range. In general, the tracks were centred approximately on our first rough determination of a *new* galactic plane, but the shorter tracks were displaced, to meet the additional requirement that each track should include a point on the *old* galactic equator.

A sample record on the four-channel system is given in Figure 4. This contains a group of three tracks, at the longitudes marked in the figure, separated by short periods at the South Celestial Pole. (Other tracks in the same longitude range were covered in different series of observations.)

---

* Observations are now available at integral 5° intervals, right around the old galactic equator, from either the Leiden or Sydney survey.

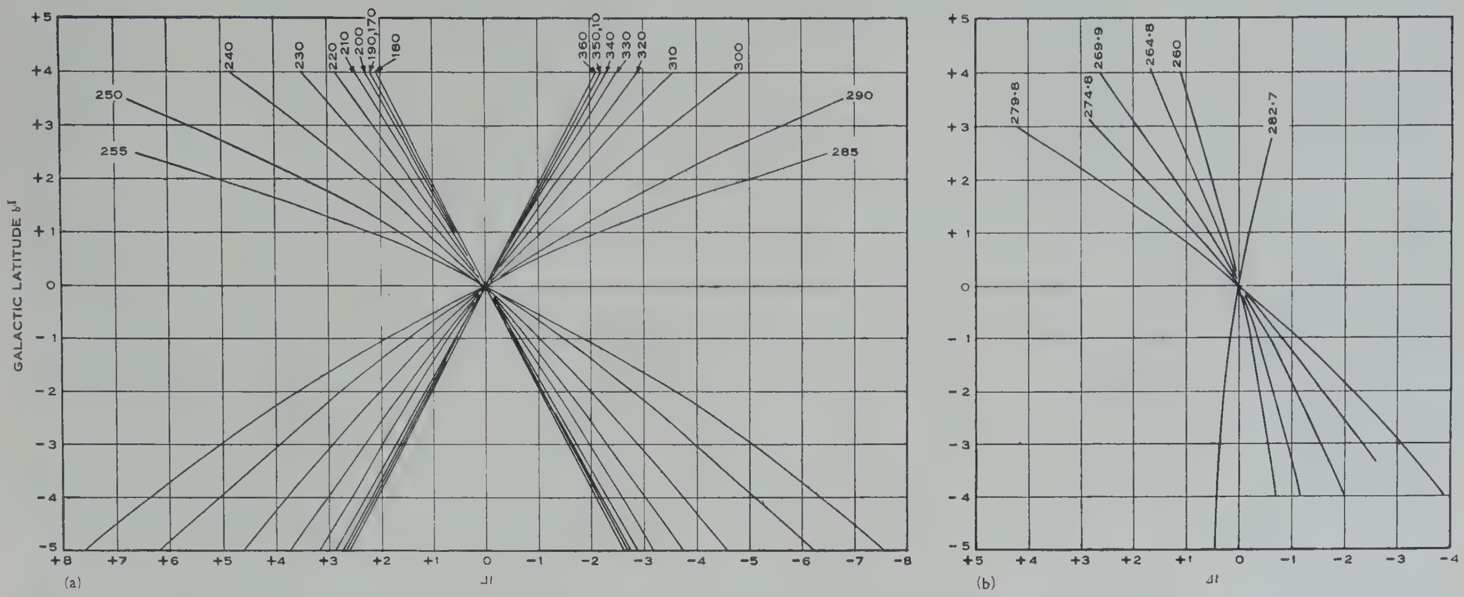

Fig. 3.—Galactic coordinates (old system) along the tracks. The abscissa is the difference between l^I at a point on the track and its value at the equator. The labels give the longitude at the equator. (*a*) Constant-declination tracks. Intermediate tracks can be found by interpolation. (*b*) Special manually operated tracks.

(c) *Frequency Coverage*

To cover the whole frequency range in which radiation could be detected, a number of runs were taken over each track with the four-channel block placed at a series of different frequencies. There was always an overlap of one channel width between successive runs and each frequency was used two or more times. In some cases, the frequency range was covered again at interlaced frequencies to give a half-channel spacing for the points.

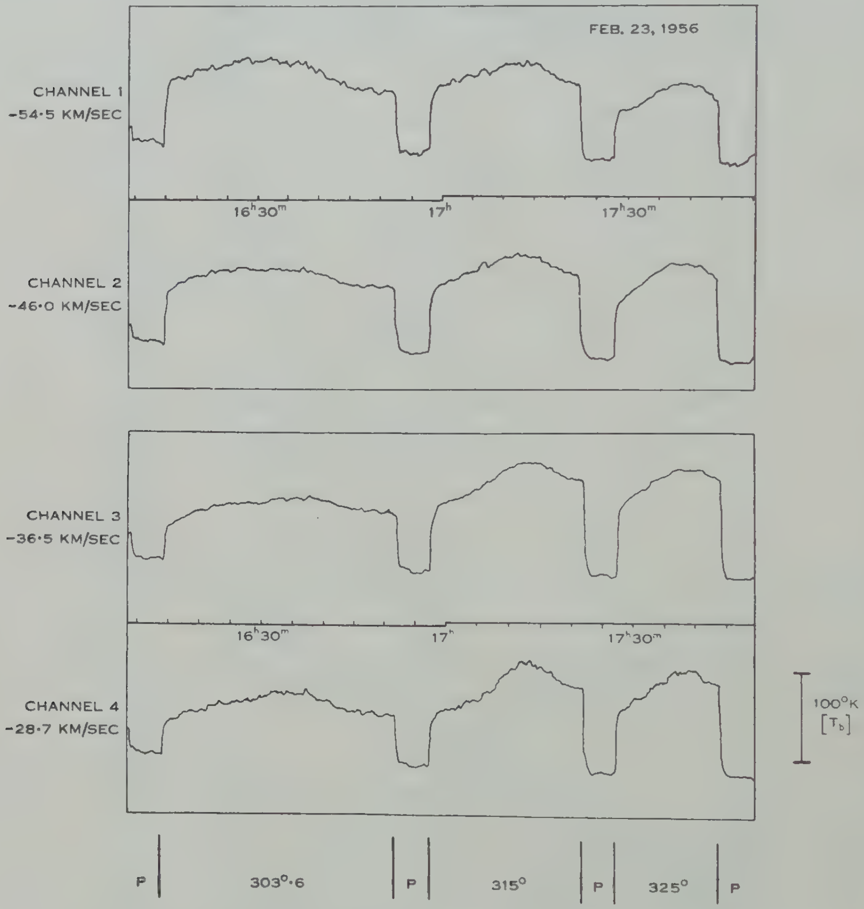

Fig. 4.—A sample four-channel record, consisting of fixed-frequency drift curves along three constant-declination tracks across the Galaxy, with check periods on the South Celestial Pole (*P*). The tracks are identified at the bottom of the diagram. (The radial velocities in this figure are the constant observational velocities, not corrected for local motions.)

A series of runs taken over a short period of time was always fairly uniformly spaced in frequency, the points being usually a channel width apart, but a repeat series taken at a later date would in general give runs at somewhat different frequencies, thus resulting in an irregular distribution of points along the line profile. The main reason for this difference was that, for convenience of operation, a succession of longitudes would be observed at the same actual frequency on a given day. The corrections to be applied for Sun and Earth motions had a different pattern at different times of year, with the result that the final corrected velocities at a given longitude show an uneven distribution.

The manner in which the points were distributed over the velocity range covered by the line is illustrated in Figure 6 below. Over the whole programme, there were an average of 6 runs per band width. The total number of galactic crossings in the whole project was about 6000, counting the records from the four channels separately.

(*d*) *Calibration Checks*

Three types of check were done at frequent intervals throughout the survey to monitor variations in the intensity scale. These comprised observations of low- and high-level standard regions in the sky, and checks of the gain of each of the four D.C. amplifiers.

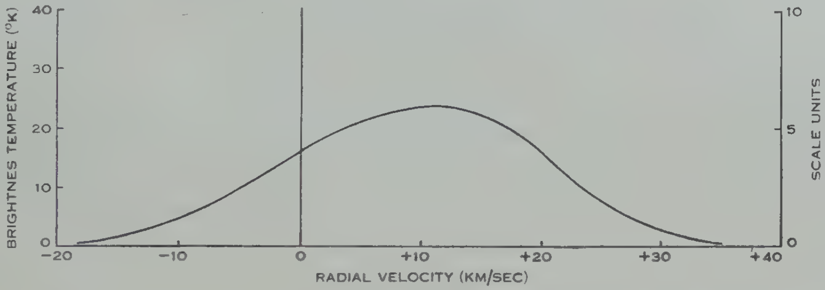

Fig. 5.—Line profile at the South Celestial Pole, the comparison point used for checking the receiver base line. (No radiation was detectable in the wings out to at least ±200 km/sec.)

The South Celestial Pole was used for low-level checks, because it was always accessible, and the intensity there is effectively zero at most velocities. There is, however, a substantial level of radiation over a range of velocity near zero. The profile at the Pole therefore had to be determined and this was done by a careful series of comparisons with the regions of the two galactic poles. The real zero level of the survey at any particular velocity is therefore the mean level near the two galactic poles. This reference level is believed to be low, because there was no detectable variation over a large area of the sky and over the whole velocity range used in the survey ; some broadly distributed radiation from the galactic halo or from beyond the Galaxy could still be present, however, as this would be difficult to detect.

The profile obtained at the celestial pole is shown in Figure 5. The nominal zero level had to be corrected for this radiation in all observations at low velocities.

For some of the runs at high radial velocities, where the galactic ridge is narrow and of low intensity, the zero level was taken from a long base line on either side of the galactic crossing, rather than from the South Pole. This method had the advantage that any effect arising from aerial movement was eliminated, but it could only be used for a small proportion of the runs, because of time limitations.

High-level check points were observed near the beginning, middle, and end of each day's programme. The positions of these standard regions are indicated in Figure 2. (The check points at 265° and 282° were alternatives.) Each of these points had to be observed at the same velocity (corrected for local motions) on each occasion, in order to obtain the standard check signal; therefore the receiver had to be retuned for a check point observation. South Pole observations, on the other hand, were always made at the frequency of the associated galactic crossing.

V. METHOD OF REDUCTION

(*a*) *Frequency*

The frequency of the centre point of the four-channel block at which an observation was taken was first determined from measurements of the two local oscillator frequencies, and the corresponding radial velocity was then corrected for the Earth's velocity relative to the local centre of rest. The corrections for points on the old galactic equator were obtained from a set of tables kindly supplied by Leiden Observatory, which give the resultant of the velocities of the Earth and the Sun,* every 5° around the (old) galactic equator and every 5 days throughout the year. To obtain the velocities at points away from the equator, additional tables were prepared giving the velocity *gradient* along constant declination lines and the special tracks, as a function of date (Gill 1955).

Finally, the velocities corresponding to the four individual channels were derived from the corrected central velocity and the known frequencies of the four narrow-band filters.

(*b*) *Intensity*

For each galactic crossing, the intensity was read from the record at a series of times corresponding to integral half-degrees of latitude (b^{I}) along a smoothed line drawn through the noise fluctuations. The relative scale factor was corrected back to a standard condition, from the associated calibrations, and the zero level was found from the mean of the pole comparisons before and after the run, adjustments being made for any radiation at the pole at the frequency of observation. (A separate correction was needed for the component of the Sun and Earth motions, in the direction of the pole.)

(*c*) *Assembly of Crossings*

In reducing the set of galactic crossings for a particular track, the objective was to produce a " contour diagram " in which the intensity is plotted as a function of radial velocity and galactic latitude.

The first step was to plot out one profile (usually for $b^{\mathrm{I}}=0$), in order to check the agreement between the various observations. This profile check enabled any obviously deviant results to be found and rejected. The scatter of the individual points in a typical case can be seen in Figure 6. The r.m.s. deviation of the observed points from the corresponding mean profile, averaged over all the tracks, amounted to ±2 °K in brightness temperature.

---

* The solar motion was taken as 20·0 km/sec directed towards $\alpha=18^{\mathrm{h}}\,00^{\mathrm{m}}$, $\delta=+30°\cdot 0$ (1900).

A diagram of this type was then used in grouping the observations at neighbouring velocities in order to form mean crossing-curves. The velocity spread inside a group was made large enough to contain a reasonable number of observations for averaging and small enough to avoid undue smoothing of the profile in the velocity direction. The velocity range covered by the points in a group averaged about 5 km/sec. Two sample comparisons between the various crossing-curves in a group are illustrated in Figure 7.

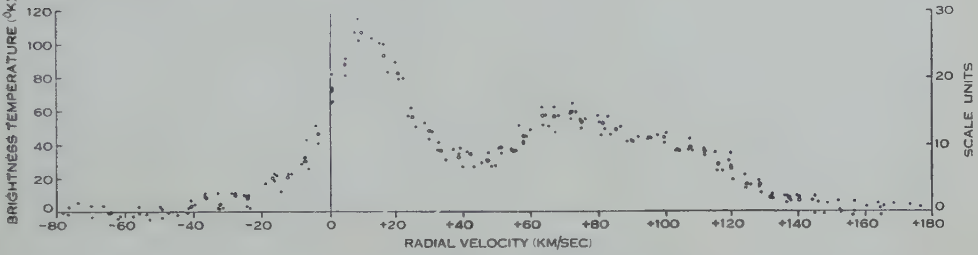

Fig. 6.—An illustration of the scatter of the points used to build up a profile ($l^{I}=230°$, $b^{I}=0°$). ● Individual points, ○ mean points.

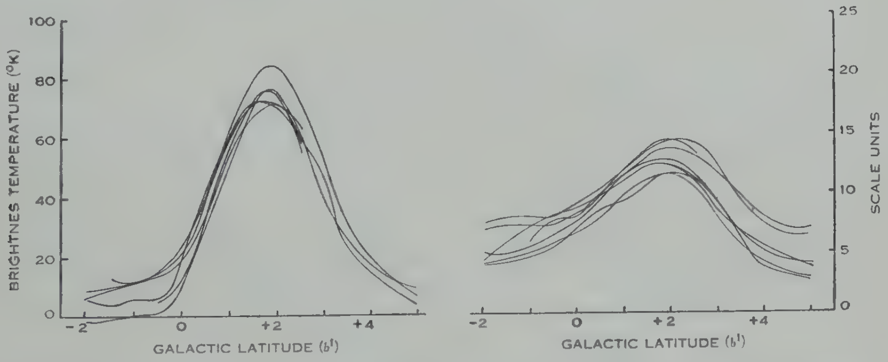

Fig. 7.—Two groups of galactic crossing-curves, illustrating the degree of reproducibility. 350° track. Velocity range: (*a*) +101·9 to +104·2 km/sec; (*b*) —11·1 to —6·8 km/sec.

A mean crossing-curve was prepared for each group by averaging the individual curves, and mean values were computed for the velocity at $b^{I}=0$ and for the velocity gradient along the track. The latitude scale was corrected at this stage for the receiver time delay.

The latitudes at which each mean crossing-curve reached a set of fixed values were then read and plotted at the appropriate velocities on a velocity–latitude grid; contours were drawn through these points, with a small amount of additional smoothing.

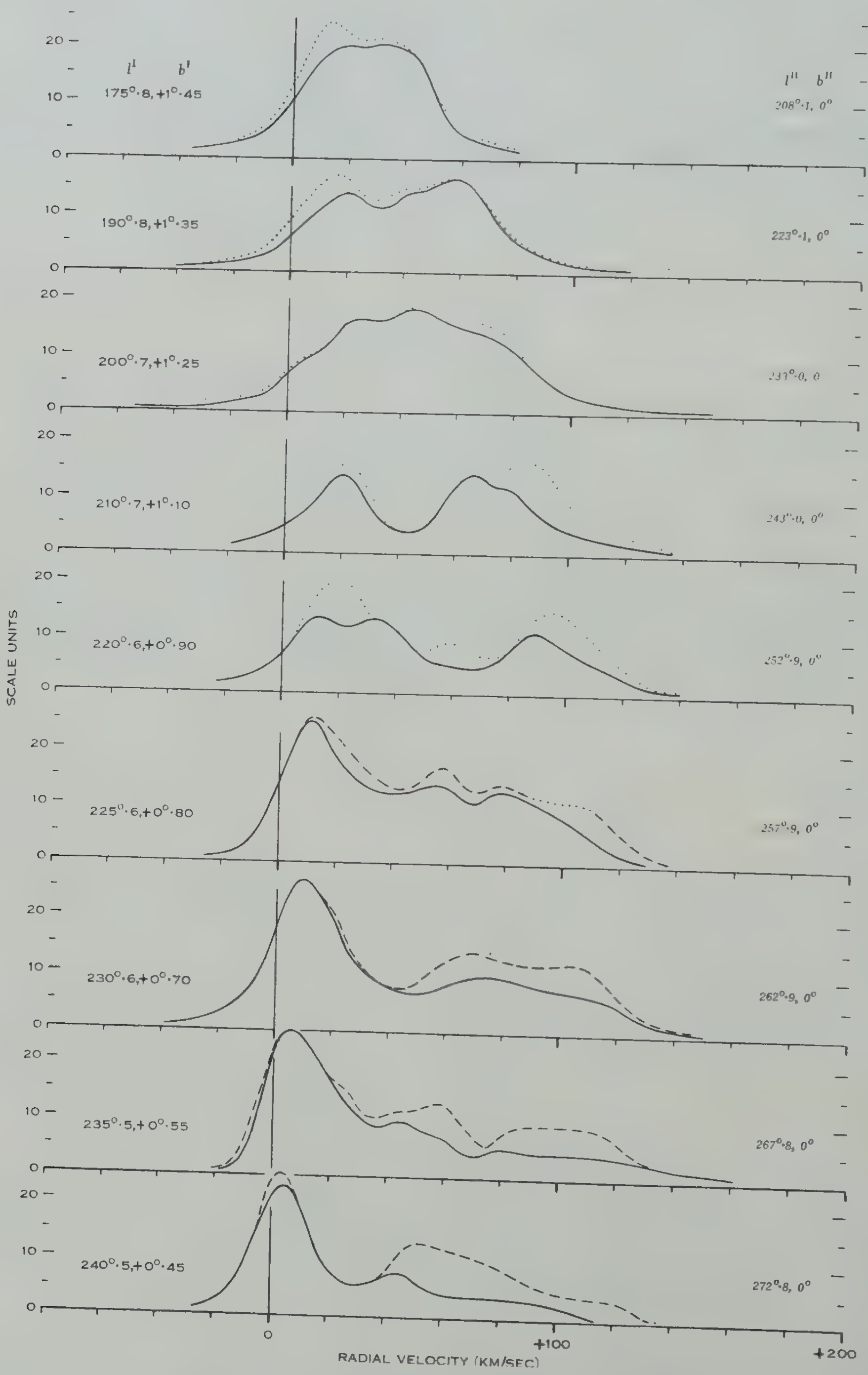

Fig. 8.—Profiles at new galactic equator ———— ; ridge-line profiles (see Section VI (*b*)) – – – · · · ·. Unit=3·2 °K in T_a, 4·1 °K in T_b.

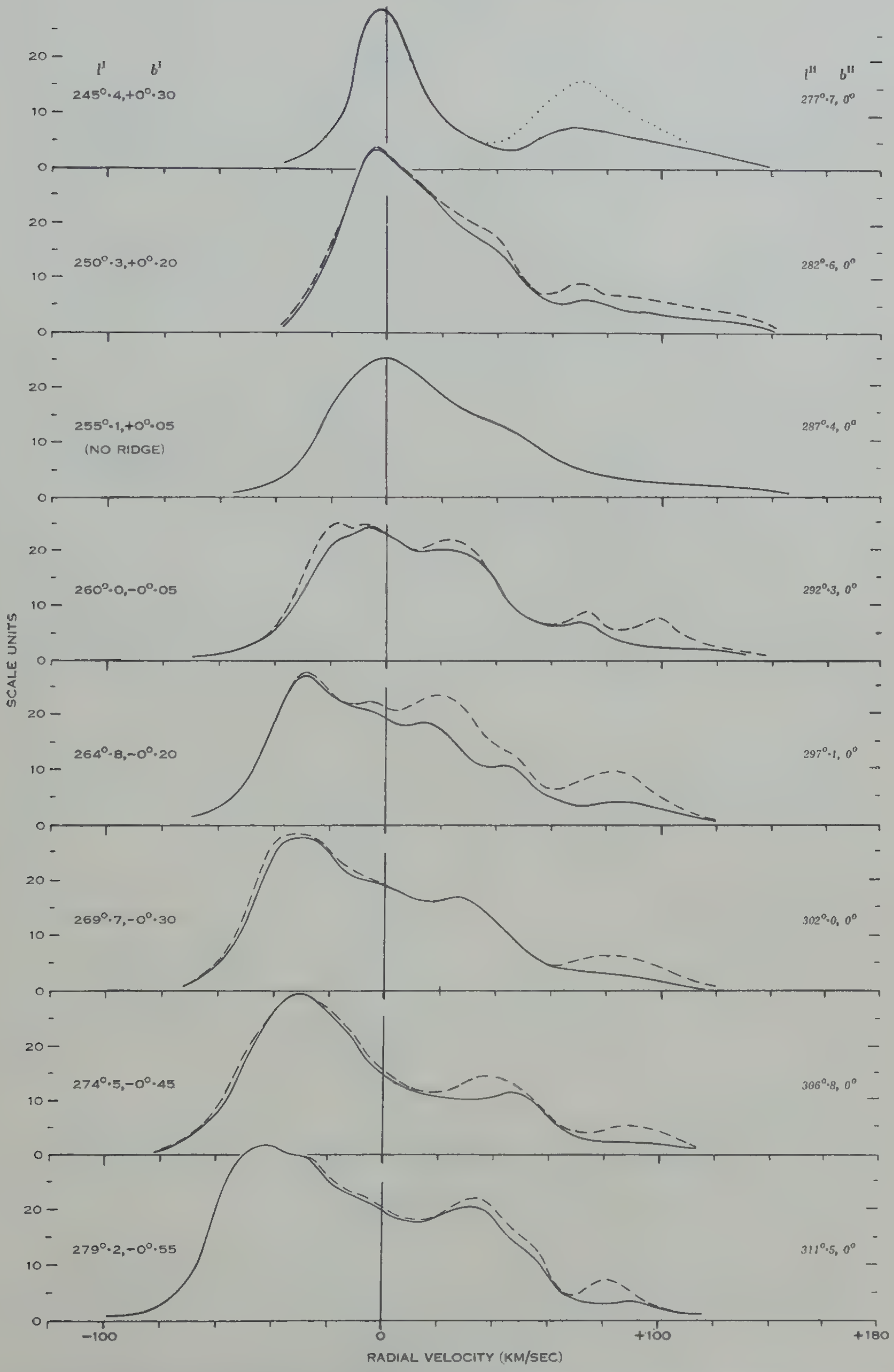

Fig. 9.—Profiles at new galactic equator ———— ; ridge-line profiles (see Section VI (*b*)) – – – · · · ·. Unit = 3·2 °K in T_a, 4·1 °K in T_b.

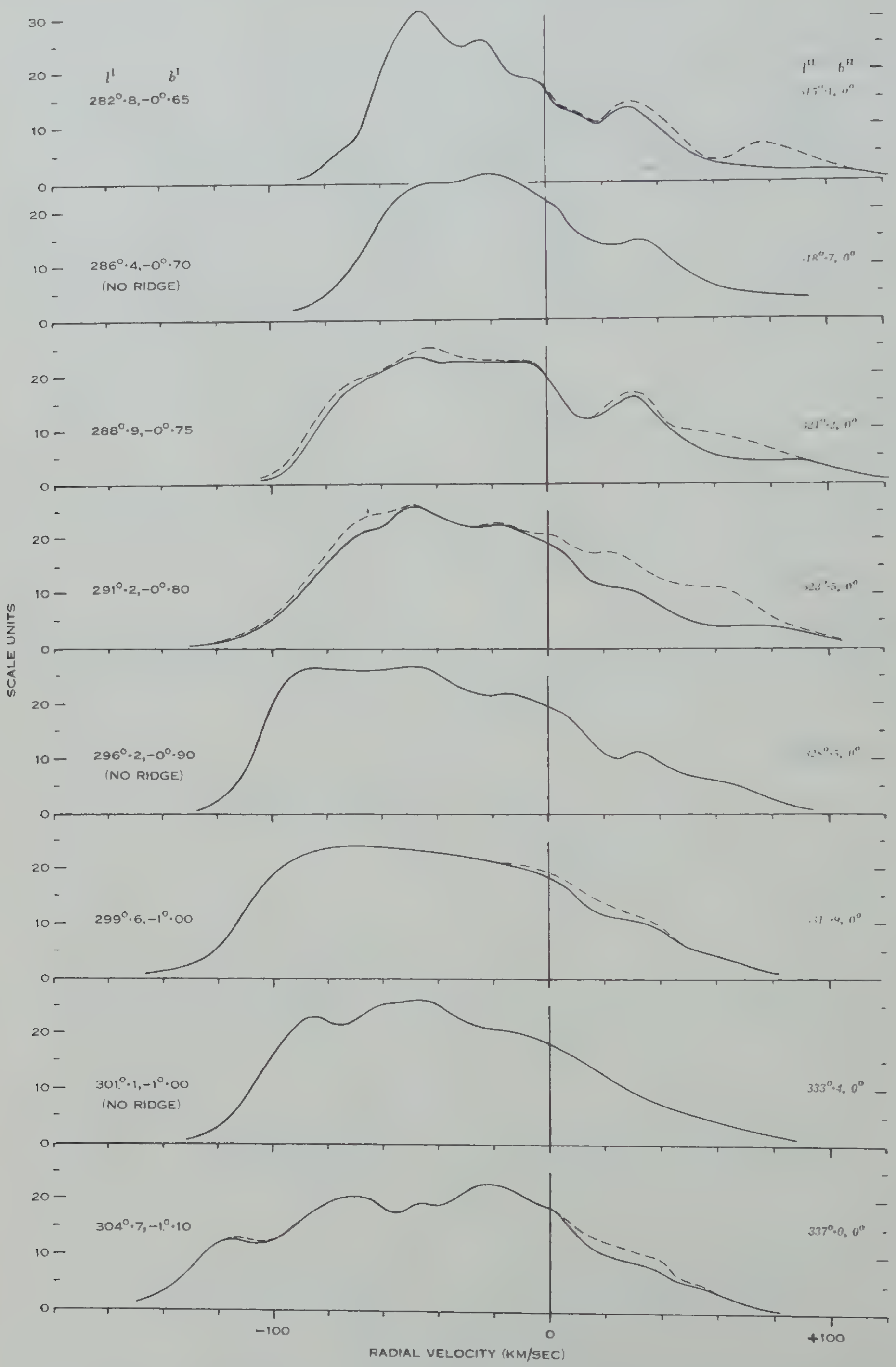

Fig. 10.—Profiles at new galactic equator ———— ; ridge-line profiles (see Section VI (*b*)) - - - - · · · ·. Unit = 3·2 °K in T_a, 4·1 °K in T_b.

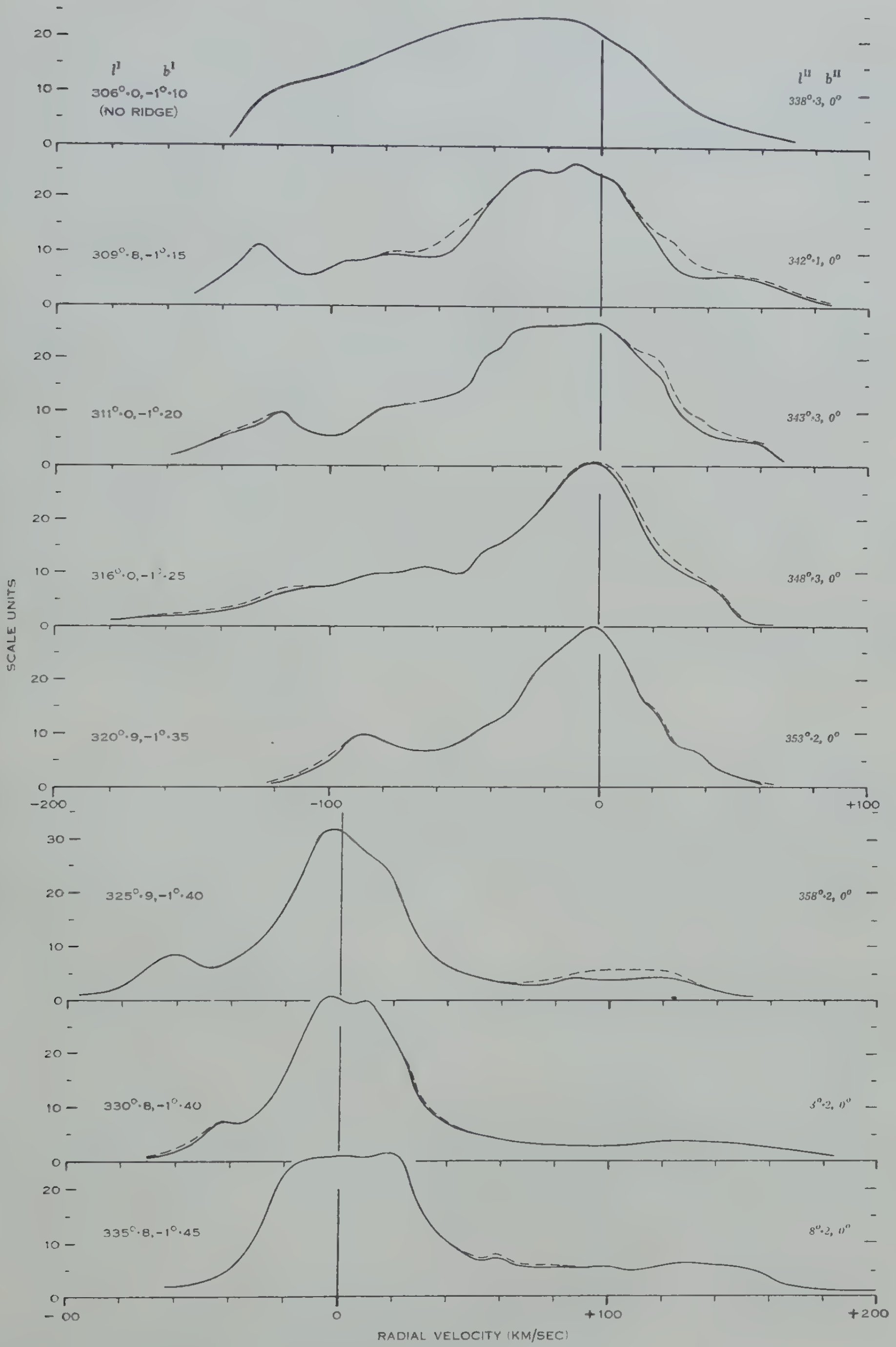

Fig. 11.—Profiles at new galactic equator ———— ; ridge-line profiles (see Section VI (*b*)) – – –· · · ·. Unit=3·2 °K in T_a, 4·1 °K in T_b.

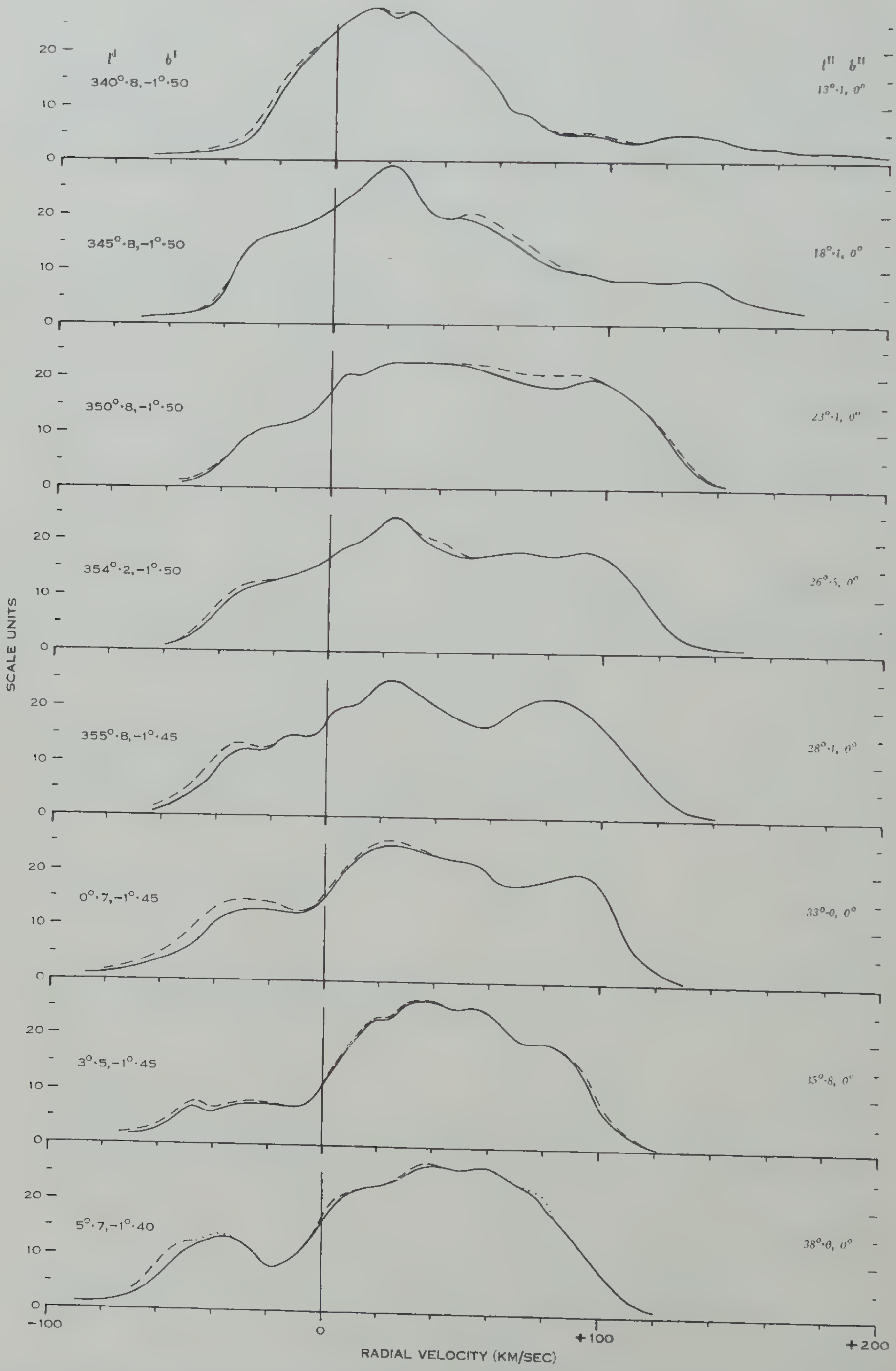

Fig. 12.—Profiles at new galactic equator ———— – ; ridge-line profiles (see Section VI (*b*)) – – –·····. Unit=3·2 °K in T_a, 4·1 °K in T_b.

VI. RESULTS OF THE SURVEY

(a) *Contour Diagrams*

The full results of the survey are presented in Plates 1–41, in the form of contour diagrams. Each diagram gives the distribution of 21 cm intensity with (old) galactic latitude and radial velocity for a particular track across the Milky Way. The longitude values given are those at which the tracks intersect the old and new galactic equators; the longitudes at other points on the tracks can be found from Figure 3.

The contour pattern presents the received intensity, with the contour levels marked in scale units; one unit is equal to 3·2 °K in aerial temperature, and 4·1 °K in brightness temperature. No corrections have been made for aerial smoothing or for continuum radiation. The zero of the intensity scale is the mean of the levels at the two galactic poles at the velocity concerned. The contour lines are dashed in regions where they are least accurate on present evidence.

The ridge-line, the line joining the maxima of the crossing-curves, has been included where possible on each diagram, as this line has special significance in galactic plane considerations. In general, the intensity labels attached to the contours lie on the ridge-line, with the centre of the circle at the point of intersection of the contour line and the ridge-line.

Contour diagrams of this form were selected as the most efficient way of displaying a large amount of information; line profiles are horizontal cross sections on these diagrams.

(b) *A Set of Profiles*

One set of profiles is also given, to aid in quick visualization, especially for demonstrating the change with longitude (see Figs. 8–12). For this purpose, profiles at points along the new galactic equator ($b^{\mathrm{II}}=0$) are the most useful. Both old and new coordinates are given in each case for the point concerned, and also the point is indicated on the latitude scale of the corresponding contour diagram, as a cross reference.

The "ridge-line profile" is also shown for each track; this curve may be regarded as the upper envelope of the family of profiles for the track concerned, or as the variation of intensity with velocity along the ridge-line of the corresponding contour diagram. It is generally shown as a dashed line, but is in dotted form in places where it is ill defined. In many places the ridge-line profile is almost identical with the galactic equator profile. In such regions the dashed line representing the ridge-line profile is discontinued, but it is to be understood as continuing along the course of the galactic equator profile. The variation of latitude and longitude along the ridge-line has been ignored in the labelling of these profiles, which are identified by the coordinates of the new galactic plane.

VII. ASSESSMENT OF RESULTS

Gathering together the earlier estimates of measuring accuracy, we have the following values for the estimated probable errors:

Position:	±0°·07 in each coordinate.
Velocity:	±0·2 km/sec.

Temperature : ±2 °K in zero level ; ±7 per cent. in scale factor, for relative measurements ; ±15 per cent. for absolute measurements of aerial temperature ; ±20 per cent. for absolute measurements of brightness temperature.

In addition, the quoted temperatures are subject to inaccuracies which may be introduced in the reduction processes, through the methods used in combining a number of runs. In particular, profiles will be less accurate than sections, because they were built up from a number of observations at discrete frequencies, taken on different days, whereas the sections were recorded directly as continuous curves. The averaging processes will have produced some smoothing in the profiles.

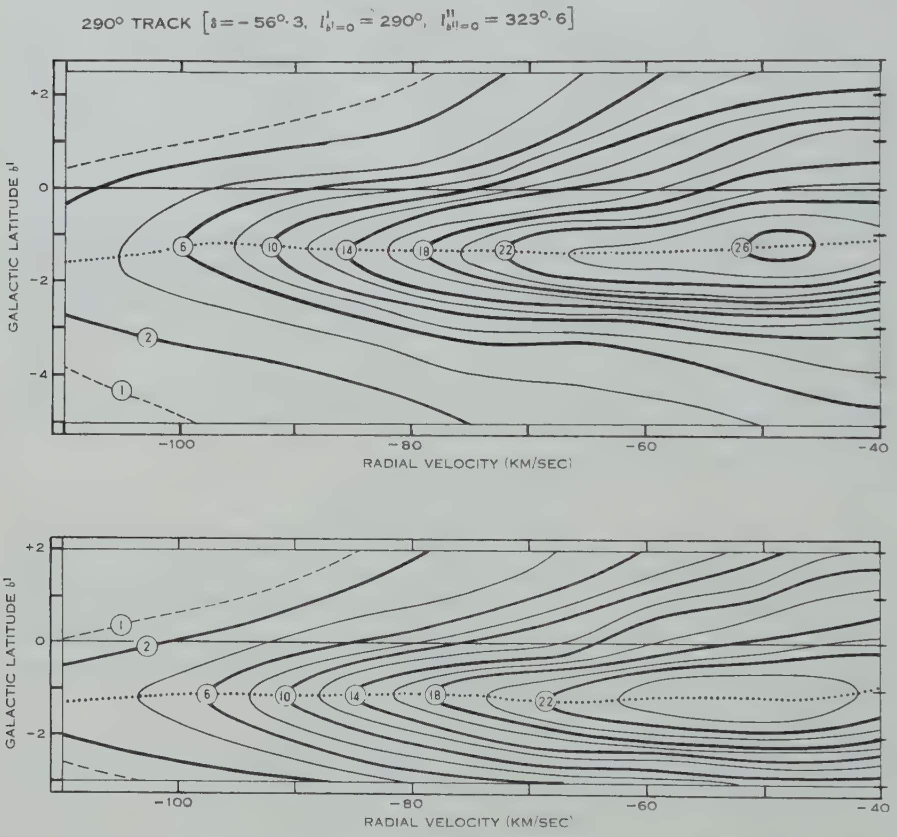

290° TRACK [$\delta = -56^\circ{\cdot}3,\ l^{I}_{b^{I}=0} = 290^\circ,\ l^{II}_{b^{II}=0} = 323^\circ{\cdot}6$]

Fig. 13.—Comparison between portions of two independently derived contour diagrams for the 290° track.

An overall assessment can best be made through comparisons with other sets of results. For this reason, two completely independent sets of observations were taken for the 290° track, and a comparison between them demonstrates the degree of reproducibility of the results. The two contour diagrams are shown in Figure 13, and the two ridge-line profiles in Figure 14.

In addition, the Sydney profiles have been compared with those from the Leiden survey over the whole region of overlap ; two examples are shown in Figure 15. The bandwidths were about the same in the two surveys ; the beamwidths, however, were significantly different, 1°·4 by 1°·4 for Sydney, and 1°·8 by 2°·8 for Leiden (Kootwijk).

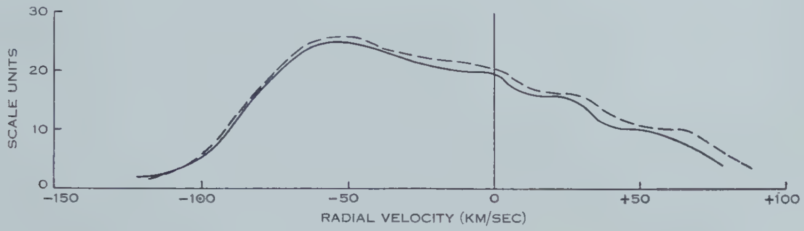

Fig. 14.—Two ridge-line profiles for the same track, derived from independent sets of observations (290° track).

The velocity scales are found to agree quite closely. In a comparison of the intensity scales, an average taken over the central parts of the profiles for the whole overlap region gave a value of 1·28 for the ratio of Sydney brightness temperatures to Leiden published temperatures. There are large uncertainties in both temperature scales, but the absolute values of the temperatures are less important than the need to establish a consistent temperature scale for combining the Sydney and Leiden surveys.

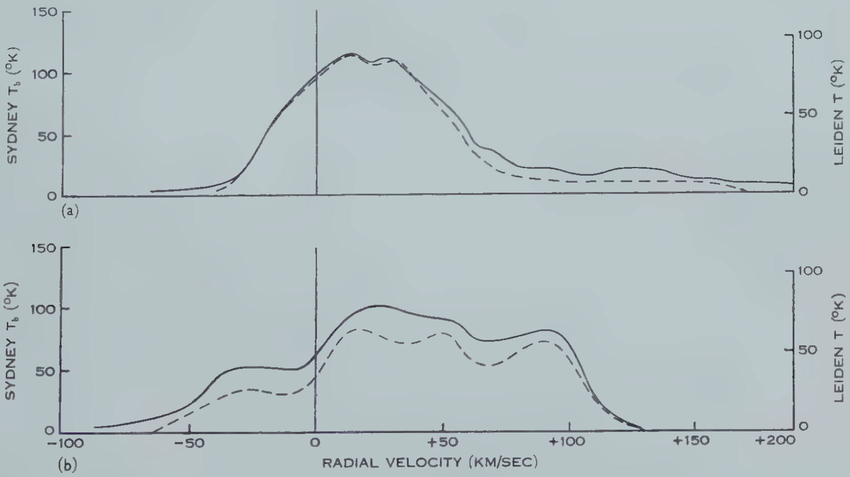

Fig. 15.—Sample comparisons between Sydney and Leiden profiles. ——— Sydney ; – – – – Leiden. (*a*) $l^{\mathrm{I}}=340°·9$, $b^{\mathrm{I}}=-1°·6$; (*b*) $l^{\mathrm{I}}=0°·9$, $b^{\mathrm{I}}=-1°·6$.

There is reasonable agreement between the shapes of the Sydney and Leiden profiles, but the Sydney ones may have some additional smoothing, resulting from the method of derivation. On the other hand, the variation with latitude should be more reliable in the Sydney case. There is a tendency for the Sydney intensities to be relatively higher in the wings of the profiles ; this appears to be mainly due to the higher resolution in latitude, since the angle subtended by the gas layer is smallest for the higher velocities.

The two sets of results are sufficiently homogeneous to be used together for building up an overall picture of the whole Galaxy. Although it would be desirable to have a closer sampling in longitude and a wider coverage in latitude, the information which is now available is adequate for deriving a coarse picture of galactic structure. This subject, and other aspects of the analysis, will be taken up in subsequent papers.

VIII. ACKNOWLEDGMENTS

B. J. Robinson, Mrs. Martha Stahr Carpenter, and R. L. Dowden were associated with the project in various periods and made substantial contributions. E. C. Holmes carried out a large part of the later observations and equipment maintenance ; Miss Pat Healy did a major share of the computational work ; and Miss Elaine Mapledorum and Mrs. Susan Paterson traced the diagrams.

IX. REFERENCES

BLAAUW, A., GUM, C. S., PAWSEY, J. L., and WESTERHOUT, G. (1959).—*I.A.U. Inform. Bull.* No. 1 : 4–6.

CHRISTIANSEN, W. N., and HINDMAN, J. V. (1952).—*Aust. J. Sci. Res.* A **5** : 437–55.

EWEN, H. I., and PURCELL, E. M. (1951).—*Nature* **168** : 356.

GILL, M. C. (1955).—C.S.I.R.O. Aust. Div. Radiophys. Rep. RPL 101.

GUM, C. S., and KERR, F. J. (1958).—C.S.I.R.O. Aust. Div. Radiophys. Rep. RPL 138.

GUM, C. S., and PAWSEY, J. L. (1958).—C.S.I.R.O. Aust. Div. Radiophys. Rep. RPL 137.

HINDMAN, J. V., and WADE, C. M. (1959).—*Aust. J. Phys.* **12** : 258–69.

VAN DE HULST, H. C., MULLER, C. A., and OORT, J. H. (1954).—*Bull. Astr. Insts. Netherlds.* **12** : 117–49.

KERR, F. J., HINDMAN, J. V., and CARPENTER, M. S. (1957).—*Nature* **180** : 677–9.

KERR, F. J., HINDMAN, J. V., and ROBINSON, B. J. (1954).—*Aust. J. Phys.* **7** : 297–314.

MULLER, C. A., and WESTERHOUT, G. (1957).—*Bull. Astr. Insts. Netherlds.* **13** : 151–95.

OHLSSON, J. (1932).—*Ann. Lund Obs.* No. 3.

OORT, J. H., KERR, F. J., and WESTERHOUT, G. (1958).—*Mon. Not. R. Astr. Soc.* **118** : 379–89.

SCHMIDT, M. (1957).—*Bull. Astr. Insts. Netherlds.* **13** : 247–68.

SEEGER, C. L., WESTERHOUT, G., and VAN DE HULST, H. C. (1956).—*Bull. Astr. Insts. Netherlds.* **13** : 89–99.

WESTERHOUT, G. (1957).—*Bull. Astr. Insts. Netherlds.* **13** : 201–46.

EXPLANATION OF PLATES 1–41

Contour diagrams showing distribution of 21 cm radiation along 41 tracks crossing the Southern Milky Way.

Contours are of constant 21 cm intensity ;

1 unit $=3\cdot 2$ °K in aerial temperature
$=4\cdot 1$ °K in brightness temperature.

Tracks.—All but six of the tracks are along constant declination lines.

The 175° track is at $\delta=+4^\circ\cdot 4$ (1955) ; it crosses the old galactic equator at $l^{\mathrm{I}}=175^\circ$ and the new equator at $l^{\mathrm{II}}=208^\circ\cdot 1$.

The tracks are not normal to the galactic equator, but in most cases cross it at steep angles. Details of all tracks are given in Figure 3 and the declination formulae for the tracks in Plates 13–18 are in Table 2.

For full description see Section VI (*a*).

21 CM SURVEY OF THE SOUTHERN MILKY WAY

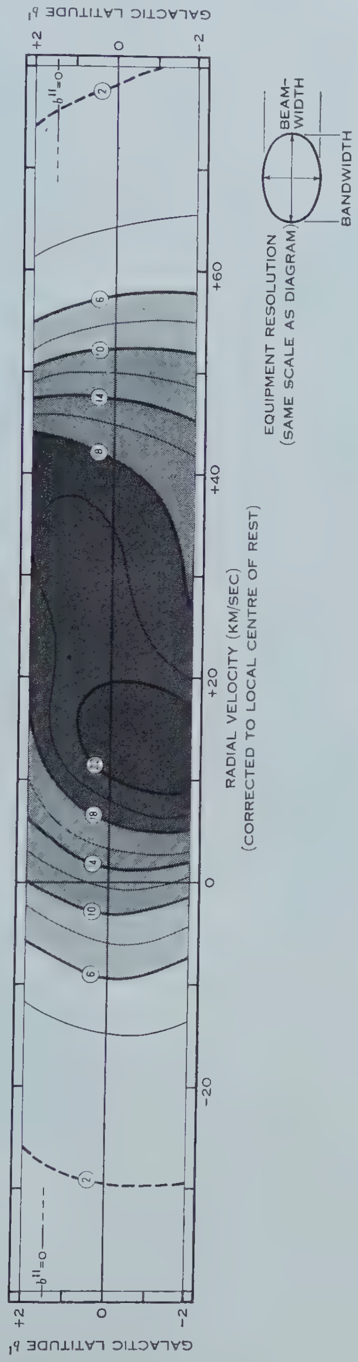

175° TRACK $\left[\delta = +4^{\circ}{\cdot}4,\ l^{I}_{b^{I}=0} = 175^{\circ},\ l^{II}_{b^{II}=0} = 208^{\circ}{\cdot}1\right]$

21 CM SURVEY OF THE SOUTHERN MILKY WAY

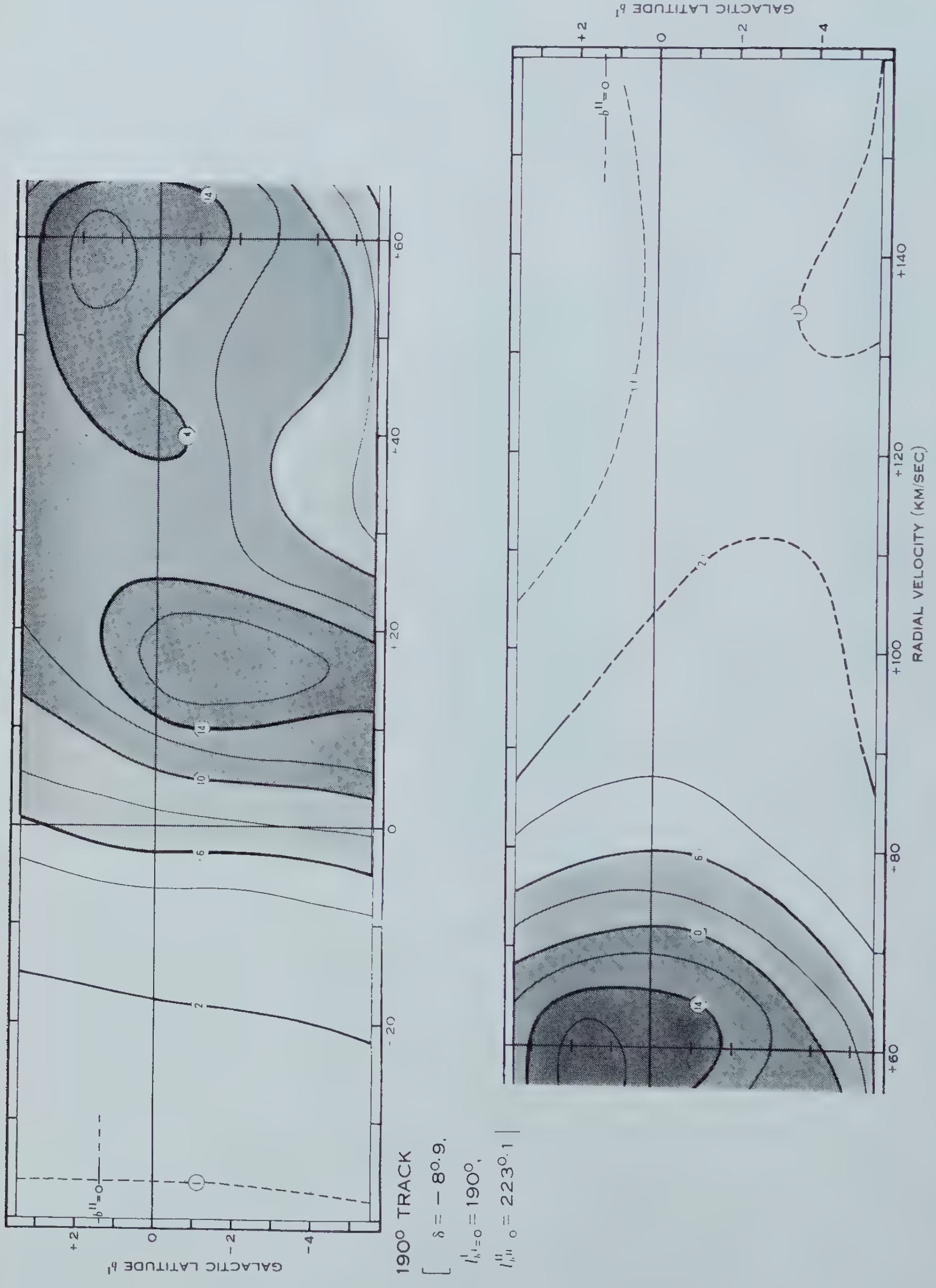

21 CM SURVEY OF THE SOUTHERN MILKY WAY

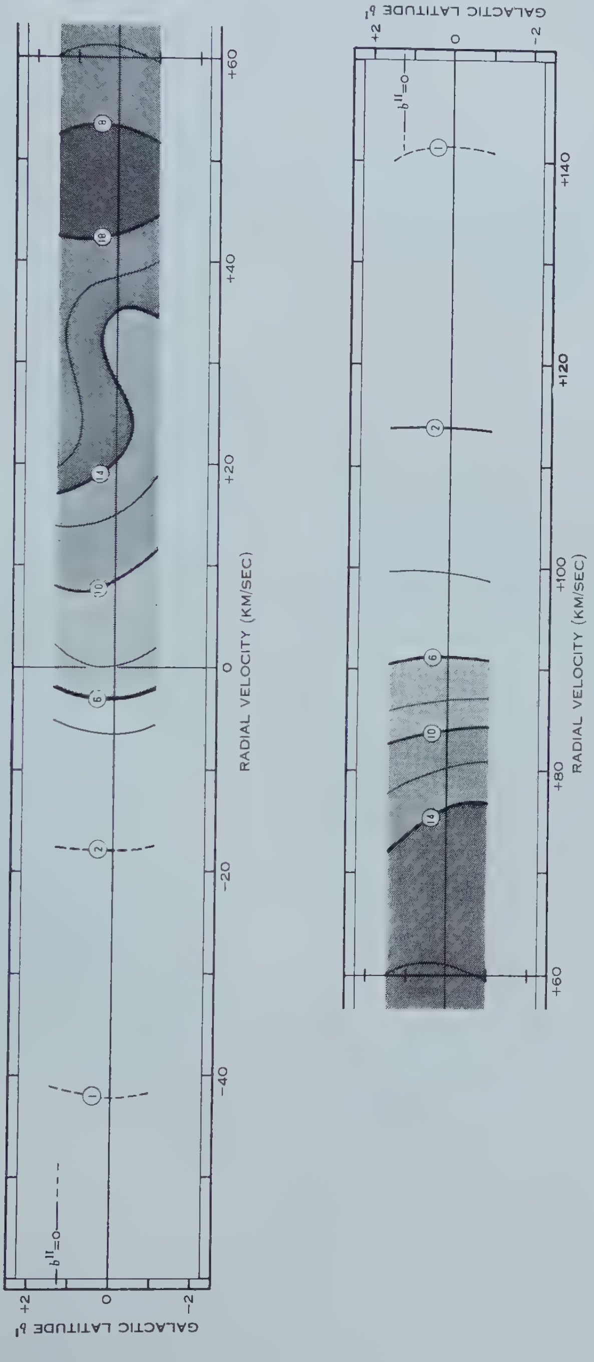

200° TRACK $[\delta = -17°.7,\ l^{I}_{b^{I}=0} = 200°,\ l^{II}_{b^{II}=0} = 233°.0]$

21 CM SURVEY OF THE SOUTHERN MILKY WAY

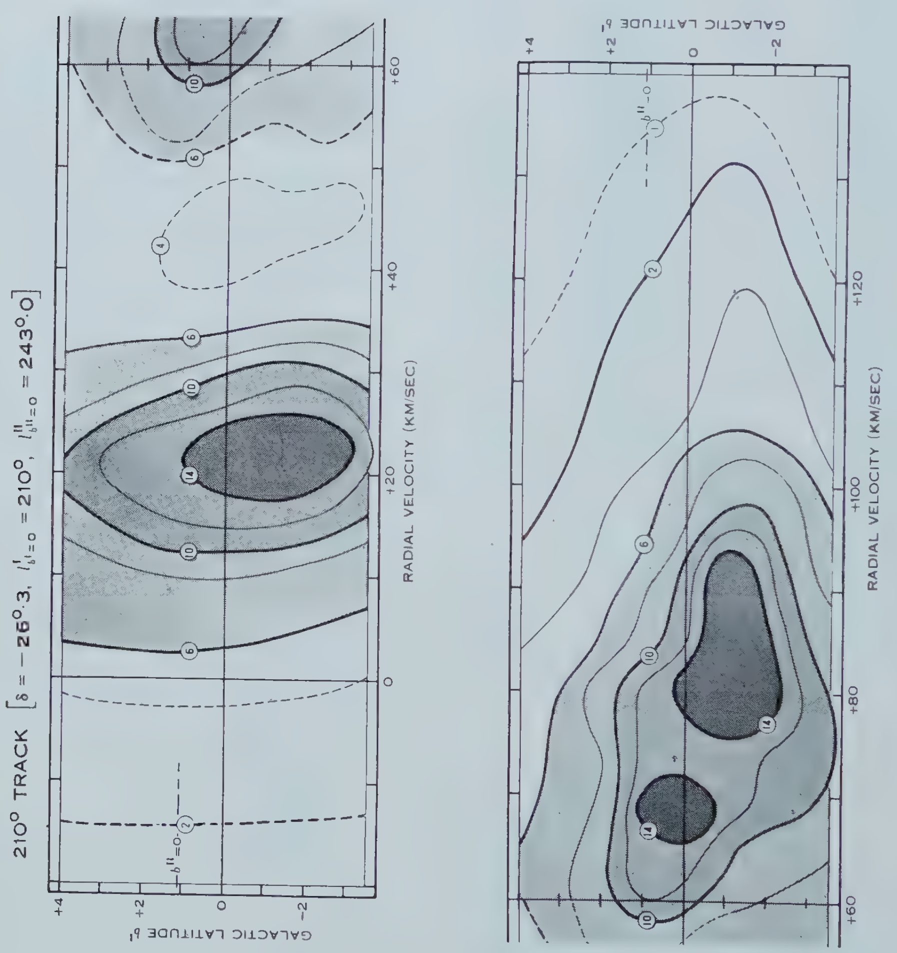

210° TRACK $\left[\delta = -26^\circ.3,\ l^{I}_{b^{I}=0} = 210^\circ,\ l^{II}_{b^{II}=0} = 243^\circ.0\right]$

21 CM SURVEY OF THE SOUTHERN MILKY WAY

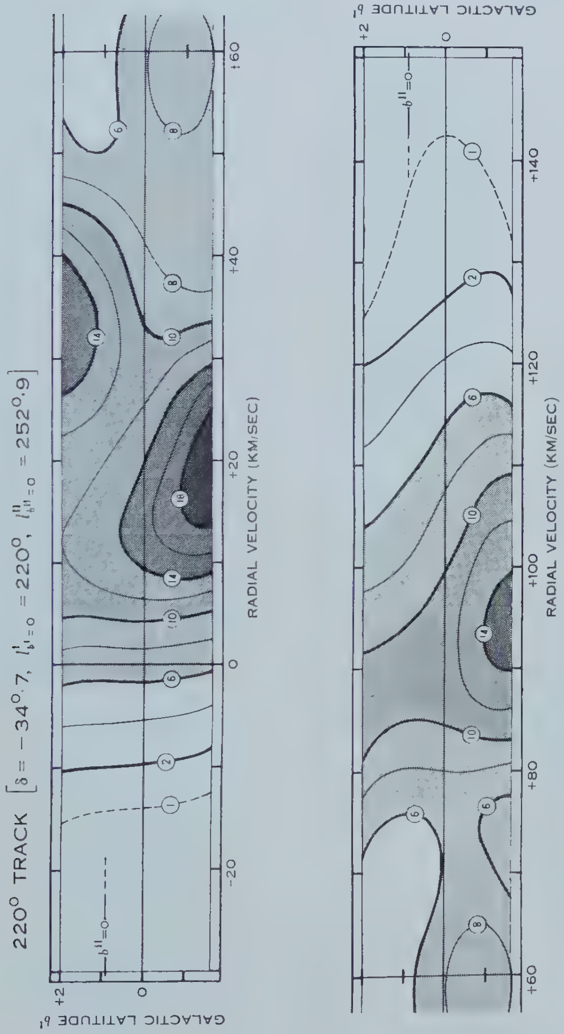
220° TRACK [$\delta = -34°.7$, $l^{I}_{b^{II}=0} = 220°$, $l^{II}_{b^{II}=0} = 252°.9$]

21 CM SURVEY OF THE SOUTHERN MILKY WAY

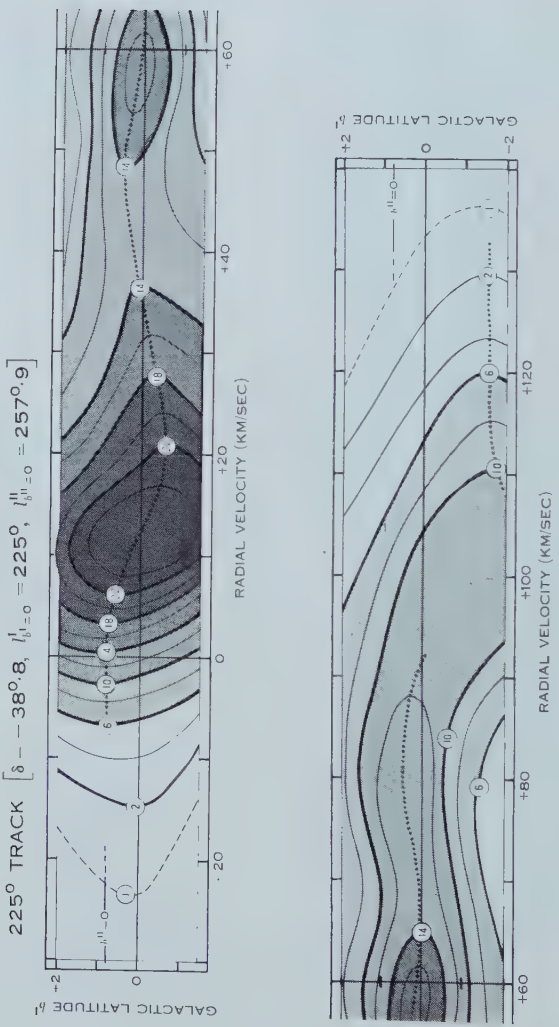

21 CM SURVEY OF THE SOUTHERN MILKY WAY

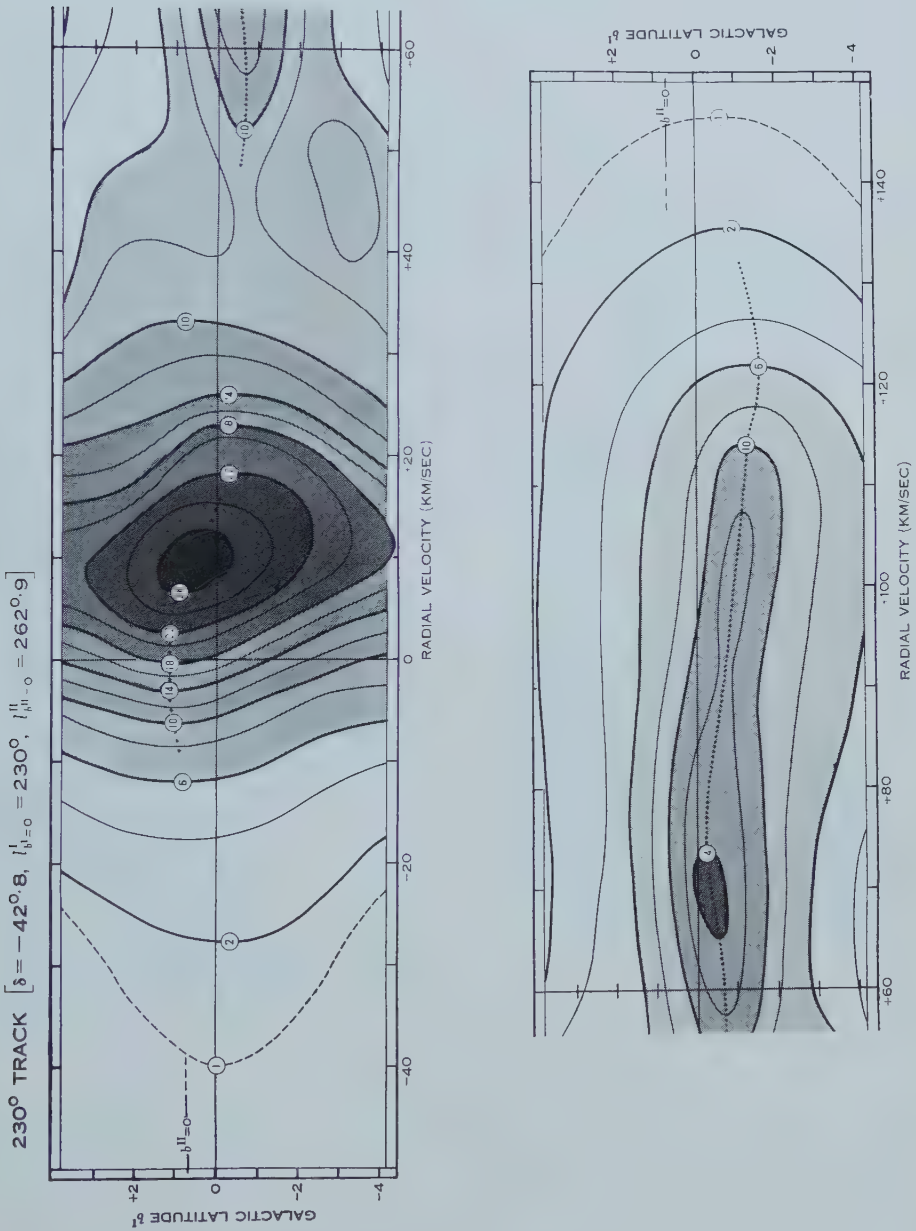

230° TRACK [$\delta = -42°.8$, $l^{I}_{b^{I}=0} = 230°$, $l^{II}_{b^{II}=0} = 262°.9$]

21 CM SURVEY OF THE SOUTHERN MILKY WAY

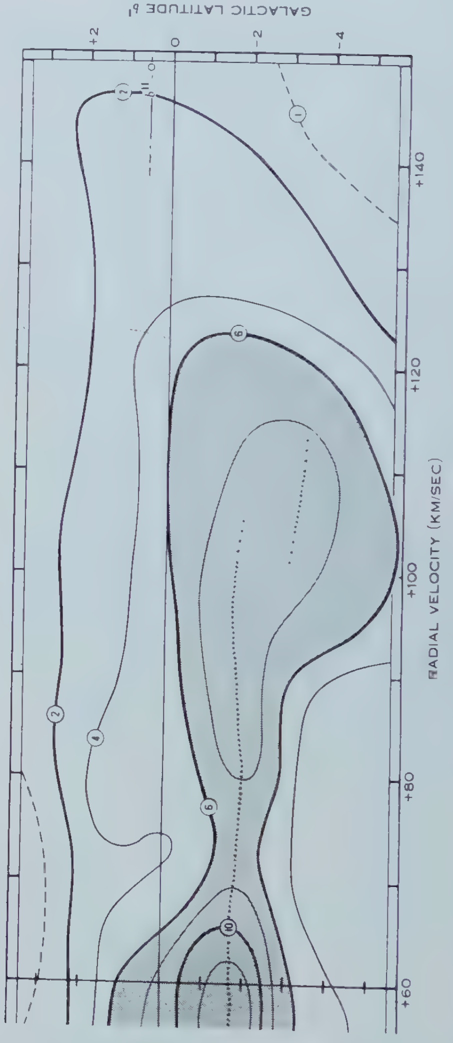

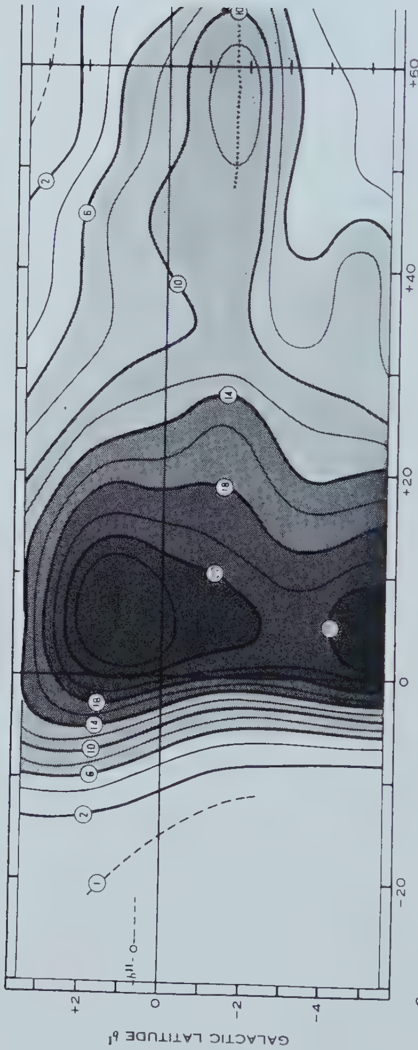

235° TRACK

$\delta = -46°.5$,

$l^{I}_{b^{II}=0} = 235°$,

$l^{II}_{b^{II}=0} = 267°.8$

21 CM SURVEY OF THE SOUTHERN MILKY WAY

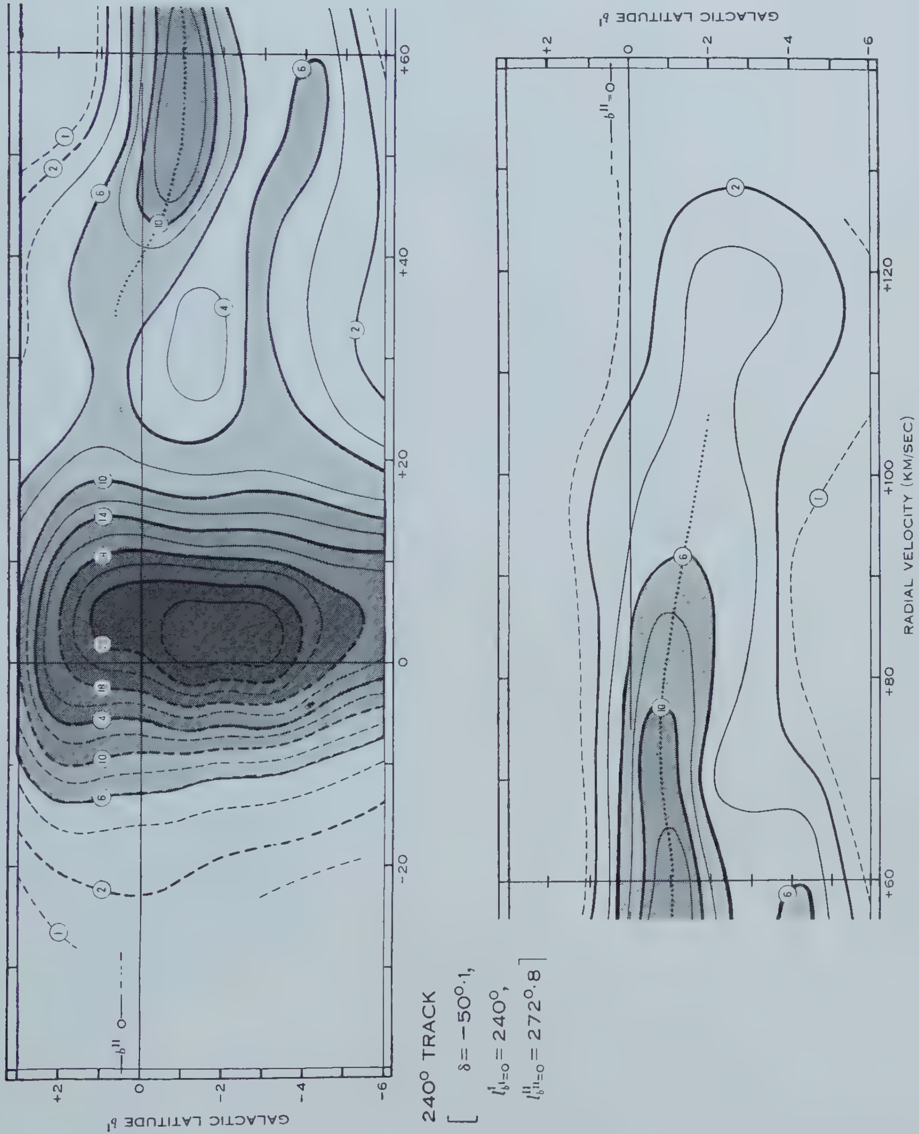

240° TRACK $\left[\delta = -50°.1,\ l^{I}_{b^{I}=0} = 240°,\ l^{II}_{b^{II}=0} = 272°.8\right]$

21 CM SURVEY OF THE SOUTHERN MILKY WAY

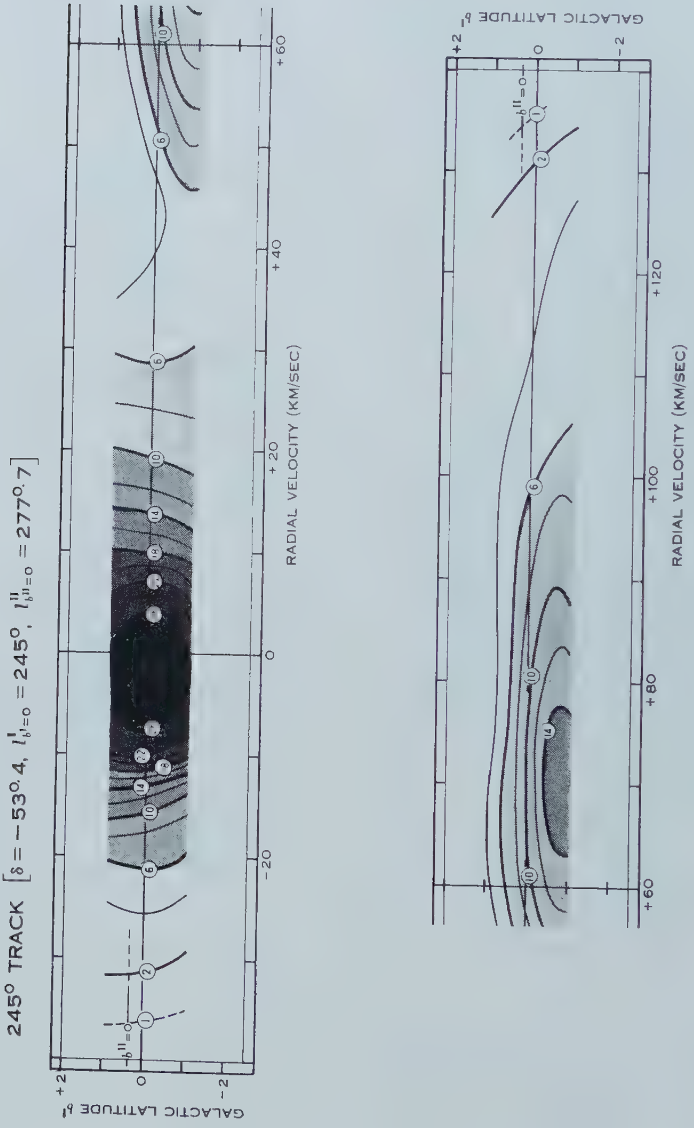

245° TRACK $[\delta = -53^\circ.4,\ l^{I}_{b^{I}=0} = 245^\circ,\ l^{II}_{b^{II}=0} = 277^\circ.7]$

21 CM SURVEY OF THE SOUTHERN MILKY WAY

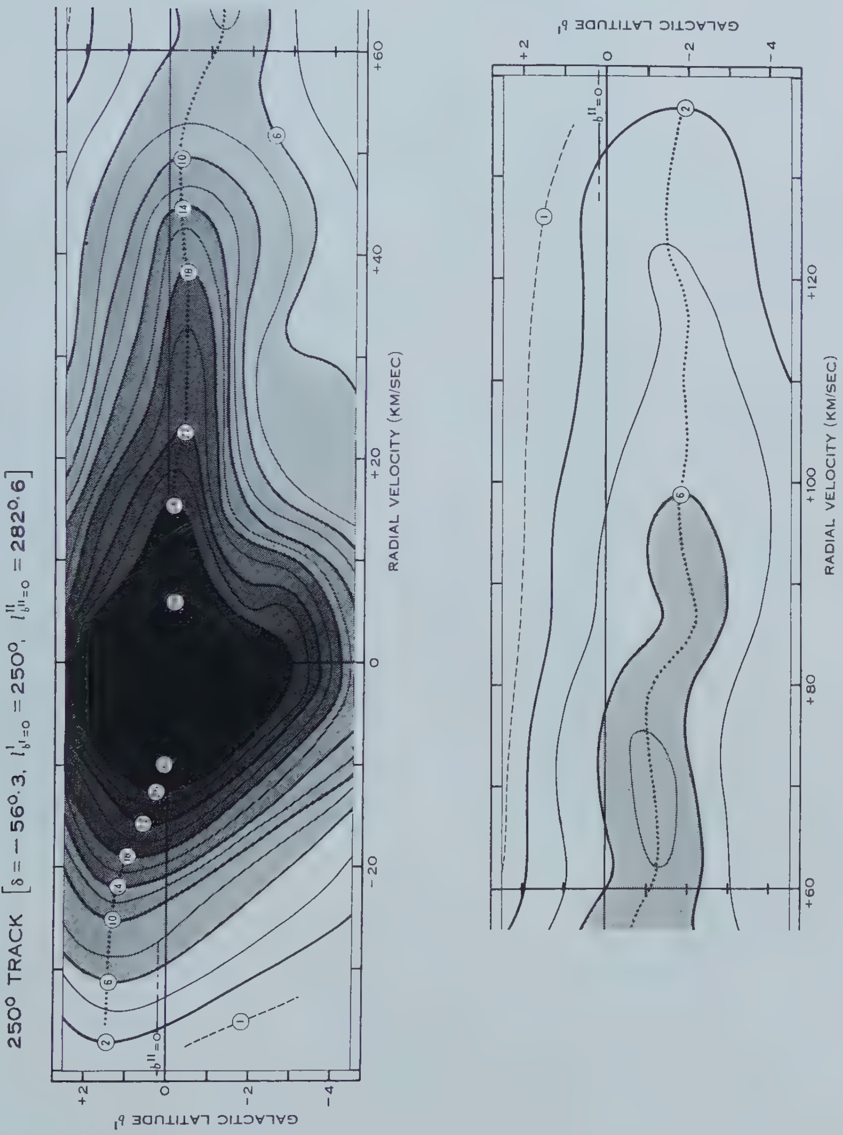

250° TRACK $[\delta = -56°.3,\ l^{I}_{b^{I}=0} = 250°,\ l^{II}_{b^{II}=0} = 282°.6]$

21 CM SURVEY OF THE SOUTHERN MILKY WAY

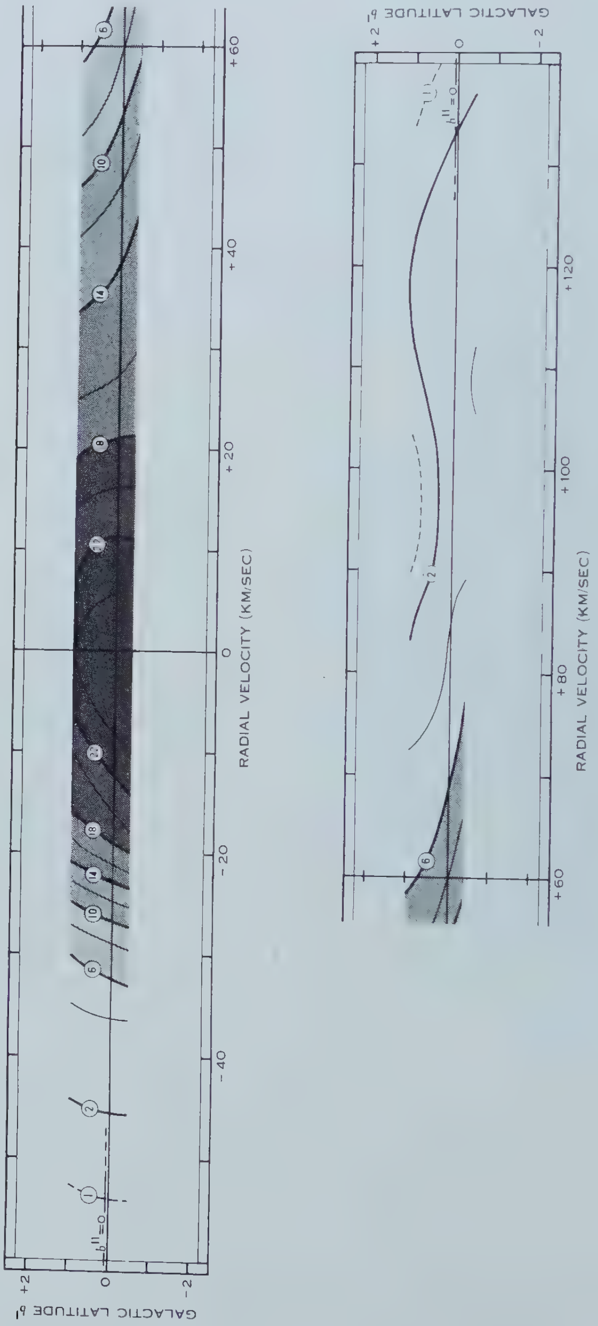

255° TRACK $\left[\delta = -58^\circ.8,\ l^{I}_{b^{I}=0} = 255^\circ,\ l^{II}_{b^{II}=0} = 287^\circ.4\right]$

21 CM SURVEY OF THE SOUTHERN MILKY WAY

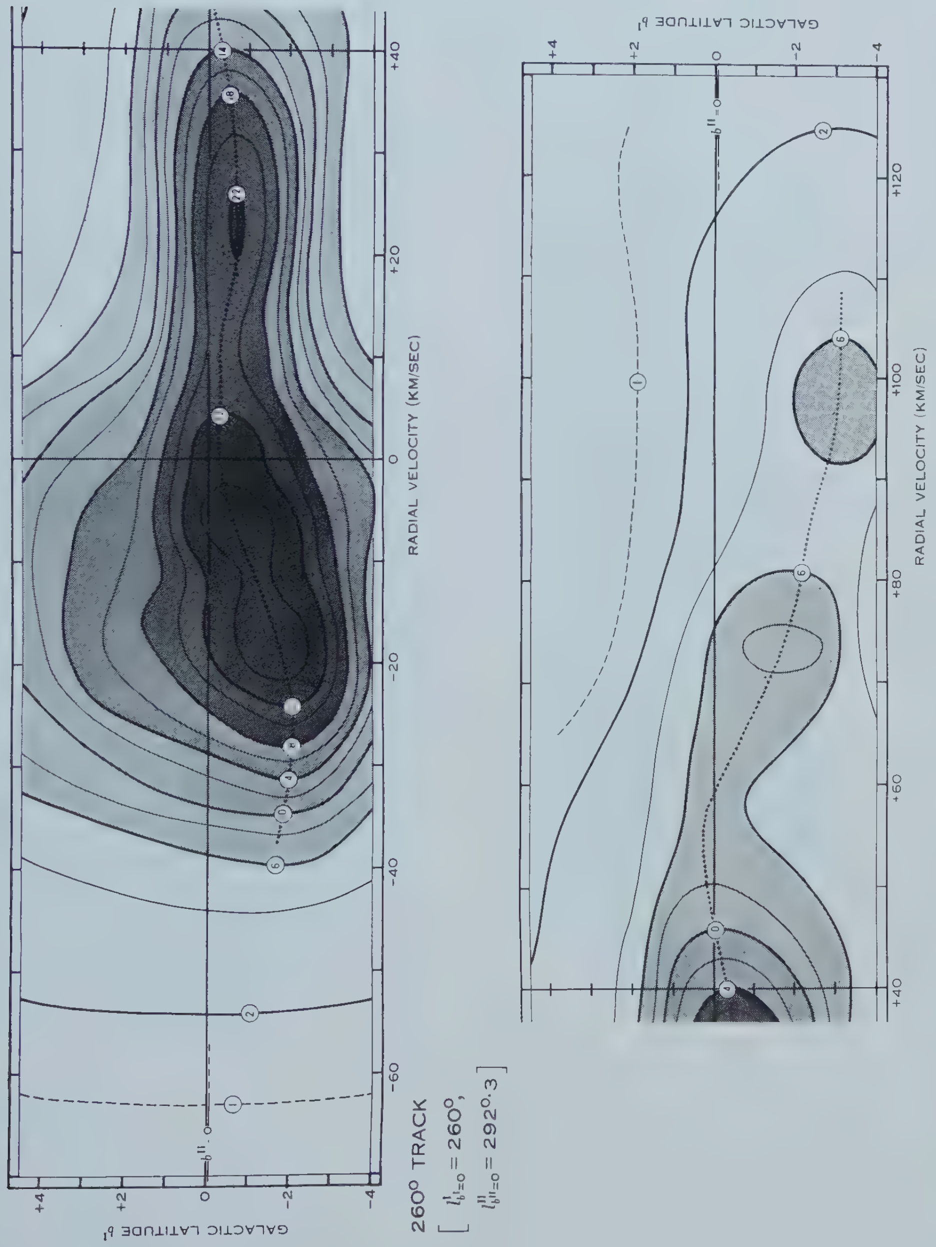

260° TRACK

$\left[\; l^{I}_{b^{I}=0} = 260^{\circ},\quad l^{II}_{b^{II}=0} = 292^{\circ}.3 \;\right]$

21 CM SURVEY OF THE SOUTHERN MILKY WAY

264°.8 TRACK $\left[l^{I}_{b^{I}=0}=264^{\circ}.8,\ l^{II}_{b^{II}=0}=297^{\circ}.1\right]$

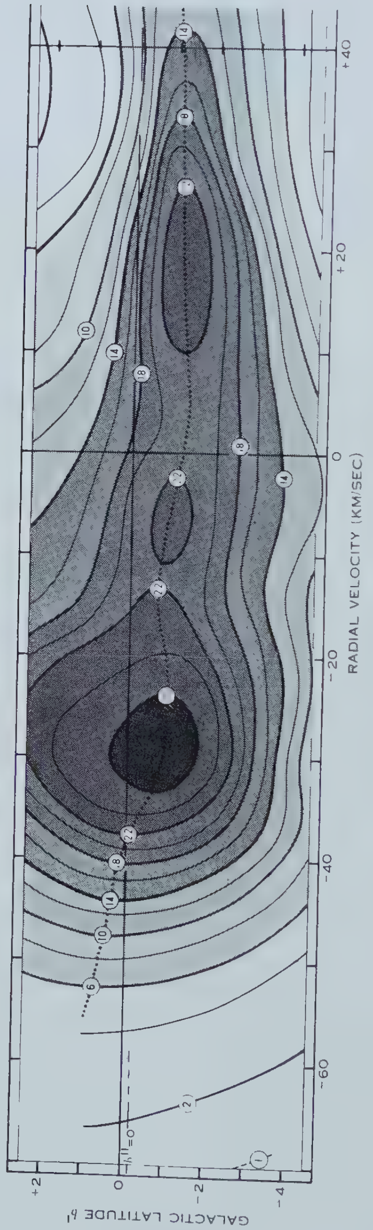

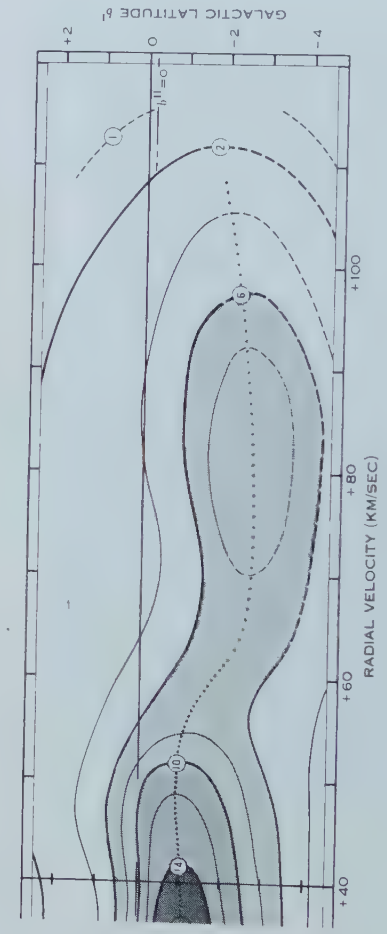

21 CM SURVEY OF THE SOUTHERN MILKY WAY

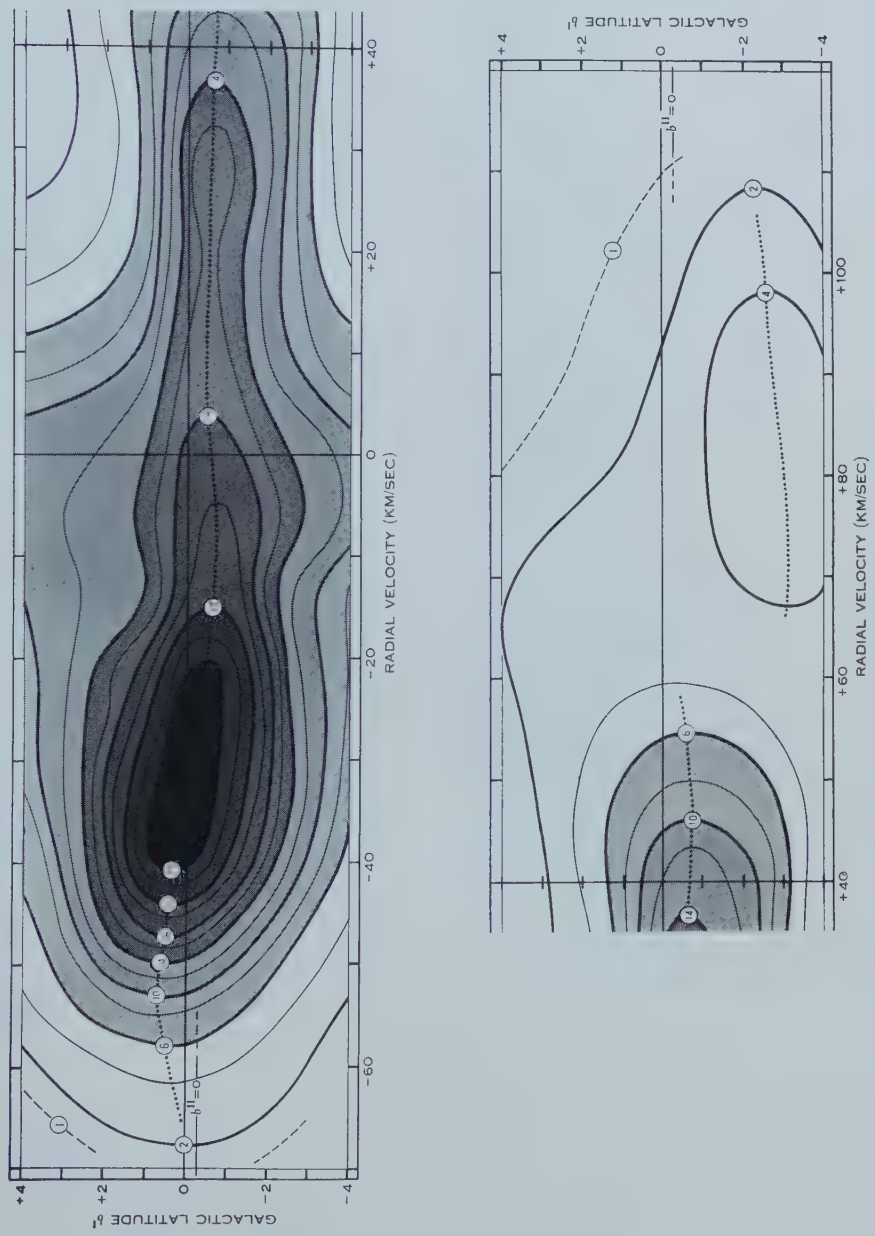

269°.9 TRACK $\left[l^{\mathrm{I}}_{b^{\mathrm{I}}=0}=269°.9,\ l^{\mathrm{II}}_{b^{\mathrm{II}}=0}=302°.0\right]$

21 CM SURVEY OF THE SOUTHERN MILKY WAY

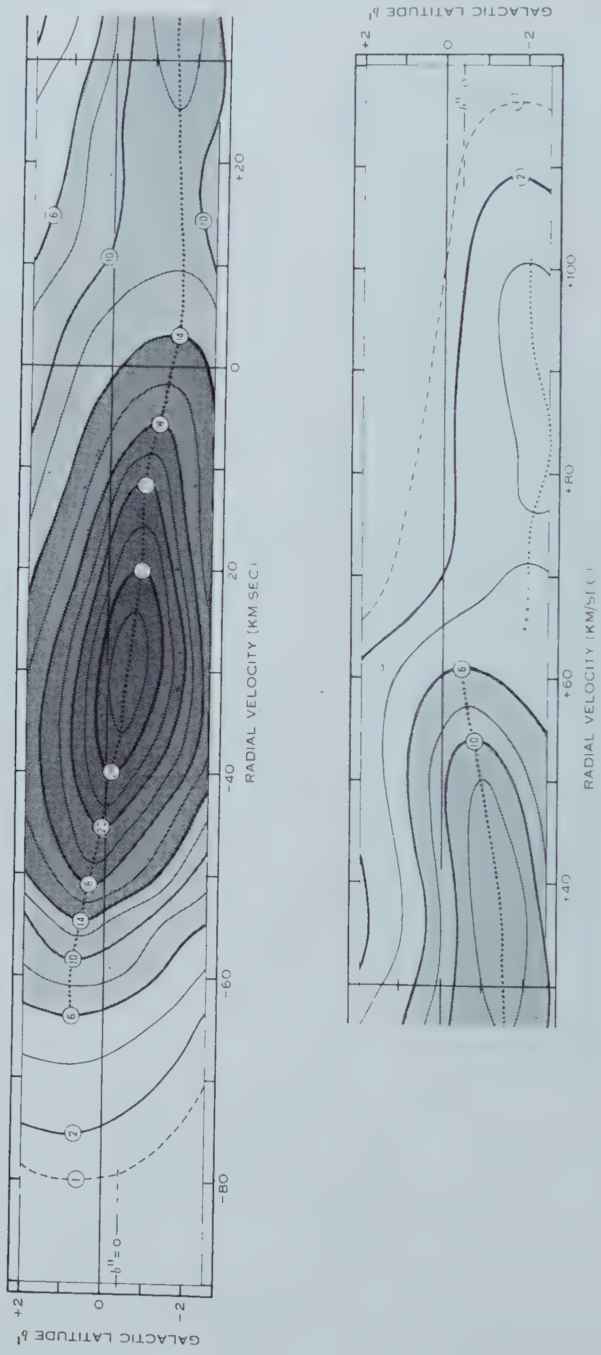

274°·8 TRACK $\left[l^{I}_{b^{I}=0} = 274°·8 \quad l^{II}_{b^{II}=0} = 306°·8\right]$

21 CM SURVEY OF THE SOUTHERN MILKY WAY

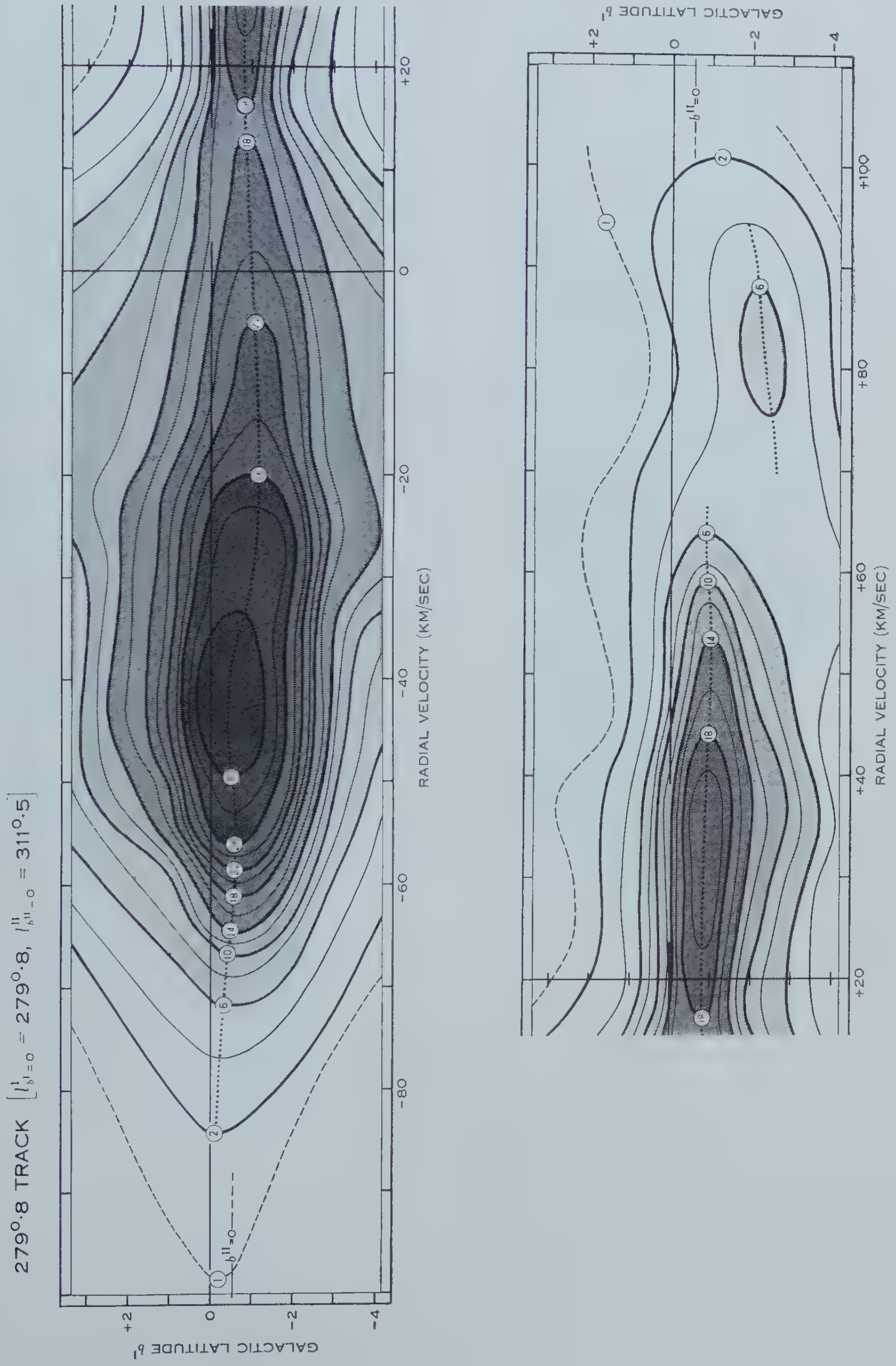

279°.8 TRACK $[l^{\rm I}_{b^{\rm I}=0} = 279^\circ.8,\ l^{\rm II}_{b^{\rm II}=0} = 311^\circ.5]$

21 CM SURVEY OF THE SOUTHERN MILKY WAY

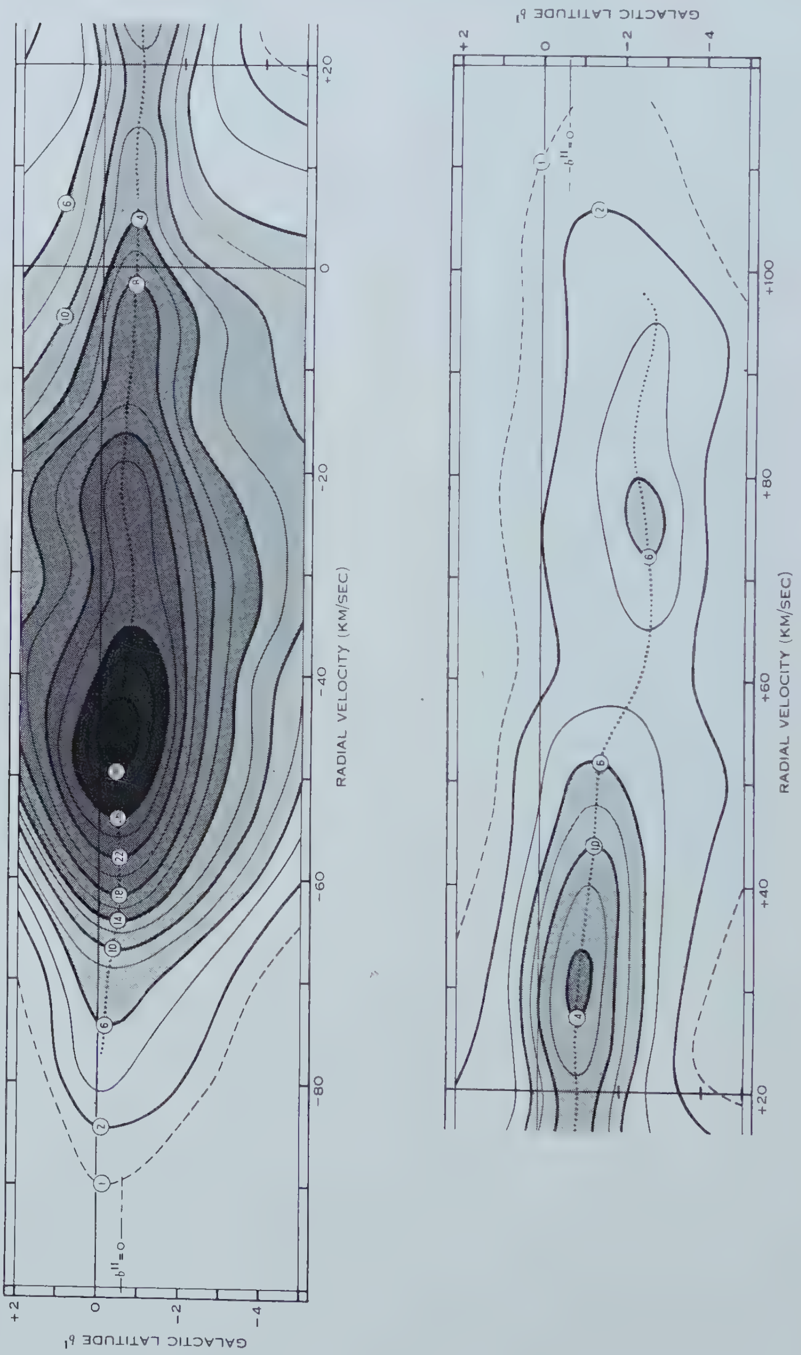

282°.7 TRACK $\left[l^I_{b^I=0} = 282^\circ.7,\ l^{II}_{b^{II}=0} = 315^\circ.0\right]$

21 CM SURVEY OF THE SOUTHERN MILKY WAY

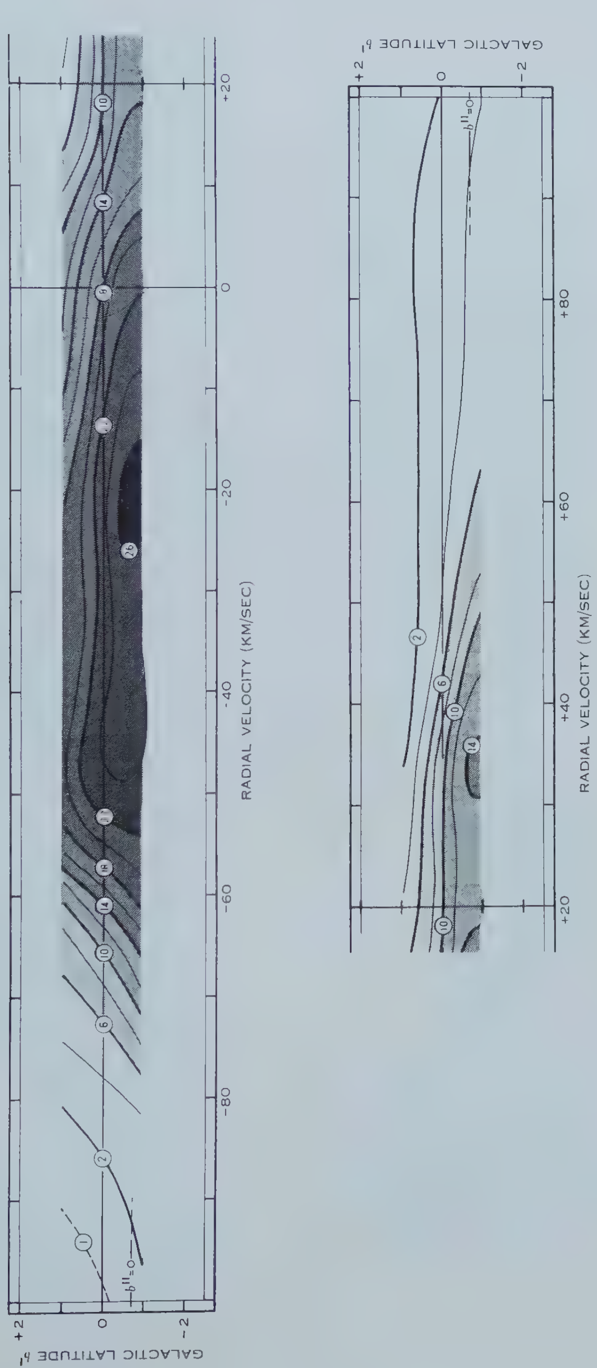

285° TRACK [$\delta = -58°\cdot 8$, $l^{I}_{b^{I}=0} = 285°$, $l^{II}_{b^{II}=0} = 318°\cdot 7$]

21 CM SURVEY OF THE SOUTHERN MILKY WAY

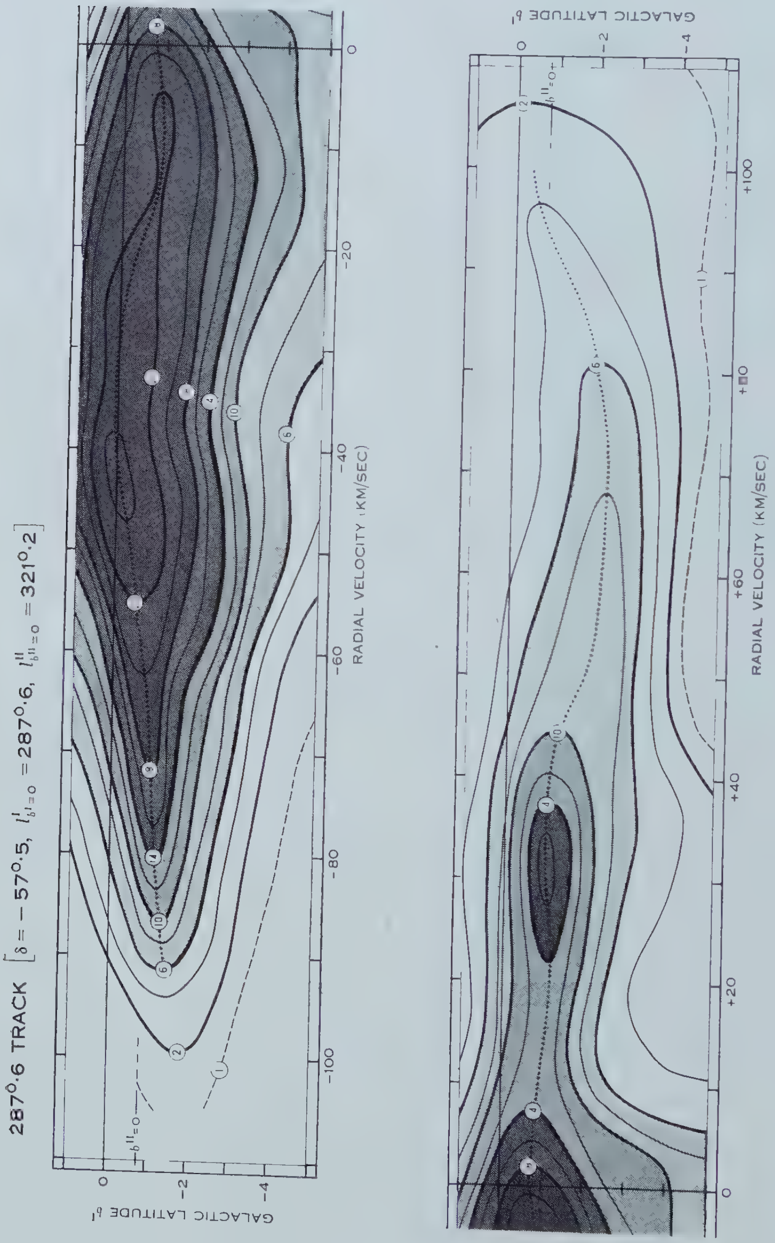
287°.6 TRACK $[\delta = -57°.5,\ l^{I}_{b^{I}=0} = 287°.6,\ l^{II}_{b^{II}=0} = 321°.2]$

21 CM SURVEY OF THE SOUTHERN MILKY WAY

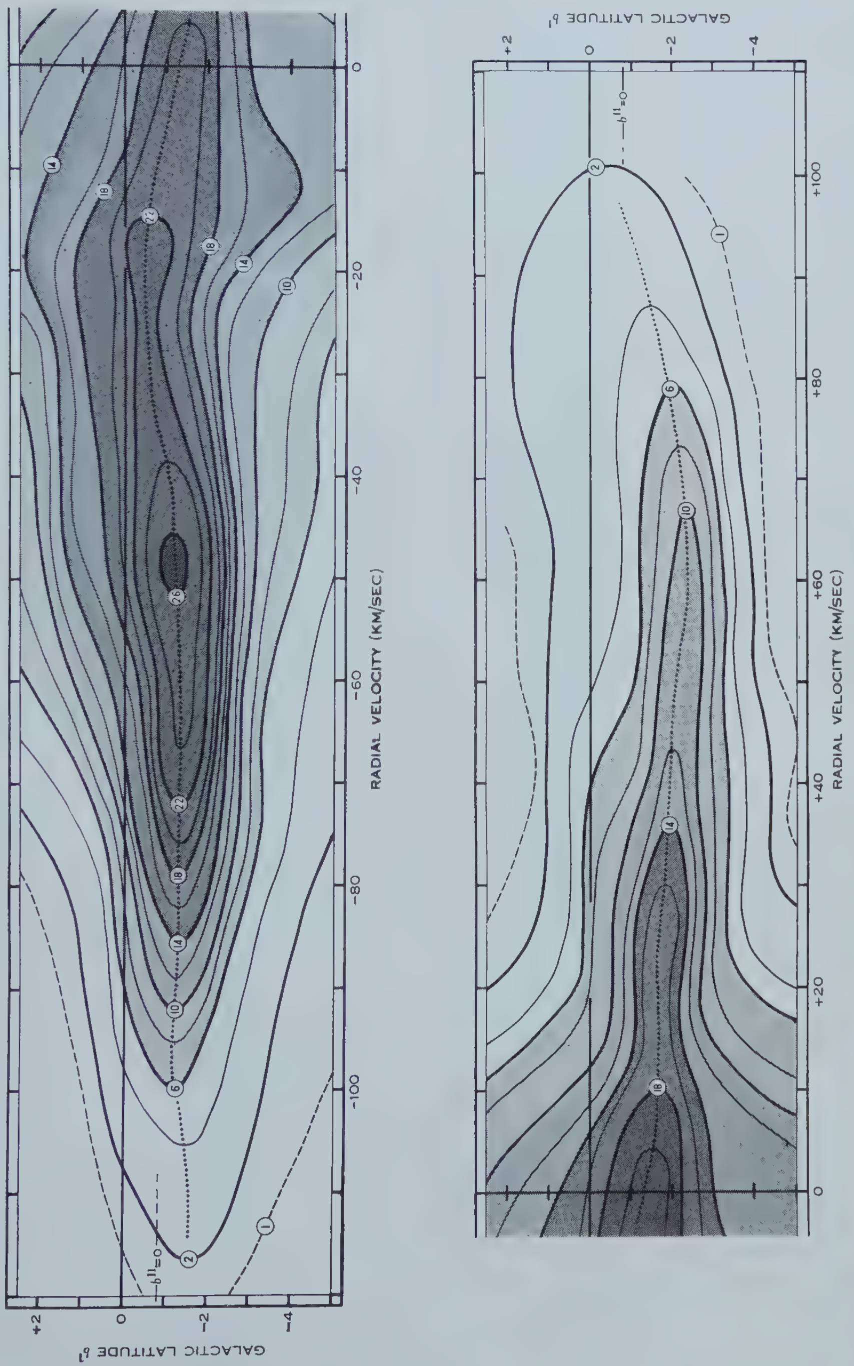

290° TRACK $[\delta = -56°.3,\ l^{I}_{b^{I}=0} = 290°,\ l^{II}_{b^{II}=0} = 323°.5]$

21 CM SURVEY OF THE SOUTHERN MILKY WAY

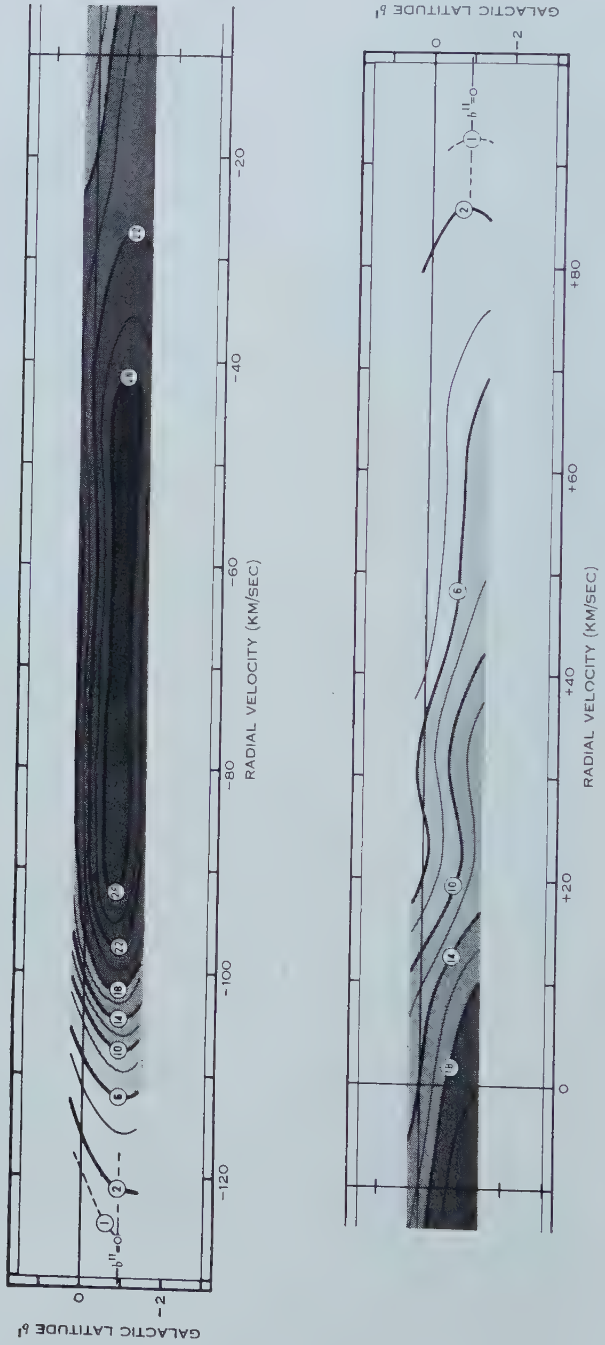

295° TRACK $\left[\delta = -53^{\circ}\cdot 3,\ l^{I}_{b^{I}=0} = 295^{\circ},\ l^{II}_{b^{II}=0} = 328^{\circ}\cdot 5\right]$

21 CM SURVEY OF THE SOUTHERN MILKY WAY

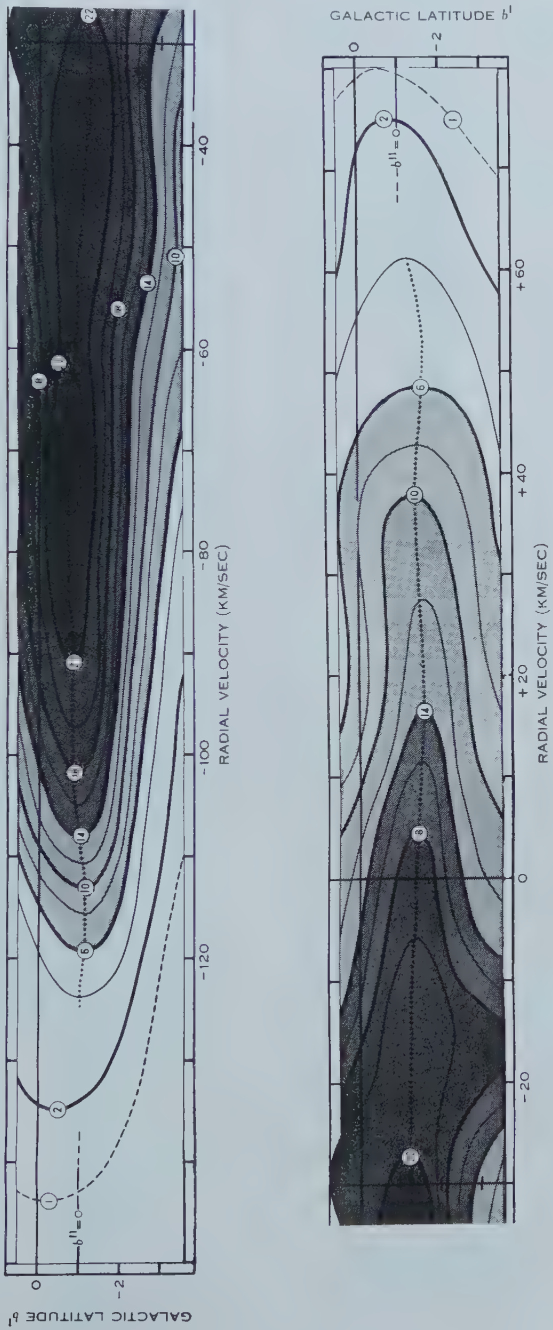

298°.5 TRACK $[\delta = -51°.0,\ l^{I}_{b^{I}=0} = 298°.5,\ l^{II}_{b^{II}=0} = 331°.9]$

21 CM SURVEY OF THE SOUTHERN MILKY WAY

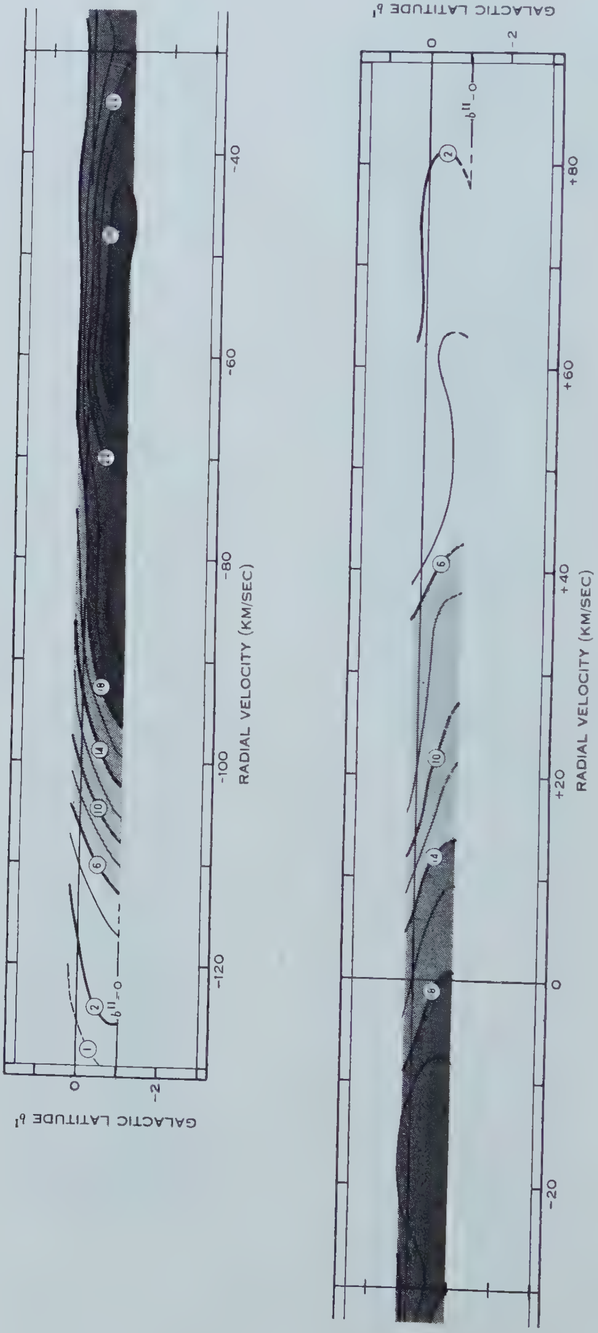

300° TRACK $\left[\delta = -50^{\circ}\cdot 0,\ l^{I}_{b^{I}=0} = 300^{\circ},\ l^{II}_{b^{II}=0} = 333^{\circ}\cdot 4\right]$

21 CM SURVEY OF THE SOUTHERN MILKY WAY

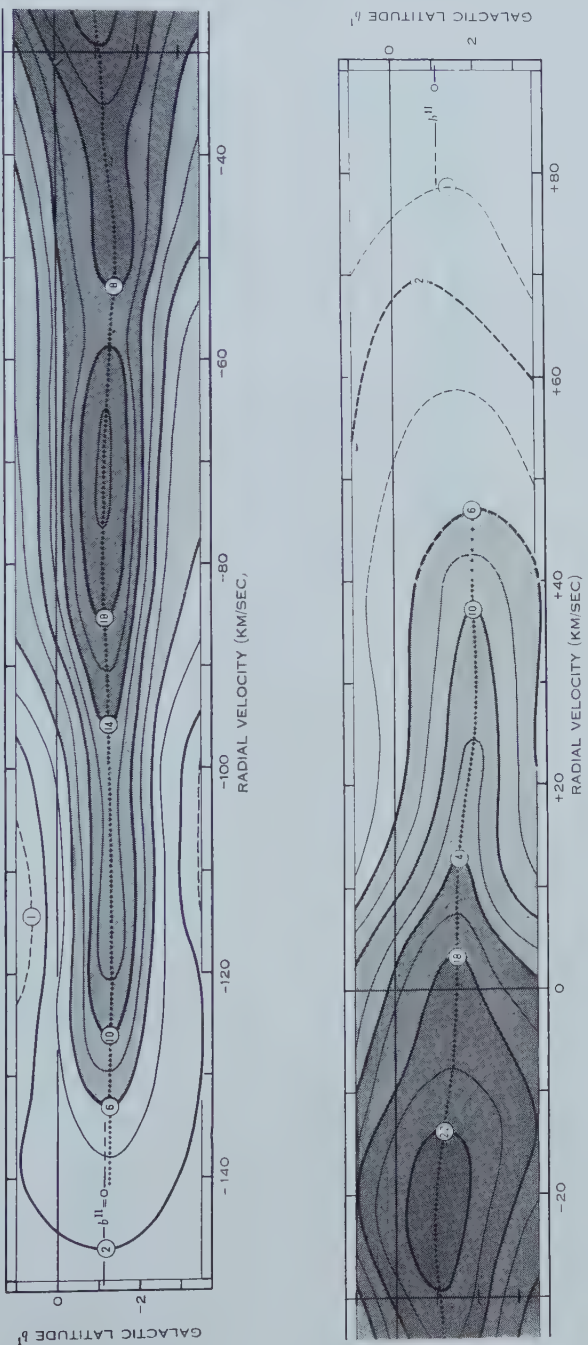

303°.6 TRACK $[\delta = -47°.4,\ l^{I}_{b^{I}=0} = 303°.6,\ l^{II}_{b^{II}=0} = 337°.0]$

21 CM SURVEY OF THE SOUTHERN MILKY WAY

305° TRACK $\left[\delta = -46°.4,\ l^{I}_{b^{I}=0} = 305°,\ l^{II}_{b^{II}=0} = 338°.3\right]$

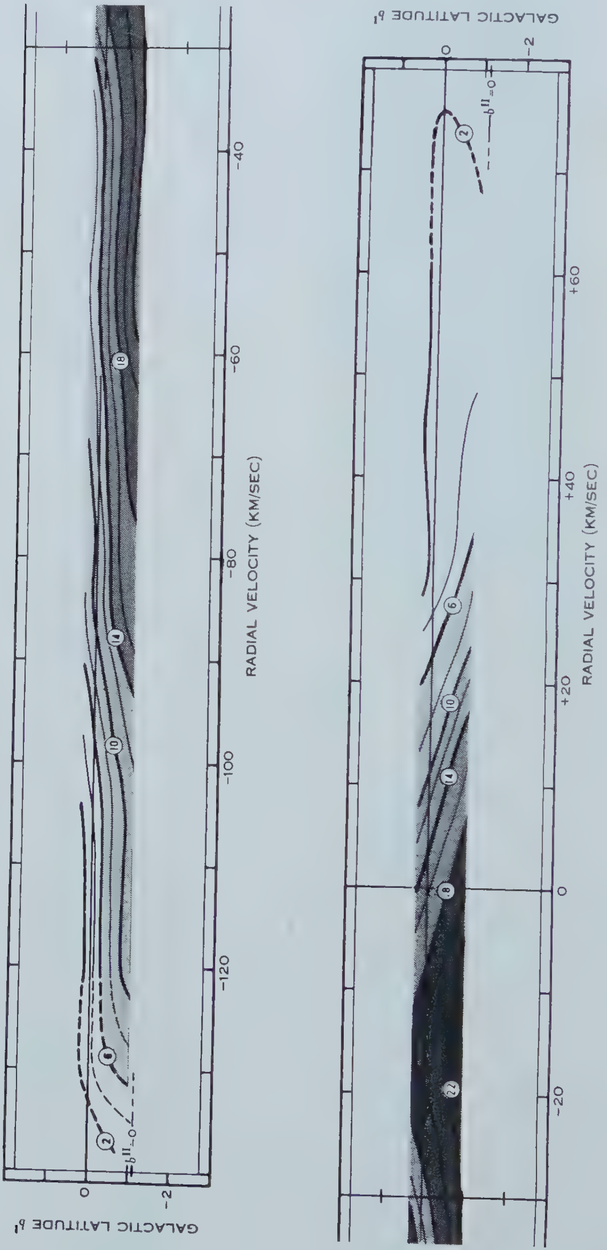

21 CM SURVEY OF THE SOUTHERN MILKY WAY

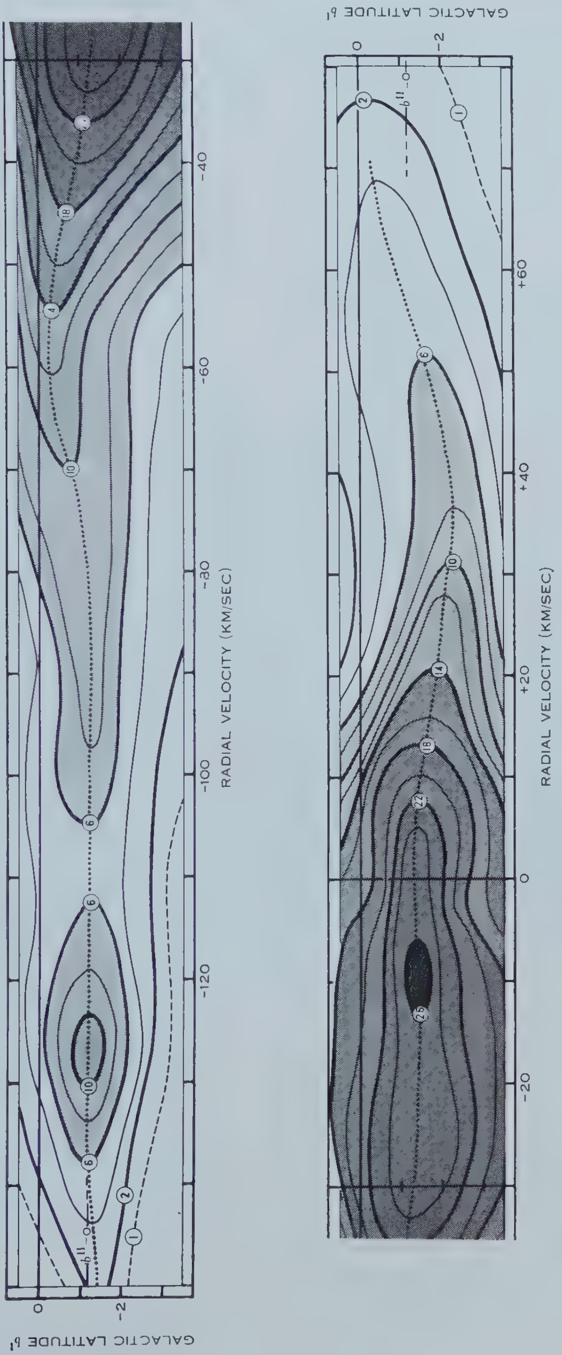

308°.8 TRACK $\left[\delta=-43°.6,\ l^{I}_{b^{II}=0}=303°.8,\ l^{II}_{b^{II}=0}=342°.1\right]$

21 CM SURVEY OF THE SOUTHERN MILKY WAY

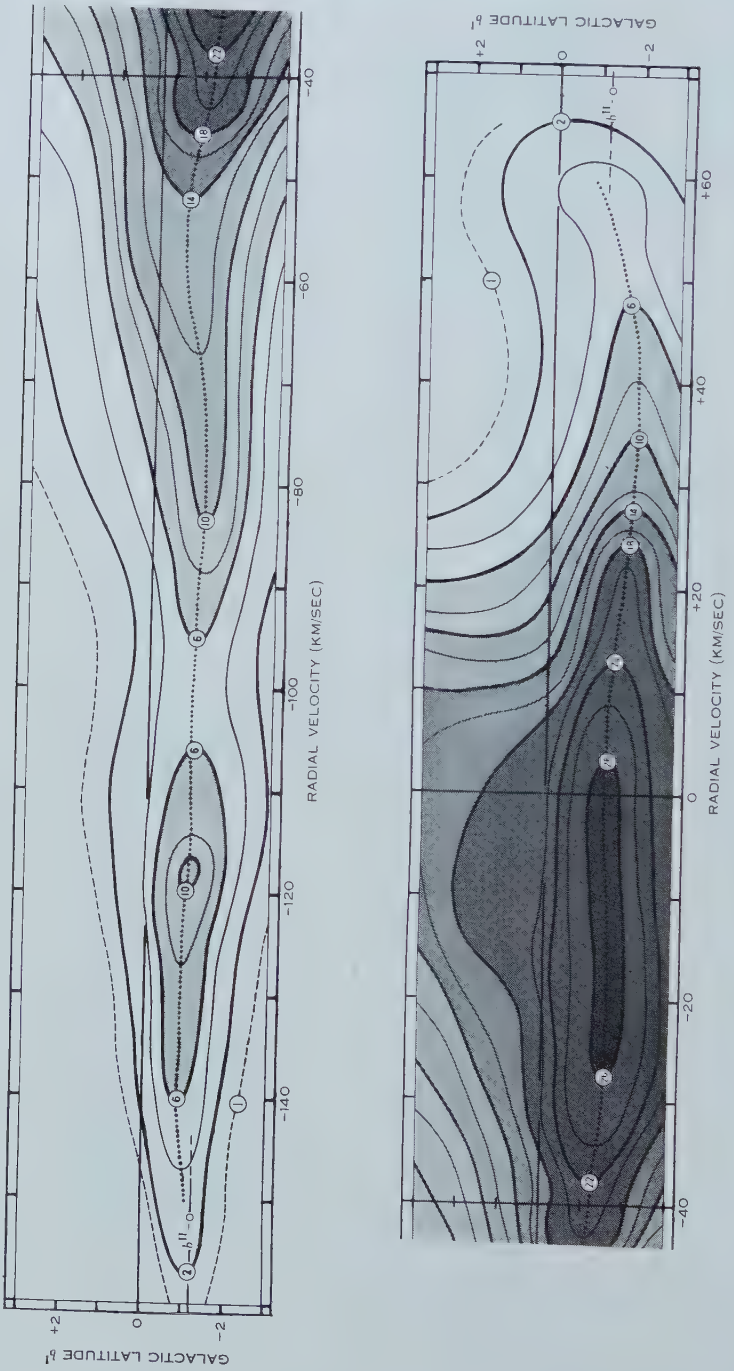

310° TRACK $\left[\delta = -42^\circ.7,\ l^{I}_{b^{I}=0} = 310^\circ,\ l^{II}_{b^{II}=0} = 343^\circ.3\right]$

21 CM SURVEY OF THE SOUTHERN MILKY WAY

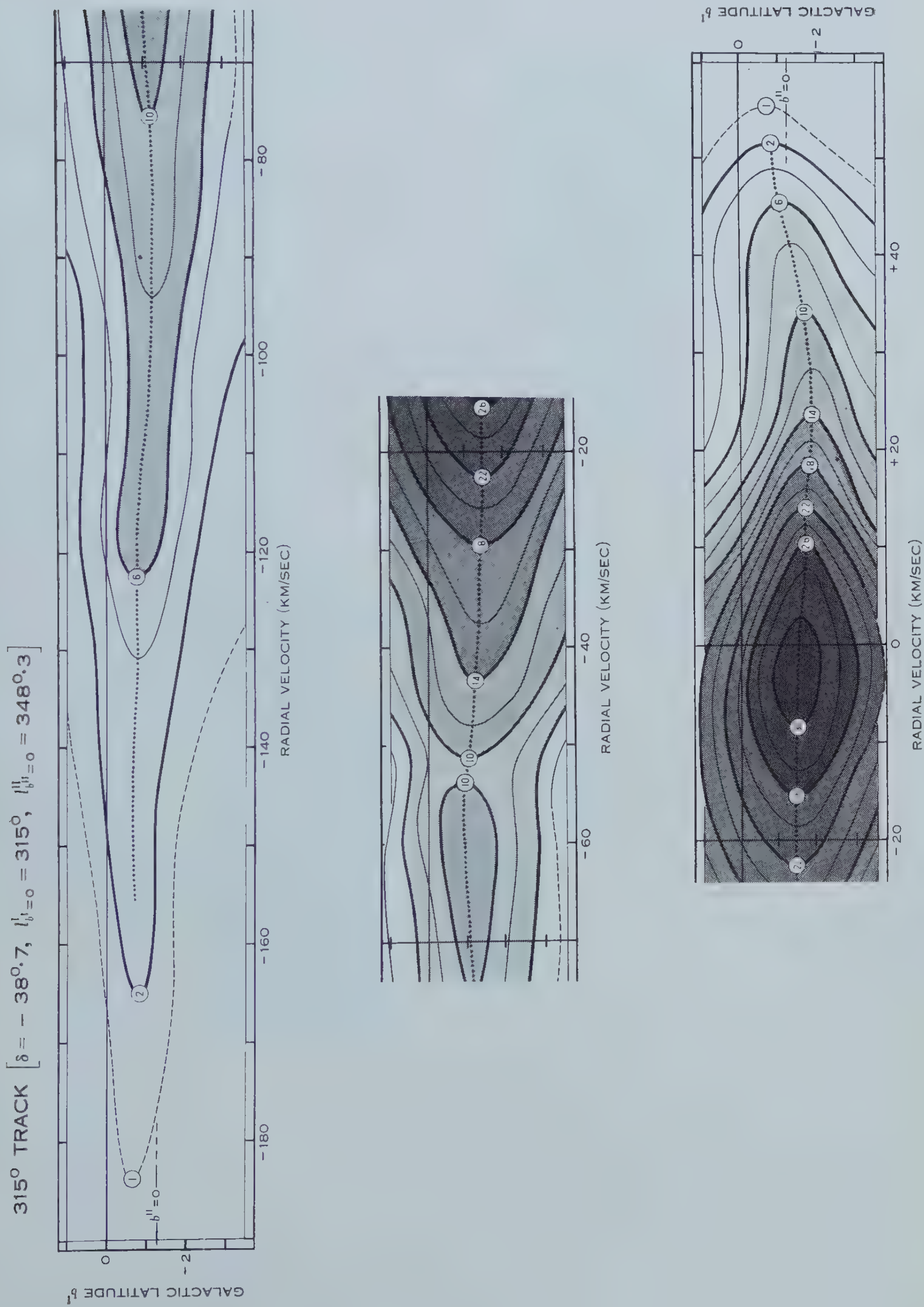

315° TRACK $\left[\delta = -38^\circ.7,\ l^{\mathrm{I}}_{b^{\mathrm{I}}=0} = 315^\circ,\ l^{\mathrm{II}}_{b^{\mathrm{II}}=0} = 348^\circ.3\right]$

21 CM SURVEY OF THE SOUTHERN MILKY WAY

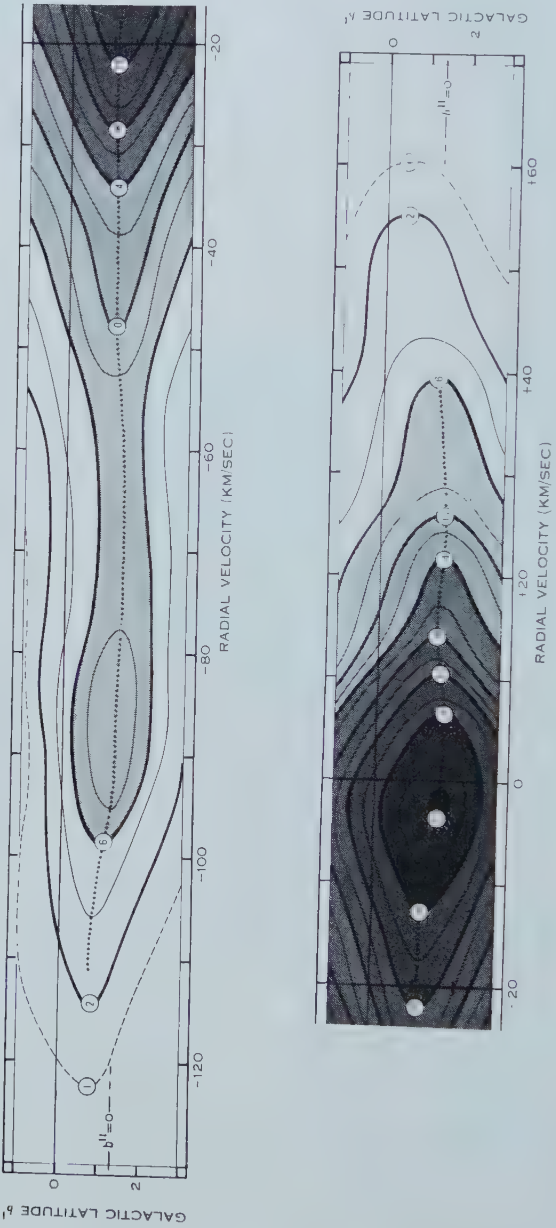

320° TRACK $\left[\delta = -34^\circ.6,\ l'_{b'=0} - 320^\circ,\ l''_{b''=0} = 353^\circ.2\right]$

21 CM SURVEY OF THE SOUTHERN MILKY WAY

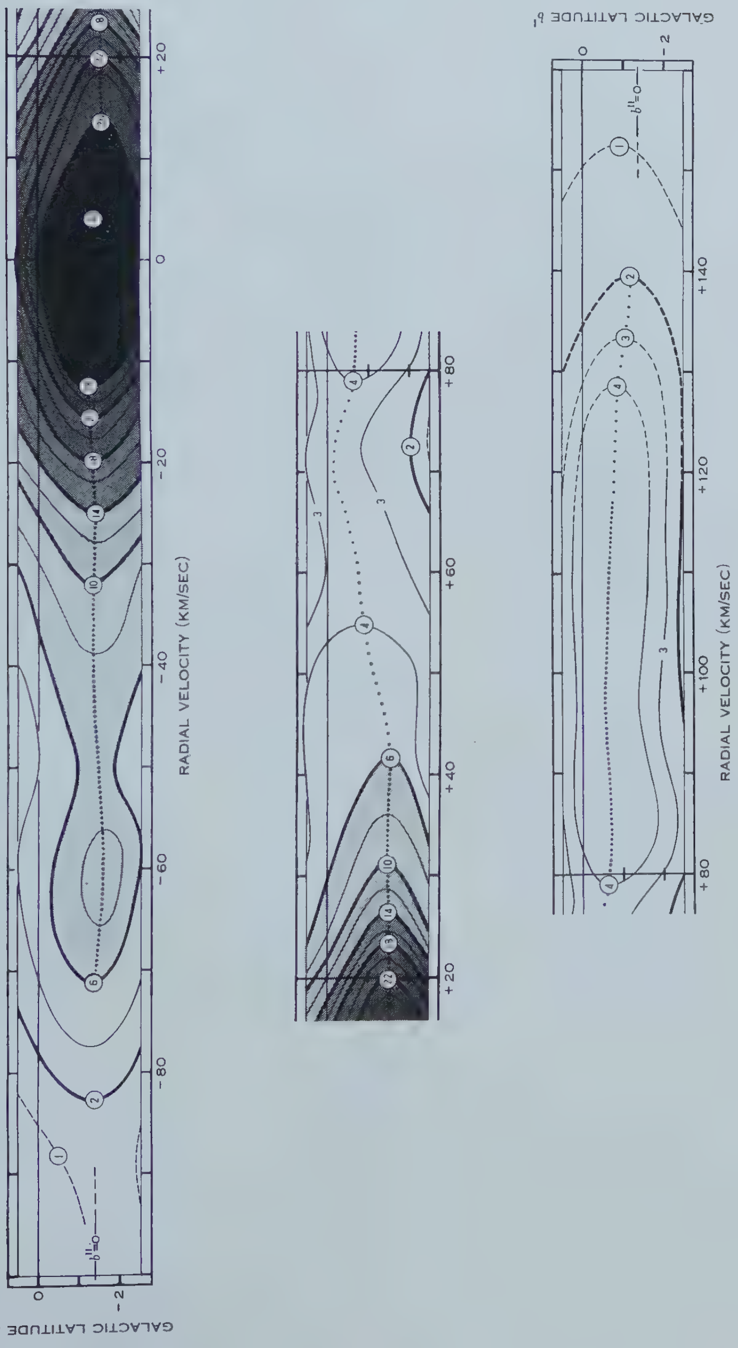

325° TRACK $\left[\delta = -30°.5,\ l^{I}_{b^{I}=0} = 325°,\ l^{II}_{b^{II}=0} = 358°.2\right]$

21 CM SURVEY OF THE SOUTHERN MILKY WAY

330° TRACK $\left[\delta = -26°.2,\ l^{I}_{b^{I}=0} = 330°,\ l^{II}_{b^{II}=0} = 3°.2\right]$

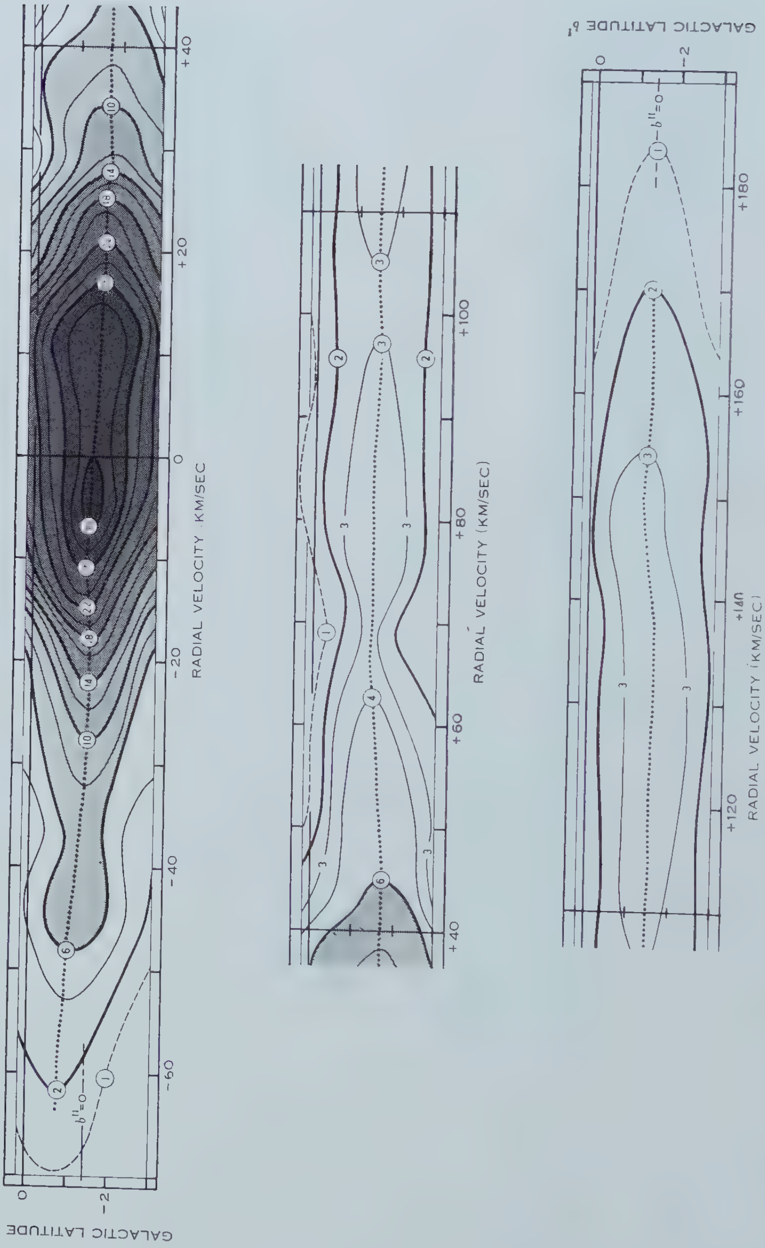

21 CM SURVEY OF THE SOUTHERN MILKY WAY

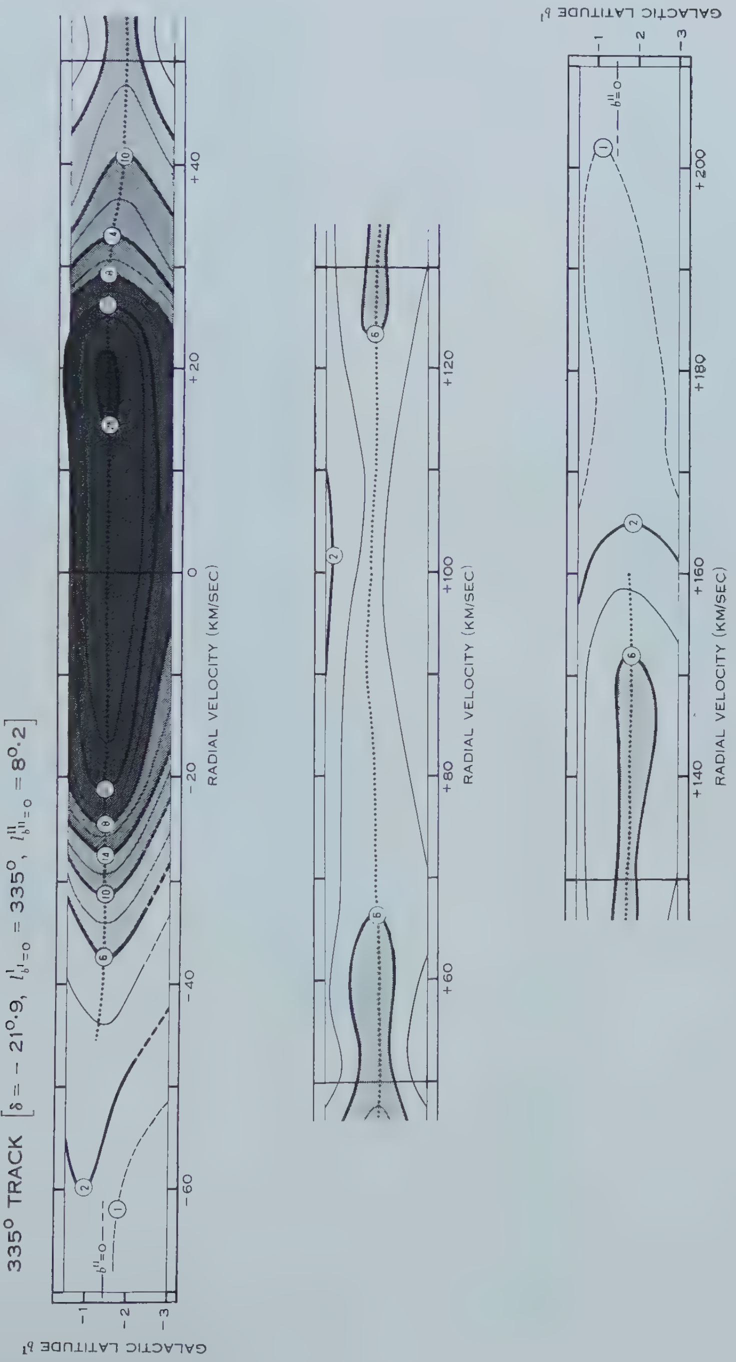

21 CM SURVEY OF THE SOUTHERN MILKY WAY

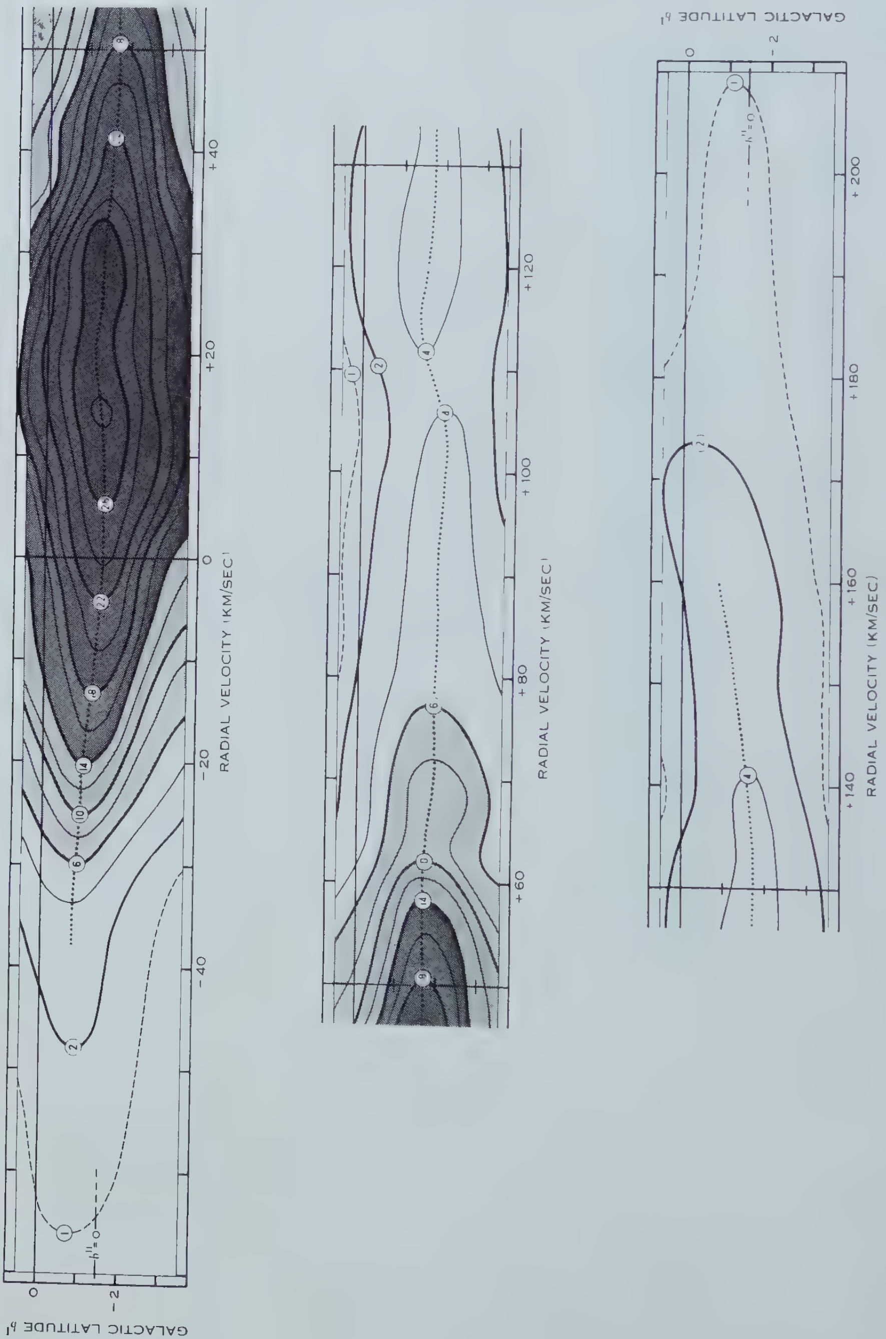

340° TRACK $[\delta = -17°.6,\ l^{I}_{b^{I}=0} = 340°,\ l^{II}_{b^{II}=0} = 13°.1]$

21 CM SURVEY OF THE SOUTHERN MILKY WAY

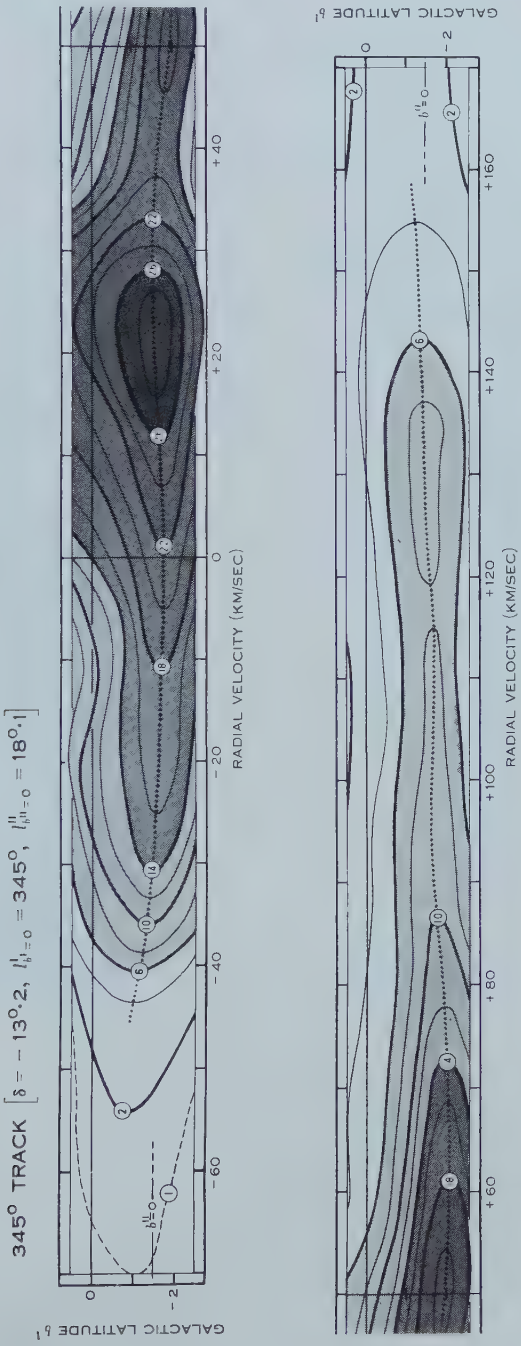

345° TRACK $[\delta = -13°{\cdot}2,\ l^I_{b^{II}=0} = 345°,\ l^{II}_{b^{II}=0} = 18°{\cdot}1]$

21 CM SURVEY OF THE SOUTHERN MILKY WAY

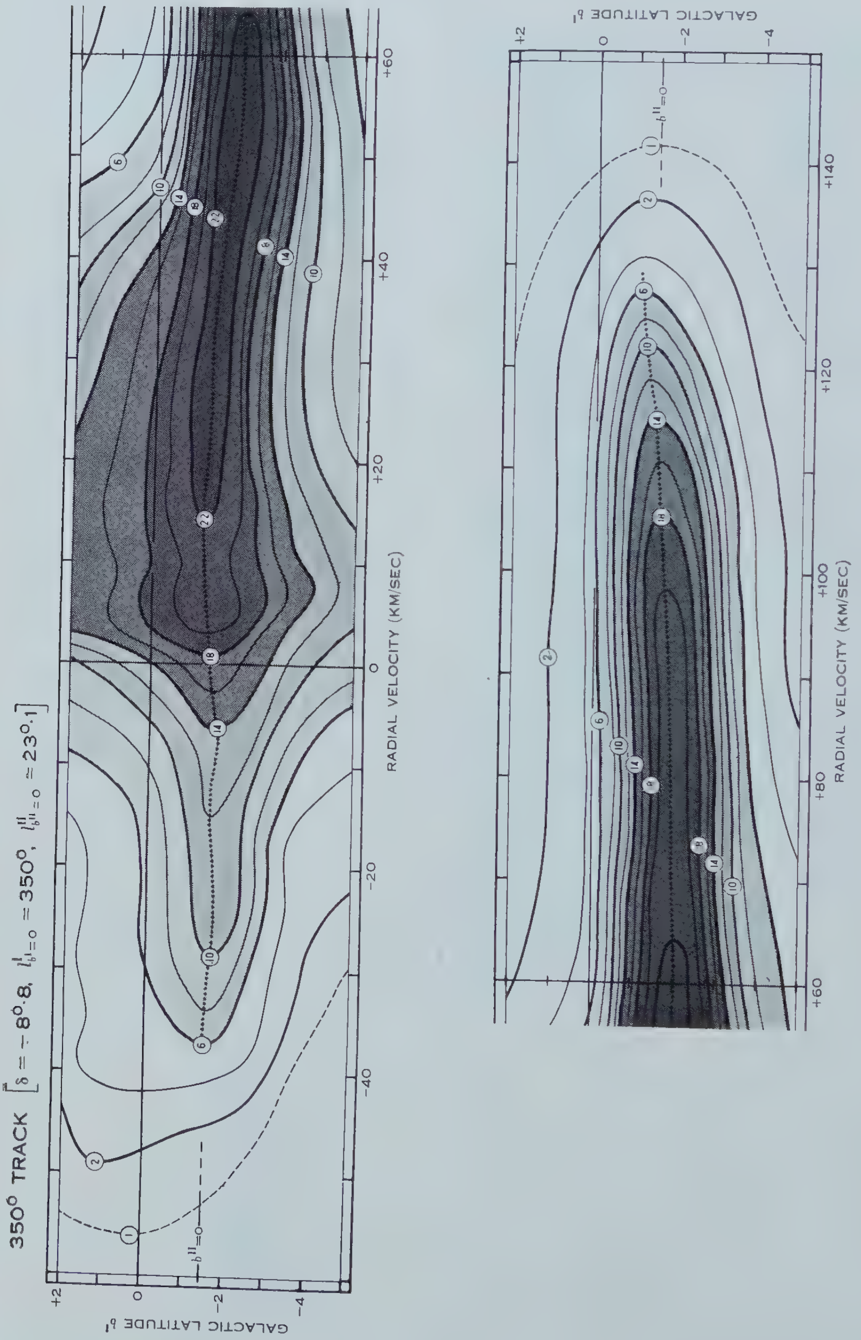

21 CM SURVEY OF THE SOUTHERN MILKY WAY

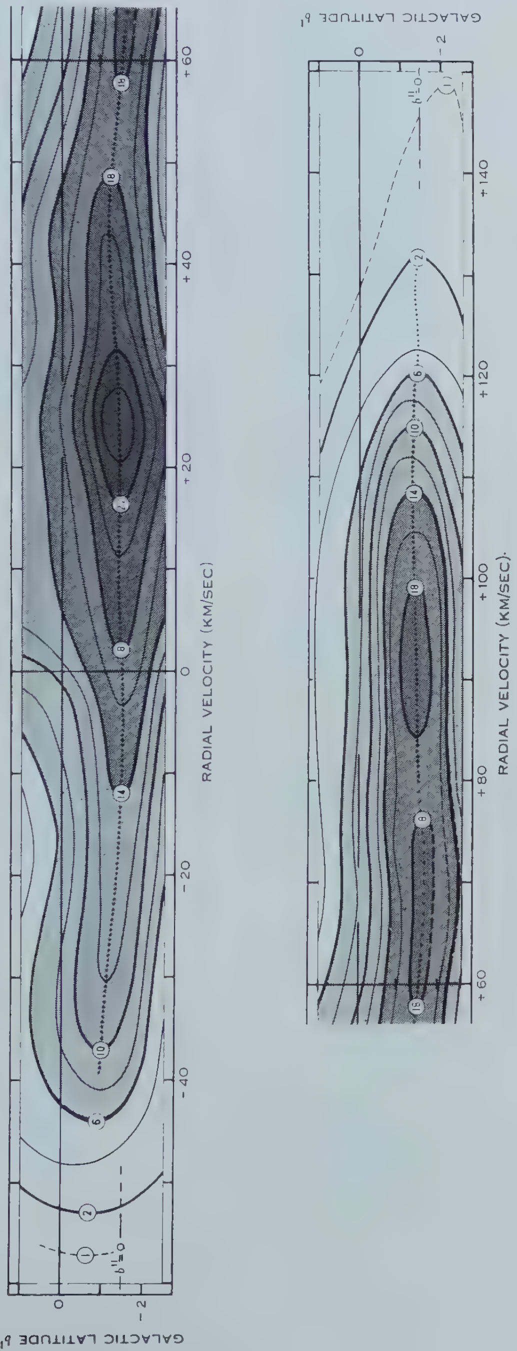

353°.4 TRACK $\left[\delta = -5^{\circ}.8,\ l^{I}_{b^{I}=0} = 353^{\circ}.4,\ l^{II}_{b^{II}=0} = 26^{\circ}.5\right]$

21 CM SURVEY OF THE SOUTHERN MILKY WAY

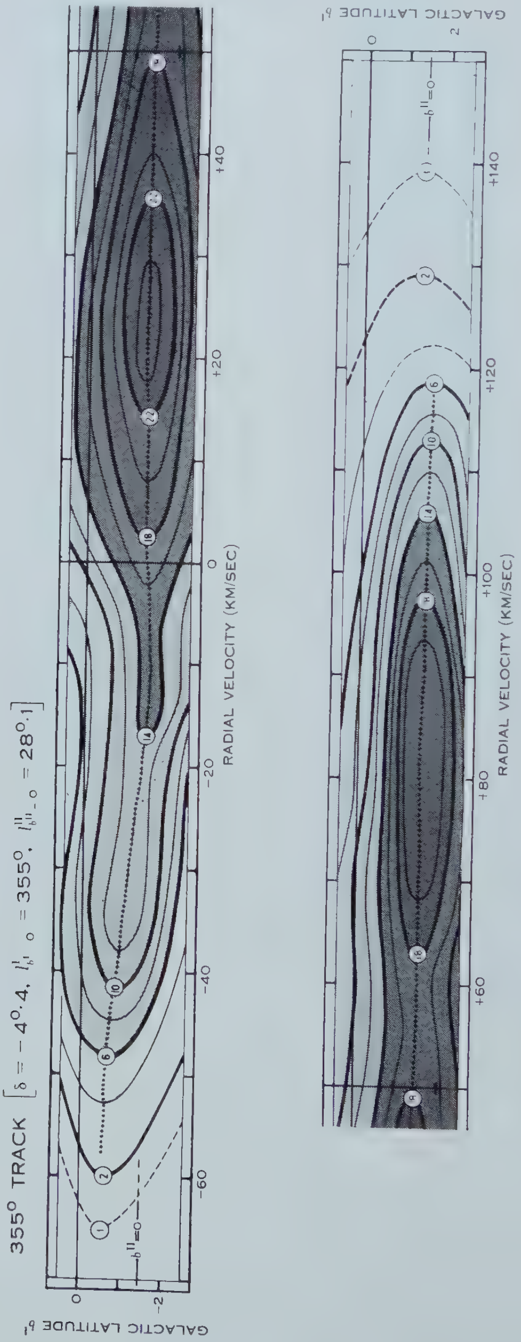

355° TRACK $[\delta = -4^\circ.4,\ l^{I}_{b^{I}=0} = 355^\circ,\ l^{II}_{b^{II}=0} = 28^\circ.1]$

21 CM SURVEY OF THE SOUTHERN MILKY WAY

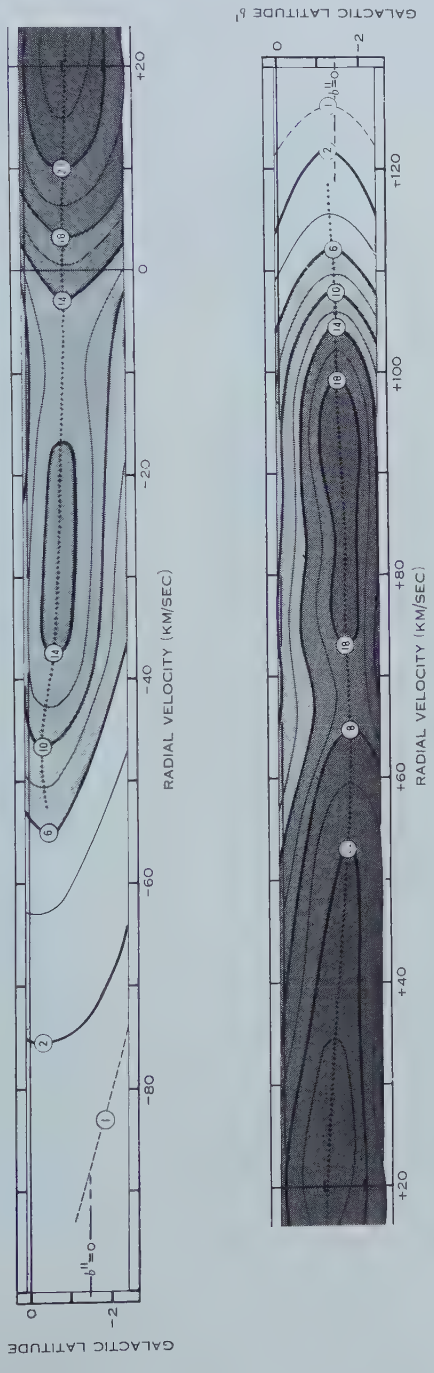

360° TRACK [$\delta = +0°.1$, $l^{I}_{b^{I}=0} = 360°$, $l^{II}_{b^{II}=0} = 33°.0$]

21 CM SURVEY OF THE SOUTHERN MILKY WAY

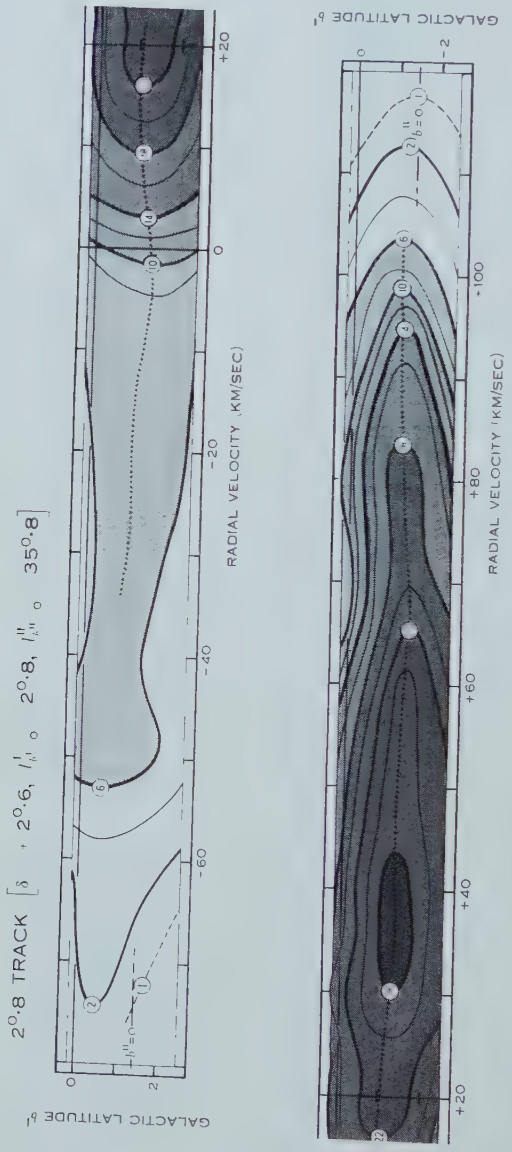

21 CM SURVEY OF THE SOUTHERN MILKY WAY

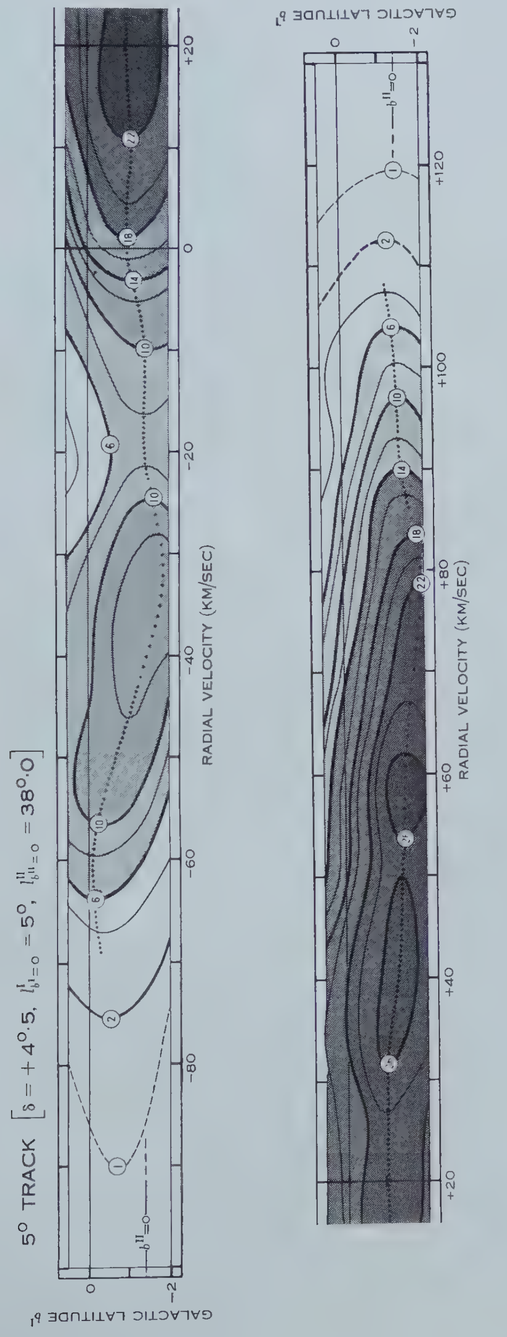

5° TRACK $[\delta = +4^\circ.5,\ l^{\mathrm{I}}_{b^{\mathrm{I}}=0} = 5^\circ,\ l^{\mathrm{II}}_{b^{\mathrm{II}}=0} = 38^\circ.0]$

SHORT COMMUNICATIONS

SPINS AND PARITIES OF LEVELS OF ^{9}Be BELOW 15 MeV*

By H. H. Thies† and B. M. Spicer†

In a recent study of the cross section of the reaction $^9\mathrm{Be}(\gamma,n)$ (Thies, Spicer, and Baglin 1959), distinct maxima were observed at 11·25 and 13·25 MeV. The maximum at 11·25 MeV was identified with the known level at 11·3 MeV and the 13·25 MeV maximum was attributed to absorption by one level at that energy. The nearly equal widths of the 11·25 and 13·25 MeV peaks justify this assumption. These peaks were attributed to $M1$ or $E1$ absorption by Thies, Spicer, and Baglin (1959).

A recent experiment on the electro-disintegration of ^{9}Be (Barber 1958) shows that, for excitations from 6 to 17 MeV, this nucleus is excited predominantly by $E1$ transitions and not $M1$ transitions. As the 11·25 and 13·25 MeV maxima are the only significant contributions to the (γ,n) cross section in the energy region 10–15 MeV, it is concluded that they are due to $E1$ transitions. In this case, the corresponding levels can have only the following assignments: $J=1/2$, $3/2$, $5/2^+$ (since the ground state of ^{9}Be is $J=3/2^-$).

The parameters of the 1·7 MeV level in ^{9}Be have been given by the photo-disintegration experiment of Connors and Miller (1956). From their results, the integrated cross section for absorption into this level is of the same order as that into the 11·25 and 13·25 MeV levels. Therefore, it may be tentatively inferred that this level is also excited by an $E1$ transition and is thus of even parity. This level was also observed (B. M. Spicer, unpublished data) in a betatron experiment on the $^9\mathrm{Be}(\gamma,n)$ reaction, in which the yield curve was measured in steps of 30 keV from threshold to 4·5 MeV. However, this experiment did not detect any effect due to the known levels at 2·43 or 3·05 MeV. Therefore, these levels either have odd parity (and are therefore excited by weaker $M1$ or $E2$ transitions) or even parity and $J\geqslant 7/2$.

The known levels of ^{9}Be will be considered below and spin and parity assignments made on the basis of present knowledge from charged particle reactions and the above considerations.

1·7 MeV level.—D. W. Miller (1958) has established beyond doubt the existence of an excited state at 1·7 MeV. In the charged particle reactions a spectrum edge from three-body break-up makes observation of this level difficult. Miller gives several independent arguments supporting the assignment of $J=1/2^+$ for this state, but leaves open the possibility $J=1/2^-$ as this contention seemed to be supported by the interpretation of the (γ,n) experiment of Connors

---

* Manuscript received March 20, 1959.

† Physics Department, University of Melbourne.

and W. C. Miller (1956). These authors referred to unpublished work of Mast, in which it was stated that a shell model calculation had shown the 1·7 MeV level to be excited by an $M1$ transition. However, an abstract of a report by Mast and Mullin (1956) shows that this γ-transition takes place to a state having $J=1/2^+$. This work is stated to be an intermediate coupling shell model calculation.

Thus, considering all available evidence, the assignment for the 1·7 MeV state is $J=1/2^+$.

2·43 MeV level.—The work of Summers-Gill (1958) on the inelastic scattering of protons, deuterons, and α-particles from ^{9}Be gives $J=5/2^-$ as the only possible assignment. The interpretation of the angular distributions for scattering used the theory of Austern, Butler, and McManus (1953). His assignment is in agreement with the non-appearance of the level in the (γ,n) study referred to above. This evidence indicates the weakness of $M1$ transitions in this nucleus.

3·05 MeV level.—Bockelman, Leveque, and Buechner (1956) placed the lower limit of 280 keV on the width of this level. Using the Wigner sum rule on reduced widths of levels, they state that $J\leqslant 3/2$. This being so, the (γ,n) result of Spicer (unpublished data) requires that the parity be odd. This is consistent with a $J=1/2^-$ assignment for a level near 3 MeV from intermediate coupling shell model calculations of Kurath (1956).

4·8 MeV level.—This level has width 1·2 MeV (Almqvist, Allen, and Bigham 1955). The intermediate coupling prediction is for three levels near this energy, having $J=3/2^-$, $5/2^-$, $7/2^-$ respectively. This may explain the large observed width (see Fig. 1).

6·8 MeV and 7·9 MeV levels.—Benveniste, Finke, and Martinelli (1956) measured the angular distribution of inelastically scattered protons which leave ^{9}Be in these levels. Bombardment was with 31 MeV protons, and the distributions were analysed using the direct interaction theory of Austern, Butler, and McManus (1953). Benveniste, Finke, and Martinelli's interpretation has been criticized by Summers-Gill (1958) on the ground that the interaction radius they use is unrealistically small. In his own work, Summers-Gill established the radius to be used from elastic scattering data, and obtained good fits to his data with values of the radius between 4·5 and 5·5 fermis. Benveniste's results have been re-examined, using this larger radius. It was found that the angular distribution from the " 6·8 MeV level " could not be fitted with the assumption of one level, but requires two levels of opposite parity. This is in line with the findings of Benveniste, Finke, and Martinelli (1956) and is insensitive to the value of nuclear radius chosen. Thus we find that we need one level having $1/2\leqslant J\leqslant 11/2^+$ and another of lower energy having $J=1/2$, $5/2$, $7/2$, $9/2^-$, to explain the position of the peak in the angular distribution.

The 7·94 MeV level is fitted uniquely in this manner, the fit being for angular momentum transfer of 5 units in the scattering. This is consistent with the small cross section for inelastic scattering to this level. These data suggest a spin of $5/2\leqslant J\leqslant 15/2$ and even parity. In the (γ,n) experiment of Thies, Spicer, and Baglin (1959) there is substantial cross section between 6 and 8 MeV.

This, taken with Barber's (1958) electro-disintegration experiment, indicates $E1$ transitions to levels in this region. Thus the γ-absorbing levels must have $J=1/2,\ 3/2,\ 5/2^+$.

Taking these two pieces of evidence together, the spin and parity of the 7·94 MeV level is fixed at $5/2^+$. The even parity level near 6·8 MeV has $J=1/2$, $3/2,\ 5/2^+$.

9·2 MeV level.—The existence of this level is not certain. Evidence for it was found by Almqvist, Allen, and Bigham (1955) on the basis of a study of the proton groups from the reaction ^{7}Li(^{3}He,p)^{9}Be. Thies, Spicer, and Baglin (1959) note that there must be a substantial contribution to the (γ,n) cross section due to a level near 9 MeV, which is expected, on the basis of the electro-disintegration data, to have $1/2,\ 3/2,\ 5/2^+$.

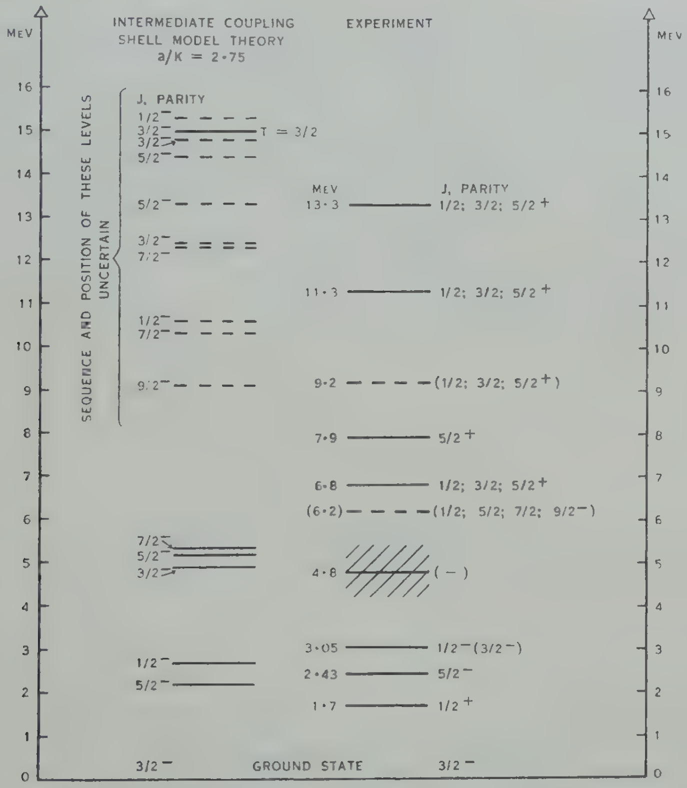

Fig. 1.—Spin and parity of levels of ^{9}Be. Assignments in parentheses are tentative.

11·3 and 13·3 MeV levels.—It has previously been noted that the spins and parities of these levels must be one of $J=1/2,\ 3/2,\ 5/2^+$.

Both French, Halbert, and Pandya (1955) and Kurath (1956) have calculated the energies of odd parity levels of ^{9}Be, for various values of the intermediate coupling parameter a/K. The spectrum of odd parity levels, as far as they are known, is consistent with an a/K value of about 2·75. This, as D. W. Miller

(1958) points out, is in line with the coupling strength required for neighbouring nuclei. The assignments indicated by the above discussion are shown in Figure 1, along with the intermediate coupling predictions of odd parity states for $a/K=2\cdot75$.

The authors wish to thank Professor Sir Leslie Martin for his interest and encouragement throughout this work. One of us (H.H.T.) wishes to thank Imperial Chemical Industries of Australia and New Zealand for a research fellowship, which was held during this work.

References

Almqvist, E., Allen, K. W., and Bigham, C. B. (1955).—*Phys. Rev.* **99** : 631A.
Austern, N., Butler, S. T., and McManus, H. (1953).—*Phys. Rev.* **92** : 350.
Barber, W. C. (1958).—*Phys. Rev.* **111** : 1642.
Benveniste, J., Finke, R. G., and Martinelli, E. A. (1956).—*Phys. Rev.* **101** : 655.
Bockelman, C. K., Leveque, A., and Buechner, W. W. (1956).—*Phys. Rev.* **104** : 456.
Connors, D. R., and Miller, W. C. (1956).—*Bull. Amer. Phys. Soc.* (II) **1** : 340.
French, J. B., Halbert, E. C., and Pandya, S. P. (1955).—*Phys. Rev.* **99** : 1387.
Kurath, D. (1956).—*Phys. Rev.* **101** : 216.
Mast, C. B., and Mullin, C. J. (1956).—*Bull. Amer. Phys. Soc.* (II) **1** : 180.
Miller, D. W. (1958).—*Phys. Rev.* **109** : 1669.
Summers-Gill, R. G. (1958).—*Phys. Rev.* **109** : 1591.
Thies, H. H., Spicer, B. M., and Baglin, J. E. E. (1959).—*Aust. J. Phys.* **12** : 21.

NOTE ON BAND TRANSMISSION IN MULTILAYER DIELECTRIC FILTERS*

By S. C. B. Gascoigne†

The existence of pass and stop bands for periodically stratified media, in particular for multilayer dielectric filters, is well known, but there seems to be no way of demonstrating this either without the use of a good deal of algebra or by appeal to relatively unfamiliar ideas, such as those of transmission line theory. Our purpose here is to show that for an infinite medium, this result can be established by a direct adaptation of the Kronig-Penney (1931) model for metal lattices. Accounts of this model are given in a number of textbooks (Rojansky 1942; Brillouin 1946) and also in undergraduate courses in this country, so that it may be considered well known. Mathematical details will accordingly be abbreviated; they may be found in the references cited.

We consider a periodically stratified medium bounded by planes normal to the x-axis. The refractive index is a step function; for $-a<x<0$ it is n_1, for $0<x<b$ it is n_2, and this structure is repeated indefinitely, with period $a+b$.

---

* Manuscript received May 25, 1959.

† Mount Stromlo Observatory, Canberra.

The differential equation satisfied by the time-independent part of an electromagnetic wave travelling in the x-direction is

$$u''+k^2n^2u=0, \qquad k=2\pi/\lambda.$$

Bounded solutions of this must have the form $u=ve^{i\mu x}$, where μ is real and v periodic with period $a+b$. Substituting for u we find that v must satisfy

$$v_1''+2i\mu v_1'+(\alpha^2-\mu^2)v_1=0, \quad -a<x<0, \ \alpha=kn_1,$$
$$v_2''+2i\mu v_2'+(\beta^2-\mu^2)v_2=0, \quad 0<x<b, \ \beta=kn_2,$$

solutions to which are

$$v_1=Ae^{i(\alpha-\mu)x}+Be^{-i(\alpha+\mu)x},$$
$$v_2=Ce^{i(\beta-\mu)x}+De^{-i(\beta+\mu)x},$$

where A, B, C, and D are constants to be fixed. Continuity and periodicity conditions are: $v_1(0)=v_2(0)$, $v_1'(0)=v_2'(0)$, $v_1(-a)=v_2(b)$, $v_1'(-a)=v_2'(b)$, and these take the form of four equations linear in A, B, C, and D. These equations have a non-trivial solution only if the determinant of the coefficients vanishes. The determinant reduces to

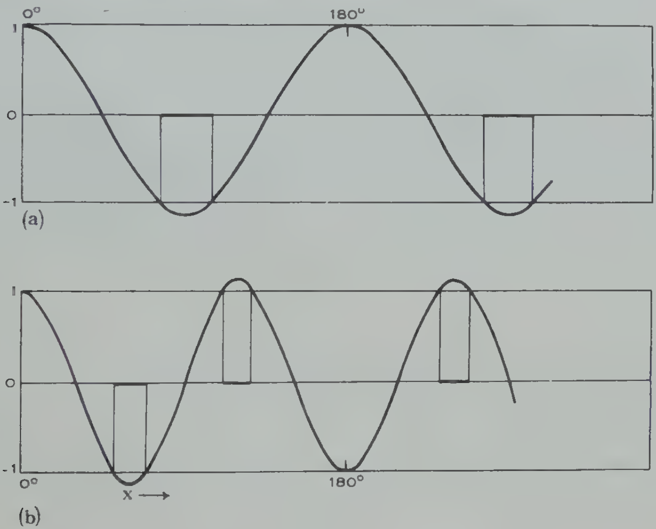

Fig. 1 (a).—Plot of $\cos^2 x - 1\cdot133 \sin^2 x$ as a function of x.
Fig. 1 (b).—Plot of $\cos x \cos 2x - 1\cdot133 \sin x \sin 2x$.

$$\cos \alpha a \cos \beta b-\frac{\alpha^2+\beta^2}{2\alpha\beta}\sin \alpha a \sin \beta b=\cos \mu(a+b),$$

or to

$$\cos kn_1a \cos kn_2b-\tfrac{1}{2}(n_1/n_2+n_2/n_1)\sin kn_1a \sin kn_2b=\cos \mu(a+b).$$

In this equation kn_1a and kn_2b are angles which measure the phase differences between the layer boundaries. The term $\frac{1}{2}(n_1/n_2+n_2/n_1)$ is clearly greater than unity, and it is then easy to show that there are values of k, and hence of λ, for which the modulus of the left-hand side is also greater than unity. Since μ must be real there can be no solution to the differential equation for these values. They constitute the stop bands or reflection bands.

As an example, suppose that $n_1=1\cdot38$ and $n_2=2\cdot30$ (the values for MgF_2 and ZnS respectively) and suppose also, as is frequently the case, that the optical thicknesses of the layers are equal, each to a quarter of a fixed wavelength λ_0. Thus, $n_1a=n_2b=\frac{1}{4}\lambda_0$, and if we put $x=\frac{1}{2}\pi\lambda_0/\lambda$, the equation becomes

$$\cos^2 x-1\cdot133 \sin^2 x=\cos \mu(a+b).$$

In Figure 1 (a) we plot the left-hand side as a function of x. The stop bands, where the left-hand side is less than -1, are indicated by heavy lines along the x-axis. They extend from 75·5 to 104·5°, from 255·5 to 284·5°, and so on; the corresponding λ-intervals are $1\cdot192$–$0\cdot861\lambda_0$, and $0\cdot352$–$0\cdot316\lambda_0$. λ_0 is near the centre of a stop band of width $0\cdot331\lambda_0$.

If one layer (it is immaterial which) has twice the thickness of the other, the equation becomes

$$\cos x \cos 2x-1\cdot133 \sin x \sin 2x=\cos \mu(a+b),$$

and we have the situation in Figure 1 (b). The stop bands extend from 51·3 to 68·0°, 112·0 to 128·7°, and so on, the corresponding λ-intervals being $1\cdot754$–$1\cdot323\lambda_0$, and $0\cdot804$–$0\cdot699\lambda_0$. λ_0 is now at the centre of a pass band.

Actual filters have, of course, only a finite number of layers, and an exact theory for these becomes complicated. The positions of the bands are very much as indicated above, but the transition between pass and stop bands is more gradual. In particular, the transmission falls appreciably near the edges of the pass bands.

References

Brillouin, L. (1946).—"Wave Propagation in Periodic Structures." p. 180. (McGraw-Hill: New York.)

Kronig, R., and Penney, W. G. (1931).—*Proc. Roy. Soc.* A **130**: 499.

Rojansky, V. (1942).—"Introductory Quantum Mechanics." p. 270. (Prentice-Hall: New York.)

PERIODICITIES IN SOLAR RADIO NOISE EMISSION*

By N. C. Gerson†

In a recent article, Roberts (1958) described solar radio wave emissions in the range 40–80 Mc/s. The investigations were a continuation of work initiated earlier by Wild and McCready (1950) on the dynamic radio-frequency spectrum, and by Wild, Murray, and Rowe (1954) employing a 40–240 Mc/s spectrograph.

Recent work by Gerson and Gossard (1959) extended the observational range to lower frequencies, 2–30 Mc/s. These workers determined the dispersion of the echoes, $\Delta f/\Delta t^2$ (cycles/sec^2), and because of the sweep-frequency nature of the bursts termed the phenomena " sweepers ". They also noted that many sweepers occur in trains with recurrence rates ranging (for the limited period of their study) from 1 to 140 sec. Most sweeper trains, however, had periods of 2–20 sec.

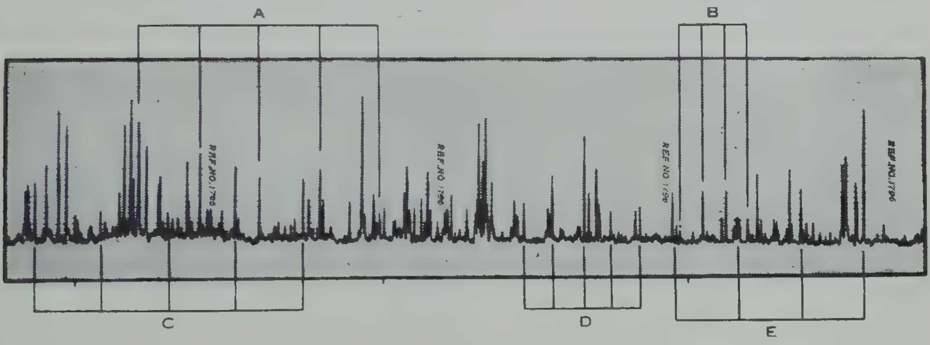

Fig. 1

It is the purpose of this note to indicate the presence of sweeper trains in the work of Roberts (1958). Figure 1 is a reproduction of his Figure 1 (*c*) where

Table 1

SWEEPER TRAINS

Description	Number of Elements	Total Duration (sec)	Period (sec)
A	5	937	234
B	4	268	89
C	5	1042	260
D	5	459	115
E	4	746	249

---

* Manuscript received May 29, 1959.

† Vice Chairman, Arctic Committee, U.S. National Committee for the IGY.

the elements of several sweeper trains (A–E) have been indicated. Periods of the trains are given in Table 1.

The sweeper trains are believed to arise from a relaxation effect taking place in the solar chromosphere. The subject is being discussed elsewhere.

References

Gerson, N. C., and Gossard, W. H. (1959).—*J. Atmos. Terr. Phys.* (In press.)
Roberts, J. A. (1958).—*Aust. J. Phys.* **11** : 215.
Wild, J. P., and McCready, L. L. (1950).—*Aust. J. Sci. Res.* A **3** : 387.
Wild, J. P., Murray, J. D., and Rowe, W. C. (1954).—*Aust. J. Phys.* **7** : 439.

THE LORENTZ TRANSFORMATIONS*

By G. Builder†

Sir Harold Jeffreys (1958) has asserted that my analysis of the clock paradox (Builder 1957) is based on concealed hypotheses ; but the hypotheses to which he refers are ones that he claims are involved in the derivation of the Lorentz transformations and in the currently accepted methods of using them. He holds that the transformations cannot be shown to be unique and he infers that predictions based on them are not necessarily correct and " cannot be right in any case " when applied to systems that are inertial at the time considered but that have been subject to acceleration at some other time. He claims that " standard works on relativity still start from the postulated invariance of the velocity of light, which can be stated in the form $ds=0$ is equivalent to $ds'=0$ " and asserts that it is inferred, without any disclosed justification, first that $ds'=kds$ and then that $k=1$ and $ds=ds'$. He holds that the last step cannot be rigorously justified, for he mentions the two possibilities $k=1$ and $k=(1-u^2/c^2)^{-\frac{1}{2}}$ and remarks that : " The question is which, if either, is right ".

Whatever some standard works may do, the literature also abounds with standard works and with a wealth of papers which trace carefully the empirical and logical basis of the restricted theory. It seems clear that Jeffreys has himself taken insufficient account of the essentially empirical character of the theory. He does not adduce the *principle of relativity* or discuss its empirical background either in his present paper (1958) or in his book " Scientific Inference " (1957) ; it is not surprising that his discussion indicates that the " postulated invariance of the velocity of light " is not by itself sufficient to establish a unique set of coordinate transformations.

Jeffreys shows that the inference that $ds'=kds$ is justified if it refers only to the restricted class of coordinate systems that are inertial ; but this restriction

---

* Manuscript received June 1, 1959.

† School of Physics, University of Sydney.

was already implied in the empirical basis of the theory and in the consequent formulation of the equality $ds' = k ds$. He then states that the further step of putting $k=1$ requires " some comparison of scales " in the two systems ; and he seems to suggest that this is possible only if there are observers in both systems who can make *mutual* scale comparisons. On the contrary, the empirical evidence generalized in the principle of relativity makes such direct scale comparisons superfluous. This evidence, based on the Michelson-Morley and related experiments, was obtained solely by sets of terrestrial measurements, each set being made using a single arrangement of measuring apparatus which was subjected to a spatial rotation and/or was subjected to acceleration by the orbital motion of the Earth so that its motion, in the astronomical inertial coordinate system, was different at different times. Thus the formulation of the principle of relativity was based on experience of situations in which the same measuring devices were utilized in different inertial coordinate systems and in which the measuring devices were transferred from one such system to another by means of non-destructive accelerations.

The empirical background of the principle of relativity thus showed that the scales of measurement in different inertial coordinate systems could be specified by requiring that they be compatible with the transfer of measuring devices from one system to another. This was implicit in Einstein's (1905) discussion of coordinate systems in which the measuring devices used would be identical if compared together at rest, and also in his discussion of the behaviour of devices initially at rest and then set into uniform motion. This specification of scales, when taken together with the prescribed method for synchronization of clocks and with the principle that all inertial coordinate systems are equally privileged in the description of natural phenomena, requires that the coordinate transformations form a group with $k=1$ (e.g. Einstein 1905 ; Poincaré 1905 ; Eddington 1920). Thus, in the context of the restricted theory, just as in the context of Newtonian relativity, every physical device, so long as it does not lose its identity by destructive treatment, itself remains a standard for the scales of measurement of any inertial coordinate system in which it is at rest.

The enormous power of useful prediction displayed by the restricted theory of relativity depends on the fact that this specification of scales eliminates the need for mutual scale comparisons in each particular case ; at the same time, the accuracy of the predictions demonstrates the validity of this specification. Thus, if a device be in uniform motion in our own inertial coordinate system S, we can simply assert that the description of its behaviour that would be given by hypothetical observers in the coordinate system S' in which it is at rest would be the same as the description that would be given by us if it were at rest in our own system S ; we can then use the Lorentz transformations to predict uniquely how the moving device will appear to behave when observed in our own system S. The accuracy of predictions made in this way has been repeatedly confirmed by experiment and this experimental evidence is quite incompatible with $k=(1-u^2/c^2)^{-\frac{1}{2}}$.

In discussing the relative retardation of clocks, Jeffreys supposes that an observer R remains at rest in an inertial coordinate system, and that an observer

M travels away from R with uniform velocity u_1 in R's system to a distance X and then returns with uniform velocity $-u_2$; R and M are supposed to have identical clocks which are to be compared at the beginning and end of the experiment; the time recorded on R's clock between M's departure and return would be $T_R=X(1/u_1+1/u_2)$ and that recorded on M's clock would be

$$T_M=X\left\{\frac{k_1}{u_1}\left(1-\frac{u_1^2}{c^2}\right)^{\frac{1}{2}}+\frac{k_2}{u_2}\left(1-\frac{u_2^2}{c^2}\right)^{\frac{1}{2}}\right\}.$$

He then comments: "If $k=(1-u^2/c^2)^{-\frac{1}{2}}$, $T_M=T_R$ and Dingle's result follows. If $k=1$ Builder's result* follows. The question is which, if either, is right."

However, it has been shown above that the restricted theory entails that $k=1$. It is also to be noted that the value $k=(1-u^2/c^2)^{-\frac{1}{2}}$ would require that the observed "rate" of M's clock would be unaffected by its motion, for in this case each of the terms in the expression for T_M would become identical with those in the expression for T_R. This is completely incompatible with available experimental evidence, for Ives and Stilwell (1938, 1941) and Otting (1939) have confirmed, by measurements on the frequency of the light emitted by atoms in canal rays, that the observed rate of processes in systems in motion is reduced by the factor $(1-u^2/c^2)^{\frac{1}{2}}$, as predicted by using the Lorentz transformation; this has also been confirmed by observations that the decay time of μ-mesons increases enormously with increase in their velocity. Thus the suggestion that k might have the value $(1-u^2/c^2)^{-\frac{1}{2}}$ is clearly wrong.

Jeffreys then puts forward a further argument which I am quite unable to follow. He states that "M's clock is compared with R's before departure and $k=1$". He then assumes that it is necessary that M and R should "compare scales" during M's journey, e.g. by measurement of transverse displacements, but he points out that M must be subjected to some elastic deformation while being set in motion at the beginning of his journey and claims that this will vitiate any comparison of scales. This leads him somehow, and certainly without any justification, to infer that "Builder's result cannot be right in any case".

Even if such a "comparison of scales" were necessary, which it is not, it would need to be made during the intervals X/u_1 and X/u_2 during which M moves uniformly, and not during the short intervals τ required for acceleration. Jeffreys explicitly concedes in his previous paragraph that "the time τ does not matter since it is small anyhow and does not increase indefinitely with X". Thus any elastic deformation suffered by M's equipment during its acceleration is irrelevant. On the other hand, there would be no elastic deformation of M's equipment during its uniform motion and any comparison of scales that might then be made would obviously be consistent with $k=1$ just as when M and R were at rest together.

However, it is worth remarking that, once we start to consider the elastic properties of real bodies, or even of ideal bodies, we cannot pass lightly over the question of the behaviour of M's clock during acceleration. There would be no difficulty in taking this into account in the hypothetical experiment here considered, since the only accelerations involved are those necessary to set M into uniform motion away from R, to reverse his motion, and bring him to rest again with R. Effects of these accelerations could be calculated, or measured experimentally, and allowance could be made for them; they could in any case be made negligible by using moderate accelerations followed by long periods of uniform motion. On the other hand, in the general case in which the motions of the clocks are arbitrary, the effects of acceleration on the rates of real clocks might well far exceed the predicted relativistic effects. Even an assumption that the clocks are to be ideal in some relativistic sense is not without difficulties, and this is important in considering the postulatory basis of the general theory of relativity.

---

* That is, the result predicted by Einstein (1905).

References

Builder, G. (1957).—*Aust. J. Phys.* **10**: 246.

Eddington, A. S. (1920).—"Report on the Relativity Theory of Gravitation." (Fleetway Press: London.)

Einstein, A. (1905).—*Ann. Phys., Lpz.* (4) **17**: 891.

Ives, H. E., and Stilwell, G. R. (1938).—*J. Opt. Soc. Amer.* **28**: 215.

Ives, H. E., and Stilwell, G. R. (1941).—*J. Opt. Soc. Amer.* **31**: 369.

Jeffreys, H. (1957).—"Scientific Inference." (Cambridge Univ. Press.)

Jeffreys, H. (1958).—*Aust. J. Phys.* **11**: 583.

Otting, G. (1939).—*Phys. Z.* **40**: 681.

Poincaré, H. (1905).—*C.R. Acad. Sci., Paris* **140**: 1504.

A NEW METHOD FOR MEASURING THE ATTACHMENT OF SLOW ELECTRONS IN GASES*

By L. G. H. Huxley,† R. W. Crompton,† and C. H. Bagot†

Introduction

Recent determinations of attachment and ionization coefficients have been carried out using a number of different techniques including (i) a method due in the first instance to Lozier using an electron beam (Craggs, Thorburn, and Tozer 1957; Tozer, Thorburn, and Craggs 1958), (ii) a development of Townsend's original method of determining ionization coefficients by the measurement of ionization currents between parallel plane electrodes of variable separation (Geballe and Harrison 1952, 1953), and (iii) a modification of Doehring's method depending on measurements of time of flight (Chanin, Phelps, and Biondi 1959). In experiments of the second and third type it is not possible to estimate experimentally the mean energy of the electrons and, if the coefficients are to be

---

* Manuscript received July 10, 1959.

† Department of Physics, University of Adelaide.

expressed as functions of electron energy, it is necessary to use the results of independent experiments.

Swarm experiments are particularly suitable when electrons of low mean energy are to be studied, since the presence of gas at relatively high pressure enables small energies to be maintained in the presence of high electric field strengths. Moreover, it is possible to measure simultaneously the coefficient of attachment α_a and the ratio W/D of drift velocity W to diffusion coefficient D for electrons, from which their mean energy may be estimated. Bailey and his colleagues (Healey and Reed 1941) developed a technique whereby pairs of values of α_a and W/D were obtained by measuring currents received by a series of electrodes of which all but the last contained a slit through which a fraction of the beam of electrons and ions passed. The purpose of this note is to describe briefly a new method of measuring the parameters and to report the results of preliminary experiments. Whereas no account was taken of the effect of ionizing collisions in the earlier work, it is possible with the present method to calculate the effect of such collisions on the measured values of α_a and W/D and an extension of the method will enable all three parameters to be determined.

Theoretical and Experimental Investigation

In a recent paper one of us (Huxley 1959) has given an account of a theoretical investigation of the structure of a stream of electrons and ions drifting and diffusing in a gas when ionization by collision and molecular attachment are present. If the source of the stream is a small hole in the cathode and the stream is entirely intercepted by an anode consisting of a central disk and two annuli, it has been shown that the expression for R, the ratio of the current received by the inner annulus to the total current received by both annuli, is given by

$$R=1-\frac{\dfrac{h}{d_b}\exp(\lambda h-\mu d_b)+\dfrac{\lambda h\alpha_a}{\mu}\displaystyle\int_0^1\exp(\lambda hs)\left\{\exp\left[-\mu h\left(\frac{b^2}{h^2}+s^2\right)^{\frac{1}{2}}\right]-\exp\left[-\mu h\left\{\frac{b^2}{h^2}+(2-s)^2\right\}^{\frac{1}{2}}\right]\right\}\mathrm{d}s}{\dfrac{h}{d_a}\exp(\lambda h-\mu d_a)+\dfrac{\lambda h\alpha_a}{\mu}\displaystyle\int_0^1\exp(\lambda hs)\left\{\exp\left[-\mu h\left(\frac{a^2}{h^2}+s^2\right)^{\frac{1}{2}}\right]-\exp\left[-\mu h\left\{\frac{a^2}{h^2}+(2-s)^2\right\}^{\frac{1}{2}}\right]\right\}\mathrm{d}s}. \quad \ldots\ldots\ldots\ldots\ldots\ldots \quad (1)$$

where h=length of the diffusion space,

$d_b=\sqrt{(b^2+h^2)}$,

$d_a=\sqrt{(a^2+h^2)}$, where a and b are the inner and outer radii of the inner annulus,

$2\lambda=W/D=\dfrac{\text{drift velocity of electrons}}{\text{diffusion coefficient of electrons}}=40\cdot 29Z/k_1$,

k_1=Townsend's energy factor,

$\mu^2=\lambda^2+2\lambda\alpha$,

$\alpha=\alpha_a-\alpha_i$=(attachment coefficient)−(ionization coefficient).

For the purpose of analysing the results of the present experiments it was assumed that ionization was small so that α could be set equal to α_a with little error.

Accordingly, sets of curves were prepared showing R as a function of μ and α_a for given values of h, from which μ and α_a may be found by measuring R at two values of h.

The experimental procedure is essentially as follows. A stream of electrons, having already acquired a steady state of motion in a uniform electric field Z, enters the diffusion chamber through a small hole in the cathode and moves through the gas under the same uniform field Z to the anode. The anode consists of separately insulated sections, the mode of division being described above. The purpose of the disk, which remains earthed throughout the course of the experiment, is to collect a central stream of unwanted ions which may have entered the diffusion chamber with the electrons. The experimental parameters are chosen so that all the ions entering at the source are collected by the central disk and so that an inappreciable current of electrons and ions falls outside the larger annulus.

In the present apparatus it is possible to vary the chamber length h continuously from 1 to 10 cm by means of an induction motor drive. Since the motor (excluding the field coils) and drive are totally enclosed within the evacuated envelope containing the diffusion apparatus it is possible to adjust the length without contaminating the sample of gas being investigated.

The procedure for determining α_a and k_1 simultaneously is as follows. At a given value of gas pressure p and electric field Z measurements of the ratio R are made at $h=2$ and 5 cm. The values of α_a and μ which satisfy equation (**1**) are found by a series of successive approximations using the graphs of R as a function of μ and α_a for the two values of h. As the first approximation α_a is set equal to 0 and, using the appropriate theoretical curves, the value of μ corresponding to the ratio R_2 for $h=2$ cm is determined. Using this value of μ, a closer approximation to α_a is obtained using the ratio R_5 obtained at $h=5$ cm and the theoretical curves for this value of h. The new value of α_a is used together with R_2 to determine a closer approximation to μ and so on. It was found that the values of α_a and μ converged quite rapidly to limiting values, usually after three " cycles ".

Having determined μ and α_a, k_1 is determined as follows. Since $\mu^2=\lambda^2+2\lambda\alpha_a$, when $\alpha_i=0$, then $\mu-\lambda=2\lambda\alpha_a/(\mu+\lambda)\simeq\alpha_a$, since $\alpha_a\ll\mu$, so that $\lambda=\mu-\alpha_a$ to a sufficient degree of accuracy. Then, since $2\lambda=W/D=40\cdot29\,Z/k_1$ at 15 °C,

$$k_1=20\cdot15\,Z/\lambda.$$

As a check on the reliability and self-consistency of the method a set of values of α_a for $Z/p=5$ V cm^{-1} (mm Hg)$^{-1}$ has been derived from measurements made with four different combinations of pressure p and diffusion chamber length h. In addition, an exact analysis of the composition of the mixed stream of electrons and ions, taking into account the diffusion of the ions formed by attachment, was undertaken by Dr. C. A. Hurst of the Department of Mathematical Physics. He showed that the ion current terms in the expression for R must be modified by correction factors which are functions of h, k_1, and α, but calculation showed their effect to be negligible in analysing the results of the present experiments.

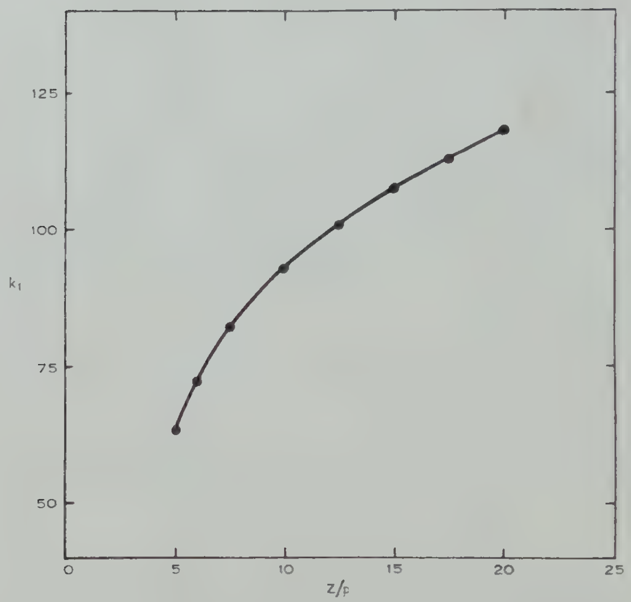

Fig. 1.—Townsend's energy factor k_1 plotted as a function of Z/p.

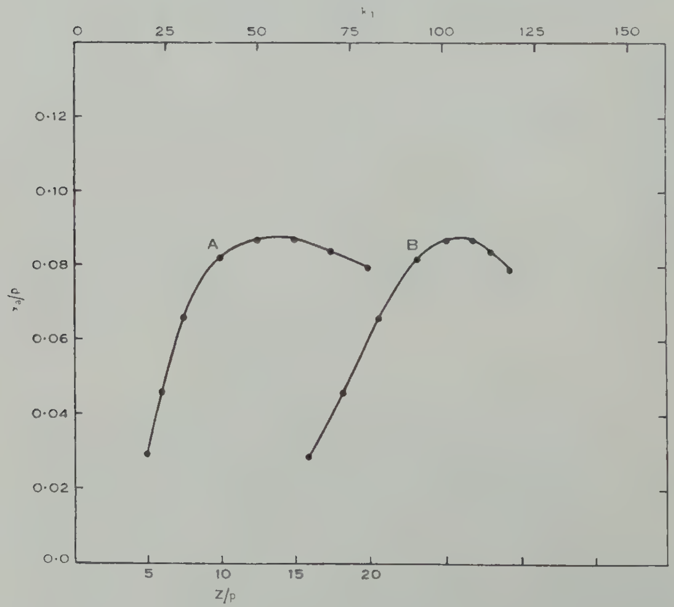

Fig. 2.—Curve A, α_a/p plotted as a function of Z/p. Curve B, α_a/p plotted as a function of Townsend's energy factor k_1.

Results

The two tables and two diagrams given summarize the first measurements made with the new method. In a sample of oxygen at 2 mm Hg pressure values of α_a/p have been obtained in the range $5 \leqslant Z/p \leqslant 20$ V cm^{-1} (mm Hg)$^{-1}$ from coupled measurements of R made at $h=2$ and 5 cm. The electron energy factor k_1 has also been derived from the measurements in this range by the process explained earlier. Table 1 summarizes the results obtained at a pressure of 2 mm Hg, while Table 2 shows the self-consistency of the method for various combinations of pressure and chamber length. Figures 1 and 2 present the results in graphical form.

TABLE 1

SUMMARY OF THE RESULTS IN OXYGEN FOR $5<Z/p<20$ V CM^{-1} (MM Hg)$^{-1}$

Z/p	α_a	μ	λ	α_a/p	k_1
5	0·058	3·24	3·18	0·029	63·3
6	0·092	3·41	3·32	0·046	72·8
7·5	0·133	3·79	3·66	0·066	82·6
10	0·164	4·48	4·32	0·082	93·3
12·5	0·174	5·16	4·99	0·087	101
15	0·173	5·79	5·62	0·087	108
17·5	0·168	6·41	6·24	0·084	113
20	0·158	6·97	6·81	0·079	118

The results obtained for $Z/p=20$ V cm^{-1} (mm Hg)$^{-1}$ were further analysed to determine the effect of ionization by collision upon the calculated values of α_a. Geballe and Harrison (1953) have published values of α_i/p as a function of Z/p for values of $Z/p>25$ V cm^{-1} (mm Hg)$^{-1}$, from which, by use of Townsend's formula $\alpha_i/p=A \exp[-B/(Z/p)]$ (Loeb 1955), a value of $\alpha_i/p=0 \cdot 012$ for $Z/p=20$ V cm^{-1} (mm Hg)$^{-1}$ was estimated. This value of α_i/p was used to recalculate a section of the theoretical curves appropriate to the analysis of the results obtained at $p=2$ mm Hg for $Z/p=20$ V cm^{-1} (mm Hg)$^{-1}$. A value of $\alpha_a=0 \cdot 162$ resulted from the reassessment compared with the value 0·158 obtained previously when ionization was ignored; k_1 was modified

TABLE 2

SHOWING THE SELF-CONSISTENCY OF THE RESULTS AT $Z/p=5$ V CM^{-1} (MM Hg)$^{-1}$ FOR DIFFERENT VALUES OF p AND h

Oxygen Pressure (mm)	From Measurements at $h=2$ and 5 cm	From Measurements at $h=2$ and 10 cm
5	0·032	0·031
10	0·032	0·033

correspondingly from $k_1 = 118$ to $k_1 = 117$. In the range of values of $Z/p < 20$ V cm^{-1} (mm Hg)$^{-1}$ over which α_i/p is appreciable, α_i/p decreases and α_a/p increases as Z/p decreases, so that the discrepancy of $2\frac{1}{2}$ per cent. in α_a/p at $Z/p = 20$ V cm^{-1} (mm Hg)$^{-1}$ represents the maximum discrepancy to which the values in Table 1 are subject due to the assumption that $\alpha_i = 0$.

Throughout the experiments the ratios R were measured to an accuracy of the order of 1 per cent. An examination of the theoretical curves shows that an error of this magnitude will in general lead to an error in α_a of approximately 5 per cent., although a somewhat larger error may be expected for small values of μ, that is, where measurements at small values of Z/p are carried out at low pressure. The discrepancy between the value of α_a/p at $Z/p = 5$ V cm^{-1} (mm Hg)$^{-1}$ obtained at a pressure of 2 mm Hg and the more consistent values obtained at 5 and 10 mm Hg may be accounted for on this basis. Values of k_1 are less affected by experimental error in the ratio R, and the results for this parameter obtained at pressures of 2, 5, and 10 mm Hg agree to within 2 per cent.

The authors wish to express their indebtedness to Dr. B. I. H. Hall, formerly of this Department, for carrying out the initial calculation of some of the theoretical curves and to Mr. J. Gascoigne for the construction of the diffusion apparatus.

References

Chanin, L. M., Phelps, A. V., and Biondi, M. A. (1959).—*Phys. Rev. Letters* **2**: 344.
Craggs, J. D, Thorburn, R, and Tozer, B. A. (1957).—*Proc. Roy. Soc.* A **240**: 473.
Geballe, R., and Harrison, M. A. (1952).—*Phys. Rev.* **85**: 372.
Geballe, R., and Harrison, M. A. (1953).—*Phys. Rev.* **91**: 1.
Healey, R. H., and Reed, J. W. (1941).—"The Behaviour of Slow Electrons in Gases." (Amalgamated Wireless: Sydney.)
Huxley, L. G. H. (1959).—*Aust. J. Phys.* **12**: 171.
Loeb, L. B. (1955).—"Basic Processes of Gaseous Electronics." (University of California Press.)
Tozer, B. A., Thorburn, R., and Craggs, J. D. (1958).—*Proc. Phys. Soc.* **72**: 1081.

AUSTRALASIAN MEDICAL PUBLISHING CO. LTD.
SEAMER AND ARUNDEL STS., GLEBE, SYDNEY

DRIFT OF A CHARGED PARTICLE IN A MAGNETIC FIELD OF CONSTANT GRADIENT

By P. W. Seymour*

[*Manuscript received June* 8, 1959]

Summary

A simple expression for the drift velocity of a charged particle moving in an inhomogeneous magnetic field has been obtained by Alfvén, who, in his first-order theory, considered the inhomogeneity as a small perturbation of a uniform field.

In this paper, by use of a different approach, an exact solution is obtained for the drift velocity of a charged particle moving in a magnetic field of constant gradient, $B_z=\lambda x$. The method easily yields as approximations Alfvén's result and the case of circular orbit, and includes the case of zero mean field, for which perturbation methods are inappropriate.

I. Motion in a Magnetic Field of Constant Gradient

Consider first the motion of an electron, and suppose the magnetic field is in the z-direction and is represented by $B_z=\lambda x$. Then, from the non-relativistic equation of motion we have, in the absence of electric field,

$$m\mathrm{d}\mathbf{w}/\mathrm{d}t=-(e/c)\mathbf{w}\times\mathbf{B}, \quad \dots\dots\dots\dots\dots\dots \quad (1)$$

where the electron charge is $-e$.

The z-component of $\mathbf{w}$ is constant, and need not be considered explicitly. The other components vary as

$$\left.\begin{aligned} m\mathrm{d}w_x/\mathrm{d}t&=-(e/c)\lambda x w_y,\\ m\mathrm{d}w_y/\mathrm{d}t&=+(e/c)\lambda x w_x. \end{aligned}\right\} \quad \dots\dots\dots\dots\dots\dots \quad (2)$$

$w^2=w_x^2+w_y^2$ is constant, and, in the notation of Figure 1, $w_x=w\cos\psi$, $w_y=w\sin\psi$. Substitution of these relations in (2) gives

$$\mathrm{d}\psi/\mathrm{d}t=e\lambda x/mc. \quad \dots\dots\dots\dots\dots\dots \quad (3)$$

Since $w=\mathrm{d}s/\mathrm{d}t$, where s denotes distance along the electron trajectory

$$\mathrm{d}\psi/\mathrm{d}s=e\lambda x/mcw. \quad \dots\dots\dots\dots\dots\dots \quad (4)$$

Thus

$$\frac{\mathrm{d}^2\psi}{\mathrm{d}s^2}=\frac{e\lambda}{mcw}\frac{\mathrm{d}x}{\mathrm{d}s}=\frac{e\lambda}{mcw}\cos\psi, \quad \dots\dots\dots\dots \quad (5)$$

and so

$$\left(\frac{\mathrm{d}\psi}{\mathrm{d}s}\right)^2=\frac{2e\lambda}{mcw}\sin\psi+\text{constant}. \quad \dots\dots\dots\dots \quad (6)$$

---

* Department of Theoretical Physics, Research School of Physical Sciences, Australian National University, Canberra.

From (4) and (6)

$$x = \pm\sqrt{\{x_0^2 + (2mcw/e\lambda)\sin\psi\}}, \quad \ldots\ldots\ldots\ldots\ldots \quad (7)$$

where x_0 is the value of x when $\psi=0$.

For x positive, (3) gives

$$t = \frac{mc}{e\lambda}\int\frac{d\psi}{\sqrt{\{x_0^2+(2mcw/e\lambda)\sin\psi\}}}. \quad \ldots\ldots\ldots\ldots \quad (8)$$

Also, since

$$\frac{dy}{ds} = \sin\psi, \quad \ldots\ldots\ldots\ldots\ldots\ldots\ldots\ldots\ldots\ldots\ldots\ldots\ldots\ldots \quad (9)$$

(4) gives

$$y = \frac{mcw}{e\lambda}\int\frac{\sin\psi\, d\psi}{\sqrt{\{x_0^2+(2mcw/e\lambda)\sin\psi\}}}. \quad \ldots\ldots\ldots\ldots \quad (10)$$

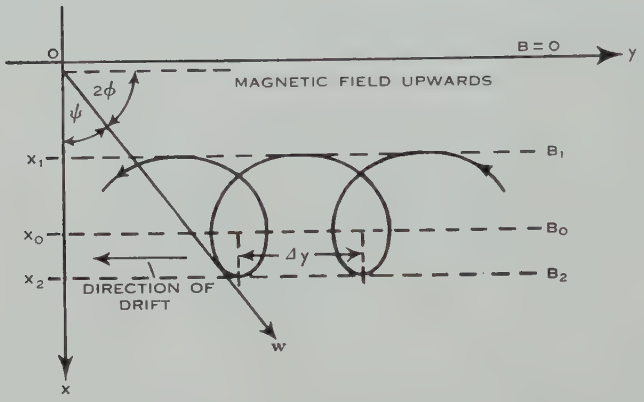

Fig. 1.—Electron drift in a magnetic field $B_z=\lambda x$: Case 1, motion does not cross the line $B=0$.

II. Comparison with Alfvén's Result

For motion which does not cross the line $B=0$, as in Figure 1, (10) gives the y-drift per cycle exactly as

$$\Delta y = \rho_0\int_0^{2\pi}\frac{\sin\psi\, d\psi}{\sqrt{\{1+2(\rho_0/x_0)\sin\psi\}}}, \quad \ldots\ldots\ldots\ldots \quad (11)$$

where $B_0=\lambda x_0$, and $\rho_0=mcw/eB_0$ is the orbit's radius of curvature for field strength B_0.

When $\rho_0 \ll x_0$, which implies electron orbital motion far from the y-axis, a first-order result for the drift velocity in the y-direction can be readily obtained. After expansion of the denominator in (11), integration gives approximately

$$\Delta y = -\pi\rho_0^2/x_0 = -\pi\lambda\rho_0^2/B_0.$$

Similarly, from (8) the periodic time in this case is $T=2\pi\rho_0/w$, and so the corresponding drift velocity in the y-direction is given by

$$w_D = \Delta y/T = -\tfrac{1}{2}\rho_0\lambda w/B_0. \quad \ldots\ldots\ldots\ldots\ldots \quad (12)$$

This is the result obtained by Alfvén (1940, 1950), and discussed by Post (1956) and Spitzer (1956).

When B_0 has a fixed value and λ approaches zero, we obtain the circular orbit result for a homogeneous magnetic field, i.e. $w_D=0$ and $T=2\pi\rho_0/w=2\pi/\omega_c$, where $\omega_c=eB_0/mc$ is the so-called cyclotron angular frequency.

III. Exact Solution in Terms of Elliptic Integrals

To complete the exact solution, two cases require consideration.

Case 1. *Electron does not enter Region of Reversed Magnetic Field*

For an electron motion which does not cross the line $B=0$, as shown in Figure 1, the limits of x are, from (**7**),

$$\left.\begin{aligned} x_1&=\surd(x_0^2-2mcw/e\lambda) \text{ for } \psi=3\pi/2,\\ x_2&=\surd(x_0^2+2mcw/e\lambda) \text{ for } \psi=\pi/2,\end{aligned}\right\} \quad \ldots\ldots\ldots \quad (\mathbf{13})$$

so that $0\leqslant x_1<x_0<x_2$.

Using the substitution $\psi=\frac{1}{2}\pi-2\varphi$, we obtain from (**10**) the drift per cycle in the y-direction as

$$\Delta y=\frac{2mcw}{eB_2}\int_0^{\pi}\frac{(1-2\sin^2\varphi)\mathrm{d}\varphi}{\surd(1-k_1^2\sin^2\varphi)}, \quad \ldots\ldots\ldots\ldots \quad (\mathbf{14})$$

where $\lambda x_2=B_2$ and $k_1^2=4mcw/e\lambda x_2^2=4\rho_2/x_2$, if ρ_2 is the orbit's radius of curvature for field strength B_2.

When $x_1\geqslant0$, (**13**) gives $x_2\geqslant\surd(4mcw/e\lambda)\geqslant\surd(x_2^2k_1^2)$, so that the upper limit of k_1^2 is unity.

Reduction of (**14**) to standard form for elliptic integrals results in

$$\begin{aligned}\Delta y&=x_2\left\{2\int_0^{\pi/2}\surd(1-k_1^2\sin^2\varphi)\mathrm{d}\varphi-[2-k_1^2]\int_0^{\pi/2}\frac{\mathrm{d}\varphi}{\surd(1-k_1^2\sin^2\varphi)}\right\}\\ &=-x_2\{2[K-E]-k_1^2K\}, \quad \ldots\ldots\ldots\ldots\ldots\ldots\ldots\ldots \quad (\mathbf{15})\end{aligned}$$

where K and E are complete elliptic integrals of the first and second kind respectively, of modulus k_1 (Dwight 1947).

The periodic time is derived from (**8**) as

$$T=\frac{4mc}{eB_2}\int_0^{\pi/2}\frac{\mathrm{d}\varphi}{\surd(1-k_1^2\sin^2\varphi)}=x_2\frac{k_1^2}{w}K. \quad \ldots\ldots\ldots \quad (\mathbf{16})$$

The exact drift velocity is, therefore, from (**15**) and (**16**),

$$w_D=\frac{\Delta y}{T}=-w\left\{\frac{2}{k_1^2}\left[1-\frac{E}{K}\right]-1\right\}. \quad \ldots\ldots\ldots\ldots \quad (\mathbf{17})$$

Since $\{(2/k_1^2)[1-E/K]-1\}\geqslant0$ for $0\leqslant k_1^2\leqslant1$, the drift velocity is always in the negative y-direction.

When $k_1^2\ll1$, Alfvén's result $w_D=-\frac{1}{8}wk_1^2$ is again obtained.

When $k_1^2=1$, which occurs when $x_1=0$, we have $w_D=-w$, and the electron moves along the line $B=0$.

For $x<0$, the electron drift pattern is precisely the mirror image in the y-axis of that shown in Figure 1. Again the drift is always in the negative y-direction.

Case 2. *Electron enters Region of Reversed Magnetic Field*

Consider now a motion in which the electron crosses the line $B=0$, and thus enters a reversed magnetic field, as shown in Figure 2. Let ψ_0 be the value of ψ when $x=0$ and $w_x>0$. Then in place of (7)

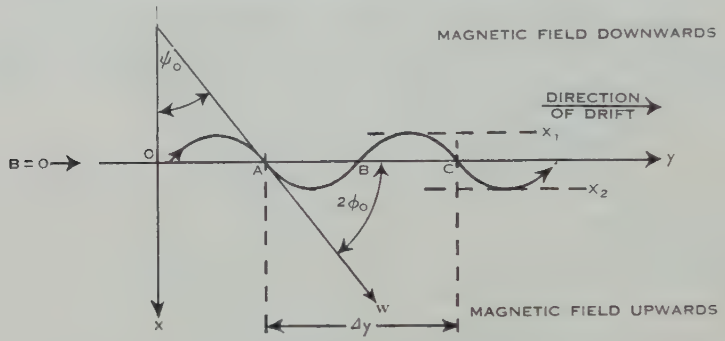

Fig. 2.—Electron drift in a magnetic field $B_z=\lambda x$: Case 2, motion crosses the line $B=0$.

$$x=\pm\sqrt{\{(2mcw/e\lambda)(\sin\psi-\sin\psi_0)\}}, \quad \ldots\ldots\ldots\ldots\ldots \quad (18)$$

and so the limits of x are now

$$x_2=-x_1=\sqrt{\{(2mcw/e\lambda)(1-\sin\psi_0)\}} \quad \text{for } \psi=\tfrac{1}{2}\pi. \quad \ldots\ldots \quad (19)$$

In this case various drift patterns may occur, as shown in Figure 3, but each pattern possesses symmetry about the y-axis. It is therefore convenient to introduce the term " zero mean field " to describe the field condition at the y-axis.

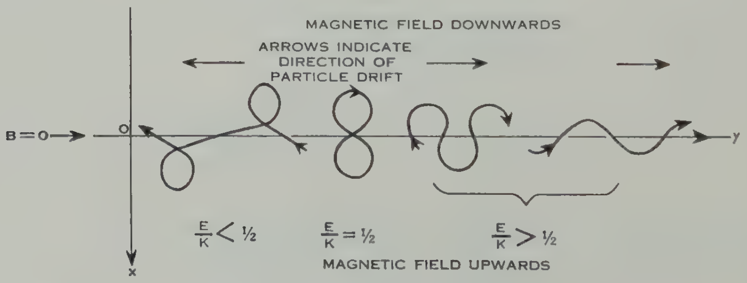
MAGNETIC FIELD DOWNWARDS
ARROWS INDICATE DIRECTION OF PARTICLE DRIFT
B=O
O
Y
$\frac{E}{K}<\frac{1}{2}$
$\frac{E}{K}=\frac{1}{2}$
$\frac{E}{K}>\frac{1}{2}$
MAGNETIC FIELD UPWARDS
X

Fig. 3.—Typical electron drift patterns in terms of E/K for Case 2.

Introducing as before $\psi=\frac{1}{2}\pi-2\varphi$, then $\psi_0=\frac{1}{2}\pi-2\varphi_0$. From Figures 2 and 3, $-\frac{1}{2}\pi\leqslant\psi_0\leqslant+\frac{1}{2}\pi$, $0\leqslant\varphi_0\leqslant\frac{1}{2}\pi$, and the above limits thus reduce to

$$x_2=-x_1=2\sqrt{(mcw/e\lambda)}\sin\varphi_0. \quad \ldots\ldots\ldots\ldots \quad (20)$$

Utilizing the properties of symmetry exhibited by the drift pattern of, say, Figure 2, then for positive x in (**18**) we obtain from (**4**) and (**9**)

$$\Delta y = AC = 2AB = \frac{2mcw}{e\lambda}\int_{\psi_0}^{\pi-\psi_0} \frac{\sin\psi\,\mathrm{d}\psi}{\sqrt{\{(2mcw/e\lambda)(\sin\psi-\sin\psi_0)\}}}$$

$$= 8\sqrt{\left(\frac{mcw}{e\lambda}\right)}\left\{\int_0^{\varphi_0} \frac{\cos^2\varphi\,\mathrm{d}\varphi}{\sqrt{(\sin^2\varphi_0-\sin^2\varphi)}} - \tfrac{1}{2}\int_0^{\varphi_0}\frac{\mathrm{d}\varphi}{\sqrt{(\sin^2\varphi_0-\sin^2\varphi)}}\right\}. \quad \ldots\ldots\ldots\ldots (\mathbf{21})$$

If another variable of integration θ is defined by $\sin\varphi = \sin\varphi_0 \sin\theta$, (**21**) may be transformed to

$$\Delta y = 8\sqrt{\left(\frac{mcw}{e\lambda}\right)}\left\{\int_0^{\pi/2}\sqrt{(1-k_2^2\sin^2\theta)}\,\mathrm{d}\theta - \tfrac{1}{2}\int_0^{\pi/2}\frac{\mathrm{d}\theta}{\sqrt{(1-k_2^2\sin^2\theta)}}\right\}$$

$$= 8\sqrt{(mcw/e\lambda)}(E-\tfrac{1}{2}K). \quad \ldots\ldots\ldots\ldots (\mathbf{22})$$

where $k_2 = \sin\varphi_0 = x_2\sqrt{(e\lambda/4mcw)}$, using (**20**).

Similarly

$$T = 4\sqrt{(mc/e\lambda w)}K, \quad \ldots\ldots\ldots\ldots (\mathbf{23})$$

and the drift velocity in this case is

$$w_D = w(2E/K-1). \quad \ldots\ldots\ldots\ldots (\mathbf{24})$$

When $k_2 \ll 1$, $E/K \approx 1-\frac{1}{2}k_2^2$ and

$$w_D \approx w(1-k_2^2) \sim w, \quad \ldots\ldots\ldots\ldots (\mathbf{25})$$

as expected from Figure 2.

For $E/K = \frac{1}{2}$, corresponding to $\varphi_0 \approx 65°$, the drift velocity becomes zero. As φ_0 increases beyond 65° ($E/K < \frac{1}{2}$) the drift velocity becomes negative, as in Case 1. Figure 3 gives typical drift patterns for $E/K < \frac{1}{2}$, $E/K = \frac{1}{2}$, and $E/K > \frac{1}{2}$. Since in this Case w_D becomes $+w$ and $-w$ for $k_2 = 0$ and $k_2 = 1$ respectively, it follows that at the limit $\varphi_0 = 0$ the electron moves along the line $B = 0$ in the positive y-direction, while at the limit $\varphi_0 = \frac{1}{2}\pi$ it moves along the same line in the negative y-direction. Thus the drift patterns of Cases 1 and 2 coincide in the limits $k_1 = 1$ and $k_2 = 1$.

For positively charged particles, the principal results are that the formulae for k_1 and k_2 remain unchanged, if the particle charge is $+e$, whereas the w_D are changed only in sign.

Since $\mathrm{d}x/\mathrm{d}s = \cos\psi$, it can be readily ascertained that the drift velocity in the x-direction is zero in all cases.

IV. Discussion of Results

The drift velocity results obtained in Cases 1 and 2 for an electron are shown plotted against the parameter $x_2\sqrt{(e\lambda/4mcw)}$ in Figure 4. This parameter is k_2 in the region of Case 2, and $1/k_1$ in the region of Case 1. For $1/k_1 \to \infty$, we have the well-known region of Alfvén drift velocities. In spite of the smallness of Alfvén drift velocities relative to particle velocities, it has been considered that charge separation effects could be obtained in a plasma and that these might lead to motion of the plasma towards the region of weakest magnetic field (Post 1956). Larger drift velocities, of the order of the particle velocities, are expected, however, in the region $x_2\sqrt{(e\lambda/4mcw)}\lesssim 1$. Thus, if the magnetic field within a plasma varies in a direction normal to the field and somewhere changes sign, the motion of the charged particles in the neighbourhood where it changes sign may lead to larger charge separation effects than in the Alfvén region.

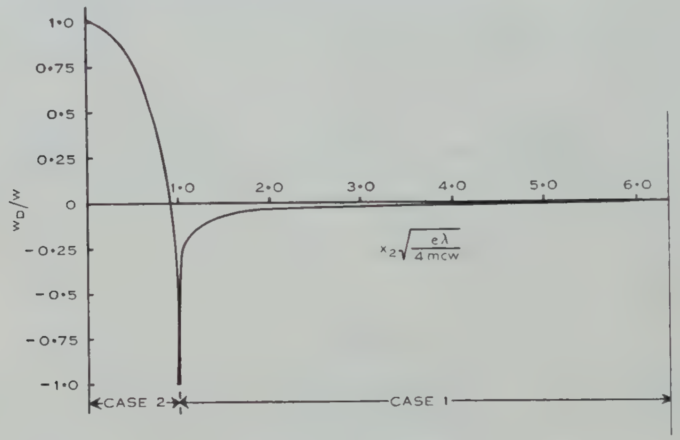

Fig. 4.—Variation of w_D/w with $x_2\sqrt{(e\lambda/4mcw)}$ for Cases 1 and 2.

V. Acknowledgments

The author is indebted to Professor K. J. Le Couteur, who suggested the problem and gave guidance during the course of the investigation, and to Dr. F. C. Barker for helpful discussions.

VI. References

Alfvén, H. (1940).—On the motion of a charged particle in a magnetic field. *Ark. Mat. Astr. Fys.* **27A**, No. 22.

Alfvén, H. (1950).—" Cosmical Electrodynamics." pp. 13–23. (Clarendon Press : Oxford.)

Dwight, H. B. (1947).—" Tables of Integrals and Other Mathematical Data." Revised Ed. pp. 234–6. (The Macmillan Company : New York.)

Post, R. F. (1956).—Controlled fusion research—an application of the physics of high temperature plasmas. *Rev. Mod. Phys.* **28** : 353–5.

Spitzer, L., Jr. (1956).—" Physics of Fully Ionized Gases." pp. 6–7. (Interscience Publishers : New York and London.)

RADIO ECHO OBSERVATIONS OF THE GEMINID METEOR STREAM

By A. A. Weiss*

[*Manuscript received July* 29, 1959]

Summary

Measurements of radiant coordinates and echo rates from 1952 to 1957 are summarized. A mean radiant of $\alpha=113\cdot4°$, $\delta=31\cdot4°$ at solar longitude $\odot=260\cdot2°$, a small radiant area, and a markedly asymmetrical distribution of meteors across the stream, with a maximum echo rate at $\odot=260\cdot8°$, all agree with northern hemisphere radio echo observations made between 1949 and 1954.

I. Introduction

With the exception of 1954, observations of the Geminid meteor stream have been made each year from 1952 to 1957. The observations prior to 1956 have already been published (Weiss 1955, 1957). This paper describes the 1956 and 1957 observations and summarizes the measurements of radiant coordinates and echo rates so far obtained.

The observations have been made with two equipments, the 27 Mc/s " wind " equipment and the 67 Mc/s radiant survey equipment. The wind equipment is essentially a C.W. system with a wide-beam aerial directed to the zenith (Robertson, Liddy, and Elford 1953). The radiant equipment (Weiss 1955) is a radar system with two narrow-beam aerials directed at low elevation along azimuths 35·5° S. of E. (termed the N aerial) and 14° N. of E. (S aerial); for the observations in 1956 and 1957 the transmitter peak pulse power was increased to 50 kW. The methods of measuring radiant coordinates, and the accuracy obtained, have been described adequately in the papers cited.

The line densities of electrons in the faintest trails detected by either equipment are close to 10^{11} electrons/cm, corresponding roughly to visual magnitude +7.

II. The Observations for 1956 and 1957

Radiant positions and echo rates are listed in Table 1. The daily shower echo rate is the echo rate remaining after subtraction of the estimated number of sporadic echoes for the periods 23–00½ hr (N aerial) and 03–04 hr (S aerial) from the total numbers of echoes detected during the corresponding periods each day.

III. Radiant Position and Diameter

Radiant positions on individual days are plotted in Figure 1. The radiant ephemeris, estimated by the method of least squares, is:

$$\alpha=113\cdot4°+0\cdot90\ (\odot-260\cdot2)°,$$
$$\delta=\ 31\cdot4°+0\cdot10\ (\odot-260\cdot2)°.$$

---

* Division of Radiophysics, C.S.I.R.O., at Department of Physics, University of Adelaide.

Table 1

RADIANTS AND TOTAL ECHO RATES FOR THE GEMINID SHOWER, 1956–1957

Date	Radiant Coordinates				Total Echo Rate			
	1956		1957		1956		1957	
	α	δ	α	δ	N	S	N	S
Dec. 8						4	14	
9					0		0	
10	109	+31				14	17	
11	112	+33			8		24	
12	114	+34	114	+35		34	44	22
13	114	+34			60		58	
14	115	+33	114	+34			64	38
15	116	+33			20		5	
Sporadic echo rate/hr	..	..	..	..	18	22	26	54

The mean radiants for the wind equipment, which are averages over several days, have been excluded. The daily motion in Right Ascension, 0·90±0·24°, is slightly smaller than those given by Lovell (1954) for radio, photographic, and visual measurements. The small daily motion in declination, 0·10±0·50°, is in the opposite sense to the small negative value given by Lovell, but because

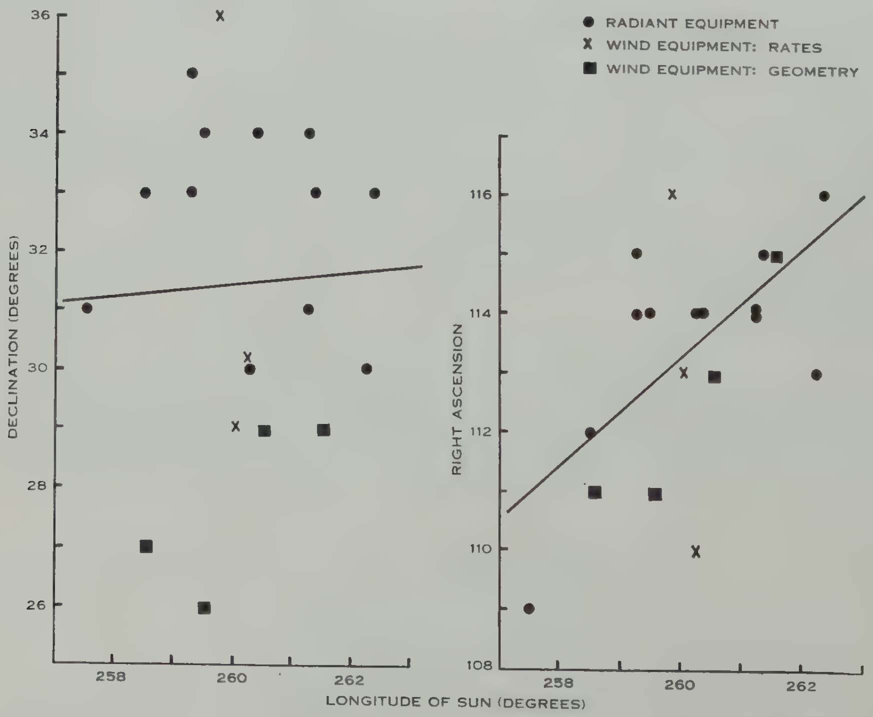

Fig. 1.—Coordinates of the Geminid radiant. The full lines are the least square fits for the daily motions.

of the large standard deviation no significance can be attached to the reversal of direction. In fact, the daily motions found here must be accorded considerably less weight than the northern hemisphere determinations, since at Adelaide the Geminid radiant is unfavourably situated (maximum elevation $<25°$) and the shower echo rate exceeds the sporadic rate for only a few days near the time of maximum activity. The mean radiant of 113·4°, +31·4° at $\odot = 260 \cdot 2°$, however, agrees well with the radio radiant of 112·9°, +31·9° given by Davidson (1956) for the same epoch.

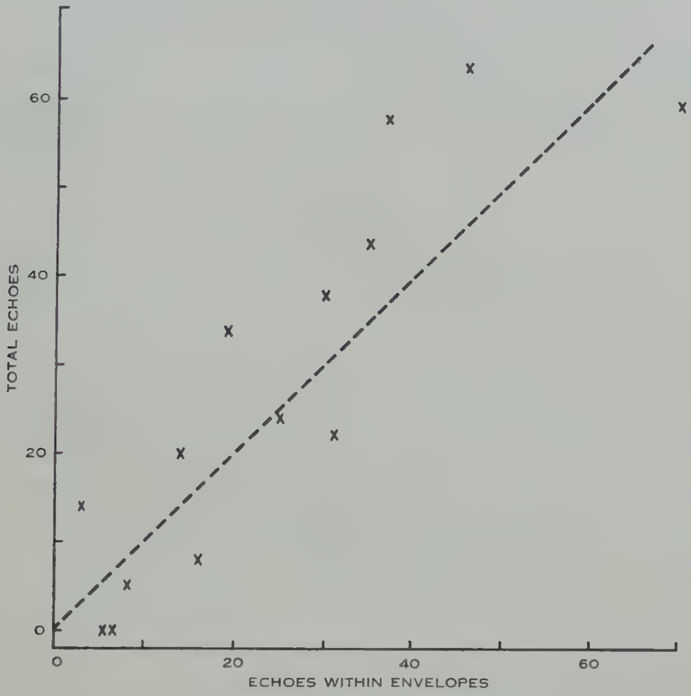

Fig. 2.—Comparison between total numbers of shower echoes each day, and the numbers of echoes falling inside the range-time envelopes corresponding to a point radiant.

Direct measurement of the radiant diameter is precluded by the low echo rate, which even at maximum activity is barely double the sporadic rate (see Table 1). It is, however, possible to compare the total shower echo rate, as listed in Table 1, with the number of shower echoes detected inside range-time envelopes on the corresponding days. This comparison is made in Figure 2, using range-time envelopes which exclude only a small proportion of meteors whose line densities exceed $\alpha = 10^{14}$ electrons/cm at the reflection points. Since an analysis of echo durations indicates that $\alpha \sim 8 \times 10^{13}$ electrons/cm for the largest Geminid meteors detected, Figure 2 suggests that almost all the Geminid echoes are contained within the range-time envelopes corresponding to a point radiant. The scatter in this diagram is attributed to random fluctuations in the sporadic echo rate. The actual diameter of the radiant must then be very small. This confirms the small radiant area found by Bullough (1954) for somewhat brighter meteors, and lends support to his supposition that the large visual radiant area is due to subsidiary radiants whose activity proceeds almost wholly from bright meteors.

IV. Shower Activity

The dependence of shower activity on solar longitude has been determined from the total number of shower echoes detected each day whilst the radiant lies within the collecting areas of the aerials. For the wind equipment this is the total time, 9 hr, for which the radiant is above the local horizon. The narrow collecting sectors of the radiant equipment lead to much shorter collection times, the times of passage of the radiant being 1·3 and 1·0 hr for the N and S aerials respectively. Corrections have been applied to allow for the slight variations in equipment sensitivity which have occurred from year to year, assuming a constant sporadic meteor flux and with mass distribution parameters $s=1\cdot5$ for the Geminids and $s=2\cdot0$ for sporadics. The value of $s=1\cdot5$, given by Browne *et al.* (1956), has been confirmed locally by an analysis of echo rates at different equipment sensitivities. Radiant equipment echo rates reduced to the 1957 N aerial rate as standard, and wind equipment rates reduced to 1952, are listed in Table 2. Echo rates measured simultaneously in both channels of the radiant equipment have been averaged ; such averages are marked by an asterisk in the table.

Table 2

reduced total echo rates

Date	Wind Equipment reduced to 1952			Radiant Equipment reduced to 1957 N Aerial		
	1952	1953	1955	1953	1956	1957
Dec. 8	0	28	—	20	8	14
9	27	18	—	11	0	0
10	14	62	0	17	28	17
11	87	46	94	—	10	24
12	92	96	66	13*	68	36*
13	154	156	121	87	72	58
14	93	180	128	69*	—	57*
15	15	46	135	40	24	5

* Average for N and S aerials.

The individual measurements and the mean activity curve are plotted in Figure 3, after increasing all radiant echo rates by a factor of 2·10. It is seen that deviations of up to ±20 per cent. from the mean occur from year to year in the reduced echo rate at maximum. Although this is greater than the ±7 per cent. deviation found by Davidson (1956) from the northern hemisphere observations, a discrepancy of this magnitude could well be due to the low echo rate, as compared with the sporadic rate, of the stream at Adelaide. Our results, then, confirm the remarkable consistency of the echo rate from year to year. The abnormally high echo rate in 1954 (Davidson 1956) seems to have been an isolated event.

The asymmetrical shape of the activity curve closely resembles that of Bullough (1954). A peak activity at $\odot = 260 \cdot 8°$ over the period 1952–1957 is identical with Bullough's determination for the years 1949–1953. This agreement as to the epoch of maximum activity is important, as it provides a firm initial value for a test of the prediction by Plavec (1950) of a rapid backward shift of the node of this stream, in consequence of which the date of maximum activity moves backwards by one day in 60 years.

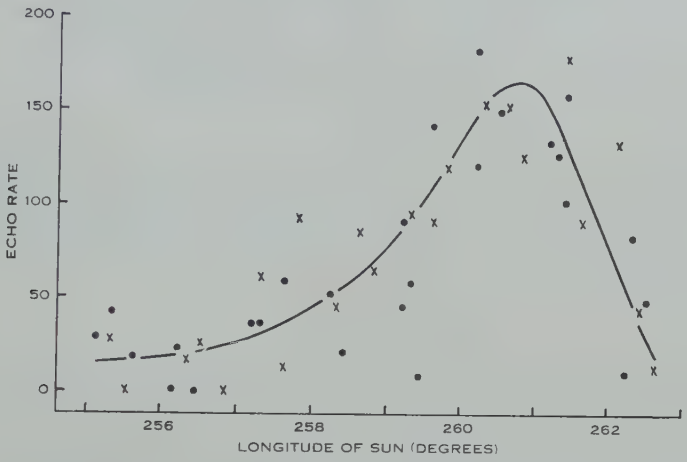

Fig. 3.—Reduced total echo rates for the Geminid radiant. × wind equipment rates ; ● radiant equipment rates multiplied by 2·10.

V. References

Browne, I. C., **Bullough**, K., **Evans**, S., and **Kaiser**, T. R. (1956).—*Proc. Phys. Soc.* B 69 : 83.

Bullough, K. (1954).—*Jodrell Bank Ann.* **1** : 68.

Davidson, T. W. (1956).—*Jodrell Bank Ann.* **1** : 116.

Lovell, A. C. B. (1954).—" Meteor Astronomy." (Clarendon Press : Oxford.)

Plavec, M. (1950).—*Nature* **165** : 362.

Robertson, D. S., **Liddy**, D. T., and **Elford**, W. G. (1953).—*J. Atmos. Terr. Phys.* **4** : 255.

Weiss, A. A. (1955).—*Aust. J. Phys.* **8** : 148.

Weiss, A. A. (1957).—*Aust. J. Phys.* **10** : 299.

HIGH RESOLUTION OBSERVATIONS OF THE GRANULAR STRUCTURE OF SUNSPOT UMBRAE

By R. J. Bray* and R. E. Loughhead*

[*Manuscript received June 12, 1959*]

Summary

High resolution photographs of sunspot umbrae have confirmed the existence of an umbral granulation, resembling the photospheric granulation but differing in regard to lifetime and cell size. Bright structures in the form of " loops " are also seen. Quite apart from the granulation, the intensity contours of spot umbrae show a detailed and complex structure.

I. Introduction

Apart from occasional " light-bridges " (Waldmeier 1955), sunspot umbrae usually appear in published photographs as uniformly dark areas. However, Chevalier (1916) reported the existence in spot umbrae of a bright granular structure, and this was later confirmed visually by Thiessen (1950). More recently, Rösch (1957) has published photographs showing evidence of this structure and has drawn attention to the need for further observations.

In the present paper an account is given of a systematic attempt to photograph detail in sunspot umbrae and, in particular, to obtain better observations of the umbral granules. The results are based on photographs selected from eleven films of six different spots. In agreement with Rösch's observations, these photographs reveal the existence of granules in spot umbrae (Plates 1 (*b*), 2 (*c*)). Measurements, although based on only a small number of granules, indicate that the " cell size " of the umbral granulation is less than that of the photospheric granulation ; moreover, the lifetime is found to be greater. In addition to granulation, " loop " structures are sometimes seen (Plate 3 (*c*)). Finally, in agreement with the observations of Das and Ramanathan (1953), it is found that the (smoothed) intensity profile of a spot umbra is not rectangular ; large spots often contain several intensity minima, each pair being separated by a " saddle ".

II. Instrument

The observations were made with the 5-in. photoheliograph (Loughhead and Burgess 1958) of the C.S.I.R.O. Division of Physics Solar Observatory. This instrument is designed to photograph any selected region of the solar disk on 35 mm film at 5-sec intervals, the 16 mm image formed by the objective being magnified by a second lens to a diameter of 20 cm. The effective wavelength is 5400 Å and the theoretical limit of resolution is $0 \cdot 8$ sec of arc.

---

* Division of Physics, C.S.I.R.O., University Grounds, Chippendale, N.S.W.

In order to photograph detail in the umbra of a spot it is necessary to give an exposure greater than that required for the penumbra or surrounding photospheric granulation. The necessary increase in exposure depends both on the size of the spot and on position in the umbra. Exposure factors ranging from two to seven were used; the latter value is normally sufficient for recording detail in the darkest region of the umbra of a very large spot. Apart from the removal of a 50 per cent. neutral filter normally present in the light path, the increases in exposure were achieved by using longer exposure times.

In the absence of any precautions, the contrast of the faint umbral detail would be reduced by scattered light from the penumbra and surrounding photosphere. To eliminate scattered light from the magnifying lens and two auxiliary prisms which divert the beam to the camera, prime-focus diaphragms were constructed, with diameters ranging from 0·06 to 0·22 mm. This range is adequate for the larger umbrae encountered on the 16 mm primary solar image. The diaphragms were made of thin aluminium foil, the holes being pierced with a fine, burnished needle. Any selected diaphragm could be mounted in a small metal box containing a central aperture. This box was carried on a Hilger micrometer microscope stage, which provided fine motions in two directions at right angles to the optical axis, thus permitting the diaphragm to be positioned on any part of a spot umbra. In addition, motion of the box along the optical axis allowed the diaphragm to be brought into the focal plane; to reduce heating, air was sucked through perforations in the front surface of the box (cf. Loughhead and Burgess 1958).

Any remaining scattered light is due to scattering in the Earth's atmosphere and at the 5-in. objective. Atmospheric scattering is usually low at the site of the Solar Observatory, some 30 miles south-west of Sydney. In addition, the objective is a cemented doublet—a type of lens inherently free from scattered light; it was cleaned regularly during the course of this work.

III. Observational Technique

The diaphragm selected for any given spot depended on the size and shape of the umbra. If this was circular, a diaphragm was usually selected which just included the inner edge of the penumbra, as seen in the telescope eyepiece (the umbra appears somewhat smaller on a visual image than on normal photographs such as Plates 1 (*a*), 2 (*a*), and 3 (*a*)). However, a smaller diaphragm was used when only the detail at the darkest point was required. If the spot was elliptical, a diaphragm was selected which just included the inner edge of the penumbra at the ends of the minor axis.

For a large umbra, such as that illustrated in Plate 3, the observing procedure was as follows: the spot was photographed without a diaphragm every 5 sec for a period of 5 min, using an overexposure factor of three. This sequence served to reveal the structure in the neighbourhood of the umbra-penumbra boundary and, in the subsequent examination of photographs taken through a diaphragm, helped to locate the position of the diaphragm relative to the spot. The appropriate diaphragm was then inserted and a 20 min sequence with an overexposure factor of five was obtained in order to show the structure of the outer umbra. Retaining the diaphragm, a further 20 min sequence was obtained, using an overexposure factor of seven ; this sequence served to reveal the structure of the core of the umbra. Finally, a repetition of the first sequence was followed by a 15 min sequence of normal photographs and a photometric calibration.

A similar procedure was used for smaller umbrae, such as that illustrated in Plate 1, except that overexposure factors ranging from 2 to 5 instead of from 3 to 7 were employed.

During the period September 1958 to February 1959, 11 films were obtained of six different sunspots of various sizes. Although photography was confined to days of exceptionally good seeing, examination of the films reveals less than 40 umbral photographs whose quality approaches the theoretical performance of the telescope. However, many others provide useful supporting data. The umbral granulation was found to be more difficult to photograph successfully than the photospheric granulation ; our experience shows that this can be attributed partly to the greater exposure times required.

IV. The Detail in Sunspot Umbrae

Plates 1–3 illustrate the typical detail to be seen in sunspot umbrae.

Plate 1 (*a*) is a normal photograph of a fairly large spot and the surrounding photospheric granulation. The umbra is divided into two parts by a light-bridge, which itself shows some granular structure. Plate 1 (*b*) shows, on twice the scale, a fourfold overexposure taken through a diaphragm centred on the upper part of the umbra. A number of umbral granules can be distinguished, including three faint ones at the dark core of the umbra. They are more closely packed than the photospheric granules (Section VI).

Plate 2 (*a*) is a normal photograph of a somewhat larger spot ; on the original negative a faint light-bridge can be seen across the centre of the umbra. Plates 2 (*b*) and 2 (*c*) show twofold and threefold overexposures respectively, roughly centred on the light-bridge ; the scale of these photographs is twice that of Plate 2 (*a*).

As shown in Plate 2 (*b*), the light-bridge consists of bright segments, an elongated portion near the middle being particularly prominent. On the right-hand border of the umbra there are several bright granules ; these granules are apparently detached from the penumbral filaments and are much brighter than those within the umbra proper. Examination of other films has shown them to be a characteristic feature of the umbra-penumbra boundary* (cf. Secchi 1875).

In Plate 2 (*c*) the centre of the light-bridge is overexposed, but its " wings " begin to appear. Above the light-bridge a number of umbral granules are now visible. The exposure is insufficient to show any granulation in the lower portion of the umbra (which the negative shows to be darker than the upper) or in the central region of the upper part ; overexposures greater than threefold are not available for this spot. It is clear that there are two points of minimum intensity separated by a saddle which, on an overexposure, appears as a light-bridge. Note the small variation in brightness of the granules in its neighbourhood.

---

* They are not to be confused with the bright regions sometimes found on the *penumbra* side of the umbra-penumbra boundary (Bray and Loughhead 1957 ; Loughhead and Bray 1958 : cf. Plate 1).

Finally, Plate 3 (*a*) shows the main spot* of the largest group which has appeared to date during the current sunspot maximum. On the same scale Plate 3 (*b*) shows a threefold overexposure made without a diaphragm. The outline is essentially an *isophote* of the umbra; it differs considerably from the outline of the umbra shown on the normal exposure. In addition, the left-hand region of the umbra is now seen to be brighter than the rest; it shows several umbral granules, whereas only one particularly bright granule is visible in the main portion.

Plate 3 (*c*) is a sevenfold overexposure taken through a diaphragm roughly centred on one of the points of minimum intensity; it is reproduced on twice the scale of Plate 3 (*a*) and (*b*). The umbral granulation is only faintly visible on the negative, probably owing to mediocre seeing, and fails to appear on the print. However, there is one striking feature, a bright loop which appears to consist of four elongated granules. Similar loops have been seen in other umbrae. This photograph shows clearly that the umbral intensity profile is far from rectangular.

The nature of the umbral detail shown by Plates 1–3 is in general confirmed by the rest of the observational material. In particular, umbral granules similar to those illustrated have been seen on all the films except one. Often the granules appear faint or indistinct, but this can usually be attributed to incorrect exposure or poor seeing. One fairly large spot failed to show more than one or two granules, although the exposure was correct and the seeing, judged by other criteria, appeared fair. In this case it is possible that the quality of the seeing has been wrongly assessed. Granulation has also been observed in the umbrae of small spots and in pores only a few seconds of arc in diameter. In such cases the granulation often appears on negatives taken with a normal exposure.

V. Lifetimes of the Umbral Granules

The film of the spot shown in Plate 2 provided nine photographs of sufficient quality to enable an estimate to be made of the lifetimes of the umbral granules; these photographs extend over a period of 32 min 42 sec. In estimating the lifetimes a method was employed similar to that used in determining the lifetimes of the photospheric granules (Bray and Loughhead 1958*b*).

Four of the granules were observed throughout the entire period (two of them failed to appear on one photograph) and therefore provide clear evidence that some granules last for at least half an hour. Four others were reliably identified for periods ranging from 4 to 10 min. However, for various reasons the non-appearance of these granules at other times cannot be taken as definite evidence of their non-existence. Hence all the above values represent only *lower limits* to the true lifetimes. A longer series of high quality photographs might well show that the true values are actually higher.

---

* The diffuse bright streak crossing the penumbra (top, left) is not a photographic defect but is a real feature of a type which has been noticed before.

Despite the small number of lifetimes estimated, it is clear that some umbral granules are longer lived than the photospheric granules, whose lifetimes according to the best available estimates are of the order of 10 min (Macris 1953 ; Bray and Loughhead 1958*b*).*

VI. "Cell Size" of the Umbral Granulation

Simple measurements of the diameters of individual umbral granules provide at best only a rough guide to the true sizes, owing to their dependence on photographic contrast and on the combined instrumental profile of telescope and atmosphere (cf. Bray and Loughhead 1958*b*). However, the mean "cell size" of the pattern, i.e. the average distance between the centres of adjacent granules, is independent of these effects, provided individual granules are actually resolved. This quantity therefore provides a more reliable parameter for characterizing the scale of the pattern.†

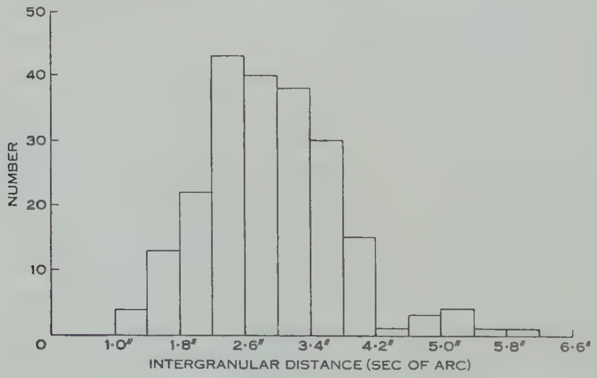

Fig. 1.—"Cell size" of the photospheric granulation : the histogram gives the distribution of the distances between the centres of adjacent granules, measured for a group of 92 granules. The most probable value is 2·6 sec of arc and the mean value 2·9 sec. The cell size of the umbral granulation is found to be 2·0 sec (see text).

To determine the mean cell size the distances between the centres of adjacent granules have been measured for the groups of granules in the umbrae of the spots illustrated in Plates 1 (*b*) and 2 (*c*) ; these are the only two spots for which sufficiently good photographs of the umbral granulation are available. The first group gave four values ranging from 1·7 to 2·0 sec of arc, with a mean of 1·9 sec. The second group gave 11 values ranging from 1·5 to 2·3 sec together with one value of 2·7 sec, giving a mean of 2·0 sec. Although based on small numbers of granules, the results for the two spots are concordant and give an overall mean of 2·0 sec of arc for the cell size of the umbral granulation.

---

* Penumbral filaments are also longer lived than the photospheric granules, having lifetimes of the order of several hours (Bray and Loughhead 1958*a*).

† Nakagawa (1959) has used a similar parameter in an experimental verification of Chandrasekhar's theory of convection in conducting liquids in the presence of a magnetic field.

It is interesting to compare this result with the mean cell size of the photospheric granulation, derived from measurements of a good-quality photograph (Bray and Loughhead 1958*b*: cf. Plate 1) taken with the same instrument. The results, which were derived from a group of 92 granules, are given in Figure 1. The mean value is 2·9 sec of arc, the most probable value being about 2·6 sec. The mean cell size of the umbral granulation in the two spots measured is therefore significantly less than that of the photospheric granulation.

All measurements were corrected for foreshortening.

VII. CONCLUSION

The observations described in this paper have confirmed the existence of granulation in the umbrae of sunspots; this resembles the photospheric granulation but differs in regard to lifetime and cell size. The intensity profile of a spot umbra is not rectangular (Das and Ramanathan 1953). A large umbra often possesses several intensity minima, each pair being separated by a " saddle ". Thus, quite apart from the granulation, the intensity contours of spot umbrae show a detailed and complex structure. What relationship, if any, does this structure bear to the umbral magnetic field distribution? Recent progress in plotting magnetic fields (e.g. Nikulin, Severny, and Stepanov 1958) leads one to hope that with improved spatial resolution this question may soon be answered.

The similarity of the umbral granulation to the photospheric granulation raises the question of whether the umbral granules, like the photospheric granules (Loughhead and Bray 1959), are to be identified with convection cells. If so, it follows that even the strong magnetic fields present in large spots fail to suppress the convective motions. These questions will be discussed more fully in a later paper.

VIII. ACKNOWLEDGMENTS

The authors wish to thank Mr. D. G. Norton for making the diaphragms and designing their mount, and for help in securing the observations. They would also like to thank Mr. H. Gillett for processing the films and making the enlargements.

IX. REFERENCES

BRAY, R. J., and LOUGHHEAD, R. E. (1957).—*Observatory* **77**: 201.
BRAY, R. J., and LOUGHHEAD, R. E. (1958*a*).—*Aust. J. Phys.* **11**: 185.
BRAY, R. J., and LOUGHHEAD, R. E. (1958*b*).—*Aust. J. Phys.* **11**: 507.
CHEVALIER, S. (1916).—*Ann. Obs. Zô-Sè* **9**: B.10.
DAS, A. K., and RAMANATHAN, A. S. (1953).—*Z. Astrophys.* **32**: 91.
LOUGHHEAD, R. E., and BRAY, R. J. (1958).—*Aust. J. Phys.* **11**: 177.
LOUGHHEAD, R. E., and BRAY, R. J. (1959).—*Nature* **183**: 240.
LOUGHHEAD, R. E., and BURGESS, V. R. (1958).—*Aust. J. Phys.* **11**: 35.
MACRIS, C. (1953).—*Ann. Astrophys.* **16**: 19.
NAKAGAWA, Y. (1959).—*Proc. Roy. Soc.* **A 249**: 138.
NIKULIN, N. S., SEVERNY, A. B., and STEPANOV, V. E. (1958).—*Izv. Crim. Astrophys. Obs.* **19**: 3.
RÖSCH, J. (1957).—*Astronomie* **71**: 129.
SECCHI, A. (1875).—" Le Soleil." 2nd Ed., Vol. I, p. 84. (Gauthier-Villars: Paris.)
THIESSEN, G. (1950).—*Observatory* **70**: 234.
WALDMEIER, M. (1955).—" Ergebnisse und Probleme der Sonnenforschung." 2nd Ed., p. 185. (Geest u. Portig: Leipzig.)

EXPLANATION OF PLATES 1–3

PLATE 1

(*a*) Sunspot photographed at $1^h\,36^m$ E.A.S.T. on September 1, 1958. Heliographic coordinates: 204° W., 6° S.; heliocentric angle, 23°.

(*b*) Fourfold overexposure taken at $11^h\,44^m$ through a small diaphragm centred on the upper portion of the umbra. Several umbral granules are distinctly shown, including three faint ones at the core of the umbra. The scale of (*b*) is twice that of (*a*).

PLATE 2

(*a*) Sunspot photographed at $12^h\,25^m$ E.A.S.T. on September 19, 1958. Heliographic coordinates: 303° W., 19° S.; heliocentric angle, 28°.

(*b*) Twofold overexposure taken at $10^h\,39^m$ through a diaphragm. Note the discrete structure of the light-bridge and the bright granules at the umbra-penumbra boundary.

(*c*) Threefold overexposure taken at $11^h\,19^m$. The part of the umbra above the light-bridge is brighter than that below, and shows clear umbral granulation.

The approximate position of the diaphragm relative to the spot is shown by the white circle. The scale of (*b*) and (*c*) is twice that of (*a*).

PLATE 3

(*a*) Sunspot photographed at $2^h\,40^m$ E.A.S.T. on January 12, 1959. Heliographic coordinates: 253° W., 11° N.; heliocentric angle, 25°.

(*b*) Threefold overexposure taken at $12^h\,34^m$ without a diaphragm. Note that the apparent umbral outline differs from that in (*a*); a few umbral granules can be seen in the left-hand portion.

(*c*) Sevenfold overexposure taken at $2^h\,10^m$ through a diaphragm, whose location is shown by the white circle in (*a*). Note the bright " loop " structure (lower, left) and the gradual decrease in intensity towards the core of the umbra. Granulation fails to appear owing to mediocre seeing. The scale of (*c*) is twice that of (*a*) and (*b*).

GRANULAR STRUCTURE OF SUNSPOT UMBRAE

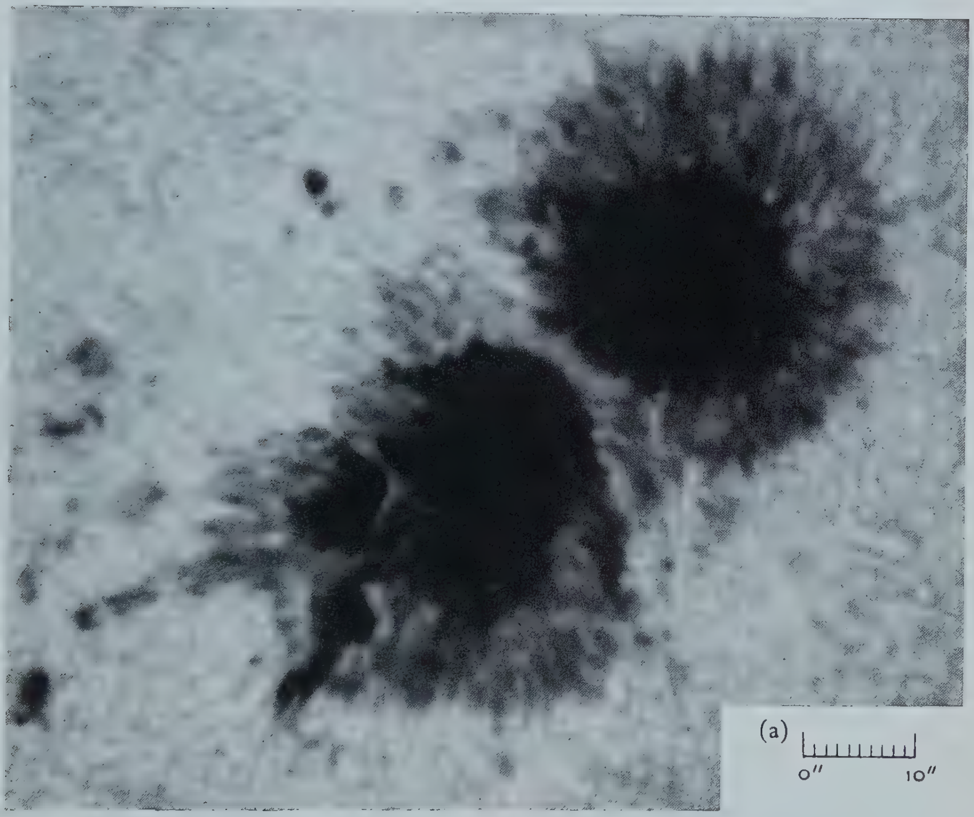
(a)

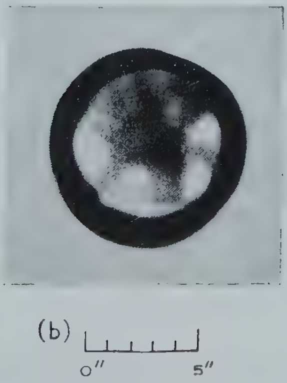
(b)

GRANULAR STRUCTURE OF SUNSPOT UMBRAE

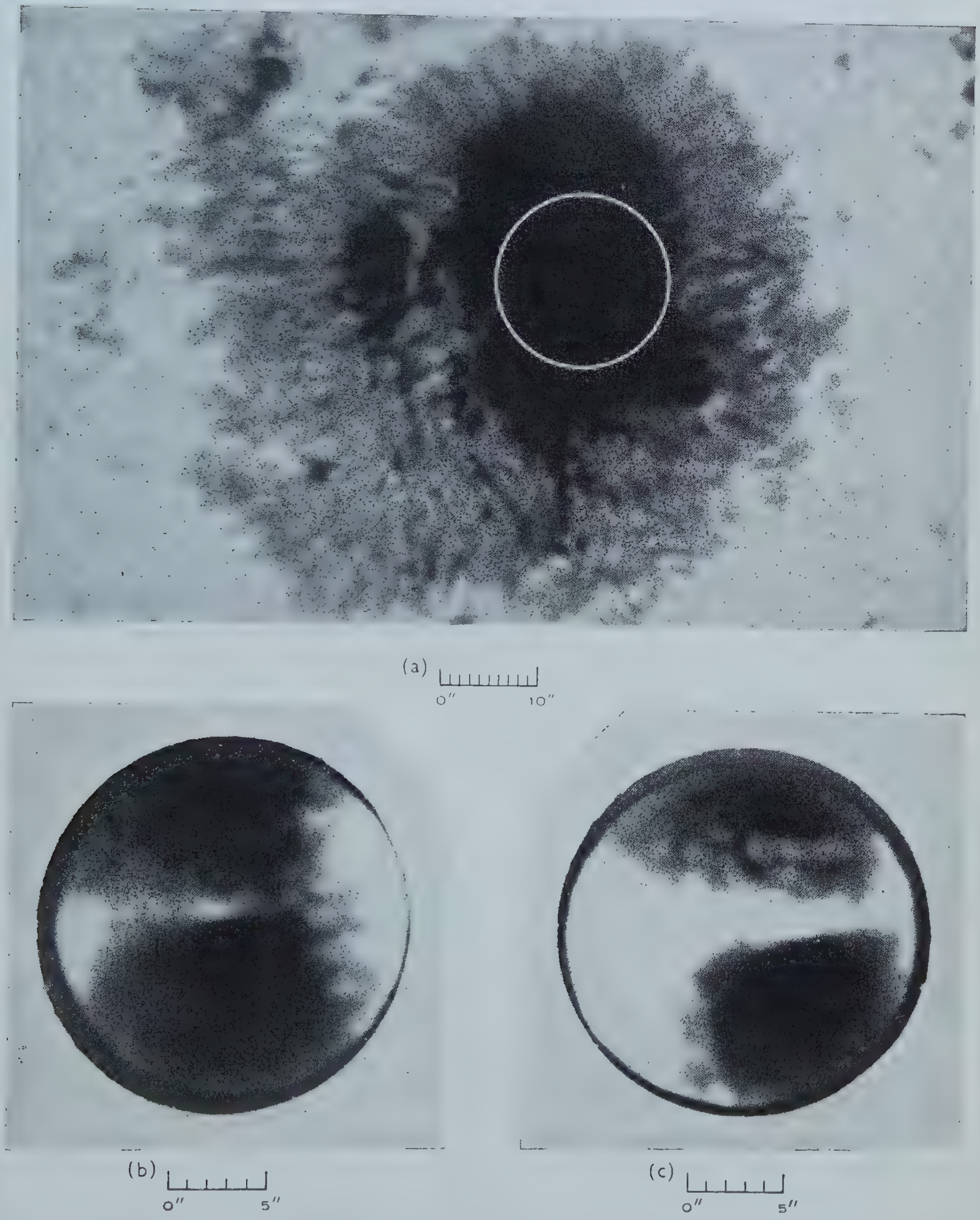

GRANULAR STRUCTURE OF SUNSPOT UMBRAE

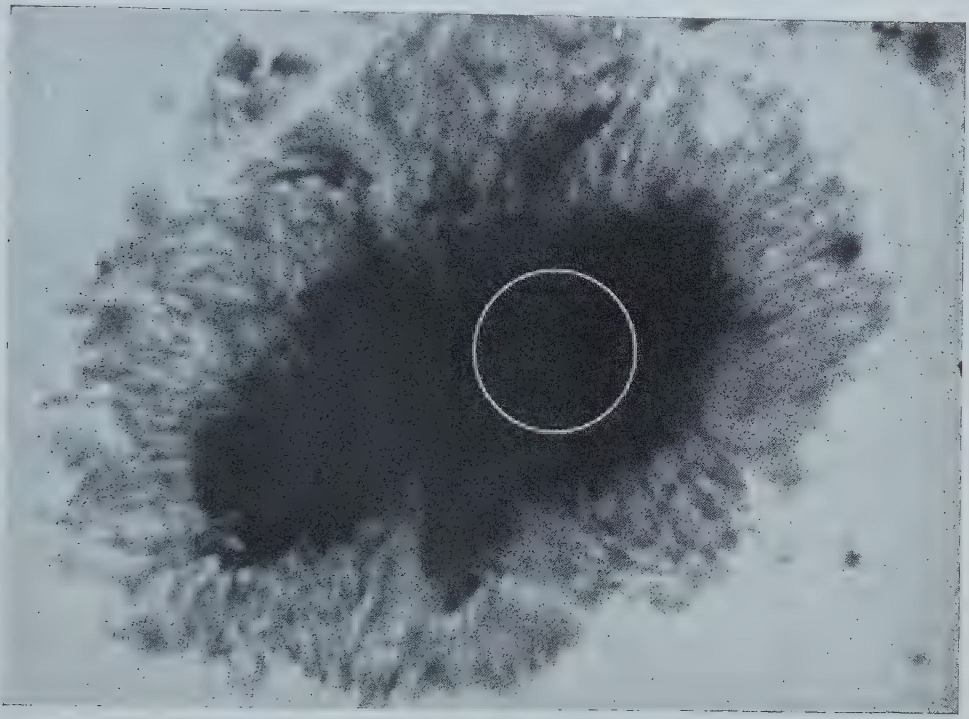
(a)

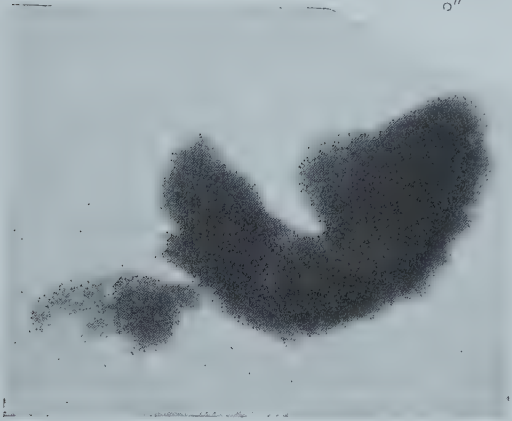
(b)

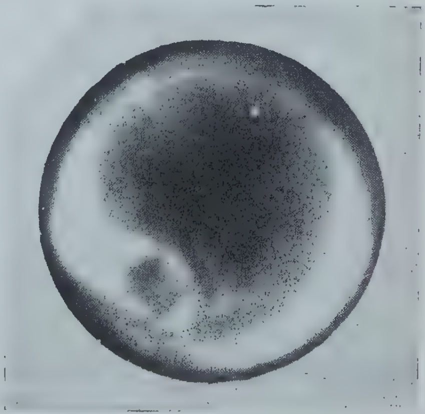
(c)

SOLAR RADIO BURSTS OF SPECTRAL TYPE II

By J. A. Roberts*

[*Manuscript received June 29, 1959*]

Contents

Page
Summary 327
I. Introduction 328
II. Bursts of spectral type II 329
  (*a*) Equipment 329
  (*b*) Spectral characteristics of type II bursts 329
  (*c*) Occurrence 331
  (*d*) Intensity and polarization 331
III. The frequency range of type II bursts 332
IV. The rates of frequency drift and the inferred speeds 333
V. Harmonic structure 336
  (*a*) Relative intensities 336
  (*b*) Harmonics higher than the second 336
  (*c*) Group delay between harmonics 338
  (*d*) The harmonic ratio and the position on the disk 339
VI. Band splitting 341
  (*a*) Observations 341
  (*b*) Interpretation 342
VII. The herring-bone structure 343
  (*a*) Observations 343
  (*b*) Interpretation 344
VIII. Compound type III–type II bursts 345
  (*a*) Observations 345
  (*b*) Interpretation 346
IX. Type II bursts and chromospheric flares 347
X. Type II bursts and geomagnetic storms 350
XI. Conclusion 353
XII. Acknowledgments 354
XIII. References 354

Summary

The characteristics of bursts of spectral type II are studied in a sample of 65 bursts. Approximately half the bursts show harmonic structure and about half are compound type III–type II events. Band splitting, the doubling of both the fundamental and second harmonic bands, is also relatively common. A rather less common feature is the appearance of herring-bone structure in which the slowly drifting band of the type II burst appears to be a source from which rapidly drifting elements diverge towards lower and higher frequencies.

Statistics are given of the rate of occurrence of the bursts, their frequency range, the rate of frequency drift, and the harmonic ratio.

---

* Division of Radiophysics, C.S.I.R.O., University Grounds, Chippendale, N.S.W.

Many of the type II bursts occurred near or after the maximum of a chromospheric flare. However, only about 3 per cent. of flares (of Class 1 or greater) are accompanied by type II bursts, although the figure rises to 30 per cent. for Class 3 flares.

There is a greater tendency for the geomagnetic field to be disturbed in the few days following a type II burst than there is after large flares which are not accompanied by type II bursts, or after large radio bursts of spectral type III. Statistically the greatest disturbance occurs after about two days, implying a mean speed of travel of about 1000 km/sec.

I. Introduction

One of the challenging discoveries made by the early investigators of solar radio emission was the existence of a class of intense metre-wavelength " burst " in which the emission appeared first at the higher frequencies (several hundred megacycles per second) and in the following minutes drifted slowly downward in frequency to perhaps 10 Mc/s. These bursts were first recognized from records made simultaneously at a number of discrete frequencies (Payne-Scott, Yabsley, and Bolton 1947), and were later studied with a dynamic spectrum analyser (Wild and McCready 1950 ; Wild 1950). Wild and McCready introduced the designation *spectral type II* for the bursts. They gave as the defining characteristic the drift of spectral features, with time, from high to low frequencies at a rate of the order of $\frac{1}{4}$ Mc/s per sec.

The observations made over the past five years with the Dapto radio-spectrograph have fully confirmed the existence of a distinct class of solar burst conforming with this definition. A total of 65 such bursts were recorded in the period from September 1952 to March 1958, and the present paper presents an analysis of these events. While many of the properties of the bursts have already been described in the literature, there is at present no comprehensive review of a large sample of bursts. This paper is an attempt to meet this need.

The main features of the bursts are described in Section II and are illustrated by a selection of records reproduced in the plates. The frequency range and the rate of frequency drift are discussed in Sections III and IV, while the following four sections deal with features which appear prominently in many of the bursts but are not universal characteristics of the type. The majority of these features have already been described in publications by Wild and his collaborators, but the " herring-bone structure " (Section VII) has not been described previously.* In this variation of the type II burst the characteristic slowly drifting band appears to be a source from which rapidly drifting, short-duration bursts emerge. In some cases the rapidly drifting elements have both positive and negative slopes, so that in the frequency-time plane the burst has the appearance of a herring-bone.

In two further sections of the paper statistics are given of the association of type II bursts with solar flares (Section IX) and with geomagnetic storms (Section X).

Although the paper is primarily intended as a summary of the observational material, some discussion of the results is given. In this, the plasma hypothesis is adopted, i.e. it is assumed that the bursts represent radiation from oscillations induced in the coronal plasma by the outward passage of a disturbance. This theory suffers from severe difficulties as regards the coupling of the oscillations to the radiation field, but it appears to be the most hopeful of the theories proposed to date. (See e.g. Wild, Murray, and Rowe 1954; Ginzburg and Zhelezniakov 1958, 1959; Wild, Sheridan, and Trent 1959.)

---

* A brief account of the " herring-bone structure " was presented by the author at the I.A.U.-U.R.S.I. Radio Astronomy Symposium at Paris in August 1958.

II. BURSTS OF SPECTRAL TYPE II

(a) *Equipment*

The observations reported in this paper were made with the Dapto radiospectrograph, which has been briefly described by Wild, Murray, and Rowe (1954). In this instrument the receiver sweeps through the frequency range of 40–240 Mc/s every half second,* and the output is used to intensity modulate the spot of a cathode-ray tube. The spot is deflected in synchronism with the sweeping of the receiver frequency so that when it is photographed on film moving slowly and continuously at right angles to the deflection, a complete dynamic spectrum is built up on the film in a manner similar to the formation of a television image. Examples of records of type II bursts made with this equipment will be found in Plates 1–5.

At the lower frequencies the weakest signals that can be clearly detected with the equipment have flux densities of about† 5×10^{-21} W m^{-2} (c/s)$^{-1}$, and with the normal adjustment of the equipment flux densities up to about 5×10^{-19} W m^{-2} (c/s)$^{-1}$ can be comfortably accommodated on the film. At higher intensities saturation in both the receiver and the film can lead to loss of detail. At the higher frequencies the sensitivity decreases by a factor of up to 5 times.

Arrangements are also available for determining the polarization of the incoming radiation over the whole range of frequencies (Komesaroff 1958).

(b) *Spectral Characteristics of Type II Bursts*

The records reproduced in Plates 1–5 have been chosen to illustrate the chief characteristics of the 65 bursts which have been classified as spectral type II. The common feature in these bursts is the drift of some of the main spectral features from high to low frequencies at rates of up to 1 Mc/s per sec. The total duration of the bursts is of the order of minutes. This definition of the type is sufficiently wide to embrace all the 65 bursts and at the same time is sufficiently narrow to exclude the majority of other bursts on the records.

Although all the bursts have these features in common, it is seen that they differ widely amongst themselves and that some exhibit other outstanding characteristics. We may list seven notable features which are present in some, but not all, bursts of this class.

(i) *Narrow Bandwidth*.—In the majority of the bursts the drifting bands are remarkably narrow, the bandwidths being as low as a few megacycles per second. The theoretical implications of this observation have been emphasized by Wild, Murray, and Rowe (1954). While narrow bandwidths are common, they do not occur invariably, as is illustrated by the burst of February 14, 1956 (Plate 2).

---

* Since September 1957 the upper limit of the range has been 200 Mc/s.

† Flux densities are specified for one plane of polarization.

(ii) *Harmonic Structure.*—In approximately 60 per cent. of the bursts the drifting bands appear in harmonic pairs. This feature, described by Wild, Murray, and Rowe (1954), is evident in all the examples in Plates 1, 3, and 4. It is discussed in detail in Section V.

(iii) *Band Splitting.*—Many of the bursts show a secondary doubling of the bands, which is illustrated by the examples in Plate 4. In these events both the fundamental and the second harmonic bands are split into a pair of ridges with a separation which is usually small compared with that between the two harmonics. This phenomenon was described in the original paper by Wild (1950). Some statistics and a theoretical discussion are given in Section VI.

(iv) *Multiple Bands.*—In some of the bursts there are several " independent " drifting bands which are neither harmonically related nor caused by band splitting. They are presumably generated by separate disturbances travelling through the corona. Although these bands are not harmonically related, each may be accompanied by a second harmonic, as in the events of January 19, 1956 (Plate 3) and January 15, 1958 (Plate 2). Furthermore, each of the fundamental and second harmonic bands may themselves be split as in the event of August 6, 1957 shown in Plates 1 and 4. The resulting band structure is quite complex. Other bursts with large numbers of drifting bands have been observed, but it has not been possible to analyse them in this way. Some of these bursts begin suddenly over a wide range of frequencies.

(v) *Compound Type III–Type II Bursts.*—Another characteristic common to approximately half the bursts is the appearance of a group of type III bursts preceding the type II burst by some minutes (Plate 1). Section VIII contains a more detailed description of this phenomenon, which was first described by Wild, Roberts, and Murray (1954).

(vi) *Herring-bone Structure.*—A somewhat less common feature is the appearance of the herring-bone structure mentioned in the introduction. Plate 5 contains examples of this structure, which is discussed in Section VII.

(vii) *Other Fine Structure.*—Besides the herring-bone structure various other forms of fine structure are seen in the bursts. The drifting bands are rarely smooth and continuous but fluctuate in intensity over periods of seconds. In some cases the bands consist of a series of short-duration, narrow-band bursts which themselves show the type II frequency drift. Examples are seen in Plate 3 in the events of November 15, 1955 and January 19, 1956. On other occasions some or all of the " sub-bursts " forming the bands are much more amorphous and resemble the narrow-band type I bursts.

For examples see the events of November 13, 1957 and August 6, 1957 illustrated in Plate 4. Fine structure of the type described by Haddock (1958), in which the sub-bursts resemble type III bursts of short duration, is of course present in the bursts with herring-bone structure, but otherwise was not a noticeable feature in the bursts.

(c) *Occurrence*

Type II bursts are rare by comparison with types I and III. Figure 1 shows that even near sunspot maximum such bursts occur only about once in 50 hr on the average, whereas at this time the average rate of occurrence of type I and type III bursts is probably one every few minutes. The figure indicates a marked increase in occurrence towards sunspot maximum, but many more observations are needed to delineate the details of the solar cycle variation.

On a shorter time scale the bursts are not randomly distributed in time either. On three occasions two type II bursts have been recorded within a few hours of one another, and many of the other bursts occur on days grouped closely together. Furthermore, there are several examples of events which really consist of two type II bursts separated by only a few minutes in time. Some of these are compound bursts in which the double type II burst is preceded by two groups of type III bursts with a similar time separation. In Plate 1 the earlier event on August 6 is of this nature.

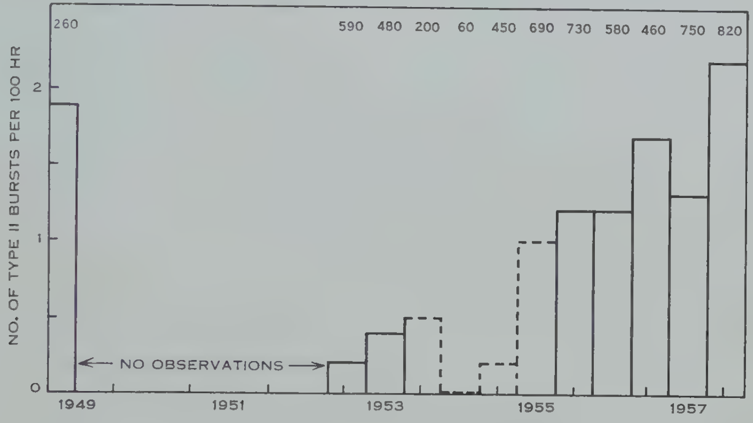

Fig. 1.—Showing the frequency of occurrence of type II bursts. The numbers at the top of the figure show the number of hours of observation in each 6-monthly period. The observations in 1949 are those made by Wild and McCready (1950) with the original solar radio-spectrograph (70–130 Mc/s). During the period near sunspot minimum (1954), where the histogram is shown dashed, the observing time was confined entirely to occasions when sunspots were visible on the disk.

From this clustering of type II bursts it is inferred that some active regions on the Sun produce many type II bursts, while others do not produce any. The correlations with solar flares discussed in Section IX are fully in accord with this deduction.

(d) *Intensity and Polarization*

The peak intensities of type II bursts range from the limit of detection up to several times 10^{-18} W m^{-2} (c/s)$^{-1}$. Intensities in excess of 10^{-19} W m^{-2} (c/s)$^{-1}$ are not uncommon. These high intensities, together with the durations of minutes or tens of minutes, led Wild (1950) to identify type II bursts as the " outbursts " recorded on single-frequency equipments. However, it is now recognized that many of these outbursts are large groups of intense type III bursts. Such events are more common than strong type II bursts and often have very great intensities. In some compound type III–type II events the energy in the type III part outweighs that in the type II burst (e.g. the events of August 6, 1957 illustrated in Plate 1).

Evidence on the polarization of type II bursts is very incomplete. However, there are sufficient measurements available to show that these bursts are usually not strongly polarized (Komesaroff 1958). More recent measurements have confirmed Komesaroff's finding and have further shown that even split-band type II bursts are not strongly polarized.

III. The Frequency Range of Type II Bursts

In the course of a type II burst the frequency of emission may drift over hundreds of megacycles per second, but in no recorded case does the *fundamental* band extend over the whole frequency range of the equipment. Typically, the burst begins suddenly with the fundamental and second harmonic beginning nearly simultaneously (Plates 1, 3, and 4). At this onset the frequency of the fundamental is commonly below 80 Mc/s and no case is known in which the fundamental band extends above 120 Mc/s (Fig. 2). In a number of the more intense bursts the fundamental band continues to the lower limit of the observed range at 40 Mc/s and occasionally the second harmonic also extends to this limit. In other cases, however, both the fundamental and second harmonic bands stop suddenly and almost simultaneously before reaching 40 Mc/s (Plates 3 and 4). In a few such cases the emission begins again at a later time, and in the frequency-time plane the later emission lies along an extension of the earlier ridge-line (Plate 2, event of December 6, 1957). It is as if the burst consisted of a pair of continuous harmonic ridges, but for part of the time the emission ceased.

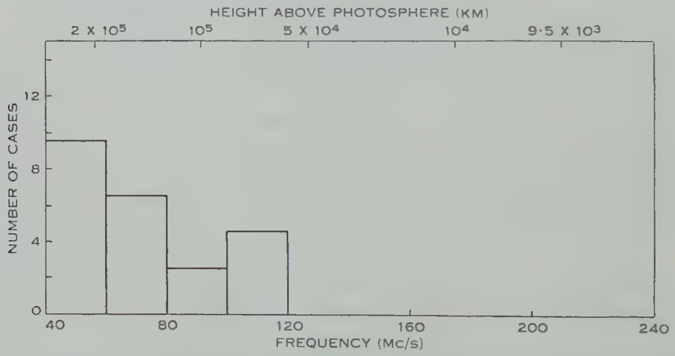

Fig. 2.—Histogram showing the distribution of the starting frequency of the fundamental band of 23 harmonic type II bursts. The height scale is derived on the assumption of emission at the plasma frequency in a Baumbach-Allen model corona.

In seeking an explanation of these sudden changes, one first notices that, because the effects occur nearly simultaneously in the fundamental and second harmonic bands, they cannot be caused by changes in the propagation conditions in the Sun or in the ionosphere. The refractive index of an ionized medium is so strongly dependent on the frequency (f^{-2}) that the fundamental and second harmonic bands would be affected quite differently. To explain the phenomenon on the plasma theory it seems necessary to suppose that some critical condition must be satisfied before the travelling disturbances will excite the corona to radiate. With such an assumption it is possible to account for the sudden onset of the type II bursts and also for the occurrence of several sections of a ridge with the intervening parts missing.

Whatever this unknown condition for emission may be, it is evidently rarely satisfied in the lower corona (below the 100 Mc/s plasma level). This is inferred from the observation that the fundamental band rarely extends into this range, although the evidence of the compound bursts (Section VIII) strongly suggests that the exciting disturbances travel outward through this region.

IV. The Rates of Frequency Drift and the Inferred Speeds

Figure 3 (*a*) shows the rate of frequency drift in type II bursts as a function of the frequency. These measurements relate to 24 bursts with clear harmonic structure and apply to the fundamental band. Where the rate of drift was measured at a number of frequencies in the one burst the measured values are joined by a line: where the drift was measured at only one frequency the value is shown by a cross. The mean drift rate is seen to increase from 0·04 Mc/s per sec at 30 Mc/s to 0·35 Mc/s per sec at 90 Mc/s. The spread of the observed values also increases with the frequency, but the spread of values expressed as a percentage of the mean is fairly constant.

According to the plasma hypothesis, when the height distribution of electron density in the corona is known the observed drift rates can be converted to equivalent radial components of speed. The actual distribution of electron density at the time and place of a burst is not known, and it is customary to use the densities given by one of the coronal models based on averaged eclipse observations. Such a procedure will not yield reliable results, since the coronal density varies with time, particularly above sunspots. Indeed, Wild, Sheridan, and Trent (1959) have recently measured the direction of arrival of the different frequencies in type II bursts and have shown that, while the results qualitatively support the plasma hypothesis, they require the scale of the corona to be several times greater than in the conventional models. However, in the absence of detailed knowledge of the electron densities in the corona, it appears worth while to discuss the drift rates in terms of an averaged model, whilst bearing in mind that the results may be correct to order of magnitude only. The speeds so obtained are likely to be low, perhaps by a factor of three.

With these considerations in mind, we proceed to a discussion of the drift rates in Figure 3 (*a*), adopting the Baumbach-Allen model corona (Allen 1947). The broken curves in Figure 3 (*a*) show the drift rates expected in such a corona for disturbances with radial speeds of 300, 500, 700, and 1000 km/sec. It is seen that these curves embrace the observed values fairly well; below 60 Mc/s the curve for 500 km/sec is almost the line of medians. For five of these bursts actual height-time plots based on the same model are given in Figure 4. As was

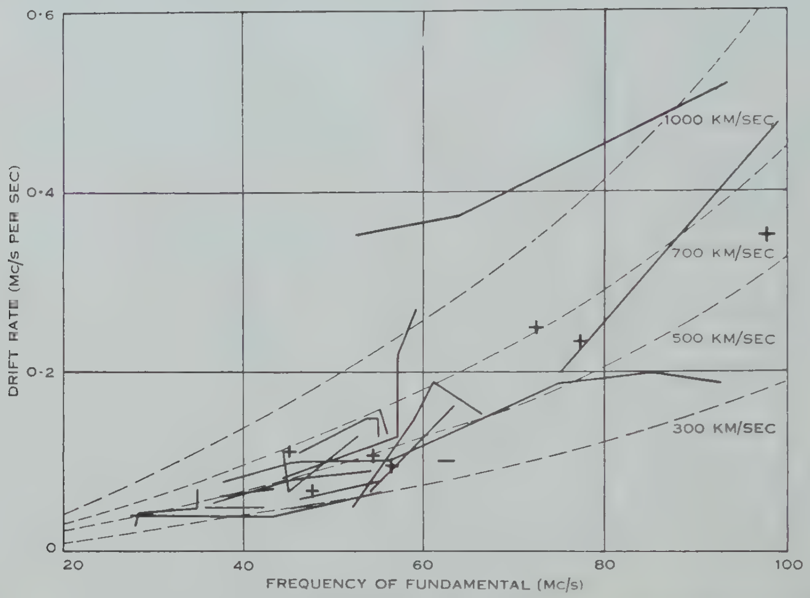

Fig. 3 (*a*).—Showing the frequency dependence of the drift rate in the fundamental band of 24 harmonic type II bursts. Where the frequency drift was measured at a number of frequencies in the one burst the measured values are joined by a line: where the drift was measured at only one frequency the value is shown by a cross. The dashed curves show the drift rates expected for disturbances moving through a Baumbach-Allen model corona at constant radial speeds of 300, 500, 700, and 1000 km/sec.

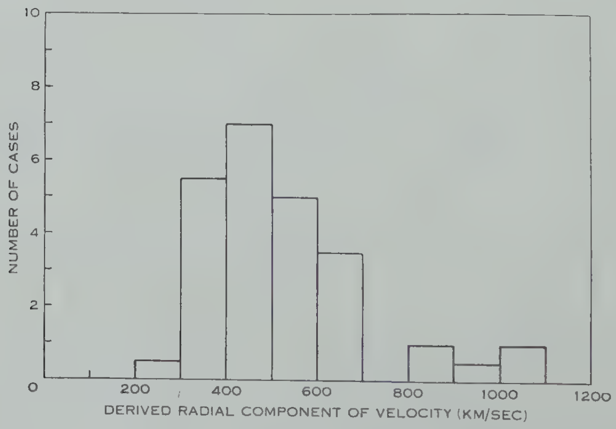

Fig. 3 (*b*).—Histogram of the derived mean radial speeds of the 24 harmonic type II bursts included in Figure 3 (*a*). Baumbach-Allen model corona.

suggested by the comparisons in Figure 3 (*a*), many of these graphs are essentially straight lines. This somewhat surprising result perhaps indicates that the actual density distribution along the trajectory of the disturbance differs from the model mainly by a change in the height scale.

In passing, it may be noted that a gravitational deceleration would not be expected to be detectable except when the true radial speed was below about 350 km/sec.

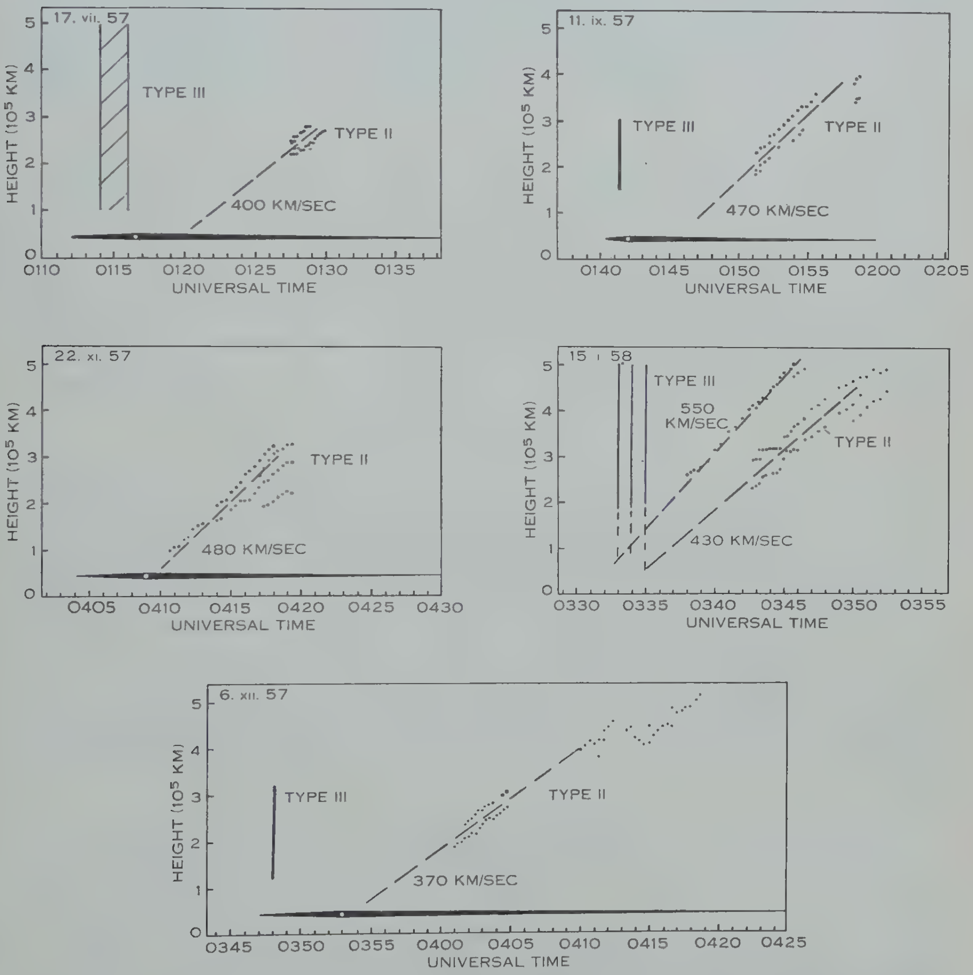

Fig. 4.—Derived height-time plots for five harmonic type II bursts. Reproduction of the spectral records of three of these bursts will be found in Plates 1 and 2. The graphs assume that emission occurs at the fundamental and second harmonic of the local plasma frequency in a Baumbach-Allen model corona. For the events of July 17, 1957 measurements were made on the fundamental band: in all other cases on the second harmonic. Where two nearly parallel series of points appear in these graphs they refer to a split band (Section VI). Preceding type III bursts are shown on the figures and known flares (beginning, maximum, and end) are indicated by the heavy tapered lines at the bottom of the graphs.

Because the height-time plots are essentially straight lines, a single speed can be assigned to each burst ; a histogram of these " radial velocities " is given in Figure 3 (*b*). The mean and median are both close to 500 km/sec, there are few values below 300 km/sec, but there appears to be a long tail on the high velocity side extending beyond 1000 km/sec. Of course, at this stage it is not clear whether the histogram really shows the distribution of radial speeds of the type II disturbances or whether it merely reflects changes in the electron density distribution in the corona. However, since the true velocities are almost certainly greater than those given in this figure, it is apparent that the disturbances travel at speeds well in excess of the speed of sound in the corona, which is ~170 km/sec. Whatever the nature of the disturbances, therefore, it is probable that the shock fronts accompanying them are the agencies which excite the oscillations in the corona.

Before concluding this section, mention should be made of one case (April 5, 1957, 0004–0013 U.T.) in which the frequency drift was at first in the usual sense of decreasing frequency but then reversed and continued for some minutes in the positive sense, with an *absolute* value quite typical of type II bursts. This event is thus analogous with the type III U bursts (Haddock 1958 ; Maxwell and Swarup 1958), and is most simply explained by supposing that the type II disturbance reached a maximum height and then fell back towards the Sun. Suggestions of a similar behaviour can be seen in one or two other events.

V. Harmonic Structure

An outstanding feature of the stronger type II bursts is the appearance of fundamental and second harmonic bands. This harmonic structure is clearly visible in 60 per cent. of the bursts recorded and in an even higher percentage of those bursts which are of at least moderate intensity and consist of well-defined ridges. All the examples of type II bursts in Plates 1, 3, and 4 have harmonic bands, and the structure can also be seen in many of the examples in the other plates. The correspondence in detail between the two bands is quite remarkable and leaves no doubt that both are generated in the same process. As the measured ratio of the frequencies of the two maxima always lies close to 2 (Fig. 5), it is clear that the two bands are harmonics radiated from a common oscillating source.

(*a*) *Relative Intensities*

The intensities of the two harmonic bands are usually quite similar. However, there are cases in which one or the other harmonic is the more intense. If the harmonics were generated by a non-linear oscillation one would expect the relative intensities of the harmonics to depend on the intensity of the event, the second harmonic being relatively stronger in the stronger events. The evidence does not support this prediction ; there are a number of examples of quite weak bursts in which the second harmonic is somewhat stronger than the fundamental.

(*b*) *Harmonics Higher than the Second*

No examples of first, second, and third harmonics are known. For 11 of the 35 harmonic bursts in this analysis a third harmonic would have been detected if its intensity had been as great as that of the second harmonic, and for 4 of these cases it would still have been detected at $\frac{1}{5}$ of the second harmonic intensity. Since in 9 of the 11 cases, including all of the 4 cases mentioned, the intensity of the second harmonic was similar to that of the fundamental, we conclude that the intensities of the first two harmonics are often similar, but that the third harmonic is considerably less intense.

For most non-linear oscillations, including plasma oscillations (Smerd 1955), the ratio of the energy in the third harmonic to that in the second is similar to the ratio of the energy in the second harmonic to that in the fundamental. It would seem, therefore, that the observed intensity ratios could be explained most directly by supposing that the oscillations are not sufficiently non-linear to radiate appreciable third harmonic, and that the radiation efficiency in the fundamental mode is considerably less than that in the second harmonic. It is interesting to note that the model suggested by Wild, Murray, and Rowe (1954) achieved this effect by inhibiting the escape of much of the fundamental band. While the evidence presented below (Section V (*d*)) suggests that this model is not correct in detail, some similar phenomenon may explain the observed intensity ratios.

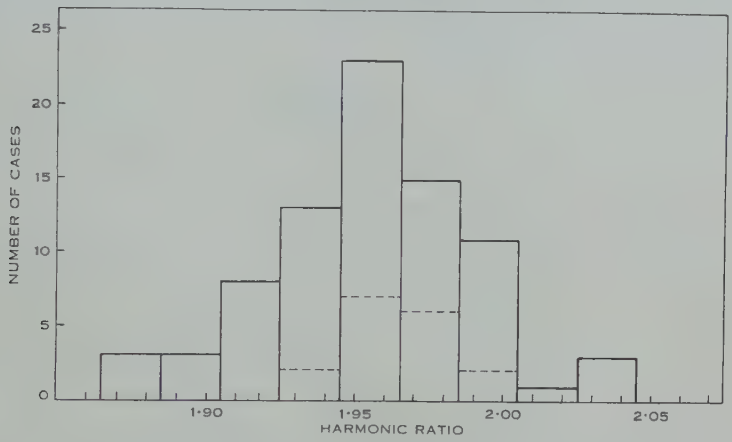

Fig. 5.—Histogram of the harmonic ratio measured as the ratio of the frequencies of maximum intensity in discrete narrow-band features. Data for 19 bursts. The histogram shown in full lines includes all measurements with equal weight: for the dashed curve the mean ratio in each burst has been used, and each burst has been given unit weight.

Although no examples of first, second, and third harmonics are known, there is one case in which it is possible that the second, third, and fourth harmonics have been observed: the corresponding fundamental band would have been below the frequency limit of the equipment. Part of the record of the dynamic spectrum of this burst is reproduced in Plate 3 (event of April 25, 1956) and graphs of the ridge-lines in the intensity-time plane are given in Figure 6. The graphs are designed to test the idea that the three bands are in the frequency ratio 2 : 3 : 4. The bands are shown at the observed frequencies by full lines, and the high frequency band is replotted at half the frequency (dashed lines) and at three-quarters of the frequency (dash-dot lines). There is seen to be a close correspondence between the observed and replotted bands, indicating that the frequencies of the bands are closely in the ratio of 2 : 3 : 4 throughout their duration.

On the basis of this evidence it would seem likely that these bands are the second, third, and fourth harmonics of a fundamental band lying below 40 Mc/s. It is only the absence of a third harmonic in many other bursts of similar or greater intensity that suggests that there may be another explanation of this structure. One possibility is that the upper two bands are the two parts of a split second-harmonic band (Section VI) and that the 3 : 4 ratio is fortuitous. However, the frequency separation of these bands (~25 Mc/s) is greater than usual in split bands.

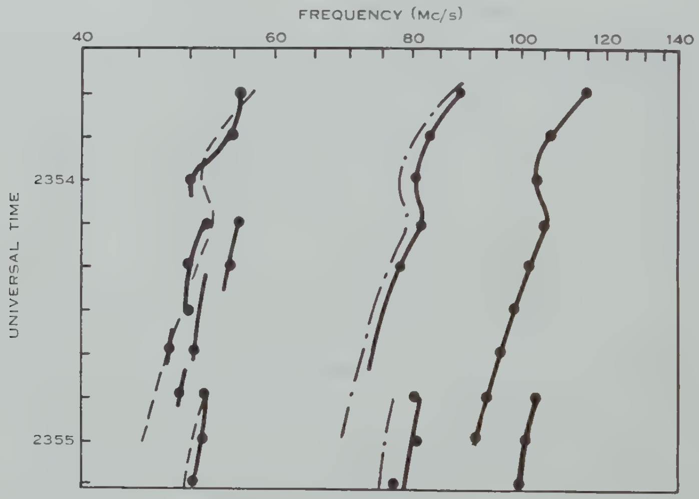

Fig. 6.—The full curves show the ridge-lines in the frequency-time plane for the type II burst of April 25, 1956 (Plate 3). The dashed lines show the highest frequency band replotted at half the frequency, and the dash-dot lines show the same band replotted at three-quarters of the frequency.

(c) *Group Delay between Harmonics*

Sharply defined features in harmonic bursts occur in the fundamental band about 1 sec after they occur in the second harmonic band. This delay is thought to be the result of a lower velocity of propagation for the fundamental mode. For frequencies near the local plasma frequency the group velocity in the corona is very low. Following the methods of Jaeger and Westfold (1950), it may be shown that, for central rays in a Baumbach-Allen model corona, the travel time for radiation at the fundamental frequency to come from the plasma frequency level is greater by approximately $\frac{3}{4}$ sec than the time for radiation at the second harmonic frequency to come from the same point. The general agreement between these predicted and observed delays may be taken as further evidence for the plasma hypothesis.

(*d*) *The Harmonic Ratio and the Position on the Disk*

In their discussion of the first recorded harmonic type II bursts, Wild, Murray, and Rowe (1954) showed that the ratio of the peak frequencies in the two bands was usually somewhat less than 2. This is a general effect and is clearly evident in Figure 5. For the two bursts which they studied, these authors compared the frequency profiles of the harmonic bands by replotting the second harmonic profile at half the frequency. This comparison showed that the lower frequencies in the fundamental band appeared to have been removed, an effect which accounted for the frequency ratio being less than 2. It was suggested that these lower frequencies had been unable to escape from the Sun in the direction of the Earth, and it was shown that this could be explained on a standard model of ray propagation in a spherically symmetric corona. For a source in the centre of the disk it was predicted that the lower half of the fundamental band would be removed but the ratio of the peak frequencies would be 2 : 1 ; for a source away from the centre of the disk a greater part of the fundamental band would be removed and the ratio would be less than 2 : 1.

Although further observations have confirmed that the ratio of the peak frequencies is usually less than 2, they do not support this theory in detail. Figure 7 gives the results of a study of the variation of the harmonic structure with the distance of the burst from the centre of the disk. Direct measurements of the positions of the type II bursts are not available but a rough measure of the position may be obtained from the association with optical events (Section IX). Figure 7 (*a*) shows that two harmonics can be received from almost any position on the disk, whereas the theory referred to above predicts that no significant part of the fundamental band should escape in bursts beyond $\sim 0 \cdot 5 R_{\odot}$. Furthermore, the harmonic ratio shows no significant variation with the position of the burst on the disk (Fig. 7 (*b*)), and it certainly does not decrease with radial distance in the way predicted by the theory and shown by the dashed curve in this figure.

Properly calibrated frequency profiles are not available for many of the bursts included in the present study but in the five cases which were examined the frequency ratio was close to 2 and the profiles of the two harmonics were similar in shape. If any of the lower frequencies had been removed from the fundamental band it was quite a minor effect. The prediction of the theory, that the entire low frequency half of the fundamental band should be absent, was not fulfilled.

It seems possible that a modification of the theory along the following lines may provide an explanation of these results. Firstly, it is supposed that small-scale irregularities in the corona near the plasma frequency level cause radiation in the fundamental band to be scattered through large angles and so to escape from the Sun in a wide beam. This modification ensures that both harmonics can be received from most parts of the disk and that the harmonic ratio is not a critical function of the position of the burst on the disk. It seems necessary to invoke small-scale irregularities for this purpose (small compared with the size of the source). Large-scale structures would modify the ray paths, and in favourable circumstances it might be possible for both the fundamental and second harmonic of the plasma frequency to be received from a source well away from the centre of the disk. However, large-scale structures will not destroy the strong beaming of the fundamental frequency, so that in most cases only the second harmonic could be received. We may note that the observations of occultations of the radio source in Taurus have already provided evidence for the existence of small-scale irregularities in the corona.

The second modification needed in the theory is to suppose that the bandwidth of the emission at any one time is determined primarily by the range of densities in the excited region of the corona and not by the natural bandwidth of emission of a homogeneous region of the plasma. In radiation from a region of the plasma which is small enough to be considered homogeneous, the lower half of the fundamental band will still be removed, i.e. for such regions the results will be somewhat like those for the centre of the disk in the absence of irregularities. However, the observed frequency profile is now supposed to be an integration of many such " filtered " profiles centred on neighbouring frequencies. The shape of the resulting profile will be determined by the distribution of the excitation. The profile of the fundamental will resemble that of the second harmonic but its peak frequency will exceed half the peak frequency of the second harmonic by a frequency of the order of the natural bandwidth of the oscillations of a homogeneous element of plasma. On this basis the observed mean harmonic ratio of $\sim 1 \cdot 95$ (Fig. 5) is taken to imply that the natural bandwidth of the plasma oscillations is only a few per cent. This agrees very well with the theoretical predictions made from considerations of Landau damping (Berz 1956).

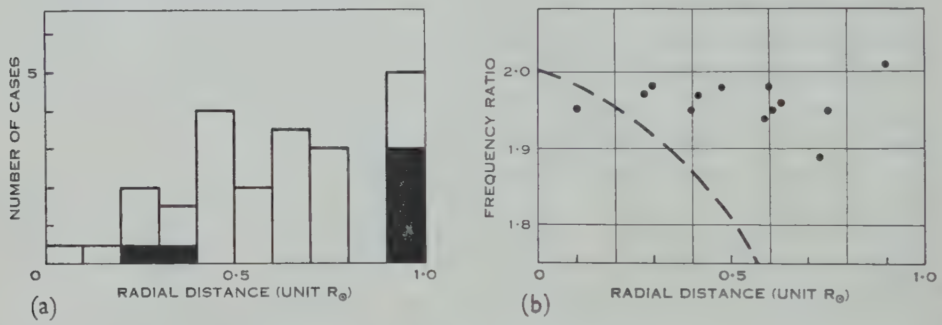

Fig. 7 (*a*).—Distribution of type II bursts with radial distance from the centre of the solar disk. Unshaded regions refer to bursts with fundamental and second harmonic bands : shaded regions to bursts with a single band at such frequencies that harmonic structure could have been detected if it had been present. Indefinite cases in which harmonic structure may or may not have been present are omitted. The radial distances are those of the associated optical events, which in 19 cases were flares of Class 1 or greater and in the remaining 3 cases were prominences ejected beyond the limb (Giovanelli and Roberts 1958).

The trend seen in this figure for more bursts to occur at larger radial distances presumably arises from the increase with distance of the area of the (flare-producing) solar surface associated with a fixed interval of radial distance.

Fig. 7 (*b*).—The dependence on radial distance of the ratio of the frequencies of corresponding features in harmonic bursts. The points show the mean values in each of 13 bursts : the curve shows the predicted ratio for a spherically symmetric corona (Wild, Murray, and Rowe 1954).

VI. Band Splitting

(a) *Observations*

Wild (1950) and Wild, Murray, and Rowe (1954) pointed out that in many type II bursts the individual harmonic bands are themselves double. Several examples of this phenomenon are shown in Plate 4. Each harmonic band is split into two ridges, which are separated by the order of 10 Mc/s in the fundamental band. The details of the split-band structure are duplicated in the second harmonic, where the splitting is twice as great. In many cases the two parts of the split band are similar, but this is not always so. For example, in the event of December 6, 1957, illustrated in Plate 4, the lower frequency ridge is considerably narrower than the higher frequency one. In a few cases a trebling of the band has been observed.

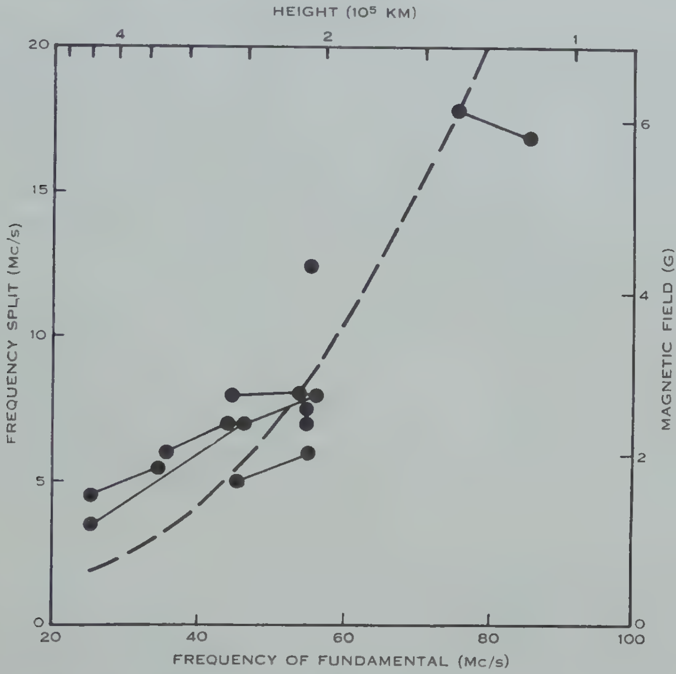

Fig. 8.—The frequency separation in split bands as a function of the mean frequency of the band. The points show the measured values, those which are joined referring to the same burst. The dashed curve shows the variation of the gyro frequency (ordinate) with the coronal plasma frequency (abscissa) for a Chapman model sunspot of surface field 3000 G and with the Baumbach-Allen model of coronal electron densities. For this curve the scales may be relabelled to show magnetic field as a function of height, the change from frequency to magnetic field being according to the relation $f_H = 2 \cdot 9$ Mc/s per gauss, and that from frequency to height following the Baumbach-Allen model (data from Smerd 1950).

The measured values of the frequency splitting are shown in Figure 8 as a function of the mean frequency of the two parts of the band. All the points for any one burst are joined by a fine line. Although in individual bursts there is little evidence for a consistent variation of the splitting with frequency, the overall result is a variation from approximately 5 Mc/s separation at 30 Mc/s, to 18 Mc/s separation at 80 Mc/s. All these results are referred to the fundamental, although, where possible, the measurements were made on the second harmonic, which is less likely to be distorted by propagation effects.

The dashed curve in this figure shows the gyro frequency above a model sunspot as a function of the plasma frequency. It is discussed below in connexion with the explanation of the band splitting.

(*b*) *Interpretation*

The close correspondence between the two parts of a split band, including the appearance of features in the two parts at similar times, suggests that the radiation is produced in a common source emitting at two different frequencies. It appears unlikely that the two parts are produced by two different disturbances which travel out through the corona. Further evidence for this view is found in the narrow range of frequency separations observed at any one frequency (Fig. 8). Wild and co-workers suggested that the double band structure might be the result of magnetic splitting, analogous to the Zeeman effect. Unfortunately, the theory of the oscillation of a plasma in the presence of a magnetic field is at present somewhat confused. Westfold (1949) suggested that such a plasma has three proper frequencies of vibration which are the three frequencies for which the refractive index is zero. On the other hand Gross (1951), Sen (1952), and Bayet (1954) have taken the frequencies of plasma oscillations in a magnetic field to be the two frequencies for which the refractive index is very great. As we shall see, neither of these theories appears to predict all the observed properties of the split bands.

The three frequencies for which the refractive index vanishes are the plasma frequency f_p, and the frequencies $\sqrt{(f_p^2+\frac{1}{4}f_H^2)}\pm\frac{1}{2}f_H$, where f_H is the gyro (cyclotron) frequency of the electrons.* For small magnetic fields ($f_H^2 \ll f_p^2$) the latter two frequencies are approximately $f_p \pm \frac{1}{2}f_H$. It is believed that the lower of these two frequencies cannot escape from the Sun but is reflected by an overlying stop region (see e.g. Pawsey and Bracewell 1955). Hence, in the fundamental band two peaks should be observed at the frequencies f_p and $f_p+\frac{1}{2}f_H$. To this extent the theory fits the observations, since the observed splitting could be explained by the presence of fields $\sim$5 G in the corona. Indeed, Figure 8 shows that the observed variation of the magnitude of the split with the frequency of the burst agrees well with that predicted on a current model of the variation of the magnetic field of a sunspot with height. However, it is necessary to add that our knowledge of the magnetic fields at these heights is extremely limited.

The difficulty with this theory is that, when the values of f_p and f_H are chosen to fit the observations, it is found that the second harmonics of *all three* frequencies should escape from the Sun. Since in most cases only two peaks are seen in the second harmonic band, it seems that this theory cannot be correct, at least in its present form.

---

* $f_p=(Ne^2/\pi m)^{\frac{1}{2}}=0\cdot 9\times 10^4 N^{\frac{1}{2}}$ Mc/s, where N is the electron density in cm^{-3}; $f_H=eH/2\pi mc=2\cdot 9H$ Mc/s, where H is the magnetic field in gauss.

The alternative theory predicts only two frequencies of oscillation, but only one of these is close to the plasma frequency. The frequencies near which the refractive index becomes very great are

$$[\tfrac{1}{2}\{f_p^2+f_H^2\pm\sqrt{(f_p^4-2f^2f_H^2\cos 2\theta+f_H^2)}\}]^{\frac{1}{2}},$$

where θ is the angle between the magnetic field and the direction of propagation. When $f_H^2 \ll f_p^2$ the upper sign yields a frequency $\sim f_p$ while the lower sign leads to a value $\sim f_H$ or less. Thus this theory of the oscillation of a plasma in a magnetic field does not predict a splitting of the plasma level into two frequencies close to the plasma frequency. It predicts one oscillation at a frequency near the plasma frequency and one at a frequency below the gyro frequency.

To decide whether the observed doubling of the bands could be the result of magnetic splitting evidently requires the development of a more complete theory, e.g. the extension of the work of Akhiezer and Sitenko (1952) and Pines and Bohm (1952) to cover the case of a charged particle projected through a plasma which is pervaded by a steady magnetic field. If such a theory should show that oscillations occur at two frequencies separated by $\sim f_H$, then the data of Figure 8 would support the identification of the observed splitting as magnetic splitting. Such an identification would provide a very valuable tool for the measurement of magnetic fields high in the corona, in a region not at present accessible to optical observations.

The observed lack of polarization of the split bands is a further difficulty for this type of theory. If the two parts of a split band represent radiation in two different modes, then they would be expected to have distinctive polarizations. Furthermore, provided the properties of the corona change sufficiently slowly with height, the radiation would remain in the same mode throughout its passage through the corona and would emerge with a distinctive polarization. This conclusion is in conflict with the observation that the split bands are substantially randomly polarized.

Randomization could be achieved by combining the emission from regions in which the magnetic field directions were different. However, to be consistent with the observed narrow bandwidths, the magnetic field would have to reverse in a distance $\sim 10^4$ km.

VII. The Herring-bone Structure

(a) *Observations*

On April 26, 1956 from 0154 to 0205 U.T. a unique burst was recorded. Two sections of the record of this event are reproduced at the top of Plate 5. The dominant feature is a rapid succession of short-lived, broad-band elements. These have fast frequency drifts of both positive and negative signs and appear to diverge from a narrow-band feature which drifts from high to low frequencies at a rate typical of a type II burst. The resulting appearance in the frequency-time plane resembles a herring-bone. In the later stages of the burst the rapidly drifting elements extend over a much smaller range of frequencies, and at times the " backbone " is missing, i.e. the narrow-band, slowly drifting feature exists only as a gap between the rapidly drifting elements diverging in the two directions.

From this part of the burst it is clear that the structure is by no means as regular as the term herring-bone may suggest. In particular, the elements which drift in the positive and negative sense do not occur in pairs.

No other event closely resembling this has been recorded, but quite a number of type II bursts contain structure which is similar to the later stages of this event (section from 0201·5 to 0202·5 U.T.). For example, the section of the type II burst on April 8, 1958 which is reproduced in this plate contains similar structure. In such bursts the herring-bone form is much less clearly developed. The rapidly drifting elements extend over only 5 or 10 Mc/s, and often the drift rates are lower, and the elements are of rather longer duration, than those in the event of April 26, 1956.

There are rather more examples of events in which only half the herring-bone is present, i.e. rapidly drifting elements extend from the type II band towards the lower frequencies but not towards the higher frequencies. Again, there is one outstanding event of this nature in the records. This occurred on July 6, 1956 from 0245 to 0300 U.T. Part of the record is reproduced in Plate 5. The burst began as a fairly typical harmonic type II, but after the burst had been in progress for approximately 3 min, rapidly drifting elements suddenly appeared extending from the low frequency side of each of the harmonic bands (see Plate 5). These elements have higher drift rates and are of even shorter duration than those in the event of April 26. The drift rates are greater than those commonly seen in type III bursts and the durations (at one frequency) are very short, often less than 1 sec.

Plate 1 contains an example of a somewhat similar event which occurred on January 24, 1957. In this case the rapidly drifting elements are much weaker and more diffuse but they resemble type III bursts more closely. In still other cases the rapidly drifting elements would undoubtedly be classified as type III bursts: the event of January 19, 1956 shown in Plate 3 is in this class, but the type III elements are difficult to see in the reproduction.

There are very few type II bursts in which the herring-bone structure is a dominant feature, but vestiges of it can be seen in perhaps 20 per cent. of all type II events. It is possible that the structure reported by Haddock (1958) is of a similar nature. This author describes the type II bursts which he has observed as being composed of elements in which the dominant drift rate is typical of the type III bursts.

(b) *Interpretation*

On the plasma hypothesis the herring-bone structure implies that the outward-travelling disturbance responsible for the type II band is a source which ejects rapidly travelling disturbances producing the type III elements. In cases where both positively and negatively drifting elements are present the fast ejections must travel both into and out from the Sun: in the other cases either only outward ejections occur, or radiation from the inward-travelling ejections cannot reach the Earth. To explain the similarity between successive elements (and their short duration at one frequency) it is necessary to suppose that the ejections all occur within the same narrow range of directions and have closely similar speeds. The very sudden onset of the ejections in the burst of July 6, 1956 (Plate 5) suggests that the coronal properties changed in some critical way in a distance certainly less than 1000 km.

As discussed in Section IV, it seems likely that the disturbances producing the regular bands in type II bursts are shock fronts accompanying supersonic ejections. We do not know of a mechanism whereby such a shock front could produce fast, beamed ejections with speeds several hundred times as great as the shock front. However, if, as Westfold (1957) and others have suggested, the corona is able to support other shock waves of a different nature and having speeds appropriate to type III bursts, then it is perhaps possible that such shock waves are generated by the sonic shock when it encounters sudden changes in the corona. Shock waves so generated might be beamed in the direction of the original shock motion (and the reverse) and this could account for the nature of the type III elements. It may also be worth considering whether a sonic shock, on reaching a region of lower temperature in the corona, might not " break " in the manner of a water wave approaching a beach and throw off high speed particles.

It is perhaps significant that the frequency drift rate in the type II section of the event on July 6, 1956 is considerably greater than the usual. The inferred speed of the disturbance is over 1000 km/sec (Fig. 3 (*a*)). However, the drift rate in the event of April 26, 1956 is not unusually great.

VIII. Compound Type III–Type II Bursts

(*a*) *Observations*

Wild, Roberts, and Murray (1954) drew attention to the tendency for a type II burst to be preceded by a group of type III bursts, which apparently formed part of the same event. The present more extensive observations have shown that this is a common occurrence : 36, or 60 per cent., of the bursts were preceded by a type III event which appeared to be unambiguously associated with the type II burst. Some examples are given in Plate 1. Often the type III events are outstanding : they may consist of groups of 10 or more bursts and may contain considerably more energy than the type II burst. Such is the case in the events of August 6, 1957, illustrated in Plate 1, and December 19, 1957, illustrated in Plate 2. In other cases, however, the type III event may be weak and perhaps consist of only one or two bursts. Examples of this type are seen in Plate 2 (events of December 6, 1957 and January 15, 1958) and in Plate 3 (event of November 15, 1955).

Occasionally type III bursts occur at the time of a type II burst, but not in a preceding group (Plate 2, event of January 15, 1958). Also in rare cases a preceding group is of very great duration, containing many tens of bursts and some of these may overlap the type II burst (see Plate 4, event of November 13, 1957).

For the apparently associated events the time delay between the type III group and the onset of the type II burst ranges from 1 to 18 min. The median value is $5\frac{1}{2}$ min, and 50 per cent. of the values lie between 4 and $9\frac{1}{2}$ min.

(*b*) *Interpretation*

The explanation of the compound type III–type II burst, proposed by Wild, Roberts, and Murray (1954), involved the ejection of two sets of disturbances from a single explosion, supposed to occur low in the solar atmosphere at the time of the type III event. The first set of disturbances, travelling with speeds of $0 \cdot 1$–$0 \cdot 3c$, were supposed to produce the type III bursts ; the other disturbance, with a speed ~500 km/sec, was responsible for the type II burst. In support of this explanation it was shown that for the three events studied the velocity lines of the two parts of the burst diverged from an origin in the lower corona within 10^5 km of the photosphere.

Table 1

COMPILATION OF DATA ON HARMONIC COMPOUND BURSTS

(The heights of intersection are for a Baumbach-Allen model corona)

Date	Frequency (Mc/s)	Time Delay of Type II Burst after Type III Event (min)	Drift Rate in Type III Burst Fundamental (Mc/s per sec)	Height of Intersection of Trajectories (10^5 km)
9. vi.55	45	8½	0·11	−0·8
5. vii.55		6 to 13	0·13	−3·5 to −0·2
24. i.57		11	0·08	−0·6
17. vii.57		12½ to 14	0·06	−0·4 to −0·2
6.viii.57		5½ to 7	0·11	−0·2 to +0·4
2. ix.57		2 to 13	0·05	+0·3 to +2·2
11. ix.57		10 to 11½	0·08	−0·7 to −0·3
6. xii.57		16	0·06	−0·8
15. i.58		{ 5½	0·08	+1·1
		10	0·06	+0·4
19. i.56	50	7	0·05	+1·2
6.viii.57		4 to 5½	0·12	+0·6 to +0·8
15. xi.55	60	3	0·1	+1·2
18. xi.55		6	0·13	−0·4

The height-time plots given in Figure 4 include four examples of compound bursts. For one of these events (January 15, 1958) the velocity lines similarly diverge from a common point in the corona within 10^5 km of the photosphere. For the other events, however, the point of intersection lies somewhat below the photosphere. The results of a study of all the harmonic compound bursts are shown in Table 1. It is seen that the apparent origin from which the disturbances diverge usually lies within 10^5 km of the photosphere, but is quite often below it. In view of the uncertainties in the electron density distribution, it thus seems that the hypothesis of a common origin is reasonable, but it is not possible to determine the height of origin by extrapolating the velocity lines in this way.

IX. Type II Bursts and Chromospheric Flares

The relationship of type II bursts to solar flares can be studied most satisfactorily when continuous optical observations of the Sun are available for the periods of the radio spectral observations. A combined study of this nature, covering 18 type II bursts, has been reported recently by Giovanelli and Roberts (1958). These authors found definite optical associations for 70 per cent. of the bursts and ambiguous associations for another 10 per cent. Most of the optical events were bright flares showing particle ejections.

Unfortunately optical observations of the Sun were not made at Sydney at the times of many of the type II bursts reported in this study. In the analysis of this section, therefore, the reports of flares seen at Sydney, which were kindly supplied by Dr. R. Giovanelli of the Division of Physics, C.S.I.R.O., have been supplemented by the reports of flares appearing in the " Quarterly Bulletin of Solar Activity " (to December 1956), in the " Daily Maps of the Sun " issued by the Fraunhofer Institute, and in " Solar-Geophysical Data " issued by the National Bureau of Standards. For the times of each of the 65 type II bursts the above-mentioned flare reports were examined. For 28 of the bursts, flares of Class I or greater were reported at times which suggested that they were related to the bursts. This relationship is indicated in Figure 9. Figure 9 (*a*) refers to the 15 bursts for which the beginning of the flare was observed. For each event it shows all the bursts of type II or type III and all the flares of Class I or greater which were reported in the period from 10 min before to 2 hr after the beginning of the relevant flare. Figure 9 (*b*) gives similar data for the remaining 13 bursts. In this case the period covered is from 20 min before to 2 hr after the beginning of the type II burst.

It is obvious from these diagrams that the flares and type II bursts are associated. A clear pattern is evident, with the type II burst beginning near the maximum of the flare and continuing after it, while in the case of a compound burst the type III event usually occurs before the flare maximum. This diagram is similar to those given by Dodson and co-workers (Dodson, Hedeman, and Owren 1953 ; Dodson 1958) showing the relationship of flares to bursts observed on single-frequency recorders. However, as already discussed in Section VIII, it does not seem to be possible at present to identify unambiguously the spectral types in Miss Dodson's analysis. The diagram also agrees with that given by Dodson (1958) for 13 of the bursts in the present study.

Since not all flares are observed, the associations listed in Figure 9 give only a lower limit for the percentage of the type II bursts which are accompanied by flares. Indeed, the last two years have seen a remarkable increase in the percentage of the bursts which are accompanied by reported flares, an effect which presumably may be attributed to the improved coverage of the flare patrols. Flares of Class I or greater were reported at the times of 64 per cent. of the 25 type II bursts recorded since July 1, 1957 ; for the 10 bursts since December 1, 1957, the figure is 80 per cent. It is clear, therefore, that the majority of type II bursts are accompanied by flares, not including sub-flares.

Although most type II bursts are associated with flares, it is actually rare for a flare to be accompanied by a type II burst. This is made clear in Table 2

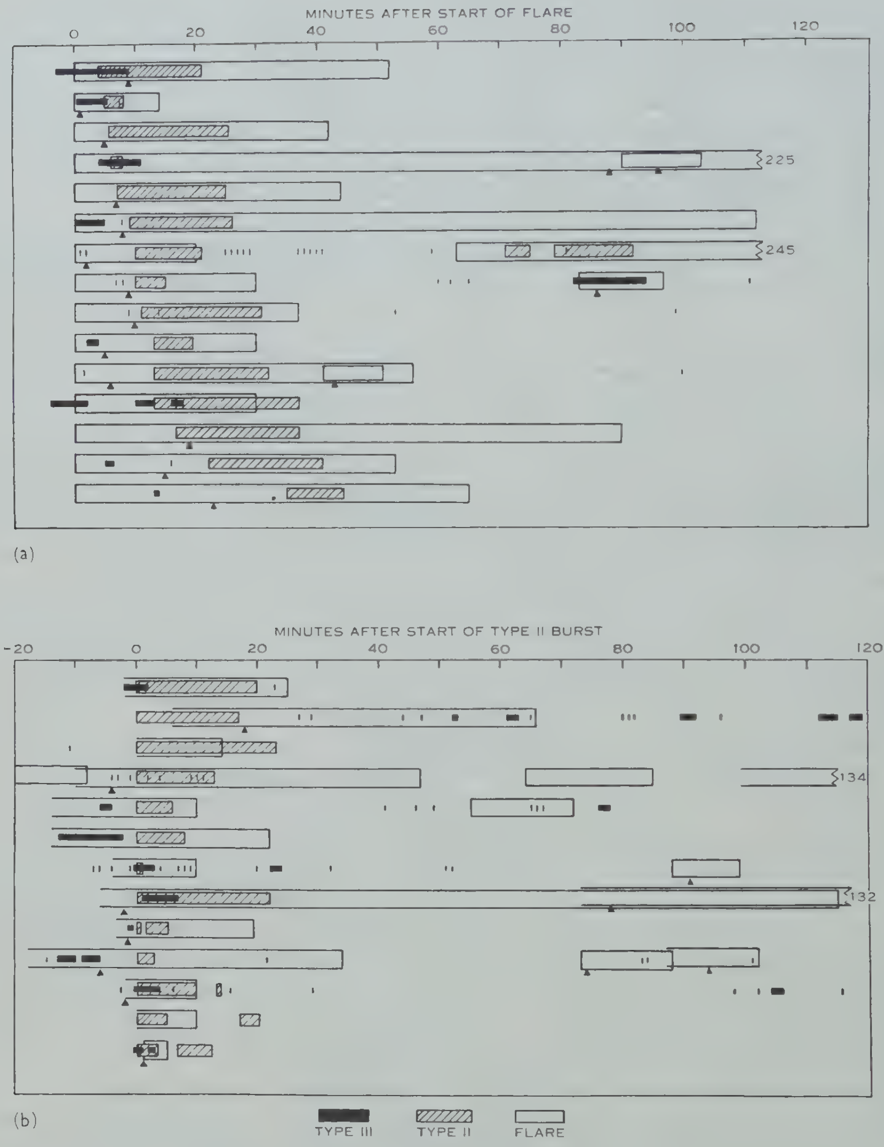

Fig. 9.—Showing the temporal relationship of flares and associated type II bursts.

(*a*) Data for 15 cases in which the beginning of the associated flare was observed. The figure shows all the bursts of spectral types II and III and all the flares of Class I or greater which occurred within the period from 10 min before to 2 hr after the beginning of the associated flare. Type III bursts are shown by heavy lines, type II bursts by shaded rectangles, and flares by open rectangles. The maxima of flares are indicated by solid triangles.

(*b*) Similar data for another 13 cases in which the beginning of the associated flare was not observed. In this case the period covered is from 20 min before to 2 hr after the start of the type II burst.

which gives the distribution by importance class of the 702 flares reported during the observing hours of the radio-spectrograph from January 1955 to March 1958 and also gives the number (and percentage) of these flares which were accompanied by type II bursts. It is seen that only about 3 per cent. of flares of Class I or greater are associated with type II events. However, the percentage increases rapidly with the importance of the flare, and approximately 30 per cent. of Class 3 flares are accompanied by bursts. Evidently some rare condition must be satisfied before a flare is accompanied by a type II burst. Since many flares are accompanied by visible ejections, we may conclude that the presence of an ejected stream is not a sufficient criterion for the occurrence of a type II burst. If only those ejections with supersonic speeds are effective (see Section IV and Giovanelli and Roberts (1958)), the numerical agreement would probably be better. Data on the frequency of occurrence of supersonic ejections from flares would be of interest in this connexion.

TABLE 2

ANALYSIS OF FLARES AND TYPE II BURSTS BY IMPORTANCE CLASS

Flare importance	1	2	3	1, 2, or 3
Number of flares during radio observations	566	120	16	702
Number of flares accompanied by type II bursts	11	8	5	24
Percentage of flares accompanied by type II bursts	2	7	31	3

TABLE 3

ANALYSIS OF FLARES AND TYPE II BURSTS BY DISK LONGITUDE

Disk longitude of flare ..	0–30°	31–60°	61–90°
Number of flares accompanied by type II bursts	14	9	5
Percentage of all flares observed (from Goldberg, Dodson, and Müller 1954)	41	36	23
Relative probability of a flare being accompanied by a type II burst	1	0·7	0·6

Table 3 gives the distribution with disk longitude of the flares accompanied by type II bursts. Rather more such flares are seen near the centre of the disk than at the limb. However, a similar comment applies to all the flares observed

(Goldberg, Dodson, and Müller 1954) so that the probability of a flare being accompanied by a type II burst is relatively independent of the longitude of the flare. This implies that the type II radiation is emitted in a broad cone, in contrast to the type I radiation which is thought to be beamed radially outwards.

It is clear from a study of these flare associations that some active regions on the Sun are very prolific in producing type II bursts, while others produce none at all. In an attempt to determine what parameters are responsible for this behaviour, a statistical investigation was made of the effect of the type of spot group. Groups were classified according to their Zurich class (as given in the Fraunhofer Institute " Daily Maps of the Sun ") and also according to their Mt. Wilson magnetic class. No significant dependence on either of these parameters was found.

X. Type II Bursts and Geomagnetic Storms

When particle streams with speeds $\sim 10^3$ km/sec were suggested as the source of type II bursts it was natural to try to identify these streams with those causing magnetic storms and aurorae on the Earth. However, it was not possible to identify particular magnetic storms unambiguously with individual type II bursts, and, as Wild, Murray, and Rowe (1953) emphasized, the inferred speeds of about 500 km/sec for type II bursts were smaller by a factor of 2 or 3 than those implied by the delay of magnetic storms after important flares. The present sample of type II bursts is large enough for statistical methods to be used in searching for possible effects of these bursts on the geomagnetic field, and in this section the results of a superposed epoch analysis are given.

Figure 10 shows the mean value of the magnetic index A_p for the period from 8 days before to 13 days after a type II burst. The A_p values appear to be high from $1\frac{1}{2}$ to $2\frac{1}{2}$ days after a type II burst, the maximum value being about $1\frac{1}{2}$ times the quiet value. The significance of this increase has been tested by dividing the data into two halves. The dashed curves in Figure 10 show the corresponding results for the first 30 and the second 30 bursts separately. Both of these curves contain the peak on the second day, while, by contrast, the other (lower) peaks in the full curve appear in only one or the other of the dashed curves. This provides considerable grounds for believing the peak on the second day to be real. The significance may also be tested by computing a standard deviation from all the points and in this way it is found that the probability of the peak value occurring by chance in a normal distribution is about 1 in 10^3.

The form of this curve is similar to that found by Dodson (1958) for the geomagnetic variability after " major early bursts " at frequencies $\leqslant 200$ Mc/s. However, in her analysis Miss Dodson found a longer period of high magnetic variability extending from approximately 2 to 7 days after the burst. The maximum variability occurred on the 3rd and 4th days after the burst and not on the second as found here. We have already referred in Section VIII to the difficulty of correlating the spectral and single-frequency classifications of bursts : the tests reported later in this section may be taken as suggesting that the bursts used by Miss Dodson contained a high proportion of type II events, but this is no more than a suggestion.

We may also mention that a curve similar to that in Figure 10 was prepared for the 37 type II bursts observed with the Harvard radio-spectrograph from October 1956 to December 1957 (Maxwell, Stone, and Swarup 1957). This curve did not show any pronounced peak but did show a period of enhanced geomagnetic variability for approximately 10 days after the bursts. This suggests that there may be some difference between the events classified as type II by the two groups of workers. However, the statistics are limited and more data are needed.*

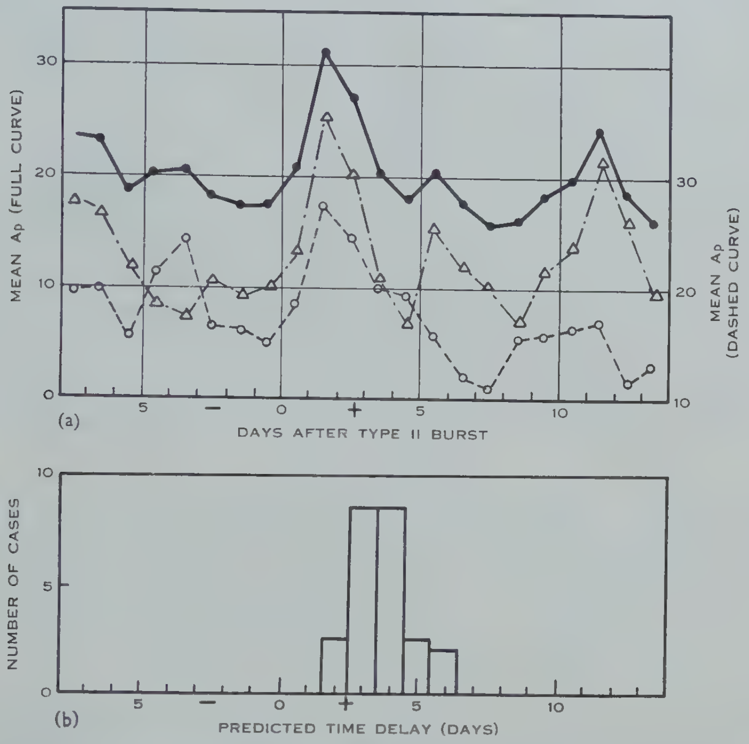

Fig. 10 (*a*).—Superposed epoch diagram showing the mean value of the geomagnetic index A_p on days before and after 60 type II bursts recorded in the period January 1955 to March 1958. The dashed lines give the corresponding diagrams for the first 30 and the second 30 bursts separately. Note that these latter curves are plotted on a displaced scale of A_p.

Fig. 10 (*b*).—The predicted time delays inferred from the frequency drift rates in 24 of the type II bursts in which harmonic structure could be clearly recognized. It is assumed that the type II disturbances move radially outwards through a Baumbach-Allen model corona and cause emission at the local coronal plasma frequency.

Figure 10 indicates a tendency for the geomagnetic field to be considerably disturbed on the first, second, and third days after a type II burst. With the purpose of determining whether the type II bursts were the significant events, similar superposed epoch diagrams were prepared showing

---

* A similar analysis for Harvard and Sydney type II bursts was reported by A. R. Thompson at the I.A.U.-U.R.S.I. Paris Symposium on Radio Astronomy in August 1958.

(i) the mean value of A_p before and after 70 flares, of importance 2 or greater, known not to be accompanied by type II bursts and occurring on days for which neither Sydney nor Harvard reported type II bursts (Fig. 11 (*a*)), and

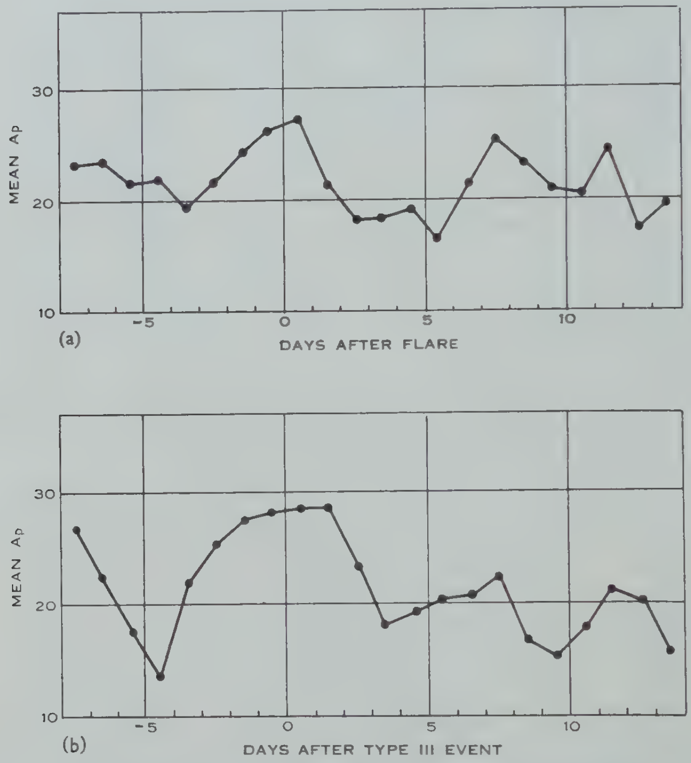

Fig. 11 (*a*).—Superposed epoch diagram showing the mean magnetic variability (mean A_p) on days following 70 flares of importance 2 or 3, which were *not* accompanied by type II bursts and which occurred on days when neither Sydney nor Harvard reported a type II burst. (The flares included are those satisfying the above conditions which were reported during the observing periods of the Dapto radio-spectrograph from June 1955 to November 1957.)

Fig. 11 (*b*).—A similar superposed epoch diagram for days following 53 outstanding type III radio events reported by Sydney in the period from July to December, 1957, on days when neither Sydney nor Harvard reported a type II burst. The type III events chosen are those groups of bursts of intensity class 2 or 3 and with durations $\geqslant 1$ min.

(ii) the mean value of A_p before and after 53 days on which at least one group of strong type III bursts was reported by Sydney, and no type II burst was reported by Sydney or Harvard (Fig. 11 (*b*)). Neither of these diagrams indicates an increase in storminess beginning a day or more after the events in question. Indeed, neither contains a peak of such apparent significance as that found after the type II events. This evidence therefore suggests that the occurrence of a type II burst gives a more positive indication of the ejection of magnetic storm particles from the Sun than is given either by the occurrence of an important flare or of a radio " outburst " of spectral type III.

Both the plasma hypothesis and the suggested association with geomagnetic storms can be tested by comparing the travel time of $1\frac{1}{2}$ to 2 days indicated by Figure 10 (*a*) with the travel times inferred from the frequency drift rates of the bursts. Figure 10 (*b*) shows to the same scale as Figure 10 (*a*) a histogram of the inferred travel times to the Earth for 24 of the bursts with clear harmonic structure. This figure contains the same data as Figure 3 (*b*), presented in a different way. The figure is based on the assumption of radial motion of the type II disturbances through a Baumbach-Allen model corona.

The mean time delay inferred in this way is seen to be about $3\frac{1}{2}$ days, or twice the mean delay of the geomagnetic disturbance after the burst. However, as already indicated, the velocities inferred from the Baumbach-Allen model are almost certainly low by a factor ~ 2, so that the agreement is considerably better than is suggested by these figures. Indeed, it may not be too optimistic to hope that the direct measurements of the motion of the sources of type II bursts now being made by Wild, Sheridan, and Trent (1959) may make it possible to associate a particular magnetic storm with a particular type II burst.

XI. Conclusion

In concluding this review it is appropriate to consider the definition of the bursts of spectral type II. The 65 bursts included in this study all appear to belong to a fairly well-defined class having the common characteristics of a drift of some of the main spectral features from high to low frequencies at rates of up to 1 Mc/s per sec, and a duration of the order of minutes (Section II (*b*)). They are clearly of the class which Wild and McCready (1950) designated as spectral type II, and indeed the definition given by these authors (Section I) appears to have been very well chosen.

The definition outlined above differs from Wild and McCready's definition in two points. Firstly, their specification of the drift rate as " of the order of $\frac{1}{4}$ Mc/s per sec " is replaced by " up to 1 Mc/s per sec ". It is clear from Figure 3 (*a*) that the observed drift rates are frequency dependent, and while $\frac{1}{4}$ Mc/s per sec is fairly representative in the frequency range in which Wild and McCready made their observations (70–130 Mc/s), it is not appropriate at the lower frequencies. The suggested new phrasing is purposely somewhat loose, but appears at present to be fairly adequate to define the class. However, further observations may make it necessary to specify the drift rate more closely, e.g. by stating it to be of the order of $0 \cdot 05$ Mc/s per sec at 30 Mc/s and $0 \cdot 3$ Mc/s per sec at 100 Mc/s, or perhaps by some simple functional dependence such as $0 \cdot 1(f/50)^{1 \cdot 5}$ Mc/s per sec, where the frequency f is in megacycles per second.

It will be noticed that the wording is chosen so as to include type II " U " bursts and bursts with pronounced herring-bone structure provided only that *some* of the main features show the typical type II drift.

The second departure from Wild and McCready's definition is to specify that the duration is of the order of minutes. This restriction was made to exclude from the class some bursts which have drift rates similar to type II bursts, but durations of only a few seconds. Such bursts are sometimes seen in the "tails" of type III bursts, and, as indicated in Section II (*b*) (vii), type II bursts are themselves sometimes composed of many such sub-bursts. Further observations may show that these bursts are in fact of the same nature as the type II bursts, but they have not been included in the present discussion except when they formed a drifting band having a duration of the order of minutes.

As worded, the suggested definition would properly include some of the drifting bands of type I bursts described by Wild (1957). In part, this reflects the lack of certainty that these events are fundamentally different from type II bursts. Most of the drifting bands of type I bursts can be excluded by requiring that the events be distinct and not part of a storm, or by using one of the more restrictive definitions of the frequency drift rate suggested above, which would exclude all but the most rapidly drifting of the bands of type I bursts. However, the bands of type I bursts occur with a wide variety of drift rates and in varying degrees of isolation, so that in a few cases it appears to be impossible to determine from the dynamic spectrum alone whether the event is of type I or of type II. Further observations of other parameters (polarization, position, and movement) may provide a means of distinguishing these events or may provide additional evidence of a continuous transition between events which are at present classified as type I and type II.

The present sample of bursts does not include events which by virtue of their slow rate of drift or association with a type I storm can be clearly classed as drifting bands of type I bursts. There are less than five events included which may perhaps be of type I.

XII. Acknowledgments

This study was made possible by the long series of records which have been obtained with the C.S.I.R.O. Radiophysics Laboratory's Dapto spectrograph. This project is under the direction of Mr. J. P. Wild, to whom the author acknowledges his indebtedness for many helpful discussions and much advice and encouragement. In the observational phases of the programme, acknowledgment should also be made of the work of Messrs. J. D. Murray, K. V. Sheridan, W. C. Rowe, M. Komesaroff, J. Joisce, and G. H. Trent. For considerable assistance with the analysis of the records I have to thank Mr. D. McLean, and in this connexion thanks are also due to Mrs. P. M. Hodgson and to Miss P. L. Wilkins and Miss J. A. Boorman. Dr. J. L. Pawsey, Dr. R. Q. Twiss, and Mr. S. F. Smerd contributed helpful comments on the interpretation of the observations.

XIII. References

Akhiezer, A. I., and Sitenko, A. G. (1952).—*J. Exp. Theor. Phys.* **23** : 161.

Allen, C. W. (1947).—*Mon. Not. R. Astr. Soc.* **107** : 426.

Bayet, M. (1954).—*J. Phys. Radium* **15** : 258.

Berz, F. (1956).—*Proc. Phys. Soc. Lond.* B **69** : 939.

Dodson, Helen W. (1958).—*Proc. Inst. Radio Engrs., N.Y.* **46** : 149.

Dodson, Helen W., Hedeman, E. Ruth, and Owren, L. (1953).—*Astrophys. J.* **118** : 169.

Ginzburg, V. L., and Zheleznakov, V. V. (1958).—*Astr. J., Moscow* **35** : 694.

GINSBURG, V. L., and ZHELEZNIAKOV, V. V. (1959).—I.A.U.-U.R.S.I. Symposium on Radio Astronomy, Paris 1958. p. 574. (Stanford Univ. Press.)

GIOVANELLI, R. G., and ROBERTS, J. A. (1958).—*Aust. J. Phys.* **11** : 353.

GOLDBERG, L., DODSON, HELEN W., and MÜLLER, EDITH A. (1954).—*Astrophys. J.* **120** : 83.

GROSS, E. P. (1951).—*Phys. Rev.* **82** : 232.

HADDOCK, F. T. (1958).—*Proc. Inst. Radio Engrs., N.Y.* **46** : 3.

JAEGER, J. C., and WESTFOLD, K. C. (1950).—*Aust. J. Sci. Res.* A **3** : 376.

KOMESAROFF, M. (1958).—*Aust. J. Phys.* **11** : 201.

MAXWELL, A., STONE, P. H., and SWARUP, G. (1957).—Spectral classification of solar radio activity. Summary of data in the frequency range 100–580 Mc/s. (Harvard University, Solar Department of Harvard College Observatory.)

MAXWELL, A., and SWARUP, G. (1958).—*Nature* **181** : 36.

PAWSEY, J. L., and BRACEWELL, R. N. (1955).—" Radio Astronomy." p. 88. (Clarendon Press : Oxford.)

PAYNE-SCOTT, RUBY, YABSLEY, D. E., and BOLTON, J. G. (1947).—*Nature* **160** : 256.

PINES, D., and BOHM, D. (1952).—*Phys. Rev.* **85** : 338.

SEN, H. K. (1952).—*Phys. Rev.* **88** : 816.

SMERD, S. F. (1950).—*Proc. Instn. Elect. Engrs.* III **97** : 447.

SMERD, S. F. (1955).—*Nature* **175** : 297.

WESTFOLD, K. C. (1949).—*Aust. J. Sci. Res.* A **2** : 169.

WESTFOLD, K. C. (1957).—*Phil. Mag.* **2** : 1287.

WILD, J. P. (1950).—*Aust. J. Sci. Res.* A **3** : 399.

WILD, J. P. (1957).—I.A.U. Symposium No. 4, Radio Astronomy. p. 321. (Cambridge Univ. Press.)

WILD, J. P., and MCCREADY, L. L. (1950).—*Aust. J. Sci. Res.* A **3** : 387.

WILD, J. P., MURRAY, J. D., and ROWE, W. C. (1953).—*Nature* **172** : 533.

WILD, J. P., MURRAY, J. D., and ROWE, W. C. (1954).—*Aust. J. Phys.* **7** : 439.

WILD, J. P., ROBERTS, J. A., and MURRAY, J. D. (1954).—*Nature* **173** : 532.

WILD, J. P., SHERIDAN, K. V., and TRENT, G. H. (1959).—I.A.U.-U.R.S.I. Symposium on Radio Astronomy, Paris 1958. p. 176. (Stanford Univ. Press.)

EXPLANATION OF PLATES 1–5

PLATE 1

Reproductions of the dynamic spectra records of four compound type III–type II bursts. Time increases from left to right, wavelength from bottom to top, and the intensity is indicated by the degree of whiteness. Sharp features at constant frequency are interfering signals due to mobile communications, etc. Diffuse features at constant frequency arise from variations in receiver gain.

All four type II bursts contain two harmonic bands. The event on July 17 and the earlier event on August 6 have " split bands " ; that on January 24 appears to be the source of diffuse type III bursts (" herring-bone structure "). The earlier event on August 6 is double—there are two intense clusters of type III bursts and each is followed after a delay of 5 or 6 min by a harmonic split-band type II burst.

PLATE 2

Examples of dynamic spectral records of type II bursts on a more compressed time scale. These records were prepared by photomechanically compressing the original records made on 35 mm film at $\frac{1}{2}$ in. per minute (see Wild 1957). Interfering signals appear as sharp features at constant frequencies : many are visible in the record of December 6, 1957. The dark lines parallel to the time axis are caused by the change from one range to the next, while the narrow dark lines parallel to the frequency axis seen in some of the records are simply short gaps in the observations.

The event of December 6, 1957 is a simple harmonic burst with band splitting ; that of January 15, 1958 is a compound type III–type II event in which the type II burst contains two separate sets of harmonic bands, the second of which are split bands ; the burst of February 14, 1956 contains broad diffuse bands ; and the event of December 19, 1957 is a compound type III–type II event, with a large cluster of type III bursts and complex structure in the type II burst.

Plate 3

Spectral records of type II bursts with outstanding harmonic structure. The first two examples have fundamental and second harmonic bands, the third event (April 25, 1956) may be an example of a second, third, and fourth harmonic (see text).

The curved, diagonal lines in these records are due to mains frequency interference.

Plate 4

Sample records of the dynamic spectra of type II bursts containing two harmonic bands, each of which is split into a pair of closely spaced ridges. In each case only part of the whole event is reproduced ; for three of the cases the full event is shown in Plate 1 or 2.

Plate 5

Illustrating the herring-bone structure in type II bursts. Only a small part of the burst is shown in each case : two sections of the burst on April 26, 1956 are included.

Plate 1

SOLAR RADIO BURSTS OF SPECTRAL TYPE II

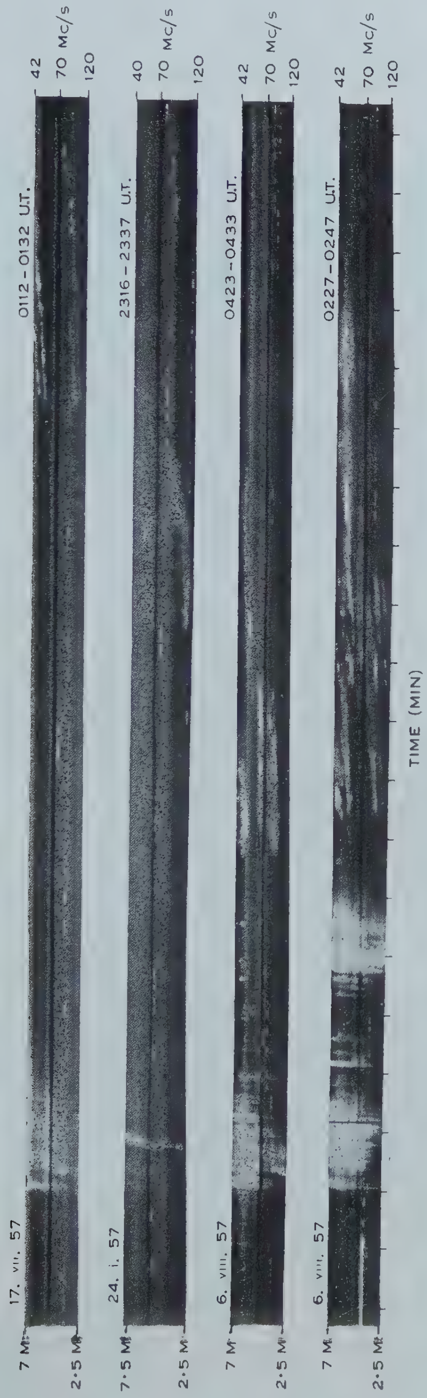

SOLAR RADIO BURSTS OF SPECTRAL TYPE II

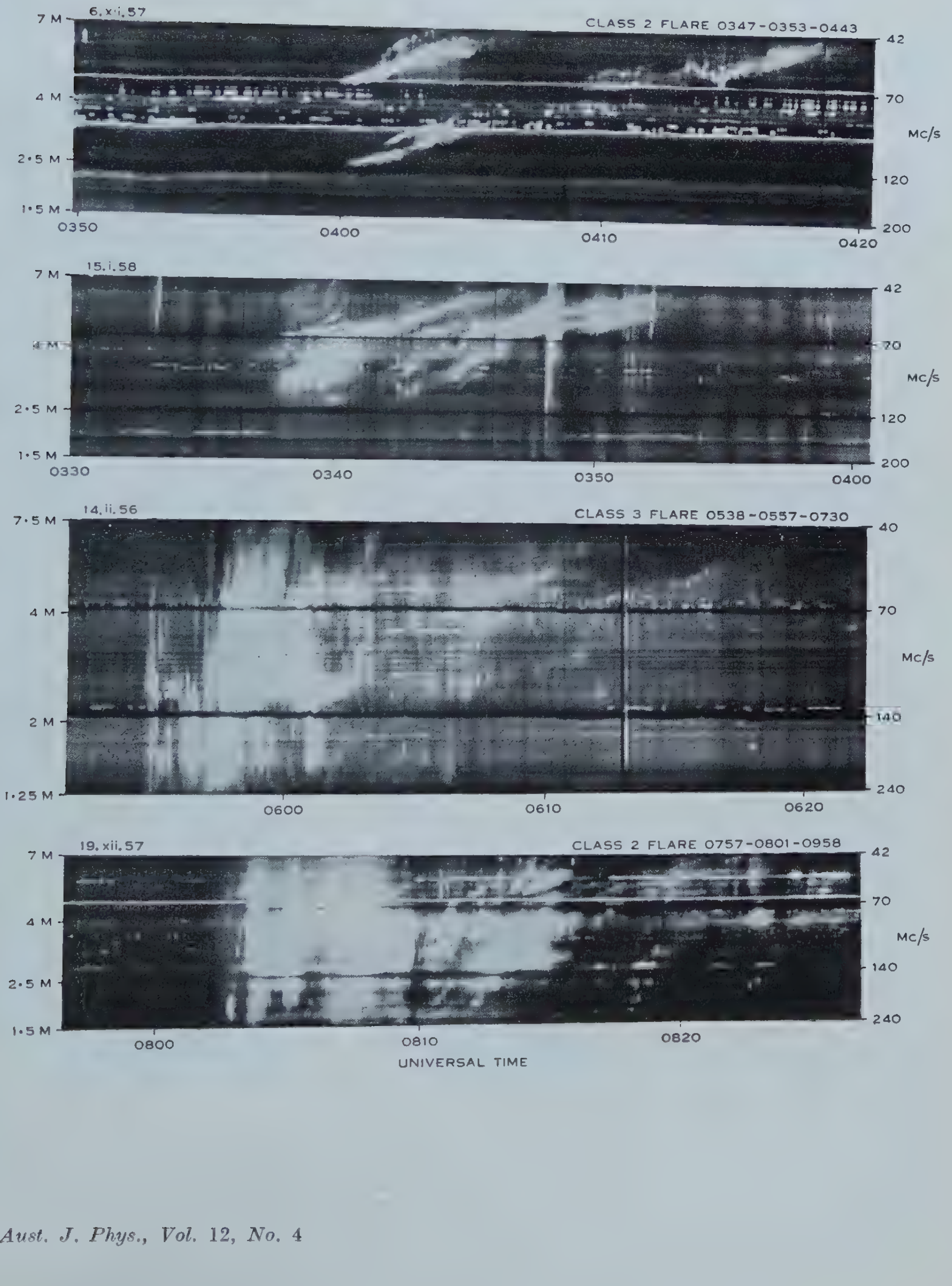

PLATE 3

SOLAR RADIO BURSTS OF SPECTRAL TYPE II

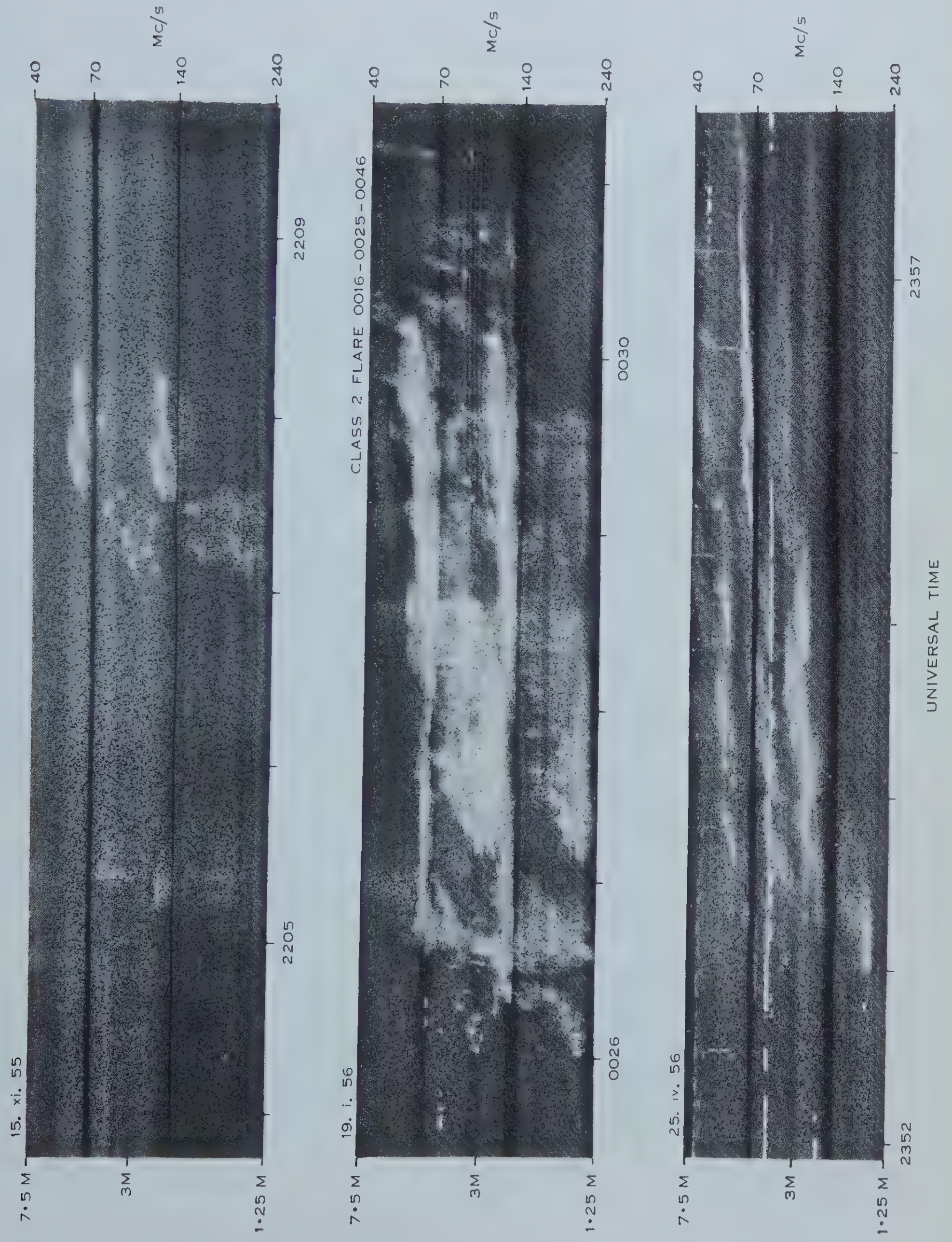

SOLAR RADIO BURSTS OF SPECTRAL TYPE II

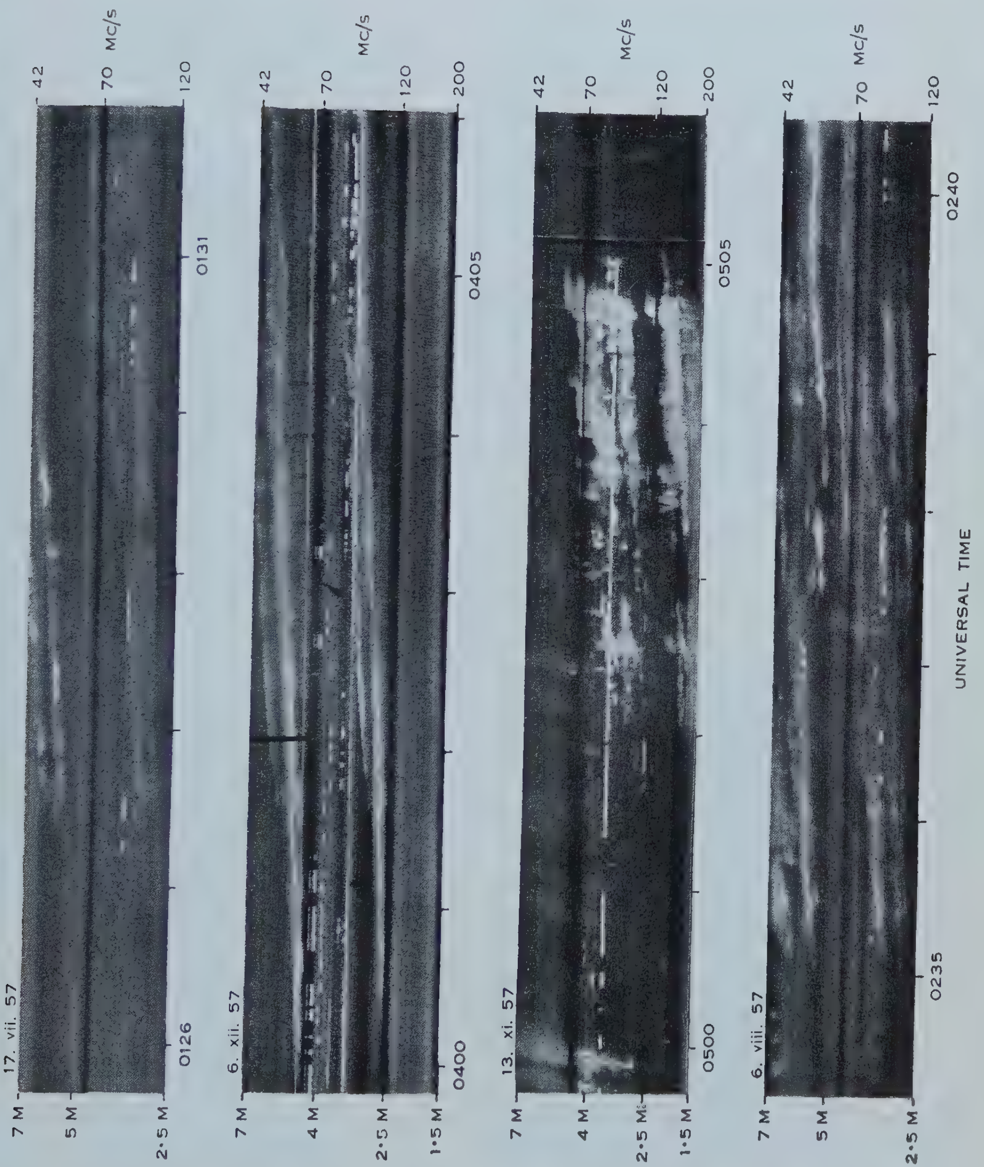

SOLAR RADIO BURSTS OF SPECTRAL TYPE II

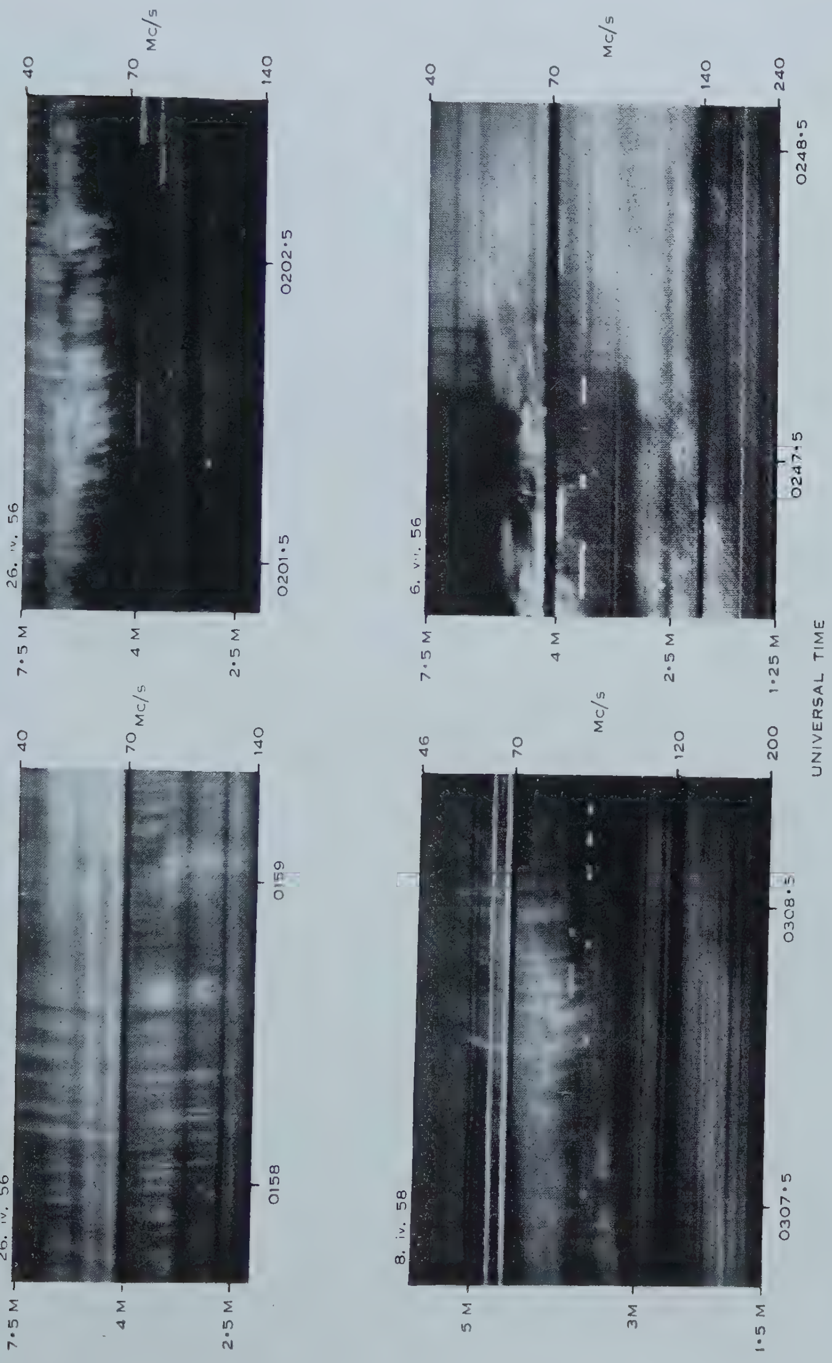

LOCATION OF THE SOURCES OF 19 Mc/s SOLAR BURSTS

By C. A. Shain* and C. S. Higgins*

[*Manuscript received July* 8, 1959]

Summary

By using large aerials in a new way, it has been possible to locate, with considerable accuracy, the sources of 19 Mc/s solar bursts. The positions of these sources have been correlated with the positions of optically active regions associated with them, and the radial distances of the radio sources from the centre of the Sun have been deduced. In 1950–1951, $18 \cdot 3$ Mc/s bursts came from sources at a radial distance estimated as $3 \cdot 4R_0$; more reliable data in 1957 indicated that the sources of $19 \cdot 7$ Mc/s bursts were at a radial distance of $2 \cdot 9R_0$. It is thought that these measurements give the distances of the fundamental plasma levels in coronal streamers.

I. Introduction

The progress of radio astronomy has been closely linked with the development of equipment and novel techniques for obtaining high angular resolving power. In the application of new direction-finding techniques it is often simpler to study solar radio emission than cosmic sources, because in some circumstances the Sun, or at least some part of it, is the outstandingly bright object in the sky. In particular, at about 20 Mc/s, the undisturbed Sun is very faint, but solar bursts commonly have intensities many times the intensity of the galactic background. Observations of solar radio spectra (Wild, Murray, and Rowe 1954) have shown that these bursts most probably originate at a level in the corona where the plasma frequency is equal to the frequency on which the bursts are observed; they are often associated with solar flares.

Since the sources of metre-wavelength radio emission must be well above the chromosphere, bursts from sources away from the centre of the solar disk will appear substantially displaced from the position of the associated optical phenomenon (Payne-Scott and Little 1951) and, conversely, if these displacements can be measured, we can obtain information about the actual height in the corona of the appropriate plasma level.

Some years ago, in 1950, an aerial system constructed near Sydney for cosmic noise observations (Shain and Higgins 1954) was used in a novel way to measure with useful accuracy the positions, in one coordinate only, of the sources of $18 \cdot 3$ Mc/s bursts from the Sun. Although these observations gave a clear indication that the sources of emission were rather higher in the corona than might have been expected on the basis of the Baumbach-Allen model of the corona, they could not be correlated in detail with optical data, simply because adequate optical data were not available. More recently we have again made

---

* Division of Radiophysics, C.S.I.R.O., University Grounds, Chippendale, N.S.W.

solar position measurements, this time using the east-west array of the 19·7 Mc/s cross-type aerial (Shain 1958) and, as these measurements were made during the International Geophysical Year, optical information is much more complete.

The aim of the present paper is to present the results of these observations and to deduce from them the apparent heights of origin of the bursts, and hence of the plasma levels in the corona. This information could then be combined with similar results obtained from observations at other frequencies (see, for example, Wild, Sheridan, and Neylan 1959) to construct a model of the coronal electron density distribution, but no attempt will be made to do this here.

II. Observational Technique

Since most solar noise bursts last for times of the order of 10 sec, any direction-finding equipment designed to observe these bursts must be able to operate very rapidly. In the metre-wavelength range the usual method involves interferometers employing widely spaced aerials and rapid variation of the phase paths to the receiver. Little and Payne-Scott (1951) operated at a single frequency and used a fast, mechanical phase changer ; Wild and Sheridan (1958) use fixed lines but sweep in frequency.

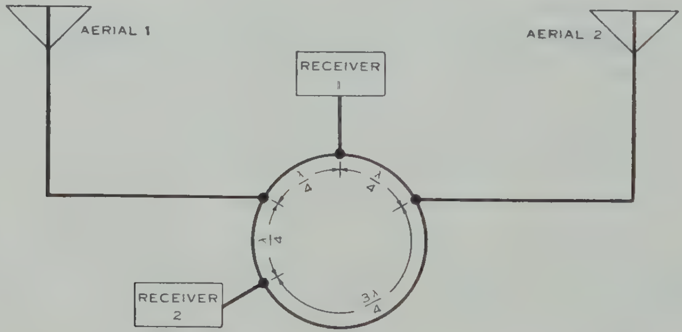

Fig. 1.—The arrangement of aerials and receivers.

For the present work, no attempt was made to sweep in phase. Two similar aerials were connected by equal feeders to a bridge, and two separate receivers to the other corners of the bridge (see Fig. 1). The feature of such a bridge (Westcott 1948) is that the two receivers are quite independent of one another in operation, and the aerials are connected to Receiver 1 in-phase, but to Receiver 2 out-of-phase. Now, if the Sun is in the primary beams of the aerials and a burst occurs, in general the burst amplitude as recorded by the two receivers will be different, and the ratio of the amplitudes is a function only of the angle between the source direction and the line joining the two arrays. If r is the ratio of the in-phase (power) amplitude to the out-of-phase amplitude, and φ the angle between the source and the line joining the aerials,

$$r=\cot^2\left(\frac{\pi d}{\lambda}\cos\varphi\right),$$

where d is the separation between the aerials and λ the wavelength. If the aerials are on an east-west line,

$$\cos \varphi = \cos \delta \sin h,$$

where δ and h are the declination and hour angle respectively of the source.

In practice, Aerials 1 and 2 (Fig. 1) were actually two halves of one large array. The earlier series of observations (in 1950–1951) used the 30-dipole array which has been described previously (Shain and Higgins 1954). For the later series (in 1957) an exactly similar arrangement was used. Although, for galactic work, it is normally operated as a complete array 3500 ft long, the east-west array of the 19·7 Mc/s Cross may be divided into two, with separate feeders for the eastern and western arms, and these separate arms formed Aerials 1 and 2 of Figure 1.

As in all interferometer observations there are ambiguities in position at intervals corresponding to the various values of φ which give the same value of r. In one way these ambiguities are more serious than with the conventional interferometer technique, because amplitudes are measured without regard to phase and near a maximum or minimum of the interferometer pattern the same ratio is measured at two fairly close positions. It is therefore desirable to compute positions for only those bursts for which the ratio is in the range, say, $0 \cdot 2 < r < 5$. On the other hand, by using the two halves of the one array there is virtually no gap between the " interferometer " aerials and, apart from the centre lobe and the two neighbouring lobes, all the lobes are of very small amplitude.

The two receivers were either two communications receivers or two sections of the receiver used with the 19·7 Mc/s Cross. The important requirements of the receivers are that they should be tuned to exactly the same frequency and that the overall time constants, including the recorders, should be the same. Intensity calibrations for each receiver were included on all the records. The accuracy with which the two receivers must be set to the same frequency depends on the spectral characteristics of the bursts. In this connexion it is of interest to note that on several occasions, not included in the present study, certain short-duration bursts have been recorded with very different intensities (allowing for aerial and receiver instrumental effects) at frequencies only 40 kc/s apart at about 19·7 Mc/s. For the present work the frequencies to which the receivers were tuned differed by no more than 1 kc/s.

A typical pair of records is shown in Figure 2; the apparent positions deduced from the ratios of burst amplitudes are shown in the lowest section of the figure.

Although the observations were all made near solar transit, so that " spherical " refraction in the ionosphere would have had only a negligible effect on measurements of hour angle, the diurnal variation of electron density produces horizontal gradients which give rise to appreciable " wedge " refraction in the east-west direction. Corrections to the observed source positions were made using the data of Komesaroff and Shain (1959), derived from observations of discrete sources of cosmic noise. In that paper it was shown that the applications of the corrections described there greatly reduced the scatter of the observed positions (to about $\pm 0^{\circ}\cdot 1$) but there remained a systematic displacement in Right Ascension. It is now known that this effect arose out of the assumption that the time variation of the critical frequency of the ionosphere could be interpreted as a spatial variation along a line of constant latitude. Further study of the data from the ionospheric sounding stations in eastern Australia and at Watheroo, Western Australia, has shown that this assumption was not fully justified, and a more complete correction for ionospheric refraction is now possible (Komesaroff and Shain, in preparation).

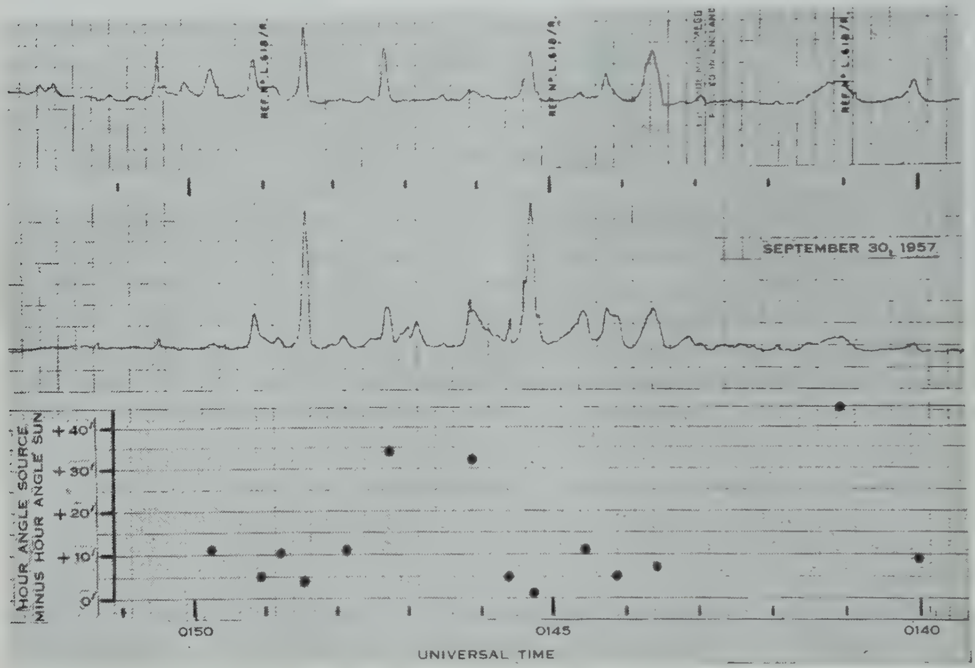

Fig. 2.—The two records for September 30, 1957. The "out-of-phase" record is on top and the "in-phase" record underneath. The lowest section of the figure shows the positions derived from the ratios of burst intensities, after making a small and constant correction for ionospheric refraction. It is clear that most of the bursts come from one source, but three bursts probably arose in another source further to the west. Only the main source has been listed in Table 2.

Because of the high intensity of solar bursts, the accuracy obtainable in reading the source positions from the records is very high, the uncertainty being only a small fraction of the beamwidth of the whole aerial array (17° to half-power at 18·3 Mc/s in 1950–1951 and 1°·5 at 19·7 Mc/s in 1957). The main source of uncertainty for the 19·7 Mc/s observations, and a contributing source for the 18·3 Mc/s observations, arises in the estimation of the ionospheric refraction, especially as interpolation from hourly data is necessary in order to estimate the ionospheric parameters. Therefore, although we have listed the positions of the radio sources to the nearest 5 min of arc, estimates of the probable uncertainties of the positions for any one day are $\pm 0^{\circ}\cdot 1$ and $\pm 0^{\circ}\cdot 3$ for the 1957 and 1950–1951 observations respectively.

It should be noted that, since there is no phase-switching involved, the rate at which direction-finding observations can be made is limited only by the overall time constant of the system. By using suitably rapid recorders, it should be possible to detect any changes in apparent position which might occur even during bursts lasting only 1 sec. Position changes have been observed during some bursts, or series of bursts, lasting several minutes, but these will not be considered in the present paper.

III. OBSERVATIONAL DATA

(a) *18·3 Mc/s Observations in 1950–1951*

The dates and times of the 1950–1951 observations are listed in Table 1, together with the positions of some optical regions with which the radio emission on the various days might reasonably be associated. As mentioned above, there were many long gaps in the optical observations during the periods of interest so that some of these associations are doubtful, and also some radio data

TABLE 1

1950–1951 OBSERVATIONS

Date	Hour Angle Radio Source minus Hour Angle Sun (min. of arc)		Optical Active Region	Hour Angle Optical Source minus Hour Angle Sun (min of arc)
	18·3 Mc/s	97 Mc/s		
1950				
Nov. 16 ..	0	+2·5	(8) Flare	0
17 ..	+20	+5·5	—	—
1951				
Jan. 30 ..	+10	+7·5	(7)	+ 4
Feb. 1 ..	+40	+15	(7) Flare	+ 9
2 ..	+20		(5) Flare	+ 6
24 ..	— 5		(13)	— 1
Mar. 16 ..	—40		(18)	—13
17 ..	—25		(18)	—12·5
18 ..	—35		(18)	—12
19 ..	+10		(18)	— 9·5
20 ..	—10		(18)	— 7
22 ..	—10		(18)	— 0·5
24 ..	+ 5		(18)	+ 5·5
25 ..	+50		(18)	+ 8·5
26 ..	+80		(18)	+11

had to be omitted because there was no clear identification with any particular optically active region. In Table 1 the regions are identified by the numbers given in the appropriate issue of the *Quarterly Bulletin on Solar Activity* ; the word " Flare " is added if a solar flare was observed during the time of observation on any day. Since the aerial was practically on an east-west line and the observations were limited to times near transit of the Sun, the position measured was the difference between the hour angles of the source and of the centre of the Sun. On four days for which 18·3 Mc/s data are available the Potts Hill 97 Mc/s swept-phase interferometer (Little and Payne-Scott 1951) was operating, although not necessarily at the same times, and Mr. A. G. Little has kindly supplied the positions deduced from these observations; these, too, are included in Table 1.

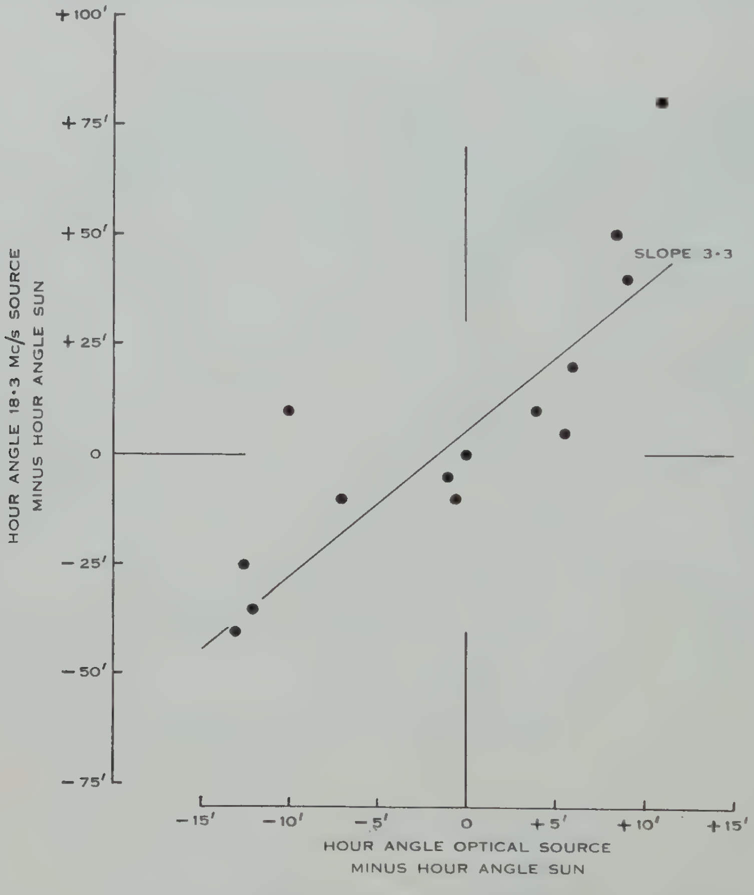

Fig. 3 (*a*).—The observed east-west displacements from the centre of the Sun of the 18·3 Mc/s sources plotted against the positions of the associated optically active regions; data from Table 1.

In Figure 3 (*a*) the east-west displacement between the radio source and the Sun's centre is plotted against the corresponding optical displacements. There is clearly a strong correlation between the two quantities, but this must be partly due to observational selection—to a certain extent the few optical data were chosen to fit the radio data. In view of all the uncertainties, no significance is attached to the fact that the line in Figure 3 (*a*) does not pass exactly through the origin. Figure 3 (*b*) shows the 18·3 Mc/s positions plotted against the corresponding 97 Mc/s positions for the few occasions on which both measurements were available.

In spite of the uncertain optical identifications, one thing is clear from Table 1 and Figure 3 (*a*), namely, that the radio sources lie far out in the corona : the east-west displacements of the radio sources range up to 50 min of arc, whereas the diameter of the optical disk is only 16 min of arc. Further, Figure 3 (*b*) shows that the 18·3 Mc/s bursts must come from a region much further out even than the region of origin of 97 Mc/s bursts.

(*b*) *19·7 Mc/s Observations in 1957*

Table 2 gives the circumstances of the position measurements made with the large 19·7 Mc/s array in 1957 ; the rather narrow primary beam of the aerial restricted the observations to times within about 15 min of solar transit. On the majority of days listed in the table the bursts were observed at times when solar flares were visible on the Sun and it appears reasonable to associate the radio bursts and the flares. On other days there were no flare observations just at the time of the radio observations. For these days the " adopted optical source " has been taken as the McMath Plage Region (MPR) which produced most flares and sub-flares during the 6 hr on either side of the time of observation. The plage regions are identified by the numbers published in the Central Radio Propagation Laboratory's monthly " Solar-Geophysical Data "* from which also some of the flare information was taken. Other flare information came from the patrol observations of the C.S.I.R.O. Division of Physics, Sydney.

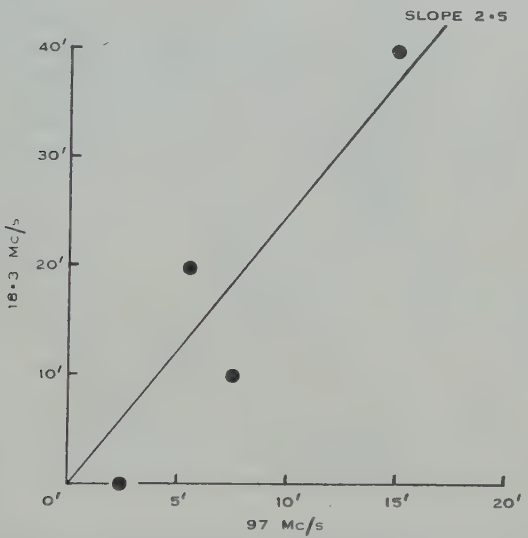

Fig. 3 (*b*).—The east-west displacements of 18·3 and 97 Mc/s sources on four days.

It is impossible to decide with certainty, from the single-frequency observations, the spectral type of the radiation being studied, but comparison with the

---

* U.S. National Bureau of Standards, Central Radio Propagation Laboratory, Series CRPL–F Part B, Issued Monthly.

Table 2
1957 observations

Date	Times of Bursts Analysed (U.T.)		Hour Angle 19·7 Mc/s Source minus Hour Angle Sun (min of arc)	Adopted Heliographic Position of Optical Source		Hour Angle Optical Source minus Hour Angle Sun (min of arc)	Optical Source	Concurrent Radio Spectral Observations
	First	Last		Lat.	Long.			
1957								
Aug. 26 ..	0153·0	0206·4	—40	N 28	E 82	—15·5	MPR 4124	U, III before and after
			—15	S 30	E 64	— 9	MPR 4125	
28 ..	0151·2	0203·7	—15	S 28	E 38	— 2·5	Flare Mitaka 0122–0135–0154	III 0146, 0200
30 ..	0148·5	0152·8	+30	S 25	W 33	+11	Flare Sydney 0133–0216–	Weak I all day IIIg 0159, 0200 ; IIIb 0201
Sept. 23 ..	0145·4	0153·8	—30	N 18	E 62	—14	MPR 4159	
24 ..	0141·0	0142·2	+80	N 13	W 62	+11	Flare Sydney 0142–0143–0148	Weak I all day III 0141, 0142
25 ..	0141·4	0149·0	+35	N 24	W 85	+11	Flare Hawaii <0132– –>0138	U, III before and after
27 ..	0140·4	0153·3	—35	N 16	E 50	—12	MPR 4162	Strong I all day
			0	N 18	E 3	— 2	MPR 4159	III storm all day
28 ..	0142·2	0151·2	+ 5	N 18	W 11	+ 1	MPR 4159	No observations
			+30	S 15	W 45	+12	MPR 4157	
30 ..	0140·1	0149·8	+ 5	N 18	W 37	+ 5·5	MPR 4159	U, III before and after
Oct. 1 ..	0145·0	0202·4	—10	N 29	E 23	— 7	Flare Sydney 0131–0139–0148 Flare Sydney 0158–0200–0204	No observations
2 ..	0149·5	0153·3	—30	S 20	E 40	— 6	MPR 4167	III after
4 ..	0151·0	0153·4	—60	N 20	E 94	—15·5	Flare Sydney 0149–0152–0200	III before and after
17 ..	0136·4	0145·6	+30	S 13	W 28	+ 9	Flare Sydney 0143–0154–0205	IIIg 0138, 0139 ; IIIb 0141
25 ..	0136·0	0142·0	+15	N 13	W 7	+ 1	Flare Sydney 0131–0145–0159	III before
Nov. 15 ..	0133·0	0152·0	+30	N 15	W 37	+ 5	Flare Sydney 0136–0138–0144	III before
18 ..	0138·0	0206·0	+20	N 5	W 50	+11	Flare Sydney 0120– –0230 Flare Hawaii 0126–0132–0138	U 0204–0205
Dec. 9 ..	0201·0	0204·0	—15	S 20	E 8	— 1	Flare Sydney 0157–0201–0226	IIIG 0200–0203

Dapto radio-spectrograph data for the days concerned suggests that in almost all cases the radiation was type III. The doubtful cases are those when type I storms were observed at Dapto, in particular on September 27, 1957; one of the two positions observed on this day probably refers to type I emission, the other to type III. There may have been a few cases of type V bursts, but types II and IV can be excluded as they occur together and the spectra of type II bursts are such that any reaching to 20 Mc/s would have been identifiable on the spectrograph records.

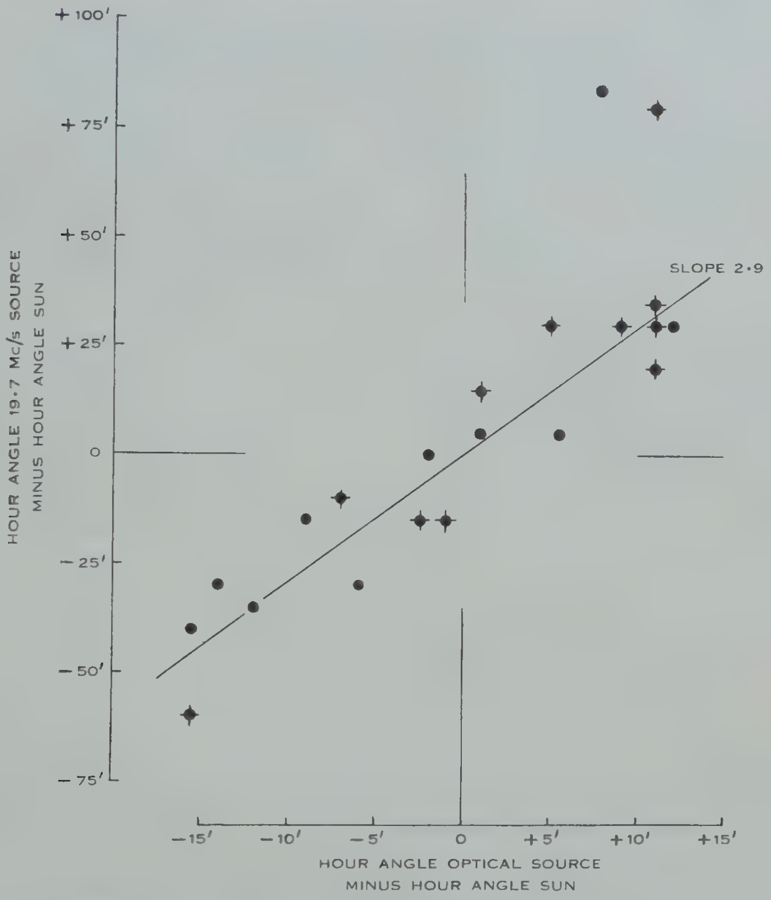

Fig. 4.—The observed east-west displacements from the centre of the Sun of the 19·7 Mc/s sources plotted against the positions of the associated " adopted optical source "; data from Table 2. The points marked with a cross correspond to radio sources directly associated with solar flares.

The east-west displacements of the radio and optical sources from the centre of the Sun are compared in Figure 4. As with the earlier observations, again there is good correlation and it can be inferred that the radio sources must be well out in the corona. This point is discussed in more detail below.

IV. HEIGHT OF THE SOURCES OF EMISSION

From their study of the radio-spectrograph data, Wild, Murray, and Rowe (1954) concluded that there was strong evidence that " fundamental " type III bursts at any frequency were generated at the corresponding plasma level in the corona. In interpreting our observations, we may consider two greatly different coronal models.

Firstly, if the corona were smooth and spherically symmetrical, the critical " escape surface ", from below which radiation cannot reach the Earth, is everywhere higher than the plasma level, so, for radiation to reach the Earth from a source at the plasma level, it is necessary to modify the simple model by introducing scattering near the escape surface. We then have the kind of situation illustrated in Figure 5 (*a*) : the source of bursts in the plasma level radially above the optical source, but the observable position probably referring to the intersection of the escape surface and the radius through the source. With the comparatively smooth, regular model of the corona, the ray path suffers appreciable refraction in the outermost regions of the corona and the apparent position as measured at the Earth is moved back towards the centre of the Sun. We have considered in detail the apparent movement of a radio source across the Sun's disk on the basis of this model and, surprisingly, it appears that the refraction almost counterbalances the effect of the increased height of the escape surface as the source nears the limb. It follows that, to within the accuracy involved in the assumption that the radio source is radially above the optical source, the observations can be interpreted as if the source moves around the plasma level surface with no refraction after leaving the source. The slope of the line through the points on diagrams such as Figures 3 (*a*) and 4 then gives directly the distance of the plasma level from the Sun's centre in units of the radius of the optical Sun.

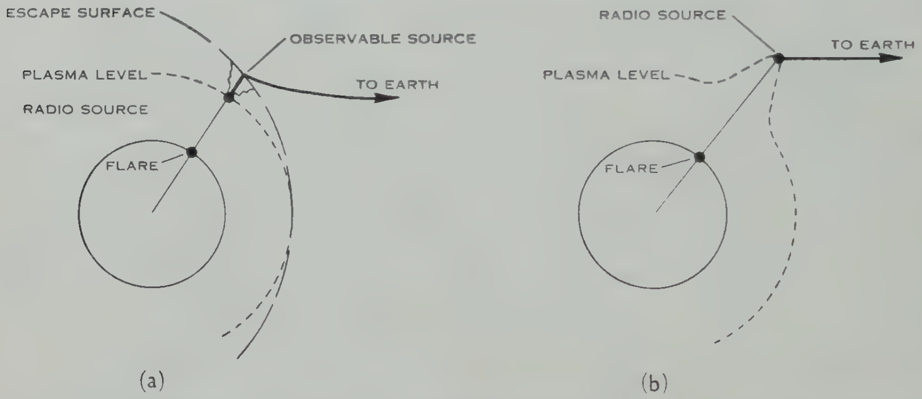

Fig. 5.—Illustrating two possible coronal models considered in the interpretation of the radio position observations.

On the other hand, there are, in fact, generally large irregularities in the corona, the coronal streamers (van de Hulst 1953), and as these are specially prominent over active regions it is probable that the radio sources are actually in coronal streamers. The disturbance exciting the source will probably travel along the streamer and the source might be expected to be at the highest point of the surface of equal electron density corresponding to the plasma frequency, as in Figure 5 (*b*). Provided the streamer is fairly narrow there will be little refraction in the " normal " outer corona, because the electron density there will be much lower than in the streamer. In this case also, then, we can deduce the height of the source directly from the observations, but this would be the height of the plasma " level " in a coronal streamer and not in the normal corona.

In either case it appears reasonable to assume that on the average the initiating disturbances travel radially outwards from the optical active region, although for any particular disturbance there may be considerable departures from radial motion.

Turning to the observational results, from Figure 3 (*a*) we deduce that in 1950–1951 the 18·3 Mc/s sources were at a radial distance of $3{\cdot}5R_0$ from the centre of the Sun (R_0 being the Sun's optical radius), although this value is rather uncertain because of the scatter of the points and the basic uncertainties in identifying the optical sources. Again, from Figure 3 (*b*) we find that the 18·3 Mc/s sources were at a distance about 2·5 times the distance of the 97 Mc/s sources. Taking the Baumbach-Allen model of the corona (Smerd 1950), the distance of the 97 Mc/s plasma level is $1{\cdot}15R_0$, but Payne-Scott and Little (1951) estimated that the sources of 97 Mc/s noise storms were not less than $0{\cdot}3R_0$ above the visible surface. In conjunction with Figure 3 (*b*) this would lead to a radial distance of $3{\cdot}2R_0$ for the 18·3 Mc/s sources, in good agreement with the value from Figure 3 (*a*) ; the average gives $3{\cdot}4R_0$.

For the later and more reliable 19·7 Mc/s observations, the slope of the line in Figure 4 indicates a radial distance of $2{\cdot}9R_0$ for 19·7 Mc/s sources in 1957.

V. Discussion

The immediate inference that might be drawn from the results of the previous section is that the sources of 19 Mc/s bursts are much higher than the " normal " 19 Mc/s plasma level (radial distance about $1{\cdot}8R_0$ (Smerd 1950 ; van de Hulst 1953)), but this simple interpretation requires further consideration, for the following reason. It was pointed out above that the spectral type of the bursts cannot be decided with certainty from the single-frequency records and there is a possibility that the derivation of a large height for the 19 Mc/s plasma level is due to the fact that the bursts studied were actually harmonics of 10 Mc/s bursts ; the 10 Mc/s plasma level is certainly higher than the 19 Mc/s level. Before considering this question more closely, it may be remarked that even the 10 Mc/s level in the normal corona is only at a radial distance of about $2{\cdot}25R_0$, and it would appear to be established that the bursts originated in coronal streamers where electron densities are rather higher at any height than in the normal corona.

If some of the bursts observed were fundamental bursts and some harmonics, the scatter of the points in an idealized diagram like Figures 3 (*a*) and 4 would increase for sources near the limb. There are, of course, other factors contributing to the scatter in these figures: observational errors, departures from radial motion of the initiating disturbances, and differences in the electron density distribution for different streamers. In Figure 4, particularly, the scatter appears to be much the same all the way along the line and, in fact, a very large part of this must be due to observational errors. It follows that any component of the scatter due to a mixture of fundamental and harmonic bursts is small, and one or other must predominate.

Wild, Murray, and Rowe (1954) have shown that the disturbances which initiate the bursts travel outwards through the corona, but are often brought to rest before escaping from the Sun. The height at which this occurs varies from burst to burst, but one would expect that the 19 Mc/s level would be excited more often than the higher 10 Mc/s level, so that most of the bursts observed were fundamentals.

TABLE 3

DERIVED HEIGHTS OF PLASMA LEVELS

Year	Frequency (Mc/s)	Electron Density (cm^{-3})	Radial Distance from Centre of the Sun
1950–51 . .	18·3	$4\cdot1\times10^6$	$3\cdot4R_0$
1957	19·7	$4\cdot8\times10^6$	$2\cdot9R_0$

Although the evidence is not conclusive, we incline to the view that the radial distances of the plasma levels, derived in this paper, refer to the fundamental plasma frequencies. The results are brought together in Table 3. Of the two sets of observations, the 19·7 Mc/s is the more reliable, but the earlier result is in good agreement, considering all the uncertainties involved and the time interval between the observations.

VI. REFERENCES

VAN DE HULST, H. C. (1953).—" The Sun." (Ed. G. P. Kuiper.) Ch. 5. (Univ. Chicago Press.)

KOMESAROFF, M. M., and SHAIN, C. A. (1959).—*Nature* **183**: 1584.

LITTLE, A. G., and PAYNE-SCOTT, RUBY (1951).—*Aust. J. Sci. Res.* A **4**: 489.

PAYNE-SCOTT, RUBY, and LITTLE, A. G. (1951).—*Aust. J. Sci. Res.* A **4**: 508.

SHAIN, C. A. (1958).—*Proc. Inst. Radio Engrs., N.Y.* **46**: 85.

SHAIN, C. A., and HIGGINS, C. S. (1954).—*Aust. J. Phys.* **7**: 130.

SMERD, S. F. (1950).—*Proc. Instn. Elect. Engrs.* III **97**: 447.

WESTCOTT, C. H. (1948).—*Wireless Engr.* **25**: 215.

WILD, J. P., MURRAY, J. D., and ROWE, W. C. (1954).—*Aust. J. Phys.* **7**: 439.

WILD, J. P., and SHERIDAN, K. V. (1958).—*Proc. Inst. Radio Engrs., N.Y.* **46**: 160.

WILD, J. P., SHERIDAN, K. V., and NEYLAN, A. A. (1959).—*Aust. J. Phys.* **12**: 369.

AN INVESTIGATION OF THE SPEED OF THE SOLAR DISTURBANCES RESPONSIBLE FOR TYPE III RADIO BURSTS

By J. P. Wild,* K. V. Sheridan,* and A. A. Neylan†

[*Manuscript received August* 3, 1959]

Summary

The paper describes an investigation aimed at finding out whether solar radio bursts of spectral type III are due to disturbances which travel out through the corona with velocities exceeding $0\cdot 1c$, as predicted by the well-known hypothesis that the emissions are due to plasma oscillations. If the proposition is correct, emissions at different frequencies would be generated at different levels in the corona—the lower the frequency the higher the source. This property is tested by simultaneous directional observations at a number of frequencies between 40 and 70 Mc/s, using a swept-frequency interferometer.

The system and performance of the interferometer are described, and errors in position-finding due to ionospheric refraction are discussed.

Results for type III bursts show that different frequencies are generated at different levels in the corona according to the predicted sequence ; they therefore strongly support the plasma hypothesis. It is concluded that the corona is considerably denser in the regions where type III sources are generated than in the average corona as depicted by conventional models ; and an origin in coronal streamers is suggested.

The derived velocities of type III disturbances are found to be considerably greater than those previously deduced from spectral data alone. The range of velocities now inferred extends from $0\cdot 2c$ to $0\cdot 8c$, with an average of $0\cdot 45c$. The significance of these very high velocities is discussed. For this purpose new evidence is discussed relating to the " type V " continuum emission which follows certain type III events. The combined type III–V events, which are known to correlate closely with chromospheric flares and sub-flares, are interpreted in terms of streams of relativistic electrons with energies $\gtrsim 2$ MeV which travel along magnetic lines of force in spiral paths. It is suggested that, in its outward passage, such a stream excites plasma oscillations in the surrounding coronal gas (yielding the type III burst), while, under favourable circumstances, the electrons themselves emit synchrotron radiation (yielding the type V burst.) A possible connexion between the energetic solar electrons and the corpuscular radiation surrounding the Earth is suggested.

I. Introduction

Bursts of spectral type III, which on many days dominate the records of solar activity in the metre-wavelength spectrum, are recognized by the rapid drift in the frequency of maximum intensity from high to low frequencies (Wild and McCready 1950). The earliest spectral observations showed that the frequency drift could be interpreted as a very fast outward movement of a disturbance through the solar corona ; the outward velocity was calculated

---

* Division of Radiophysics, C.S.I.R.O., University Grounds, Chippendale, N.S.W.

† Division of Radiophysics, C.S.I.R.O. ; present address : Mount Stromlo Observatory, Canberra.

to be in the range 3×10^4 to 10^5 km/sec, i.e. one-tenth to one-third the velocity of light (Wild 1950). This interpretation was based on the *plasma hypothesis*, namely, that the radio emission was due to plasma oscillations excited in the coronal gas surrounding a suitable kind of localized disturbance. Since the plasma frequency decreases with height in the solar corona, the observed drift from high to low frequencies corresponds to an outward movement of the disturbance. The quantitative conversion of frequency drift to velocity was made using a standard empirical model of the solar corona.

This interpretation was not taken particularly seriously until subsequent observations revealed that in some type III bursts the sources radiated in two bands corresponding to a fundamental frequency and its second harmonic: this strongly suggested that plasma oscillations were responsible (Wild, Roberts, and Murray 1954). However, since the deduced velocities are far in excess of those of any known optical phenomenon, it is obviously important to test their validity by direct means.

In the present paper* we describe an experimental test of the hypothesis using directional observations. The hypothesis predicts that, when a type III source is ejected outwards from near the limb of the Sun, the radio source should appear beyond the limb and its angular displacement from the limb should increase as the frequency decreases. This prediction is tested using a swept-frequency interferometer capable of measuring the east-west coordinate of the source position as a function of both time and frequency.

The instrument is described in Section II. Its principal limitation is imposed by the effects of ionospheric refraction, and a discussion of these effects is therefore given in Section III. The experimental results on type III bursts are presented and interpreted in Sections IV, V, and VI. Section VII gives a description and interpretation of bursts of spectral type V which frequently accompany type III bursts; this discussion is a necessary preliminary to Section VIII, where the physical nature of the type III bursts is considered.

The interferometer described in this paper is operated in conjunction with the Dapto solar radio-spectrograph whose frequency was initially 40–210 Mc/s, and is now 24–210 Mc/s. Much of the discussion of results depends on combining observations made with the two techniques.

Sample spectra of type III bursts are shown in Plate 1 and some properties of type III bursts are listed below. The quantities given apply at frequencies around 100 Mc/s unless otherwise stated, although the spectral type has been recognized over a wide frequency range between about 20 and 600 Mc/s.

Rate of frequency drift	20 Mc/s per sec
Instantaneous bandwidth	10–100 Mc/s
Duration of single burst	3–10 sec
Duration of group ($\sim$10) of bursts	$\frac{1}{2}$–2 min
Maximum intensity	$\sim 10^{-18}$ W m^{-2} (c/s)$^{-1}$

---

* A preliminary sample of the results of this paper was discussed at the Paris Symposium on Radio Astronomy 1958 (Wild, Sheridan, and Trent 1959).

Apparent angular size	~6 min of arc at 65 Mc/s, increasing with decreasing frequency (see Wild and Sheridan 1958)
Polarization	Varies between random and strongly circular or elliptical (Komesaroff 1958)
Frequency of occurrence	Up to several groups per hour at times of strong activity
Optical correlation	Marked correlation with solar flares and micro-flares (Loughhead, Roberts, and McCabe 1957). The bursts occur close to the time when the flare shows its initial sudden expansion (Giovanelli 1958).

II. The Swept-frequency Interferometer

The function of the interferometer used in this investigation is to measure one coordinate (parallel to the observer's east-west line) of the centroid of an isolated source situated on or near the Sun's disk. The measurement can be made effectively simultaneously at five to ten different frequencies between 40 and 70 Mc/s at successive times separated by $\frac{1}{2}$ sec. The accuracy of measurement is about ± 1 min of arc.

The principles of operation and technical details of the swept-frequency interferometer in its initial form have been discussed in a previous paper (Wild and Sheridan 1958). Major features have since been added as a result of operating experience. Firstly, an additional interferometer system with a short base line has been incorporated for lobe identification. Secondly, a more convenient display system has been used and an automatic system of "following" and calibration has been incorporated. The latter facilities have resulted in a reduction, by an order of magnitude, of the time required to analyse the records, which is a major factor in the feasibility of the experiment.

In the outline of the whole system given below, emphasis will be given to the new features. A simplified diagram of the system is given in Figure 1.

(a) *The Principle of Position Measurements*

Two aerials, 1 km apart on an east-west line, are connected to a central receiver whose frequency is swept twice per second through the range 40–70 Mc/s. The relative length of the aerial feeder lines is capable of extensive variation in steps of 15 m; it is regulated throughout the day in such a way that the excess length s of the path travelled by signals coming from the direction of the centre of the Sun's disk via the west aerial over that via the east aerial is constrained to lie within the limits $45\ \text{m} \leqslant s \leqslant 60\ \text{m}$. This regulation is controlled by a computor which is described later.

It is readily seen that a broad-band source of emission situated at the centre of the Sun's disk will induce coherent signals in the two aerial channels, and that when added together the envelope of the instantaneous spectrum that would be given by either one of the channels alone now becomes modulated by an interference pattern, whose maxima occur at the frequencies

$$f_n = n(c/s),$$

where c is the velocity of light and n assumes integral values. For a source whose centroid lies a small angular distance, φ radians, east of centre, the frequency of maxima are given by

$$f_n = nc/(s + a'\varphi),$$

where a' denotes the foreshortened base line of the interferometer as viewed from the direction of the Sun.

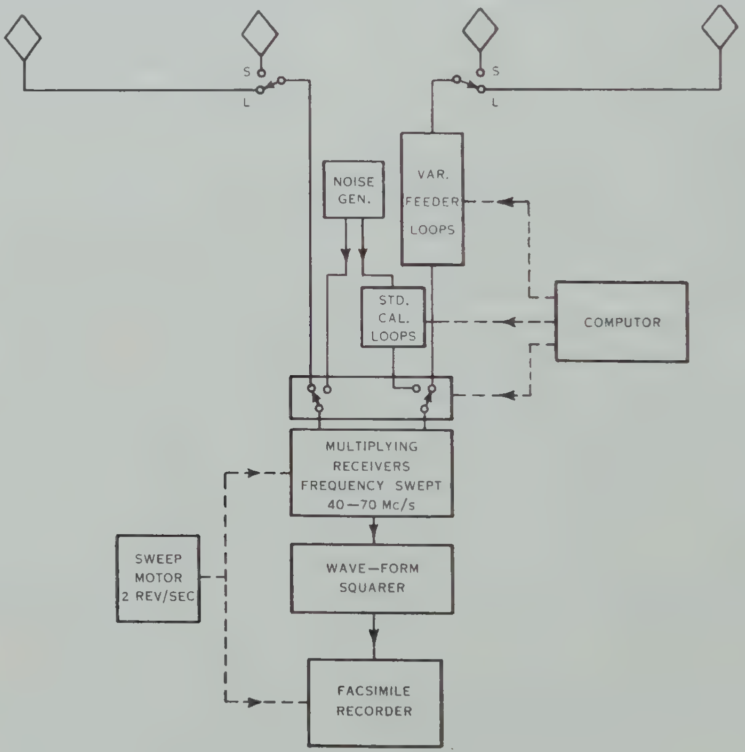

Fig. 1.—Simplified block diagram of the swept-frequency interferometer. Short-base and long-base interferometers are selected by the S/L switch.

In practice the signals in the two channels are combined by a process of multiplication rather than addition, and hence the output " spectrum " consists of the modulation pattern alone, i.e. positive and negative swings in the interference pattern are symmetrical about the zero line. Under the adopted conditions the zero line is crossed at five to ten frequencies (given by $f_n \pm \frac{1}{4}$) and so, if means are provided to determine the correct lobe number n, the angle φ can be measured at each of these frequencies.

(*b*) *The Method of Display*

In the new system of display each swept-frequency modulation pattern delivered by the interferometer is converted into a square waveform (by passing the waveform through a high-gain amplifier that cuts off the extremities of the positive and negative swings) and displayed as a single intensity-modulated line on paper records using a facsimile recorder.* Successive traces at $\frac{1}{2}$ sec intervals are recorded one below the other, partially overlapping, as in ordinary records of dynamic spectra. Each zero point can then be recognized as a sudden change between a black and a white region.

Figure 2 represents an idealized record of a solar source; the first part (between 1159 and 1203 local apparent time) shows a broad-band source *fixed* on the Sun's disk, the second (between 1203·5 and 1204·5) a source which changes position and becomes dispersive with time. Between 1159 and 1200 the swept-frequency pattern gradually drifts and expands owing to the decrease in s with the westward movement of the Sun through the sky. At 1200, s has decreased to 45 m, at which stage the relative feeder length is automatically changed to make $s=60$ m. The new compressed pattern then proceeds to expand again until s has once again decreased to 45 m at about 1203·5. This procedure is repeated continually throughout the observing period. Of course, the record appears banded only when sufficiently intense solar radiation is being received; at other times it consists of random noise.

(*c*) *Calibration of the Record*

In the method used to analyse the records, the first step is to generate a reference pattern, superimposed on the actual paper record, corresponding to a source situated precisely at the centre of the Sun's disk. To do this, the pair of aerial feeders are, at precisely controlled intervals of time, automatically disconnected from their receiver terminals and replaced for a few seconds by a pair of calibration lines connected to a broad-band noise generator. The latter delivers along the calibration lines a pair of mutually isolated but phase-coherent noise signals. The lengths of the two calibration lines are identical, except that one of them contains an additional loop of length l appropriate to the position of the centre of the Sun at that instant of time. By this means the pattern due to a central solar source is completely simulated. In practice, four standard l-values are used for calibration, namely 60, 55, 50, and 45 m; thus the extreme values are used at the beginning and end of each main switching period. The appropriate times at which the calibrations are inserted are calculated by a clock-driven computor described below.

---

* Facsimile recorders were developed primarily for the reception of newspaper photographs transmitted by radio. Electro-sensitive recording paper (9 in. wide in the present case) is fed between and in contact with two stainless steel electrodes. One electrode is a thin bar extending across the width of the paper; the other is a single-turn helical wire mounted on a cylindrical former whose axis extends across the width of the paper. Rotation of the helix through one revolution sweeps the point of contact with the paper from one side to the other. The signal is applied as a potential difference between the electrodes. The electrolytic current flowing at any instant between the electrodes deposits ferric ions into the paper, causing it to blacken in the appropriate spot with a density which increases with the current. The recorder used in this experiment was the product of Hogan Laboratories, New York.

The calibration patterns appear in Figure 2 as brief sections of extra blackness. The continuous pattern corresponding to a central solar source is then given with sufficient accuracy by joining adjacent calibration marks by straight lines, shown dashed in the figure. It is then a simple matter to measure the time displacement between the actual pattern and the reference pattern, and hence determine φ at any desired frequency and time (see Section II (*f*)).

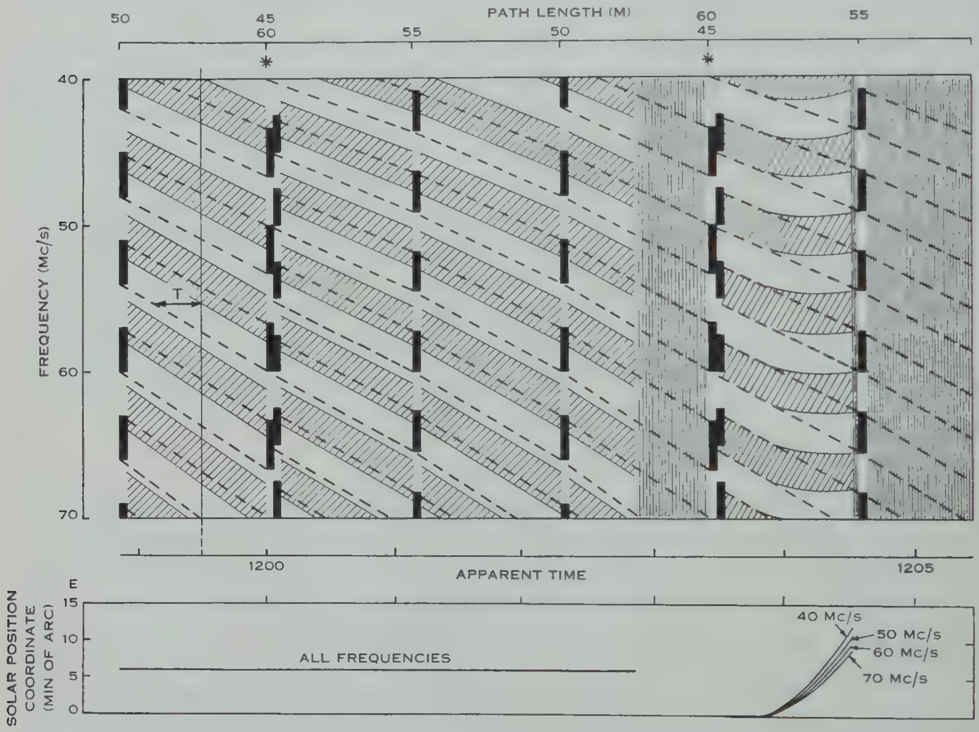

Fig. 2.—Idealized record obtained with the swept-frequency interferometer. The hatched bands, which appear black on the actual record, are produced by a hypothetical solar source, whose position is shown in the lower part. The dotted lines are drawn manually on the record by joining the appropriate calibration marks. The asterisks indicate times at which the relative lengths of the aerial feeder lines are changed by 15 m.

Rapid movements in the position of a source can be recognized by inspection, as illustrated in the latter part of Figure 2. In the example given, the source is initially at the centre of the Sun and all frequencies arrive from this direction. As it moves outwards towards the east, different frequencies are shown arriving from different directions.

(*d*) *The Computor*

Let us designate by l' the difference in the path length travelled by plane waves arriving from the direction of the centre of the Sun's disk to the two *aerials* of the interferometer. Then the system described above requires a computor which delivers pulses at those times when, for integral values of p, l' assumes the values :

(i) $l' = p \times 15$ metres, for the purpose of changing the relative lengths of the aerial feeder lines in steps of 15 m, and

(ii) $l' = p \times 5$ metres, for the purpose of controlling the calibration system.

Clearly, a system that satisfies (ii) can be made to satisfy (i) also by selecting every third pulse.

Now, for an east-west interferometer, l' is given by the well-known equation

$$l' = a \sin H \cos \delta,$$

where a is the distance between aerials, H the hour angle, and δ the declination of the centre of the Sun's disk. Hence to satisfy (ii), we require pulses to be delivered at times corresponding to the hour angles H_p given by

$$\tfrac{1}{5} a \sin H_p \cos \delta = p,$$

where a is measured in metres. The declination δ changes only slowly with time, and for present purposes can be regarded as constant throughout one 4-hr period of observation. For a reason which will become apparent, let the last equation be written in the form

$$\{(\tfrac{1}{5} a/A) \cos \delta\}(A \sin H_p) = p,$$

where $A = 1{\cdot}3750 \times 10^4$.

To produce the desired sequence of pulses (see Fig. 3) we have made use of a small commercially available hand calculator (*Curta*) which is capable of adding a number to itself m times, with an accuracy exceeding 1 in 10^7, by m rotations of a shaft. The number $(\tfrac{1}{5} a/A) \cos \delta$ (appropriate to the daily value of δ) is set up on the calculator and the shaft is driven at a variable rate such that the cumulative number of revolutions measured from noon is $A \sin H$. The cumulative product, $\tfrac{1}{5} a \cos \delta \sin H$, therefore appears on the register, and arrangements are made for a pulse to be delivered when the digit corresponding to integral values of p changes its value.

The variable drive of the computor shaft is achieved by using a constant-speed, crystal-controlled, synchronous motor driven at the rate $A(\mathrm{d}H/\mathrm{d}t)$, which is exactly 1 rev/sec with the chosen value of A. This is the maximum driving rate required, and indeed approximates closely to the required rate during a considerable period around noon, since then $H \approx \sin H$. The motor is normally connected to the calculator's shaft, but it is occasionally declutched for exactly one revolution at times determined by a *standard* programmed tape to compensate for the difference between AH and $A \sin H$ in the cumulative number of revolutions. The interferometer is operated daily for about 4 hr centred on noon, and during this time the motor makes some 10^4 revolutions, of which less than 10^3 are declutched. The computor delivers pulses with an accuracy of about ± 1 sec.

(*e*) *The Complete Record: Ambiguity Resolution and Polarization*

Figure 4 shows an actual record taken during a period of prolonged, broad-band, intense emission from the Sun. It contains the basic features shown in the idealized record of Figure 2 (viz. the patterns due to the source and calibration signals), but contains additional information of two kinds.

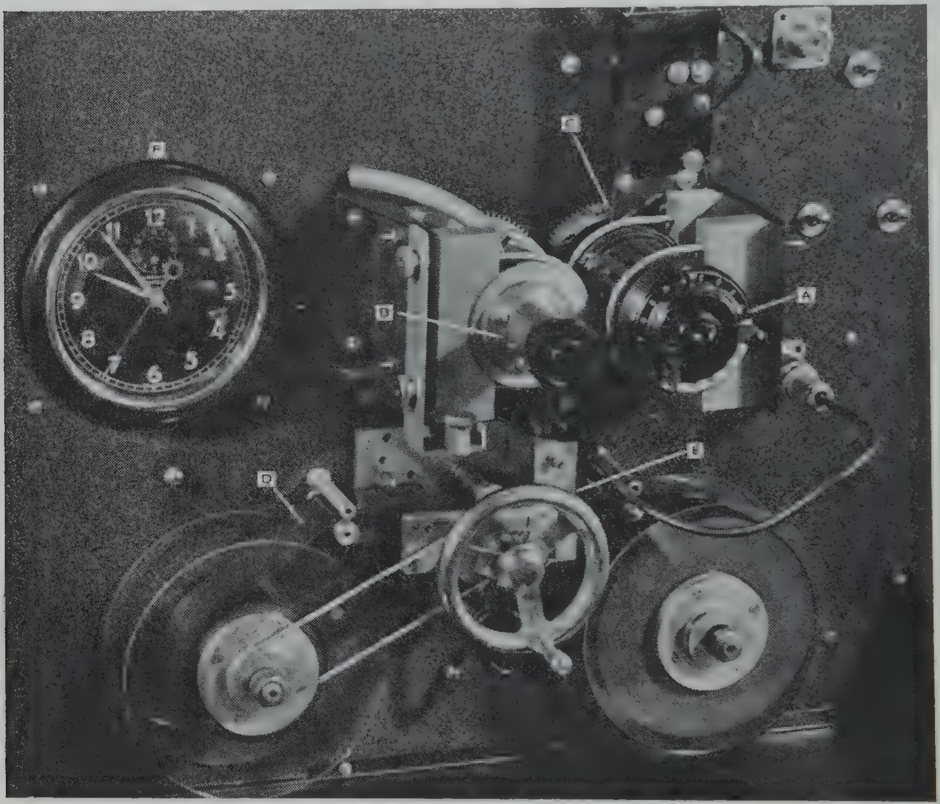

Fig. 3.—The computor used to control the interferometer. A digital calculator *A* is driven by a synchronous motor (behind panel) *via* a magnetic clutch *B*. The appropriate shaft of the calculator operates a photoelectric switch *C* to deliver the output pulse. The magnetic clutch is controlled by a photoelectric switch *E*, which is operated by a programmed tape *D*. The clock *F*, which is set to read local apparent time, is mechanically coupled to the programmed tape.

Firstly, there are periods of about 3 sec (selected by the operator) during which the aerials of the short-base ($\frac{1}{4}$ km) interferometer are substituted for those of the long-base one. As previously intimated, this information is essential to identify the correct lobe (i.e. the correct dark band on the record) associated with the long-base interferometer. While the lobe separation of the long-base system is only about 20 min of arc, that of the short-base system is about 80 min of arc, i.e. sufficiently great to avoid confusion in all but exceptional cases.

The ratio of the two base lines is made equal to $4\pm0{\cdot}0001$. It can be shown that this choice allows the same computor etc. to be used for both systems:

in the case of the short-base system the feeder-line switching is controlled by a " memory system " that takes note only of every fourth pulse fed to the long-base system, and similarly the record analyst takes note only of every fourth calibration on the record. In practice the operator can change from long- to short-base operation by pressing a switch which interchanges the aerials and automatically resets the aerial line lengths.

The second additional facility shown on the record is the provision of short periods of a few seconds (again selected by the operator), during which the rhombic aerials of the normal interferometer are replaced by a pair of coaxial rhombics with mutually perpendicular planes of polarization. These are connected to the receiving system through lengths of line that differ by a fixed amount (45 m), and cause a swept-frequency interference pattern to be generated when coherent signals are received in the two aerials. Measurement of the phase of this pattern yields information on the type of *polarization* (random, circular, linear, or elliptical) being received. The system is essentially similar to that described by Komesaroff (1958) but the accuracy of phase measurement is enhanced by the use of the multiplying receiving system and improved display. Information on polarization will not be discussed in the present paper.

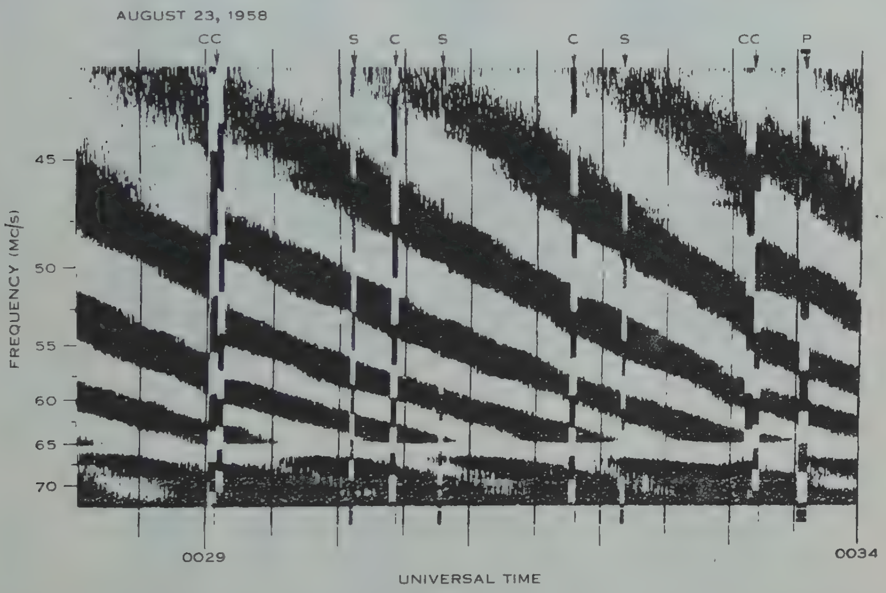

Fig. 4.—Photographic reproduction of an actual facsimile record obtained with the swept-frequency interferometer during a prolonged solar radio storm. The interferometer is operated with the receiver connected to the long-base (1 km) aerial system except for short intervals indicated as follows : *S*, short-base ($\frac{1}{4}$ km) system ; *P*, polarization aerial system ; *C*, calibration system. The horizontal bands between 65 and 70 Mc/s are due to interference from television stations.

Records of type III bursts, where the coherent interferometer pattern appears only for brief periods of time, are basically similar. Examples are shown in Figure 5.

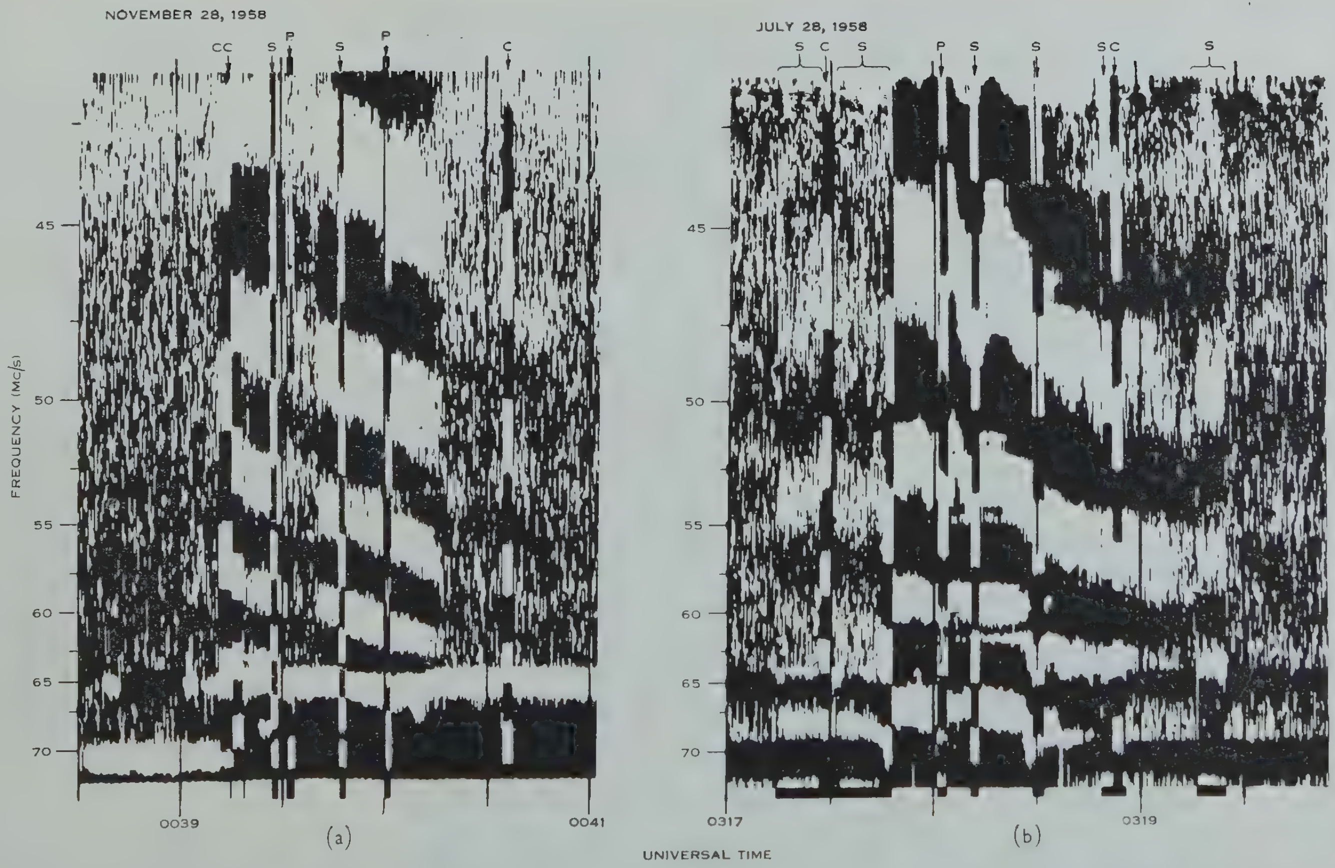

Fig. 5.—Interferometer records of groups of type III bursts. (*a*) is a "normal" record, in which the position at a given frequency remains constant, while (*b*) is an extreme example in which the position shows rapid changes. Details are as in Figure 4.

(*f*) *Analysis of the Records*

The procedure for analysing records of type III bursts consists of the following steps :

(i) Corresponding calibration points are joined on the paper by pencilled lines, so as to give the pattern corresponding to a central solar source. This is performed for both the long-base system (in detail) and the short-base system (as necessary).

(ii) At a selected time during the life of the bursts (or more than one time if source movements are evident), the time delay T between the actual source and calibration source may be read at each frequency defining the edge of a black band. Measurement of the quantity T is illustrated on the left-hand side of Figure 2. Now it is clear that if T is positive (in the sense that a point on the pattern of the actual source *follows* the corresponding one on the calibration source, as in Fig. 2), then the source must have drifted through the appropriate interferometer lobe *after* the centre of the disk, i.e. the source is east of centre. Further, it may simply be shown that the magnitude of the angular position coordinate φ is then given in radians by*

$$\varphi=\frac{\cos H\cos\delta}{\sqrt{(1-\sin^2 H\cos^2\delta)}}\,\frac{\mathrm{d}H}{\mathrm{d}t}T.$$

In practice the quantity φ, rather than T, is read directly from the record by using a " slide-rule " device to make the numerical conversion. Values of φ can be determined at about ten frequencies for a given time.

(iii) To standardize the frequency values, the results are expressed in terms of averages within five adjacent frequency bands. These bands are 5 Mc/s in width, and centred on the standard values 45, 50, 55, 60, and 65 Mc/s. (The 65 Mc/s is often unreliable owing to interference from television signals.)

(iv) The final results required for solar purposes are conveniently expressed in terms of the *position coordinates*, P_{45}, P_{50}, P_{55}, P_{60}, and P_{65}, at the five frequencies. This quantity is defined as the projected distance (normally measured in units of the photospheric radius R_0) between the centre of the disk and the source, measured in the terrestrial east-west direction. It is evident that the position coordinate is given by

$$P_f=(R_0/\Omega)\varphi(f),$$

where Ω is the semi-angle subtended by the photosphere at the Earth.

---

* This may be derived from Section IV *A* (2) of Wild and Sheridan (1958), subject to the note below, or more directly from first principles.

Note.—We take this opportunity of correcting an error in the section cited in the above paper. In Figure 11 of that paper, ΔH should be replaced by $\Delta H\cos\delta$, and equations **(10)**–**(14)** modified accordingly. Using the notation of that paper (e.g. r for the present φ), the final equations **(13)** and **(14)** should read, respectively :

$$r=(\sin\theta-\sin H_0\cos\delta_0)(1-\sin^2 H_0\cos^2\delta_0)^{-\frac{1}{2}},$$
$$\psi=\pm\tan^{-1}(\tan H_0\sin\delta_0).$$

For some purposes (e.g. optical identifications) it is also required to specify the orientation of the lobes on the solar disk. This is given by the angle ψ between the lobes and the solar diameter through the north point of the Sun at noon, thus*

$$\tan \psi = \pm \tan H \sin \delta.$$

(*g*) *An Empirical Correction*

The correct functioning of the interferometer depends on each radio-frequency line and loop of the system possessing its assigned electrical length and sufficient uniformity to avoid unwanted phase errors. The measures taken to meet these requirements were described by Wild and Sheridan (1958). An excellent test of the whole system is provided by observations of reasonably static solar radio storms that continue throughout a 4-hr observing period. Such records were examined closely for signs of instrumental defects, e.g. sudden changes in apparent positions at times when the line lengths were switched. With one exception, such changes were found to be entirely absent within the accuracy of measurement (±1 min of arc). The exception referred to positions in the 60 Mc/s band, which invariably showed a sudden change of 5 min of arc at noon, when the main loop system was transferred from the eastern to the western line. This error is believed due to the cumulative addition of phase errors in the 15 m loop system which would occur at harmonics of 20 Mc/s. A uniform correction of 2·5 min of arc was therefore applied to all 60 Mc/s positions, westward before noon and eastward after. The efficacy of this correction may be judged from inspection of Figure 6, now to be discussed.

III. IONOSPHERIC REFRACTION

A serious threat to the success of the experiment is imposed by the unknown errors in position measurement caused by refraction in the ionosphere of the incident solar radiation, particularly irregular refraction. Since the angular deviation caused by refraction at an ionospheric gradient increases approximately with the square of the wavelength, it is desirable to design the experiment in the first place so as to observe at the highest acceptable frequencies. The reasons for choosing a frequency range as low as 40–70 Mc/s have been discussed previously (Wild and Sheridan 1958). Briefly, they depend on (1) a desire to observe the fundamental frequency emitted in type III bursts ($f \lesssim 90$ Mc/s) and (2) the fact that the effect we are looking for is itself more pronounced at low frequencies. We must therefore be resigned to the troublesome effects of ionospheric distortion.

A convenient comprehensive test of ionospheric effects is again provided by observations of the relatively stable solar sources responsible for storms of long duration. A reduced record of such a storm is shown in Figure 6 (*a*). At any one time all frequencies appear to arrive from the same position to within about ±2 min of arc and this position changes only slightly during the course of the storm. This movement appears to be solar rather than ionospheric in

---

* See previous footnote.

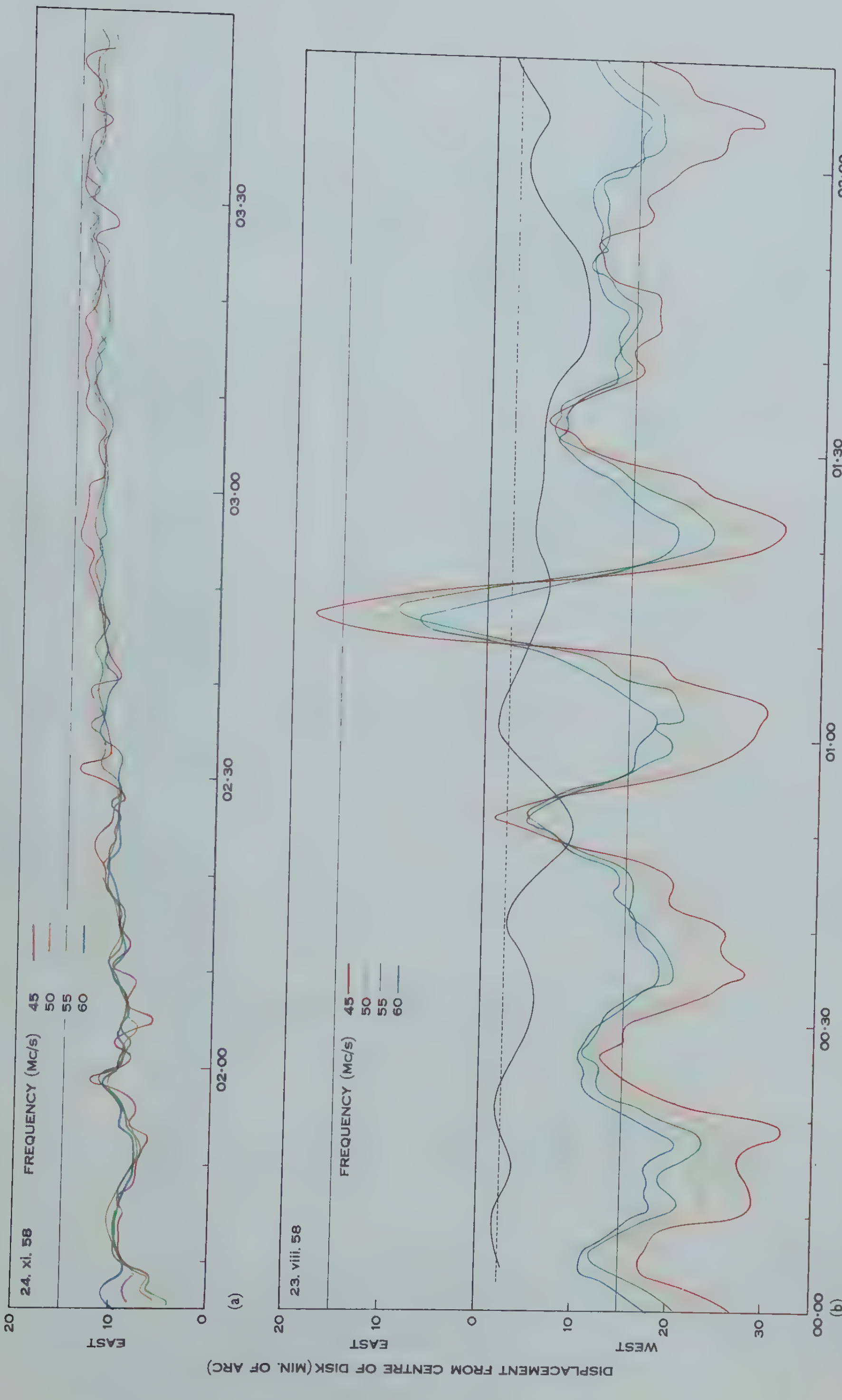

Fig. 6.—The variation of source position with time at four frequencies during prolonged solar radio storms. In (*a*) all frequencies arrive simultaneously from about the same position. In (*b*) there are large, quasi-periodic variations which are believed due to ionospheric refraction. The full black line shows the position of the unrefracted source if certain simplifying assumptions are made. The dotted black line shows the optical position of the centre of the sunspot believed responsible for the emission.

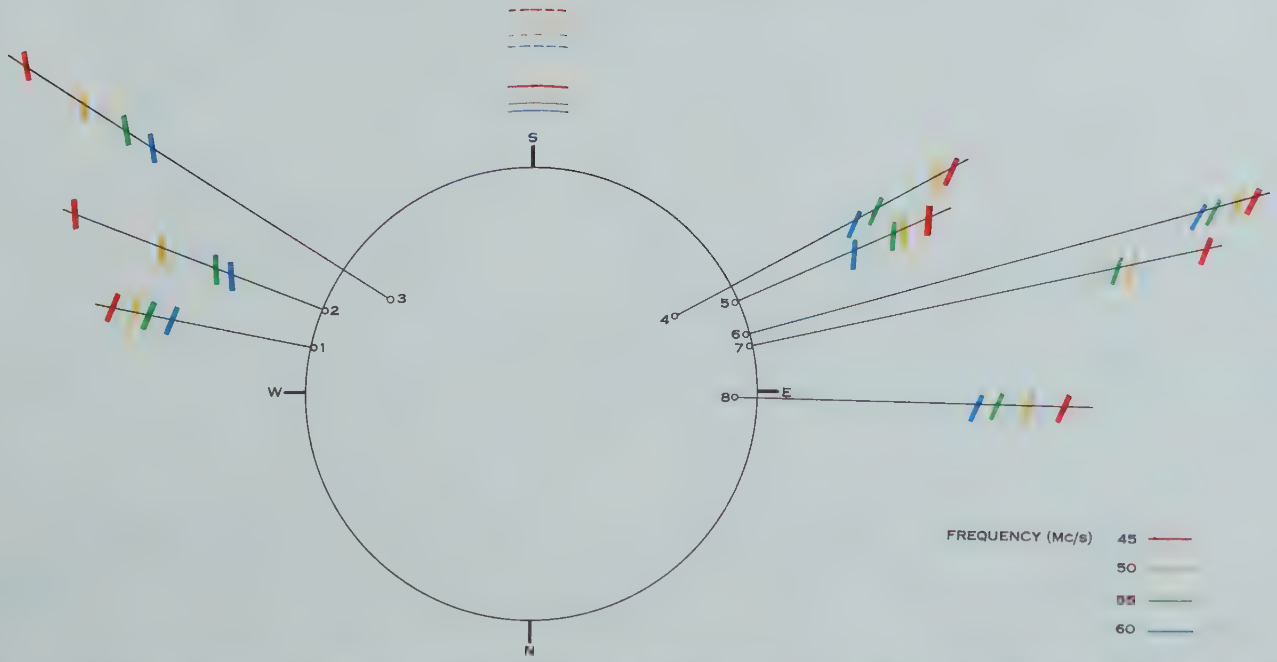

Fig. 7.—The source positions of eight type III bursts (coloured lines) associated with limb flares (optical positions shown as open circles). The lines on which the radio sources are located by the interferometer are shown in part only, viz. that part which is close to the radial line drawn through the optical flare. The circular arcs show the levels of the fundamental (full lines) and second harmonics (dotted lines) of the plasma frequency, assuming the Baumbach-Allen corona.

origin, since refraction would cause a systematic dispersion of positions with frequency. We may therefore conclude that on such occasions ionospheric effects are quite unimportant.

In contrast to this behaviour, records are also obtained in which the position swings wildly from side to side. An example is given in Figure 6 (*b*), where deviations of as much as 20 min of arc are present. The amount of deviation depends on frequency in a remarkably systematic way—the lower the frequency the greater the deviation. This is qualitatively consistent with the effects to be expected from ionospheric refraction. To test this quantitatively, let us attempt to fit the data to a scheme depending on two simplifying assumptions: (1) that all frequencies emitted by the source originated from the same position at any one time as in Figure 6 (*a*), and (2) that the deviations are due to refraction in a slowly varying, " thin " ionospheric wedge. Then it can simply be shown that the angular position coordinate at frequency f is given by

$$\varphi(f)=\varphi(\infty)+kf^{-2},$$

where k is independent of f but varies with the gradient of the refracting wedge. Evidently, $\varphi(\infty)$ is the true position of the source. A plot of $\varphi(f)$ versus f^{-2} at any instant should therefore give a straight line which intersects the $\varphi(f)$ axis at $\varphi(\infty)$. The procedure was applied to Figure 6 (*b*) at time intervals of 5 min. It was found that in most cases a straight line could be drawn through each set of observational points on the plot of $\varphi(f)$ versus f^{-2}. The consequent values of $\varphi(\infty)$ are indicated by the full black line. This may be compared with the dotted black line which shows the position coordinate of the centre of a large sunspot which was almost certainly responsible for the storm. Bearing in mind the obvious oversimplification of the initial assumptions, the relatively small difference between the two black lines strongly suggests that the observed deviations in the radio positions are mainly due to ionospheric refraction.* When such conditions prevail, observations of the positions of individual short-lived solar phenomena may be seriously in error. Such errors are a likely contributory cause of the scatter component in the statistical analysis discussed below in Section IV (*b*) (ii).

IV. POSITION MEASUREMENTS OF TYPE III BURSTS

The observations presented here were made between June and December 1958, and the analysis is based on about 100 groups of type III bursts.

(*a*) *The Variation of Position with Time at a Given Frequency*

Inspection of the unreduced records showed that in the majority of cases the position at any given frequency remained constant to within about ±1 min of arc throughout the lifetime of an individual burst. Also bursts of a group were usually located in the same position (e.g. Fig. 5 (*a*)). Exceptions to this rule sometimes occurred (e.g. Fig. 5 (*b*)) when the position appeared to dart about between two or more fixed positions.

---

* The quasi-periodic nature of the positional variations evident in Figure 6 (*b*) may be of considerable interest in ionospheric studies. The period is about 22 min; in another record taken on July 13, 1958, a similar periodicity was present. This periodicity seems to indicate a very large-scale structure in the irregular ionosphere. Assuming the time variations to be due only to the rotation of the ionosphere through the line joining Sun and observer (i.e. zero " wind " velocity) and also that the refraction occurs at a height of 200 km, we deduce a periodic variation in the irregular ionosphere with scale size about 25 km.

(*b*) *The Variation of Position with Frequency*

In general the position of a type III source showed systematic variations with frequency. This question is critical in testing the validity of the plasma hypothesis, and it is interesting to consider first the most direct test of the hypothesis, i.e. to examine the radio positions of events associated with chromospheric flares situated near the limb.

(i) *Events associated with Limb Flares.*—The identification of flares associated with type III bursts is a procedure which requires considerable caution. Both flares and bursts tend to be numerous on the same days, and the probability of chance coincidences is high. We have therefore counted only those cases in which (1) the burst occurs between the start and maximum of the flare and (2) both burst and flare are so isolated that confusion is extremely unlikely. On this basis eight limb-flare events were recognized.* The optical and radio positions are shown in Figure 7 ; each radio position is presented as a small section of the line on which the centroid of the source is located by the interferometer, viz. the section centred on the radial line through the flare.

In each case the radio positions are seen to lie beyond the optical limb, and the distance from the centre increases systematically with decreasing frequency. Since higher frequencies invariably arrive before lower frequencies in type III bursts, these results strongly support the hypothesis that the different frequencies originate at different levels in the path of a disturbance travelling outwards through the solar corona. If it is assumed that the path of the disturbance is in fact radial and that the relative positions are not distorted by refraction, we can combine the positions of Figure 7 with the corresponding drift rates given by the dynamic spectra to calculate the velocity of the disturbance. Velocities thus calculated are found to lie in the range $\frac{1}{4}c$ to c. These values are considerably greater than those previously inferred from spectral data.

(ii) *Statistical Analysis of Radio Positions.*—The *spread* of position with frequency, clearly evident in Figure 7, is examined in Figure 8 (*a*) using the complete set of radio observations. The purpose of the figure is to investigate statistically how the amount of spread varies with position on the Sun. Thus the abscissa represents the position coordinate at 60 Mc/s and the ordinate the difference between the position at 60 Mc/s and that at 45 Mc/s. Each dot represents an observed burst or homogeneous group of bursts. Roughly, the points are seen to be scattered about a straight slanting line passing through the origin. Hence we shall refer to this diagram in terms of two components—the *linear* and *scatter* components.

---

* The optical data on flares was kindly supplied by Dr. R. G. Giovanelli and Miss M. McCabe of the Division of Physics, C.S.I.R.O., to whom the authors are obliged for much helpful cooperation.

The linear component is shown in Figure 8 (*b*), in which mean values of the ordinates of Figure 8 (*a*) have been plotted for successive narrow ranges of the abscissa. It may be interpreted in terms of the simple model shown in Figure 9, where different frequencies are assumed to originate at different fixed levels in the solar atmosphere. In the idealized case, when refraction is negligible and when the lobes of the interferometer pattern lie normal to the plane of the figure, it is readily seen that the spread $(P_{45}\text{–}P_{60})$ is a linear function of position (P_{60}).

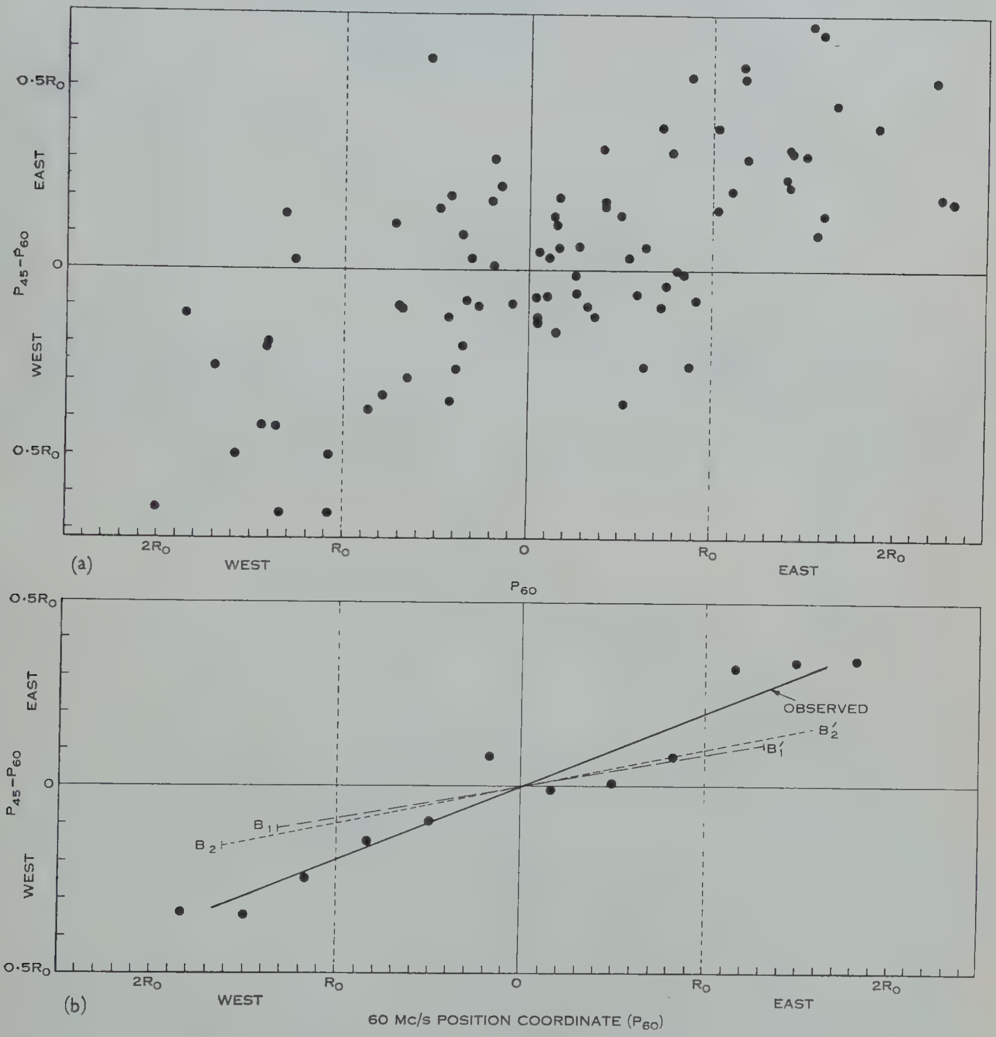

Fig. 8.—Showing the distribution with 60 Mc/s position on the disk of the amount of the " position spread " in type III bursts (as measured by the difference between 45 and 60 Mc/s position coordinates). In (*a*) each burst or group of bursts is shown as a dot. In (*b*) the mean positions in each abscissa-group are shown. The line through the observed points is compared with that predicted by the plasma hypothesis assuming the Baumbach-Allen corona. The predicted lines refer to sources originating at the fundamental plasma frequency (B_1B_1') and at the second harmonic of the plasma frequency (B_2B_2').

Thus the presence of a systematic (linear) component in Figure 8, which contains ten times as many events as Figure 7, provides further evidence that different frequencies originate at different levels. Moreover, the gradient and extent of this line can be used to obtain information on the electron density distribution of the solar corona (see Section V (*b*)).

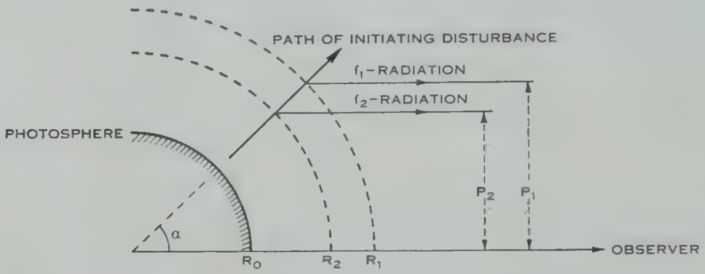

Fig. 9.—Idealized diagram showing the radio emission from a radially ejected type III disturbance.

The scatter component can be due to several causes, e.g. irregular refraction in the terrestrial and solar atmospheres, variations in the heights of emission levels from event to event, variations in the angle between the path of the disturbance and the radial direction, and variations due to different angles between the path of the disturbance and the scanning direction of the interferometer.

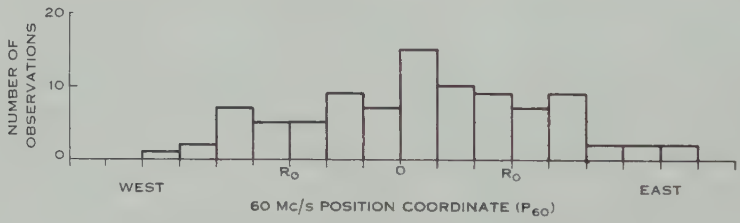

Fig. 10.—Distribution across the disk of 60 Mc/s sources of type III bursts.

The data of Figure 8 may be used to derive the approximate mean radial distances, R_{45} and R_{60}, at which sources of 45 and 60 Mc/s bursts radiate. We first plot the distribution of 60 Mc/s position coordinates (Fig. 10): the distribution is seen to be fairly uniform* between $\pm 1\cdot 66R_0$, where the number of events drops sharply. Hence we infer

$$R_{60} \approx 1\cdot 66R_0.$$

For the separation between the 60 and 45 Mc/s levels, Figure 8 (*b*) gives $R_{45}-R_{60} \approx 0\cdot 34R_0$ (from the value of $P_{45}-P_{60}$ at $P_{60}=1\cdot 66R_0$), whence

$$R_{45} \approx 2\cdot 0R_0.$$

---

* The number of events (56) on the eastern side considerably exceeds that (36) on the western side; while this difference may have arisen because the observing period was too short to be completely representative, it is certainly consistent with an effect of east-west asymmetry noted in the distribution of bursts by Hey, Parsons, and Phillips (1948), Hey and Hughes (1955), and Loughhead, Roberts, and McCabe (1957).

Finally, to investigate the velocity of the inferred travelling disturbances, we calculate the " east-west component of the apparent transverse velocity " of each event. This is given by $(P_{45}-P_{60})/(t_{45}-t_{60})$, where t_{45} and t_{60} denote the times of maximum intensity at frequencies of 45 and 60 Mc/s. Figure 11 shows how this velocity varies from centre to limb, using the 60 Mc/s position coordinate as abscissa. Each point represents the mean of about ten bursts, and the total length of the vertical lines through each point denotes the standard deviation. The velocity is seen to increase from about zero at the centre to about $0\cdot5c$ at the radio limb. Thus, neglecting the possible effects of systematic refraction, we again find evidence for radial-like disturbances with mean outward velocities of about $0\cdot5c$.

Discussion of velocities will be continued in Section VI.

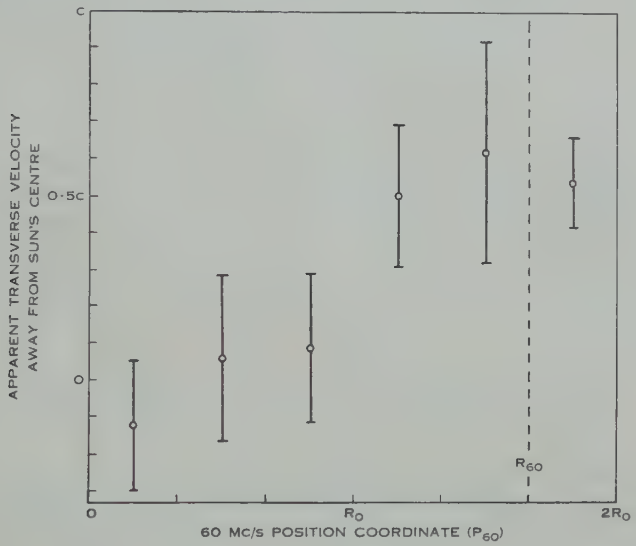

Fig. 11.—The variation with 60 Mc/s position on the disk of the transverse component of the apparent outward velocity of type III disturbances. Each point represents the mean of about ten values of independent events, and total lengths of the vertical lines signify the standard deviations.

V. Implications of the Plasma Hypothesis

The evidence given above that the height of origin of type III bursts increases with decreasing frequency strongly favours the widely accepted hypothesis that the frequency emitted from a given level in the corona is either the fundamental plasma frequency or its second harmonic. We now explore some of the consequences of applying this hypothesis to the present observations.

(*a*) *The Escape of Fundamental and Second Harmonic Frequencies*

If the solar atmosphere is assumed to be smooth and spherically symmetrical with its electron density decreasing monotonically outwards, then the fundamental plasma frequency can escape from its level of origin only along a radial path (see Jaeger and Westfold 1950; Wild, Murray, and Rowe 1954). The second harmonic, on the other hand, is free to escape through a wide cone of angles around the radial direction. One might predict, therefore, that those type III bursts which contain *both* harmonics should be found only near the centre of the disk, and that events recorded elsewhere should be purely second harmonic.

To investigate this prediction we have plotted (Fig. 12) the distribution across the Sun of the percentage of events showing both harmonics. While the number of these events is small (20), there seems to be a definite indication of a gradual rise from centre to limb and possibly a more sudden decline beyond the limb. In the majority of these cases the fundamental was more intense than the harmonic. Thus it is found that the fundamental can escape from the whole radio disk, whence the prediction of the simple theory is directly contradicted.

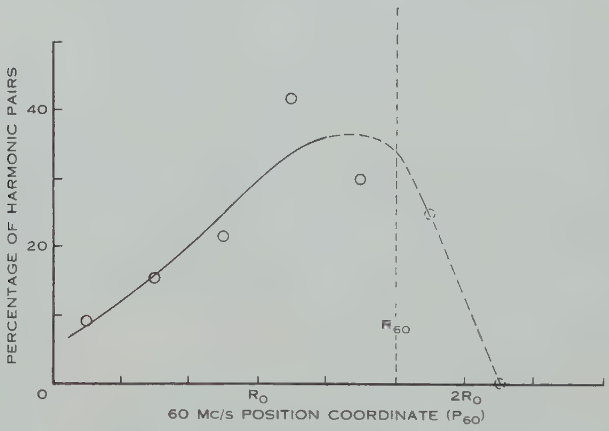

Fig. 12.—Distribution with 60 Mc/s position on the disk of the percentage of type III bursts which show recognizable harmonics.

The form of the distribution of Figure 12 could arise in the following way. The small number of recognizable harmonic pairs near the centre is caused by the second harmonic being usually swamped by the fundamental. The swamping effect gradually decreases with distance from the centre, so causing a gradual increase in the number of recognizable pairs. On the other hand the apparent absence of pairs beyond the normal radio limb could be due to the *absence* of a fundamental in events taking place very close to and actually round the limb. This interpretation is consistent with evidence given by Roberts (1959) for type II bursts which are believed to originate at the same levels as the type III bursts. In the present discussion we shall assume that, across the " normal " radio disk, the fundamental frequency dominates the second harmonic to the extent that the latter can be neglected. This assumption applies to the low frequencies in question, and is certainly not valid at high frequencies (e.g. $\gtrsim$150 Mc/s).

The escape of the fundamental plasma frequency through a wide cone of angles becomes possible if the solar atmosphere is pervaded by small-scale irregularities (see Roberts 1959). Indeed, the existence of such irregularities seems essential to the survival of the plasma hypothesis.

The path followed by a ray escaping outwards from the plasma level through an irregular but quasi-spherical atmosphere requires detailed consideration beyond the scope of the present paper. We may merely surmise that near its start the path meanders through the highly refracting irregularities in all directions, while on the average the direction of escape is radial, i.e. the mean path is deviated *away* from the centre of the disk. Subsequently we should expect the path to curve *inwards* owing to the effects of spherical refraction (Jaeger and Westfold 1950). As pointed out by Shain and Higgins (1959), these two opposing effects are likely to be comparable in magnitude. For the purposes of the present discussion, therefore, it seems reasonable to make the simplifying assumption that the measurement of the position of sources located at the plasma level is unaffected by refraction in the solar atmosphere. In this connexion it is noteworthy that there is evidence for no refraction for other types of emission, believed to be broad-band emission from a fixed source (see Fig. 6 (*a*) and Wild, Sheridan, and Trent 1959).

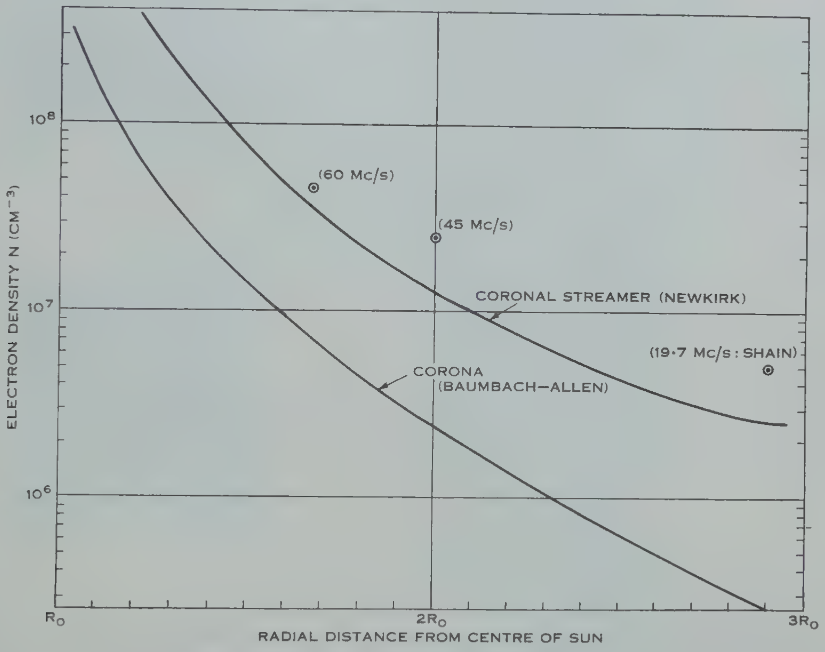

Fig. 13.—Electron densities in the solar corona as a function of radial distance from the centre of the Sun. The lower curve is the standard Baumbach-Allen model; the upper curve is that given by Newkirk for the corona above an average active centre (1956–1958). The experimental points refer to the active regions in which type III sources are generated, the latter being supposed to originate at the fundamental plasma level. The 45 and 60 Mc/s points emerge from the present analysis, while the 19·7 Mc/s point is due to Shain and Higgins (1959).

(b) *The Radial Distribution of Electron Density*

The heights of several plasma levels in the " normal " corona, as represented by the Baumbach-Allen model, are shown as coloured arcs (full lines) at the top of Figure 7. These levels are seen to be considerably lower and closer together than those actually observed. The same conclusion emerges from Figure 8 (*b*), where the linear component calculated from the Baumbach-Allen model (B_1B_1') is seen to be less steep and less extended than the observed line. Thus, if the assumptions discussed in (*a*) are substantially correct, type III bursts must originate in locally dense regions of the corona.

Identifying the mean radial distances R_{45} and R_{60} (see Section IV) with those of the 45 and 60 Mc/s plasma levels in type III source regions, we obtain the values of electron density plotted in Figure 13. In the same figure is given a third point (19·7 Mc/s) obtained by Shain and Higgins (1959) during a similar part of the current solar cycle, using a somewhat similar method. These points are shown in relation to the " normal " (Baumbach-Allen) coronal model and a model coronal streamer given by Newkirk (personal communication). The latter is based on many observations during the years 1956–1958 made with the white-light coronameter of the High Altitude Observatory, Boulder, Colorado. It is in close agreement with a detailed study of three streamers made by Schmidt (1953).

The radio values are seen to be an order of magnitude greater than the normal coronal densities. On the other hand they are similar to, though slightly greater than, those of the model streamer. This result suggests that type III disturbances may actually travel out along coronal streamers.

VI. The Distribution of Velocities

The results of Section IV led to the conclusion that the mean velocity of type III disturbances is of the order of $0 \cdot 5c$. The methods used were direct, but the conclusion depended to a great extent on the relatively small number of events which occurred near the limb. We now attempt to evaluate, necessarily by less direct means, the approximate radial velocity of each event, and hence arrive at a distribution of velocities.

For this purpose we shall assume that at a given frequency, f Mc/s, all bursts originate at the same radial distance, R_f, as in Figure 9. Using the values of R_{45} and R_{60} previously determined, the approximate radial component of velocity of a disturbance can be determined by

$$v=(R_{45}-R_{60})/(t_{45}-t_{60}).$$

When $v\sim c$, however, appreciable corrections are required to take account of the finite difference in the times taken by the two frequencies to propagate from their point of origin to the observer. The time delay then depends on the heliocentric angle α between the path of the disturbance and the Sun-Earth line (Fig. 9), and is given by

$$t_{45}-t_{60}=\left(\frac{1}{v}-\frac{1}{c}\cos\alpha\right)(R_{45}-R_{60})+\tau(\alpha),$$

SPEED OF TYPE III SOLAR RADIO DISTURBANCES

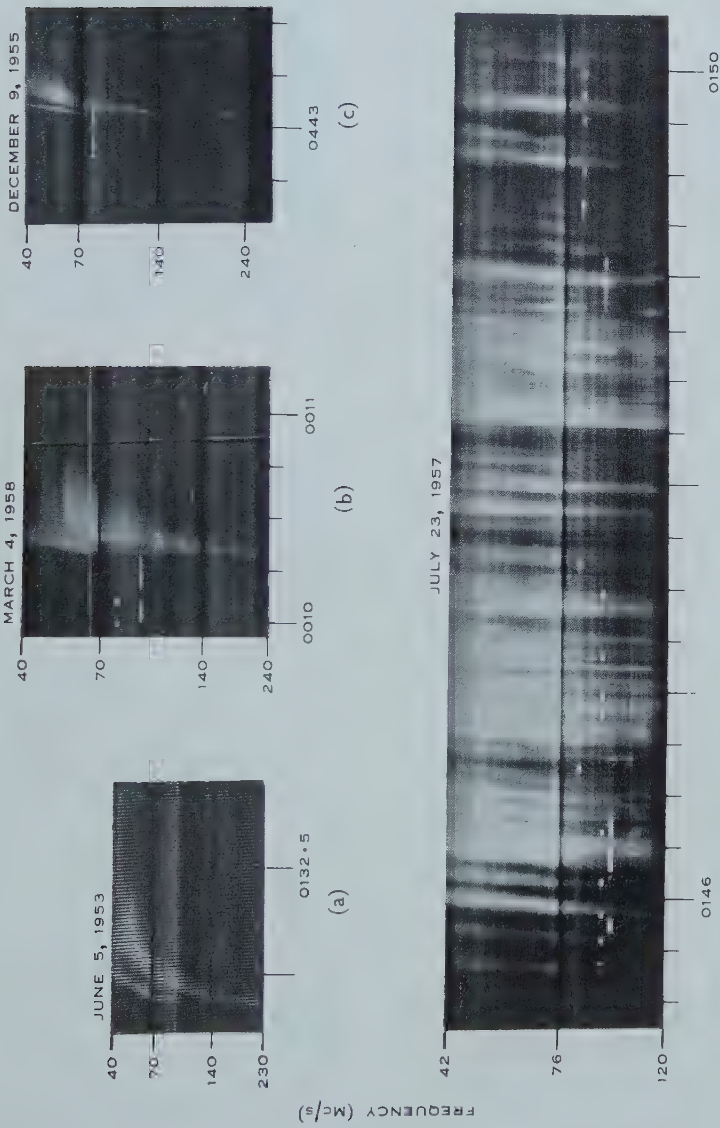

Examples of dynamic spectra of type III bursts. (*a*), (*b*), and (*c*) show individual bursts in which first and second harmonics can be recognized; (*d*) shows a typical large group of bursts. Scale of time: 4 divisions per min.

SPEED OF TYPE III SOLAR RADIO DISTURBANCES

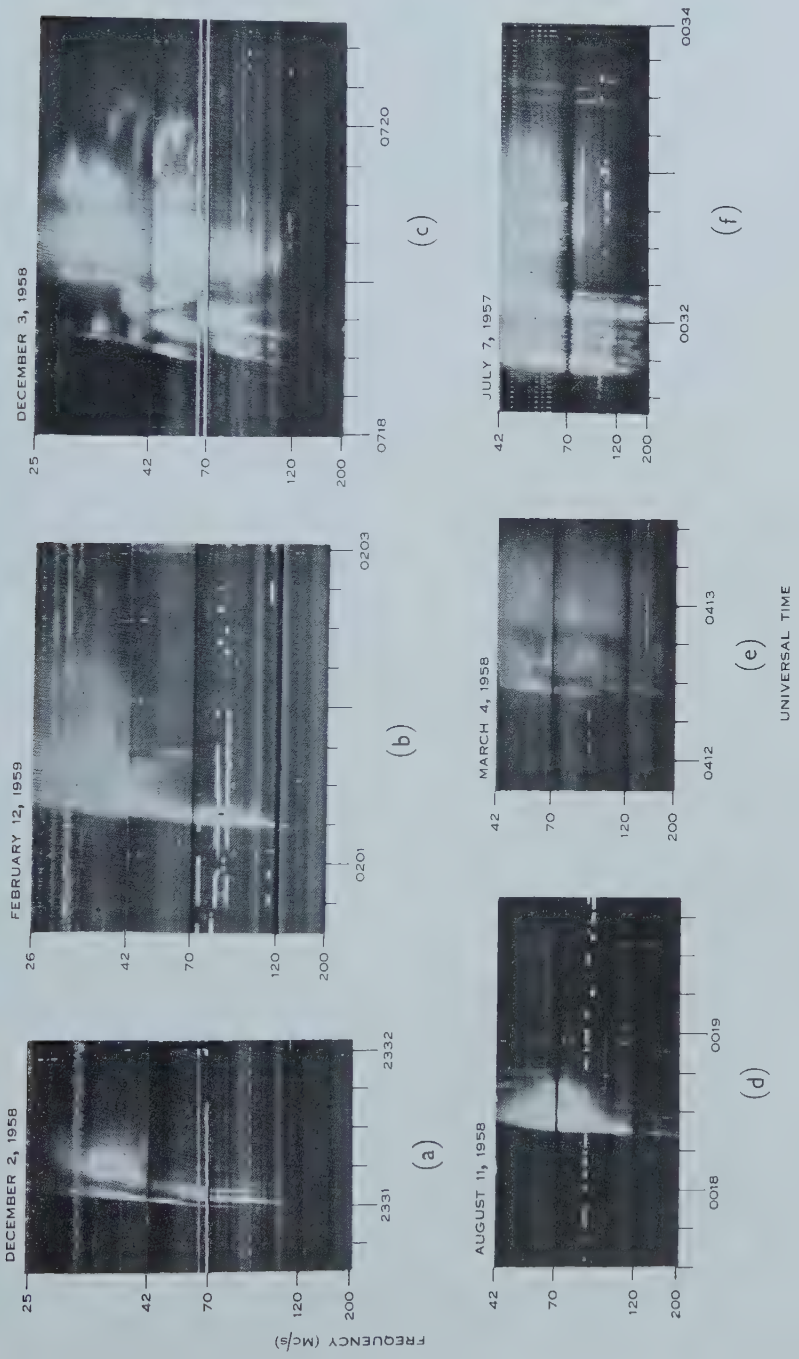

Examples of type III bursts which are followed by pronounced type V emission.

in which the first term on the right-hand side is obtained from simple geometric considerations on the assumption that the velocity of propagation is exactly c, and the second term $\tau(\alpha)$ is the correction required to allow for departures from this assumption. The correction $\tau(\alpha)$ can become appreciable when the path of propagation passes through regions whose refractive index departs significantly from unity (e.g. when the plasma hypothesis applies). Its evaluation is difficult and depends on the model atmosphere assumed. For the present purpose we calculate $\tau(\alpha)$ assuming that the propagation of each frequency can be regarded as rectilinear propagation through a spherically symmetrical atmosphere whose radial distribution of electron density is considerably greater than normal, viz. that given by the upper curve in Figure 14. Details of the calculation of $\tau(\alpha)$ are given in Appendix I, where an approximate analytical method is developed for treating the case of rectilinear propagation in any spherically symmetrical atmosphere. The adopted function $\tau(\alpha)$ is shown in Figure 16 in Appendix I.

For comparison with experimental data, we make use of the approximation*

$$P_{60} \approx R_{60} \sin \alpha,$$

and use the previous equation to plot values of $t_{45}-t_{60}$ as a function of P_{60} for various values of c (Fig. 14). Also to illustrate the effect of the badly known correction $\tau(\alpha)$, a curve corresponding to $v=c$ is given when $\tau(\alpha)$ is set equal to zero (dashed line).

On the same graph, each observed burst is represented as a closed or open circle. The latter refer to type III bursts which are confused by the presence of another form of emission (spectral type V) discussed subsequently.

While the observational points are widely scattered, the great majority lie between $P_{60}=0$ and $P_{60}=R_{60}$. The few points which lie outside this range are mainly subject to confusion by type V emission. We shall, of necessity, ignore these wayward points. In the main body of the diagram ($P_{60} \leqslant R_{60}$), there appears to be a significant upward sweep of points in the sense that both the mean and the minimum value of $t_{45}-t_{60}$ appear to increase with t_{60}. The same trend is present in the derived curves of constant velocity.

In this graph the abscissae of observational points are subject to errors of various kinds, e.g. the effects of refraction, non-radial paths, and limitations due to one-dimensional scanning. Inspection of the figure shows, however, that, except very near the limb, the determination of velocity is fairly insensitive to errors in the abscissae.

Figure 15 (full line) shows the distribution of the radial component of velocities derived directly from Figure 14. All points in the range $P_{60} \leqslant R_{60}$ were used, except two in which the derived velocity exceeded c. Owing to the uncertainty of the function $\tau(\alpha)$, a second distribution (dotted line) was evaluated setting $\tau(\alpha)=0$. The difference in the two distributions is slight except near the high velocity tail; this result means that the derived distribution does not critically depend on whether the radiation is supposed to originate at the fundamental plasma level or not.

---

* This is strictly true only when the path of the disturbance lies in the same plane as the axis of the interferometer; it is approximately true for all radial disturbances originating at low heliographic latitudes.

The distribution shows a mean velocity of 0·45*c*. A striking feature is the abrupt low velocity cut-off at about 0·2*c*. The maximum velocity, whose determination is more hazardous, appears to lie within about 25 per cent. of the velocity of light.

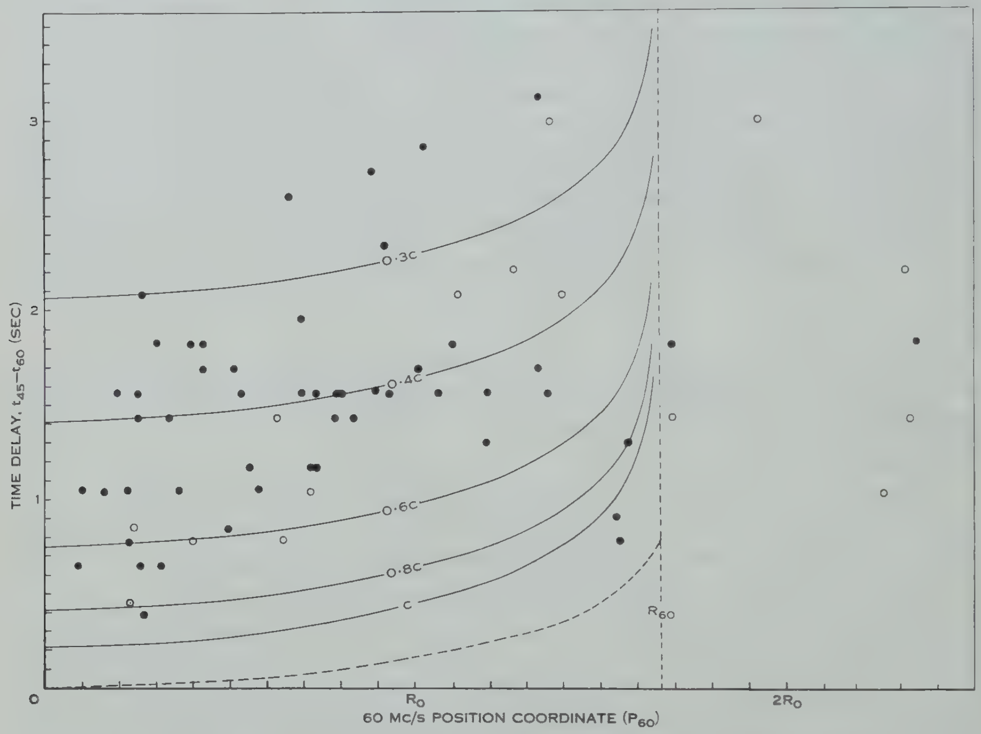

Fig. 14.—The distribution with 60 Mc/s position on the disk of the time interval between times of maximum intensity at 60 and 45 Mc/s for observed type III bursts. Each circle (full or open) represents an independent event. The curves show lines of constant velocity for type III disturbances, in terms of the velocity of light, *c*. These curves depend on assumptions described in the text. Those type III bursts which are followed by substantial type V emission are distinguished by open (as opposed to full) circles.

VII. Bursts of Spectral Type V

An important clue to the nature of type III disturbances is provided by a feature only briefly mentioned so far, namely, that certain type III bursts are followed by the broad-band diffuse afterglow known as the type V burst (Wild, Sheridan, and Trent 1959). The nature and origin of this emission will therefore be discussed before the origin of type III bursts is considered.

(*a*) *Description*

The type V burst may be defined as broad-band continuum radiation lasting for as long as 1 minute or more after a type III burst ; appreciable type V emission occurs with perhaps 1 in every 3 or 4 groups of type III bursts. Examples of type V spectra are given in Plate 2. In some cases the emission appears merely as a diffuse prolongation of the type III burst, in others as a detached blob or patchiness. The bursts radiate most strongly at frequencies below about 150 Mc/s, and sometimes the high frequency boundary has the form of a relatively sharp cut-off. The bandwidth is a substantial fraction of the mid frequency. Intensities as high as 10^{-18} W m^{-2} $(c/s)^{-1}$ are sometimes observed. No evidence of harmonic structure has been noted, and the spectra show no characteristics which suggest an origin in plasma oscillations. It is suggested that the type V emission is much more likely to be synchrotron radiation from relativistic electrons spiralling in the local magnetic field. A similar suggestion has been made by Boischot and Denisse (1957) to explain the type IV emissions which are also of broad bandwidth, but which follow type II bursts and persist for periods of hours.

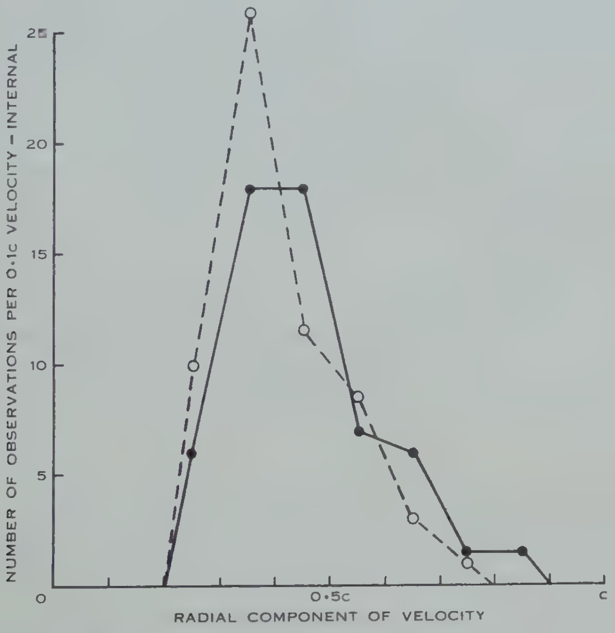

Fig. 15.—Distribution of velocities (radial component) of type III disturbances. The full line is derived directly from Figure 14; the dotted line shows the effect of neglecting the correction term $\tau(\alpha)$.

(*b*) *The Synchrotron Hypothesis*

To test the feasibility of the synchrotron hypothesis, we note that synchrotron radiation from an electron of energy E (MeV) spiralling with an angle of pitch Θ in a magnetic field of flux density B (gauss) shows a maximum in its spectrum at the frequency f_c, given by

$$f_c = 16BE^2 \sin\Theta \quad (\text{Mc/s}),$$

and that above this frequency the energy falls off rapidly. Hence, for $f_c = 100$ Mc/s, $BE^2 \approx 6$. Taking $1 \cdot 5$ G as a reasonable upper limit to the coronal magnetic field, and $\sin\Theta \sim 1$, we find that electron energies of at least 2 MeV are required.

The total power radiated by each electron is approximately $6\times10^{-22}B^2E^2\sin^2\Theta$ watts, and, assuming this power to be radiated in an effective bandwidth of $\frac{1}{2}f_c$, it can be calculated that the maximum flux density at the Earth due to each electron is

$$S=2\cdot7\times10^{-52}B\,\overline{\sin\Theta}\ \ \mathrm{W\,m^{-2}\,(c/s)^{-1}}.$$

Hence, neglecting self-absorption, the total number of electrons required to generate a flux density of 10^{-18} W m^{-2} (c/s)$^{-1}$ is

$$n=\frac{3\cdot7\times10^{33}}{B\,\overline{\sin\Theta}}$$
$$\gtrsim3\times10^{33},$$

since it may be assumed that $B\,\overline{\sin\Theta}\lesssim1\cdot2$. In the presence of self-absorption, rough thermodynamic arguments indicate that for electron energies of a few million electron-volts the radiating area of the source must be an appreciable fraction of the Sun's disk to yield the observed intensity ; this is supported by a preliminary source size measurement made at Dapto, where a value of 14 min of arc was obtained. We may therefore reasonably assume a radiating volume with linear dimensions of $\sim5\times10^5$ km, i.e. a volume of $\sim10^{32}$ cm^3. It follows that the required density of energetic electrons need be no greater than 30 cm^{-3}. A comparable figure (100 cm^{-3}) was deduced by Boischot and Denisse in their explanation of type IV bursts.

This brief discussion of type V bursts should be regarded as tentative in its quantitative aspects, since a detailed analysis of the observational material is required. In its support we may also mention a preliminary finding that the bursts are often polarized and that there are sometimes indications of linear polarization.

A number of the type III bursts used in the present analysis were accompanied by type V bursts. As previously mentioned, these are distinguished in Figure 14 by the open circles. While the number of cases shown is small, there appears to be a relatively higher probability for type V events to occur well away from the centre of the disk. This may imply that the magnetic fields tend to be radial, since synchrotron emission is beamed normal to the direction of the field. We may also note that events can occur far beyond the radio limb when synchrotron radiation is responsible for the emission.

VIII. On the Physical Nature of Type III Disturbances

Our interpretation of type V bursts requires the temporary existence high in the corona of a cloud of spiralling electrons with energy in excess of 2 MeV, i.e. with velocities within a few per cent. of the velocity of light. The minimum height at which radiation of a given frequency can escape is the corresponding plasma level. Thus, for example, the 45 Mc/s radiation in type V bursts would, according to our previous figures, originate at a radial distance of not less than $2R_0$. Now, it is known that many type V bursts, like the type III bursts that precede them, correlate very closely with the onset of chromospheric flares and sub-flares. We may therefore reasonably presume that the supply of fast electrons originates low in the solar atmosphere and that they are transported with great rapidity to the heights whence the synchrotron radiation is emitted. Since the velocities of type III disturbances are found to be comparable with the velocity of light, it is extremely tempting to associate this act of transportation of the type V electrons with the type III disturbance. The fact that the majority of the type III disturbances are rather slower than the speed of million-volt electrons would be expected if the electrons travel along lines of magnetic force in a spiral path. Such electrons would travel through the corona practically unimpeded by collisions. We suggest specifically, therefore, that the disturbance responsible for initiating the plasma radiation in type III bursts is associated with a corpuscular stream ejected at the beginning of a flare and containing, in some cases at least, more than 3×10^{33} electrons with energy greater than 2 MeV. In some cases the electrons, following the magnetic field configuration, are returned to the Sun, giving rise to the variety of type III spectrum described by Maxwell and Swarup (1958) as the " inverted U " (see example in Plate 2 (*c*)). In other, more frequent, cases the electrons are guided out into interplanetary space, yielding the " normal " type III spectrum. It seems an attractive possibility that such electrons may be responsible for the corpuscular radiation round the Earth which has recently been observed with satellites (see, for instance, Van Allen 1959).

A possible objection to the theory is that the electron stream would pass too rapidly into the Sun or out of the solar atmosphere to explain the relatively long duration (~1 min) of the type V burst. It may therefore be necessary to postulate the existence of magnetic irregularities capable of trapping the type V electrons in the outer corona. Such irregularities would also ensure a supply of electrons with high pitch angles capable of generating synchrotron radiation near optimum power.

IX. Acknowledgments

Of the many members of the staff of the Radiophysics Laboratory who have contributed to the substance and preparation of this paper, the authors wish to thank particularly Mr. G. H. Trent, Mr. J. Joisce, and Mr. P. J. Collins for valuable assistance in assembling the equipment and in taking observations, Mrs. Marjorie Gorzkos for performing a large quantity of painstaking analysis, and Mr. K. R. McAlister and Mr. K. W. Anderson for the mechanical design of the computor and aerials. The authors also wish to thank Mr. C. A. Shain and Mr. D. J. McLean for helpful discussion and checking of the manuscript, and Dr. J. L. Pawsey for his interest in this work.

X. References

Boischot, A., and Denisse, J. F. (1957).—*C.R. Acad. Sci., Paris* **245** : 2194.
Giovanelli, R. G. (1958).—*Aust. J. Phys.* **11** : 350.
Hey, J. S., and Hughes, V. A. (1955).—*Mon. Not. R. Astr. Soc.* **115** : 605.
Hey, J. S., Parsons, S. J., and Phillips, J. W. (1948).—*Mon. Not. R. Astr. Soc.* **108** : 354.
Jaeger, J. C., and Westfold, K. C. (1950).—*Aust. J. Sci. Res.* A **3** : 376.
Komesaroff, M. (1958).—*Aust. J. Phys.* **11** : 201.
Loughhead, R. E., Roberts, J. A., and McCabe, Marie K. (1957).—*Aust. J. Phys.* **10** : 483.
Maxwell, A., and Swarup, G. (1958).—*Nature* **181** : 36.
Roberts, J. A. (1959).—*Aust. J. Phys.* **12** : 327.

Schmidt, M. (1953).—*Bull. Astr. Insts. Netherlds.* **12**: 61.
Shain, C. A., and Higgins, C. S. (1959).—*Aust. J. Phys.* **12**: 357.
Van Allen, J. A. (1959).—*Nature* **183**: 430.
Wild, J. P. (1950).—*Aust. J. Sci. Res.* A **3**: 541.
Wild, J. P., and McCready, L. L. (1950).—*Aust. J. Sci. Res.* A **3**: 387.
Wild, J. P., Murray, J. D., and Rowe, W. C. (1954).—*Aust. J. Phys.* **7**: 439.
Wild, J. P., Roberts, J. A., and Murray, J. D. (1954).—*Nature* **173**: 532.
Wild, J. P., and Sheridan, K. V. (1958).—*Proc. Inst. Radio Engrs., N.Y.* **46**: 160.
Wild, J. P., Sheridan, K. V., and Trent, G. H. (1959).—I.A.U.-U.R.S.I. Symposium on Radio Astronomy, Paris 1958. p. 176. (Stanford Univ. Press.)

Appendix I

Evaluation of the Excess of Time, t, *taken by a Radio-frequency Signal to escape along a Straight Path from its Plasma Level in a Spherically Symmetrical Ionized Atmosphere over that taken by Radiation travelling along the Same Path with the Velocity of Light*

It is well known that the radial distribution of electron density, $N(r)$, in the solar corona can be simulated by an exponential function over a moderate range of r. Therefore, let the distribution be written in the form

$$N(r)=N_0 e^{-\beta(r)r}, \qquad \ldots\ldots\ldots\ldots\ldots\ldots (1)$$

where in cases of interest $\beta(r)$ is a relatively slowly varying function.

Let the point of origin of the disturbance be specified in polar coordinates (R,α), with the pole at the centre of symmetry and $\alpha=0$ directed along the path of escape (see Fig. 9). Take rectangular coordinates (x,y) through the centre, such that the x coordinate is directed along $\alpha=0$; then the path of the disturbance is given by

$$y=R\sin\alpha,$$

and

$$x^2=r^2-R^2\sin^2\alpha \quad (R\cos\alpha\leqslant x\leqslant\infty). \qquad \ldots\ldots (2)$$

The excess time is given by the integral

$$t=\frac{1}{c}\int_{R\cos\alpha}^{\infty}\left(\frac{1}{\mu}-1\right)\mathrm{d}x, \qquad \ldots\ldots\ldots\ldots (3)$$

where c is the velocity of light and the refractive index μ is given in terms of the plasma frequency

$$f_p=e(N/\pi m)^{\frac{1}{2}} \qquad \ldots\ldots\ldots\ldots\ldots\ldots (4)$$

(where e and m denote the electronic charge and mass), by

$$\mu^2=1-f_p^2(r)/f^2. \qquad \ldots\ldots\ldots\ldots\ldots\ldots (5)$$

In the present treatment we shall restrict ourselves to the case when the frequency is equal to the plasma frequency at $r=R$, namely,

$$f=f_p(R), \qquad \ldots\ldots\ldots\ldots\ldots\ldots (6)$$

but the treatment is capable of generalization to all frequencies. Combining equations (1), (2), (4), (5), and (6), we obtain the expression

$$x^2 = -R^2 \sin^2 \alpha + \{\beta(r)\}^{-2}\{\beta(R)R - \log(1-\mu^2)\}^2. \qquad \ldots\ldots \quad (7)$$

In using equation (7) to evaluate the integral (3), we shall assume that contributions towards the excess time come predominantly from a small range of r immediately above R, where the refractive index is small. This assumption is suggested by the computations of Jaeger and Westfold, and can be justified *a posteriori*. Hence, since $\beta(r)$ is a slowly varying function, we write $\beta(r) = \beta(R) \equiv \beta$, and equation (7) simplifies to

$$x^2 = -R^2 \sin^2 \alpha + \{R - \beta^{-1} \log(1-\mu^2)\}^2. \qquad \ldots\ldots\ldots \quad (8)$$

The central path.—Consider first the special case when the path of escape is along the x-axis ($\alpha = 0$). Equations (3) and (8) then give

$$t = \frac{2}{\beta c}\int_0^1 \frac{d\mu}{1+\mu} = \frac{2 \log 2}{c\beta}. \qquad \ldots\ldots\ldots\ldots\ldots \quad (9)$$

In practice the value of β is conveniently measured directly as a gradient in a plot of $\log N$ versus r. As an example, for the Allen-Baumbach model of the solar corona with $f = 60$ Mc/s, we find $\beta(R) = 5 \cdot 9 R_0$, giving $t = 0 \cdot 235 R_0/c = 0 \cdot 55$ sec. This value is some 15 per cent. lower than that computed by numerical integration by Jaeger and Westfold. However, the calculated *differential* time excess $t_{60} - t_{100}$ for the escape of 60 and 100 Mc/s signals from their respective plasma levels is found to agree with Jaeger and Westfold's value (approx. $0 \cdot 08$ sec) to within about 3 per cent. This example confirms what we might have expected intuitively—that the approximate method is more reliable for the calculation of differential values of time excesses as compared with absolute values.

General case.—For the general case ($0 \leqslant \alpha \leqslant \frac{1}{2}\pi$), we write (8) in the form

$$x^2 = R^2 \cos^2 \alpha - 2R\beta^{-1} \log(1-\mu^2)[1 - (2R\beta)^{-1} \log(1-\mu^2)].$$

In the solar atmosphere $2R\beta \sim 15$, and μ is small in the region of interest. Hence we neglect the last term in the square brackets and obtain*

$$t \approx \frac{2R}{\beta c}\int_0^1 \{R^2 \cos^2 \alpha - 2R\beta^{-1} \log(1-\mu^2)\}^{-\frac{1}{2}}(1+\mu)^{-1} d\mu$$

$$\approx \frac{2R}{\beta c}\int_0^1 \{R^2 \cos^2 \alpha + 2R\beta^{-1}\mu^2\}^{-\frac{1}{2}}(1+\mu)^{-1} d\mu,$$

since $\log(1-\mu^2) \approx -\mu^2$ in the region of interest. This may be integrated using a substitution of the form $S = 1+\mu$, and we obtain

$$t \approx 2(R/c)(2\beta R + \beta^2 R^2 \cos^2 \alpha)^{-\frac{1}{2}} \log\{(1 + 2(\beta R)^{-1} \sec^2 \alpha)^{\frac{1}{2}} + 1\}. \qquad \ldots \quad (10)$$

---

* The fact that the neglected term exceeds $(2R\beta)^{-1}$ for values of $\mu > 0 \cdot 8$, and indeed becomes infinite as $\mu \rightarrow 1$, suggests that the upper limit of the integral should not be taken beyond about $0 \cdot 8$. However, it is found that doing so would scarcely affect the final value of t. This emphasizes the dominant role of the region of small μ values.

For the values used in this paper, the excess time delays computed from equation (**10**) for the central ray agreed with those computed directly from equation (**9**) to within about 5 per cent.

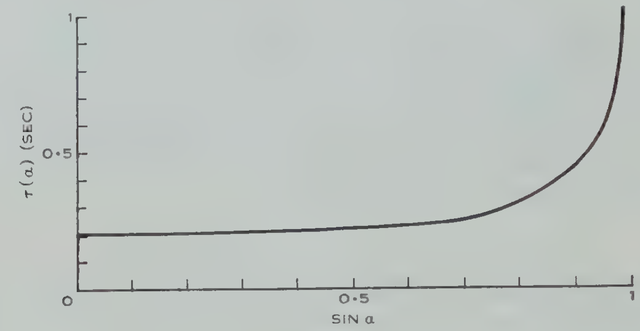

Fig. 16.

Application to particular case.—For the purposes of Section IV, we wish to evaluate the quantity

$$\tau(\alpha)=t(\beta_{45})-t(\beta_{60}), \quad \ldots\ldots\ldots\ldots\ldots\ldots \quad (\mathbf{11})$$

where β_{45} and β_{60} refer to the values of β at the 45 and 60 Mc/s plasma levels of the atmosphere whose radial distribution is given by the upper curve of Figure 13. It is found graphically that $\beta_1=3\cdot36/R_0$ and $\beta_2=4\cdot56/R_0$, and the corresponding values of R, as used in Section IV, are $R_{45}=2\cdot0R_0$ and $R_{60}=1\cdot66R_0$. Substituting in equations (**10**) and (**11**), we obtain the function $\tau(\alpha)$ shown in Figure 16.

AN ASSOCIATION BETWEEN SOLAR RADIO BURSTS AT METRE AND CENTIMETRE WAVELENGTHS

By A. A. Neylan*

[*Manuscript received August* 3, 1959]

Summary

From a study of simultaneous metre and centimetre solar radio bursts, it appears that the type III events which coincide with centimetre bursts are frequently followed by a particular form of broad-band emission. This last burst, termed type V, is observed mainly below 150 Mc/s on radio spectrum records where it resembles a bright glow lasting for about 1 min. Synchrotron radiation has been suggested as the mechanism for type V bursts.

The accompanied centimetre burst lasts a length of time comparable with that of the metre bursts, is indistinguishable in intensity from unaccompanied centimetre bursts, and, on present evidence, may be due to either thermal or synchrotron radiation.

A stream of highly energetic particles ejected from a flare region on the Sun is suggested as the cause of both events, exciting centimetre bursts in or near the chromosphere and type V bursts at large heights in the corona.

I. Introduction

It is well known that certain disturbances on the Sun generate radio emission over a very large range of frequencies, from wavelengths of a few millimetres up to tens of metres. The major radio outbursts are associated with large flares, and are to be observed on both short and long wavelengths, lasting for tens of minutes or more. Besides these, many smaller radio disturbances are known to occur in both wavelength bands.

The great majority of the smaller sporadic disturbances at metre wavelengths are known to belong to a definite spectral class, namely, type III (Wild, Roberts, and Murray 1954). The single type III burst is a brief disturbance lasting some 5 or 10 sec and drifting with time from high to low frequencies at the rate of some 20 Mc/s per sec. In general, groups of type III bursts are much more frequent than centimetre bursts.

The purpose of the present investigation is to find out if there is any connexion between type III bursts at metre wavelengths and the " lesser " disturbances at centimetre wavelengths: and if so, to search for features in the type III burst which distinguish those which are from those which are not accompanied by centimetre bursts.

In the present analysis, which covers the period July 1957 to March 1958, records from the Radiophysics Laboratory spectrograph at Dapto (40–240 Mc/s) were studied in conjunction with single-frequency data (1000, 2000, 3750, and 9400 Mc/s) from the Research Institute of Atmospherics, Nagoya. The

---

* Division of Radiophysics, C.S.I.R.O., University Grounds, Chippendale, N.S.W.; present address: Mount Stromlo Observatory, Canberra.

sensitivity of the Dapto equipment is such that bursts of flux density less than about 50×10^{-22} W m^{-2} (c/s)$^{-1}$ in one plane of polarization are not recorded. The equipment used at Nagoya has been described by Tanaka and Kakinuma (1956, 1958). For 1000, 2000, and 3750 Mc/s the threshold of detectability is 10×10^{-22} W m^{-2} (c/s)$^{-1}$ and for 9400 Mc/s it is 20×10^{-22} W m^{-2} (c/s)$^{-1}$.

II. Observations and Analysis

A perusal of the records showed metre bursts to be far more frequent than centimetre bursts, so that the majority of metre bursts occur unaccompanied by short wavelength emission. Of some 2000 type III events less than 10 per cent. occurred while a centimetre burst was in progress. On the other hand, there are a number of centimetre bursts of comparable intensity which are unaccompanied by metre bursts.

(a) *Recognition of a New Feature—the Type V Burst*

On examining the spectrum records of those type III's accompanied by centimetre disturbances, it was noted that a particular feature tended to repeat itself. The burst normally began with a type III burst which was followed immediately or almost immediately by a second disturbance. The latter was a broad band enhancement of radio emission extending over a frequency range of 100 Mc/s or so and lasting for up to about 1 min. Three examples of this " continuum " radiation, which has been designated a type V burst (Wild, Sheridan, and Trent 1959), are given in Plate 1. In some cases the type V merges with the type III, whereas in others the two are detached, but in no case is there clear evidence of frequency drift in the type V event. On the high frequency side, the burst often shows a steep downward gradient in the energy spectrum, which occurs on the average at about 100 Mc/s.

(b) *Association of Type V with Centimetre Bursts*

To test the correlation of type III plus type V events with high frequency bursts, two groups of events were chosen.

Group A consisted of 27 clear and distinct cases of type III events followed by type V, which occurred during the period July 1957 to March 1958. The examples in Plate 1 are from this group. Of the group A events, 20 out of 27 occurred nearly simultaneously with bursts at centimetre wavelengths. Except in two cases where the centimetre disturbance lasted much longer than the metre burst, the durations of corresponding centimetre and metre bursts were similar.

Group B consisted of 26 spectrograph events selected at random from the same 9-month period, July 1957 to March 1958. The basis of selection was that the events be sharply defined type III bursts which were not accompanied or followed by continuum at metre wavelengths (see Plate 2). These events were used as a control group. Of the 26 events, it was found that only one burst occurred at the time of a centimetre burst.

While the number of events in groups A and B is not large, it seems sufficient to suggest strongly that the probability of a type III burst being accompanied by a centimetre burst is considerably increased by the type III being followed by a type V continuum.

(c) *Association of Type V Bursts with Flares*

Covington and Harvey (1958) have reported that "there is a strong probability, almost a certainty, that every 10 cm burst is associated with some flare". Since type V bursts show a good correlation with centimetre bursts, one might expect them to be frequently associated with flares.

Such is the case. A list of 15 distinct type V events was compiled which occurred at times when flare data were available. Of these 14 occurred during flares, and in half the cases the radio burst began within a minute of the quoted maximum of the flare. These maxima all appeared to be of the sudden explosive type, described by Giovanelli (1958) as "puffs".

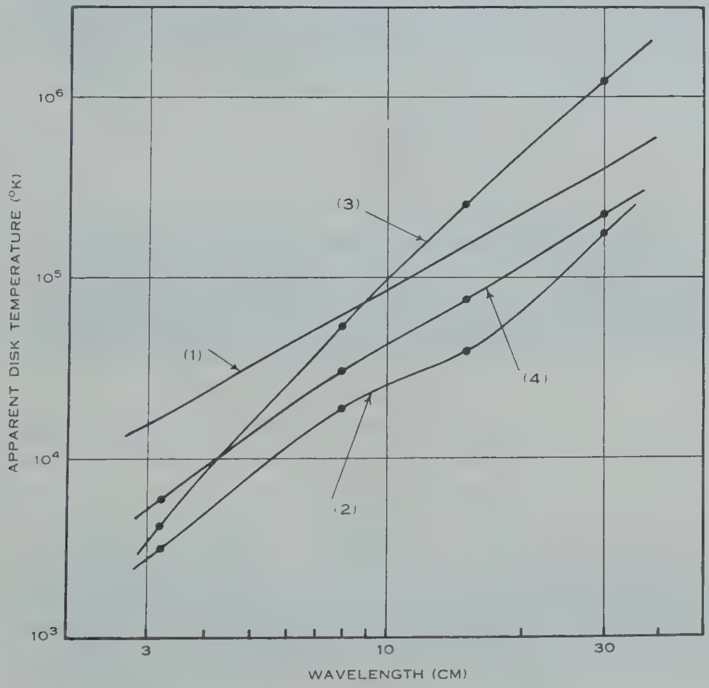

Fig. 1.—Intensities of various forms of solar radio emission in terms of apparent disk temperatures is given as a function of wavelength: (1) mean quiet Sun at sunspot maximum; (2) mean intensity of 20 centimetre bursts which accompanied type III–type V events; (3) maximum values of the accompanied centimetre bursts; (4) mean intensity of 25 centimetre bursts unaccompanied by metre-wavelength activity.

The association of puffs, high frequency events, and type III–type V events is neatly exemplified (Plate 3) by a flare, 0157–0226 Universal Time, December 9, 1957, which showed two sudden eruptions, or puffs, with an interval of about 15 min between peak intensities. During the 29 min while the flare was observed, radio emission recorded by the spectrograph was confined almost entirely to two short but outstanding bursts which coincide with the puffs at 0201 and 0216 hr.

During the same period only two events were reported on 2000 Mc/s, each lasting for 1 min and commencing at 0201 and 0216 hr respectively. Bursts at 3750 and 9400 Mc/s were also reported to begin at 0216 hr, lasting 2 and 1 min respectively.

(d) *Intensity of Centimetre Bursts*

Having found a feature which tends to distinguish between those type III's which are and are not accompanied by centimetre bursts, one now asks whether the centimetre bursts which accompany type III are distinguishable from other centimetre bursts. In particular, are the type V-accompanied centimetre bursts more intense as a group than unaccompanied centimetre bursts ?

Means of the peak intensities for these two classes of events are presented in Figure 1 in terms of apparent disk temperatures. Centimetre bursts which were associated with Group A events composed the " accompanied " group. Maximum values at the various frequencies for these events are also plotted, illustrating the considerable spread of the observations. The mean " unaccompanied " curve was derived from the intensities of 25 representative centimetre bursts chosen solely on the basis of their occurring at times when there was no activity at metre wavelengths. Mean values for the quiet Sun at sunspot maximum, based on international solar radio emission data as published in the I.A.U. Quarterly Bulletin on Solar Activity, kindly supplied by Mr. S. F. Smerd, are included for comparison.

It is evident from Figure 1 that the accompanied and unaccompanied bursts are of comparable intensity.

III. DISCUSSION

The close association between type V bursts and centimetre bursts poses the question of what is the physical relation between the two phenomena.

Firstly, do both bursts come from the same region ? Interferometer data on source positions, supported by theoretical considerations of the levels of zero refractive index in the solar atmosphere, place the source of the type V emission in the upper corona. The accompanying centimetre burst is believed to come from a much lower level. For example, Christiansen (personal communication) states that, using his highly directive equipment at 20 cm, he has never observed a burst on the limb as high as 100,000 km. This implies that the centimetre burst is not merely a high frequency component of the type V radiation but is a distinct burst originating lower in the solar atmosphere. This inferred spatial separation of the sources of type V and centimetre bursts into coronal and probably chromospheric regions leaves unexplained the simultaneity of the two events.

For the type V bursts, synchrotron radiation has been suggested (Wild, Sheridan, and Neylan 1959), and this involves the transport of a large number of highly energetic particles into the upper corona. It is now suggested that the particle stream acts as the physical link between the two bursts and that the centimetre burst occurs as a direct result of the passage of this electron stream through the chromosphere and lower levels of the corona. The radiation generated could be either thermal or synchrotron ; present evidence does not differentiate between these two mechanisms.

SOLAR RADIO BURSTS AT METRE AND CENTIMETRE WAVELENGTHS

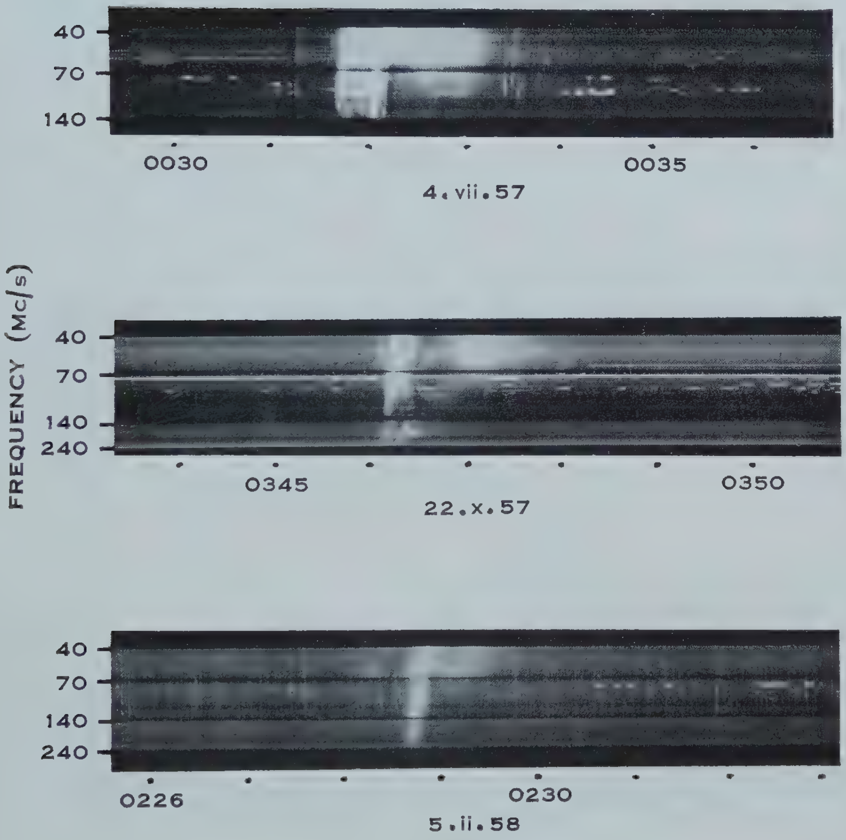

Three examples of type III bursts followed by the broad-band type V burst. These events tend to occur simultaneously with centimetre bursts.

SOLAR RADIO BURSTS AT METRE AND CENTIMETRE WAVELENGTHS

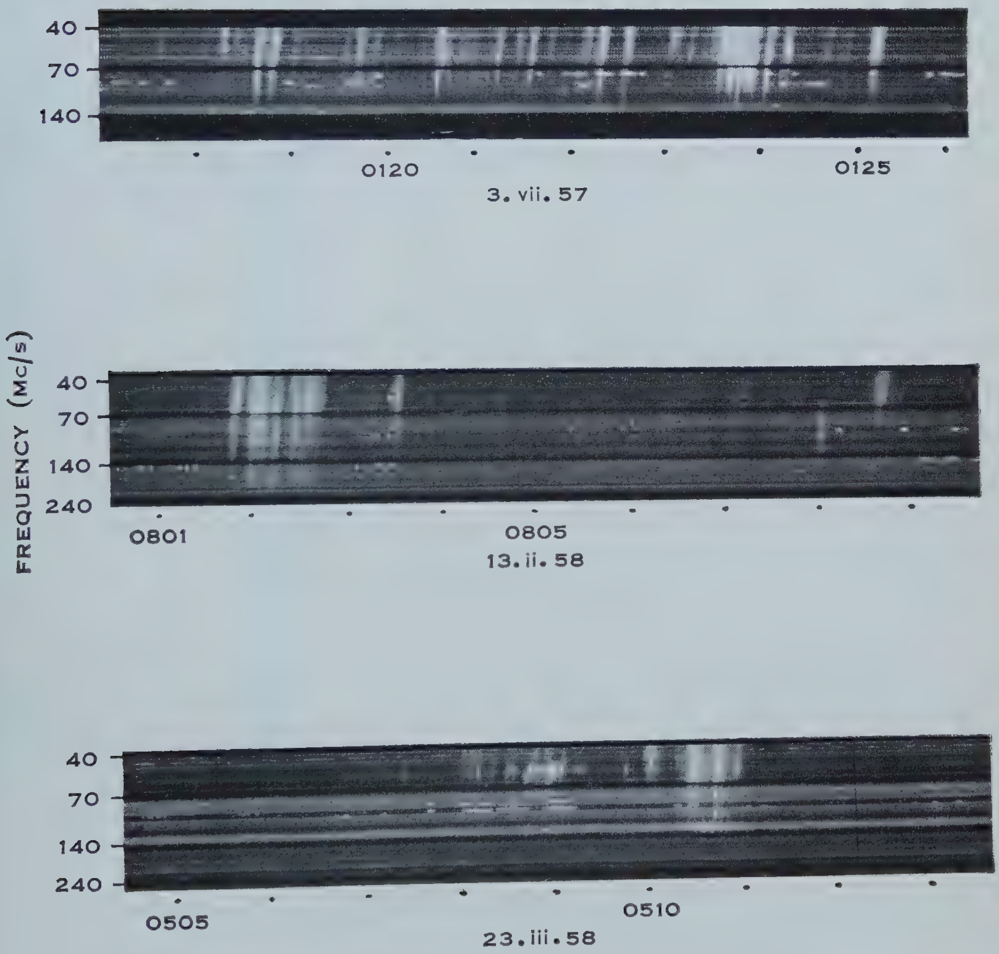

Three examples of "sharp" type III bursts of the kind which were found to be generally unaccompanied by centimetre bursts.

SOLAR RADIO BURSTS AT METRE AND CENTIMETRE WAVELENGTHS

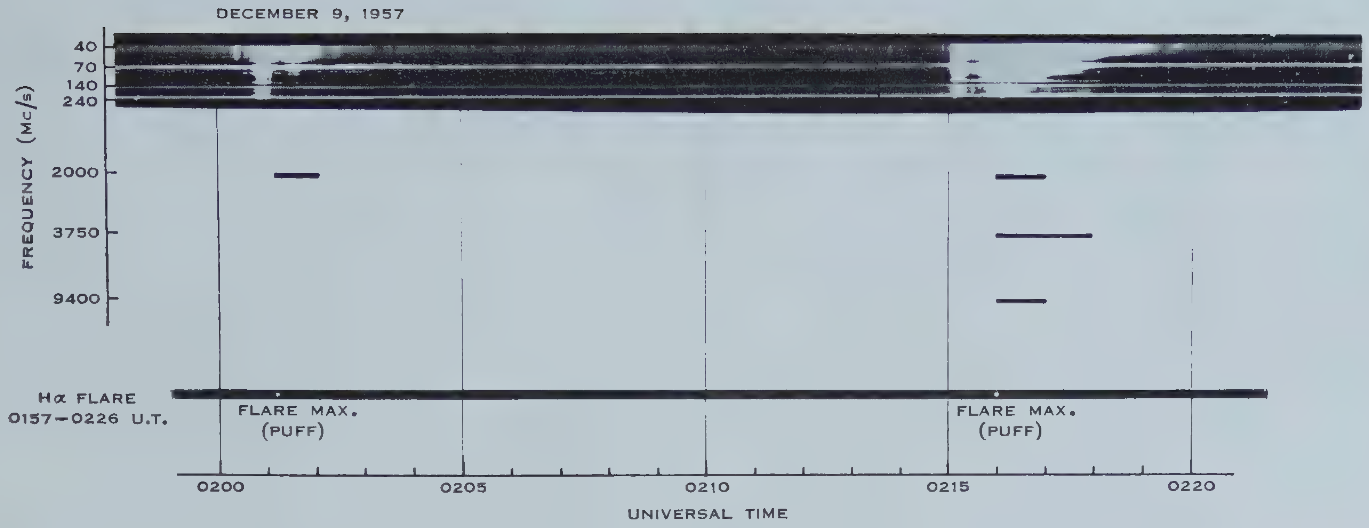

Radio and optical data showing the association of type V bursts, centimetre bursts, and flare-puffs. At top, the Dapto radio spectrum record is reproduced. Heavy horizontal lines represent the duration of the centimetre bursts and of the flare.

On the one hand, the intensities of the accompanied bursts shown in Figure 1 seem to be low enough to permit the possibility of thermal radiation. Assuming a source size area of the order of one-tenth of the solar disk the corresponding mean brightness temperatures range from tens of thousands of degrees at 3 cm to some millions at 30 cm wavelength. It is feasible to think of a dense particle stream causing this emission by collisional heating. Observations of the angular size of the source are needed to develop this argument.

On the other hand, a consistent explanation of the centimetre burst can be given in terms of synchrotron radiation generated by the same stream of electrons in its passage through the chromosphere and lower corona. The strong tendency for a centimetre burst to accompany a type III burst only when the latter is accompanied by a type V burst is then readily explained by supposing that the stream must possess a minimum number of relativistic electrons in order to generate synchrotron radiation either in the chromosphere or corona. Furthermore, the common occurrence of centimetre bursts in the absence of type III bursts could be explained by the same (synchrotron) mechanism if it is supposed that in these cases the stream is prevented from reaching the upper corona, e.g. by a re-entrant magnetic field configuration.

IV. ACKNOWLEDGMENTS

The author wishes to acknowledge his indebtedness to Professor A. Kimpara of the Research Institute of Atmospherics, Nagoya University, and to Professor S. Suzuki of Tokyo Astronomical Observatory, Mitaka, for their assistance and for the very complete data on centimetre-wavelength solar emission which they have made available. The author wishes to thank Mr. J. P. Wild, under whose direction the observations were made, for his very helpful guidance and Mr. S. F. Smerd for many useful discussions.

The work was undertaken at the C.S.I.R.O. Division of Radiophysics Laboratory while the author was in receipt of a C.S.I.R.O. research grant.

V. REFERENCES

COVINGTON, A. E., and HARVEY, G. A. (1958).—*J.R. Astr. Soc. Canad.* **52**: 161.

GIOVANELLI, R. G. (1958).—*Aust. J. Phys.* **11**: 350.

TANAKA, H., and KAKINUMA, T. (1956).—*Proc. Res. Inst. Atmos. Nagoya Univ.* **4**: 60.

TANAKA, H., and KAKINUMA, T. (1958).—*Proc. Res. Inst. Atmos. Nagoya Univ.* **5**: 81.

WILD, J. P., ROBERTS, J. A., and MURRAY, J. D. (1954).—*Nature* **173**: 532.

WILD, J. P., SHERIDAN, K. V., and NEYLAN, A. A. (1959).—*Aust. J. Phys.* **12**: 369.

WILD, J. P., SHERIDAN, K. V., and TRENT, G. H. (1959).—I.A.U.-U.R.S.I. Symposium on Radio Astronomy, Paris 1958. p. 176. (Stanford Univ. Press.)

SOLAR RADIO EMISSION OF SPECTRAL TYPE IV AND ITS ASSOCIATION WITH GEOMAGNETIC STORMS

By D. J. McLean*

[*Manuscript received August 5, 1959*]

Summary

A new type of solar radio event, the type IV storm, first described by Boischot, has been identified on Dapto radio-spectrographic records. It has been shown to be distinguishable from type I storms by (i) its smooth spectrum, (ii) its close association with type II bursts, and (iii) its remarkably close association with geomagnetic storms. In common with some type I storms, all type IV storms are found to be associated with very large solar flares.

It appears possible to explain the production of type IV emission and the occurrence of the related phenomena in terms of a single cloud of gas which moves through the Sun's corona.

I. Introduction

It has long been known that large outbursts of solar radio emission from the Sun are sometimes followed by periods of prolonged radio "storms" (e.g. Hatanaka and Moriyama 1950; Payne-Scott and Little 1952). Until recently these outburst-associated storms were presumed to be particular cases of "noise storms" which dominate the metre-wavelength radio records of the Sun over certain active periods and which are now called type I storms. The spectral records of type I storms show that they consist of many narrow-band, short-lived bursts, superposed on a background of continuum radiation.

More recently, Boischot (1958), observing the Sun with a multi-element interferometer at 169 Mc/s, has made a distinction between the ordinary noise storm (type I) and storms to which he gives the new classification of type IV. What Boischot has described is a long-duration ($\sim\frac{1}{2}$–6 hr), very smooth increase in intensity of solar radio emission extending through metre and decimetre wavelengths. These events are preceded by high intensity, short-duration outbursts which Boischot identifies as type II bursts (the characteristics of a type II burst are briefly described near the beginning of Section II), and are closely associated with very big flares (importance 2 or greater). The type IV sources are generally of larger diameter than those of type I noise storms (7–12 min of arc for a type IV, a little less for a type I source). They show rapid motion, generally away from the centre of the disk, at speeds of $\sim$1000 km/s, during the first few minutes of their existence. After this they remain steady until the storm fades, or possibly drift back slightly before fading. Boischot also presents some evidence that the flares associated with big cosmic ray increases are often, perhaps always, associated with type IV storms.

---

* Division of Radiophysics, C.S.I.R.O., University Grounds, Chippendale N.S.W., and School of Physics, University of Sydney.

Observing with a radio-spectrograph, Haddock (1958) has reported that, while type IV storms occur mainly after type II bursts, similar events are occasionally observed without any type II burst.

Recently Wild, Sheridan, and Trent (1959), working with a two-element, swept-frequency interferometer, have observed the motions of type IV sources over a range of frequencies, and they report that, at any one time, all frequencies arrive from the same direction (with a little scatter). This observation is taken as evidence that the mechanism of emission is not plasma oscillations, since radiation emitted from plasma oscillations will be restricted to frequencies near the fundamental (and second harmonic) of the plasma frequency in the region of the source and so a wide range of frequencies cannot be emitted from the same point. (In the case of type II and type III bursts, which are believed to be radiation from plasma oscillations, Wild, Sheridan, and Trent do observe different frequencies arriving from different directions.) However, Wild's observations are consistent with a suggestion by Boischot and Denisse (Boischot 1958) that the type IV radiation could be produced by synchrotron emission from high energy electrons spiralling in a magnetic field.

In the present paper it is proposed (1) to present the results of a recent study of spectral records of those solar radio storms which last only a few hours (" discrete storms "), with emphasis on the distinction between type I and type IV storms, (2) to describe the association of type IV storms with other solar and terrestrial events, and (3) to suggest, in the light of the evidence presented, a theory of the evolution of the type IV event.

II. OBSERVATIONS

Since 1952, solar radio-spectrograph records have been made at Dapto, N.S.W., on equipment described briefly by Wild, Murray, and Rowe (1954). These records were examined, mainly but not exclusively at times immediately after flares of importance 2 or greater and after outbursts which appeared on the spectral records as type II bursts, and all periods of greater than 10 min and less than about 5 hr duration, during which the observed intensity was appreciably greater than the quiet-Sun level over part or all of the observed frequency range, noted as discrete storms. The record of October 21/22, 1958, at the bottom of Plate 1, shows the start of a typical storm at 2341 U.T., preceded by an example of a type II burst from 2328 to 2342 U.T. It can be seen in the latter that there is a narrow band of high intensity activity at a frequency which drifts from $\sim$100 Mc/s to 40 Mc/s in about 10 min and that all the details are reproduced at a frequency which is approximately twice the fundamental frequency. This pair of bands is generally considered to be the fundamental and second harmonic of the frequency of plasma oscillations at the source region in the solar corona, the frequency drift being due to the motion of the source. For a fuller discussion of type II observations and theory see Roberts (1959).

The period studied was from 1952 to 1958. Only 22 discrete storms were found, of which perhaps 12 could be classified as type IV, the other 10 as type I. Possibly other such events have been obscured by what appear to be continuous periods of several days of type I noise storms. It appears probable from Boischot's work, which is supported by the present, non-exhaustive, examination of the Dapto records, that all type IV events may be associated with flares.

(*a*) *The Distinction between Type I and Type IV Storms*

In order to examine the possible distinction between type I and type IV storms the set of 22 storms was divided into two groups by two different classifications, one dependent on the prevalence or absence of bursts, and the other on whether or not the event was associated with a type II burst. Both these depend on characteristics capable of recognition from spectra alone. The two pairs of groups were then compared to see whether or not the classifications could be shown to be nearly equivalent.

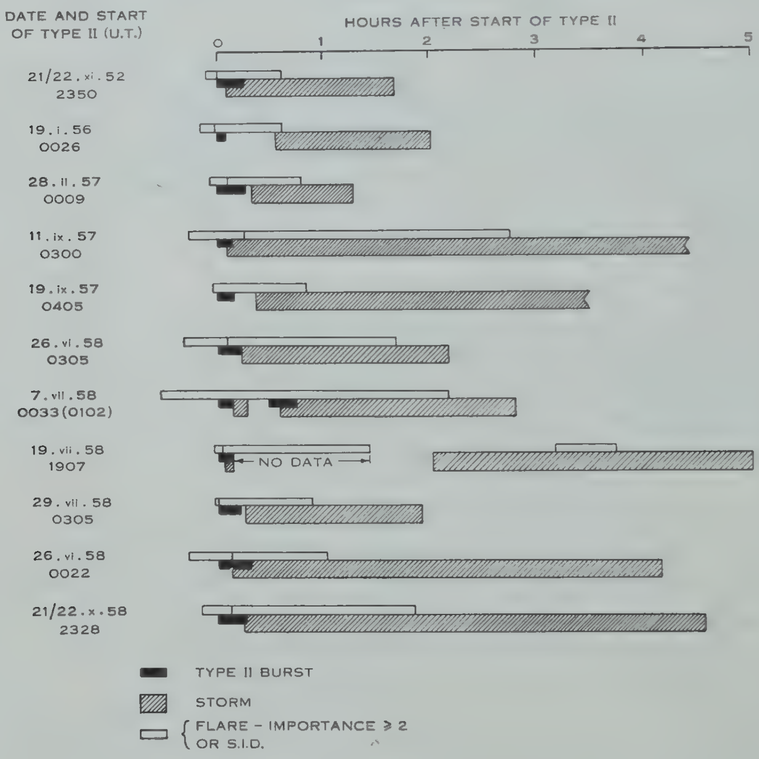

Fig. 1 (*a*).—Schematic diagram showing durations of radio storms which follow type II bursts and their relations in time to the type II and big flare event. These storms are shown later to be all the type IV storms observed.

In the first classification we divide the storms into groups of those showing many bursts which we term " bursty " and those showing few which we term " smooth ". Storms of the former type satisfy the definition of type I storms given in the introduction, i.e. a long series of very short, narrow-band bursts, superposed on a broad-band continuum—the bursts being the dominant feature.

SOLAR RADIO EMISSION OF SPECTRAL TYPE IV

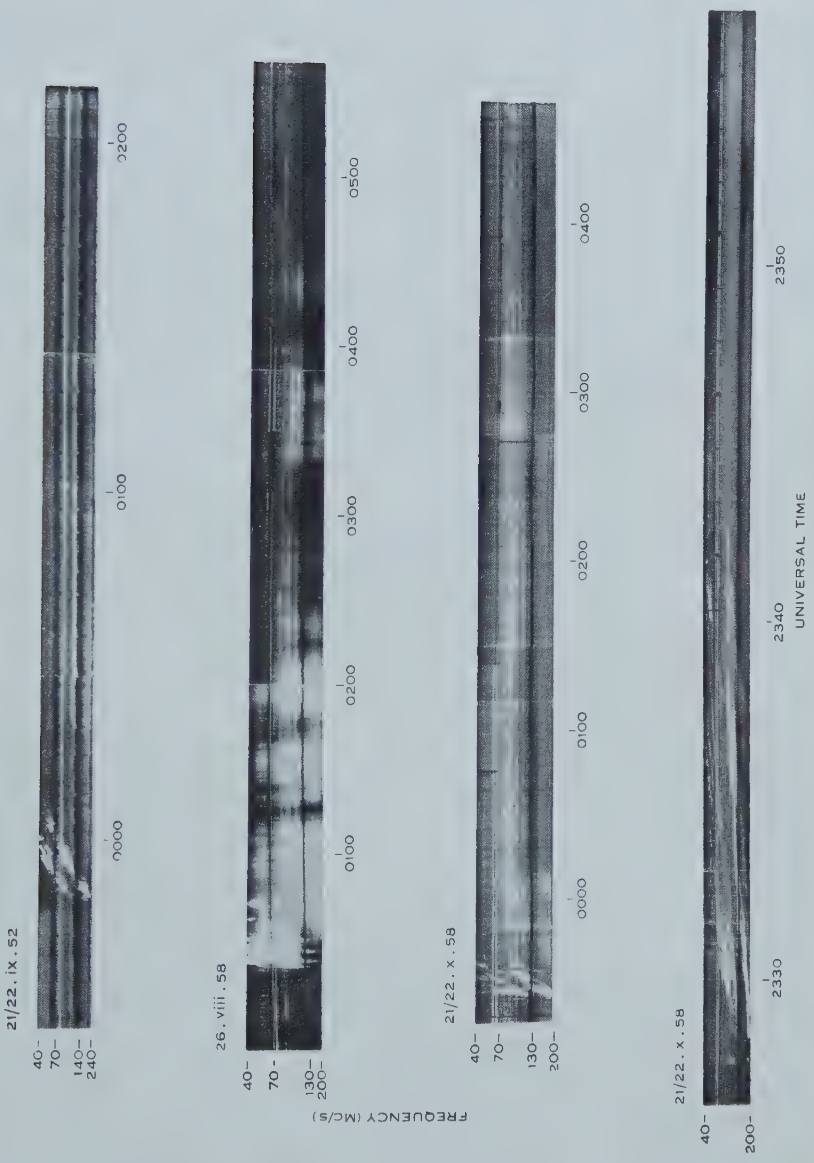

The latter (smooth) type consist almost entirely of a smooth, very broad-band, sometimes intense, increase in radio emission, which in many cases rises quickly to a maximum and then decays slowly. In other cases multiple maxima, about half an hour apart, are observed, as in the event of August 26, 1958, in Plate 1. Total durations are of the order of a few hours.

The start of these smooth storms often shows more detailed structure. Frequently the continuum exhibits a low frequency cut-off, drifting towards lower frequencies at a rate typical of type II bursts. Sometimes the event starts as two broad bands, about 20 Mc/s wide, which merge within a few minutes into even broader continuum. Also, sometimes the storm starts with a few bursts (which do not resemble a type II burst) then blurs out after a few minutes and the storm continues as a smooth continuum.

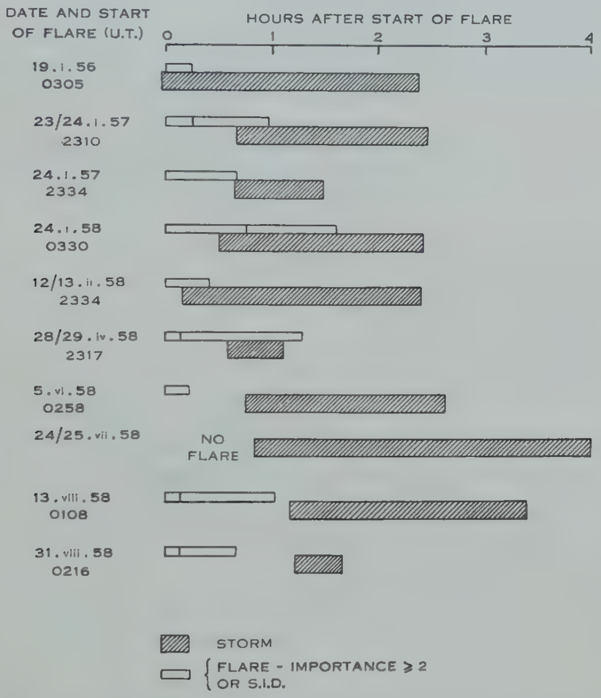

Fig. 1 (*b*).—Similar to Figure 1 (*a*), showing the durations and flare relationships of radio storms not associated with type II bursts. These are all type I storms.

Plate 1 shows examples of the " spectral appearance " of this smooth type of storm. It will be shown that this type is distinctive in other respects, justifying Boischot's extension of the spectral classification to distinguish it from type I.

The second classification is by the presence or absence of an associated type II burst. This could be decided from the available records in most cases but in two cases Harvard spectral data in CRPL " Solar Geophysical Data " were consulted.

Figure 1 (*a*) shows the time relationships of events which have been interpreted as being associated ; the differently shaded rectangles represent the times and durations of type II bursts, type II associated storms, and big flares (or S.I.D.'s which are indicative of big flares.) The events involved are sufficiently rare to make precise criterion for association unnecessary. The association can be judged from inspection of Figure 1 (*a*).

Figure 1 (*b*) shows the times of flares and related storms not associated with type II bursts and has been included here for comparison with Figure 1 (*a*) in a later discussion of flare associations.

The two classifications are compared in Table 1 which shows the correlation between type II–associated and smooth storms.

TABLE 1

CORRELATION BETWEEN TYPE II BURSTS AND SMOOTH STORMS

	Smooth	Bursty	Total
Type II–associated	12	0	12
Non-type II–associated	1	9	10
Total	13	9	22

Clearly the correlation is good and hence the distinction between type I (or bursty) and type IV (or smooth) storms emphasized. In fact, from this table it appears that the simplest definition of a type IV storm, and the easiest to apply from a spectral point of view, is " a storm which closely follows a type II burst ". Some care is needed, however, since in one case, which occurred since the data for this paper were collected, a type IV was observed at frequencies above 40 Mc/s, associated with a type II burst which was observed only at frequencies below 40 Mc/s. Hence Haddock's observation on equipment which had a low frequency limit of 100 Mc/s, of smooth storms without an associated type II burst is not contrary to the above conclusion. For the purposes of the rest of this paper, therefore, an event has been classed as a type IV storm if it closely followed a type II burst. This implies, as Table 2 shows, that the storm also fitted the original description of a smooth storm.

III. THE ASSOCIATION OF TYPE IV STORMS WITH FLARES AND GEOMAGNETIC STORMS

(*a*) *Flares*

As Figures 1 (*a*) and 1 (*b*) show, most of the events examined, whether type IV or type I storms, are associated with the occurrence of large solar flares. In only one case is there no evidence of flare association, and at that time there appears to have been no flare patrol. Four cases are consistent with flare association but the evidence is either confused (due to the occurrence of more than one suitable flare or in one case due to the occurrence of two storms during the one flare) or indirect (i.e. inferred from ionospheric effects). The remaining

17 all occur between ½ and 2 hr after the start of a big flare. Hence in almost every case there is evidence of close flare association.

Clearly, due to the mode of selection, this is not very significant for type I events, since the records were only examined systematically after big flares and type II bursts, and those events following type II bursts are type IV storms. However, as Roberts (1959) pointed out, approximately half the total number of type II bursts are associated with flares of importance 1, and it is therefore significant that all type IV events were associated with flares of importance 2 or greater. The probability of this occurring by chance is about 1/5000.

TABLE 2

DISTRIBUTION OF TYPE IV AND TYPE I STORMS WITH IMPORTANCE OF FLARE

	Uncertain or None	Imp. 2	Imp. 3	Imp. 3+	Total
Type IV	2	2	6	2	12
Type I	3	5	2	0	10
Total ..	5	7	8	2	22

When cases are split amongst the flare importance classes as in Table 2, there seems to be a strong tendency for type IV storms to associate with big flares, bigger than do type I storms; two-thirds of the observed cases are associated with flares of importance 3 or 3+.

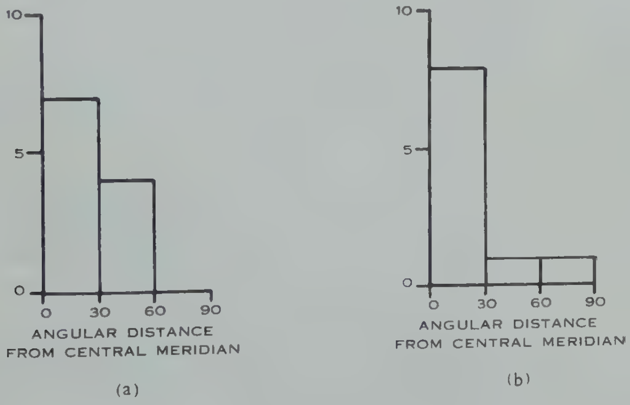

Fig. 2.—Distribution with central meridian distance (*a*) of flares associated with an observed type IV storm and (*b*) of importance 3 flares known to be not associated with a type II storm.

Another aspect of the type IV–flare relationship is the distribution with central meridian distance of type IV–associated flares. The observed distribution, in Figure 2 (*a*), shows no cases more than 60° from the central meridian. This may be due to (1) angle discrimination or (2) biased sampling.

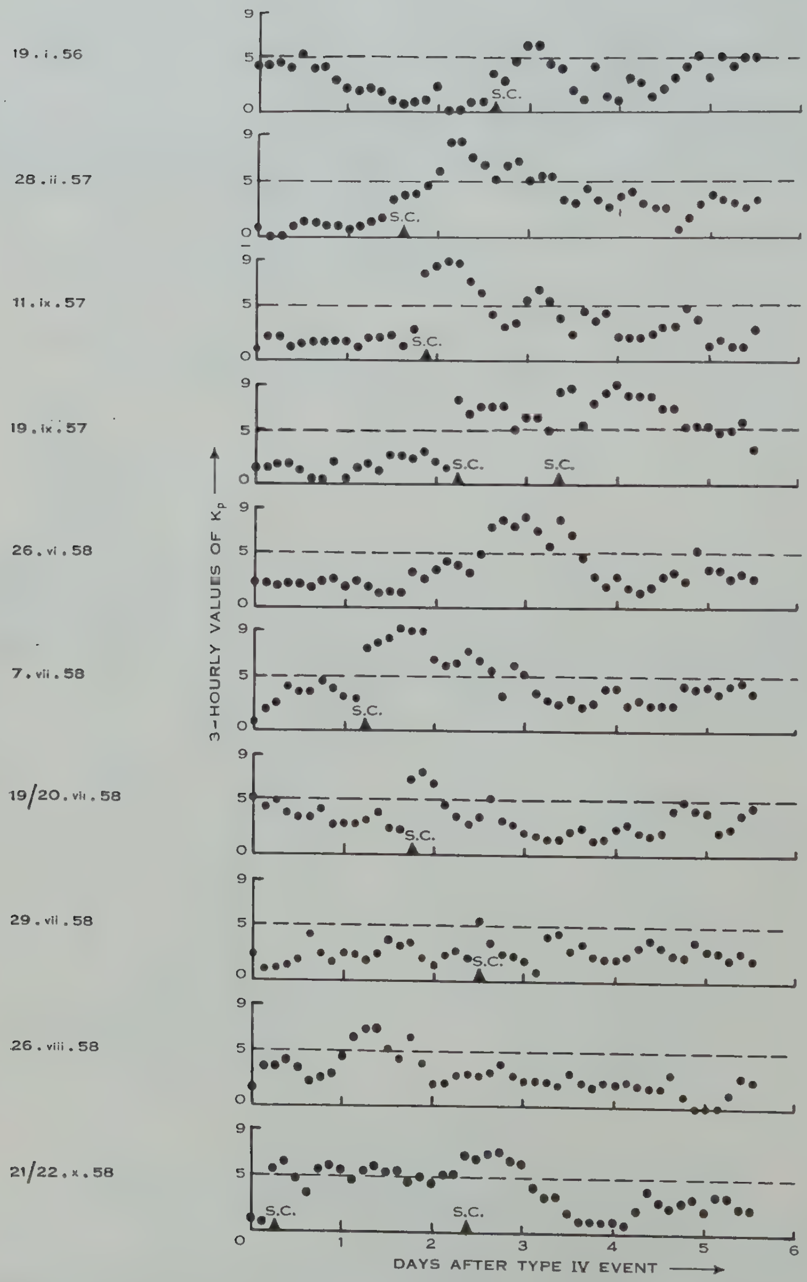

Fig. 3.—Values of K_p (geomagnetic index) plotted at 3-hourly intervals for a period from 0 to 5½ days after each of the ten most recent type IV storms observed.

Since no type IV storm has been observed without an associated flare, seeing difficulties involved in flare observations near the limb cannot cause this effect. However, if a type II burst were less likely to be observed if its associated flare were near the limb than near the centre of the disk, the observed effect might be produced. Again, it is not believed that any of the storms observed without type II bursts, can be identified as a type IV, contrary to what would be expected if the distribution of Figure 2 (*a*) were due to angular discrimination in the observability of type II bursts rather than type IV storms. Also, Roberts (1959) has shown that there does not appear to be any significant discrimination against observations of type II bursts associated with flares near the limb.

Since these arguments appear to eliminate the possibility of biased sampling, Figure 2 (*a*) is interpreted as an angular discrimination in the observability of type IV storms.

It might be argued that the observed effect is due to absorption. If this were the case the same effect should be observed for type II bursts, since these are believed to originate from the lowest level in the corona from which the radiation can escape without being completely absorbed. However, type II bursts are observed even associated with flares on the limb (Roberts 1959). The explanation therefore appears to be that the emission is confined to a cone whose axis is in or near the plane of the solar meridian through the associated flare.

For comparison, Figure 2 (*b*) shows the spatial distribution of ten flares of importance 3, occurring during the radio observing periods, but not associated with any observable type IV storm. If all importance 3 flares were associated with type IV storms, the flares in Figure 2 (*b*) should all lie outside the range associated with observable type IV's. Figure 2 (*b*) therefore shows that not all importance 3 flares are associated with type IV storms. This is as expected from Roberts' observation that not all importance 3 flares are associated with type II bursts.

(*b*) *Geomagnetic Storms*

Figure 3 shows plots of K_p, an index of geomagnetic variability, at 3-hourly intervals, for several days after each of the ten most recent type IV events. In all cases, except perhaps one, there is seen to be evidence of a magnetic storm commencing between 1 and 3 days after the type IV, and in most cases there is an associated sudden commencement.

To compare this apparent effect with that produced by other types of events, especially those intimately associated with type IV storms, the superposed epoch method was used. In Figure 4 is plotted the mean K_p index, before and after each of the following :

(*a*) The ten type IV storms used above.
(*b*) The ten type I storms, associated with flares, used earlier in this paper.
(*c*) The ten importance 3 flares occurring in radio observing periods, but not associated with any type IV, also used earlier.
(*d*) Thirty-six type II bursts, none of which occurred within four days of a known type IV storm observed from Sydney.

As can be seen, the correlation of geomagnetic storms with type IV storms is outstanding and is probably the only significant one; certainly type II bursts, without type IV storms following them, do not appear to be associated in any but a small percentage of cases. This is in direct agreement with Sinno and Hakura (1958), but the conclusion is different from that of Dodson (1958), who associates geomagnetic storms with "major early bursts". (Figure 1 (*a*) shows that type IV storms generally occur after the maximum of a flare.)

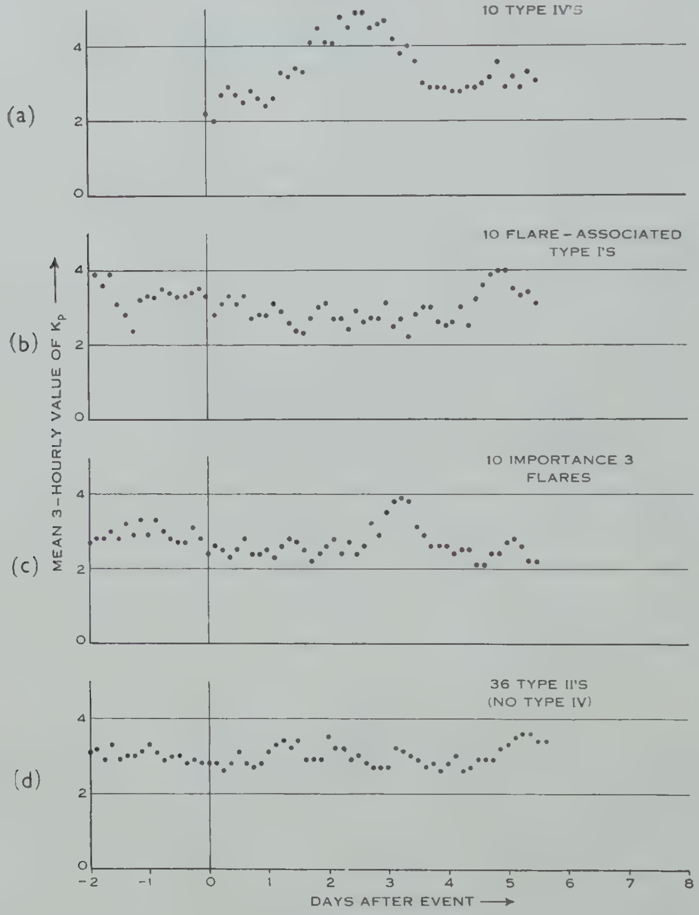

Fig. 4.—The mean value of K_p for each 3-hourly period before and after (*a*) type IV storms (10 events); (*b*) type I storm (10 events); (*c*) importance 3 flares, not associated with type IV storms (10 events); and (*d*) type II bursts, not associated with type IV storms (36 events).

It is interesting to note that the previously mentioned restriction of the type IV–associated flares to within 60° of the central meridian, is similar to the restriction to within ~45° of the central meridian of flares associated with magnetic storms (Kiepenheuer 1953).

Apparently type IV radiation and magnetic-storm clouds are confined to roughly the same cone of emission. Hence, if a magnetic storm followed a type IV storm occurring anywhere on the Sun, it would be reasonable, from the direction of the Earth, to expect to see both or neither. This is relevant to a consideration of the percentage of geomagnetic storms associated with type IV's (which has not been investigated yet).

It appears from Figure 3 that occurrence of a type IV storm will become a reliable guide for the prediction of terrestrial disturbances 1–3 days later.

IV. A Hypothesis of Origin

Boischot and Denisse (Boischot 1958) have already proposed synchrotron radiation, from relativistic electrons spiralling in a magnetic field, as the mechanism for type IV emission.

Since type II bursts, geomagnetic storms, and flares have been shown above to be closely associated with type IV storms, the following results and ideas arising from previous work are relevant.

(i) Type II bursts are believed to be produced by plasma oscillations in the solar corona (Wild, Murray, and Rowe 1954; Wild, Sheridan, and Trent 1959); such oscillations could be excited by the passage of a shock front ahead of a fast moving column of gas (Westfold 1957; Roberts 1959).

(ii) Geomagnetic storms are thought to be due to the arrival at the Earth of a cloud of plasma ejected from the solar corona, and carrying trapped magnetic fields and high energy protons (Kiepenheuer 1953; Gold 1959).

(iii) Type IV sources are observed with velocities of 500–3000 km/sec; type II sources and magnetic storm clouds are believed to have velocities of the same order (Boischot 1958; Wild, Sheridan, and Trent 1959).

(iv) Boischot (1958) has observed type IV sources to have diameters of $\sim$7–12 min of arc.

In addition it has been shown in this paper that:

(v) Although not unique, a fairly typical description of the start of a type IV is as follows: a type II burst occurs, then, after a short delay of minutes, a smooth increase of intensity commences at high frequencies and rises gradually to a maximum in a period of about 10 min. Lower frequencies appear at later times, the effect being that of a low frequency cut-off drifting to lower frequencies at roughly the same rate as the type II. This can be observed fairly easily for the event of August 26, 1958, in Plate 1.

(vi) The spectrum is essentially smooth and changes slowly with time.

(vii) As stated above, a type II burst, geomagnetic storm, and large flare are all closely associated with the occurrence of a type IV.

In the rest of this paper, the outline of a hypothesis is presented which appears capable of combining these facts and ideas and of explaining the spectral observations. This is done by considering the sequence of events in 4 phases, illustrated diagrammatically in Figures 5 (*a*) to 5 (*d*).

First phase (Fig. 5 (*a*)).—A flare occurs low in the solar atmosphere, in the region of high magnetic field associated with a sunspot group. It has been

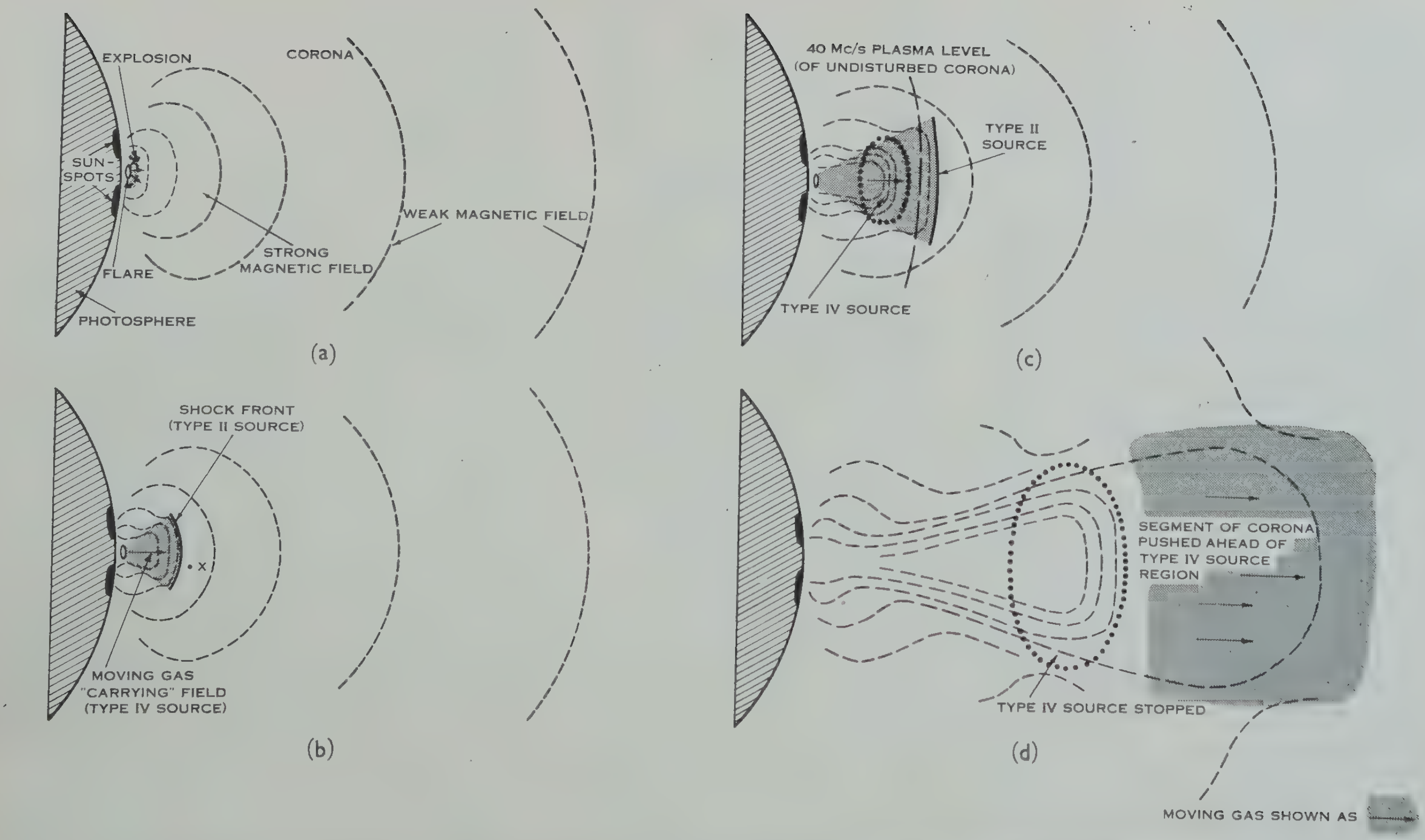
EXPLOSION
CORONA
SUN-SPOTS
WEAK MAGNETIC FIELD
STRONG MAGNETIC FIELD
FLARE
PHOTOSPHERE
(a)
SHOCK FRONT (TYPE II SOURCE)
x
MOVING GAS "CARRYING" FIELD (TYPE IV SOURCE)
(b)
40 Mc/s PLASMA LEVEL (OF UNDISTURBED CORONA)
TYPE II SOURCE
TYPE IV SOURCE
(c)
SEGMENT OF CORONA PUSHED AHEAD OF TYPE IV SOURCE REGION
TYPE IV SOURCE STOPPED
(d)
MOVING GAS SHOWN AS

Fig. 5.—A simple representation showing a possible mode of development of a type IV storm and its relation to flares, type II bursts, and geomagnetic storms (see text).

postulated that an explosion of some sort occurs near the start of the flare and ejects a column of gas, which travels radially outwards from the region of the flare.

Second phase (Fig. 5 (*b*)).—The column travels with a velocity of about 1000 km/sec. For such a high velocity the front of the column will be bounded by a shock front. This is a sharp discontinuity between the stationary corona, as yet unaffected by the explosion, and the moving gas constituting the column which is at a higher temperature and pressure. As the shock front reaches a point such as X in Figure 5 (*b*) the gas near X is compressed and accelerated to the velocity of the column, thus becoming a homogeneous part of the column. In this way the boundary of the column moves forward relative to the gas in the column, i.e. the shock front moves faster than the gas comprising the column.

As mentioned earlier, the shock front is assumed to excite plasma oscillations in the corona, which in turn produce the type II radiation. This has already been shown to fit the observations in most respects (Roberts 1959). Also, it is well known (e.g. Westfold 1957) that magnetic fields which are in the coronal gas before it is accelerated by the explosion are " frozen in " and carried by the gas.

It is not unreasonable to expect that a small percentage of particles in the column will have been accelerated to high energies (1 MeV would be sufficient to explain the observed effect) either by the explosion, or by the rapidly changing fields in the shock front, or by both. Under suitable conditions these will be trapped within the column by the frozen-in magnetic fields and the electrons will radiate continuously over a wide frequency range (Schwinger 1952). This is taken to be the type IV emission.

Boischot's cosmic ray evidence suggests that during the first or second phase extremely high energy protons might be generated, which under favourable conditions (not necessarily immediately) might be liberated from the magnetic fields to give rise to terrestrial cosmic ray increases (see Piddington 1958).

Third phase (Fig. 5 (*c*)).—When the disturbance reaches greater heights in the corona, the gas in the forward part of the column, which has been accelerated by the shock front, does not contain such strong, frozen-in magnetic fields and so the conditions are unfavourable for the generation of synchrotron emission in this region. The type II source (near the shock front) and the type IV source (in the region of the high magnetic fields and moving with the velocity of the gas in the column) therefore tend to become separated. Hence, at the time shown in Figure 5 (*c*), a single-frequency record of solar emission at 40 Mc/s would show the type II burst to be already over and the type IV storm not yet started. (Following other workers, we have here assumed that the type II radiation comes from just in front of the shock front; its frequency is then determined by the undisturbed coronal density.) Owing to the nature of the shock front, the gas in the column will be maintained at a higher density than the gas in the surrounding corona and so the plasma frequency (which is the low frequency cut-off for transmission of radiation) will be higher here than in the adjacent corona. Hence, the type IV source will not be observed at, say, 40 Mc/s till the gas in and ahead of the source has expanded to the density at the 40 Mc/s plasma level in the undisturbed corona, which is unlikely to occur until after the type IV source crosses the original position of this level. This is the explanation of the observed delay between a type II burst and the associated type IV storm and the drifting cut-off frequency. An exactly similar discussion can of course be applied to, say, 30 Mc/s observations, which should not show the type IV radiation till after the source passes through the 30 Mc/s level, which is above the 40 Mc/s level—hence the drifting cut-off.

The rise time may be explained by postulating a long extent of the type IV source in the direction of motion. It is clear from the above discussion that, while the leading edge of the source is " visible " at 40 Mc/s, the tail of the source may still lie in denser gas which absorbs 40 Mc/s radiation. Hence, as each part of the storm becomes visible, the observed intensity rises.

The observed value of rise time seems to agree with that estimated by assuming that all the type IV emission at a given frequency becomes visible at the same height in the corona. Boischot (1958) observes type IV sources $\sim$10 min of arc across, which is roughly 4×10^5 km. A source 4×10^5 km long with a velocity of 10^3 km/sec should take about 7 min to cross a particular level in the corona. This is the order of the observed time for a type IV storm to rise from zero to maximum intensity at a given frequency.

Fourth phase (Fig. 5 (*d*)).—The type IV source is observed to stop moving high in the corona. No attempt is made here to postulate a stopping mechanism. It is postulated, however, that the stopping mechanism is such that the segment of the corona, which has been pushed out ahead of the type IV source region and which has already been considered not to emit type IV radiation owing to the insufficient magnetic field, is not stopped. In that case, this moving cloud of gas, carrying weak magnetic fields and possibly high energy protons, becomes the magnetic storm cloud, travelling with the velocity the type IV source had initially.

This completes the suggested outline for the explanation of type IV emission. Two points, predicted by the hypothesis, which it should be possible to test from interferometric measurements, are :

(i) that the type IV source should follow the type II source along the same path,

(ii) that the type II source should travel appreciably faster than the type IV source.

V. Conclusion

There are at least two distinct types of solar radio storm observable at metre wavelengths. One is the type I, which has long been recognized ; the other is the type IV, only recently distinguished from type I by Boischot.

The type IV storm is a smooth, long-duration, enhancement of radio emission from the Sun, which is closely associated with very big flares and nearly always follows a type II burst. However, it appears necessary to allow the possible existence of a small amount of burst structure in the definition of a type IV storm, especially early in the storm. On the other hand, the type I storm is distinguished by its extremely bursty nature and its non-association with type II bursts. Further, type I storms of less than, say, 10 hr duration may be associated with flares, but the tendency appears to be towards less important flares than those associated with type IV storms.

Evidence has been produced that the occurrence of a type IV storm is a very significant event in the prediction of a geomagnetic storm commencing 1–3 days later. Large flares and type II bursts, both of which are commonly associated with type IV storms, do not appear to be followed by geomagnetic storms if they are not associated with type IV storms. Further, type I storms do not appear to be associated with geomagnetic storms, which is also a useful point of distinction between type I and type IV storms. The type IV storm appears therefore to be a valuable prediction guide.

A hypothesis has been proposed in which type II bursts, type IV storms, and magnetic storms are all observable effects of the one cloud of gas ejected from near the photosphere by an explosion.

VI. Acknowledgments

This work was done while the author, who is a student at the University of Sydney, was attached to the Radiophysics Laboratory. The author especially wishes to thank Mr. J. P. Wild for considerable direction, discussion, and assistance during this study; also Dr. J. L. Pawsey for acting as a supervisor. Further, the author wishes to thank all those people whose work has made this study possible, by producing, processing, and analysing the records.

VII. References

Boischot, A. (1958).—*Ann. Astrophys.* **21**: 273.

Dodson, H. W. (1958).—*Proc. Inst. Radio Engrs., N.Y.* **46**: 149.

Gold, T. (1959).—*Nature* **183**: 355.

Haddock, F. T. (1958).—*Proc. Inst. Radio Engrs., N.Y.* **46**: 3.

Hatanaka, T., and Moriyama, F. (1950).—*Rep. Ionosphere Res. Japan* **4**: 173.

Kiepenheuer, K. O. (1953).—" The Sun." (Ed. G. P. Kuiper.) (Univ. Chicago Press.)

Payne-Scott, Ruby, and Little, A. G. (1952).—*Aust. J. Sci. Res.* A **5**: 32.

Piddington, J. H. (1958).—*Phys. Rev.* **112**: 589.

Roberts, J. A. (1959).—*Aust. J. Phys.* **12**: 327.

Schwinger, J. (1952).—*Phys. Rev.* **75**: 1912.

Sinno, K., and Hakura, Y. (1958).—*Rep. Ionosphere Res. Japan* **12**: 296.

Westfold, K. C. (1957).—*Phil. Mag.* **2**: 1287.

Wild, J. P., Murray, J. D., and Rowe, W. C. (1954).—*Aust. J. Phys.* **7**: 439.

Wild, J. P., Sheridan, K. V., and Trent, G. H. (1959).—I.A.U.-U.R.S.I. Symposium on Radio Astronomy, Paris 1958. p. 176. (Stanford Univ. Press.)

Explanation of Plate 1

" Spectral appearance " of type IV storms. The first three examples are reproductions of spectral records in which the time scale has been considerably compressed by a special photomechanical process. The fourth shows the start of the third event on a more normal time scale.

In all cases, frequency and time scales are as marked and intensity is shown by the whiteness of the record.

Horizontal white lines are due to interference from radio transmitters and horizontal black lines mark the limits of the individual frequency bands in the equipment.

THE ETA CARINAE NEBULA AND CENTAURUS A NEAR 1400 Mc/s

II. PHYSICAL DISCUSSION OF THE ETA CARINAE NEBULA

By C. M. Wade*

[*Manuscript received June 30, 1959*]

Summary

The 1400 Mc/s observations of NGC 3372 described in Paper I (Hindman and Wade 1959) are discussed. Comparison of the flux densities at 85·5 Mc/s (Mills, Little, and Sheridan 1956) and at 1400 Mc/s leads to a value of 10,000 ± 1000 °K for the electron temperature of the nebula. Unpublished optical measurements of the distribution of surface brightness across the object, made by Gum, indicate that there is a dense core about 24 min of arc in diameter, surrounded by a much less dense region with a diameter of 120 min of arc. Adopting the optically determined distance of 1400 parsecs (Hoffleit 1953), we find r.m.s. densities of 71 ions cm^{-3} in the core and 11 ions cm^{-3} in the outer region. The total mass of the object is not more than 25,000 solar masses. It is shown that several O-stars probably are needed to maintain the ionization of the nebula.

I. Introduction

The present paper is a sequel to an earlier one (Hindman and Wade 1959) which described observations of the Eta Carinae Nebula (NGC 3372) at a frequency near 1400 Mc/s. The main results in the previous paper may be summarized as follows :

(i) the flux density of NGC 3372 near 1400 Mc/s is $5\cdot 82\times 10^{-24}\ \mathrm{W\,m^{-2}\,(c/s)^{-1}}$, with an estimated uncertainty less than ±20 per cent,

(ii) the apparent surface brightness distribution appears to be fairly symmetrical,

(iii) the source shows a high degree of concentration towards its centre.

The objective of the present paper is to infer the temperature, density, and mass of the object from the available radio data. We shall consider also its excitation.

The physical discussion to follow rests upon several assumptions. These are.

(i) *The radio emission of the nebula is purely thermal.*

(ii) *The ionized region has a uniform electron temperature.* While this assumption is undoubtedly somewhat idealized, arguments presented by Spitzer (1954) show that the range of electron temperatures within a given nebula is not likely to be very great.

(iii) *The mass distribution within the nebula is spherically symmetrical.* This needs to be only approximately true for the discussion given below. The assumption is supported by the observed absence of any marked asymmetry in the distribution of the radio emission of the source.

---

* Division of Radiophysics, C.S.I.R.O., University Grounds, Chippendale, N.S.W.

(iv) *The nebular gas consists entirely of singly ionized atoms.* This assumption is probably quite sound, since the only elements likely to be present in significant amounts are hydrogen and helium. Swihart (1952) has shown that, under such conditions as we expect to prevail in NGC 3372, helium is almost entirely in the singly ionized state; moreover, the He II and H II zones are almost exactly coincident. Therefore the numbers of positive and negative ions should be equal and Kramers' law may be used in the form appropriate for fully ionized hydrogen.

The discussion requires a knowledge of the solid angle subtended by the nebula and of the distribution of relative optical depth over its projected surface. Ideally, we should like to determine these from radio-frequency observations. Because of the insufficient angular resolution of the available instruments, however, the existing radio data consist mainly of measurements of flux density. Therefore it is necessary, in our case, to estimate the angular size and optical depth distribution from optical observations.

II. Geometrical Preliminaries

(*a*) *The Apparent Surface Distribution of Optical Depth*

Consider a spherically symmetrical nebula situated at some distance from the observer. The optical depth at a point on the projected surface of the sphere will depend only on the angular distance of the point from the centre. The ratio of the optical depth at fractional radius x to that at the apparent centre may be expressed by some function $g(x)$. Letting $x=1$ at the outer boundary of the object, we have $g(0)=1$ and $g(1)=0$. The values of $g(x)$ for intermediate radii depend upon the distribution of opacity within the sphere, the relationship being expressed by a form of Abel's integral equation

$$g(x)=\frac{2r_0\varkappa_0}{\tau_0}\int_x^1\frac{yh(y)\mathrm{d}y}{\sqrt{(y^2-x^2)}}, \quad \ldots\ldots\ldots\ldots\ldots\ldots \quad (1)$$

where r_0 is the radius of the nebula, $\varkappa_0$ is the absorption coefficient at its centre, and τ_0 is the optical depth through its apparent centre. $h(y)$ is the ratio of the absorption coefficient at fractional radius y to $\varkappa_0$. Equation (1) has a unique solution (Bracewell 1956):

$$h(y)=-\frac{\tau_0}{\pi r_0\varkappa_0}\int_y^1\frac{g'(x)\mathrm{d}x}{\sqrt{(x^2-y^2)}}. \quad \ldots\ldots\ldots\ldots\ldots \quad (2)$$

Equations (1) and (2) provide a means of converting between corresponding distributions of opacity and optical depth.

C. S. Gum (unpublished data) has measured the distribution of surface brightness, in Hα light, along a line passing across the centre of NGC 3372 at position angle 335°, as shown in Plate 1. Since the object is optically thin in Hα, the radio surface brightness distribution at high frequencies should be very similar to that measured by Gum. The diameter along which his measurement was made appears to be relatively unaffected by the rather erratic obscuration overlying most of the nebula. The optical measurement is consistent with an optical depth distribution of the form

$$g(x)=\begin{cases}\dfrac{(1-c)\sqrt{(\alpha^2-x^2)}+c\sqrt{(1-x^2)}}{\alpha+c(1-\alpha)}, & 0\leqslant x\leqslant\alpha,\\[2ex] \dfrac{c\sqrt{(1-x^2)}}{\alpha+c(1-\alpha)}, & \alpha<x\leqslant 1,\end{cases} \quad \ldots\ldots (3)$$

where $\alpha=0\cdot2$ and $c=0\cdot025$. The rather complicated expression of these equations is due to the desirability of having the opacity model (equation (4)) stated in the simplest possible form. Figure 1 shows the agreement between the above distribution and that measured by Gum, for an adopted angular diameter of 120 min of arc. The two distributions differ appreciably only where $x<0\cdot1$. The difference in that region is to be expected, because that is where Gum's line of measurement cuts across one of the strong lanes of absorbing matter seen against the nebula at optical wavelengths. The adopted optical depth distribution is undoubtedly somewhat idealized, but errors in it have only a slight effect on the values to be derived for the electron temperature and total

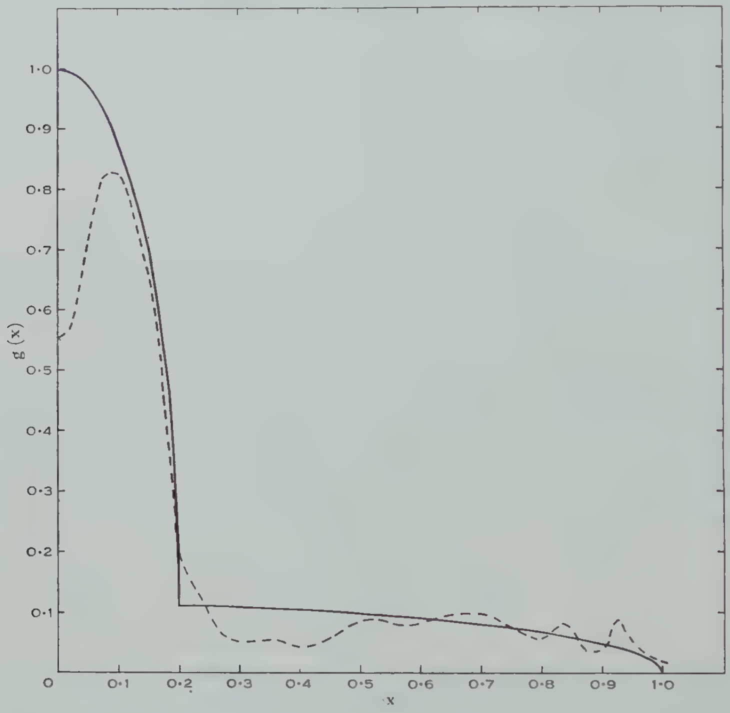

Fig. 1.—Radial optical depth distribution across NGC 3372. The quantity plotted is relative optical depth g as a function of fractional angular radius x; $x=1$ at 60′ from the centre.

...... Distribution in p.a. 335°, based on optical measurements by C. S. Gum.

——— Adopted distribution.

mass, and the discussion of the excitation of the object is entirely independent of the geometry. The calculation of density and emission measure are more sensitive to errors in $g(x)$, and hence less weight should be attached to the values found for these quantities. Figure 2 shows the form of $h(y)$ corresponding to equations (3),

$$h(y)=\begin{cases}1, & 0\leqslant y\leqslant\alpha,\\ c, & \alpha<y\leqslant 1.\end{cases} \quad \ldots\ldots\ldots\ldots\ldots\ldots \quad (4)$$

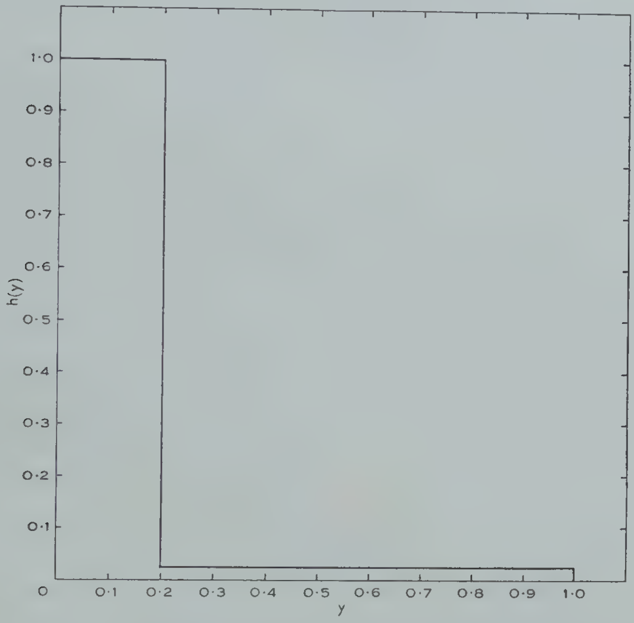

Fig. 2.—Radial opacity distribution corresponding to the adopted optical depth distribution. The relative opacity h is plotted as a function of fractional radius y. $\alpha=0\cdot 2$, $c=0\cdot 025$.

Other model-dependent parameters needed in the ensuing discussion may be derived from equations (3) and (4). These are:

$$\bar{g}=2\int_0^1 xg(x)\mathrm{d}x=0\cdot 0994,$$

$$u=\left[2\bar{g}\int_0^1 h(y)\mathrm{d}y\right]^{\frac{1}{2}}=0\cdot 2091.$$

The numerical values have been calculated for $\alpha=0\cdot 2$ and $c=0\cdot 025$.

(b) *The Apparent Flux Density*

The apparent flux density (defined by Mills, Little, and Sheridan 1956) of a nebula at a particular frequency, in units of W m^{-2} (c/s)$^{-1}$, is

$$F_{app}=2\cdot 04\times 10^{-35}\varphi^2 f_{mc}^2(T_e-T_b)\psi(\tau_0), \quad \ldots\ldots\ldots\ldots \quad (5)$$

where φ is its angular diameter in minutes of arc, f_{mc} is the frequency in Mc/s, T_e is the electron temperature of the nebular gas, and T_b is the brightness temperature (assumed to be uniform) of the sky background at the position of the nebula. $\psi(\tau_0)$ is the value of $1-e^{-\tau(x)}$ averaged over the projected surface of the object. If $T_b \ll T_e$, the apparent and true flux densities are equal.

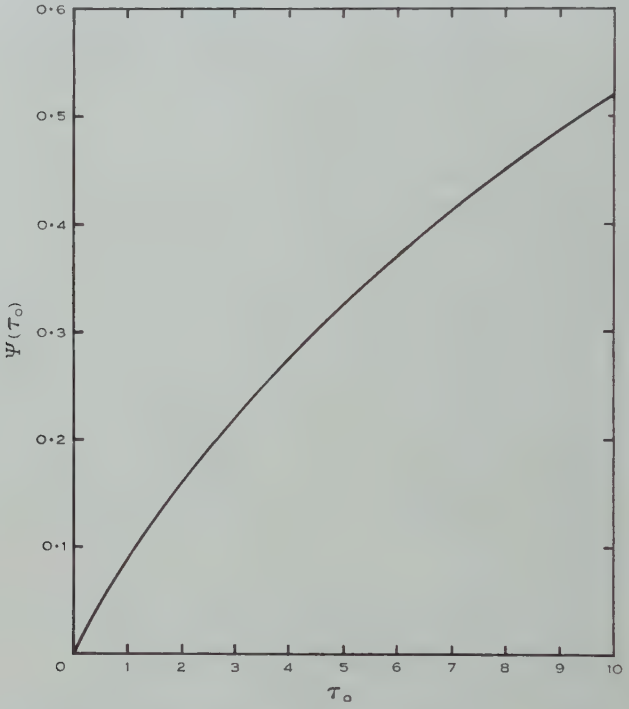

Fig. 3.—The optical depth parameter $\psi(\tau_0)$ for $\alpha=0\cdot2$, $c=0\cdot025$.

Figure 3 shows $\psi(\tau_0)$ in the range $0 \leqslant \tau_0 \leqslant 10$ for the adopted optical depth distribution $g(x)$. If $\tau_0 \ll 1$, we have simply

$$\psi(\tau_0)=\bar{g}\tau_0. \qquad \ldots\ldots\ldots\ldots\ldots\ldots \quad (6)$$

III. The Electron Temperature

The flux density of a thermal radio source depends only weakly on frequency as long as the object is optically thin. The optical depth increases rapidly with decreasing frequency, however, causing the emitted flux to drop fairly sharply at the lower frequencies. The spectrum in the region of decreasing flux density is quite sensitive to the electron temperature of the source ; this circumstance permits one to find the electron temperature of a nebula by comparing the flux densities measured at two well-separated frequencies, provided that the optical depth is appreciable at one at least of the frequencies. The observations of

THE ETA CARINAE NEBULA AND CENTAURUS A. II

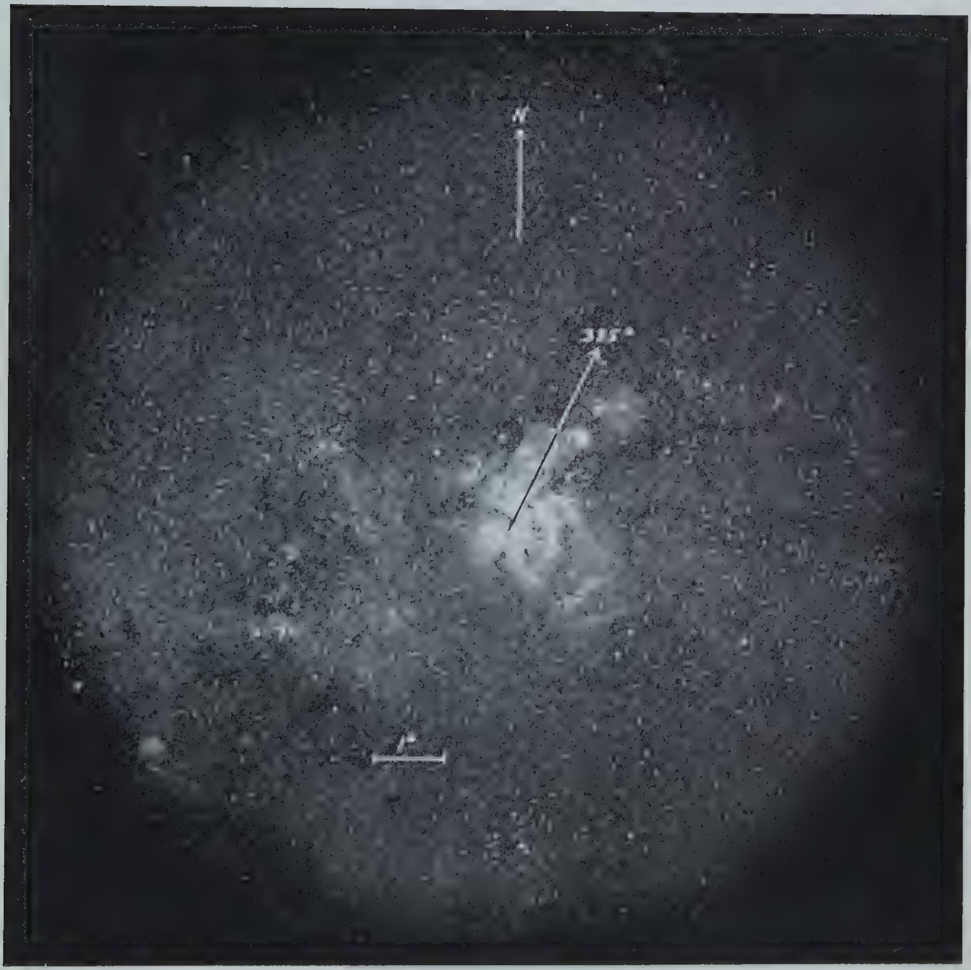

Photograph of NGC 3372 in Hα light, taken with the 8-in. $f/1$ Meinel-Pearson Schmidt camera at the Mount Stromlo Observatory. The line along which C. S. Gum measured the surface brightness of the object is indicated. North is at the top, with east to the left.

NGC 3372 at 85·5 Mc/s by Mills, Little, and Sheridan (1956) fall in the range of intermediate optical depths ; hence they are suitable for comparison with the 1400 Mc/s data.

The method, which was described by the author in a previous paper (Wade 1958), may be outlined as follows.

(i) The ratio of the optical depths at the projected centre of a nebula at the two frequencies must be equal to the ratio of the absorption coefficients, which is :

$$\frac{\tau_{0,1}}{\tau_{0,2}}=\frac{\zeta_1}{\zeta_2}\left(\frac{f_2}{f_1}\right)^2, \qquad \ldots\ldots\ldots\ldots\ldots\ldots\ldots (7)$$

where

$$\zeta=9\cdot 70\times 10^{-3}\ln 3kT_e/2hf.$$

The subscripts 1 and 2 denote the two frequencies ; in the present case we may take these to be 85·5 and 1400 Mc/s respectively. h and k are Planck's and Boltzmann's constants and f is the frequency in cycles per second. For temperatures in the vicinity of 10,000 °K, we have

$$\tau_{0,1}/\tau_{0,2}=326.$$

(ii) Using equations (5) and (6) and Figure 3, one may find the ratio of the central optical depths from the radio-frequency observations, assuming a value for the electron temperatures. If the assumed temperature is correct, the computed optical depth ratio will be equal to that required by equation (7). The simplest means of arriving at the correct temperature is to assume several values and compute the optical depth ratio corresponding to each. The temperature can then be found graphically from a plot of optical depth ratioversus electron temperature.

Mills, Little, and Sheridan (1956) found that the apparent flux density of NGC 3372 at 85·5 Mc/s is $3\cdot 42\times 10^{-24}$ W m^{-2} (c/s)$^{-1}$.* Hill, Slee, and Mills (1958) give 4700 °K for the brightness temperature of the sky near NGC 3372 at 85·5 Mc/s. This value must consist of two parts : (*a*) the true background temperature, i.e. the emission arising beyond NGC 3372, and (*b*) the emission occurring between the source and the Sun, which we shall call the *foreground component*. It is difficult to estimate reliably the relative strengths of the two components. Extrapolation of unpublished observations at 19·7 Mc/s by C. A. Shain (personal communication) leads to an estimate of 1400 °K for the foreground component. This is consistent with data obtained at 85·5 Mc/s (B. Y. Mills, personal communication) ; hence we adopt the above value, leaving a true background temperature of 3300 °K at 85·5 Mc/s. At 1400 Mc/s, the background temperature is less than 5 °K and may be neglected. Taking $\varphi=120$ min of arc, we can draw Figure 4 ; the intersection of the two curves gives an electron temperature of 10,000 °K. The principal sources of possible error in this result are.

---

* Because of an error in calibration, the flux density published by Mills and his co-authors was too low by a factor slightly greater than two (Mills, personal communication). The correction has been incorporated in the figure given above.

(i) *The experimental uncertainties in the flux densities,* which lead to an uncertainty of ±700 °K.

(ii) *The uncertainty in the magnitude of the foreground component at 85·5 Mc/s.* The error due to this cause is probably not greater than ±300 °K.

The net uncertainty is therefore less than ±1000 °K.

The electron temperature deduced above is in good agreement with the 8000–10,000 °K expected on theoretical grounds (Spitzer 1954). It also accords well with the recent optical determinations by Pronyk (1957), who found that the temperature ranges from 7500 to 11,000 °K in NGC 1976 and from 7600 to 9000 °K in IC 405; in both cases the temperature tends to decrease with increasing distance from the exciting stars.

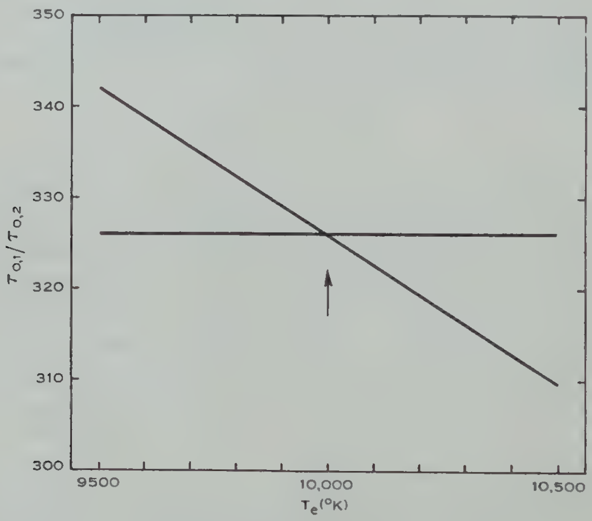

Fig. 4.—Determination of the electron temperature of NGC 3372.

IV. Density and Total Mass

If a nebula is optically thin, the r.m.s. density at its centre, in ions per cubic centimetre, is given by (see Appendix I)

$$n_0 = 1 \cdot 05 \times 10^{16} \frac{T_e^{\frac{1}{4}} F^{\frac{1}{2}}}{(\zeta R)^{\frac{1}{2}} \varphi^{3/2} u}, \qquad \ldots\ldots\ldots\ldots\ldots \quad (8)$$

provided $T_b \ll T_e$, which is usually true at the frequencies where $\tau_0 \ll 1$. F is the true flux density of the nebula, and R is its distance in parsecs. Hoffleit (1953) has estimated the distance to NGC 3372 as 1400 parsecs, using available optical data. With the 1400 Mc/s flux density, we find that the r.m.s. density of the core region is 71 ions cm^{-3}. This agrees fairly well with Bok's (1932) early result of 60 ions cm^{-3}, derived from optical data. The density of the outer region may be found by multiplying the core value by $c^{\frac{1}{2}}$; it is 11 ions cm^{-3}.

An upper limit to the total mass of the nebula may be set by assuming that the r.m.s. densities are equal to the actual average ion densities, and integrating over the volume of the object. Before doing this, however, one must know the relative abundances of the hydrogen and helium components of the gas. No direct determination of the abundance ratio in NGC 3372 is available; but Mathis (1957) has evaluated it for the Orion Nebula (NGC 1976), finding that one helium ion is present for each eight of hydrogen, in good agreement with the ratio of about one in ten found in stellar atmospheres and nebulae by various other workers (see Allen 1955, p. 28). Adopting the eight to one ratio, we find that the total mass of NGC 3372 is less than or equal to 25,000 solar masses.

V. The Central Emission Measure

The surface brightness of a nebula may conveniently be described by its *emission measure*, which is defined (Strömgren 1948) as

$$\varepsilon=\int_S n_e n_i \mathrm{d}s,$$

where n_e and n_i are the electron and ion densities, and S is the path length of the line of sight through the ionized region in parsecs. Since we are assuming in the present discussion that the region consists of singly ionized atoms, we may take $n_e=n_i$. The emission measure at the apparent centre of an optically thin spherical nebula is related to the flux density by

$$\varepsilon_0=1\cdot 59\times 10^{28}T_e^{\frac{1}{2}}F/\varphi^2\zeta\bar{g} \qquad \ldots\ldots\ldots\ldots\ldots \quad \mathbf{(9)}$$

(see Appendix I). Using this relation and the 1400 Mc/s flux density, we find that the central emission measure of NGC 3372 is 54,000. This may be compared with the value 80,000 ± 30,000 which Gum estimated from his unpublished optical measurements.

We have ignored the small, very intense patch of nebulosity associated with the star Eta Carinae. Since this nebulosity is less than 10 sec of arc in diameter, it can have no measurable effect on the observed flux densities. Furthermore, its connexion with NGC 3372 is doubtful (Bok 1932; Gaviola 1950). Therefore we are justified in neglecting it in the present discussion.

VI. The Excitation of NGC 3372

The effectiveness of a star as a source of nebular excitation may be inferred from the size and density of the ionized region associated with it. Considering a spherical nebula with radius r_0 and uniform ion density n, Strömgren (1939) showed that $U(\equiv n^{\frac{2}{3}}r_0)$ depends only on the spectral type and the absolute luminosity of the exciting star. The excitation parameter U may be found directly from the flux density if the object is optically thin (Wade 1958)

$$U=6\cdot 32\times 10^6 R^{\frac{2}{3}}T_e^{\frac{1}{6}}\zeta^{-\frac{1}{3}}F^{\frac{1}{3}}. \qquad \ldots\ldots\ldots\ldots\ldots \quad \mathbf{(10)}$$

The value of U derived from this equation is independent of the geometry of the nebula. Applying it to NGC 3372, we find $U=134$. According to Pottasch (1956), the value of U for a typical O5 star is 100. Since the effective U of a group of stars is the cube root of the sum of the cubes of their individual U's, the value found for NGC 3372 implies that it is excited by the equivalent, roughly, of three O5 stars. No satisfactory identification has been made of the stars responsible for the ionization of NGC 3372, but our result for *U* makes it seem likely that a group of several hot stars is imbedded in it.

VII. Conclusions

The foregoing discussion has led to the interpretation of NGC 3372 shown in Figure 5. The available radio data are consistent with a spherical nebula having an electron temperature of 10,000 ± 1000 °K, comprising a relatively small dense core and a broad tenuous envelope. Adopting the optically determined distance of 1400 parsecs, we found that the r.m.s. ion densities of the core and the envelope are respectively 71 cm^{-3} and 11 cm^{-3}. The computed central emission measure of 54,000 is in rough agreement with Gum's unpublished optical determination. The nebula almost certainly is excited by more than one O-star, since the ultraviolet flux required to maintain the ionization of such a large mass (about 25,000 solar masses) is about three times the amount which could be supplied by a single O5 star.

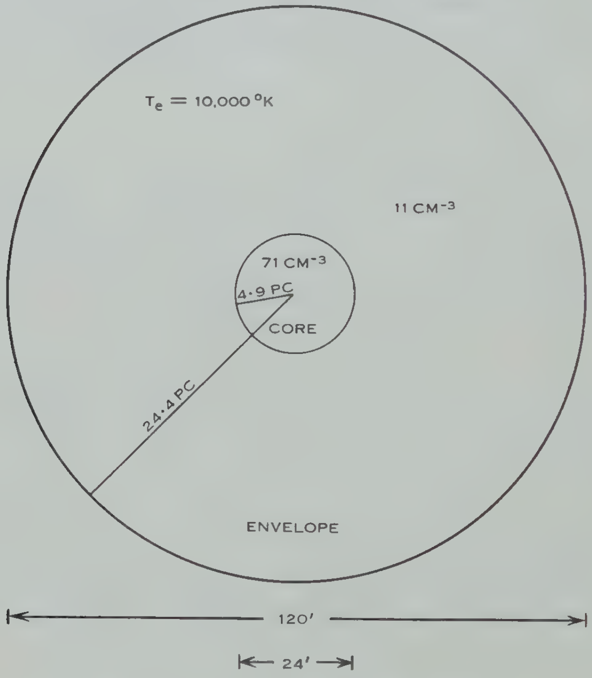

Fig. 5.—Derived model for NGC 3372.

A high resolution determination of the surface brightness distribution across the object at a high frequency (i.e. at a frequency such that the nebula is everywhere optically thin) is desirable to check the form adopted in the preceding discussion and in order to ascertain the validity of the assumption of radial symmetry. Observations of the flux density at several other frequencies will serve as a general check on the derived model.

Figure 6 shows the integrated radio-frequency spectrum implied by our model. It was computed from equation (5), assuming that

$$T_b=3300[f_{mc}/85\cdot5]^{-2\cdot70}.$$

At about 66 Mc/s, the background temperature should be equal to the electron temperature, making the object invisible at that frequency. At lower frequencies it should be seen in absorption. At the high frequencies, where the object is optically thin, about 75 per cent. of the flux arises in the envelope.

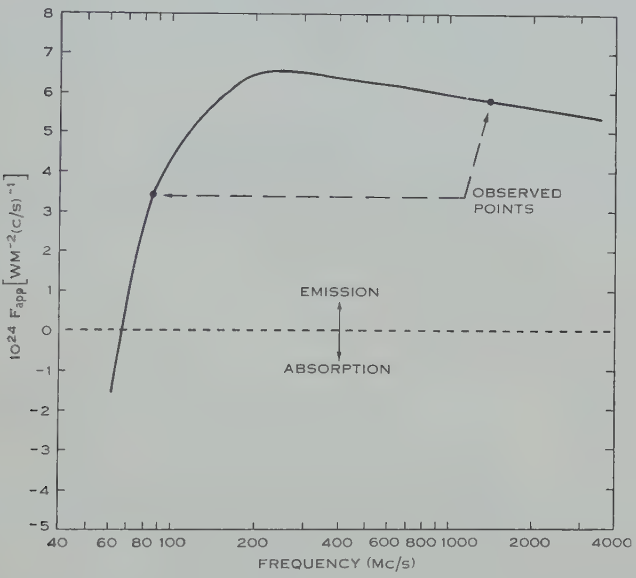

Fig. 6.—Radio spectrum of NGC 3372, computed from the derived model. The observed points are indicated.

The results obtained in the present paper agree well with previous conclusions about emission nebulae gained from theoretical and optical studies. This fact provides some confirmation of the basic physical assumption underlying the analysis; namely, that the nebula emits radio waves solely by the thermal mechanism of free-free transitions. The radio approach to the problem of determining the general physical properties of nebulae is, on the whole, simpler and more direct than contemporary optical methods. This is true of both the observational techniques and the physical theory required to discuss the observations.

VIII. ACKNOWLEDGMENTS

The author is indebted to Dr. C. S. Gum for making available his unpublished optical measurements of the surface brightness of NGC 3372, and to Dr. B. Y. Mills and Mr. C. A. Shain for helpful discussions. The work was made possible by a Junior Research Fellowship granted by the Commonwealth Scientific and Industrial Research Organization.

IX. References

Allen, C. W. (1955).—"Astrophysical Quantities." (Athlone Press: London.)
Bok, B. J. (1932).—Harv. Rept. No. 77.
Bracewell, R. N. (1956).—*Aust. J. Phys.* **9**: 198.
Gaviola, E. (1950).—*Astrophys. J.* **111**: 408.
Hill, E. R., Slee, O. B., and Mills, B. Y. (1958).—*Aust. J. Phys.* **11**: 530.
Hindman, J. V., and Wade, C. M. (1959).—*Aust. J. Phys.* **12**: 258.
Hoffleit, D. (1953).—*Ann. Harv. Coll. Obs.* **119**, No. 2.
Mathis, J. S. (1957).—*Astrophys. J.* **125**: 328.
Mills, B. Y., Little, A. G., and Sheridan, K. V. (1956).—*Aust. J. Phys.* **9**: 218.
Piddington, J. H. (1951).—*Mon. Not. R. Astr. Soc.* **111**: 45.
Pottasch, S. (1956).—*Bull. Astr. Insts. Netherlds.* **13**: 77.
Pronyk, V. I. (1957).—*Izv. Krymskoi Astrof. Obs.* **17**: 14.
Spitzer, L. (1954).—*Astrophys. J.* **120**: 1.
Strömgren, B. (1939).—*Astrophys. J.* **89**: 526.
Strömgren, B. (1948).—*Astrophys. J.* **108**: 242.
Swihart, T. L. (1952).—Master's Thesis, University of Indiana.
Wade, C. M. (1958).—*Aust. J. Phys.* **11**: 388.

Appendix I

(*a*) *Derivation of Equation* (8)

If the nebula is optically thin, we may combine equations (5) and (6) to obtain

$$F=2\cdot04\times10^{-35}\varphi^2 f_{mc}^2 T_e \bar{g}\tau_0, \qquad \ldots\ldots\ldots\ldots \quad (\mathbf{A1})$$

provided $T_b \ll T_e$, which ordinarily is true at the high frequencies where $\tau_0 \ll 1$.

According to Kramers' law (e.g. Piddington 1951), the absorption coefficient at the centre of the nebula is

$$\varkappa_0=10^{-12}\zeta n_0^2/f_{mc}^2 T_e^{3/2}, \qquad \ldots\ldots\ldots\ldots\ldots \quad (\mathbf{A2})$$

if the gas is of low density and consists only of singly ionized atoms. The optical depth through the projected centre of the nebula is

$$\tau_0=2r\varkappa_0\int_0^1 h(y)\mathrm{d}y. \qquad \ldots\ldots\ldots\ldots\ldots\ldots \quad (\mathbf{A3})$$

Now, if R is the distance to the nebula in parsecs and φ is its angular diameter in minutes of arc,

$$r_0=4\cdot48\times10^{14}R\varphi. \qquad \ldots\ldots\ldots\ldots\ldots\ldots\ldots \quad (\mathbf{A4})$$

Substituting (A2) and (A4) in (A3), we get

$$\tau_0=448R\zeta\varphi n_0^2/f_{mc}^2 T_e^{3/2}. \qquad \ldots\ldots\ldots\ldots\ldots \quad (\mathbf{A5})$$

Then, substituting (**A5**) in (**A1**) and solving for n_0, and defining

$$u=\left[2\bar{g}\int_0^1 h(y)\mathrm{d}y\right]^{\frac{1}{2}},$$

we obtain

$$n_0=1\cdot05\times10^{16}\frac{T_e^{\frac{1}{4}}F^{\frac{1}{2}}}{(R\zeta)^{\frac{1}{2}}\varphi^{3/2}u},$$

which is equation (**8**).

(*b*) *Derivation of Equation* (**9**)

According to equation (**16**) of a previous paper by the author (Wade 1958), the central emission measure of an optically thin nebula is

$$\varepsilon_0=\frac{f_{mc}^2T_e^{3/2}\tau_0}{3\cdot08\times10^6\zeta}$$

Solving (**A1**) for τ_0 and substituting in the above expression, we obtain

$$\varepsilon_0=1\cdot59\times10^{28}T_e^{\frac{1}{2}}F/\varphi^2\zeta\bar{g},$$

which is equation (**9**).

TOWARDS A METHOD FOR THE ACCURATE SOLUTION OF THE SCHRÖDINGER WAVE EQUATION IN MANY VARIABLES

I. FORMULATION OF THE METHOD FOR AN EIGENVALUE PROBLEM WITHOUT SYMMETRY CONDITIONS

By I. M. Bassett*

[*Manuscript received June 26, 1959*]

Summary

The aim of this paper and those following is to formulate and explore a new method, suitable for use with an electronic digital computer, for the solution of eigenvalue-eigenfunction problems in many variables, with the aim of applying the method to the Schrödinger wave equation.

In this method, an expression for an eigenfunction F, depending on the variables $x, y, \ldots, z$, is sought in the form

$$F=F(x, y, \ldots, z)=\sum_i f_i(x)g_i(y) \ldots h_i(z), \qquad \ldots\ldots\ldots\ldots \text{(A)}$$

which is a sum of products of functions of one variable ; the functions of one variable are represented numerically, and are determined with the aid of the variation principle, so as to give a " best " representation of F of this form. This may be contrasted with the Rayleigh-Ritz method, in which each term of the series (**A**) is, apart from a multiplying coefficient, an analytic function determined in advance, only the coefficients being determined by the variation principle. In view of this contrast, it would be expected that the present method would give a more accurate expression for F with a given number of terms, and may therefore be regarded as an attempt to solve the problem of the slow convergence of the Rayleigh-Ritz procedure for complex problems.

The method is worked out in detail only for the fundamental solution. The stationary condition by which the functions of one variable are determined is shown, subject to certain reservations, to be a minimum condition (theorem 3), and the convergence of the procedure is discussed.

A way is suggested for obtaining an initial estimate of the eigenfunction, for the iterative improvement which the method prescribes.

I. INTRODUCTION

The outstanding property of the Schrödinger wave equation from the computer's point of view is that its solution is an inseparable function of many variables. One must represent any function either by a table of numbers or by a rule by which such a table could be generated (the rule being commonly embodied in an analytic expression) or by a partial table together with a rule for generating the rest of the table. For a function of many variables, full and direct tabulation is impossible, as the following rough calculation shows. If a function of one variable requires 100 tabular entries for close enough description, then, roughly speaking, for a function of 30 variables, such as the wave function of the sodium cation, $100^{30}=10^{60}$ tabular entries would be needed. At 1 cm^2 per entry, the wave function would cover the Earth about 10^{40} times. From the impossibility of making such a table D. R. Hartree concluded that the wave equation cannot be solved accurately (Hartree 1957).

---

* Chemistry Department, University of Melbourne ; present address : Chemistry Department, University of Illinois, Urbana, Ill., U.S.A.

This problem is overcome in Rayleigh's method by using an almost entirely analytic representation of the wave function. Rayleigh's method consists in setting up, as a representation of the solution, an analytic expression containing some variable parameters, and then determining the " best " values of these parameters by using the minimum property of eigenvalues. The form of analytic expression must be more-or-less guessed. Rayleigh's method has been used in most attempts to obtain accurate *ab initio* solutions of the many-electron wave equation. The form of Rayleigh's method most used is the " Rayleigh-Ritz " method in which the analytic expression is a linear combination of given functions and the variable parameters are the coefficients of the linear combination. If the given functions form a complete set, then, in principle, by allowing enough of them to enter the linear combination, a solution of arbitrarily small inaccuracy could be obtained. However, it is not possible to tell which members of the complete set are the best ones to use except by trying them out.

The method proposed represents the eigenfunction by a partial tabulation, without restricting it. It seeks an expression for an eigenfunction depending on the variables $x, y, \ldots, z$ in the form

$$\sum_i f_i(x)g_i(y) \ldots h_i(z) \qquad \ldots\ldots\ldots\ldots\ldots\ldots \quad (*)$$

that is, a series in which each term is a product of one-dimensional functions. The one-dimensional functions are represented by tables of numbers, and are determined by the nature of the problem, through the minimum property of eigenvalues, so that each term added is a " best " term of this form ; in contrast, in the Rayleigh-Ritz method, each term is determined, apart from its multiplying coefficient, in advance. In any practical application of the Rayleigh-Ritz method, moreover, each term is a product of functions of one variable (in order that the numerical integrations should be feasible). This comparison, in view of the degree of accuracy which has been attained in some applications of the Rayleigh-Ritz method (see, for example, Boys and Price 1954), suggests that the proposed method would provide an accurate representation of wave functions sufficiently compact to be capable of being handled by a high speed electronic digital computer with a large store. The imposition of the form (*) does not restrict the solution for a reason which may be expressed loosely as follows : if

$$\chi_i(x), \quad i=1, 2, \ldots,$$

is a complete set of functions in a range $-R \leqslant x \leqslant R$, then the set of products

$$\chi_i(x)\chi_j(y) \ldots \chi_k(z), \quad i=1, 2, \ldots; \; j=1, 2, \ldots; \; \ldots; \; k=1, 2, \ldots;$$

is a complete set in

$$-R \leqslant x \leqslant R, \; -R \leqslant y \leqslant R, \; \ldots, \; -R \leqslant z \leqslant R$$

(Courant and Hilbert 1953).

Thus any function defined in the region can be expressed as a sum of products of functions of one variable.

Two suggestions have been made recently for the solution of the convergence problem presented by the Rayleigh-Ritz process. It has been suggested (Slater 1953) that a good set of one-electron functions to use in a Rayleigh-Ritz expansion would be the (complete) set of solutions of a certain self-consistent field problem. However, it is not claimed that a practical method could be based on this idea. A second suggestion (Löwdin 1955; Shull and Löwdin 1959) consists in the demonstration that a certain set of one-electron functions, the "natural spin-orbitals" must give rapid convergence. However, there does not seem to be any way of determining these without first obtaining the wave function. The present series of papers may be thought of as making another suggestion for the solution of this convergence problem.

It is assumed throughout this paper that the fundamental solution of the eigenvalue-eigenfunction or eigenvalue-eigenvector problem considered is that corresponding to the algebraically least eigenvalue; this is no restriction. This paper is concerned mainly with the determination of the least eigenvalue and its eigenfunction or eigenvector; the method is worked out in detail only for this case. It is also assumed that this eigenfunction is non-degenerate.

II. Formulation of the Method for an Eigenvalue Problem without Symmetry Conditions

In order to show clearly the basic properties of the method, it is first formulated (in Part I) not for the wave equation (from whose solutions it is necessary to select those with certain symmetry properties) but for an eigenvalue problem without symmetry conditions, which will be written

$$\mathscr{H}\psi=\lambda\psi, \quad \ldots\ldots\ldots\ldots\ldots\ldots \quad (1)$$

where ψ is a real function of n variables $(x, y, \ldots, z)$ and $\mathscr{H}$ is a real differential operator. ψ is the fundamental eigenfunction of $\mathscr{H}$ and λ is the corresponding eigenvalue. The function ψ is taken to be defined in a region $-R\leqslant x\leqslant R$, $-R\leqslant y\leqslant R$, . . ., $-R\leqslant z\leqslant R$ and to be subject to the condition that it vanish on the boundary $x=\pm R$, $y=\pm R$, . . ., $z=\pm R$ of this region. $\mathscr{H}$ is taken to be symmetric; that is, we take it that if φ and ψ are arbitrary functions (apart from satisfying conditions of differentiability and the boundary conditions)

$$\int_{-R}^{R}\cdots\int_{-R}^{R}\varphi\mathscr{H}\psi\,\mathrm{d}x\mathrm{d}y\ldots\mathrm{d}z=\int_{-R}^{R}\cdots\int_{-R}^{R}\psi\mathscr{H}\varphi\,\mathrm{d}x\ldots\mathrm{d}z.$$

Let us write

$$Q=Q(v)=\int_{-R}^{R}\cdots\int_{-R}^{R}v(x, y, \ldots, z)\mathscr{H}v(x, y, \ldots, z)\mathrm{d}x\mathrm{d}y\ldots\mathrm{d}z$$

and

$$N=N(v)=\int_{-R}^{R}\cdots\int_{-R}^{R}v^2(x, y, \ldots, z)\mathrm{d}x\mathrm{d}y\ldots\mathrm{d}z.$$

The lowest eigenvalue of (**1**) is the least value which Q/N assumes for any $v=v(x, y, \ldots, z)$ satisfying the boundary conditions, and the eigenfunction belonging to this eigenvalue is that v which gives to Q/N its least value. Let $u(x, y, \ldots, z)$ be a first guess at this lowest eigenfunction. We seek a set of n functions $f(x), g(y), \ldots, h(z)$ vanishing at $\pm R$ (so that $u+fg\ldots h$ satisfies the boundary condition for a solution of (**1**)) such that $u+fg\ldots h$ is the best expression of this form for the lowest eigenfunction. Let $g(y)=g_0(y)\ldots h(z)=h_0(z)$ be fixed, and let $\delta f=\delta f(x)$ be a variation of $f(x)$ which vanishes at $\pm R$. If $f(x)$ gives to Q/N its least value, Q/N being formed for $(u+f(x)g_0(y)\ldots h_0(z))$, then $\delta(Q/N)=0$. Now

$$\begin{aligned}\delta Q=\delta(&\int\!\ldots\!\int u\mathscr{H}u\,\mathrm{d}x\ldots\mathrm{d}z+2\int\!\ldots\!\int fg\ldots h\mathscr{H}u\,\mathrm{d}x\ldots\mathrm{d}z\\&+\int\!\ldots\!\int fg\ldots h\mathscr{H}fg\ldots h\,\mathrm{d}x\ldots\mathrm{d}z)\\=2&\int\delta f(\int\!\ldots\!\int g\ldots h\mathscr{H}u\,\mathrm{d}y\ldots\mathrm{d}z)\mathrm{d}x\\&+2\int\delta f(\int\!\ldots\!\int g\ldots h\mathscr{H}g\ldots h\,\mathrm{d}y\ldots\mathrm{d}z)f\mathrm{d}x,\end{aligned}$$

where the integrations are from $-R$ to R in each variable. Similarly,

$$\delta N=2\int\delta f(\int\!\ldots\!\int g\ldots hu\,\mathrm{d}y\ldots\mathrm{d}z)\mathrm{d}x+2\int\delta f(\int\!\ldots\!\int g^2\ldots h^2\mathrm{d}y\ldots\mathrm{d}z)f\mathrm{d}x.$$

$\delta(Q/N)=(1/N)\{\delta Q-(Q/N)\delta N\}=0$ if and only if

$$\begin{aligned}\int\delta f\{&\int\!\ldots\!\int g\ldots h\mathscr{H}u\,\mathrm{d}y\ldots\mathrm{d}z+(\int\!\ldots\!\int g\ldots h\mathscr{H}g\ldots h\,\mathrm{d}y\ldots\mathrm{d}z)f\\&-(Q/N)\int\!\ldots\!\int g\ldots hu\,\mathrm{d}y\ldots\mathrm{d}z-(Q/N)(\int\!\ldots\!\int g^2\ldots h^2\mathrm{d}y\ldots\mathrm{d}z)f\}\mathrm{d}x=0.\end{aligned}$$

If this holds for any variation δf, then f satisfies the equation

$$\begin{aligned}(&\int\!\ldots\!\int g\ldots h\mathscr{H}g\ldots h\,\mathrm{d}y\ldots\mathrm{d}z)f-(Q/N)(\int\!\ldots\!\int g^2\ldots h^2\mathrm{d}y\ldots\mathrm{d}z)f\\&+\int\!\ldots\!\int g\ldots h\mathscr{H}u\,\mathrm{d}y\ldots\mathrm{d}z-(Q/N)\int\!\ldots\!\int g\ldots hu\,\mathrm{d}y\ldots\mathrm{d}z=0.\end{aligned}\qquad\ldots\ldots\ldots\ldots\ (\mathbf{2})$$

Equation (**2**) is formed for $g(y)=g_0(y)\ldots h(z)=h_0(z)$.

If $f(x)g_0(y)\ldots h_0(z)$ is small enough, that is, if $u(x, y, \ldots z)$ is near enough to the lowest eigenfunction of (**1**), then Q/N in (**2**) can be formed for $f=0$ and taken as constant, so that (**2**) becomes simply a differential equation for f. Anyway, it is to be expected that iterative solution of (**2**) would lead to a solution $f(x)=f_1(x)$ which is "self-consistent" (i.e. which is yielded by (**2**) with Q/N formed for $u+f_1(x)g_0(y)\ldots h_0(z)$) and moreover is that f which gives to $Q(u+fg_0\ldots h_0)/N(u+fg_0\ldots h_0)$ its least value. Keeping $f=f_1$ fixed, the "best" $g=g_1$ is then determined, by solving the equation corresponding to (**2**) for g, in which the functions other than f and g are kept fixed at the same values as before. It may again be unnecessary to get a strictly self-consistent solution for g, that is, it may be sufficient to form Q/N for $(u+f_1g_0\ldots h_0)$ and treat it as a constant. The process is then repeated for each of the n functions up to $h(z)$, and the cycle then repeated as many times as is necessary to obtain reasonable convergence. The functions finally obtained, f_ω, $g_\omega, \ldots, h_\omega$, (say), determine new approximations $v_1=u+f_\omega g_\omega\ldots h_\omega$ and $Q(v_1)/N(v_1)$ to the lowest eigenfunction and eigenvalue of (**1**). Denoting the kth improved approximation by

$v_k(x, y, \ldots, z)$, v_k would be expected to converge to the lowest eigenfunction as $k \to \infty$, since this can be expressed exactly by means of a series

$$u(x, y, \ldots, z) + \sum_{k=1}^{\infty} f_k(x) g_k(y) \ldots h_k(z),$$

as noted in the introduction.

So that the numerical integrations may be practicable, $u(x, y, \ldots, z)$ and $\mathscr{H} = \mathscr{H}(x, y, \ldots, z)$ must be expressed as sums of products of functions of (or operators on) one variable. $\mathscr{H}$ could in general be so expressed only by an infinite series, which would have to be terminated in numerical work.

III. FORMULATION AS A METHOD OF SOLVING A NUMERICAL FORM OF EQUATION (1)

The method will now be reformulated, taking the same eigenvalue problem (**1**) as starting point. In this formulation the function is replaced by a vector, corresponding to a possible numerical representation of it, and the operation of differentiation of a function replaced by multiplication of the vector by a suitable matrix, which produces the appropriate finite-difference operation. There are two reasons for undertaking this second formulation. The first is to obtain a clear insight into the structure of the method, while avoiding the proverbial subtleties of the calculus of variations. While the results are obtained for one particular choice of numerical approximations, they can certainly be applied to any other sufficiently refined methods of numerical approximation which may be chosen. The second reason is that this formulation of the method could be used with advantage as it stands in the exploratory stages of the solution of a complicated problem, that is, for establishing " initial " estimates of the eigenfunction, in a way which is suggested by the example in Part II (Bassett 1959*a*).

In anticipation of the final aim, the solution of the wave equation, $\mathscr{H}$ in equation (**2**) will be taken to be of the form

$$-\frac{\partial^2}{\partial x^2} - \frac{\partial^2}{\partial y^2} - \ldots - \frac{\partial^2}{\partial z^2} + V(x, y, \ldots, z).$$

Let a function $v(x, y, \ldots, z)$ of N variables $x, y, \ldots, z$ defined in $-R \leqslant x \leqslant R$, $-R \leqslant y \leqslant R, \ldots, -R \leqslant z \leqslant R$ and vanishing on the boundaries of the region be represented by a function defined at only the r^N interior points

$$(-R+lh,\ -R+mh, \ldots, -R+ph) \quad l=1, 2, \ldots, r;\ m=1, 2, \ldots, r; \quad p=1, 2, \ldots, r. \qquad \ldots\ldots\ldots\ (\mathbf{3})$$

where $h = 2R/(r+1)$. The function so defined can be thought of as a vector of r^N elements. The function or vector will be written in the form $v(x, y, \ldots, z)$, which may be abbreviated to v; if it is convenient not to distinguish between the different kinds of elements of $v(x, y, \ldots, z)$ then it will be written $v(X)$, where X stands for the set of variables $x, y, \ldots, z$.

A function of one variable, of x say, defined in $-R \leqslant x \leqslant R$ and vanishing on the boundary is represented by a function defined at the r interior points

$$-R+lh \quad (l=1, 2, \ldots, r),$$

that is, by a vector of r elements, which will be written in the form $f(x)$. The second derivative can then be represented by $\sum_{x'} K(x, x')f(x')$ where $K(x, x')$ is the (x, x')th element of the symmetric $r \times r$ matrix

$$\begin{array}{cccccccc}
-2/h^2 & 1/h^2 & 0 & 0 & & & & \\
1/h^2 & -2/h^2 & 1/h^2 & 0 & \cdots & & & \\
0 & 1/h^2 & -2/h^2 & 1/h^2 & & & & \\
 & \cdots & & & & & \cdots & \\
 & & & & \cdots & 1/h^2 & -2/h^2 & 1/h^2 \\
 & & & & & 0 & 1/h^2 & -2/h^2.
\end{array}$$

For a function $v(x, y, \ldots, z)$ a representation of the Laplacian, the sum of the second derivatives with respect to each variable in turn, at any point (**3**) can likewise be obtained by multiplication by a symmetric $r^N \times r^N$ matrix: thus the sum of the second derivatives of $v(x, y, \ldots, z)$ is represented by

$$\sum_{x', y', \ldots, z'} L(x, y, \ldots, z;\ x', y', \ldots, z')v(x', y', \ldots, z'),$$

where

$$\begin{aligned} L(x, y, \ldots, z;\ x', y', \ldots, z') &= L(x', y', \ldots, z';\ x, y, \ldots, z) \\ &= K(x, x')\delta yy' \ldots \delta zz' + \delta xx' K(y, y') \ldots \delta zz' + \ldots + \delta xx' \delta yy' \ldots K(z, z'). \end{aligned}$$

From here on H is taken to be minus the above expression, plus the expression

$$V(x, y, \ldots, z)\delta xx' \delta yy' \ldots \delta zz',$$

which is a diagonal matrix. Using the X notation, the function obtained by operating on $v(x)$ with H is $\sum_{X'} H(X, X')v(X')$.

The integral of a function $v(x, y, \ldots, z)$ defined in $-R \leqslant x \leqslant R, \ldots, -R \leqslant z \leqslant R$ and vanishing on the boundaries is taken to be represented by

$$h^N \sum_x \sum_y \ldots \sum_z v(x, y, \ldots, z) = h^N \sum_X v(X),$$

the summation extending over the interior points (**3**).

Consider now the quotient of quadratic forms

$$\frac{\displaystyle\sum_{x, y, \ldots, z} \sum_{x', y', \ldots, z'} v(x, y, \ldots, z)H(x, y, \ldots, z;\ x', y', \ldots, z')v(x', y', \ldots, z')}{\displaystyle\sum_{x, y, \ldots, z} v^2(x, y, \ldots, z)}$$

or

$$\frac{\displaystyle\sum_X \sum_{X'} v(X)H(X, X')v(X')}{\displaystyle\sum_X v^2(X)}. \qquad \ldots\ldots\ldots\ldots\ldots\ldots \quad (4)$$

The expression (**4**) takes on its least value for a vector $v(X)$ which is a lowest eigenvector of H. That is, $v(X)$ is a solution of the equations

$$\sum_{X'} H(X, X')v(X') = \Lambda v(X) \qquad \ldots\ldots\ldots\ldots\ldots \quad (5)$$

with the least eigenvalue Λ.

Our task may now be stated exactly. It is to lay down a rule for getting a sequence

$$v_1(X),\ v_2(X),\ v_3(X),\ .\ .\ .$$

of vectors which converges to the lowest eigenvector of (5). It is assumed in this paper that there is only one such eigenvector, i.e. that the lowest eigenvalue is non-degenerate.

It is convenient to rewrite (4) using the notation

$$\begin{aligned}\sum_{x',\,y',\,\ldots,\,z'} & H(x, y, \ldots, z;\ x', y', \ldots, z')v(x', y', \ldots, z')\\ & = Hv(x, y, \ldots, z),\end{aligned}$$

so that (4) becomes

$$\frac{\displaystyle\sum_{x,\,y,\,\ldots,\,z} v(x, y, \ldots, z)Hv(x, y, \ldots, z)}{\displaystyle\sum_{x,\,y,\,\ldots,\,z} v^2(x, y, \ldots, z)}. \quad \ldots\ldots\ldots\ldots \quad (6)$$

$h^N\sum_X v(X)Hv(X)$ and $h^N\sum_X v^2(X)$ will sometimes be written $Q(v)$ and $N(v)$. The expression (6) formed for $v(x, y, \ldots, z)=u(x, y, \ldots, z)+f(x)g_0(y)\ldots h_0(z)$ takes on its least value, for given functions u and $g_0, \ldots, h_0$, for a function f which satisfies

$$\delta\{Q(u+fg_0\ldots h_0)/N(u+fg_0\ldots h_0)\}=0$$

for r independent variations δf of f

$$\begin{aligned}\frac{1}{h^N}\delta Q &= \delta \sum_{x,\,y,\,\ldots,\,z} (u+fg\ldots h)H(u+fg\ldots h)\\ &= \sum_{x,\,y,\,\ldots,\,z} (2\delta fg\ldots hHu+2\delta fg\ldots hHfg\ldots h),\\ \frac{1}{h^N}\delta N &= \delta \sum_{x,\,y,\,\ldots,\,z} (u+fg\ldots h)^2\\ &= 2\sum_{x,\,y,\,\ldots,\,z} \delta f(ug\ldots h+fg^2\ldots h^2).\end{aligned}$$

$\delta(Q/N)=0$ if and only if $\delta Q-(Q/N)\delta N=0$, that is,

$$\sum_{x,\,y,\,\ldots,\,z} \delta f\{g\ldots hHu+g\ldots hHg\ldots hf-(Q/N)ug\ldots h-(Q/N)fg^2\ldots h^2\}=0.$$

This equation, formed for r independent functions δf, is equivalent to

$$\begin{aligned}&\Big(\sum_{y\ldots z} g\ldots hHg\ldots h\Big)f-(Q/N)\Big(\sum_{y\ldots z} g^2\ldots h^2\Big)f\\ &\qquad +\sum_{y\ldots z} g\ldots hHu-(Q/N)\sum_{y\ldots z} g\ldots hu=0. \quad \ldots \quad (7)\end{aligned}$$

The transformation just carried out depends on the fact that H is symmetric. Equation (7), the central equation of the method, is the "numerical" analogue of equation (2).

The lemma and theorems 1 and 2 below lead up to theorem 3, which states that the solution f of equation (7) is, subject to certain restrictions, that f which gives to Q/N its least possible value.

Lemma. Let $H(X, X')$ be the (X, X')th element of a symmetric $m \times m$ matrix, $v = v(X)$ an m-rowed vector,

$$Q(v) = h^N \sum_{X, X'} v(X) H(X, X') v(X') = h^N \sum_X v(X) H v(X) = (v, Hv),$$

and

$$N(v) = h^N \sum_X v^2(X) = (v, v).$$

If $u = u(X)$ is also an m-rowed vector, and γ is a variable number, $Q(u+\gamma v)/N(u+\gamma v)$ cannot have a local proper minimum with respect to γ for two different values of γ.

Proof. Suppose that two such values of γ exist. We may take one value as zero, and for the other we may assume that

$$Q(u+\gamma v)/N(u+\gamma v) \leqslant Q(u)/N(u). \quad \ldots\ldots\ldots\ldots \quad (8)$$

Now $Q(u+\gamma v) = Q(u) + 2\gamma(v, Hu) + \gamma^2 Q(v)$ and $N(u+\gamma v) = N(u) + 2\gamma(v, u) + \gamma^2 N(v)$. Since Q/N is stationary at $\gamma = 0$,

$$(u, Hv) - Q(u)/N(u)(u, v) = 0, \quad \ldots\ldots\ldots\ldots\ldots \quad (9)$$

and, at $\gamma = 0$,

$$\frac{\mathrm{d}^2 Q/N}{\mathrm{d}\gamma^2} = \frac{1}{N}\left(\frac{\mathrm{d}^2 Q}{\mathrm{d}\gamma^2} - \frac{Q}{N}\,\frac{\mathrm{d}^2 N}{\mathrm{d}\gamma^2}\right).$$

The last equation implies that

$$Q(v) - \{Q(u)/N(u)\} N(v) \geqslant 0. \quad \ldots\ldots\ldots\ldots \quad (10)$$

The inequality (8) is equivalent to

$$Q(u) + 2\gamma(v, Hu) + \gamma^2 Q(v) \leqslant Q(u) + 2\gamma\{Q(u)/N(u)\}(u, v) + \gamma^2\{Q(u)/N(u)\} N(v),$$

that is, using (9),

$$\gamma^2 Q(v) \leqslant \gamma^2 \{Q(u)/N(u)\} N(v).$$

From this and equation (10) $Q(v)/N(v) = Q(u)/N(u)$ which implies that $\mathrm{d}^2(Q/N)/\mathrm{d}\gamma^2$ vanishes at $\gamma = 0$. Now Q/N has the form $(a + b\gamma + c\gamma^2)/(a' + b'\gamma + c'\gamma^2)$ and if the first and second derivatives of this function of γ vanish at $\gamma = 0$ then $a/a' = b/b' = c/c'$. Hence Q/N is independent of γ and cannot have a proper minimum with respect to γ.

Theorem 1

Let us write $\Lambda(v) = Q(v)/N(v)$ for any function v. Let $\xi = \xi(x)$ denote a function of x. Let

$$\left.\begin{aligned} &\frac{\mathrm{d}}{\mathrm{d}t}\Lambda\{u + (f + t\xi)g \,.\,.\,.\, h\}\Big|_{t=0} = 0, \\ \text{and} \quad &\frac{\mathrm{d}^2}{\mathrm{d}t^2}\Lambda\{u + (f + t\xi)g \,.\,.\,.\, h\}\Big|_{t=0} > 0. \end{aligned}\right\} \quad \ldots\ldots\ldots \quad (11)$$

Let *every* $\xi(x)$ satisfy equations (11), for $f = {}'f$. Then the same cannot be true for $f = {}''f$ unless ${}'f$ and ${}''f$ are identically equal.

Proof. Let us suppose that the theorem is false, and its conditions are satisfied by $'f$ and by $''f$, where $'f$ and $''f$ are not identically equal. Then

$$\frac{\mathrm{d}}{\mathrm{d}\alpha}\Lambda\{u+('f+\alpha(''f-'f))g\ldots h\}\Big|_{\alpha=0}=0,$$
$$\frac{\mathrm{d}^2}{\mathrm{d}\alpha^2}\Lambda\{u+('f+\alpha(''f-'f))g\ldots h\}\Big|_{\alpha=0}>0,$$
$$\frac{\mathrm{d}}{\mathrm{d}\beta}\Lambda\{u+(''f+\beta('f-''f))g\ldots h\}\Big|_{\beta=0}=0,$$
$$\frac{\mathrm{d}^2}{\mathrm{d}\beta^2}\Lambda\{u+(''f+\beta('f-''f))g\ldots h\}\Big|_{\beta=0}>0.$$

Hence, writing $\alpha=t$, $\beta=1-t$, we find that

$$\Lambda\{u+('f+t(''f-'f))g\ldots h\}$$

has a proper local minimum with respect to t for $t=0$ and $t=1$, which contradicts the lemma.

Theorem 2

If the functions $u(x, y, \ldots, z)$ and $g(y), \ldots, h(z)$ are given and

$$\Lambda(u)<\min_{\alpha,\beta,\ldots,\gamma}\Lambda\{\alpha(x)\beta(y)\ldots\gamma(z)\},$$

there is a function $f=f(x)$ for which $\Lambda\{u+f(x)g(y)\ldots h(z)\}$ assumes its least possible value. For this function f, Λ is stationary.

Proof. Since $\Lambda(v)$ is bounded below as v varies, $\Lambda(u+fg\ldots h)$ is certainly bounded below as f varies. Let l be the greatest lower bound of Λ as f varies. Then a sequence f_n exists such that $\Lambda(u+f_ng\ldots h)\to l$. If $\sum_x f_n^2(x)\to\infty$, then $\Lambda(f_ng\ldots h)\to l$, which contradicts the hypothesis. Hence $\sum_x f_n^2(x)$ is bounded, and so possesses at least one limit point, $f(x)$ say, for which $\Lambda(u+fg\ldots h)=l$, since Λ is a continuous function of the elements of f. The rest of the theorem may be deduced from the fact that Λ is a rational function in the elements of f.

Theorem 3

Let the functions $u(x, y, \ldots, z)$ and $g(y), \ldots, h(z)$ be given, and let $\Lambda(u)\leqslant\min_{\alpha,\beta,\ldots,\gamma}\Lambda\{\alpha(x)\beta(y)\ldots\gamma(z)\}$. Let $\Lambda\{u+f(x)g(y)\ldots h(z)\}<\Lambda(u)$ and let Λ be stationary with respect to f. There is only one function f which satisfies these conditions, and that gives to Λ its least possible value.

Proof. It is sufficient to show that, under the hypotheses of the theorem,

$$\frac{\mathrm{d}^2}{\mathrm{d}t^2}\Lambda\{u+(f+t\xi)g\ldots h\}\Big|_{t=0}>0$$

for any ξ. Since Λ is stationary with respect to f,

$$\frac{\mathrm{d}}{\mathrm{d}t}\Lambda\{u+(f+t\xi)g\ldots h\}\Big|_{t=0}=0.$$

It follows that

$$\frac{d^2\Lambda}{dt^2}\bigg|_{t=0}=\frac{1}{N}\left(\frac{d^2Q}{dt^2}\bigg|_{t=0}-\Lambda\frac{d^2N}{dt^2}\bigg|_{t=0}\right),$$

that is,

$$\frac{d^2\Lambda}{dt^2}\bigg|_{t=0}=\frac{1}{N(u+fg\ .\ .\ .\ h)}\{Q(\xi g\ .\ .\ .\ h)-\Lambda(u+\xi g\ .\ .\ .\ h)N(\xi g\ .\ .\ .\ h)\}.$$

By hypothesis, $Q(\xi g\ .\ .\ .\ h)/N(\xi g\ .\ .\ .\ h)=\Lambda(\xi g\ .\ .\ .\ h)>\Lambda(u+fg\ .\ .\ .\ h)$. Hence

$$\frac{d^2\Lambda}{dt^2}\bigg|_{t=0}>0.$$

IV. CONVERGENCE

There are three kinds of sequence of solutions (each member of a sequence giving an eigenvalue estimate) which the method prescribes : (i) the sequence of solutions f of equation (**7**) (of which it may be sufficient, for practical purposes, to take the first member) which should converge to a " self-consistent " solution ; (ii) the cyclic sequence of self-consistent solutions $f, g, .\ .\ .\ h, f, g, .\ .\ .\ h, .\ .\ .$ of equation (**7**) and its analogues ; (iii) the sequence of partial sums in the series expression for the eigenfunction.

In the example of Part II all three sequences converge, the first so rapidly that the first member of the sequence is sufficient.

(i) In the form which the stationary condition (**7**) assumes for a wave mechanical problem (Part III, Bassett 1959*b*), if it is looked on as a differential equation for f, the " constants " depend on f in first order. The equation is similar in this respect to the equation for the radial dependence of a one-electron function in the Hartree-Fock method with superposition of configurations (Hartree 1957) and so convergence can probably be attained in practice. In the stationary condition (**7**) itself, which applies to an eigenvalue problem without symmetry restrictions, the dependence of the " constants " on the solution is only second order, as only Q/N is so dependent, and no difficulty would be expected with convergence.

(ii) The convergence of the eigenvalue estimates belonging to the sequence (ii) is ensured by theorem 3, which shows that these eigenvalue estimates form a monotonic decreasing sequence, which is certainly bounded below, and if the product $fg\ .\ .\ .\ h$ does not converge, it must approach a range of equally acceptable functions.

(iii) The completeness of a suitable set of products of functions of one variable argues strongly, if loosely, for convergence of the sequence (iii), but the matter will be settled best by practical trial.

V. ACKNOWLEDGMENTS

The author would like to thank Dr. A. C. Hurley, Professor T. M. Cherry, and Mr. Bruce Craven for reading the manuscript at various stages of completeness and for making many helpful suggestions, and Dr. M. V. Wilkes for a germinal conversation.

VI. References

Bassett, I. M. (1959*a*).—*Aust. J. Phys.* **12**: 441.

Bassett, I. M. (1959*b*).—*Aust. J. Phys.* **12**: 449.

Boys, S. F., and Price, V. E. (1954).—*Phil. Trans.* A **246**: 451.

Courant, R., and Hilbert, D. (1953).—"Methods of Mathematical Physics." (Interscience: New York.)

Hartree, D. R. (1957).—"The Calculation of Atomic Structures." p. 16. (Chapman and Hall: London.)

Löwdin, P.-O. (1955).—*Phys. Rev.* **97**: 1474.

Shull, H., and Löwdin, P.-O. (1959).—*J. Chem. Phys.* **30**: 617.

Slater, J. C. (1953).—*Phys. Rev.* **91**: 528.

TOWARDS A METHOD FOR THE ACCURATE SOLUTION OF THE SCHRÖDINGER WAVE EQUATION IN MANY VARIABLES

II. A SIMPLE NUMERICAL ILLUSTRATION

By I. M. Bassett*

[*Manuscript received June 26, 1959*]

Summary

The method described in Part I is here applied to an eigenvalue problem in two variables

$$\mathscr{H}\psi(x,y)=\lambda\psi(x,y).$$

The results show that an accurate estimate of the fundamental eigenvalue (to seven significant figures) and eigenfunction can be obtained for this problem with only four terms in the series expression for ψ,

$$\psi=\sum_k a_k(x)b_k(y).$$

An application of the Rayleigh-Ritz method to the same problem gives a four-term solution of much lower accuracy (Table 5). The example shows that the individual functions a_k and b_k are not uniquely determined. It shows that a calculation based on a coarse interval can provide good initial estimates of the $a_k(x)$ and $b_k(y)$ and, moreover, predict the accuracy of the corresponding solution obtainable without numerical approximation.

I. Numerical Illustration

The method† described in Part I‡ has been applied to the equation

$$(-\partial^2/\partial x^2-\partial^2/\partial y^2+9xy)v(x,y)=\lambda v(x,y),$$

where the eigenfunction $v(x,y)$ is defined within and vanishes on the boundary of the square $0\leqslant x\leqslant 1$, $0\leqslant y\leqslant 1$. Three values of h were used, $\frac{1}{8}$, $\frac{1}{16}$, and $\frac{1}{32}$.

---

* Chemistry Department, University of Melbourne ; present address : Chemistry Department, University of Illinois, Urbana, Ill., U.S.A.

† In the second formulation, given in Section III, Part I, in which it is formulated as a method of solving a numerical form of the eigenfunction problem.

‡ Bassett, I. M. (1959).—*Aust. J. Phys.* **12** : 430.

For $h=\frac{1}{8}$, the matrix H is the 49×49 matrix :

$$\begin{array}{cccccccccc}
\frac{-4}{h^2}+\frac{3}{8}\cdot\frac{3}{8} & & & & & & & 1/h^2 & & \\
 & \frac{-4}{h^2}+\frac{3}{8}\cdot\frac{6}{8} & & & & & & & 1/h^2 & \\
 & & \frac{-4}{h^2}+\frac{3}{8}\cdot\frac{9}{8} & & & & & & & \\
 & & & \frac{-4}{h^2}+\frac{3}{8}\cdot\frac{12}{8} & & & & & & \cdots \\
 & & & & \frac{-4}{h^2}+\frac{3}{8}\cdot\frac{15}{8} & & & & & \\
 & & & & & \frac{-4}{h^2}+\frac{3}{8}\cdot\frac{18}{8} & & & & \\
 & & & & & & \frac{-4}{h^2}+\frac{3}{8}\cdot\frac{21}{8} & & & \\
1/h^2 & & & & & & & \frac{-4}{h^2}+\frac{6}{8}\cdot\frac{3}{8} & & \\
 & 1/h^2 & & & & & & & \frac{-4}{h^2}+\frac{6}{8}\cdot\frac{6}{8} & \\
 & & & & & & & & & \cdots \\
 & & \cdots & & & & & & &
\end{array}$$

in which the zeros have been omitted.

The equation to be solved for f, namely,

$$\sum_y gHgf-\Lambda\sum_y g^2f+\sum_y gHu-\Lambda\sum_y gu=0,$$

becomes

$$-f''\sum_y g^2+f\Big(-\sum_y g''g+9x\sum_y g^2y-\Lambda\sum_y g^2\Big)$$
$$+\sum_k\Big\{-a_k\sum_y gb_k''-a_k''\sum_y gb_k+9a_kx\sum_y gb_ky-\Lambda a_k\sum_y gb_k\Big\}=0,$$

where $u(x,y)=\sum_k a_k(x)b_k(y)$ and f'' stands for the vector whose jth element is

$$(1/h^2)[f\{(j-1)h\}-2f(jh)+f\{(j+1)h\}].$$

If the last equation is rewritten in the form

$$f''+p(x)f(x)+q(x)=0,$$

after dividing through by $-\sum_y g^2$, then the elements of f are the solution of

$$-2f(h)+f(2h)+h^2p(h)f(h)+h^2q(h)=0,$$
$$f(h)-2f(2h)+f(3h)+h^2p(2h)f(2h)+h^2q(2h)=0,$$
$$f(2h)-2f(3h)+f(4h)+h^2p(3h)f(3h)+h^2q(3h)=0,$$
$$\cdots$$
$$-2f(rh)+f\{(r-1)h\}+h^2p(rh)f(rh)+h^2q(rh)=0.$$

Results of the calculations are shown in Tables 1–5.

TABLE 1

$h=\frac{1}{8}$

	$a_0=b_0$	Term 1			Term 2			Term 3		
		$\bar{a}_1$	$\bar{b}_1$	g_0	$\bar{a}_2$	$\bar{b}_2$	g_0	$\bar{a}_3$	$\bar{b}_3$	g_0
	0·3827	0·125	0·125	0·64775962	—0·125	0·125	0·01	0·125	0·125	0·01
	0·7071	0·2272427654	0·2272948014	1·14374253	—0·164159598	0·166741626	0·01	0·15647423	0·17322713	0·01
	0·9239	0·2903877106	0·2905471896	1·40105055	—0·105516293	0·113146656	0·01	0·13417524	0·16026166	0·01
	1·0000	0·3065020806	0·3067841048	1·40476502	0·010737892	0·002453142	0·01	0·12259124	0·14493200	0·01
	0·9239	0·2760799732	0·2764400832	1·19617773	0·121094932	—0·104475358	0·01	0·14270564	0·15765280	0·01
	0·7071	0·2065678800	0·2069098306	0·84767007	0·167524435	—0·151795674	0·01	0·15328570	0·16994080	0·01
	0·3827	0·1099309538	0·1101422600	0·43193433	0·121350239	—0·111596213	0·01	0·10631966	0·12476700	0·01
Modulus of first element		1·31561279	0·75260925		0·17604305	0·12488933		0·05871633	0·00588043	
Q	5·43443226	263·37321470			263·36285907			263·41846382		
N	0·250010228	12·14228421			12·14271222			12·14527603		
Q/N	21·7368397	21·69058227			21·68896489			21·68896475		
Number of cycles ..		10			$3\frac{1}{2}$			5		
Mean square residual	1·408	0·09045			0·00001574			0·000001207		
Root mean square residual	1·187	0·3007			0·003967			0·001099		

Table 2

$h=\frac{1}{32}$

$a_0=b_0$	Term 1			Term 2			Term 3		
	$\bar{a}_1$	$\bar{b}_1$	g_0	$\bar{a}_2$	$\bar{b}_2$	g_0	$\bar{a}_3$	$\bar{b}_3$	g_0
0·0980	0·03125	0·03125	0·071574	—0·03125	0·03125	0·036241	0·03125	0·03125	0·00174273
0·1951	0·0621216443	0·0621248084	0·141453	—0·0607994448	0·0609203250	0·069125	0·061077129	0·060915748	0·00331087
0·2902	0·0922642635	0·0922737323	0·210395	—0·0873194620	0·0877365696	0·099687	0·079362905	0·087632960	0·00475409
0·3827	0·1213152603	0·1213401183	0·276127	—0·1096142003	0·1106376143	0·124819	0·100155996	0·110364443	0·00592337
0·4714	0·1489737318	0·1490202186	0·339297	—0·1269819229	0·1289021393	0·144981	0·108404481	0·128376227	0·00682318
0·5555	0·1749409837	0·1750168388	0·397962	—0·1388694202	0·1420137271	0·158795	0·107220891	0·141451815	0·00744015
0·6344	0·1989363265	0·1990524081	0·452619	—0·1449252516	0·1496710412	0·166197	0·107698016	0·149630178	0·00773929
0·7071	0·2207376205	0·2209014152	0·501779	—0·1451838148	0·1518447289	0·167380	0·099677205	0·153412671	0·00782561
0·7730	0·2401328703	0·2403525962	0·545790	—0·1397785321	0·1486600345	0·161872	0·089440800	0·153461643	0·00764220
0·8315	0·2569470834	0·2572303943	0·583606	—0·1290546694	0·1404252755	0·151091	0·080175949	0·150741236	0·00735981
0·8819	0·2710496613	0·2714009997	0·615422	—0·1135799193	0·1276219969	0·134264	0·066745610	0·146253338	0·00691877
0·9239	0·2823233882	0·2827479612	0·640657	—0·0939527258	0·1108202615	0·113709	0·059271230	0·141043304	0·00649813
0·9569	0·2907087287	0·2912071703	0·659351	—0·0710114323	0·0907408213	0·088466	0·049317375	0·136095476	0·00605303
0·9808	0·2961529187	0·2967266055	0·671381	—0·0455405185	0·0681324615	0·061413	0·047918138	0·132260950	0·00571808
0·9952	0·2986596875	0·2993054439	0·676650	—0·0185123656	0·0438460719	0·031524	0·047216460	0·130200443	0·00547472
1·0000	0·2982501533	0·2989629765	0·675446	+0·0091396180	0·0187367925	0·001877	0·049011910	0·130316140	0·00537865
0·9952	0·2949738891	0·2957470624	0·667550	+0·0364796896	—0·0063348919	—0·028513	0·055189196	0·132789238	0·00544302
0·9808	0·2889133484	0·2897373038	0·653621	+0·0625610820	—0·0305136239	—0·056687	0·062862604	0·137454864	0·00562836
0·9569	0·2801753820	0·2810379566	0·633341	0·0864836739	—0·0529831778	—0·083487	0·069321477	0·143886959	0·00597631
0·9239	0·2688761953	0·2697656294	0·607666	0·1074839441	—0·0730117453	—0·106388	0·081709045	0·151443987	0·00636195
0·8819	0·2551766424	0·2560767015	0·576199	0·1247559865	—0·0898973721	—0·126004	0·088556873	0·159199149	0·00684469
0·8315	0·2392289389	0·2401247555	0·540129	0·1377397817	—0·1030845260	—0·140492	0·098203070	0·166114233	0·00724633

TABLE 2 (*Continued*)

	$a_0 = b_0$	Term 1			Term 2			Term 3		
		$\bar{a}_1$	$\bar{b}_1$	g_0	$\bar{a}_2$	$\bar{b}_2$	g_0	$\bar{a}_3$	$\bar{b}_3$	g_0
	0·7730	0·2212243197	0·2220977013	0·499011	0·1458723800	—0·1120821827	—0·150161	0·100863513	0·171063081	0·00762817
	0·7071	0·2013458858	0·2021800389	0·454184	0·1488400165	—0·1165653912	—0·154085	0·102371152	0·172853833	0·00780633
	0·6344	0·1797972054	0·1805749120	0·405178	0·1464272821	—0·1163277042	—0·152206	0·100627142	0·170405425	0·00782438
	0·5555	0·1567930324	0·1574962466	0·353403	0·1385657697	—0·1113064413	—0·144702	0·090641957	0·162827583	0·00755159
	0·4714	0·1325311018	0·1331459924	0·298374	0·1254823944	—0·1016438153	—0·131114	0·084106310	0·149395111	0·00699514
	0·3827	0·1072397948	0·1077512310	0·241550	0·1074451315	—0·0875996927	—0·112820	0·071396304	0·129794790	0·00613349
	0·2902	0·0811374706	0·0815315836	0·182467	0·0849766464	—0·0696362033	—0·088895	0·050644888	0·104160069	0·00492102
	0·1951	0·0544171921	0·0546866907	0·122514	0·0589339328	—0·0484529881	—0·062116	0·037541913	0·073100040	0·00349462
	0·0980	0·0273073794	0·0274436751	0·061692	0·0301869423	—0·0248751081	—0·032485	0·017805372	0·037763715	0·00185428
Modulus of first element		0·61244964	0·10705947		0·04671489	0·03742186		0·01782422	0·00153148	
Q . .	5·49321185	268·34276156			268·33665109			268·37386641		
N . .	0·24999404	12·23648429			12·23706945			12·23876670		
Q/N . .	21·973371	21·92972713			21·92817914			21·92817895		
Mean sq. residual	1·45	0·0915			0·0000428			0·00000449		
Root mean sq. res.	1·20	0·303			0·00654			0·00212		
Number of cycles . .		2			2			1		

TABLE 3

$h=\frac{1}{8}$ AND $h=\frac{1}{16}$

	$h=\frac{1}{8}$			$h=\frac{1}{16}$		
	$\bar{a}_1$	$\bar{b}_1$	g_0	$\bar{a}_1$	$\bar{b}_1$	g_0
	0·125	—0·125	0·2	0·0625	—0·0625	0·0625
	0·2567267570	—0·25671942	0·2	0·1268290283	—0·1268266729	0·1303710
	0·3805350478	—0·38051271	0·2	0·1930585893	—0·1930501860	0·2056846
	0·4656209639	—0·46558162	0·2	0·2607784330	—0·2607594424	0·2893524
	0·4789506184	—0·47890051	0·2	0·3268765612	—0·3268430642	0·3772544
	0·3990173670	—0·39896985	0·2	0·3876155807	—0·3875648942	0·4638023
	0·2287914444	—0·22876210	0·2	0·4387724283	—0·4387036028	0·5421943
				0·4756925444	—0·4756067925	0·6045265
				0·4941653416	—0·4940660623	0·6432952
				0·4905300346	—0·4904227652	0·6516494
				0·4625313841	—0·4624232590	0·6249084
				0·4093291761	—0·4092284337	0·5606269
				0·3321804714	—0·3320954907	0·4598159
				0·2348250951	—0·2347632457	0·3277130
				0·1216740439	—0·1216414385	0·1706619
Modulus of first element ..	0·091266394	0·125000000		0·06527578	0·03949496	
Q	3·854003014			3·96983820		
N	0·177694173			0·18143552		
Q/N	21·688967			21·880160		
No. of cycles ..	$4\frac{1}{2}$			10		
Mean square residual	0·000261					
R.M.S. residual ..	0·0162					

TABLE 4

VALUES OF Λ AND DECREMENTS, CORRESPONDING TO SUCCESSIVE TERMS

	Term 0	Term 1	Term 2	Term 3
First solution (Tables 1 *and* 2)				
$h=\frac{1}{8}$	21·7368398	21·69058227 0·0463	21·68896489 0·00162	21·68896475 $1\cdot4\times10^{-7}$
$h=\frac{1}{16}$	21·9258745	21·8817581 0·0441	21·8801570 0·00160	21·8801570 0×10^{-7}
$h=\frac{1}{32}$	21·973371	21·92972713 0·0436	21·92817914 0·00155	21·92817895 $1\cdot9\times10^{-7}$
Second solution (Table 3)				
$h=\frac{1}{8}$	21·7368398	21·688967 0·0479		
$h=\frac{1}{16}$	21·9258745	21·880160 0·0457		

TABLE 5

COMPARISON OF MEAN SQUARE RESIDUALS OBTAINED BY THE RAYLEIGH-RITZ METHOD AND THE PRESENT METHOD

	Term 0	Term 1	Term 2	Term 3
Rayleigh-Ritz method ..	1·4	0·73	0·073	0·011
Present method ($h=\frac{1}{32}$) ..	1·4	0·092	0·000043	0·0000045

The approximate solution which is first guessed (the zeroth term) is written $a_0(x)b_0(y)$. a_0 and b_0 are equal, and are the values of $\sin \pi x$, $\sin \pi y$ at the lattice points. This choice was made since $\sin \pi x \sin \pi y$ is the exact solution of the original problem with the term $9xy$ omitted. The notation $\bar{a}_1$ means $a_1 h/|\, a_1(h)\,|$ that is, the vector obtained from a_1 by dividing by the modulus of the first element, and then multiplying by h. The moduli of the first elements are given and the vectors themselves can be calculated from these. The "number of cycles" is one if, from the initially assumed g_0, one f has been determined, and from that a new g; a cycle is a determination of an f *and* a g. The "mean square residual" is

$$\sum_{xy} (Hv-\Lambda v)^2 / \sum_{xy} v^2,$$

and the square root of this is the "root mean square residual". For $h=\frac{1}{8}$ the mean square residual was calculated from the residuals—the 7^2 individual values of $Hv-\Lambda v$. For $h=\frac{1}{32}$ the mean square residual was calculated from integrals, using the identity

$$\sum_{xy} (Hv-\Lambda v)^2 = \sum_{xy} (Hv)^2 - \Lambda Q.$$

Calculation by this method, as the mean square residual is small and Q is large, provided a sensitive check on arithmetic errors in the calculation of Λ.

The character of the solution is essentially independent of h. The shapes of the functions a_k, the sizes of the mean square residuals, the rapidity of convergence of the iterative process for determining the products $a_k(x)b_k(y)$, and the decrements of Λ (Table 4) all point to this conclusion.

These same properties would certainly persist no matter how small h were taken, so that an expression of the form

$$\sum_0^3 a_k(x)b_k(y)$$

would provide a solution of the original problem of similar accuracy. This illustrates, too, that calculations based on a coarse interval can provide good initial estimates of the eigenfunction for a refined calculation, and can be used to predict the accuracy of that refined calculation, the truncation error associated with the coarseness of the interval being irrelevant to that prediction.*

---

* The further refinement of the solution was not undertaken, as lack of computing facilities made the labour seem not worth while, in view of the strong indications already obtained that the accuracy and other characteristics of the solution are independent of h.

Two different solutions to the problem were obtained from different g_0's used in the calculation of the first term $a_1(x)b_1(y)$. One solution is shown in Tables 1 and 2 and the other in Table 3. Note that the existence of two solutions does not contradict theorem 3 (Part I).

The cyclic improvement of f and g was stopped when it seemed that no essential further changes would take place. While the vectors $a_1(x)$, $b_1(y)$ at which $\Lambda(a_0b_0+a_1b_1)$ is stationary with respect to a_1 and b_1 evidently satisfy $a_1(t)=\pm b_1(t)$, $a_1(x)$ and $b_1(y)$ were left in the slightly unsymmetrical form in which they were got.

A rough idea of the degree of accuracy of the eigenvector can be got from the magnitude of the root mean square residual. Since Λ is approximately 20, if the absolute values of the errors in v cluster around 10^{-4}, the root mean square residual must be about 2×10^{-3}. Since this is the approximate size of the root mean square residual to the third term for $h=\frac{1}{8}$ and $h=\frac{1}{32}$, the eigenvector to the third term must be right to about one part in 10,000 (the table of residuals for $h=\frac{1}{8}$ and samples of the residuals for $h=\frac{1}{32}$ showed the error to be fairly uniformly spread over the eigenvector). An approximate upper limit on the absolute error in the eigenvalue estimate can also be set in the following way: for $h=\frac{1}{8}$ and $h=\frac{1}{32}$ the third term reduces the mean square residuals by a factor of about 10, and probably reduces the error in the eigenvalue estimate by a similar factor. Those figures in the eigenvalue estimates which are unchanged by the third terms, namely, 21·688965 and 21·928179, are therefore probably correct; both are almost certainly correct to seven significant figures; this is supported by the coincidence to seven significant figures in the case of $h=\frac{1}{8}$ of the eigenvalue estimate belonging to the other solution (Table 3).

The mean square residuals obtained in a Rayleigh-Ritz calculation are shown in Table 5. For the zeroth term, $\sin\pi x\sin\pi y$ was used, and the subsequent terms were multiples of $\sin\pi x\sin 2\pi y$, $\sin 2\pi x\sin\pi y$, and $\sin 2\pi x\sin 2\pi y$ respectively; the solution to term 3 is the best linear combination of these four functions.

The accuracy obtained by the present method, and the comparison with the Rayleigh-Ritz method, are both satisfactory, but the evidence is of course not weighty. The main function of this example is to show that the equations developed are formally correct and that the method can work in a simple case.

II. ACKNOWLEDGMENTS

The author would like to thank Dr. A. C. Hurley for his helpful comments on the manuscript and would also like to thank the staff of the Melbourne University Computation Laboratory for their assistance.

TOWARDS A METHOD FOR THE ACCURATE SOLUTION OF THE SCHRÖDINGER WAVE EQUATION IN MANY VARIABLES

III. APPLICATION OF THE GENERAL METHOD TO THE WAVE EQUATION WITHOUT SPATIAL SYMMETRY

By I. M. Bassett*

[*Manuscript received June 26, 1959*]

Summary

The method of Part I is applied to the problem of finding the lowest antisymmetric eigenfunction of the wave equation for n electrons without spatial symmetry, and the lowest antisymmetric eigenfunction of given multiplicity. Knowledge of the multiplicity of the ground state is not needed. Theorem 3 of Part I, which proves the equivalence of the central stationary condition to a minimum condition, is extended to cover the present case.

I. Choice of the Spin Functions

The wave equation for n electrons moving in a field of atomic nuclei regarded as fixed point charges is, in atomic units,

$$\left(-\tfrac{1}{2}\sum_j \nabla_j^2 - \sum_\alpha \sum_j \frac{N_\alpha}{r_{\alpha j}} + \sum_{i<j} \frac{1}{r_{ij}}\right)\Psi = E\Psi, \quad \dots\dots\dots\dots (1)$$

where E is the energy, Ψ the wave function, and, if x_j, y_j, z_j are the Cartesian coordinates of the jth electron,

$$r_{ij} = \sqrt{\{(x_i - x_j)^2 + (y_i - y_j)^2 + (z_i - z_j)^2\}},$$

and, if x_α, y_α, z_α are the Cartesian coordinates of the αth nucleus, which bears the charge N_α,

$$r_{\alpha j} = \sqrt{\{(x_j - x_\alpha)^2 + (y_j - y_\alpha)^2 + (z_j - z_\alpha)^2\}},$$

and

$$\nabla_j^2 = \frac{\partial^2}{\partial x_j^2} + \frac{\partial^2}{\partial y_j^2} + \frac{\partial^2}{\partial z_j^2}.$$

We seek not merely a solution of (1), but a solution of (1) having a certain symmetry. The simplest prescription for this symmetry is that the wave function including spin is " antisymmetric ", i.e. is multiplied by -1 by an odd permutation of the electron indices. Let the spin coordinates of the n electrons be denoted by $s_1, s_2, \dots, s_n$. An arbitrary function

$$\Phi(x_1 y_1 z_1 s_1 x_2 y_2 z_2 s_2 \dots x_n y_n z_n s_n)$$

---

* Chemistry Department, University of Melbourne ; present address : Chemistry Department, University of Illinois, Urbana, Ill., U.S.A.

of space and spin coordinates can be expressed as an infinite series

$$\begin{aligned}\Phi&=\sum_k \xi_k\\ &=\sum_k f_{1k}(x_1)g_{1k}(y_1)h_{1k}(z_1)\sigma_{1k}(s_1)f_{2k}(x_2)g_{2k}(y_2)h_{2k}(z_2)\sigma_{2k}(s_2)\ldots f_{nk}(x_n)g_{nk}(y_n)h_{nk}(z_n)\sigma_{nk}(s_n),\end{aligned} \qquad \ldots\ldots\ldots\ldots \ (2)$$

where $\sigma_{jk}(s)=\delta_{s,\sigma_{jk}}$ and σ_{jk} may have the values $+1$ or -1. We shall write $\delta_{s,1}=\alpha(s)$ and $\delta_{s,-1}=\beta(s)$. If P is a permutation on the numbers $1, 2, \ldots, n$, let $\mathbf{O}_P$ denote the operation of permuting the electron indices in a function of space and spin. Let $\mathbf{Q}_R$ denote the operation of applying a rotation R to the spin coordinates alone. $\mathbf{O}_P$ and $\mathbf{Q}_R$ commute and we may express any function ξ of space and spin in the form

$$\xi=\xi^{(1)}+\xi^{(2)}+\ldots+\xi^{(S)}+\ldots,$$

where $\xi^{(S)}$ belongs to the irreducible representation $\mathsf{D}^{(S)}(R)$ of the rotation group with respect to $\mathbf{Q}_R$: that is, it has the symmetry with respect to $\mathbf{Q}_R$ which corresponds to the multiplicity S (Wigner 1931). Further, each $\xi^{(S)}$ can be written in the form ${}'\xi^{(S)}+{}''\xi^{(S)}$, where ${}'\xi^{(S)}$ is antisymmetric with respect to $\mathbf{O}_P$ and ${}''\xi^{(S)}$ contains no antisymmetric component, and both belong to $\mathsf{D}^{(S)}(R)$ with respect to $\mathbf{Q}_R$. Let $\mathbf{Q}_P$ denote the operation of applying a permutation to the spin coordinates alone. A function of spin which belongs to $\mathsf{D}^{(S)}(R)$ with respect to $\mathbf{Q}_R$ belongs to $A^{(S)}(P)$ with respect to $\mathbf{Q}_P$ where $A^{(S)}(P)$ is an irreducible representation of the permutation group whose character is the coefficient of $x^{\frac{1}{2}n-S}$ in

$$(1-x)(1+x^{\rho_1})(1+x^{\rho_2})\ldots(1+x^{\rho_\nu}),$$

where $\rho_1, \rho_2, \ldots, \rho_\nu$ are the cycle-lengths of P. Hence

$$\sum_P \chi^{(S)}(P)\mathbf{Q}_P\xi=\text{const.}\times\xi^{(S)},$$

where $\chi^{(S)}(P)$ is the character of P in $A^{(S)}(P)$, and

$$\sum_P \varepsilon_P\mathbf{O}_P\sum_{P'}\chi^{(S)}(P')\mathbf{Q}_{P'}\xi=\text{const.}\times{}'\xi^{(S)}, \qquad \ldots\ldots\ldots\ldots \ (3)$$

where $\varepsilon_P=+1$ or -1 according as P is even or odd.

This means that, given an arbitrary function ξ of space and spin, its component belonging to the irreducible representation $\varepsilon_P\mathsf{D}^{(S)}(R)$ of the direct product group of $\mathbf{O}_P$ and $\mathbf{Q}_R$ is given by the expression on the left of equation (**3**) (apart from a constant factor).

If for ξ we substitute

$$\Phi=\sum_k \xi_k$$

from (**2**), and assume that Φ is antisymmetric and has the multiplicity S, then an expression for Φ is obtained in the form

$$\sum_k \sum_P \varepsilon_P\mathbf{O}_P\sum_{P'}\chi^{(S)}(P')\mathbf{Q}_{P'}f_{1k}(x_1)g_{1k}(y_1)h_{1k}(z_1)\sigma_{1k}(s_1)\ldots f_{nk}(x_n)g_{nk}(y_n)h_{nk}(z_n)\sigma_{nk}(s_n). \qquad \ldots\ldots\ldots\ldots \ (4)$$

This expression is, in general, the sum of $2s+1$ orthogonal functions, one belonging to each of the $2s+1$ rows of $\varepsilon_P \mathsf{D}^{(S)}(R)$. Those terms, for which

$$\tfrac{1}{2}(\sigma_{1k}+\sigma_{2k}+\ldots+\sigma_{nk})=m,$$

belong to the mth row, the rows being numbered $-m$ to $+m$. Hence, if the spin functions are restricted to satisfy $\frac{1}{2}(\sigma_{1k}+\sigma_{2k}+\ldots+\sigma_{nk})=m$, where $|m|\leqslant S$, the expression (**4**) belongs to the mth row of $\varepsilon_P \mathsf{D}^{(S)}(R)$. Since the eigenvalues of (**1**) are independent of m, for the purpose of calculating an eigenvalue it is sufficient to choose $m=0$, if n is even, and $m=\frac{1}{2}$, if n is odd.

For example, for $n=3$, $S=1$ taking $\sigma_{1k}(s)=\alpha(s)$, $\sigma_{2k}(s)=\beta(s)$, $\sigma_{3k}(s)=\alpha(s)$ and using the abbreviation

$$\varphi_1(X_j)=f_1(x_j)g_1(y_j)h_1(z_j)$$

the series is

$$\Sigma \sum_P \varepsilon_P \mathbf{O}_P \sum_{P'} \chi^{(1)}(P')\mathbf{Q}_{P'}\varphi_1(X_1)\alpha(s_1)\varphi_2(X_2)\beta(s_2)\varphi_3(X_3)\alpha(s_3), \quad \ldots\ldots \ (5)$$

where the subscript k has been omitted on the first summation sign and on the φ's. The elements of the group of permutations on 1, 2, 3 are (1), (12), (23), (31), (123), and (132). The characters are

$$\chi^{(1)}(1)=2,\ \chi^{(1)}(12)=\chi^{(1)}(23)=\chi^{(1)}(31)=0,\ \chi^{(1)}(123)=-1=\chi^{(1)}(132).$$

Hence the expression (**5**) becomes

$$\begin{aligned}\Sigma[2\sum_P &\varepsilon_P \mathbf{O}_P \varphi_1(X_1)\alpha(s_1)\varphi_2(X_2)\beta(s_2)\varphi_3(X_3)\alpha(s_3)\\ &-\sum_P \varepsilon_P \mathbf{O}_P \varphi_1(X_1)\alpha(s_1)\varphi_2(X_2)\alpha(s_2)\varphi_3(X_3)\beta(s_3)\\ &-\sum_P \varepsilon_P \mathbf{O}_P \varphi_1(X_1)\beta(s_1)\varphi_2(X_2)\alpha(s_2)\varphi_3(X_3)\alpha(s_3)],\end{aligned}$$

which may be written for short

$$\Sigma[2\ \mathrm{Det}\ \{\varphi_1\alpha\varphi_2\beta\varphi_3\alpha\}-\mathrm{Det}\ \{\varphi_1\alpha\varphi_2\alpha\varphi_3\beta\}-\mathrm{Det}\ \{\varphi_1\beta\varphi_2\alpha\varphi_3\alpha\}]. \quad \ldots \ (6)$$

It follows that an eigenfunction belonging to any given eigenvalue, in particular the lowest eigenvalue, regardless of its multiplicity, can be expressed in the form

$$\sum_k \mathrm{Det}\ \{f_{1k}(x_1)g_{1k}(y_1)h_{1k}(z_1)\alpha(s_1)\ \ldots\ f_{nk}(x_n)g_{nk}(y_n)h_{nk}(z_n)\beta(s_n)\}, \quad \ldots \ (7)$$

where an equal number of α's and β's are to be taken if n is even, and one more α than β if n is odd.

In the next section, the stationary condition for the functions of one variable is based on the expression (**7**) for the wave function. If the lowest eigenvalue of multiplicity S is sought, and it is not the ground state eigenvalue, the stationary condition must be based on (**4**), wherein the σ's may, as above, be chosen so that $m=0$ (if n is even) and $m=\frac{1}{2}$ (if n is odd).

II. Derivation of the Stationary Condition for the Ground State

Application of the method of Part I (Bassett 1959*a*) to this problem, whereby the successive terms in the series expression for the eigenfunction become the determinants of (**7**), finds the lowest eigenfunction of the form (**7**), and therefore finds an eigenfunction belonging to the lowest eigenvalue which corresponds to a physical state. The determinants are built up by the type of iterative procedure described in Parts I and II (Bassett 1959*a*, 1959*b*), in which the central process is the solution of a stationary condition for a function of one variable.

Let $\mathscr{H}$ represent the differential operator in (**1**). Following the notation used in Parts I and II, let us write

$$Q=Q(\Psi)=\int\Psi\mathscr{H}\Psi\mathrm{d}\tau=(\Psi,\mathscr{H}\Psi),$$
$$N=N(\Psi)=\int\Psi^2\mathrm{d}\tau=(\Psi,\Psi),$$

where the integration is over all space and spin coordinates, and Ψ is taken to be real. Let us write $\Lambda=\Lambda(\Psi)=Q(\Psi)/N(\Psi)$. Ψ is to be expressed in the form (**7**), which we shall for the moment write

$$\Sigma\ \mathrm{Det}\ \{\varphi_1(X_1)\alpha(s_1)\ .\ .\ .\ \varphi_n(X_n)\beta(s_n)\},$$

so that

$$Q=[\Sigma\mathrm{Det}\ \{\varphi_1(X_1)\alpha(s_1)\ .\ .\ .\ \varphi_n(X_n)\beta(s_n)\},\ \mathscr{H}\Sigma\ \mathrm{Det}\ \{\varphi_1(X_1)\alpha(s_1)\ .\ .\ .\ \varphi_n(X_n)\beta(s_n)\}],$$

which, owing to the symmetry of $\mathscr{H}$ with respect to permutation of the electron indices, is equal to

$$n![\Sigma\varphi_1(X_1)\alpha(s_1)\ .\ .\ .\ \varphi_n(X_n)\beta(s_n),\ \mathscr{H}\Sigma\ \mathrm{Det}\ \{\varphi_1(X_1)\alpha(s_1)\ .\ .\ .\ \varphi_n(X_n)\beta(s_n)\}].$$

Let us write Ψ in the form

$$\Psi=u(X_1s_1\ .\ .\ .\ X_ns_n)+\mathrm{Det}\ \{f_1(x_1)g_1(y_1)h_1(z_1)\alpha(s_1)\ .\ .\ .\ f_n(x_n)g_n(y_n)h_n(z_n)\beta(s_n)\},$$

and let us determine the condition that $\Lambda=Q/N$ be stationary with respect to f_1. The variation δQ of Q, consequent on a variation δf_1 of f_1, satisfies

$$\begin{aligned}\delta Q&=2[\delta\ \mathrm{Det}\ \{f_1(x_1)g_1(y_1)h_1(z_1)\alpha(s_1)\ .\ .\ .\ f_n(x_n)g_n(y_n)h_n(z_n)\beta(s_n)\},\ \mathscr{H}\Psi]\\&=2[\mathrm{Det}\ \{\delta f_1(x_1)g_1(y_1)h_1(z_1)\alpha(s_1)\ .\ .\ .\ f_n(x_n)g_n(y_n)h_n(z_n)\beta(s_n)\},\ \mathscr{H}\Psi]\\&=2n![\delta f_1(x_1)g_1(y_1)h_1(z_1)\alpha(s_1)\ .\ .\ .\ f_n(x_n)g_n(y_n)h_n(z_n)\beta(s_n),\ \mathscr{H}\Psi].\end{aligned}$$

Similarly,

$$\delta N=2n![\delta f_1(x_1)g_1(y_1)h_1(z_1)\alpha(s_1)\ .\ .\ .\ f_n(x_n)g_n(y_n)h_n(z_n)\beta(s_n),\ \Psi].$$

$\delta(Q/N)=(1/N)\{\delta Q-(Q/N)\delta N\}=0$ if and only if

$$[\delta f_1(x_1)g_1(y_1)h_1(z_1)\alpha(s_1)\ .\ .\ .\ f_n(x_n)g_n(y_n)h_n(z_n)\beta(s_n),\ \mathscr{H}\Psi-(Q/N)\Psi]=0.$$

This is true for arbitrary δf_1 if and only if

$$\begin{aligned}\int.\ .\ .\int g_1(y_1)h_1(z_1)\alpha(s_1)\ .\ .\ .\ f_n(x_n)g_n(y_n)h_n(z_n)\beta(s_n)\{\mathscr{H}\Psi-(Q/N)\Psi\}\\\times\mathrm{d}y_1\mathrm{d}z_1\ .\ .\ .\ \mathrm{d}x_n\mathrm{d}y_n\mathrm{d}z_n\mathrm{d}s_1\ .\ .\ .\ \mathrm{d}s_n=0\qquad\ldots\ldots\ (8)\end{aligned}$$

for all x_1. The functions g_1, h_1, . . ., h_n are allotted values, and an initial guess is made at f_1, which is substituted where f_1 occurs in an integral with respect to y_1, z_1, . . ., z_n, and in Q/N, and (8) then becomes a differential equation for an improved f_1. A " self-consistent " f_1, i.e. one which, when substituted in (8) gives an equation whose solution is f_1, is the solution of the stationary condition. Theorems 1 and 2 below lead to theorem 3, which shows that this stationary condition is, subject to certain reservations, a unique minimum condition. Equation (8) can be regarded as an extended form of Hartree-Fock equation. Formulae for the individual terms on the left-hand side of (8) are complicated, but can be obtained in a straightforward way. Their number is reduced somewhat by the orthogonality of α and β spin functions.

In the following, a translation to " numerical form " as in Part I, Section 3, is assumed. H denotes the matrix which produces the finite-difference operation corresponding to $\mathscr{H}$, and the functions become vectors operated on by H.

Theorem 1

Let us write

$$D(f_1)=\mathrm{Det}\,\{f_1(x_1)g_1(y_1)h_1(z_1)\alpha(s_1)\ .\ .\ .\ f_n(x_n)g_n(y_n)h_n(z_n)\beta(s_n)\}.$$

Let ξ denote a function of x_1. Let

and

$$\left.\begin{aligned} \frac{\mathrm{d}}{\mathrm{d}t}\Lambda[u+D(f_1+t\xi)]\ \Big|_{t=0}&=0,\\ \frac{\mathrm{d}^2}{\mathrm{d}t^2}\Lambda[u+D(f_1+t\xi)]\ \Big|_{t=0}&>0.\end{aligned}\right\}\qquad\ldots\ldots\ldots\ldots\ (9)$$

Let *every* ξ for which $D(\xi)$ is not identically zero satisfy equations (9), for $f_1={}'f$; then the same cannot be true for $f_1={}''f$, unless $D({}'f)$ is identically equal to $D({}''f)$.

Proof. Let $D({}'f)$ be not identically equal to $D({}''f)$, and let us suppose that equations (9), for every ξ for which $D(\xi)$ is not identically zero, are satisfied by $f={}'f$ and by $f={}''f$. Then, since $D({}'f)-D({}''f)=D({}'f-{}''f)$ is not identically zero,

$$\begin{aligned} \frac{\mathrm{d}}{\mathrm{d}\alpha}\Lambda[u+D\{{}'f+\alpha({}''f-{}'f)\}]\ \Big|_{\alpha=0}&=0,\\ \frac{\mathrm{d}^2}{\mathrm{d}\alpha^2}\Lambda[u+D\{{}'f+\alpha({}''f-{}'f)\}]\ \Big|_{\alpha=0}&>0,\\ \frac{\mathrm{d}}{\mathrm{d}\beta}\Lambda[u+D\{{}''f+\beta({}'f-{}''f)\}]\ \Big|_{\beta=0}&=0,\\ \frac{\mathrm{d}^2}{\mathrm{d}\beta^2}\Lambda[u+D\{{}''f+\beta({}'f-{}''f)\}]\ \Big|_{\beta=0}&>0.\end{aligned}$$

Hence, writing $\alpha=t$, $\beta=1-t$, we find $\Lambda[u+D\{{}'f+t({}''f-{}'f)\}]$ has a proper local minimum with respect to t for $t=0$ and $t=1$, which contradicts the lemma of Part I.

Theorem 2

If the functions

$$u(x_1y_1z_1s_1\ .\ .\ .\ x_ny_nz_ns_n)\ \text{ and }\ g_1(y_1),\ h_1(z_1),\ .\ .\ .,\ h_n(z_n)$$

are given and

$$\Lambda(u)<\min_{\alpha_1\beta_1\gamma_1\ldots\alpha_n\beta_n\gamma_n}\Lambda[\mathrm{Det}\,\{\alpha_1(x_1)\beta_1(y_1)\gamma_1(z_1)\alpha(s_1)\ .\ .\ .\ \alpha_n(x_n)\beta_n(y_n)\gamma_n(z_n)\beta(s_n)\}],$$

there is a function f_1 for which

$$\Lambda[u+\text{Det}\,\{f_1(x_1)g_1(y_1)h_1(z_1)\alpha(s_1)\ .\ .\ .\ h_n(z_n)\beta(s_n)\}]$$

assumes its least possible value. For this f_1, Λ is stationary with respect to f_1.

Proof. The proof of Theorem 2 of Part I can be easily adapted.

Theorem 3

Let the functions

$$u(x_1y_1z_1s_1\ .\ .\ .\ z_ns_n) \text{ and } g_1(y_1),\ h_1(z_1),\ .\ .\ .,\ h_n(z_n)$$

be given and let

$$\Lambda(u)\leqslant \min_{\alpha_1,\beta_1,\gamma_1,\ldots,\gamma_n} \Lambda[\text{Det}\,\{\alpha_1(x_1)\beta_1(y_1)\gamma_1(z_1)\alpha(s_1)\ .\ .\ .\ \gamma_n(z_n)\beta(s_n)\}].$$

Let $\Lambda[u+\text{Det}\,\{f_1(x_1)g_1(y_1)h_1(z_1)\alpha(s_1)\ .\ .\ .\ h_n(z_n)\beta(s_n)\}]<\Lambda(u)$ and let Λ be stationary with respect to f_1. There is only one determinant $D(f_1)$ for which f_1 satisfies these conditions, and that gives to Λ its least possible value.

Proof. It is sufficient to show that, if ξ is such that $D(\xi)$ is not identically zero then

$$\frac{\mathrm{d}^2}{\mathrm{d}t^2}\Lambda[u+D(f_1+t\xi)]\ \Big|_{t=0}>0,$$

under the hypotheses of the theorem. Since Λ is stationary with respect to f_1,

$$\frac{\mathrm{d}}{\mathrm{d}t}\Lambda[u+D(f_1+t\xi)]\ \Big|_{t=0}=0.$$

It follows that

$$\frac{\mathrm{d}^2}{\mathrm{d}t^2}\Lambda\ \Big|_{t=0}=\frac{1}{N}\left(\frac{\mathrm{d}^2Q}{\mathrm{d}t^2}\ \Big|_{t=0}-\Lambda\frac{\mathrm{d}^2N}{\mathrm{d}t^2}\ \Big|_{t=0}\right),$$

that is,

$$\frac{\mathrm{d}^2}{\mathrm{d}t^2}\Lambda\ \Big|_{t=0}=\frac{1}{N}[Q\{D(\xi)\}-\Lambda\{u+D(f_1)\}N\{D(\xi)\}].$$

By hypothesis,

$$\frac{Q\{D(\xi)\}}{N\{D(\xi)\}}=\Lambda[D(\xi)]>\Lambda[u+D(f_1)].$$

Hence

$$\frac{\mathrm{d}^2}{\mathrm{d}t^2}\Lambda\ \Big|_{t=0}>0.$$

III. ACKNOWLEDGMENTS

The author would like to thank Dr. A. C. Hurley for reading the manuscript.

IV. REFERENCES

BASSETT, I. M. (1959*a*).—*Aust. J. Phys.* **12**: 430.
BASSETT, I M. (1959*b*).—*Aust. J. Phys.* **12**: 441.
WIGNER, E. (1931).—" Gruppentheorie und ihre Anwendung auf die Quantenmechanik der Atomspektren." p. 315. (Vieweg: Braunschweig.)

THE LATTICE THERMAL CONDUCTIVITY OF SOME GOLD ALLOYS

By J. A. Birch,* W. R. G. Kemp,* P. G. Klemens,*
and R. J. Tainsh*

[*Manuscript received July* 23, 1959]

Summary

The electrical and thermal conductivities of the following gold alloys have been measured from 2 to 90 °K : Au-0·7 per cent. Pt, Au-1·6 per cent. Pt, Au-1·8 per cent. Pt, Au-0·65 per cent. Cr, and Au-6·2 per cent. Cr. Their lattice thermal conductivities have been deduced and the effects of annealing studied. It is found that in well-annealed dilute alloys, the lattice conductivity at liquid helium temperatures approaches a value consistent with theoretical predictions. It appears that increasing solute content causes an increasing dislocation density, which cannot be reduced substantially by annealing. This effect is more pronounced in the case of the chromium alloys. The lattice thermal conductivities at liquid oxygen temperatures compared with theory reveal numerical discrepancies, similar to those found in copper alloys.

I. Introduction

From the lattice component of the thermal conductivity of dilute alloys one can deduce the lattice conductivity of the pure parent metal and thus deduce the nature and strength of the electron-phonon interaction (see, for example, reviews by Klemens 1956, 1958). Thus, silver alloys were studied by Kemp *et al.* (1956) and copper alloys by several investigators, including White and Woods (1955), Kemp, Klemens, and Tainsh (1957), and Lomer and Rosenberg (1958). We have similarly investigated gold alloys ; a preliminary report of some of these measurements has already appeared (Birch, Kemp, and Klemens 1958).

The lattice thermal conductivity $\varkappa_g$ is limited by various processes, each of which contributes approximately additively to $W_g=1/\varkappa_g$, that is,

$$W_g=W_E+W_D+W_U+W_P+W_I, \quad \ldots\ldots\ldots\ldots \quad (1)$$

where W_E is the resistivity due to the scattering of phonons by conduction electrons, W_D by dislocations, W_P by point defects, W_I by static imperfections other than dislocations and point defects, and W_U is the resistivity due to three-phonon interactions.

Now W_E and W_D both vary as T^{-2}, and these resistivities are most important at liquid helium temperatures, while W_U and W_P, varying as T, are most important at liquid oxygen temperatures ; other imperfections have an intermediate temperature dependence and, if they affect $\varkappa_g$ significantly, do so at intermediate temperatures.

Most interest lies in the value of W_E, obtained from the value of W_gT^2 at liquid helium temperatures in well-annealed specimens. Cold-worked specimens have higher values of $(W_gT^2)_{\mathrm{He}}$, no doubt due to an appreciable dislocation resistance W_D. However, there is also some doubt as to whether annealed specimens are really sufficiently free of dislocations for W_D to be negligible, and values of $(W_g)_{\mathrm{He}}$ observed on annealed specimens may only be upper bounds for W_E.

---

* Division of Physics, C.S.I.R.O., University Grounds, Chippendale, N.S.W.

It has been commonly observed that $(W_gT^2)_{\mathrm{He}}$ increases with solute content, and, as this increase occurs irrespective of whether alloying increases or decreases the electron concentration, and also occurs if the electron concentration is unchanged (gold in copper measured by Kemp, Klemens, and Tainsh 1957), one suspects that this increase may be due to a dislocation resistance, the number of dislocations retained after equivalent annealing treatment increasing with solute content.

Kemp, Klemens, and Tainsh found support for this view from a reduction of $(W_gT^2)_{\mathrm{He}}$ of three copper-zinc alloys when increasing the annealing temperature. If the annealing temperature is critical, then it should be possible to achieve further reductions in dislocation density by annealing just below the melting point. This is extremely difficult in copper-zinc alloys because of the danger of zinc evaporation, but is quite feasible in gold-platinum alloys, which were available to us and seemed in any case suitable for deriving $\varkappa_g$ of pure gold by extrapolation, since gold-platinum forms a continuous solid solution. We have therefore measured the gold-platinum alloys not only after annealing at moderately high temperatures (700–750 °C), but also after annealing just below the melting point. The alloys selected contained about 1·8 and 0·7 per cent. Pt respectively, and a less complete study was made of a 1·6 per cent. Pt alloy. It was found that the 0·7 per cent. Pt alloy showed a value of $(W_gT^2)_{\mathrm{He}}$ when annealed, which was only slightly higher than the theoretical value of $(W_ET^2)_{\mathrm{He}}$; other alloys, however, had lower lattice conductivities owing to the presence of dislocations.

Since terminal values of W_D seem in general to decrease with solute content, it was hoped to obtain low dislocation densities by using a solute element of high specific resistivity, thus lowering the solute content. An alloy of 0·65 per cent. chromium was therefore measured, but W_D remained high.

This alloy had been prepared by diluting a commercially available Au-6·2 per cent. Cr alloy, and, since the latter alloy shows an anomalous electrical resistance change on annealing (Linde 1954), its lattice thermal conductivity was also measured to search for a corresponding anomalous change of lattice conductivity on annealing. No such effect was found, but this alloy showed extremely high values of W_g both before and after annealing.

In addition to studies at helium temperatures, there is also some interest in the value of W_g/T at liquid oxygen temperatures, as this gives information about the magnitude of W_U and about W_P due to a known concentration of solute atoms.

II. MEASUREMENTS

The measurements of thermal and electrical conductivity were carried out in the range 2–90 °K using differential gas thermometers and a galvanometer amplifier, with common points of attachment on to the specimen rod. The apparatus used has been described by White (1953) and by Kemp *et al.* (1956).

TABLE 1

ELECTRICAL RESISTIVITIES AND LATTICE THERMAL CONDUCTIVITIES

Specimen	Condition	ρ_0 ($\mu\Omega$ cm)	$\rho_{90}-\rho_0$ ($\mu\Omega$ cm)	$\rho_{293}-\rho_0$ ($\mu\Omega$ cm)	$(\varkappa_g/T^2)_{\mathrm{He}}$ (W cm^{-1} deg^{-3})	$(\varkappa_g/T)_{\mathrm{Ox}}$ (W cm^{-1} deg^{-2})
Au-0·7% Pt	Drawn (80% red.)	0·857	0·61	2·25	$5\cdot8\times10^{-4}$	4·3
	Ann. 750 °C	0·816	0·63	2·27	$2\cdot6\times10^{-3}$	6·2
2·6 mm dia.	Ann. 1050 °C	0·820	0·62	2·29	$2\cdot6\times10^{-3}$	6·2
Au-1·6% Pt	Ann. 700 °C	1·64	0·71	2·47	$1\cdot75\times10^{-3}$	—
3 mm dia.	Ann. 1050 °C	2·04	0·66	2·28	$1\cdot8\times10^{-3}$	6·0
Au-1·8% Pt	Ann. 700 °C	1·85	0·66	2·40	$1\cdot5\times10^{-3}$	4·6
	Ann. 900 °C	1·83	0·72	2·46	$1\cdot6\times10^{-3}$	4·6
3 mm dia.	Ann. 1082 °C	1·95	—	2·52	$1\cdot8\times10^{-3}$	4·6
Au-6·2% Cr	As drawn	27·3	3·9	5·8	$1\cdot07\times10^{-4}$	4
	Ann. 200 °C	28·8	3·5	4·7	$1\cdot43\times10^{-4}$	4
2 mm dia.	Ann. 500 °C	27·9	3·4	4·9	$2\cdot2\times10^{-4}$	4
Au-0·65% Cr	As drawn	3·04	—	1·8	$4\cdot0\times10^{-4}$	—
	Ann. 500 °C	2·83	0·64	1·95	$1\cdot1\times10^{-3}$	7
3·2 mm dia.	Ann. 1050 °C	2·96	—	—	$1\cdot2\times10^{-3}$	7
Pure gold	——	—	0·60	2·20	$2\cdot9\times10^{-3}$*	35†

* Theoretical estimate (Klemens 1954).

† Theoretical estimate (Leibfried and Schloemann 1954; see also Klemens 1958).

The gold-platinum specimens were prepared by Messrs. Garrett, Davidson, and Matthey (Sydney), the approximate compositions being checked from values of the residual electrical resistivity, using data of Linde (1939; see also Gerritsen 1956) for the specific resistivity of platinum in gold (1·01 $\mu\Omega$ cm per atomic per cent.). In the case of Au-1·6 per cent. Pt the composition deviated appreciably from the expected composition (1 per cent. Pt), and this was confirmed subsequently by chemical analysis.* Since this discrepancy was not satisfactorily explained, we are inclined to give less weight to the results from this alloy. The specimens were received in the "as drawn" condition and were annealed *in vacuo* at the temperatures stated in Table 1 for 4 hr. The 0·7 per cent. Pt alloy was homogenized at 1050 °C and then drawn, reducing its cross section by 80 per cent.; in this case the three specimens were distinct, but in all other alloys annealing was cumulative.

The Au-6·2 per cent. Cr alloy (composition in atomic per cent.) was supplied by Messrs. Sigmund Cohn (New York); annealing was in an atmosphere of helium for 12 hr. It was later diluted about ten times with pure gold by Messrs. Garrett, Davidson, and Matthey to provide Au-0·65 per cent. Cr. The latter alloy was annealed *in vacuo* cumulatively for 4 hr.

---

* We are indebted to Mr. D. A. Sinclair, Branch Superintendent, Defence Standards Laboratory, Sydney, for this analysis.

III. Results

Electrical resistivity data of the various specimens are summarized in Table 1. The thermal conductivities of some of the specimens are given as function of temperature in Figures 1 and 2.

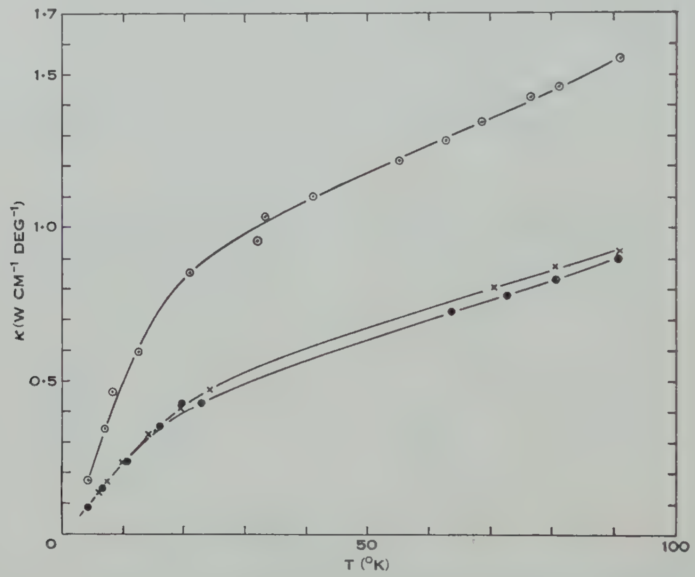

Fig. 1.—Thermal conductivity of gold-platinum alloys. Au-0·7% Pt annealed at 1050 °C ⊙ ; Au-1·6% Pt annealed at 1050 °C ● ; Au-1·8% Pt annealed at 1082 °C ×.

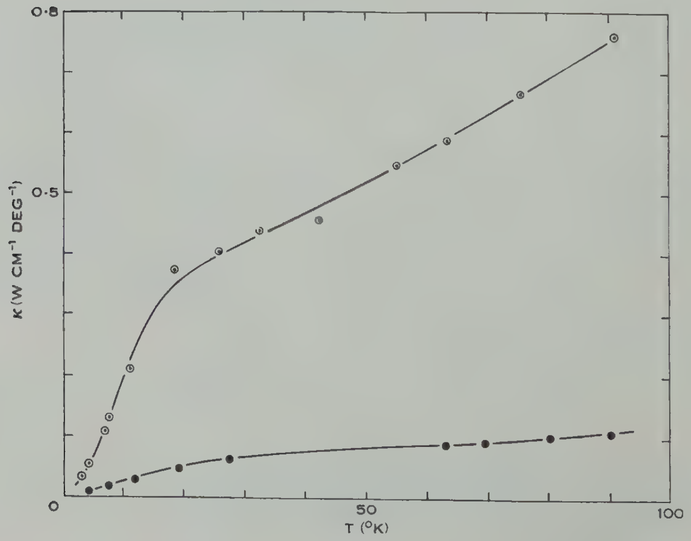

Fig. 2.—Thermal conductivity of gold-chromium alloys. Au-0·65% Cr annealed at 1050 °C ⊙ ; Au-6·2% Cr annealed at 500 °C ●.

The lattice thermal conductivity was deduced from measured values of $\varkappa(T)$ and ρ_0 (residual electrical resistivity), as described, for example, by Kemp *et al.* (1956) and by Klemens (1958), using the relations

$$\varkappa=\varkappa_e+\varkappa_g, \qquad (2)$$

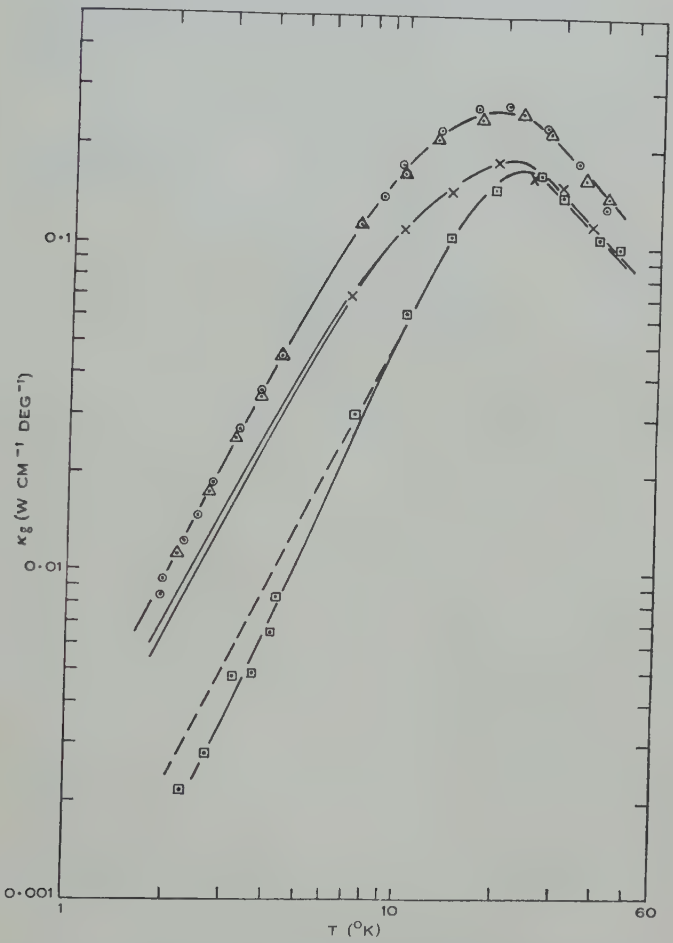

Fig. 3.—Lattice thermal conductivity of gold-platinum alloys. Au-0·7% Pt deformed ⊡, annealed at 750 °C △, annealed at 1050 °C ⊙, dashed line: extrapolated T^2 variation; Au-1·8% Pt ×. For the latter alloy at low temperatures the upper curve is for specimen annealed at 1082 °C, the lower curve for that annealed at 700 °C; the coefficients of the T^2 dependence were determined from curves of $\varkappa/T$ against T, as described by Kemp *et al.* (1956).

where the electronic conductivity $\varkappa_e$ is given by

$$1/\varkappa_e=W_i+\rho_0/LT, \qquad (3)$$

$L=2\cdot45\times10^{-8}$ V^2/deg^2 being the Sommerfeld value of the Lorenz number and W_i the ideal electronic thermal resistivity. For W_i we took the values for pure

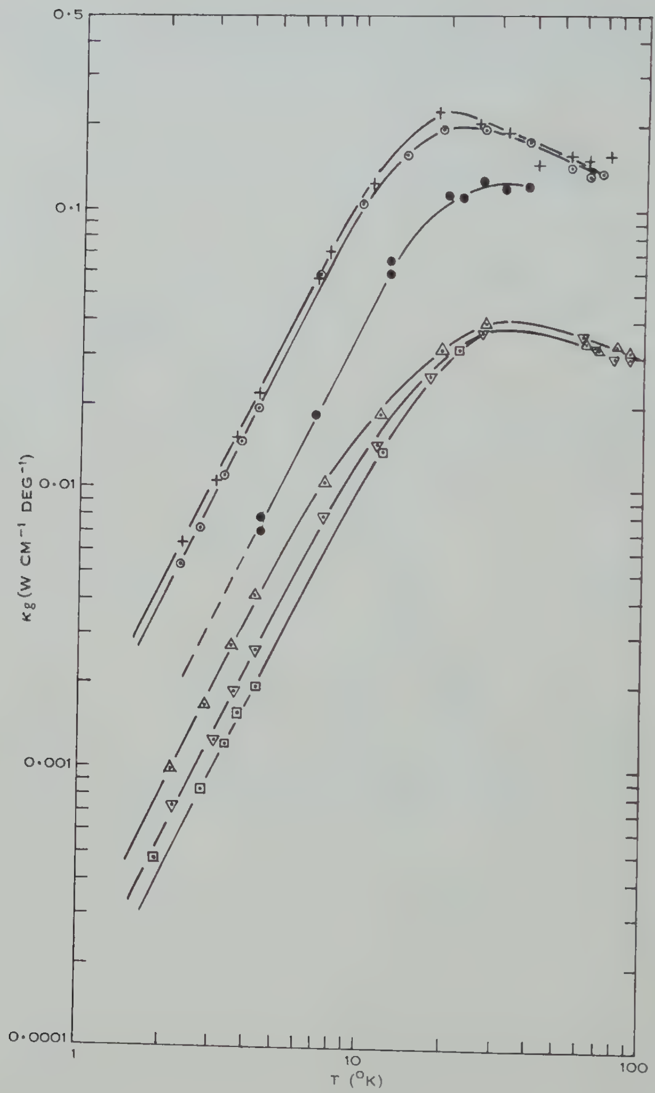

Fig. 4.—Lattice thermal conductivity of gold-chromium alloys. Au-0·65% Cr deformed ●, annealed at 500 °C ⊙, annealed at 1050 °C + ; Au-6·2% Cr deformed ⊡, annealed at 200 °C ▽, annealed at 500 °C △.

gold (White 1953), corrections due to the change of W_i with composition (Klemens 1959) being unimportant in the present alloys.

The values of $\varkappa_g$ for the various alloy specimens are displayed in Figures 3 and 4, except for the two Au-1·6 per cent. Pt specimens, the curves for which are practically coincident with that of Au-1·8 per cent. Pt annealed at 1082 °C. Values of $\varkappa_g/T^2$ at helium temperatures and of $\varkappa_g/T$ at oxygen temperatures are also shown in Table 1.

IV. DISCUSSION

(a) *Low Temperature Results*

Consider the lattice conductivities at temperatures well below 20 °K. It is seen that $(\varkappa_g/T^2)_{\mathrm{He}}$ is least for the 6·2 per cent. Cr alloy, is higher for the 0·65 per cent. Cr alloy, higher still for the 1·8 and 1·6 per cent. Pt alloys, and highest for the annealed 0·7 per cent. platinum alloy. In general it seems sufficient to anneal at moderate temperatures (500–750 °C) to increase $(\varkappa_g/T^2)_{\mathrm{He}}$ substantially: annealing above 1000 °C produces relatively small changes only, and none in the 0·7 per cent. Pt alloys. Thus, while some reduction in dislocation density can be effected by annealing close to the melting point, the most important factor in determining $(\varkappa_g/T^2)_{\mathrm{He}}$ is the composition; chromium is much more effective in decreasing $(\varkappa_g/T^2)_{\mathrm{He}}$ than platinum.

The present results do not allow a clear distinction between the possibilities that the increase of $(W_gT^2)_{\mathrm{He}}$ is due to a change in W_E or to an additional dislocation resistance. The insensitivity of the 0·7 per cent. Pt and, to a lesser extent, the 0·65 per cent. Cr and the 1·6 per cent. Pt alloys to further annealing at 1050 °C would indicate a change in W_E, but the results for the 1·8 per cent. Pt alloy, showing a relatively small change from 700 to 900 °C, but a larger change from 900 to 1082 °C, indicate a sluggish removal of dislocations, which requires very high annealing temperatures, and may well be incomplete.

Irrespective of why $(W_gT^2)_{\mathrm{He}}$ increases with solute content, we obtain from the two annealed Au-0·7 per cent. Pt specimens an estimate of $(W_ET^2)_{\mathrm{He}}$ which is probably not greatly in error. From the present results $(W_ET^2)_{\mathrm{He}} \ngtr 0\cdot 38\times 10^3$ W^{-1} cm deg^3. White, Woods, and Elford (1959) have recently obtained* a slightly lower value of $0\cdot 36\times 10^3$ for a dilute gold-iron alloy (0·13 per cent. Fe). The theoretical value of $(W_ET^2)_{\mathrm{He}}$ for gold is $0\cdot 35\times 10^3$, obtained by Klemens (1954) from the observed value of W_i/T^2, assuming $\theta_D=170$ °K and further assuming that the electrons interact equally strongly with transverse and with longitudinal phonons. On the other hand, the assumption of no interaction between electrons and transverse waves, but coupling between the polarization branches, leads to $(W_ET^2)_{\mathrm{He}}=7\times 10^3$ W^{-1} cm deg^3. The present results, and those of White, Woods, and Elford, clearly favour the former coupling scheme, as proposed by Makinson (1938). Thus gold behaves similarly to copper and silver in this regard.

Since the Fermi surface of gold is most probably not spherical (Klemens 1956; Cohen and Heine 1958), the agreement between the observed values of $(W_gT^2)_{\mathrm{He}}$ and the theoretical estimate of $(W_ET^2)_{\mathrm{He}}$ confirms the theoretical prediction that the ratio W_E/W_i is not sensitive to small departures from sphericity.

If we assume that W_E is the same for all alloys and changes in $(W_gT^2)_{\mathrm{He}}$ with composition are due to dislocations, we can deduce $(W_DT^2)_{\mathrm{He}}$ for the various specimens and calculate the corresponding dislocation densities, using a relation obtained by Klemens (1955) as subsequently modified by a numerical factor (Klemens 1958):

---

* We are indebted to Dr. G. K. White for communicating these results in advance of publication.

$$\begin{aligned} W_D T^2 &= 0{\cdot}17 \frac{vh^2}{K^3} N b^2 \\ &= 3{\cdot}9 \times 10^{-9} N \quad \mathrm{W}^{-1}\,\mathrm{cm\ deg}^3, \qquad \ldots\ldots\ldots\ (4) \end{aligned}$$

where N (in lines/cm^2) is the dislocation density, v the sound velocity, h and K the Planck and Boltzmann constants, and b the Burgers vector. In Table 2 are given values of $(W_D T^2)_{\mathrm{He}}$, obtained by assuming the theoretical value of $0{\cdot}35 \times 10^3$ for $(W_E T^2)_{\mathrm{He}}$, and also values of N calculated using (4).

TABLE 2

DISLOCATION DENSITIES

Specimen	Condition	$W_D T^2$ (10^3 W^{-1} cm deg^3)	N (10^{11} cm^{-2})
Au-0·7% Pt	Drawn (80% red.)	1·4	3·6
	Ann. 750 °C	0·04 (?)	0·1 (?)
	Ann. 1050 °C	0·04 (?)	0·1 (?)
Au-1·8% Pt	Ann. 700 °C	0·32	0·82
	Ann. 900 °C	0·28	0·72
	Ann. 1082 °C	0·21	0·54
Au-0·65% Cr	As drawn	2·1	5·4
	Ann. 500 °C	0·57	1·5
	Ann. 1050 °C	0·49	1·3
Au-6·2% Cr	As drawn	9·0	23
	Ann. 200 °C	6·6	17
	Ann. 500 °C	4·2	11

In attempting to explain the large number of dislocations in alloys remaining after annealing (comparable to the number introduced by deformation in the case of the chromium alloys) one naturally thinks of the movement of dislocations being impeded by the solute atoms. Either the solute atoms act as obstacles themselves or some other imperfections, associated with the solute atoms, act in this way. The action of impurities as obstacles has recently been demonstrated by Johnston and Gilman (1959) in the case of lithium fluoride. There are two effects: the impurities not only anchor the dislocations and tend to make them immobile, but, if the dislocations have broken away and are mobile, their velocities are decreased by a very large factor. It is not unlikely that solute atoms in gold play a similar role.

It is interesting to note that the two less dilute alloys (1·8 per cent. Pt, 6·2 per cent. Cr) have curves of $\varkappa_g$ against T which differ in shape from those of the other two alloys, for they appear truncated around 10 °K. Furthermore, there is less change on annealing in that temperature region than at lower temperatures (none in the case of 1·8 per cent. Pt). The thermal resistivity at these intermediate temperatures is not inconsistent with a thermal resistivity due to stacking faults, for stacking faults should contribute a resistivity $W_S \propto T^{-1}$ (Klemens 1957). This identification cannot be made with confidence, but, if it is provisionally adopted, the stacking fault probability can be calculated from the additional thermal resistivity. If a stacking fault is regarded as an extended dislocation, then the dislocation densities of Table 2 and the stacking fault probabilities can be used to obtain the average width of the stacking fault ribbon. This turns out to be about 40 Å in the 6·2 per cent. Cr alloy and 100 Å in the 1·8 per cent. Pt alloy. It is possible that the high values of the dislocation density in these alloys are a result of the additional inhibition of dislocation movement due to these stacking faults.

(*b*) *Results at Liquid Oxygen Temperatures*

At temperatures above about $\frac{1}{4}\theta_D$ (θ_D is the Debye temperature) theory indicates that $W_U \propto T$ (e.g. review by Klemens 1958), while $W_P \propto T$ below and up to θ_D. Thus in the absence of other imperfections W_g should vary as T above about 40 °K. In the case of the platinum alloys $\varkappa_g$ varies indeed as T^{-1} above about 30 °K up to about 50 °K—at higher temperatures $\varkappa_g$ can no longer be evaluated with confidence, but presumably this temperature dependence continues to higher temperatures. Values of $(\varkappa_g T)_{\text{Ox}}$ shown in Table 1 are values taken in the former temperature region. In the case of the chromium alloys, $\varkappa_g$ varies more slowly than T^{-1} at the highest temperatures at which $\varkappa_g$ could be determined. Values of $(\varkappa_g T)_{\text{Ox}}$ derived from $\varkappa_g$ at 90 °K and shown in Table 1 will thus in general underestimate $\varkappa_g$ in the true T^{-1} region, which is presumably attained at higher temperatures.

The difference in $(\varkappa_g T)_{\text{Ox}}$ between the 0·7 per cent. Pt and the 1·8 per cent. Pt alloy is presumably due to a point defect resistance $W_P \propto T$, and most likely originates from the scattering of phonons by the platinum atoms. This would make the resistivity due to 1 per cent. Pt atoms $W_P/T = 5\cdot0 \times 10^{-2}$ W^{-1} cm. Correcting the observed value of $(W_g/T)_{\text{Ox}}$ of the 0·7 per cent. Pt alloy for the contribution due to W_P of the platinum atoms, we obtain $(W_U/T)_{\text{Ox}} = 0\cdot125$, that is, the intrinsic value of $(\varkappa_g T)_{\text{Ox}}$ is about 8·0 W cm^{-1}. A similar extrapolation of the chromium alloys to zero chromium content is much less certain, but gives the same result. White, Woods, and Elford (1959) also obtained a value of 8 W cm^{-1} for $(\varkappa_g T)_{\text{Ox}}$ of their Au-0·13 per cent. Fe alloy.

This may be compared with a theoretical value of $\varkappa_g T = 35$ W cm^{-1} derived, with some approximations, by Leibfried and Schloemann (1954). The discrepancy of a factor 4 is slightly greater than that found in copper and silver alloys (see Klemens 1958).

The thermal point defect resistivity W_P of platinum in gold is considerably higher than one would have expected from their small difference in atomic mass. Theoretically (Klemens 1955), the point defect resistivity is given by

$$\begin{aligned} W_P/T &= \frac{12\pi^2}{0\cdot90}\,\frac{a^3}{hv^2}nS^2 \\ &= 21\cdot7nS^2 \text{ W}^{-1}\text{ cm}, \qquad \ldots\ldots\ldots\ldots\ldots \ (5) \end{aligned}$$

where a^3 is the atomic value, n the defect concentration per atom, and S^2 a numerical constant. If a point defect scatters only in virtue of its mass difference,

$$S^2 = (\Delta M/M)^2/12, \quad \ldots\ldots\ldots\ldots\ldots\ldots \quad (6)$$

M and ΔM being the normal atomic mass and the deviation from it. For platinum in gold, $S^2 = 0 \cdot 9 \times 10^{-5}$, while the present results indicate $S^2 = 0 \cdot 23$. The scattering of phonons by the platinum atoms is thus due to such effects as the distortion of the lattice around the solute atoms, and the difference in the binding forces due to gold-platinum and gold-gold adjacencies. A similar situation prevails in regard to zinc in copper and cadmium in silver (Klemens 1958).

For chromium in gold we obtain from the results of the present paper $(W_p/T)_{\text{Ox}} = 2 \cdot 0 \times 10^{-2}$ W^{-1} cm per atomic per cent., or $S^2 = 0 \cdot 09$. From the mass difference alone, by equation (**6**), S^2 should be $0 \cdot 045$, so that the chromium atoms scatter not only due to the mass difference, but also through misfit.

It is interesting to note that in the case of the 0·7 per cent. Pt alloy, but not in the case of the two chromium alloys, $(W_g/T)_{\text{Ox}}$ is significantly larger in the deformed state than after annealing. This indicates the removal of point defects during annealing with a value of $nS^2 = 3 \cdot 2 \times 10^{-3}$; but the electrical resistivity change during annealing (which may not be entirely due to point defects) is far too small to account for any point defect in concentrations of 10^{-2} to 10^{-3} per atom. The same difficulty was also found in the case of copper-zinc alloys (Kemp *et al.* 1957; Kemp, Klemens, and Tainsh 1959).

(c) *Electrical Resistivity Changes*

The change in ρ_0 of Au-0·7 per cent. Pt during annealing to 750 °C is small, but comparable with similar changes commonly observed in pure gold. All gold-platinum alloys showed an increase in ρ_0 on increasing the annealing temperature to 1050 °C or higher. This may be due to contamination or to the release of platinum atoms that had segregated. The latter hypothesis seems specially likely in the Au-1·6 per cent. Pt. alloy, partly because the increase in ρ_0 is too great to be accounted for by any likely contamination and partly because the solute atoms were probably not uniformly distributed, as indicated by the deviation of the apparent platinum content from the expected composition.

The Au-0·65 per cent. Cr alloy showed a similar increase after annealing at 1050 °C.

The Au-6·2 per cent. Cr alloy showed an increase of ρ_0 after annealing, similar to that previously found by Linde (1954) on annealing gold-chromium alloys of more than 2 per cent. Cr at 450–500 °C. The present results show that this increase occurs already when annealing at 200 °C; further annealing at 500 °C causes a small decrease, as in normally behaved metals.

One possible mechanism for the resistance increase on annealing is to suppose that some chromium atoms are segregated along the dislocations after deformation; the low temperature anneal causes them to disperse into the material, thus increasing the resistivity. On this basis the observed resistance increase would indicate that 5 per cent. of the chromium atoms were thus segregated, i.e. about 0·003 per atom. On the other hand, a dislocation density of 2×10^{12} cm^{-2} (see Table 2) could accommodate only about 0·001 chromium atoms per atom, even if every dislocation were decorated by one atom per atomic plane. While a more concentrated decoration is not impossible, it appears unlikely that this is the mechanism of the electrical resistance increase.

V. ACKNOWLEDGMENTS

The authors wish to thank Dr. G. K. White for helpful discussions and Mr. J. W. Smyth for valuable technical assistance.

VI. REFERENCES

BIRCH, J. A., KEMP, W. R. G., and KLEMENS, P. G. (1958).—*Proc. Phys. Soc. Lond.* **71** : 843.

COHEN, M. H., and HEINE, V. (1958).—*Advanc. Phys.* **7** : 395.

GERRITSEN, A. N. (1956).—" Encyclopedia of Physics." Vol. 19, Pt. 2. (Springer : Berlin.)

JOHNSTON, W. G., and GILMAN, J. J. (1959).—*J. Appl. Phys.* **30** : 129.

KEMP, W. R. G., KLEMENS, P. G., SREEDHAR, A. K., and WHITE, G. K. (1956).—*Proc. Roy. Soc.* A **233** : 480.

KEMP, W. R. G., KLEMENS, P. G., and TAINSH, R. J. (1957).—*Aust. J. Phys.* **10** : 454.

KEMP, W. R. G., KLEMENS, P. G., and TAINSH, R. J. (1959).—*Phil. Mag.* (In press.)

KEMP, W. R. G., KLEMENS, P. G., TAINSH, R. J., and WHITE, G. K. (1957).—*Acta Met.* **5** : 303.

KLEMENS, P. G. (1954).—*Aust. J. Phys.* **7** : 57.

KLEMENS, P. G. (1955).—*Proc. Phys. Soc. Lond.* A **68** : 1113.

KLEMENS, P. G. (1956).—" Encyclopedia of Physics." Vol. 14, Pt. 4. (Springer : Berlin.)

KLEMENS, P. G. (1957).—*Canad. J. Phys.* **35** : 441.

KLEMENS, P. G. (1958).—*Solid State Physics* **7** : 1.

KLEMENS, P. G. (1959).—*Aust. J. Phys.* **12** : 199.

LEIBFRIED, G., and SCHLOEMANN, E. (1954).—*Nachr. Akad. Wiss. Göttingen, Math-phys. Kl.* **IIa** (4) : 71.

LINDE, J. O. (1939).—Thesis : Lund.

LINDE, J. O. (1954).—*J. Appl. Sci. Res.* B **4** : 73.

LOMER, J. N., and ROSENBERG, H. M. (1958).—" Low Temperature Physics and Chemistry." p. 394. (Univ. Wisconsin Press : Madison.)

MAKINSON, R. E. B. (1938).—*Proc. Camb. Phil. Soc.* **34** : 474.

WHITE, G. K. (1953).—*Proc. Phys. Soc. Lond.* A **66** : 559.

WHITE, G. K., and WOODS, S. B. (1955).—*Canad. J. Phys.* **33** : 58.

WHITE, G. K., WOODS, S. B., and ELFORD, T. M. (1959).—*Phil. Mag.* (In press.)

SHORT COMMUNICATIONS

THE IONOSPHERE OF JUPITER*

By H. Rishbeth†

It has been suggested that the radio-frequency emissions from Jupiter are due to plasma oscillations in the planet's ionosphere (e.g. Gardner and Shain 1958). This note shows that, according to standard theory, sufficient ionization may be produced by solar radiation; but it does not attempt to explain the actual cause of the disturbances.

Evidence so far available suggests that the radiation from Jupiter is strongest at frequencies near 20 Mc/s (Gardner and Shain 1958). If this is taken to be the fundamental frequency of a plasma oscillation, then the corresponding electron density is $N=5\times10^6$ cm^{-3}, a value which is seldom approached in the terrestrial ionosphere. Since the intensity of the ionizing radiation is presumably much less than at the Earth, the required electron density will only be attained if the recombination coefficient α is very low. It is suggested that this may be so.

The relevant theory is that of Chapman (1931), who considers the absorption of monochromatic radiation in an isothermal atmosphere. The theory may be expected to give rough quantitative results even if its assumptions are not strictly true.

Let I be the intensity of ionizing radiation incident vertically at the top of the atmosphere and q the rate of production of ionization. Let n be the number density of the ionizable constituent, H its scale height, and A its ionization cross section. Then, at the level of maximum production, under conditions of equilibrium:

$$q=\alpha N^2, \qquad (1)$$

$$q=I\mathrm{e}^{-1}/H, \qquad (2)$$

$$1=nAH. \qquad (3)$$

Also

$$H=kT/mg, \qquad (4)$$

where k is Boltzmann's constant, T the temperature, g the acceleration due to gravity, and m the mean molecular mass, which may be written as $\mu\times$(mass of hydrogen atom).

A model of the Jovian atmosphere has been proposed by Kuiper (1952). It consists of a troposphere—a region in which the temperature decreases upwards—and an isothermal stratosphere: at the tropopause, which is near the level of the visible clouds, the pressure is of the order of 1 terrestrial atmosphere and the temperature is about 90 °K. The suggested percentage com-

---

* Manuscript received June 9, 1959.

† Cavendish Laboratory, Cambridge, England.

position by weight of the atmosphere is H_2 63·5, He 35, and heavy gases (CH_4, NH_3, etc.) 1·5, whence $\mu=2\cdot5$. With $g=2600$ cm sec^{-2}, this gives $H\simeq10$ km.*

However, in the terrestrial F region the temperature is much higher than in the stratosphere: the same may be true of Jupiter. Furthermore, the molecular weight may decrease with altitude, for two reasons. Firstly, diffusive separation of gases may occur; and secondly, hydrogen is probably dissociated at great heights in the atmosphere. Thus an alternative estimate of H can be made, in which these possible effects are combined so as to increase H: if $T=300$ °K (say) and $\mu=1$, then $H\simeq100$ km.

Comparison is best made with the F_1 region of the terrestrial ionosphere, in which the maximum rate of ion production occurs: the greater electron density in the F_2 region is due to conditions which may not exist in Jupiter's atmosphere. In the F_1 region, H is about 30 km, and $q=500$ cm^{-3} sec^{-1} for moderate sunspot numbers. Since similar ultraviolet wavelengths are involved in each case, it is reasonable to take

$$I_J/I_E=R_E^2/R_J^2=1/27, \quad \ldots\ldots\ldots\ldots\ldots\ldots \quad (5)$$

where R is the radius of the planetary orbit and the subscripts E, J refer to the Earth and Jupiter. Use of (1), (2), and (5), with the desired value $N=5\times10^6$ cm^{-3}, shows that if $H_J=10$ km, then $q_J\simeq50$ cm^{-3} sec^{-1} and α must not exceed 2×10^{-12} cm^3 sec^{-1}; but if $H_J=100$ km, then $q_J\simeq5$ cm^{-3} sec^{-1} and $\alpha\leqslant2\times10^{-13}$ cm^3 sec^{-1}. Typical F_1-region values are $N=3\times10^5$ cm^{-3} and $\alpha=5\times10^{-9}$ cm^3 sec^{-1}.

The altitude of the ionized region in the Jovian atmosphere may be estimated by means of equation (3). For the principal gases of the Earth's atmosphere the ionization cross section A is 10^{-17} or 10^{-18} cm^2: similar values are probably appropriate to the Jovian situation, and with a scale height H of 10 or 100 km, the equation gives n as 10^{10} to 10^{12} cm^{-3} (similar to that in the F_1 region). At the tropopause of Kuiper's model, the number density is of order 10^{20} cm^{-3}. Thus between the tropopause and the ionosphere the number density decreases by a factor of about 10^9, corresponding to a difference in altitude of $9 \ln 10=21$ scale heights, or a few hundred kilometres. The ionosphere thus lies well above the level of the visible clouds.

The recombination processes operative in the terrestrial ionosphere have been discussed by Bates and Massey (1946, 1948). They are:

(i) Radiative recombination: coefficient about 10^{-12} cm^3 sec^{-1}.

(ii) Dissociative recombination (involving molecular ions); coefficient 10^{-8} or 10^{-9} cm^3 sec^{-1}.

The latter process is important either if the ionizable gas is composed of diatomic or polyatomic molecules, or if monatomic ions can transfer their charge to a molecular constituent. No other recombination process is likely to be more rapid than (i).

---

* Kuiper proposes an alternative composition, with helium as the predominant constituent and $\mu=3\cdot3$: the adoption of this model makes no substantial difference to the subsequent discussion.

The coefficients quoted are rough values, applicable to conditions in the Earth's atmosphere, and it is plausible that for the constituents of Jupiter's atmosphere they will be of similar magnitude. Then, if process (i) alone occurs, the required electron density seems feasible; but if process (ii) is operative, it does not—so it is necessary to consider whether any constituent gas is likely to give rise to molecular ions in the ionosphere.

It may be estimated that hydrogen will be dissociated above the level at which $n \sim 10^{13}$ cm^{-3}, a few scale heights below the level of the ionosphere. The principal constituent of the ionosphere is thus atomic hydrogen, and molecular hydrogen will be comparatively rare. Although H_2 molecules will absorb a small proportion of the ionizing radiation, and the resulting H_2^+ ions can recombine dissociatively, most of the radiation is available for the production of H^+ ions. Since the ionization potential of H_2 exceeds that of H, there can be no formation of H_2^+ ions by transfer of charge from the H^+ ions. Moreover, the pressure is probably too low to permit the formation of He_2^+ ions, and CH_4 and NH_3 are likely to be dissociated well below the ionosphere. Consequently, the H^+ ions cannot recombine by a dissociative process.

The essential difference between the two ionospheres, therefore, is that whereas in the terrestrial F region the principal ion (O^+) can react with neutral molecules to form molecular ions, the H^+ ions in the Jovian ionosphere can only recombine by the radiative process. Provided electrons are not removed too quickly by diffusion, and rough calculation suggests that they are not, the values $\mu=1$, $T=100$ °K, $\alpha=10^{-12}$ cm^3 sec^{-1} yield $N \simeq 4\times10^6$ cm^{-3}, which is satisfactory.

The ionization will be removed by recombination in a time of order $\alpha N \sim 10^5$ or 10^6 sec. This is longer than the rotation period of Jupiter ($3\cdot6\times10^4$ sec), so the electron density will show little diurnal variation.

The above considerations suggest that Jupiter may possess an ionosphere with a critical frequency of order 20 Mc/s, and that it lies a few hundred kilometres above the level of the visible clouds. However, the correlation between the radio-frequency activity and the planet's rotation period (Shain 1956) implies that the sources of excitation are fixed with respect to the cloud system. Possibly surface or atmospheric phenomena cause disturbances in the overlying ionosphere.

The author wishes to thank Dr. K. Weekes of the Cavendish Laboratory for many helpful discussions during the preparation of this paper.

References

Bates, D. R., and Massey, H. S. W. (1946).—*Proc. Roy. Soc.* A **187**: 261.
Bates, D. R., and Massey, H. S. W. (1948).—*Proc. Roy. Soc.* A **192**: 1.
Chapman, S. (1931).—*Proc. Phys. Soc. Lond.* **43**: 26.
Gardner, F. F., and Shain, C. A. (1958).—*Aust. J. Phys.* **11**: 55.
Kuiper, G. P. (1952).—" The Atmospheres of the Earth and Planets." 2nd Ed. Ch. XII. (Univ. Chicago Press.)
Shain, C. A. (1956).—*Aust. J. Phys.* **9**: 61.

ANALYSIS OF COMPOSITE SPECTRAL–SENSITIVITY FUNCTIONS*

By J. S. Anderson,† E. A. Faulkner,‡ and D. F. Klemperer‡

In measurements of the photoelectric effect on semiconductors two types of relationship have been found between the frequency of incident radiation ν and the observed photoelectric current I_{obs}. In one type, the plot of log I_{obs} against ν fits the theoretical Fowler curve (Fowler 1931); in other cases, however, a curve is obtained which is in two parts, each of which can be fitted to a separate Fowler curve. Thus Suhrmann, Wedler, and Dierk (1958*a*, 1958*b*) obtained "composite" curves from bismuth films, and we have found both types of behaviour with evaporated nickel films undergoing stepwise oxidation. The problem of interpreting such composite curves is quite a general one.

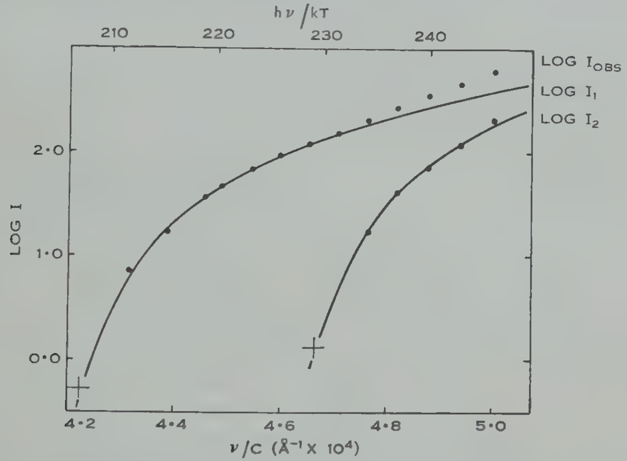

Fig. 1.—Fowler-type plot for photoelectric emission from a partially oxidized nickel surface; curves are computed from Fowler's equation. The work functions are 5·21 eV ($4\cdot23\times10^{-4}$ Å^{-1}) and 5·76 eV ($4\cdot67\times10^{-4}$ Å^{-1}).

A composite curve may be interpreted in terms of two emitting mechanisms which act independently. The observed photoelectric current is then the sum of the individual currents, so that

$$\begin{aligned}\log I_{\text{obs}} &= \log\,(I_1+I_2)\\ &= \log\,\{A_1\varphi(\nu-\nu_1)+A_2\varphi(\nu-\nu_2)\},\end{aligned}$$

where φ is the Fowler function and ν_1 and ν_2 are the two threshold frequencies. Such a relationship, in a restricted range of frequency, gives a very good fit to two Fowler curves intersecting at a frequency slightly above that of the higher threshold ν_2. (The exact point of intersection for lines of best fit depends on the value of A_1/A_2 and on the ratio of the frequency range employed to the interval between the two threshold frequencies.)

---

* Manuscript received August 7, 1959.

† Department of Chemistry, University of Melbourne.

‡ Division of Tribophysics, C.S.I.R.O., University of Melbourne.

The value of ν_2 may be obtained from a second plot of log $(I_{\text{obs}}-I_1)$ against ν, where I_1 is obtained by extrapolation of the first Fowler curve ; the method is illustrated in Figure 1, using some of our (unpublished) results. We have usually found it more convenient, however, to use a different method based on the fact that $\varphi(\nu-\nu')$ approaches $0\cdot5(\nu-\nu')^2$ as $(\nu-\nu')$ increases : when $(\nu-\nu')$ is greater than $5kT/h$, the discrepancy is usually small compared with the experimental error, and in this region a plot of $I_{\text{obs}}^{\frac{1}{2}}$ against ν can be readily fitted to a pair of intersecting straight lines. The value of ν_2 can be calculated from the parameters of these lines ; alternatively, values of I_2 can be obtained numerically and a third straight line can be drawn which is extrapolated to determine ν_2, as shown in Figure 2.

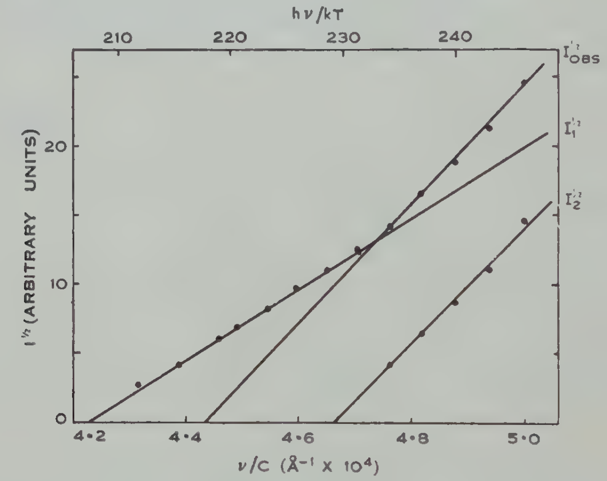

Fig. 2.—Square-root plot for the results in Figure 1.

The values of ν_2 are not the same as the values of second threshold frequency derived by the method of Suhrmann, Wedler, and Dierk. On the basis of a particular band model which is not fully elaborated in their papers, these authors have applied a graphical analysis of Fowler plots which differs from our method. For a typical set of their results (Suhrmann, Wedler, and Dierk 1958*a*, p. 101, Fig. 4) their analysis leads to threshold values of 4·25 and 4·37 eV ; when treated by our method (which assumes the operation of two independent types of emitting region) the same experimental results give threshold values of 4·25 and 4·6 eV, so that the separation is changed by a factor of three. Likewise, the value of A_1/A_2, which is 0·6 according to the analysis of Suhrmann, Wedler, and Dierk, becomes unity in our method. It is therefore necessary in any such case to consider results in relation to a particular model.

References

Fowler, R. H. (1931).—*Phys. Rev.* **38** : 45.

Suhrmann, R., Wedler, G., and Dierk, E.-A. (1958*a*).—*Z. Phys.* **153** : 96.

Suhrmann, R., Wedler, G., and Dierk, E.-A. (1958*b*).—*Z. Phys. Chem.* N.F. **18** : 255.

THE EXTENDED COMPONENT OF CENTAURUS A*

By C. M. Wade†

The strong southern radio source Centaurus A (IAU 13S4A) was one of the first to be identified with an optically observable object. Bolton, Stanley, and Slee (1949) suggested that the radio emission was associated with the peculiar galaxy NGC 5128, and this identification has been strengthened by more recent positional measurements (Mills 1952). NGC 5128 is a most unusual object, appearing to be a spheroidal galaxy transected by a heavy belt of obscuring matter (Baade and Minkowski 1954*a* ; Sérsic 1958). Its distance is uncertain, but it is likely to be about 1 megaparsec away (Baade, personal communication).

Early interferometric observations (Mills 1953 ; Bolton *et al.* 1954) indicated that the radio source comprises two distinct components : an intense source with an angular size of a few minutes of arc, coincident in position with NGC 5128 ; and a much fainter source of far greater size surrounding NGC 5128. This has been confirmed by subsequent pencil-beam observations at 19·7 Mc/s (Shain 1958), 85·5 Mc/s (Sheridan 1958), and 1400 Mc/s (Hindman and Wade 1959 ; Heeschen, personal communication). These show that the extended component covers a solid angle of more than 20 square degrees ; that it subtends about 8° of declination and 3° of Right Ascension ; and that NGC 5128 lies near its centre. The main features of the source remain much the same over the entire frequency range (more than 6 octaves).

Figures 1 and 2 reproduce the distributions found in the two surveys made with aerial beamwidths of less than 1°, at 85·5 Mc/s and at 1400 Mc/s (Heeschen, personal communication). Their close resemblance is quite striking in view of the great difference between the frequencies at which they were obtained. The two components of the source are shown clearly. Some structure is evident in the extended part, the most outstanding feature being a strong, broad maximum about 2° south of the central source associated with NGC 5128. Heeschen's observations (Fig. 2) also suggest complex structure in the northern part. The extended component has no known optical counterpart, although it accounts for 75 per cent. of the total flux at metre and decimetre wavelengths. While there is little doubt that the central source is physically associated with NGC 5128, there is a possibility that the larger source is a separate object accidentally aligned with it. The extended source is not likely to lie within our own galaxy, however, since it is some 20° from the Milky Way plane ; also, its centre is very close to NGC 5128. Thus it seems probable that the extended source is physically associated with NGC 5128.

---

* Manuscript received October 12, 1959.

† Division of Radiophysics, C.S.I.R.O., University Grounds, Chippendale, N.S.W.

The extended component can be seen most clearly if the effects of the central source (which we shall call *Source a*) are removed from the observed distribution. We have done this with the 85·5 Mc/s observations shown in Figure 1. Since

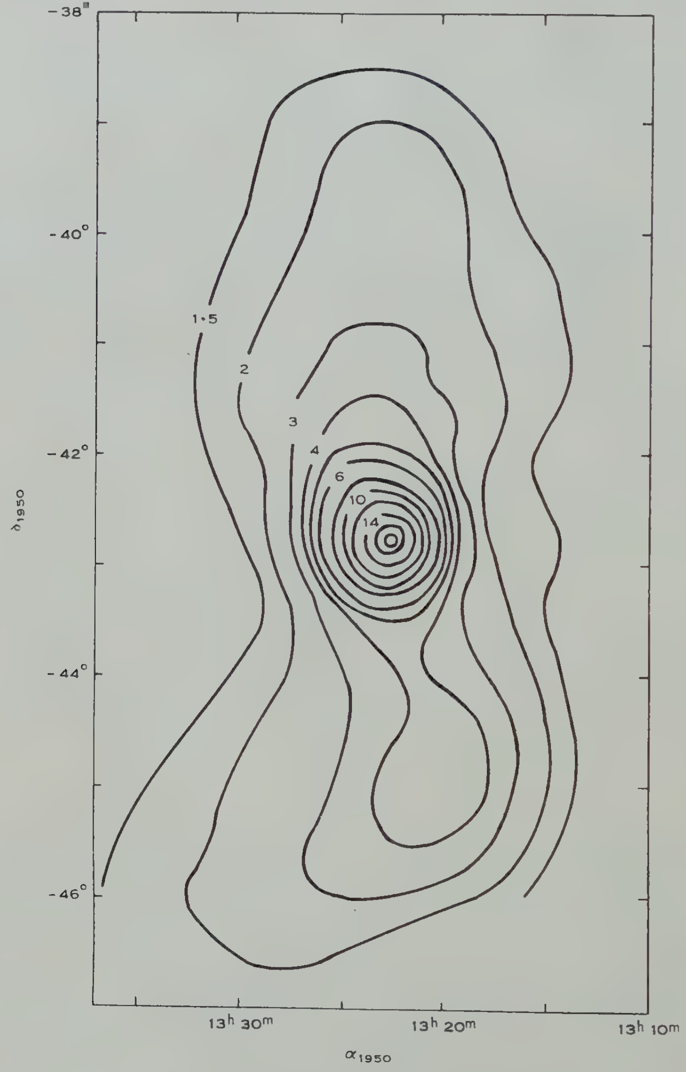

Fig. 1.—Centaurus A at 85·5 Mc/s ; aerial beamwidth 50 min of arc. Contour interval, 3000 °K. This chart is similar to one published by Sheridan (1958), but differs in minor details. It is based on Sheridan's observations but includes quantitative beam-asymmetry corrections.

Source *a* is much smaller than the 50 min of arc beamwidth, its contribution has the same shape as the aerial radiation pattern. Trial subtractions assuming various intensities for Source *a* show that its effects seem to be completely removed from the observed distribution if its flux density is equal to 25 per cent.

of the total. Upon removing Source *a* from the 85·5 Mc/s distribution, we are left with the picture shown in Figure 3. The new distribution has two broad, strong maxima: one is that previously noted, at $\alpha_{1950}=13^{\mathrm{h}}\ 21^{\mathrm{m}}$, $\delta_{1950}=-44^{\circ}\cdot7$; and the other is similar to it in size and intensity, at $\alpha_{1950}=13^{\mathrm{h}}\ 24^{\mathrm{m}}$, $\delta_{1950}=-42^{\circ}\cdot1$. We shall call these *Source b* and *Source c* respectively. Source *b* was resolved well in the original observations, but the beam-broadened radiation of Source *a*

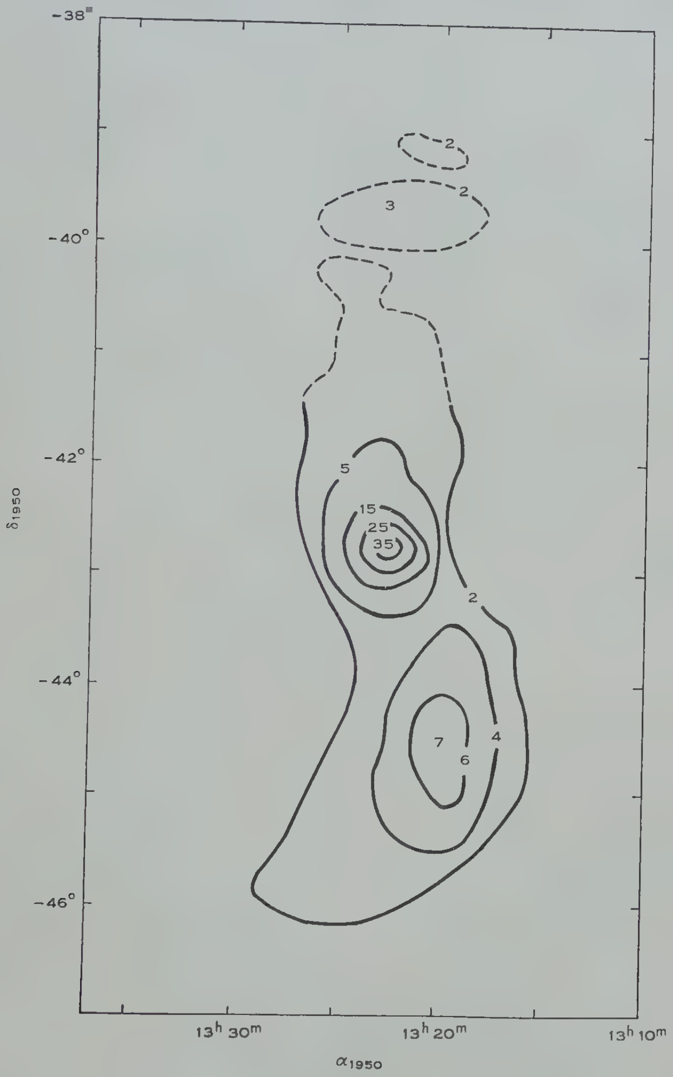

Fig. 2.—Centaurus A at 1400 Mc/s; aerial beamwidth 36 min of arc. Contours are marked in degrees of aerial temperature. These are preliminary observations made by D. S. Heeschen with the 85-ft radio telescope at the National Radio Astronomy Observatory (Green Bank, West Virginia), and they are reproduced here with his permission.

effectively masked Source *c*. One should not attach too much significance to the finer details in Figure 3, but the major features probably are shown with reasonable accuracy. The dimensions of Sources *b* and *c* are respectively about 1°·7 by 2°·6 and 1°·5 by 2°·4 between half-brightness points. The separation of their centres is 2°·7.

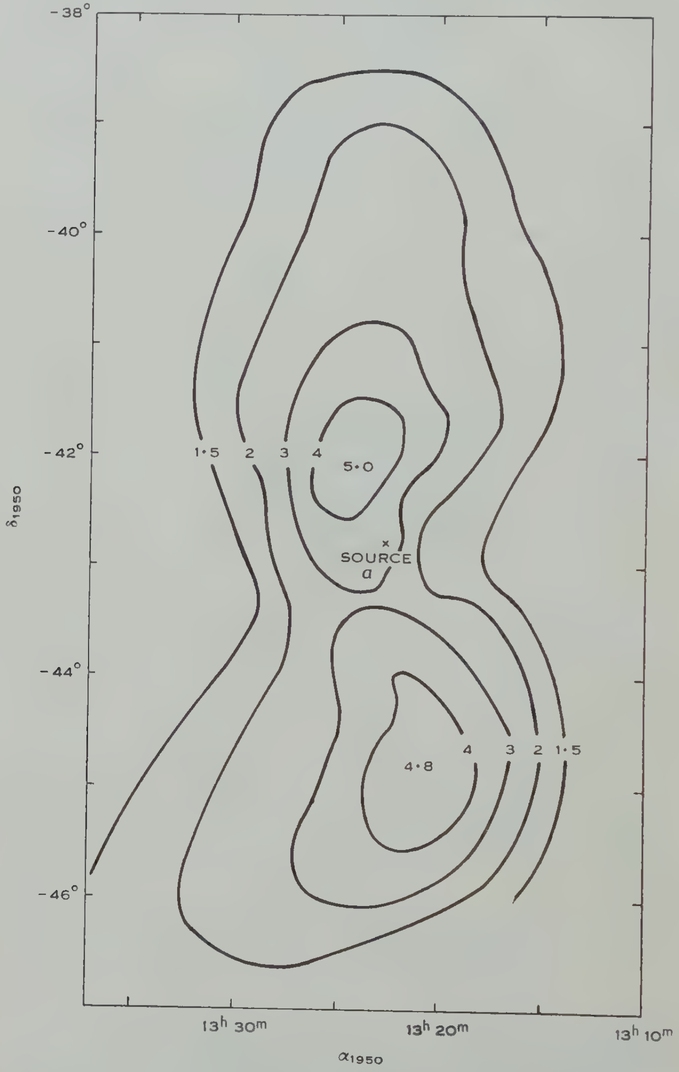

Fig. 3.—85·5 Mc/s contours of Centaurus A after subtraction of the radiation due to Source *a*. The position of Source *a* is indicated.

The fact that the central source accounts for some 25 per cent. of the total flux at both 85·5 and 1400 Mc/s (Hindman and Wade 1959) implies that Source *a* and the extended component both have similar spectral laws at metre and decimetre wavelengths. On the other hand, Source *a* contributes only 11 per cent. of the total at 19·7 Mc/s (Shain 1958). Shain (1959) suggests that the low value at 19·7 Mc/s is due to ionized hydrogen in NGC 5128 lying between Source *a* and the observer.

The dimensions of the extended component are enormous; assuming its distance is 1 megaparsec, we find that it has a linear size of roughly 50 kpc by 150 kpc. It fills a volume of at least 2×10^{14} cubic parsecs. This is about 500 times greater than the volume of the associated galaxy, NGC 5128. Hence the extended component is far too large to be a "galactic halo" in the usual sense. Another case of such a vast radio-emitting region outside the associated galaxy is Cygnus A (IAU 19N4A). It is of interest to compare these two sources.

Cygnus A is associated with a close pair of interacting galaxies (Baade and Minkowski 1954*b*). The system has a red-shift of 16,830 km/sec, which corresponds to a distance of about 150 megaparsecs if we assume that the Hubble constant is between 100 and 120 km $\mathrm{sec}^{-1}\,\mathrm{Mpc}^{-1}$. According to interferometric measurements by Jennison and Das Gupta (1956), the radio emission comes from two areas of nearly equal intensity separated by about 85 sec of arc, each having angular dimensions of about 35 by 45 sec of arc between half-brightness points. The radio positional data are not sufficiently precise to permit an accurate determination of the relative configuration of the galaxies and the radio areas, but the galaxies probably lie somewhere between the two radio centres. This is reminiscent of Centaurus A, where a peculiar galaxy is seen between two large radio-emitting regions (Sources *b* and *c*). Table 1 illustrates the good agreement between the linear separation and dimensions of the components of each source. There is no evidence of a central source in Cygnus A corresponding to Source *a* in Centaurus, but it should be remembered that most of the radiation from Centaurus A originates in the extended component; Source *a* is a relatively minor feature which presumably is due to local conditions in some part of NGC 5128 or the dark band. Thus Source *a* does not affect seriously the overall similarity in the apparent forms of the Centaurus and Cygnus sources. On the other hand, there are some marked differences between the two objects. Optically the associated galaxies appear to be dissimilar, although they are very unusual systems in each case. There is also a great disparity in the emitted radio fluxes, Cygnus A being intrinsically about 3×10^4 times more powerful than Centaurus A.

TABLE 1

COMPARISON OF CENTAURUS A AND CYGNUS A

Quantity	Centaurus A	Cygnus A
Distance	~1 Mpc	~150 Mpc
Linear separation of the radio components perpendicular to the line of sight	~50 kpc	~60 kpc
Linear dimensions of radio components to half-brightness ..	~30 kpc by 40 kpc	~25 kpc by 35 kpc

Although the similarities between Centaurus A and Cygnus A could well be fortuitous, it might be worth while to investigate the possibility that these objects represent a distinct class of very large binuclear extragalactic sources. This will require an adequate knowledge of the structure of a sufficient number of extragalactic sources. Criteria will be needed for distinguishing physical radio binaries from chance coincidences, and optical identifications would be desirable for any physical pairs found.

The author is indebted to Mr. K. V. Sheridan for making available his 85·5 Mc/s observational material; to Dr. D. S. Heeschen for permission to reproduce his unpublished 1400 Mc/s observations; and to the Commonwealth Scientific and Industrial Research Organization for a Junior Research Fellowship.

References

Baade, W., and Minkowski, R. (1954*a*).—*Astrophys. J.* **119**: 215.
Baade, W., and Minkowski, R. (1954*b*).—*Astrophys. J.* **119**: 206.
Bolton, J. G., Stanley, G. J., and Slee, O. B. (1949).—*Nature* **164**: 101.
Bolton, J. G., Westfold, K. C., Stanley, G. J., and Slee, O. B. (1954).—*Aust. J. Phys.* **7**: 96.
Hindman, J. V., and Wade, C. M. (1959).—*Aust. J. Phys.* **12**: 258.
Jennison, R. C., and Das Gupta, M. K. (1956).—*Phil. Mag.* **1**: 65.
Mills, B. Y. (1952).—*Aust. J. Sci. Res.* A **5**: 456.
Mills, B. Y. (1953).—*Aust. J. Phys.* **6**: 452.
Sérsic, J. L. (1958).—*Observatory* **78**: 24.
Shain, C. A. (1958).—*Aust. J. Phys.* **11**: 517.
Shain, C. A. (1959).—I.A.U.-U.R.S.I. Symposium on Radio Astronomy, Paris 1958. p. 328. (Stanford Univ. Press.)
Sheridan, K. V. (1958).—*Aust. J. Phys.* **11**: 400.

INDEX

PAGE

Alloys, Deviation from Matthiessen's Rule and Lattice Thermal Conductivity of .. 199

Anderson, J. S., Faulkner, E. A., and Klemperer, D. F.—
  Analysis of Composite Spectral-sensitivity Functions .. 469

Argon, Liquid, Electron Mobility in 105

Auroral Arcs at Middle Latitudes, Photometric Observations of Subvisual Red 197

Baglin, J. E. E.—*See* Thies, H. H. 21

Bagot, C. H.—*See* Huxley, L. G. H. 303

Bassett, I. M.—
  Towards a Method for the Accurate Solution of the Schrödinger Wave Equation in Many Variables—
    I. Formulation of the Method for an Eigenvalue Problem without Symmetry Conditions 430
    II. A Simple Numerical Illustration 441
    III. Application of the General Method to the Wave Equation without Special Symmetry 449

Beryllium: Energy Spectrum of Protons from the ^{7}Be$(d,p)^8$Be Reaction 99

Beryllium: Spins and Parities of Levels of ^{9}Be below 15 MeV 293

Beryllium: The Photoneutron Cross Section of ^{9}Be in the Intermediate Energy Range .. 21

Birch, J. A., Kemp, W. R. G., Klemens, P. G., and Tainsh, R. J.—
  The Lattice Thermal Conductivity of Some Gold Alloys 455

PAGE

Bogle, G. S., and Symmons, H. F.—
  Zero-field Masers 1

Bray, R. J.—*See* Loughhead, R. E. 97

Bray, R. J., and Loughhead, R. E.—
  High Resolution Observations of the Granular Structure of Sunspot Umbrae .. 320

Builder, G.—
  The Lorentz Transformations 300

Calcium, Scattering of High Energy Polarized Nucleons by 248

Carbon, Scattering of High Energy Polarized Nucleons by 248

Centaurus A near 1400 Mc/s .. 258

Centaurus A, The Extended Component of 471

Conductivity, Thermal, of Alloys 199

Conductivity, Thermal, of Some Gold Alloys 455

Conductivity, Thermal, Use of Complete Temperature-Time Curves for Determination of, with particular Reference to Rocks 203

Corona, Solar, Occultations of the Crab Nebula by the .. 134

Coulomb Wave Functions, Irregular 94

Crab Nebula, Occultations of the, by the Solar Corona .. 134

Crompton, R. W.—*See* Huxley, L. G. H. 303

Detection of Time-correlated Photons by a Coincidence Counter 77

Dirac Continuum Radial Wave Functions 30

PAGE

Doyle, H. A., Everingham, I. B., and Hogan, T. K.—
Seismic Recordings of Large Explosions in South-eastern Australia 222

Duncan, R. A.—
Photometric Observations of Subvisual Red Auroral Arcs at Middle Latitudes .. 197

Electron Mobility in Liquid Argon 105

Electrons Drifting and Diffusing in a Gas when Ionization and Attachment are Present .. 171

Electrons, Slow, a New Method for Measuring the Attachment of, in Gases 303

Eta Carinae Nebula near 1400 Mc/s 258

Eta Carinae Nebula, Physical Discussion of the 418

Everingham, I. B.—*See* Doyle, H. A. 222

Expansion, Thermal, of Solids .. 237

Explosions, Large, Seismic Recordings of 222

Faculae Bordering Small Sunspots near the Limb, Observations of 97

Faulkner, E. A.—*See* Anderson, J. S. 469

Filters, Dielectric, Note on Band Transmission in Multilayer .. 296

Fletcher, G. C.—
The Thermal Expansion of Solids 237

Gardner, F. F.—
The Effect of Sudden Ionospheric Disturbances (S.I.D.'s) on 2·28 Mc/s Pulse Reflections from the Lower Ionosphere .. 42

Gascoigne, S. C. B.—
Note on Band Transmission in Multilayer Dielectric Filters 296

PAGE

Geomagnetic Storms, Solar Radio Emission of Spectral Type IV and its Association with 404

Gerson, N. C.—
Periodicities in Solar Radio Noise Emission 299

Giovanelli, R. G.—
Radiative Transfer in Non-uniform Media 164

Gold Alloys, The Lattice Thermal Conductivity of Some 455

Goodwin, G. L.—
A Discussion of Ionospheric Demodulation near Gyro Frequency 157

Gum, C. S.—*See* Kerr, F. J. .. 270

Higgins, C. S.—*See* Shain, C. A. 357

Hindman, J. V.—*See* Kerr, F. J. 270

Hindman, J. V., and Wade, C. M.—
The Eta Carinae Nebula and Centaurus A near 1400 Mc/s. I. Observations 258

Hogan, T. K.—*See* Doyle, H. A. 222

Huxley, L. G. H.—
The Structure of a Stream of Electrons and Ions Drifting and Diffusing in a Gas when Ionization by Collision and Molecular Attachment are Present 171

Huxley, L. G. H., Crompton, R. W., and Bagot, C. H.—
A New Method for Measuring the Attachment of Slow Electrons in Gases .. 303

Hydrogen Gas, Neutral, in the Taurus-Orion Region .. 127

Ionosphere, Effect of Sudden Ionospheric Disturbances on 2·28 Mc/s Pulse Reflections from the Lower 42

Ionosphere of Jupiter 466

Ionospheric Demodulation near Gyro Frequency 157

Ions Drifting and Diffusing in a Gas when Ionization and Attachment are Present .. 171

PAGE

Jaeger, J. C.—
  The Use of Complete Temperature-Time Curves for Determination of Thermal Conductivity with particular Reference to Rocks .. 203
Jupiter, The Ionosphere of .. 466

Kemp, W. R. G.—*See* Birch, J. A. 455
Kerr, F. J., Hindman, J. V., and Gum, C. S.—
  A 21 cm Survey of the Southern Milky Way .. 270
Klemens, P. G.—
  Deviation from Matthiessen's Rule and Lattice Thermal Conductivity of Alloys .. 199
  See also Birch, J. A... .. 455
Klemperer, D. F.—*See* Anderson, J. S. 469

Learner, A., and Robson, B. A.—
  Irregular Coulomb Wave Functions 94
Lines, Spectral, The Shape of: Tables of the Voigt Profile .. 184
Lithium: A Search for Levels of ^{7}Li Between 9·0 and 9·55 MeV Excitation .. 231
Little, A. G.—*See* Twiss, R. Q... 77
Lorentz Transformations .. 300
Loughhead, R. E.—*See* Bray, R. J. 320
Loughhead, R. E., and Bray, R. J.—
  Observations of Faculae Bordering Small Sunspots near the Limb 97

McGee, R. X., and Murray, J. D.—
  Neutral Hydrogen Gas in the Taurus-Orion Region observed with a Multichannel 21 cm Line Receiver .. 127
McLean, D. J.—
  Solar Radio Emission of Spectral Type IV and its Association with Geomagnetic Storms 404

PAGE

Maser, Amplifier, Optimum Line Width in a Reflection Cavity 218
Masers, Zero-field 1
Matthiessen's Rule, Deviation from, of Alloys 199
Meteor Height Distribution, Theory of the Radio-echo, in a Non-isothermal Atmosphere 54
Meteor Stream, Geminid, Radio Echo Observations of the .. 315
Meteor Trails, Elevation, Height, and Electron Density of Echoing Points of 65
Meteor Trails, Temporal Variation of the Heights of Reflection Points of 116
Milky Way, Southern, A 21 cm Survey of the 270
Murray, J. D.—*See* McGee, R. X. 127

Neylan, A. A.—
  An Association between Solar Radio Bursts at Metre and Centimetre Wavelengths .. 399
  See also Wild, J. P. .. 369
Nickel: The ^{58}Ni(n,p)^{58}Co, ^{58}Ni($n,2n$)^{57}Ni, and ^{58}Ni(n,np)^{57}Co Cross Sections at 14·1 MeV 103
Nucleons, High Energy Polarized, Scattering by Complex Nuclei 248

Occultations of the Crab Nebula by the Solar Corona .. 134
Orion: Neutral Hydrogen Gas in the Taurus-Orion Region .. 127

Particle, Charged, Drift of, in a Magnetic Field of Constant Gradient 309
Perlman, H. S., and Robson, B. A.—
  Dirac Continuum Radial Wave Functions 30
Photoneutron Cross Section of ^{9}Be in the Intermediate Energy Range 21
Photons, Detection of Time-correlated, by a Coincidence Counter 77

PAGE

Posener, D. W.—
  The Shape of Spectral Lines: Tables of the Voigt Profile $(a/\pi)\int_{-\infty}^{\infty} e^{-y^2}dy/\{a^2+(v-y)^2\}$ 184

Protons, Energy Spectrum of, from the ^{7}Be$(d,p)^8$Be Reaction 99

Purser, K. H.—
  A Search for Levels of ^{7}Li between 9·0 and 9·55 MeV Excitation 231

Purser, K. H., and Titterton, E. W.—
  The ^{58}Ni$(n,p)^{58}$Co, ^{58}Ni$(n,2n)^{57}$Ni, and ^{58}Ni$(n,np)^{57}$Co Cross Sections at 14·1 MeV 103

Radiation, Cosmic Radio: A 21 cm Survey of the Southern Milky Way 270

Radiation, Cosmic Radio: Neutral Hydrogen Gas in the Taurus-Orion Region observed with a Multichannel 21 cm Line Receiver 127

Radiation, Cosmic Radio: Physical Discussion of the Eta Carinae Nebula .. 418

Radiation, Cosmic Radio: The Eta Carinae Nebula and Centaurus A near 1400 Mc/s 258

Radiation Cosmic Radio: The Extended Component of Centaurus A 471

Radio Bursts, Location of the Sources of the 19 Mc/s Solar .. 357

Radio Bursts, Solar, Association between, at Metre and Centimetre Wavelengths 399

Radio Bursts, Solar, of Spectral Type II 327

Radio Bursts, Type III, Investigation of the Speed of the Solar Disturbances responsible for 369

Radio Emission, Solar, of Spectral Type IV and its Association with Geomagnetic Storms 404

PAGE

Radio Noise Emission, Periodicities in Solar 299

Relativity: The Lorentz Transformations 300

Rishbeth, H.—
  The Ionosphere of Jupiter .. 466

Roberts, J. A.—
  Solar Radio Bursts of Spectral Type II 327

Robson, B. A.—
  Scattering of High Energy Polarized Nucleons by Complex Nuclei 248
  See also Learner, A. .. 94
  See also Perlman, H. S. .. 30

Seymour, P. W.—
  Drift of a Charged Particle in a Magnetic Field of Constant Gradient .. 309

Shain, C. A., and Higgins, C. S.—
  Location of the Sources of 19 Mc/s Solar Bursts .. 357

Sheridan, K. V.—*See* Wild, J. P. 369

Slee, O. B.—
  Occultations of the Crab Nebula by the Solar Corona in June 1957 and 1958 .. 134

Smith, W. E.—
  The Microwave Spectra of Isotopic Molecules of Sulphur Dioxide 109

Solids, Thermal Expansion of .. 237

Spear, R. H.—
  The Energy Spectrum of Protons from the ^{7}Be$(d,p)^8$Be Reaction 99

Spectra, Microwave, of Isotopic Molecules of Sulphur Dioxide 109

Spectral-sensitivity Functions, Analysis of Composite .. 469

Spicer, B. M.—*See* Thies, H. H. 21, 293

Stacey, F. D.—
  Electron Mobility in Liquid Argon 105

Sudden Ionospheric Disturbances, Effect of, on 2·28 Mc/s Pulse Reflections from the Lower Ionosphere 42

PAGE

Sulphur Dioxide, Microwave Spectra of Isotopic Molecules of 109

Sun : Association between Solar Radio Bursts at Metre and Centimetre Wavelengths .. 399

Sun : Investigation of the Speed of the Solar Disturbances responsible for Type III Radio Bursts 369

Sun : Location of the Sources of the 19 Mc/s Solar Bursts .. 357

Sun : Periodicities in Solar Radio Noise Emission .. 299

Sun : Solar Radio Bursts of Spectral Type II 327

Sun : Solar Radio Emission of Spectral Type IV and its Association with Geomagnetic Storms 404

Sunspot Umbrae, High Resolution Observations of the Granular Structure of .. 320

Sunspots, Small, Observations of Faculae bordering, near the Limb 97

Symmons, H. F.—*See* Bogle, G. S. 1

Tainsh, R. J.—*See* Birch, J. A. 455

Taurus-Orion Region, Neutral Hydrogen Gas observed in the 127

Thies, H. H., and Spicer, B. M.—
  Spins and Parities of Levels of ^{9}Be below 15 MeV .. 293

Thies, H. H., Spicer, B. M., and Baglin, J. E. E.—
  The Photoneutron Cross Section of ^{9}Be in the Intermediate Energy Range .. 21

Titterton, E. W.—*See* Purser, K. H. 103

Transfer, Radiative, in a Non-uniform Medium 164

PAGE

Troup, G. J.—
  The Optimum Line Width for the Transition used in a Reflection Cavity Maser Amplifier 218

Twiss, R. Q., and Little, A. G.—
  The Detection of Time-correlated Photons by a Coincidence Counter .. 77

Voigt Profile, Tables of the .. 184

Wade, C. M.—
  The Eta Carinae Nebula and Centaurus A near 1400 Mc/s. II. Physical Discussion of the Eta Carinae Nebula .. 418
  The Extended Component of Centaurus A 471
  See also Hindman, J. V. .. 258

Wave Equations, Schrödinger, Towards a Method for the Accurate Solution of the, in many Variables 430, 441, 449

Wave Functions, Dirac Continuum Radial 30

Wave Functions, Irregular Coulomb 94

Weiss, A. A.—
  Elevation, Height, and Electron Density of Echoing Points of Meteor Trails .. 65
  Radio-echo Observations of the Geminid Meteor Stream 315
  Theory of the Radio-echo Meteor Height Distribution in a Non-isothermal Atmosphere 54
  The Temporal Variation of the Heights of Reflection Points of Meteor Trails .. 116

Wild, J. P., Sheridan, K. V., and Neylan, A. A.—
  An Investigation of the Speed of the Solar Disturbances responsible for Type III Radio Bursts 369

DATE DUE

OVERNIGHT FEB 28 '76

RES. JUL 8 '78

OCT 25 '79 PER

NOV 8 1982

HIGHSMITH 45-220

4

3 8198 303 614 539
THE UNIVERSITY OF ILLINOIS AT CHICAGO